

# Modeling of Water Quality, Quantity, and Sustainability

Guest Editors: Yongping Li, Guohe Huang, Yuefei Huang, and Xiaosheng Qin





---

# **Modeling of Water Quality, Quantity, and Sustainability**

Journal of Applied Mathematics

---

## **Modeling of Water Quality, Quantity, and Sustainability**

Guest Editors: Yongping Li, Guohe Huang, Yuefei Huang,  
and Xiaosheng Qin



---

Copyright © 2014 Hindawi Publishing Corporation. All rights reserved.

This is a special issue published in "Journal of Applied Mathematics." All articles are open access articles distributed under the Creative Commons Attribution License, which permits unrestricted use, distribution, and reproduction in any medium, provided the original work is properly cited.

## Editorial Board

- Saeid Abbasbandy, Iran  
Mina B. Abd-El-Malek, Egypt  
Mohamed A. Abdou, Egypt  
Subhas Abel, India  
Mostafa Adimy, France  
Carlos J. S. Alves, Portugal  
Mohamad Alwash, USA  
Igor Andrianov, Germany  
Sabri Arik, Turkey  
Francis T.K. Au, Hong Kong  
Olivier Bahn, Canada  
Roberto Barrio, Spain  
Alfredo Bellen, Italy  
Jafar Biazar, Iran  
Hester Bijl, The Netherlands  
Anjan Biswas, Saudi Arabia  
S. P.A. Bordas, USA  
James Robert Buchanan, USA  
Alberto Cabada, Spain  
Xiao Chuan Cai, USA  
Jinde Cao, China  
Alexandre Carvalho, Brazil  
Song Cen, China  
Q. S. Chang, China  
Tai-Ping Chang, Taiwan  
Shih-sen Chang, China  
Rushan Chen, China  
Xinfu Chen, USA  
Ke Chen, UK  
Eric Cheng, Hong Kong  
Francisco Chiclana, UK  
J.-T. Chien, Taiwan  
C. S. Chien, Taiwan  
Han H. Choi, Republic of Korea  
Tin-Tai Chow, China  
M. S. H. Chowdhury, Malaysia  
Carlos Conca, Chile  
Vitor Costa, Portugal  
Livija Cveticanin, Serbia  
Eric de Sturler, USA  
Orazio Descalzi, Chile  
Kai Diethelm, Germany  
Vit Dolejsi, Czech Republic  
Bo-Qing Dong, China  
Magdy A. Ezzat, Egypt
- Meng Fan, China  
Ya Ping Fang, China  
A. M. Ferreira, Portugal  
Michel Fliess, France  
M. A. Fontelos, Spain  
Huijun Gao, China  
B. J. Geurts, The Netherlands  
Jamshid Ghaboussi, USA  
Pablo González-Vera, Spain  
Laurent Gosse, Italy  
K. S. Govinder, South Africa  
Jose L. Gracia, Spain  
Yuantong Gu, Australia  
Zhihong GUAN, China  
Nicola Guglielmi, Italy  
F. G. Guimarães, Brazil  
Vijay Gupta, India  
Bo Han, China  
Maoan Han, China  
Pierre Hansen, Canada  
Ferenc Hartung, Hungary  
Xiaoqiao He, Hong Kong  
Luis Javier Herrera, Spain  
J. Hoenderkamp, The Netherlands  
Ying Hu, France  
Ning Hu, Japan  
Zhilong L. Huang, China  
Kazufumi Ito, USA  
Takeshi Iwamoto, Japan  
George Jaiani, Georgia  
Zhongxiao Jia, China  
Tarun Kant, India  
Ido Kanter, Israel  
Abdul Hamid Kara, South Africa  
Hamid Reza Karimi, Norway  
Jae-Wook Kim, UK  
Jong H. Kim, Republic of Korea  
Kazutake Komori, Japan  
Fanrong Kong, USA  
Vadim . Krysko, Russia  
Jin L. Kuang, Singapore  
Miroslaw Lachowicz, Poland  
Hak-Keung Lam, UK  
Tak-Wah Lam, Hong Kong  
PGL Leach, Cyprus
- Yongkun Li, China  
Wan-Tong Li, China  
J. Liang, China  
Ching-Jong Liao, Taiwan  
Chong Lin, China  
Mingzhu Liu, China  
Chein-Shan Liu, Taiwan  
Kang Liu, USA  
Yansheng Liu, China  
Fawang Liu, Australia  
Shutian Liu, China  
Zhijun Liu, China  
J. López-Gómez, Spain  
Shiping Lu, China  
Gert Lube, Germany  
Nazim I. Mahmudov, Turkey  
O. D. Makinde, South Africa  
F. J. Marcellán, Spain  
G. Martín-Herrán, Spain  
Nicola Mastronardi, Italy  
M. McAleer, The Netherlands  
Stephane Metens, France  
Michael Meylan, Australia  
Alain Miranville, France  
Ram N. Mohapatra, USA  
Jaime E. M. Rivera, Brazil  
Javier Murillo, Spain  
Roberto Natalini, Italy  
Srinivasan Natesan, India  
Jiri Nedoma, Czech Republic  
Jianlei Niu, Hong Kong  
Roger Ohayon, France  
Javier Oliver, Spain  
Donal O'Regan, Ireland  
M. Ostoja-Starzewski, USA  
Turgut Öziş, Turkey  
Claudio Padra, Argentina  
R. M. Palhares, Brazil  
Francesco Pellicano, Italy  
Juan M. Peña, Spain  
Ricardo Perera, Spain  
Malgorzata Peszynska, USA  
James F. Peters, Canada  
M. A. Petersen, South Africa  
Miodrag Petkovic, Serbia

Vu Ngoc Phat, Vietnam  
Andrew Pickering, Spain  
Hector Pomares, Spain  
Maurizio Porfiri, USA  
Mario Primicerio, Italy  
M. Rafei, The Netherlands  
Roberto Renò, Italy  
Jacek Rokicki, Poland  
Dirk Roose, Belgium  
Carla Roque, Portugal  
Debasish Roy, India  
Samir H. Saker, Egypt  
Marcelo A. Savi, Brazil  
Wolfgang Schmidt, Germany  
Eckart Schnack, Germany  
Mehmet Sezer, Turkey  
N. Shahzad, Saudi Arabia  
Fatemeh Shakeri, Iran  
Jian Hua Shen, China  
Hui-Shen Shen, China  
F. Simões, Portugal  
Theodore E. Simos, Greece

A.-M. A. Soliman, Egypt  
Xinyu Song, China  
Qiankun Song, China  
Yuri N. Sotskov, Belarus  
P. C. Spreij, The Netherlands  
Niclas Strömberg, Sweden  
Ray KL Su, Hong Kong  
Jitao Sun, China  
Wenyu Sun, China  
XianHua Tang, China  
Alexander Timokha, Norway  
Mariano Torrisi, Italy  
Jung-Fa Tsai, Taiwan  
Ch Tsitouras, Greece  
K. Vajravelu, USA  
Alvaro Valencia, Chile  
Erik Van Vleck, USA  
Ezio Venturino, Italy  
Jesus Vigo-Aguiar, Spain  
M. N. Vrahatis, Greece  
Baolin Wang, China  
Mingxin Wang, China

Qing-Wen Wang, China  
Guangchen Wang, China  
Junjie Wei, China  
Li Weili, China  
Martin Weiser, Germany  
Frank Werner, Germany  
Shanhe Wu, China  
Dongmei Xiao, China  
Gongnan Xie, China  
Yuesheng Xu, USA  
Suh-Yuh Yang, Taiwan  
Bo Yu, China  
Jinyun Yuan, Brazil  
Alejandro Zarzo, Spain  
Guisheng Zhai, Japan  
Jianming Zhan, China  
Zhihua Zhang, China  
Jingxin Zhang, Australia  
Shan Zhao, USA  
Chongbin Zhao, Australia  
Renat Zhdanov, USA  
Hongping Zhu, China

# Contents

**Modeling of Water Quality, Quantity, and Sustainability**, Yongping Li, Guohe Huang, Yuefei Huang, and Xiaosheng Qin

Volume 2014, Article ID 135905, 3 pages

**Discussion on Muskingum versus Integrator-Delay Models for Control Objectives**, Yolanda Bolea, Vicenç Puig, and Antoni Grau

Volume 2014, Article ID 197907, 11 pages

**Conceptual Model for Simulating the Adjustments of Bankfull Characteristics in the Lower Yellow River, China**, Yuanjian Wang, Xudong Fu, and Guangqian Wang

Volume 2014, Article ID 852174, 12 pages

**River Flow Estimation from Upstream Flow Records Using Support Vector Machines**, Halil Karahan, Serdar Iplikci, Mutlu Yasar, and Gurhan Gurarslan

Volume 2014, Article ID 714213, 7 pages

**Mathematical Modeling and Simulation of SWRO Process Based on Simultaneous Method**,

Aipeng Jiang, Qiang Ding, Jian Wang, Shu Jiangzhou, Wen Cheng, and Changxin Xing

Volume 2014, Article ID 908569, 11 pages

**Water Demand Forecast in the Baiyangdian Basin with the Extensive and Low-Carbon Economic Modes**, T. L. Qin, D. H. Yan, G. Wang, and J. Yin

Volume 2014, Article ID 673485, 10 pages

**A Conjunction Method of Wavelet Transform-Particle Swarm Optimization-Support Vector Machine for Streamflow Forecasting**, Fanping Zhang, Huichao Dai, and Deshan Tang

Volume 2014, Article ID 910196, 10 pages

**Identification of Contamination Control Strategy for Fluid Power System Using an Inexact Chance-Constrained Integer Program**, Y. Q. Huang, S. L. Nie, and H. Ji

Volume 2014, Article ID 146413, 19 pages

**Accurate Simulation of Contaminant Transport Using High-Order Compact Finite Difference Schemes**, Gurhan Gurarslan

Volume 2014, Article ID 396738, 8 pages

**Numerical Simulation of Flow and Suspended Sediment Transport in the Distributary Channel Networks**, Wei Zhang, Qiong Jia, and Xiaowen Chen

Volume 2014, Article ID 948731, 9 pages

**Calculation of the Instream Ecological Flow of the Wei River Based on Hydrological Variation**, Shengzhi Huang, Jianxia Chang, Qiang Huang, Yimin Wang, and Yutong Chen

Volume 2014, Article ID 127067, 9 pages

**Monthly Optimal Reservoirs Operation for Multicrop Deficit Irrigation under Fuzzy Stochastic Uncertainties**, Liudong Zhang, Ping Guo, Shiqi Fang, and Mo Li  
Volume 2014, Article ID 105391, 11 pages

**Spatial and Temporal Variation of Annual Precipitation in a River of the Loess Plateau in China**, Cui Shen and Huang Qiang  
Volume 2014, Article ID 827120, 11 pages

**A Physically Based Runoff Model Analysis of the Querétaro River Basin**, Carlos Javier Villa Alvarado, Eladio Delgadillo-Ruiz, Carlos Alberto Mastachi-Loza, Enrique González-Sosa, and Ramos Salinas Norma Maricela  
Volume 2014, Article ID 586872, 12 pages

**Study on Spacing Threshold of Nonsubmerged Spur Dikes with Alternate Layout**, Xiaomeng Cao, Zhenghua Gu, and Hongwu Tang  
Volume 2013, Article ID 945984, 8 pages

**Mathematical Modeling for Water Quality Management under Interval and Fuzzy Uncertainties**, J. Liu, Y. P. Li, and G. H. Huang  
Volume 2013, Article ID 731568, 14 pages

**Testing a Conceptual Lumped Model in Karst Area, Southwest China**, Peng Shi, Mi Zhou, Simin Qu, Xi Chen, Xueyuan Qiao, Zhicai Zhang, and Xinxin Ma  
Volume 2013, Article ID 827980, 10 pages

**Detecting Runoff Variation of the Mainstream in Weihe River**, Qiang Huang and Jingjing Fan  
Volume 2013, Article ID 356474, 8 pages

**Uncertainty Analysis of Multiple Hydrologic Models Using the Bayesian Model Averaging Method**, Leihua Dong, Lihua Xiong, and Kun-xia Yu  
Volume 2013, Article ID 346045, 11 pages

## Editorial

# Modeling of Water Quality, Quantity, and Sustainability

Yongping Li,<sup>1</sup> Guohe Huang,<sup>2</sup> Yuefei Huang,<sup>3</sup> and Xiaosheng Qin<sup>4</sup>

<sup>1</sup> MOE Key Laboratory of Regional Energy Systems Optimization, S-C Resources and Environmental Research Academy, North China Electric Power University, Beijing 102206, China

<sup>2</sup> Environmental Systems Engineering Program, Faculty of Engineering and Applied Science, University of Regina, Regina, SK, Canada S4S 0A2

<sup>3</sup> State Key Laboratory of Hydro-Science and Engineering, Tsinghua University, Beijing 100084, China

<sup>4</sup> School of Civil & Environmental Engineering, Nanyang Technological University, Blk NI-01c-82, 50 Nanyang Avenue, Singapore 639798

Correspondence should be addressed to Yongping Li; [yongping.li@iseis.org](mailto:yongping.li@iseis.org)

Received 5 August 2014; Accepted 5 August 2014; Published 26 August 2014

Copyright © 2014 Yongping Li et al. This is an open access article distributed under the Creative Commons Attribution License, which permits unrestricted use, distribution, and reproduction in any medium, provided the original work is properly cited.

For decades, water shortage, flooding, and water deterioration problems have led to a variety of adverse impacts on socioeconomic development and human life. Challenges of water quality and quantity management adhering to the principle of sustainable development have been of significant concerns to many researchers and decision makers [1–6]. These issues are highly complicated, involving a large number of social, economic, environmental, technical, and political factors, coupled with complex spatial variability and cascading effect [7, 8]. Climate change and human interference could affect the related management systems at a regional scale and lead to more significant spatial and temporal variations of water quantity and availability as well as the associated environmental and ecological conditions. Such complexities force researchers to develop more robust mathematical methods and tools to analyze the relevant information, simulate the related processes, implement mitigation strategies, assess the potential impacts/risks, and generate sound decision alternatives. Therefore, it is desired that mathematical techniques be developed to aid decision makers in formulating and adopting cost-effective and environment-benign water management plans and policies.

The paper “River flow estimation from upstream flow records using support vector machines” by H. Karahan et al. proposed a novel architecture for flood routing model and validated the model efficiency on several problems by employing support vector machines. The results showed that the proposed architecture advances the model performance

under noisy and missing data conditions and the support vector machines can be powerful alternative in modeling flood routing.

The paper “Mathematical modeling and simulation of SWRO process based on simultaneous method” by A. Jiang et al. developed a spiral-wound model for simulating seawater reverse osmosis (SWRO) process. The model was described by differential and algebraic equations with some inequality and equality constraints of equipment and water quality. A case study of a SWRO plant was used to validate the formulated model and solution method. The study work was helpful to gain an in-depth insight into the mechanism of SWRO process and had a significant potential for helping in energy saving through the optimized operation.

The paper “Water demand forecast in the Baiyangdian Basin with the extensive and low-carbon economic modes” by T. L. Qin et al. analyzed the effects of extensive and low-carbon economic modes on water demand of the Baiyangdian Basin, China. Results can support generation of environmental conservancy target and water resources allocation scheme under many conflicting factors being balanced due to complexities of the real-world problems.

The paper “A conjunction method of wavelet transform-particle swarm optimization-support vector machine for streamflow forecasting” by F. Zhang et al. developed a wavelet transform particle swarm optimization support vector machine (WT-PSO-SVM) model to forecast monthly streamflow of Tangnaihai hydrology station in the Yellow River.

The model integrated the advantages of the best versatility, robustness and effectiveness of SVM, the best global searching ability, and the simple implementing procedure of PSO for parameter selection. The results demonstrated that the advanced model could forecast monthly streamflow in situations without formulating models for the internal structure of the watershed compared with the conventional SVM model.

The paper “*Identification of contamination control strategy for fluid power system using an inexact chance-constrained integer program*” by Y. Q. Huang et al. developed an inexact chance-constrained integer programming method for planning contamination control of fluid power system. The model is good at examining the reliability of satisfying (or risk of violating) system constraints under uncertainties expressed as probability distributions and discrete intervals. The results can be used for generating decision alternatives and thus help designers identify desired strategies under various environmental, economic, and system-reliability constraints.

The paper “*Accurate simulation of contaminant transport using high-order compact finite difference schemes*” by G. Gurarslan carried out numerical simulation of advective-dispersive contaminant transport by using high-order compact finite difference schemes combined with second-order MacCormack and fourth-order Runge-Kutta schemes. Numerical experiments were conducted for the aim of demonstrating efficiency and high-order accuracy of the current methods. It was exhibited that the methods are capable of achieving high accuracy and efficiency with minimal computational effort, by comparisons of the computed results with exact solutions.

The paper “*Numerical simulation of flow and suspended sediment transport in the distributary channel networks*” by W. Zhang et al. presented a 1D flow and suspended sediment transport model to simulate the hydrodynamics and suspended sediment transport in the distributary channel networks and applied it to the Pearl River networks. The model was extensively calibrated and validated against field measurements to provide an accurate representation of water level and discharge, as well as suspended sediment transport in the networks, demonstrating that the model could simulate the hydrodynamics and suspended sediment concentration in the distributary channel networks.

The paper “*Calculation of the instream ecological flow of the Wei River based on hydrological variation*” by S. Huang et al. analyzed the variation of instream ecological flow of the Wei River Basin, through employing the heuristic segmentation algorithm, the law of tolerance and ecological adaptation theory, and a modified Tennant method. This study suggested that the heuristic segmentation algorithm is suitable to detect the mutation points of flow series and minimum instream ecological flow can be identified by the modified Tennant method. The results are helpful for the manager to reasonably allocate water resources and support the river’s ecosystem sustainability.

The paper “*Monthly optimal reservoirs operation for multicrop deficit irrigation under fuzzy stochastic uncertainties*” by L. Zhang et al. proposed an uncertain monthly reservoirs operation and multicrop deficit irrigation model

under conjunctive use of underground and surface water in Shiyang River Basin, China. Uncertainties in reservoir management shown as fuzzy probability were treated through chance-constraint parameter for decision makers. The results of reservoir operation policy, irrigation scheme, and water resources allocation could be used to provide decision support for local managers.

The paper “*Spatial and temporal variation of annual precipitation in a river of the Loess Plateau in China*” by C. Shen and H. Qiang analyzed the spatial and temporal patterns of annual precipitation in the Weihe Basin, where Mann-Kendall method was used to discriminate the variation points of precipitation series. The results indicated that there was an overall reduction in annual precipitation across the basin and there were two spatial patterns during the study period. The findings have significant implications for the variations research of runoff in the basin, as variation points in the annual precipitation series at each meteorological station in the basin were detected.

The paper “*A physically based runoff model analysis of the Querétaro River Basin*” by C. J. V. Alvarado et al. used a physically based model to analyze water balance by evaluating the volume rainfall-runoff using SHETRAN and hydrometric data measurements in 2003. The results were compared with five ETp different methodologies in the Querétaro River Basin in central Mexico. This study work can be a strong base for sustainable water management in a basin, the prognosis and effect of land-use changes, and availability of water and also can be used to determine application of known basin parameters, basically depending on land-use, land-use changes, and climatological database to determine the water balance in a basin.

The paper “*Study on spacing threshold of nonsubmerged spur dikes with alternate layout*” by X. Cao et al. built a numerical model combining the standard  $k-\varepsilon$  model, finite volume method, and rigid lid assumption to investigate the spacing threshold of nonsubmerged double spur dikes with alternate layout and the same length in straight rectangular channel. The results of four sets of additional conditions illustrated that the generalization of empirical formula is satisfactory and the precision of interpolation is higher than that of extrapolation.

The paper “*Mathematical modeling for water quality management under interval and fuzzy uncertainties*” by J. Liu et al. proposed an interval fuzzy credibility-constrained programming method for supporting river water quality management. The model is good at dealing with different types of uncertainties (i.e., interval numbers and possibility distributions) in water quality management and can also be used to analyze reliability of satisfying system constraints. A real-world case (i.e., Xiangxi River in the Three Gorges Reservoir Region) was used to demonstrate the methodology’s applicability. The solutions are useful for managers in making decisions of water quality management, considering tradeoffs between system benefit and environmental requirement.

The paper “*Testing a conceptual lumped model in Karst area, Southwest China*” by P. Shi et al. used Xin’anjiang model for modeling hydrological response of Sancha River Valley (a typical karst area located in the southwest of China).

The performance of the model was evaluated based on the model's ability to reproduce the streamflow and baseflow. Suitable parameters such as percentage of bias (PBIAS), Nash-Sutcliffe efficiency (NSE), coefficient of determination ( $R^2$ ), and standard deviation (RSR) which could reflect the hydrological and geomorphic condition were calculated between the simulated and measured flow for both calibration and validation period. The results suggested that the model structure and parameters are of reasonable validity and are feasible to describe the hydrologic processes in this region.

The paper “*Detecting runoff variation of the mainstream in Weihe River*” by Q. Huang and J. Fan analyzed the variation change in runoff through using the Mann-Kendall method. The results indicated that runoff variation changes point is 1990 for most of the catchments. The attribution analysis showed that the primary drivers of the shift in runoff variation changes are human activities rather than climate change, as water consumption increased sharply in the 1990s.

The paper “*Uncertainty analysis of multiple hydrologic models using the Bayesian model averaging method*” by L. Dong et al. employed the Bayesian model averaging (BMA) method to construct a three-member predictions ensemble and a nine-member predictions ensemble for ensemble hydrologic prediction as well as for uncertainty analysis. Compared with the previous studies of the BMA, this study focused on the comparison of the prediction uncertainty interval generated by BMA with that of each individual model under two different BMA combination schemes. It was found that BMA is useful for dealing with two issues: (1) assessing the relative performances of multiple competing models for the same problem and (2) handling uncertain control variables.

In summary, the effective mathematical methods for modeling water quantity, quality, and sustainability are becoming one of the most important goals pursued by governments, industries, communities, and researchers. These 16 papers submitted to this special issue mainly focus on exposition of innovative methodologies for tackling problems in fields of hydrologic prediction, water resources allocation, pollution mitigation, flood/drought control, and climate change impact assessment and adaptation planning. These research works will enhance the capability of decision makers in exploring comprehensive and ambitious plans for managing water systems, with an aim of achieving better sustainability.

## Acknowledgment

We wish to extend our thanks to those who contributed to this issue.

Y. P. Li  
G. H. Huang  
Y. F. Huang  
X. S. Qin

## References

- [1] Y. P. Li, G. H. Huang, and S. L. Nie, “Planning water resources management systems using a fuzzy-boundary interval-stochastic programming method,” *Advances in Water Resources*, vol. 33, no. 9, pp. 1105–1117, 2010.
- [2] Y. P. Li, G. H. Huang, and S. L. Nie, “Optimization of regional economic and environmental systems under fuzzy and random uncertainties,” *Journal of Environmental Management*, vol. 92, no. 8, pp. 2010–2020, 2011.
- [3] X. S. Qin, G. H. Huang, and Y. P. Li, “Risk management of BTEX contamination in ground water—an integrated fuzzy approach,” *Ground Water*, vol. 46, no. 5, pp. 755–767, 2008.
- [4] M. C. Kirnbauer and B. W. Baetz, “Allocating urban agricultural reuse strategies to inventoried vacant and underutilized land,” *Journal of Environmental Informatics*, vol. 20, no. 1, pp. 1–11, 2012.
- [5] T. Y. Xu and X. S. Qin, “Solving water quality management problem through combined genetic algorithm and fuzzy simulation,” *Journal of Environmental Informatics*, vol. 22, no. 1, pp. 39–48, 2013.
- [6] A. S. Mahiny and K. C. Clarke, “Simulating hydrologic impacts of urban growth using SLEUTH, multi criteria evaluation and runoff modeling,” *Journal of Environmental Informatics*, vol. 22, no. 1, pp. 27–38, 2013.
- [7] G. H. Huang and J. Xia, “Barriers to sustainable water-quality management,” *Journal of Environmental Management*, vol. 61, no. 1, pp. 1–23, 2001.
- [8] Y. P. Li, G. H. Huang, Y. F. Huang, and H. D. Zhou, “A multistage fuzzy-stochastic programming model for supporting sustainable water-resources allocation and management,” *Environmental Modelling and Software*, vol. 24, no. 7, pp. 786–797, 2009.

## Research Article

# Discussion on Muskingum versus Integrator-Delay Models for Control Objectives

**Yolanda Bolea, Vicenç Puig, and Antoni Grau**

*Automatic Control Department, Technical University of Catalonia (UPC), Pau Gargallo 5, 08028 Barcelona, Spain*

Correspondence should be addressed to Yolanda Bolea; [yolanda.bolea@upc.edu](mailto:yolanda.bolea@upc.edu)

Received 25 January 2014; Revised 19 June 2014; Accepted 19 June 2014; Published 14 August 2014

Academic Editor: Guohe Huang

Copyright © 2014 Yolanda Bolea et al. This is an open access article distributed under the Creative Commons Attribution License, which permits unrestricted use, distribution, and reproduction in any medium, provided the original work is properly cited.

A comparative study about two models, Muskingum and integrator-delay (ID) models, for canal control is presented. The former is a simplified hydrological model which is very simple and extensively used in hydraulic engineering for simulation and prediction. The latter is also a model with physical meaning and is widely used for irrigation canals control. Due to a lack of general awareness of Muskingum prediction model in regulation from the control community, authors present this comparative study with the ID control model. Both models have been studied and analyzed for control purposes. This study has been carried out and validated in a real irrigation canal, at Aghili irrigation district in Iran, using two traditional control approaches, PID with feedback and predictive control. The results demonstrate the advantages and drawbacks of both models, showing the benefits and limitations of using the widespread Muskingum model among the hydraulics scientific community for control design.

## 1. Introduction

Management of open-flow canal systems requires accurate control models of flow transfer. Open-flow canals are large parameter-distributed systems that can be described with Saint-Venant equations [1, 2]. These nonlinear partial differential equations (PDE) represent water dynamics in a precise and complete manner and, for an arbitrary geometry, there is no analytical solution. Usually numerical methods [3, 4] have been used to obtain a solution of the Saint-Venant equations. The more typical numerical methods are the characteristic method [5], the finite difference method [6], and Preissman implicit scheme [7–9]. The implicit numerical schemes are simpler than the other approaches. But the stability of their solution cannot be guaranteed and depends on the discretization time. Taking into account this fact, usually Muskingum model has been used by hydraulic engineers as a prediction model in rivers and in irrigation canals [10, 11] but so far not as a control model. Nevertheless, Saint-Venant model is not useful for automatic control purposes due to its complexity (high number of states and high computational load, etc.). Unfortunately, in control design or in the computation of control actions, the complexity of the characteristic model is

directly proportional to the complexity of the control techniques and their implementation. Modeling these systems for control design is therefore not so easy to be devised, although it is a crucial step. A classical way to control irrigation canals is to design controllers based on linear models.

Therefore, in the literature several linear control models have been already proposed for open-flow canal systems. Corrigan et al. [12, 13] proposed a model for open canal networks related to the elevation of the gate. Papageorgiou and Messmer [14, 15] and Ermolin [16] proposed an approximation for uniform flow canals derived from linearized Saint-Venant equations. Malaterre [7] used a state-space model for canal systems derived from discretized Saint-Venant equations. Baume et al. [17] obtained an infinite dimensional state-space model from linearized Saint-Venant equations. When the canal has prismatic geometry and it is in permanent regime, Baume's model has the advantage that the solution of the linearized Saint-Venant equations is exact. But usually, real canals do not fulfill the required conditions assumed in the mentioned works. To palliate these problems, Schuurmans et al. [18–20] formulated an analytical model denoted as integrator delay (ID) that is composed of two parameters: an integrator and a delay. This model is an

approximation that relates input and output flow including backwater effects when a reservoir-delay model is used. It is very popular among the control community for its easiness describing the more essential aspects of the canal frequential behavior. However, in [21], it is demonstrated that the ID model does not represent accurately the dynamics of a canal for medium and high frequencies. Another extended model for control purposes is the Hayami model [22, 23]. It is based on a first order linearization of the diffusive wave equation around the reference flow. This model is represented by a second order transfer function with delay structure. The model behaves accurately for abrupt and unexpected changes of the reference signal. Its main drawback is its usefulness only for canals with a specific geometry such as those with a reduced set of diffusion and celerity coefficients and canal length.

To overcome the drawbacks of the mentioned models so far, some relatively recent works have been developed. Improvements to the ID model have been also proposed in [24] and its LPV extension [25]. Moreover, in [26, 27], an IDZ (integrator delay zero) model is proposed. This novel model extends the ID model by adding a zero in the high frequencies leading to a better fit in this range. This fact improves the accuracy in time domain simulations, and all model parameters can be analytically computed leading to a simpler implementation. This modelling approach has been also used to generate state-space MIMO models in [28–31]. In [32], a new computational method is provided in order to obtain a frequency domain model of Saint-Venant equations linearized around any stationary regime. In [33], a mathematical model of a gate to automatically control the upstream water level is proposed in order to operate under free and submerged flows conditions (called the Vlugter gate). Munier and his colleagues, in [34], proposed a new model, called LBLR for Linear Backwater Lag-and-Route, which approximates the Saint-Venant equations linearized around a nonuniform flow in a finite channel (with a downstream boundary condition) taking into account the backwater effect. Next in [35], a new approach to compute the response time is proposed, accounting explicitly for the backwater and the feedback effects due to the downstream cross structure. The method provides a distributed analytical expression of the response time as a function of the characteristics of the canal (geometry and roughness) and the downstream cross structure.

As an alternative to the above approaches, in [36–39], linear black-box models for the canal control design have been used. These models are estimated by classical linear estimation methods [40]. They do not have hydraulic meaning and they are based only on experiments. In this case, the main drawback is the necessity of a high number of experiments, especially in the multivariable case. For this reason, some authors carried out a subspace identification [41, 42].

Interestingly, there is a model widely used in hydraulic engineering for prediction that has been barely used as a control model for controller design. This is the Muskingum model. After his experiments in the Muskingum River, McCarthy proposed a hydrological model suitable only in rivers (Muskingum model, [10, 43]) operating with input

and output flows. The model does not require a geometrical definition for the riverbed because the geometry is included in its parameters.

Muskingum model is a hydrological model and is widely used for simulation by hydraulic engineers due to its simplicity and its good results for prediction; nevertheless, it has been almost never applied in the control of flow-open channels. On the other hand, ID model is a mere control model widely used in this kind of systems and with satisfactory results. Both models are simple and simplified and, moreover, they have physical meaning. And this is the motivation that pushed this research to analyze and validate this hydrological model in the canal control and compare it with ID model. Muskingum model is very interesting for control because it is a discrete model that can be used with the most known real canal control methods based on PID and predictive control. In engineering, Muskingum model is not used mainly because it is an unknown approach and the objective of this work is also to reveal, investigate, and study the advantages and drawbacks of Muskingum model (typically used in prediction) as an open-flow canal control model. To reach this objective, a comparative study between both models (ID model and Muskingum model) has been carried out. It is well worth to note that in [44], the Muskingum model is used in predictive control. It would be of interest that hydraulic engineers as well as control engineers could use the same mathematical tools to share experiences and knowledge, because at the end they are performing complementary works in water resource management. Moreover, both communities could approach and create synergies with a higher efficacy and efficiency.

The main contribution of this research is to analyze and study whether Muskingum hydrological model is suitable as control model for typical controller design in water management as feedback control with PID and predictive control. The present paper is organized as follows. Section 2 gives a system description of Aghili irrigation canal used in our study. In Section 3, a brief explanation of Muskingum model and its relationship with the ID model is presented. Specifically, the Muskingum prediction model has been studied as a control model. To do so, it has been analyzed in open loop (in continuous time as well as in discrete time) and in closed loop (considering the effect of ZOH and sample time). In Section 4, a comparison is also performed with the ID model widely used in controller design. In Section 5, the closed-loop behaviour in continuous and discrete time is also analyzed specially when using such a model to design a feedback controller. In Section 6, both models are tested and validated in Aghili irrigation canal using two control methods: PID control with a SP scheme and predictive control. Finally, the conclusions of using the Muskingum and ID models for control are presented.

## 2. Description of the Irrigation Canal

In this section, a real irrigation canal system (Aghili canal) is described. The complete behaviour of the water in this system is represented by Saint-Venant equations as a simulation model.



FIGURE 1: (a) Map of Khuzestan Province in Iran where the Aghili irrigation map is located; (b) Aghili irrigation canal and its spillway, West and East branches start at this point (32.169147 and 48.734554 coordinates) (from Google Maps); (c) aerial picture of the start of the canal at Karun River (from Google Maps); (d) sluice gate at Karun river where the 2 km canal starts.

2.1. *System Description.* Aghili irrigation district (AID) is located in southwest Iran, in the north of Khuzestan Province (see Figure 1(a)). AID is a part of the Gotvand irrigation network. The annual (maximum versus minimum) air temperatures range from 53° to 3°C and precipitation rates from 582 mm to 152 mm, respectively. The net cultivated area in AID is about 4000 ha. The annual mean distributed water in the irrigation area is about 150 MCM (million cubic meters). AID includes a short main canal, 2 km long, along with two subsidiary canals, right branch at a length of 14.9 km and left branch at a length of 18.6 km. In this study, the 2 km canal is treated. In Figure 1(b), an aerial picture of the spillway can be seen where both branches depart from the canal. The right branch (west branch) has been studied in [45]. The total irrigation canal is composed of a main small pool equipped with an upstream sluice gate that takes water from Karun River (Figure 1(c)) with two subsidiary reaches (Figure 2(a)), as previously cited. Upstream of this gate ( $u$ ) is a dam (Figure 1(d)) of constant level  $H = 3.5$  m and the total length of the pool ( $L$ ) is 2 km (Figure 2(b)). For more information about Karun River, see [46]. This main pool is used for the control study of this paper.

To reproduce the real behaviour of this irrigation canal, a simulator developed by the group of “Modelling and Control of Hydraulic Systems” at the UPC is used [47]. It solves numerically Saint-Venant equations [1, 3, 48] which accurately describe water dynamics.

2.2. *Saint-Venant Model.* Saint-Venant model can be expressed by the conservation of mass and momentum principles equations in a one-dimensional free surface flow.

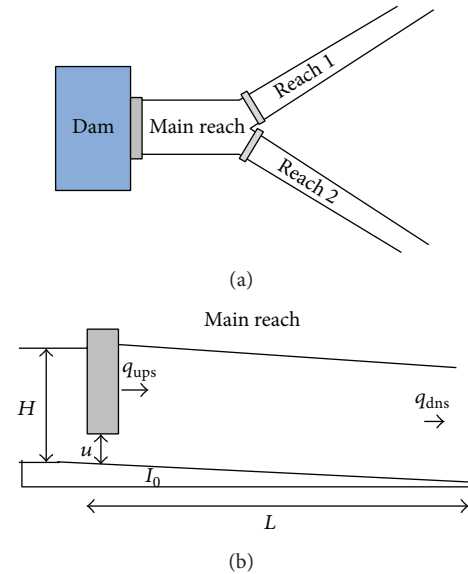


FIGURE 2: (a) Canal scheme and (b) scheme of the main reach.

Conservation mass equation:

$$\frac{\partial q}{\partial x} + \frac{\partial A}{\partial t} = 0. \tag{1}$$

Momentum equation:

$$\frac{\partial q}{\partial t} + \frac{\partial}{\partial x} \left( \frac{q^2}{A} \right) + gA \frac{\partial y}{\partial x} - gA (I_0 - I_f) = 0, \tag{2}$$

where  $Q = Q(x, t)$  is the flow ( $\text{m}^3/\text{s}$ ),  $y(x, t)$  is the level (m),  $A = A(x, t)$  is the cross-sectional area ( $\text{m}^2$ ),  $t$  is the time variable (s),  $x$  is the spatial variable (m) measured in the direction and the sense of the movement,  $y$  is the water level,  $g$  is the gravity ( $\text{m}/\text{s}^2$ ),  $I_0$  is the bottom slope, and  $I_f$  is the friction slope.

This pair of partial differential equations (1)-(2) constitutes a nonlinear and hyperbolic system for an arbitrary geometry and it lacks analytical solution [1, 3]. These equations can be solved by different numerical methods, such as Preissman, finite differences, and characteristics [48, 49]. The Saint-Venant model describes in detail the canal dynamics, and it is very useful in simulation. However, this model is too complex for controller design and furthermore it cannot be used for control design using analytical methods. As previously said, these equations are used as simulation model (solved numerically using the method of characteristics) to reproduce the complex dynamics of Aghili irrigation canal.

### 3. Physical Canal Models: Muskingum Model versus ID model

**3.1. Muskingum Model.** The Muskingum model [1, 10] relates the inflow ( $I$ ) with the outflow ( $Q$ ) of a free surface hydraulic system. This model uses the following continuity equation and a linear storage-discharge relationship:

$$I(t) - Q(t) = \frac{dV(t)}{dt}, \quad (3)$$

$$V(t) = K(\chi I(t) + (1 - \chi)Q(t)), \quad (4)$$

where  $V$  ( $\text{m}^3$ ) is the volume of water stored in the hydraulic system and  $K$  and  $\chi$  are parameters that depend on the hydraulic system.  $K$  is considered as the average pool travel time, and  $\chi$  shows the influence of the downstream condition in the hydrograph propagation with  $0 \leq \chi \leq 0.5$  (see Figure 3).

The inflow  $I$  is the input variable, also noted as  $q_{\text{ups}}$ ; the outflow  $Q$  is the output variable, also noted  $q_{\text{dns}}$ . The Muskingum model works only with upstream and downstream flows and it is not possible to obtain the water level with any direct relationship. Normally, an empirical approximation is used (e.g., Manning, Chezy or Darcy-Weisbach; in this paper, the Manning approximation is used) to relate the flow and level, adding imprecision to the results. Replacing (3) with (4) and using the Laplace transform, the relation between output flow and input flow is obtained:

$$q_{\text{dns}}(s) = G_m(s) q_{\text{ups}}(s) = \frac{(1 - K\chi s)}{(K(1 - \chi)s + 1)} q_{\text{ups}}(s). \quad (5)$$

**3.2. ID Model.** Canals are systems that can be decomposed in many dynamic elements, usually of first order, so the full model is of an order equal to the number of elements. Then, the resulting model will have an order equal to the number of pieces used to model the canal, that is, a very high order model. As discussed in [50], this very high order model would be difficult to use for control purposes but, fortunately, it is

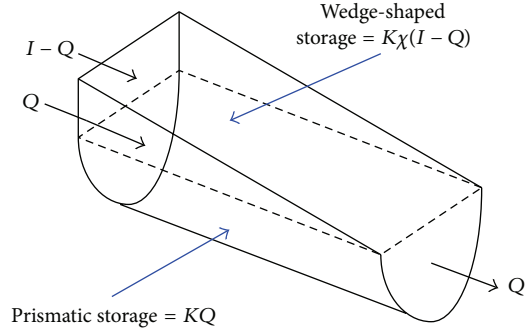


FIGURE 3: Prismatic storage and wedge-shaped storage in a pool.

possible to approximate the behaviour of such high order processes by a system with one time constant and a dead time, that is, a FOPDT. This will be shown in the following subsection.

The complete water dynamics of a single-pool irrigation canal is classically modeled with the Saint-Venant equations. However, as discussed in the previous section, for control purposes, the ID (integrator delay) model is considered as proposed by Litrico and Fromion [32] for low frequencies. The single canal reach dynamics has a relationship between downstream level  $y_{\text{dns}}$  and downstream flow  $q_{\text{dns}}$  and upstream flow  $q_{\text{ups}}$  for low frequencies. This relation can be approximated by

$$y_{\text{dns}}(s) = P_1(s) q_{\text{ups}}(s) + P_2(s) q_{\text{dns}}(s) \quad (6)$$

with

$$P_1(s) = \frac{e^{-\tau_d s}}{A_d s}, \quad (7)$$

$$P_2(s) = \frac{-1}{A_d s},$$

where  $\tau_d$  is the downstream transport delay and  $A_d$  is the downstream backwater area. Taking into account the linearized relationship between the downstream flow  $q_{\text{dns}}$  and level  $y_{\text{dns}}$  in the spillway, the following equality can be established:

$$q_{\text{dns}}(s) = \lambda y_{\text{dns}}(s), \quad (8)$$

where  $\lambda$  is a constant.

Combining (6) and (8), the following first order plus time delay (FOPDT) model can be obtained:

$$q_{\text{dns}}(s) = \frac{P_1(s)}{(\lambda - P_2(s))} q_{\text{ups}}(s)$$

$$= \frac{e^{-\tau_d s}}{(A_d \lambda s + 1)} q_{\text{ups}}(s) \quad (9)$$

$$= \frac{k}{(Ts + 1)} e^{-\tau_d s} q_{\text{ups}}(s)$$

with a gain  $k = 1$  and a time constant  $T = \lambda A_d$ .

The delay,  $\tau_d$ , can be estimated based on physical laws by

$$\tau_d = \frac{L}{v + c}, \quad (10)$$

where  $L$  is the canal length,  $v$  is the current water velocity, and  $c$  is the current celerity:  $c = \sqrt{gy}$ . For more details about this modelling approach, see [22–24, 26, 32].

**3.3. Relation between Both Models.** Comparing the ID and Muskingum model structure, it can be shown that Muskingum model can be obtained from the ID model through an approximation using the McLaren approach [51]. Then, if  $G_m$  is the open-flow canal transfer function, we obtain

$$G_m(s) = \frac{1}{Ts + 1} e^{-\tau s} \approx \frac{1 - \tau s}{Ts + 1}. \quad (11)$$

Although the delay is neither close to zero nor it can be neglected considering the system dynamics, the error produced by the approximation is not significant when  $G_m$  is discretized by a convenient sampling time; see Section 3.2. This approximated transfer function has the same structure as that of the hydrological original continuous Muskingum model, considering  $\tau = K\chi$  and  $T = K(1 - \chi)$ .

## 4. Open-Loop Behaviour of the Muskingum Model

**4.1. Continuous-Time Open-Loop Behaviour.** The behaviour of the Muskingum model in open-loop will be compared with the ID model and with the real behaviour reproduced by means of solving the Saint-Venant equations [1] using the open-flow canal presented in Section 2 of this paper. The estimated parameters of the Muskingum model for this canal are  $K = 1200$  and  $\chi = 0.2$  while in the case of ID model they are  $k = 1$ ,  $T = 12.09$  min, and  $\tau = 8.28$  min.

Equation (11) shows that the continuous Muskingum model is a model with a zero in the right half-plane (RHP), that is, with unstable inverse model (nonminimum phase model, NMP). This implies that for either step-input or instantaneous unit hydrograph response will present negative flows (i.e., when the input increases the output decreases) lacking physical meaning. This problem has been already reported in [52]. In Figure 4, the step-input response of the canal system for the case of the Muskingum and ID model is compared against the real behaviour simulated using the Saint-Venant equations. It can be noticed that continuous ID behaviour resembles the real one (simulated with the Saint-Venant equations). On the other hand, the nonminimum phase behaviour of the continuous Muskingum model is present at the beginning, although it reaches the correct steady state at the end.

**4.2. Discrete-Time Open-Loop Behaviour.** When obtaining the discrete-time Muskingum model to predict the behaviour of an open flow sewer in open-loop, the bilinear transform is usually used in the hydraulic literature. Then, applying the

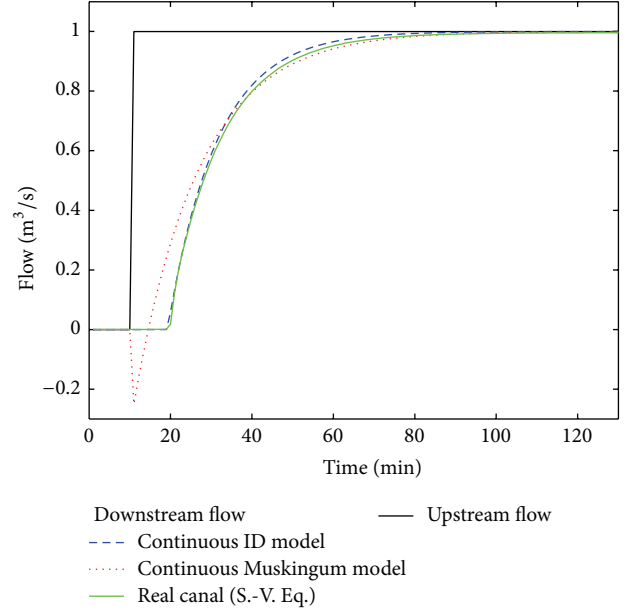


FIGURE 4: Real-step response (Saint-Venant equations) and estimated-step responses with continuous Muskingum model and continuous ID model.

bilinear transformation with sampling time  $T_s$  to (1) and (2), the following expression is obtained:

$$Q(k) = c_0 I(k) + c_1 I(k-1) + c_2 Q(k-1), \quad (12)$$

where

$$\begin{aligned} c_0 &= \frac{T_s/K - 2\chi}{2(1-\chi) + T_s/K}, \\ c_1 &= \frac{T_s/K + 2\chi}{2(1-\chi) + T_s/K}, \\ c_2 &= \frac{2(1-\chi) - T_s/K}{2(1-\chi) + T_s/K} \end{aligned} \quad (13)$$

with the condition

$$2K\chi \leq T_s \leq K \quad (14)$$

in order to provide hydrological meaning to the model. This selection guarantees that the sampling time  $T_s$  will be larger than the delay and the propagated hydrograph does not take negative values.

Then, the following transfer function can be obtained from (12)

$$\frac{Q(z)}{I(z)} = \frac{c_0 z + c_1}{z - c_2} \quad (15)$$

that corresponds to a first-order linear system with a zero and a pole. According to (15), in fact the parameters will be  $c_0$ ,  $c_1$ , and  $c_2$  and using the expressions in (13) it will be possible to compute Muskingum parameters  $K$  and  $\chi$  (bilinear transformation, see Table 1).

TABLE 1: Muskingum parameters.

Discretization type	Muskingum coefficients		
	$c_0$	$c_1$	$c_2$
With ZOH	$\frac{-\chi}{(1-\chi)}$	$\left(\frac{\chi}{1-\chi}\right) + (1 - e^{-T_s/K(1-\chi)})$	$e^{-T_s/K(1-\chi)}$
With bilinear transform	$\frac{T - 2K\chi}{2K(1-\chi) + T}$	$\frac{2K(1-\chi) - T}{2K(1-\chi) + T}$	$\frac{T + 2K\chi}{2K(1-\chi) + T}$

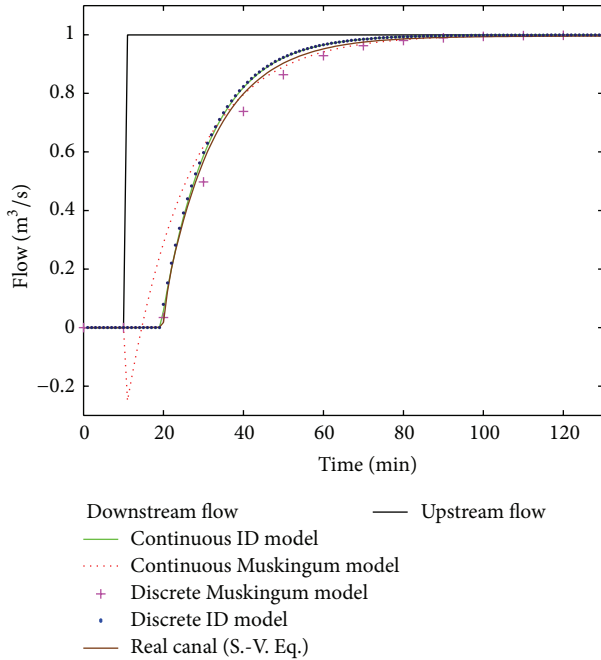


FIGURE 5: Real-step response (Saint-Venant equations) and estimated-step responses with continuous and discrete (bilinear,  $T_s = 600$  s) Muskingum models and continuous and discrete (ZOH,  $T_s = 60$  s) ID model.

In Figure 5, the open-loop response of the discrete-time Muskingum model to a unit step input is compared with the one obtained using an ID model and the real behaviour simulated using Saint-Venant equations. It can be noticed that using the sampling time suggested by rule equation (14) and the bilinear discretization method, the discrete-time Muskingum model produces good prediction results, avoiding the negative values that presented the continuous-time model.

## 5. Closed-Loop Behaviour of the Muskingum Model

The use of the Muskingum model in closed-loop canal control (digital and continuous) is discussed in this section taking into account three important features for control applications such as the effect of its structure, the inclusion of a zero-order hold (ZOH) in closed loop, and the sampling time selection. This study has been carried out considering

a PI controller synthesized by the pole placement method [53] and using the same canal system in case of the open-loop response (Section 4). The PI controller has been designed in order to obtain the following specifications: steady-state zero error for step responses, no overshoot, and desired time constant of 800 s.

**5.1. Structure.** As discussed in Section 3.1, the Muskingum model introduces a nonminimum phase zero. The effect of such zero in closed loop is the degradation of the performance because the controller has been adjusted considering that the canal behaves as a nonminimum phase plant but the real canal does not behave in such a way. In particular, the desired closed-loop behaviour is not obtained, appearing instead as an overshoot when applied to the real canal. On the other hand, when the Muskingum model is used as the plant to simulate the behaviour of the controller that also has been designed using the Muskingum model, the closed behaviour fulfills the desired behaviour but still presents the nonminimum phase dynamics (Figure 6). As a conclusion, the effect of structure mismatch between the Muskingum model and the real canal behaviour will derive in a degraded closed-loop response including more overshoot than the specified.

**5.2. Discretization Method.** When using the discrete Muskingum model for designing a closed-loop digital controller, additionally to the problem of the structure mismatch, two additional issues appear; namely, the discrete equivalent Muskingum model should include the dynamics of a ZOH and second the Shannon criteria should be fulfilled when selecting the sampling time. These problems appear since, usually in hydraulics, the Muskingum model is discretized using the bilinear transformation and with a sampling time that provides hydrological meaning to the model (see Section 3.1).

However, when using such a model in closed-loop digital control, instead a ZOH transform should be used to take into account the dynamics of the ZOH that models the D/A conversion process. This is a standard procedure in classical digital control [54]. Then, equivalent discrete-time transfer function will have the same structure as that in the case of the bilinear transform, but the parameters of the model  $c_0$ ,  $c_1$ , and  $c_2$  will be different according to Table 1.

If the discrete-time Muskingum model obtained by means of the bilinear transform is used to design the controller instead of the one obtained using the zero-order

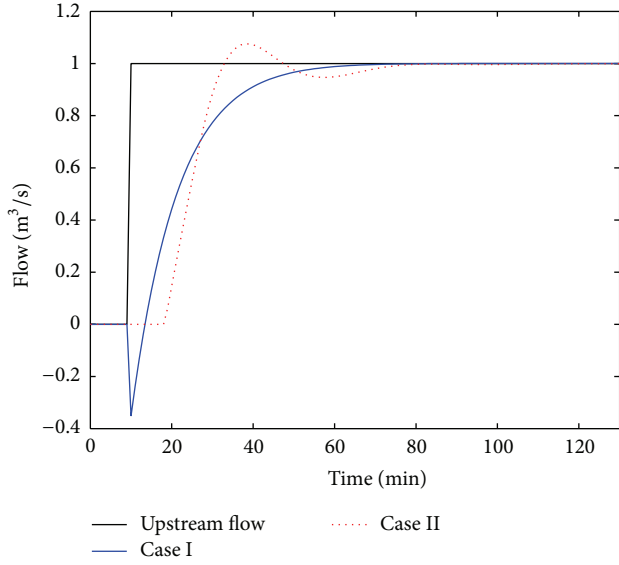


FIGURE 6: Step closed-loop response for the case I: downstream flow with PI designed by continuous Muskingum with continuous Muskingum plant; and case II: downstream flow with PI designed by continuous Muskingum with ideal ID plant.

hold transform, the closed-loop behaviour will experiment a performance degradation when applied to a discrete-time Muskingum model using the zero-order hold transform according to the results presented in Figure 7. The inclusion of the zero-order hold when applying digital control is unavoidable since the D/A converter is always present. As a conclusion, for closed-loop digital control design, the discrete-time Muskingum model should be obtained using the zero-order hold transform instead of the bilinear transform.

5.3. *Effects of the Sampling Time.* Even when discretizing the Muskingum model using the zero-order hold method, another problem appears when selecting the sampling time period satisfying the rule given in (9) in order that the discrete Muskingum model has hydrological meaning since the Shannon theorem [54] is not respected. Shannon's theorem establishes that a good sampling time should take a value at least  $T_s = T/10$ , but according to rule (14), in the best case  $T_s = K = T/(1 - \chi)$ . The selection of the sampling time following the Muskingum rule will derive again in a performance's degradation according to Figure 7 with respect to the equivalent closed-loop continuous behaviour. In fact, in this figure it can be observed that the use of the sampling time suggested by Muskingum rule increases the overshoot. On the other hand, selecting the sampling time according to Shannon's theorem derives in a closed-loop response that resembles that obtained when the continuous Muskingum model is used. However, even when using the ZOH transform method as a discretization procedure and the sampling time suggested by Shannon's theorem, the problem of the structure in the Muskingum model described in Section 5.1 still remains.

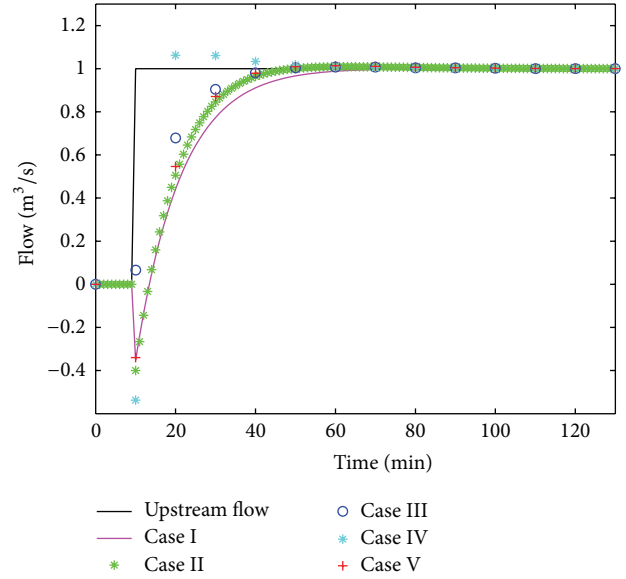


FIGURE 7: Step closed-loop response for the case I: downstream flow with PI designed by continuous Muskingum with continuous Muskingum plant; case II: downstream flow with PI designed by discrete Muskingum (ZOH and  $T_s = 60$  s) with discrete Muskingum (ZOH and  $T_s = 60$  s) plant; case III: downstream flow with PI designed by discrete Muskingum (bilinear and  $T_s = 600$  s) with discrete Muskingum (bilinear and  $T_s = 600$  s) plant; case IV: downstream flow with PI designed by discrete Muskingum (bilinear and  $T_s = 600$  s) with discrete Muskingum (ZOH and  $T_s = 600$  s) plant; and case V: downstream flow with PI designed by discrete Muskingum (ZOH and  $T_s = 600$  s) with discrete Muskingum (ZOH and  $T_s = 600$  s) plant.

## 6. Control Results for Real Plant

Finally, in order to validate both models (Muskingum and ID) for control design, the control results using the real plant (simulated by means of Saint-Venant equations) are presented in Figures 8, 9, and 10. In this section, two usual methodologies for canal feedback control using a PI and with a Smith predictor (SP) scheme [55, 56] and predictive control [50, 57, 58] are tested for this study and for validation.

6.1. *Using a PI Controller with a SP Scheme.* For the PI with a SP scheme (to compensate the delay of the system) designed by pole placement technique [59–61], it can be observed that the results considering the real plant and the continuous ID model (used as a plant) using the PI designed with discrete ID model (ZOH,  $T_s = 60$  s) (denoted as PI1) are very similar. On the other hand, the closed-loop control results for the PI designed with discrete Muskingum model (bilinear,  $T_s = 600$  s) (denoted as PI2) considering the real plant are very different from the ones obtained using the continuous Muskingum model (used as a plant). These prove the validity of the ID model for control design, while showing that the Muskingum model is not suitable for this purpose.

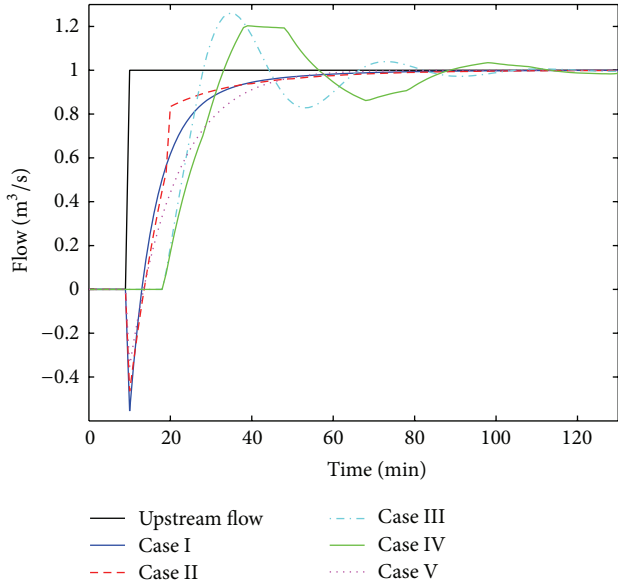


FIGURE 8: Step closed-loop response for the case I: downstream flow with PI designed by discrete Muskingum (ZOH,  $T_s = 60$  s) with continuous Muskingum plant; case II: downstream flow with PI designed by discrete Muskingum (ZOH,  $T_s = 600$  s) with continuous Muskingum plant; case III: downstream flow with PI designed by discrete Muskingum (ZOH,  $T_s = 60$  s) with continuous ID plant; case IV: downstream flow with PI designed by discrete Muskingum (ZOH,  $T_s = 600$  s) with continuous ID plant; and case V: downstream flow with PI designed by continuous Muskingum with continuous Muskingum plant.

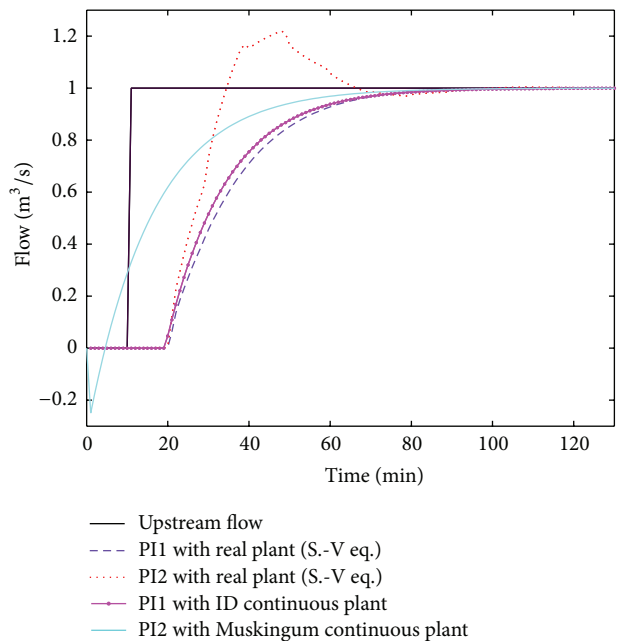


FIGURE 9: Step closed-loop response of the real irrigation plant (Saint-Venant equations) using a PI1 and a PI2; step closed-loop response of the ID continuous plant using PI1 and step closed-loop response of the Muskingum continuous plant using PI2.

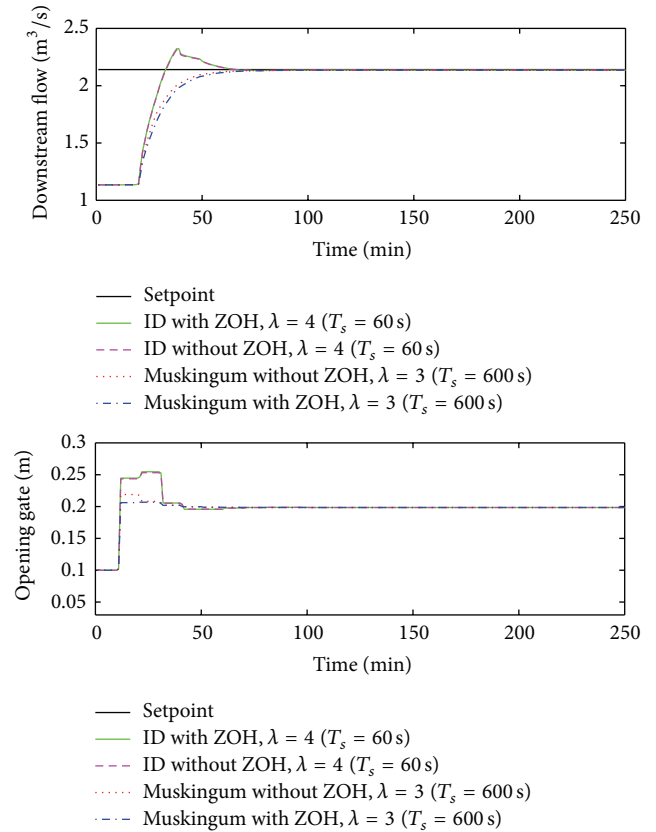


FIGURE 10: Step closed-loop response of the real irrigation plant (Saint-Venant equations) using predictive control with a Muskingum model and an ID model (both with and without ZOH) for different predictive horizon  $\lambda$  and different  $T_s$ .

6.2. *Using a Predictive Controller with a SP Scheme.* It is well known that predictive control essentially relies on the use of a model capable of forecasting the system output as a function of the system inputs on moving horizon setting and computing the control sequence making that predicted output could follow a desired trajectory through the minimization of a performance criterion. The predictive control is suitable for systems with delay and the model precision is not critical because a new predictive model is obtained from a new calibration every time the system operates.  $\lambda$ , the prediction horizon, is chosen in order to predict the transitory dynamics and to yield the adequate performance. The selection of prediction horizon will drive to a tradeoff between the abrupt control effort and the swift in the response. The precision and accuracy of predictive control have been studied with an ID model with  $T_s = 60$  s and Muskingum model with sample times that give physical meaning to Muskingum; that is,  $T_s = 600$  s. The ID model and Muskingum model provide a temporal response with approximately the same rapidity. However, the former presents more overshoot than the latter. Therefore, the predictive controller based on Muskingum model is more energetically efficient (less oscillations in the spillway movements). After analyzing the results obtained from

the simulations, it is recommended to use the Muskingum model altogether with the predictive control strategy because it is a stationary, good prediction model and the delay is implicit.

## 7. Conclusions

In this paper, the use of the Muskingum model in closed-loop digital and continuous control has been analyzed and discussed regarding three main issues: the structure of the model, the discretization method, and the selection of the sampling time. Regarding the structure of the Muskingum model in continuous time, it can be observed that it introduces a nonminimum-phase zero that produces negative responses at the beginning of the response to a step input. This behaviour is not present in the real canal making this model not useful in continuous time. Such nonminimum phase behaviour is avoided in discretizing the Muskingum model using the rule that guarantees the sampling time with the order of the delay. However, such a selection of the sampling time is not supported by Shannon's theorem. Moreover, the discretization method typically used with the Muskingum model is the bilinear transform that does not take into account the zero-order hold. However, even when using the zero-order hold method as a discretization procedure and sampling time fulfilling Shannon's theorem, the problem of the nonminimum phase introduced by the unstable zero appears again since the closed-loop behaviour in this case resembles the equivalent closed-loop continuous behaviour. As a conclusion, the Muskingum model is a good open-loop prediction model in discrete time using the suggested discretization rule in order to avoid the nonminimum phase behaviour and it is suitable for flood routing applications. For control purposes, mathematically simple control laws that can be designed (either based on the PID law or based on a predictive control strategy) with both models have been considered. These laws should allow an easy and swift computation, guaranteeing stability and convergence to the desired setpoint. However, when using the Muskingum model for designing a closed-loop controller, the results are not as good as expected. In particular, if the controller is implemented in a digital way, the mandatory inclusion of the ZOH effect and selection of the sampling time according to Shannon's theorem derive in the reappearance of the nonminimum phase behaviour that Muskingum sampling time rule avoided. Furthermore, if the sampling time is reduced in the simulation of Muskingum controller, there is an increment of oscillations in the closed-loop response. This makes the Muskingum model also not useful for digital feedback control design. But in the case of predictive control, the explained Muskingum behaviour does not influence the predictive control algorithm because this type of control requires only a good prediction model at each prediction horizon. Since the delay is implicit in the system, a prediction model is obtained when a suitable sample time is selected. Therefore, with the use of Muskingum model, energetically efficient control results are obtained, although ID model also presents reasonable results. On the other hand, when PID

controllers are designed using the ID model, the control results are temporally more efficient (less time of convergence and more rapidity) and more energetically efficient than Muskingum model. However, Muskingum model is more energetically efficient when considering a predictive law, although the speed of the response of control results is similar using both models.

## Conflict of Interests

The authors declare that there is no conflict of interests regarding the publication of this paper.

## Acknowledgment

This research has been funded by Project 2009 SGR 908 from Autonomous Government of Catalonia.

## References

- [1] V. T. Chow, *Open-Channel Hydraulics*, McGraw-Hill, 1959.
- [2] M. Gómez, *Contribución al estudio del movimiento de variable en lámina libre en las redes de alcantarillado [Ph.D. thesis]*, UPC, 1988 (Spanish).
- [3] J. A. Cunge, F. M. Holly, and A. Verwey, *Practical Aspects of Computational River Hydraulics*, Pitman Advanced Publishing, 1980.
- [4] J. P. Baume and M. Poirson, "Modélisation numérique d'un écoulement permanent dans un réseau hydraulique maillé à surface libre, en régime fluvial," *La Houille Blanche*, no. 1-2, pp. 95–100, 1984.
- [5] A. Garcia, M. Hubbard, and J. J. de Vries, "Open channel transient flow control by discrete time LQR methods," *Automatica*, vol. 28, no. 2, pp. 255–264, 1992.
- [6] J. M. Reddy, "Local optimal control of irrigation canals," *Journal of Irrigation and Drainage Engineering*, vol. 116, no. 5, pp. 616–631, 1990.
- [7] P. O. Malaterre, *Modelisation, analysis and LQR optimal control of an irrigation canal [Ph.D. thesis]*, CEMAGREF, 1994.
- [8] M.-L. Chen, *Commande Optimale et Robuste des Équations aux Dérivées Partielles Régissant le Comportement des Systèmes Hydrauliques à Surface Libre [Ph.D. thesis]*, Institut National Polytechnique de Grenoble, 2001.
- [9] P. Pognant-Gros, *De la Réduction de Modèles vers la Commande Robuste. Application à la Commande des Canaux d'Irrigation [Ph.D. thesis]*, Université de Caen, France, 2003.
- [10] G. T. McCarthy, *The Unit Hydrograph and Flood Routing*, U.S. Army Corps of Engineers, North Atlantic Division, New London, Conn, USA, 1938.
- [11] A. Das, "Parameter estimation for Muskingum models," *Journal of Irrigation and Drainage Engineering*, vol. 130, no. 2, pp. 140–147, 2004.
- [12] G. Corrigan, F. Patta, S. Sanna, and G. Usai, "A mathematical model for open-channel networks," *Applied Mathematical Modelling*, vol. 3, no. 1, pp. 51–54, 1979.
- [13] G. Corrigan, A. Fanni, S. Sanna, and G. Usai, "A constant-volume control method for open channel operation," *International Journal of Modelling and Simulation*, vol. 2, no. 2, pp. 108–112, 1982.

- [14] M. Papageorgiou and A. Messmer, "Continuous-time and discrete-time design of water flow and water level regulators," *Automatica*, vol. 21, no. 6, pp. 649–661, 1985.
- [15] M. Papageorgiou and A. Messmer, "Flow control of a long river stretch," *Automatica*, vol. 25, no. 2, pp. 177–183, 1989.
- [16] Y. A. Ermolin, "Study of open-channel dynamics as controlled process," *Journal of Hydraulic Engineering*, vol. 118, no. 1, pp. 59–72, 1992.
- [17] J. P. Baume, P. O. Malaterre, and J. Sau, "Tuning of PI controllers for an irrigation canal using optimization tools," in *Proceedings of the USCID Workshop on Modernization of Irrigation Water*, 1999.
- [18] J. Schuurmans, O. H. Bosgra, and R. Brouwer, "Open-channel flow model approximation for controller design," *Applied Mathematical Modelling*, vol. 19, no. 9, pp. 525–530, 1995.
- [19] J. Schuurmans, A. J. Clemmens, S. Dijkstra, A. Hof, and R. Brouwer, "Modeling of irrigation and drainage canals for controller design," *Journal of Irrigation and Drainage Engineering*, vol. 125, no. 6, pp. 338–344, 1999.
- [20] J. Schuurmans, A. Hof, S. Dijkstra, O. H. Bosgra, and R. Brouwer, "Simple water level controller for irrigation and drainage canals," *Journal of Irrigation and Drainage Engineering*, vol. 125, no. 4, pp. 189–195, 1999.
- [21] I. Guenova, X. Litrico, and D. Georges, "Modelling and robust PID control of an irrigation canal pool," in *Proceedings of the 23rd IASTED International Conference on Modelling, Identification, and Control*, pp. 561–566, Grindelwald, Switzerland, February 2004.
- [22] X. Litrico, *Modélisation, identification et commande robuste de systèmes hydrauliques à surface libre [Thèse de doctorat de l'ENGREF]*, Spécialité Sciences de l'Eau, 1999.
- [23] X. Litrico and D. Georges, "Robust continuous-time and discrete-time flow control of a dam-river system. (I) Modelling," *Applied Mathematical Modelling*, vol. 23, no. 11, pp. 809–827, 1999.
- [24] X. Litrico and V. Fromion, "Analytical approximation of open-channel flow for controller design," *Applied Mathematical Modelling*, vol. 28, no. 7, pp. 677–695, 2004.
- [25] Y. Bolea, V. Puig, and J. Blesa, "Linear parameter varying modelling and identification for real-time control of open-flow irrigation canals," *Environmental Modelling & Software*, vol. 53, pp. 87–97, 2013.
- [26] X. Litrico and V. Fromion, "Simplified modeling of irrigation canals for controller design," *Journal of Irrigation and Drainage Engineering*, vol. 130, no. 5, pp. 373–383, 2004.
- [27] X. Litrico, V. Fromion, J.-P. Baume, C. Arranja, and M. Rijo, "Experimental validation of a methodology to control irrigation canals based on Saint-Venant equations," *Control Engineering Practice*, vol. 13, no. 11, pp. 1425–1437, 2005.
- [28] A. J. Clemmens and J. Schuurmans, "Simple optimal downstream feedback canal controllers: theory," *Journal of Irrigation and Drainage Engineering*, vol. 130, no. 1, pp. 26–34, 2004.
- [29] A. J. Clemmens and B. T. Wahlin, "Simple optimal downstream feedback canal controllers: ASCE test case results," *Journal of Irrigation and Drainage Engineering*, vol. 130, no. 1, pp. 35–46, 2004.
- [30] B. T. Wahlin, "Performance of model predictive control on ASCE test canal 1," *Journal of Irrigation and Drainage Engineering*, vol. 130, no. 3, pp. 227–238, 2004.
- [31] P. J. van Overloop, J. Schuurmans, R. Brouwer, and C. M. Burt, "Multiple-model optimization of proportional integral controllers on canals," *Journal of Irrigation and Drainage Engineering*, vol. 131, no. 2, pp. 190–196, 2005.
- [32] X. Litrico and V. Fromion, "Frequency modeling of open-channel flow," *Journal of Hydraulic Engineering*, vol. 130, no. 8, pp. 806–815, 2004.
- [33] G. Belaud, X. Litrico, B. de Graaff, and J. Baume, "Hydraulic modeling of an automatic upstream water level control gate for submerged flow conditions," *Journal of Irrigation and Drainage Engineering*, vol. 134, no. 3, pp. 315–326, 2008.
- [34] S. Munier, X. Litrico, G. Belaud, and P. Malaterre, "Distributed approximation of open-channel flow routing accounting for backwater effects," *Advances in Water Resources*, vol. 31, no. 12, pp. 1590–1602, 2008.
- [35] S. Munier, G. Belaud, and X. Litrico, "Closed-form expression of the response time of an open channel," *Journal of Irrigation and Drainage Engineering*, vol. 136, no. 10, pp. 677–684, 2010.
- [36] N. Bedjaoui and E. Weyer, "Algorithms for leak detection, estimation, isolation and localization in open water channels," *Control Engineering Practice*, vol. 19, no. 6, pp. 564–573, 2011.
- [37] P. J. van Overloop, I. J. Miltenburg, X. Bombois et al., "Identification of resonance waves in open water channels," *Control Engineering Practice*, vol. 18, no. 8, pp. 863–872, 2010.
- [38] E. Weyer, "System identification of an open water channel," *Control Engineering Practice*, vol. 9, no. 12, pp. 1289–1299, 2001.
- [39] Y. Bolea, J. Blesa, V. Puig, and T. Escobet, "Identification of an open canal: parametric black-box vs muskingum approaches," in *Proceeding of the IEEE International Conference on Systems, Man and Cybernetics*, vol. 5, pp. 494–499, October 2002.
- [40] L. Ljung, *System Identification: Theory for the User*, Prentice Hall, Upper Saddle River, NJ, USA, 2nd edition, 1999.
- [41] A. Akhenak, E. Duviella, L. Bako, and S. Lecoeuche, "Online fault diagnosis using recursive subspace identification: application to a dam-gallery open channel system," *Control Engineering Practice*, vol. 21, no. 6, pp. 797–806, 2013.
- [42] Y. Bolea, N. Cheddor, and A. Grau, "MIMO LPV state-space identification of open-flow irrigation canal systems," *Mathematical Problems in Engineering*, vol. 2012, Article ID 948936, 16 pages, 2012.
- [43] V. Singh, *Hydrologic Systems*, vol. 1, Prentice-Hall, 1988.
- [44] X. Alvarez Brotons, M. Gomez Valentin, and J. Rodellar, *Predictive control of Irrigation Canals Using Prediction Models of Muskingum (first order) and Hayami (second order) type*, Civil Engineering School of Barcelona. Technical University of Catalonia, Barcelona, Spain, 2004.
- [45] A. Montazar and S. Isapoor, "Centralized Downstream PI controllers for the west canal of Aghili irrigation district," *Journal of Agricultural Science and Technology*, vol. 14, no. 2, pp. 375–388, 2012.
- [46] H. Borjian, "Karun River. Geography and hydrology," *Encyclopaedia Iranica*, vol. 15, no. 6, pp. 629–633, 2011.
- [47] Y. Bolea and J. Blesa, "Irrigation canal simulator (ICS)," Internal Report, Automatic Control Department, Technical University of Catalonia, 2000.
- [48] J. A. Cunge and M. Wegner, "Intégration numérique des équations d'écoulement de Barré de Saint-Venant par un schéma implicite de différences finies," *La Houille Blanche*, vol. 1, pp. 33–39, 1964.
- [49] R. W. Hamming, *Numerical Methods for Scientists and Engineers*, Dover Publications, New York, NY, USA, 2nd edition, 1973.

- [50] E. F. Camacho, *Model Predictive Control*, chapter 5, Springer, New York, NY, USA, 1999.
- [51] K. Ogata, *Modern Control Engineering*, Prentice-Hall, 2nd edition, 1993.
- [52] R. Szymkiewicz, "An alternative IUH for the hydrological lumped models," *Journal of Hydrology*, vol. 259, no. 1–4, pp. 246–253, 2002.
- [53] K. J. Åström and T. Hägglund, *PID Controller: Theory, Design and Tuning*, Instrument Society of America, Research Triangle Park, NC, USA, 2nd edition, 1995.
- [54] K. J. Åström and B. Wittenmark, *Computer-Controlled Systems. Theory and Design*, Prentice-Hall, 3rd edition, 1997.
- [55] O. J. M. Smith, "Closer control of loops with dead time," *Chemical Engineering Progress*, vol. 53, pp. 217–219, 1957.
- [56] J. E. Normay-Rico and E. Camacho, *Control of Dead-Time Processes*, Springer, New York, NY, USA, 2007.
- [57] M. Gómez, J. Rodellar, and J. A. Mantecón, "Predictive control method for decentralized operation of irrigation canals," *Applied Mathematical Modelling*, vol. 26, no. 10, pp. 1039–1056, 2002.
- [58] J. Maciejowski, *Predictive Control with Constraints*, Prentice Hall, Great Britain, UK, 2002.
- [59] R. Isermann, *Digital Control Systems*, vol. 1 of *Fundamentals, Deterministic Control*, Springer, New York, NY, USA, 2nd edition, 1989.
- [60] S. M. Shinnars, *Modern Control System: Theory and Design*, John Wiley & Sons, New York, NY, USA, 2nd edition, 1992.
- [61] J. A. Baksi and M. V. Backsi, *Modern Control Theory*, Technical Publications, Pune, India, 1st edition, 2008.

## Research Article

# Conceptual Model for Simulating the Adjustments of Bankfull Characteristics in the Lower Yellow River, China

Yuanjian Wang,<sup>1,2</sup> Xudong Fu,<sup>1</sup> and Guangqian Wang<sup>1</sup>

<sup>1</sup> State Key Laboratory of Hydrosience and Engineering, Tsinghua University, Beijing 100084, China

<sup>2</sup> Yellow River Institute of Hydraulic Research, Yellow River Conservancy Commission, Zhengzhou 450003, China

Correspondence should be addressed to Yuanjian Wang; wang-yj03@mails.tsinghua.edu.cn

Received 23 December 2013; Revised 7 February 2014; Accepted 12 May 2014; Published 5 August 2014

Academic Editor: Yuefei Huang

Copyright © 2014 Yuanjian Wang et al. This is an open access article distributed under the Creative Commons Attribution License, which permits unrestricted use, distribution, and reproduction in any medium, provided the original work is properly cited.

We present a conceptual model for simulating the temporal adjustments in the banks of the Lower Yellow River (LYR). Basic conservation equations for mass, friction, and sediment transport capacity and the Exner equation were adopted to simulate the hydrodynamics underlying fluvial processes. The relationship between changing rates in bankfull width and depth, derived from quasiuniversal hydraulic geometries, was used as a closure for the hydrodynamic equations. On inputting the daily flow discharge and sediment load, the conceptual model successfully simulated the 30-year adjustments in the bankfull geometries of typical reaches of the LYR. The square of the correlating coefficient reached 0.74 for Huayuankou Station in the multiple-thread reach and exceeded 0.90 for Lijin Station in the meandering reach. This proposed model allows multiple dependent variables and the input of daily hydrological data for long-term simulations. This links the hydrodynamic and geomorphic processes in a fluvial river and has potential applicability to fluvial rivers undergoing significant adjustments.

## 1. Introduction

The bankfull characteristics of alluvial rivers are basic research topics in fluvial processes [1, 2]. In recent years, various natural and anthropogenic disturbances (such as dam construction, water and soil conservation, enhanced water usage with rapid socioeconomic development, and evaporation and precipitation variation related to climate change) have altered the runoff and sediment yield in many large river basins. Concerns have been raised regarding adjustments to river geometries and their impacts on local flood defence and ecological safety. There is emerging interest in the temporal adjustment of bankfull characteristics for rivers subject to significant climate change or intense human interference [3].

Two kinds of approaches have been developed to quantify the variation in bankfull characteristics in terms of the timescales at which the channel adjustment is explored: geomorphic and hydrodynamic approaches. The geomorphic approach is usually based on geomorphic laws expressed by power law, hyperbolic, and exponential equations or relatively complex differential equations [4–7]. It is widely

recognised that geomorphic systems respond rapidly, immediately following the disruption of the equilibrium state, but thereafter exhibit a declining rate of adjustment as a new equilibrium or relaxed state is approached [5, 8, 9]. Applications with years or decades of geomorphic models can be found for various alluvial river basins, such as the South Island of New Zealand [10], Lower Hunter Valley in NewSouthWales [11], sand-bed streams of the American Midwest [12], Sabie River in South Africa [13], Karst landscape evolution in the Cave City in Kentucky [14], Lower Yellow River (LYR) in China [15–18], basins in southeastern Australia [19], and North Fork Toutle River in Washington [20]. The river channel slope [21], channel width [22], bankfull cross-section area and discharge [16, 17], bed level [9, 23], and channel width-depth ratio [24] have been considered as dependent variables of flow and the sediment volume flux per year.

The hydrodynamic approach reproduces channel response processes by accounting for microscale river dynamics. That is, the Saint Venant equations (continuity and momentum equations) for river flow, the sediment transport equation, and the river bed or bank deformation equations are set up to describe the instantaneous relations

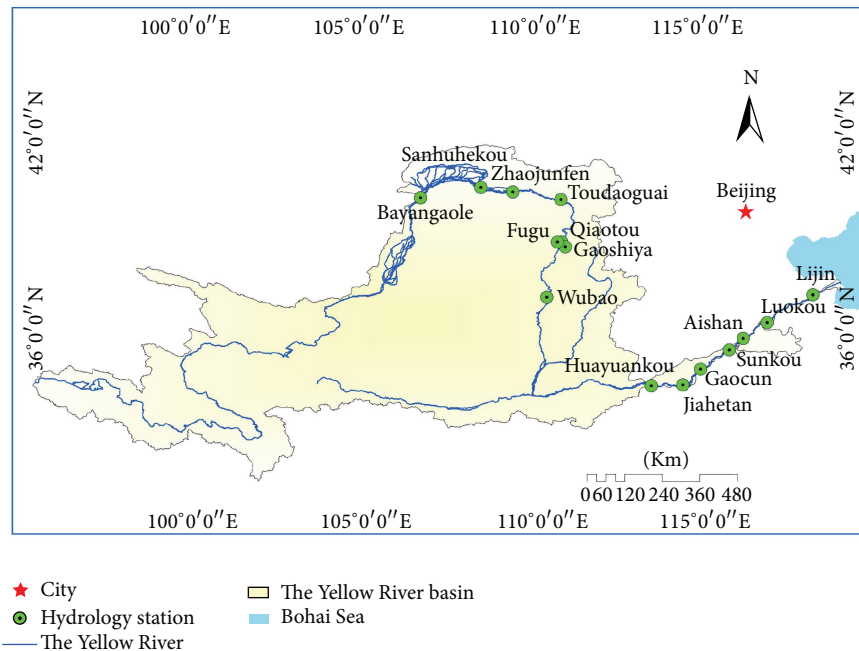


FIGURE 1: Schematic of the Yellow River basin.

between channel adjustment and the incoming flow and sediment conditions. One-, two-, and three-dimensional models for either steady flow [25–29] or unsteady flow [30–32] have been used widely to investigate channel degradation or aggradation during flood events. Recently, much effort has shifted to the long-term simulation of channel responses. The formation and evolution of meandering or wandering rivers has been simulated considering the long-term fluvial actions [33–36]. For example, Sun et al. [34] reproduced the phenomenon of channel evolution, including the shallowing and widening of the initial channel, the rhythmical sequence of alternate bars and erosional bumps, and the occurrence of meandering abrupt shifts and bank cusps. Asahi et al. [36] captured the nature process of river meandering in a computational model that considers the effects of bank erosion, the process of land accretion along the inner banks of meander bends, and the formation of channel cut-offs.

In nature, the channel response is achieved by the cumulative effects of fluvial erosion/deposition processes, which relate to both geomorphic processes and hydrodynamic events. The geomorphic approach, particularly the rate law method, can capture the overall behaviour of the channel response to seasonal or annual flow and sediment data, but it cannot account for the effects of flood events. The channel response can be characterised by a set of variables, but the coordination of multiple dependent variables has not been explored. By contrast, the hydrodynamic approach is capable of representing the details of the channel response process at small timescales, such as bank erosion, bar migration, and channel shallowing/widening. When applied on large timescales, the computational limitations and requirements for accurate resistance parameters and boundary conditions

may stop it from producing reliable simulation and predictions.

Here we propose a physics-based model linking hydrodynamic and geomorphic scales. It is intended to represent channel response processes subject to both hydrodynamic and geomorphic controls. The model adopts hydrodynamic equations and boundary equations with daily data as input. It enables the characterisation of flood events in large rivers (typically lasting for around 10 days) and the simulation of continuous response behaviour over a long-term period (years or decades). In a scientific sense, linking across hydrodynamic and geomorphic scales is an attempt to overcome the shortcomings of each scale by considering the flood details and obtaining the long-period channel response processes. It may be applied both to simulate fluvial processes over the past few decades and to forecast channel-forming processes with potential flow and sediment series in the future for large alluvial rivers like LYR.

## 2. Background of This Study

*2.1. Overview of the Study Area.* The Yellow River is the second longest river in China and supports 12% of the Chinese population (Figure 1). The river is about 5464 km long with a drainage area of 752,000 km<sup>2</sup>. The Yellow River is famous for its excessive sediment load and deficient flow. The long-term average sediment load at the Sanmenxia Dam is 1.6 billion tons per year, which ranks first in the world.

The LYR stretches from Huayuankou to Lijin, as shown in Figure 2. It is about 520 km long and exhibits variable channel patterns. It is usually divided into three geomorphological distinct reaches [37]. The upper reach from Huayuankou to

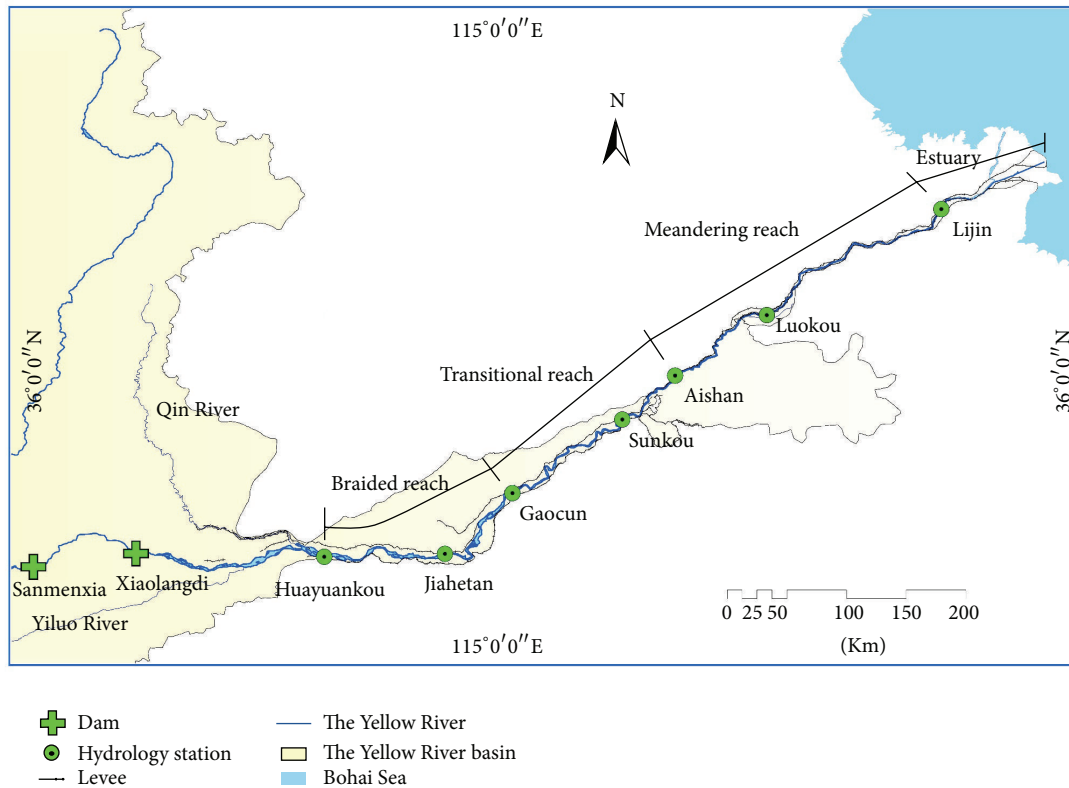


FIGURE 2: Map of the Lower Yellow River.

Gaocun is a typical wandering channel pattern. The lower reach, from Taochengpu to Lijin, is a stable meandering channel pattern. The intervening reach transitions from wandering to meandering. The LYR is a natural alluvial river because of the high suspended sediment load it carries and deposits. According to the observed data, the total deposition volume in the LYR reached about 5.52 billion  $m^3$  during the period from 1950 to 1999, of which 60% was deposited in the wandering reach.

Here, the Huayuankou and Lijin Stations were chosen to validate the effects of the model, because these two stations are representative of typical wandering and meandering reaches, respectively. They have different bankfull characteristics as a function of flow and sediment load.

For Lijin Station in the meandering reach, the bankfull characteristics are easy to determine by observing when the water fills the main channel without overtopping the banks of the floodplain (Figure 3). For Huayuankou Station, cross-sections usually exhibit a compound geometric shape (Figure 4). Given nonstationary flow and sediment discharge, the location of the main channel often shifts laterally, which makes it difficult to define the zone of the main channel and bankfull characteristics in the wandering reach. As before, earlier and later measurements of the cross-section and the upstream and downstream cross-sectional profiles were used for reference to determine the bankfull stage [32].

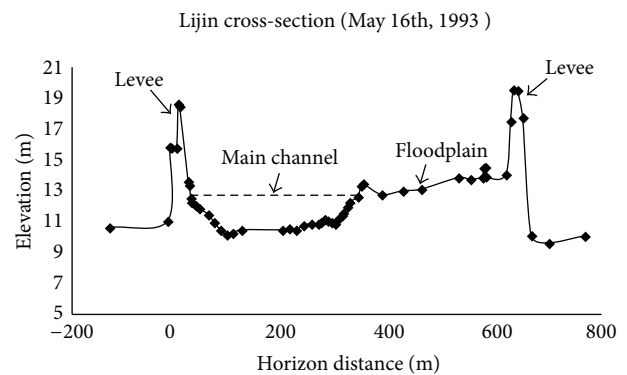


FIGURE 3: Typical cross-sectional profile at Lijin Station.

The deviation of the inner-annual distributions of flow and sediment discharge can cause different channel forms in the LYR. These two chosen reaches had similar annual mean values of flow and sediment discharge, but different annual distributions (Figure 5). The annual mean flow discharge from 1950 to 2002 was  $1248 m^3/s$  at Huayuankou Station and  $1036 m^3/s$  at Lijin Station, while the annual peak flow discharge (daily peak data) was 6014 and  $4713 m^3/s$ , respectively. The annual mean sediment discharge from 1950 to 2002 was  $32 m^3/s$  at Huayuankou Station and  $26 m^3/s$  at Lijin Station,

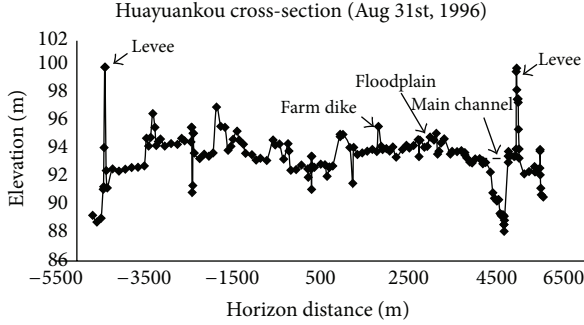


FIGURE 4: Typical cross-sectional profile at Huayuankou Station.

while the annual peak sediment discharge (daily peak data) was 653 and 330  $\text{m}^3/\text{s}$ , respectively.

Using time series analysis, a decreasing trend was detected for the annual mean and daily peak flow and sediment discharge for the two stations over the past 50 years using the Mann-Kendall method [38]. Two significant times marking mutation of the pattern of the annual mean flow discharge were detected at the stations (1969 and 1986) using the Fisher discriminant criterion [39]. The two years were linked to dam construction on the Yellow River for the Liujiaxia and Longyangxia reservoirs.

**2.2. Bankfull Characteristics in Typical Sections.** Figure 6 shows the observed bankfull characteristics (bankfull discharge  $Q_{\text{bf}}$ , bankfull area  $A_{\text{bf}}$ , bankfull width  $B_{\text{bf}}$ , and bankfull depth  $h_{\text{bf}}$ ) at Lijin Station from 1964 to 2000. All of the data were obtained from the measured profile data after the flood season each year. Table 1 shows the correlation matrix. From the figure and table, there are linear relations between  $Q_{\text{bf}}$  and  $A_{\text{bf}}$ ,  $A_{\text{bf}}$  and  $h_{\text{bf}}$ , and  $Q_{\text{bf}}$  and  $A_{\text{bf}}$ . However, the data mining indicated that the bankfull width  $B_{\text{bf}}$  varied from 400 to 600 m. For this, there were no obvious linear relations. Since these bankfull characteristics were all determined by the incoming flow and sediment conditions on a large time scale; there is no coherent geomorphic law to interpret all processes.

The same analysis for Huayuankou in the wandering reach is shown in Figure 7 and Table 2. Nonlinear relations existed more widely here than at Lijin. Except for  $A_{\text{bf}} \sim h_{\text{bf}}$ , none of the other relationships were obviously linear. The channel geometry changed so quickly and markedly that the bankfull width  $B_{\text{bf}}$  varied from 1800 to 3200 m. This showed greater variation and was more nonlinear than in the meandering reach.

### 3. Study Methodology

In previous geomorphic models, channel response to disturbances can be described using nonlinear decay functions, for which the rate law has been most widely used to describe

relaxation paths and recovery times. The rate law takes the form of a negative exponential equation:

$$\frac{dY}{dt} = -\beta(Y - Y_e). \quad (1)$$

Here,  $Y$  is a characteristic parameter of the fluvial system,  $Y_e$  is the asymptotic value of this parameter,  $\beta$  is the decay rate that quantifies how rapidly  $Y$  approaches  $Y_e$ , and  $t$  is the time since the disturbance. Many studies have shown that the rate law can simulate and predict the channel response to disturbances with seasonal or annual data [5, 40–42].

As mentioned above, the rate law is used to illustrate the channel forming macroprocess ( $10^1$ – $10^2$  years) without any physical mechanism. It smoothes the flood details and cannot account for the effects of the deviation of flood events. This paper focuses on the dynamic processes of the channel geometry of alluvial rivers. Bankfull parameters such as the bankfull discharge  $Q_{\text{bf}}$ , area  $A_{\text{bf}}$ , width  $B_{\text{bf}}$ , and depth  $h_{\text{bf}}$  all vary with time. To capture the major characteristics of the fluvial response, but allow lower computational complexity, a quasiequilibrium state was assumed. The temporal variation of the flow discharge and sediment load was distinguished for typical flood events, but the governing equations of flow and sediment transport took the form for steady flows. This suggests an intermediate timescale between the hydrodynamic and geomorphic scales. Above this, the temporal variation is accounted for, but it is neglected below this. A suitable timescale for a large river like the LYR that has a typical flood event of 10 days is 1 day. This can account for the daily variation in the flow and sediment conditions during the flood event.

The cross-sections of the LYR are mostly wide and shallow with 400–4000 m river top widths and 1–5 m river depths. As a result, the wetted perimeter  $p$  (m) can nearly be substituted by the top widths  $B$  (m). The hydraulic radius  $R$  (m) can be expressed as  $R = A/p = A/B = h$ , where  $A$  is the flow area ( $\text{m}^2$ ) and  $h$  (m) is the average river depth expressed by  $h = A/B$ . With the assumption of quasiequilibrium [43, 44], the flow continuity, momentum, sediment transport, and bed deformation equations can be expressed as

$$Q_{\text{bf}} = B_{\text{bf}} h_{\text{bf}} U_{\text{bf}}, \quad (2)$$

$$U_{\text{bf}} = \frac{1}{n} R_{\text{bf}}^{2/3} S^{1/2}, \quad (3)$$

$$CS = k_0 \left( \frac{U_{\text{bf}}^3}{g h_{\text{bf}} \omega} \right)^m, \quad (4)$$

$$(1 - \varphi) \frac{\partial \eta}{\partial t} = -\frac{\partial q_t}{\partial x}, \quad (5)$$

where  $Q_{\text{bf}}$  is the bankfull discharge ( $\text{m}^3/\text{s}$ ),  $B_{\text{bf}}$  is the bankfull channel width,  $h_{\text{bf}}$  is the bankfull channel depth,  $U_{\text{bf}}$  is the bankfull velocity (m/s),  $R_{\text{bf}}$  is the bankfull hydraulic radius (m),  $S$  is the channel slope, and  $n$  is the Manning coefficient determined by the median grain size of the bed material load and channel depth in the form  $n = h^{1/6} / [18.1 + 12.31 \lg(h/D_{65})]$  [45].

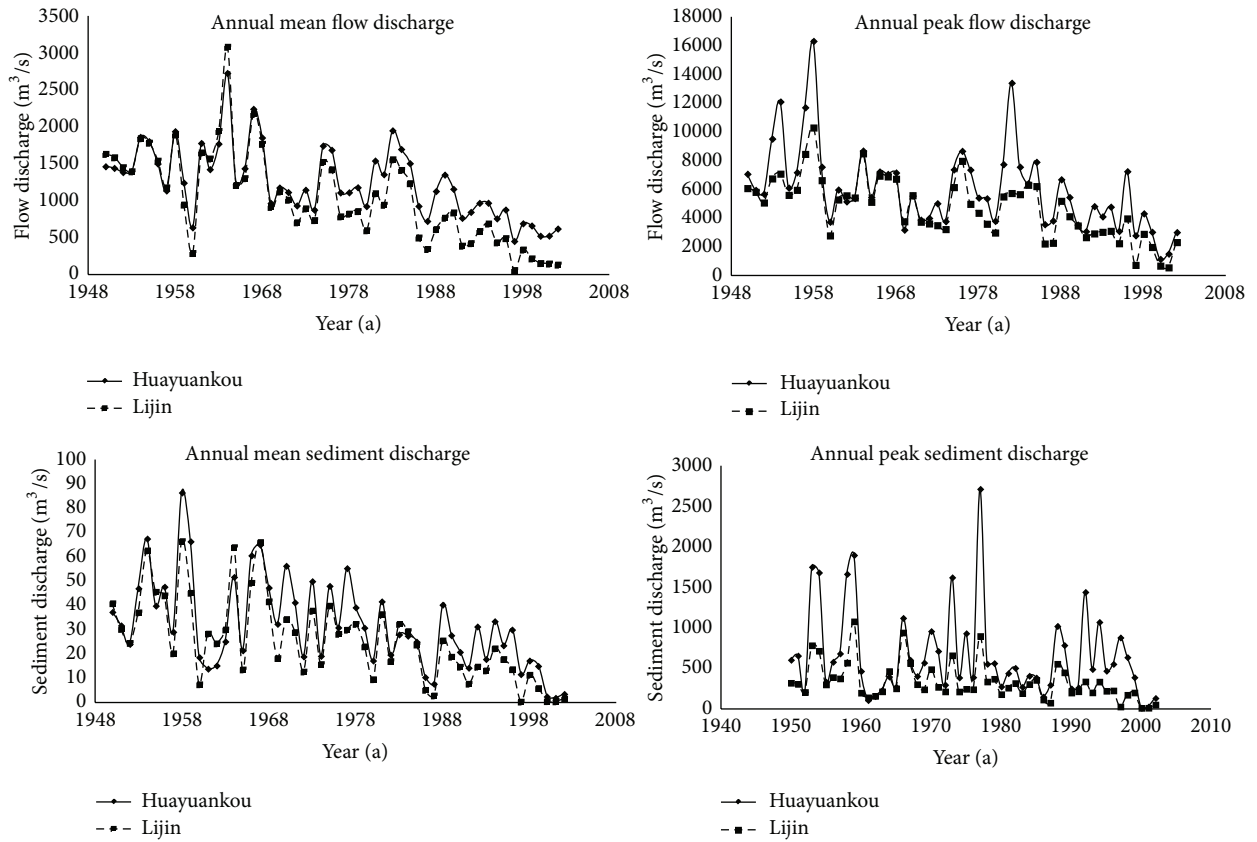


FIGURE 5: Flow and sediment discharge data at Huayuankou and Lijin Stations.

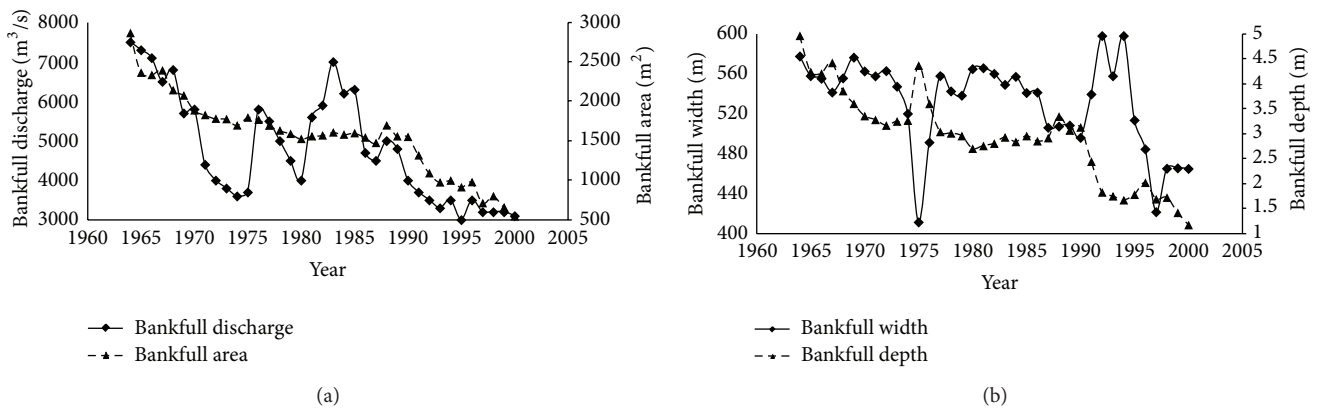


FIGURE 6: Observed bankfull characteristics at Lijin Station: (a) bankfull discharge and area; (b) bankfull width and depth.

TABLE 1: Correlation matrix of the bankfull characteristics at Lijin Station.

	Bankfull discharge	Bankfull area	Bankfull width	Bankfull depth
Bankfull discharge	1	0.80	0.45	0.74
Bankfull area		1	0.44	0.97
Bankfull width			1	0.23
Bankfull depth				1

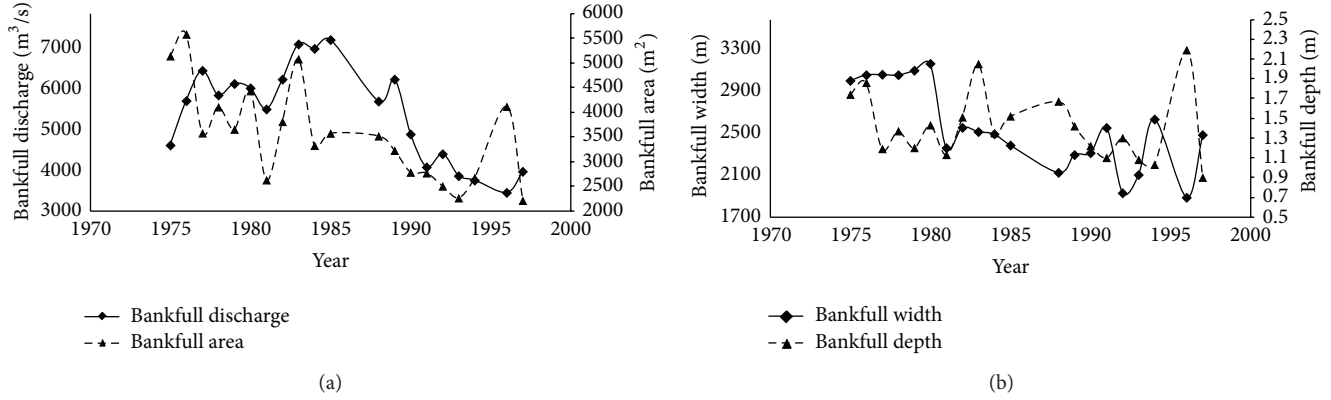


FIGURE 7: Observed bankfull characteristics at Huayuankou Station: (a) bankfull discharge and area; (b) bankfull width and depth.

TABLE 2: Correlation matrix of the bankfull characteristics at Huayuankou Station.

	Bankfull discharge	Bankfull area	Bankfull width	Bankfull depth
Bankfull discharge	1	0.41	0.35	0.23
Bankfull area		1	0.52	0.79
Bankfull width			1	-0.08
Bankfull depth				1

Equation (4) is Zhang Ruijin's sediment-carrying capacity formula [46], which is used widely for the LYR, where  $CS$  is the sediment concentration ( $\text{kg}/\text{m}^3$ ),  $\omega$  is the sediment settling velocity ( $\text{m}/\text{s}$ ) in muddy water, and  $k_0$  and  $m$  are parameters (at Huayuankou Station,  $k_0 = 0.04$  and  $m = 0.92$ ; at Lijin Station,  $k_0 = 0.03$  and  $m = 0.92$ ).  $\varphi$  is the riverbed porosity,  $\eta$  is the bed elevation ( $\text{m}$ ),  $q_t = U_{\text{bf}} h_{\text{bf}} CS$  is the total sediment transport rate in volume per unit stream width ( $\text{m}^2/\text{s}$ ), and  $x$  is the streamwise coordinate. Of these equations, (5) (i.e., the Exner equation) is for unsteady flow, whereas the others are for steady flows. This is consistent with the fact that the adjustment of the channel form takes much longer than that of the flow and sediment conditions.

These four governing equations involve two independent variables,  $Q$  and  $CS$ , but five dependent variables in the bankfull state,  $B_{\text{bf}}$ ,  $h_{\text{bf}}$ ,  $U_{\text{bf}}$ ,  $S_{\text{bf}}$ , and  $\eta$ . On a medium timescale of  $10^0$ - $10^1$  years,  $S$  changes less than  $B_{\text{bf}}$  and  $h_{\text{bf}}$ . As  $S_{\text{bf}}$  is fixed, over long periods of time for a given  $Q$  and  $CS$ , the expected channel cross-section can be obtained in terms of  $B_{\text{bf}}$  and  $h_{\text{bf}}$ .

For an alluvial river like the LYR,  $R_{\text{bf}} \approx h_{\text{bf}}$  when  $B_{\text{bf}} \gg h_{\text{bf}}$ . Under these circumstances, the bankfull depth is

$$\left(\frac{CS}{k_0}\right)^{1/m} g\omega S^{-1.5} = h_{\text{bf}}^{0.5} \left[18.1 + 12.31 \lg\left(\frac{h_{\text{bf}}}{D_{65}}\right)\right]^3. \quad (6)$$

The left-hand side of (6) is calculated from known data, and the right-hand side of the equation is an increasing function

of  $h_{\text{bf}}$ . A trial method can be used to obtain the value of  $h_{\text{bf}}$ . Then,  $B_{\text{bf}}$  and  $U_{\text{bf}}$  can be obtained as

$$U_{\text{bf}} = \left[18.1 + 12.31 \lg\left(\frac{h_{\text{bf}}}{D_{65}}\right)\right] h_{\text{bf}}^{0.5} S^{0.5}, \quad (7)$$

$$B_{\text{bf}} = \frac{Q}{\left[18.1 + 12.31 \lg\left(\frac{h_{\text{bf}}}{D_{65}}\right)\right] h_{\text{bf}}^{1.5} S^{0.5}}.$$

From (6) and (7),  $B_{\text{bf}}$  and  $h_{\text{bf}}$  are determined by the incoming steady flow and sediment discharge. Nevertheless, for alluvial rivers like the LYR, the flow discharge and sediment volume are not steady on intra- or interannual timescales. As a result, series of  $B_{\text{bf}}$  and  $h_{\text{bf}}$  should be expected instead of a fixed value. In other words, a dynamic equation including  $\partial B_{\text{bf}}/\partial t$  and  $\partial h_{\text{bf}}/\partial t$  is needed. This is the key problem to be addressed in this paper.

We rewrite (5) in integral form

$$(1 - \varphi) \int_0^L \frac{\partial A_{\text{bf}}}{\partial t} dx = (1 - \varphi) L \frac{\partial A_{\text{bf}}}{\partial t} = \int_0^L \frac{\partial Q_s}{\partial x} dx, \quad (8)$$

where  $L$  is the length of the river reach and  $Q_s = Bq_t$  is the volumetric sediment transport rate ( $\text{m}^3/\text{s}$ ). With the assumption of a rectangular channel, we have

$$\frac{1}{A_{\text{bf}}} \frac{\partial A_{\text{bf}}}{\partial t} = \frac{1}{h_{\text{bf}}} \frac{\partial h_{\text{bf}}}{\partial t} + \frac{1}{B_{\text{bf}}} \frac{\partial B_{\text{bf}}}{\partial t}. \quad (9)$$

For rivers in a stationary state, the relationship between the geometrical dimension (i.e.,  $B$  and  $h$ ) and water discharge  $Q$  that passes through this cross-section takes the form [8, 47]

$$B_{\text{bf}} = aQ_{\text{bf}}^\alpha, \quad h_{\text{bf}} = bQ_{\text{bf}}^\beta, \quad (10)$$

where  $a$  and  $b$  are coefficients that vary with the characteristics of the river basin. For the statistical results of most alluvial rivers across the world [8],  $\alpha$  and  $\beta$  are exponents, usually with  $\alpha = 0.5$  and  $\beta = 0.33$ .

For a nonstationary state,  $Q_{bf}$  is a time-dependent variable, and steady values of  $B_{bf}$  and  $h_{bf}$  do not exist. Nonetheless, the relations between bankfull channel geometry and flow discharge still work as

$$B_{bf}(t) = aQ_{bf}(t)^\alpha, \quad h_{bf}(t) = bQ_{bf}(t)^\beta. \quad (11)$$

A plot of the channel response processes is shown in Figure 8, which shows a theoretical situation where the change of water occurs by skipping from one value to another and the channel geometry parameters ( $B_{bf}$  or  $h_{bf}$ ) change synchronously. Nevertheless, a process connects the past bankfull values to the current ones. In this process, the value of  $B$  or  $h$  is neither the past bankfull value nor the current one. It is also a bankfull value including two impact input processes: the past flow process and current one. Here, we sought a rule that describes the transition between the two stable states.

Equation (11) is differentiated at time  $t$

$$\frac{\partial B_{bf}}{\partial t} = a\alpha Q_{bf}^{\alpha-1} \frac{\partial Q_{bf}}{\partial t}, \quad \frac{\partial h_{bf}}{\partial t} = b\beta Q_{bf}^{\beta-1} \frac{\partial Q_{bf}}{\partial t}, \quad (12)$$

leading to

$$\frac{1}{\alpha B_{bf}} \frac{\partial B_{bf}}{\partial t} = \frac{1}{\beta h_{bf}} \frac{\partial h_{bf}}{\partial t}. \quad (13)$$

The final form is

$$\begin{aligned} \frac{1}{B_{bf}} \frac{\partial B_{bf}}{\partial t} &= \frac{\alpha}{\alpha + \beta} \frac{1}{A_{bf}} \frac{\partial A_{bf}}{\partial t}, \\ \frac{1}{h_{bf}} \frac{\partial h_{bf}}{\partial t} &= \frac{\beta}{\alpha + \beta} \frac{1}{A_{bf}} \frac{\partial A_{bf}}{\partial t}. \end{aligned} \quad (14)$$

The computational model in a reach of the LYR is shown in Figure 9. There, inlet and outlet data appear from the entrance and exit stations of the reach.  $CS_0$  and  $CS$  are the sediment transport capacity ( $\text{kg}/\text{m}^3$ ) of the two stations;  $Q$  is the flow discharge of the reach ( $\text{m}^3/\text{s}$ ),  $D_{65}$  is the grain size of the bed material load in the 65% range (mm), and  $L$  is the length of the reach (m).

## 4. Results and Discussion

**4.1. Simulation Results.** From Jinan Station to the Lijin Station, the model uses the daily water and sediment discharge data from the 1964 to 2000: the bed slope  $S = 0.0001$ ,  $\gamma = 9800 \text{ kg}/(\text{m}^2 \cdot \text{s}^2)$ , and  $D_{65}$  is observed and changed with time every year as shown in Table 3. The simulation results are shown in Figure 10.

Figure 10 shows that two types of year cause nonnegligible errors. The first type is the years with low flow discharge and high sediment load, such as 1973 and 1997. In 1973, the annual sediment load at Lijin Station was 1.2 billion tons per

TABLE 3: Grain size of  $D_{65}$  at Lijin and Huayuankou Stations.

Year	Huayuankou/mm	Lijin/mm
1964	0.009	0.014
1965	0.027	0.014
1966	0.015	0.015
1967	0.02	0.018
1968	0.027	0.021
1969	0.016	0.009
1970	0.018	0.012
1971	0.02	0.017
1972	0.02	0.019
1973	0.018	0.018
1974	0.019	0.021
1975	0.021	0.026
1976	0.015	0.023
1977	0.019	0.014
1978	0.018	0.016
1979	0.016	0.016
1980	0.018	0.017
1981	0.018	0.027
1982	0.018	0.023
1983	0.022	0.029
1984	0.022	0.021
1985	0.023	0.021
1986	0.018	0.012
1987	0.015	0.008
1988	0.02	0.015
1989	0.024	0.018
1990	0.018	0.015
1991	0.017	0.016
1992	0.028	0.016
1993	0.022	0.021
1994	0.029	0.018
1995	0.024	0.022
1996	0.022	0.02
1997	0.027	0.016
1998	0.021	0.021
1999	0.02	0.012
2000	0.005	0.029

year or 50% more than the mean value in the past 50 years. The annual flow volume was 28.15 billion  $\text{m}^3$  per year or 10% less than the mean value in the past 50 years. In 1997, the annual sediment load at Lijin Station was 0.016 billion tons per year or 98% less than the mean value in the past 50 years. The annual flow volume was 1.86 billion  $\text{m}^3$  per year, with 227 days in the zero-flow state. In these years, deposition along the river occurred more heavily at the outlet. This was the main reason why the observed bankfull width was reduced and the calculated value was not. The second type was years with overflow events, such as what occurred in 1967 and 1988. In 1967, the maximum daily discharge was  $8510 \text{ m}^3/\text{s}$  and the observed bankfull discharge (after the flood

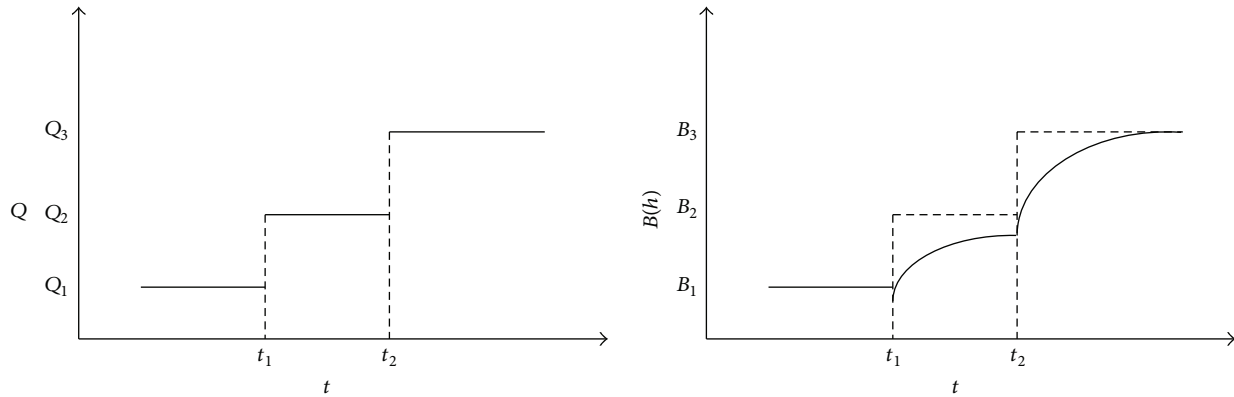


FIGURE 8: Channel response processes for the change of water and sediment flow.

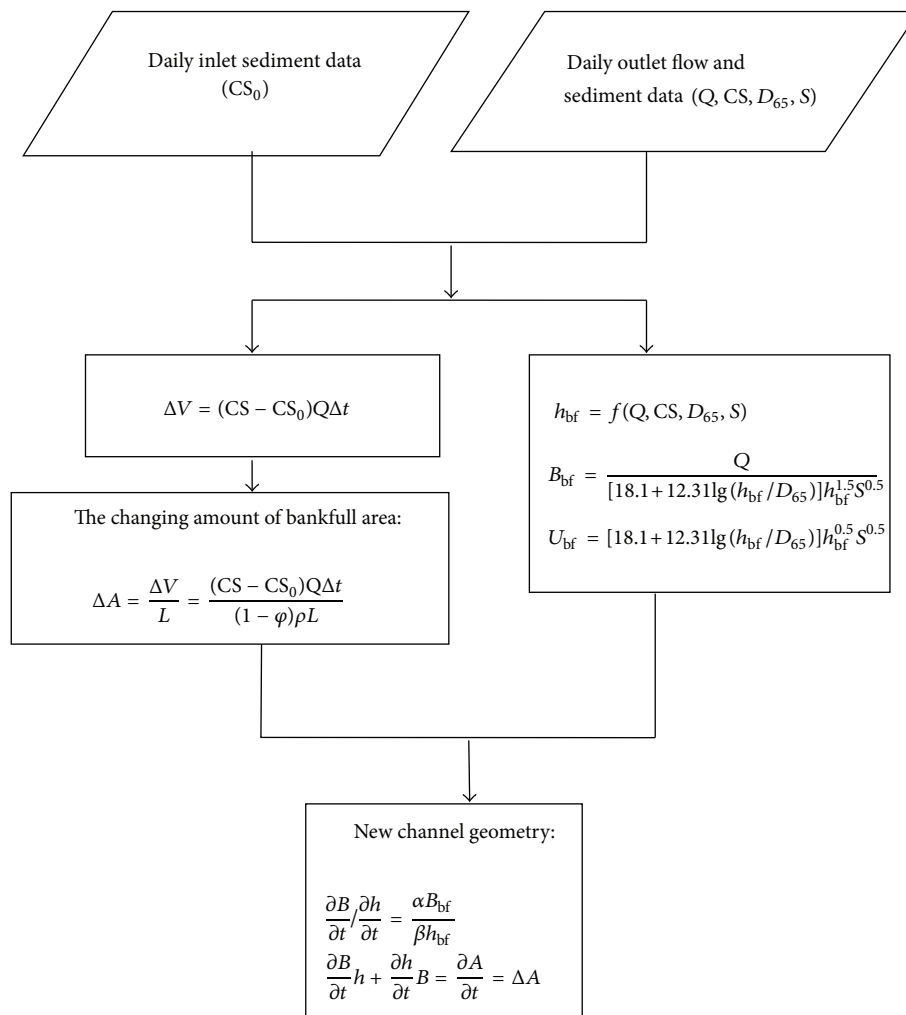


FIGURE 9: Computational process of the bankfull area computational model.

season) was 7500 m<sup>3</sup>/s. In 1988, the maximum daily discharge was 5220 m<sup>3</sup>/s and the observed bankfull discharge (after the flood season) was 5000 m<sup>3</sup>/s. However, overbank flood events were less important than the larger sediment load and smaller flow volume from the error analysis at Lijin Station. One

explanation for the smaller impact might be the fact that the overbank flood volume was not much larger than the bankfull flood at the river outlet.

The daily water and sediment discharge data for Xiaolangdi and Huayuankou Stations from 1976 to 1997 was

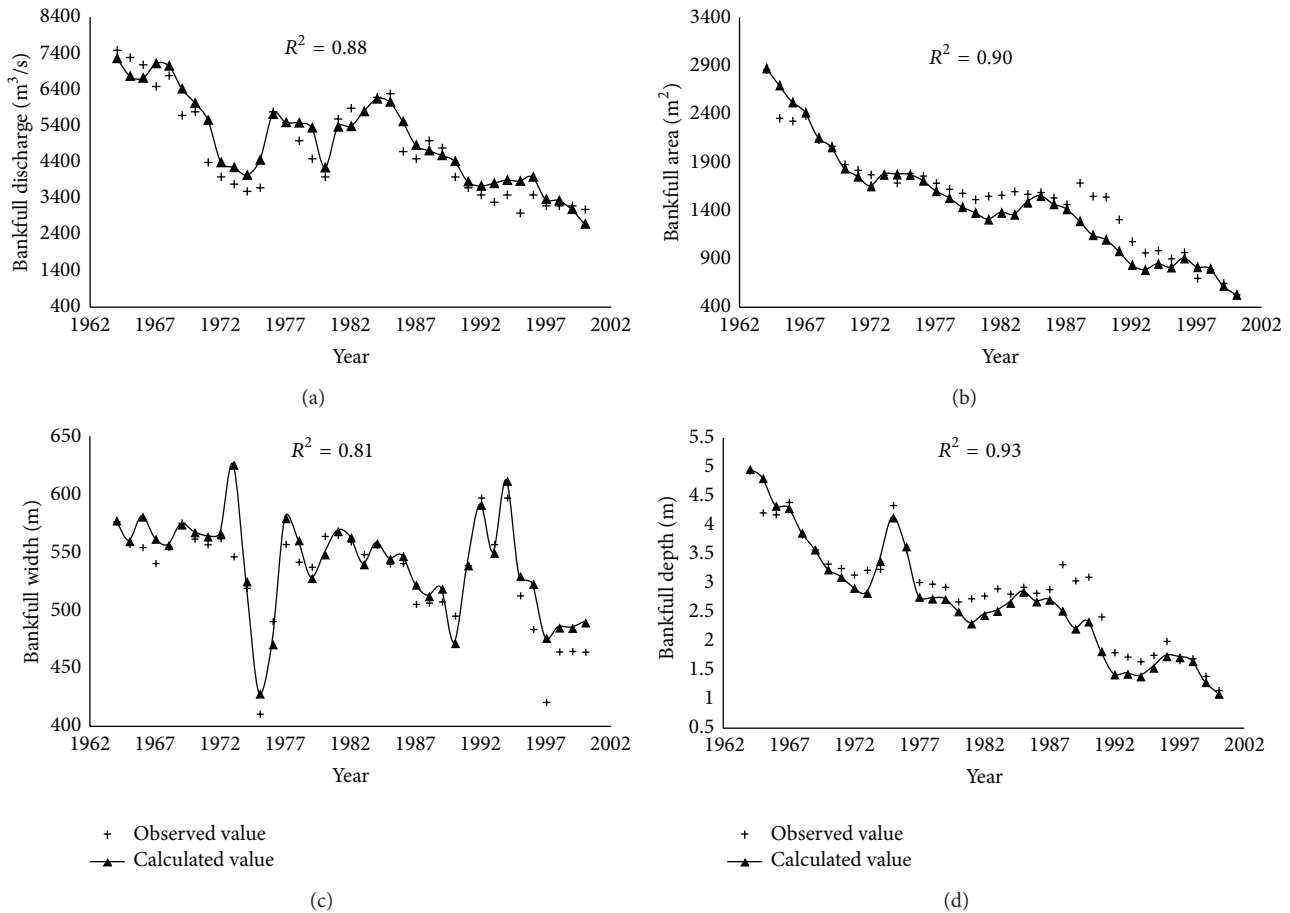


FIGURE 10: Bankfull computational results at Lijin Station for 38 years: bankfull (a) discharge; (b) area; (c) width; and (d) depth.

used in the model, together with the daily water discharge data of Heishiguan and Wuzhi Stations. The simulation results are shown in Figure 11.

The calculated errors at Huayuankou station were more obvious than those at Lijin station. Besides the first type, which included 1987 and 1992, the second type, which included 1976 ~ 1977, 1981 ~ 1983, 1988, and 1996, had more impact on the errors. 1981 ~ 1983 may be taken as an example: the max daily discharge was 7760, 13,400, and 7580 m<sup>3</sup>/s, respectively, and the bankfull discharge (after the flood season) was 5320, 6000, and 6800 m<sup>3</sup>/s. Three years of overbank flood events caused obvious river width expansion, which the methods in this paper cannot reflect.

From Figures 10 and 11, however, the calculated values still agree well with the observed values ( $R^2 > 0.7$ ). This shows that the assumptions and methods adopted in this model are reasonable in some sense.

#### 4.2. Accuracy Impact Factors for Simulations

4.2.1. *Lateral Inflow.* Two tributaries in the Xiaolangdi-Huayuankou reach and the Yiluo and Qin Rivers affected the flow and sediment discharge in the reach. Given the lack of daily sediment concentration data, a simplified study is required.

According to the statistical data from 1960 to 1996, the annual average sediment discharge of the Yiluo River (Heishiguan station) is  $0.092 \times 10^8 t$ , accounting for 0.9% of that in the main stream of the LYR. The annual average sediment discharge of the Qin River (Wuzhi station) is  $0.039 \times 10^8 t$ , accounting for 0.4% of that in the main stream of the LYR. Therefore, these two rivers are considered to be clear in the calculation for this section. This simplification might affect the accuracy in some years when the sediment load cannot be ignored.

4.2.2. *Overbank Flood.* Differences exist in the scour and silting mechanisms between overbank and normal floods. Scouring occurs when the water level rises, while silting occurs when the water level falls. Floodplain silting with channel scouring is common during overbank flood periods in the LYR.

For overbank floods with a low sediment load, for example, the flood that occurred from July 31 to August 8, 1982, the peak discharge at Huayuankou station was 15,300 m<sup>3</sup>/s and the average sediment concentration was 67 kg/m<sup>3</sup>. This caused 0.217 billion tons of sediment to be deposited in the floodplain and 0.15 billion tons to be scoured from the main channel in the Huayuankou-Aishan reach.

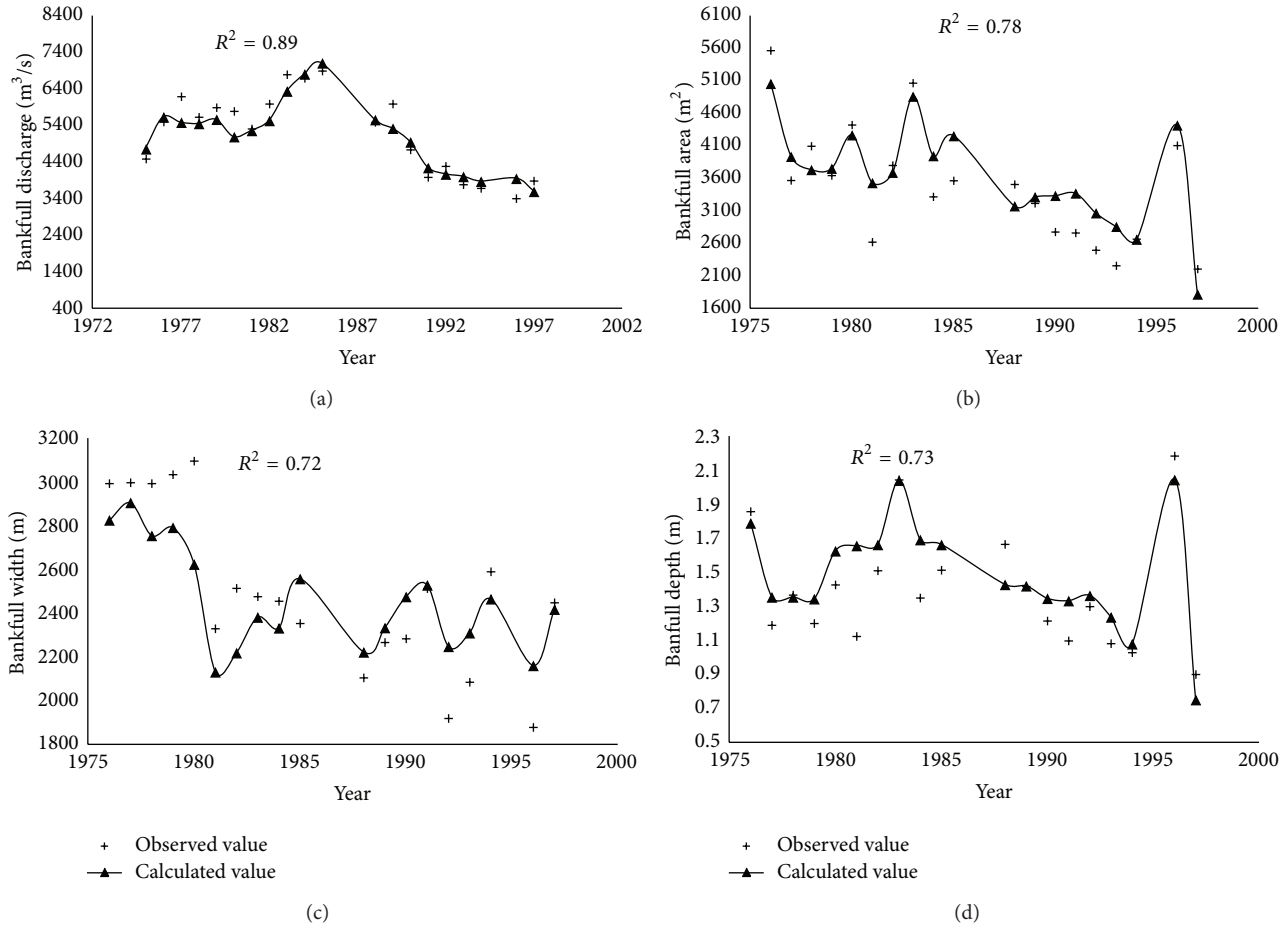


FIGURE 11: Bankfull computational results at Huayankou station for 22 years: bankfull (a) discharge; (b) area; (c) width; and (d) depth.

For overbank floods with high sediment load, for example, the flood that occurred in 1977, the peak discharge at Huayankou station was  $10,800 \text{ m}^3/\text{s}$  and the average sediment concentration was  $437 \text{ kg}/\text{m}^3$ . This caused the amount of sediment deposited in the main channel to be three times that deposited in the floodplain in the Huayankou-Aishan reach.

Consequently, the methods used in this paper are not suitable for overbank situations. The key issue is that the distribution of resistance in the floodplain and main channel is unknown. A simplified statistical method is used to deal with overbank flood events. For flows with a high sediment concentration, sediment is deposited all along the river, and a distributing coefficient  $K = V_1/V_2$  reflecting the deposition ratio between the floodplain and main channel is calibrated against all years. Here,  $V_1$  is the deposition volume in the main channel ( $\text{m}^3$ ) and  $V_2$  is in the floodplain.

For flows with a high sediment concentration, sediment is deposited all along the river ( $K = 0.32$ ), while for flows with a low sediment concentration, the main channel is scoured, the floodplain is deposited, and  $K = -0.51$ . According to statistical data, the criterion for high sediment loads is  $300 \text{ kg}/\text{m}^3$ .

**4.2.3. Channel Shape of a Uniform Reach.** Here, the chosen river reach is assumed to be uniform so that the depositing or eroding sediment volume can be distributed along the reach evenly. This assumption is much more acceptable in the Jinan-Lijin reach than in the Xiaolangdi-Huayankou reach, because there is a valley channel beyond Xiaolangdi Station that affects the sediment distribution along the Xiaolangdi-Huayankou reach. This might be an important impact factor for the accuracy of the model applied to Huayankou station.

## 5. Conclusions

- (1) Based on the equations for stable alluvial rivers, namely, the Exner equation, flow continuity, the momentum, and sediment concentration conservation equations and assuming that the riverbed slope is constant on middle timescales ( $10^0$ - $10^1$  years), we found stationary geomorphic relations for time-varying fluvial processes. We obtained a time-dependent relation for the channel geometry given nonstationary alluvial processes.
- (2) The final solutions from the equations for stable alluvial rivers simply reflect the adjusted direction

of channel geometry. The adjusted magnitude of the hydraulic geometry each day is determined by the daily input of depositing or eroding sediment volumes. The direction and magnitude give the final channel shape.

- (3) Using daily flow and sediment data to determine the adjustment direction and magnitude, the variation in the bankfull characteristics for Lijin and Huayuankou Stations in the LYR were calculated. The final results agreed closely ( $R^2 > 0.7$ ) with the observed values. This implies that the assumptions are acceptable and the method is applicable for the reservoir and channel regulation in the LYR.
- (4) Compared with the rate-law and hydrodynamic methods, the proposed method enables multiple dependent variables and the input of detailed hydrological data for long-term simulations. However, because of those assumptions for simplification, the model we provided also has some limitations. Firstly, it cannot be applied to a dramatic time-varying fluvial procedure like an overbank flow or a hyperconcentration flood, only fitting for a quasisteady fluvial process. Secondly, the time-step of one day is still large for a physics-based model which smooths the deviation of inner-daily flood process. Thirdly, the key equation in this model is derived by the experiential relations between channel geometry and hydraulic relations, which is not verified in theory. These limitations are the main sources of the model error and will be our next work in the future.

## Conflict of Interests

The authors declare that there is no conflict of interests regarding the publication of this paper.

## Acknowledgments

This study was supported financially by the China Ministry of Science and Technology through the Key Project in the National Science & Technology Pillar Program in the Twelfth Five-year Plan Period of China (Grant no. 2012BAB02B02). It was supported by the Open Program Fund of MWR Key Laboratory of Yellow River Sedimentation of the Yellow River Conservancy Commission.

## References

- [1] G. Lacey, "Flow in alluvial channels with sandy mobile beds," *Proceedings of the Institute of Civil Engineers*, vol. 11, pp. 145–164, 1958.
- [2] D. B. Simons and M. L. Albertson, "Uniform water conveyance channels in alluvial materials," *Journal of the Hydraulics Division*, vol. 86, pp. 33–71, 1960.
- [3] J. X. Xu, "The water fluxes of the Yellow River to the sea in the past 50 years, in response to climate change and human activities," *Environmental Management*, vol. 35, no. 5, pp. 620–631, 2005.
- [4] W. L. Graf, "The rate law in fluvial geomorphology," *American Journal of Science*, vol. 277, no. 2, pp. 178–191, 1977.
- [5] G. P. Williams and M. G. Wolman, *Downstream Effects of Dams on Alluvial Rivers*, Geological Survey Professional Paper no. 1286, U.S. Government Printing Office, Washington, DC, USA, 1984.
- [6] A. Simon, "A model of channel response in disturbed alluvial channels," *Earth Surface Processes & Landforms*, vol. 14, no. 1, pp. 11–26, 1989.
- [7] C. E. Thorn and M. R. Welford, "The equilibrium concept in geomorphology," *Annals of the Association of American Geographers*, vol. 84, no. 4, pp. 666–696, 1994.
- [8] D. Knighton, *Fluvial Forms and Processes: A New Perspective*, Arnold, London, UK, 1998.
- [9] N. Surian and M. Rinaldi, "Morphological response to river engineering and management in alluvial channels in Italy," *Geomorphology*, vol. 50, no. 4, pp. 307–326, 2003.
- [10] M. P. Mosley, "Semi-determinate hydraulic geometry of river channels, South Island, New Zealand," *Earth Surface Processes & Landforms*, vol. 6, no. 2, pp. 127–137, 1981.
- [11] C. Gippel, "Changes in stream channel morphology at tributary junctions, Lower Hunter Valley, New South Wales," *Australian Geographical Studies*, vol. 28, no. 2, pp. 291–307, 1985.
- [12] J. E. Pizzuto, "Flow variability and the bankfull depth of sand-bed streams of the American Midwest," *Earth Surface Processes & Landforms*, vol. 11, no. 4, pp. 441–450, 1986.
- [13] G. L. Heritage, L. J. Broadhurst, and A. L. Birkhead, "The influence of contemporary flow regime on the geomorphology of the Sabie River, South Africa," *Geomorphology*, vol. 38, no. 3–4, pp. 197–211, 2001.
- [14] C. Groves and J. Meiman, "Weathering, geomorphic work, and karst landscape evolution in the Cave City groundwater basin, Mammoth Cave, Kentucky," *Geomorphology*, vol. 67, no. 1–2, pp. 115–126, 2005.
- [15] B. Wu, G. Wang, and J. Xia, "Case study: delayed sedimentation response to inflow and operations at Sanmenxia Dam," *Journal of Hydraulic Engineering*, vol. 133, no. 5, pp. 482–494, 2007.
- [16] B. Wu, G. Wang, J. Xia, X. Fu, and Y. Zhang, "Response of bankfull discharge to discharge and sediment load in the Lower Yellow River," *Geomorphology*, vol. 100, no. 3–4, pp. 366–376, 2008.
- [17] B. Wu, J. Xia, X. Fu, Y. Zhang, and G. Wang, "Effect of altered flow regime on bankfull area of the Lower Yellow River, China," *Earth Surface Processes & Landforms*, vol. 33, no. 10, pp. 1585–1601, 2008.
- [18] B. Wu, S. Zheng, and C. R. Thorne, "A general framework for using the rate law to simulate morphological response to disturbance in the fluvial system," *Progress in Physical Geography*, vol. 36, no. 5, pp. 575–597, 2012.
- [19] T. J. Pietsch and G. C. Nanson, "Bankfull hydraulic geometry; the role of in-channel vegetation and downstream declining discharges in the anabranching and distributary channels of the Gwydir distributive fluvial system, southeastern Australia," *Geomorphology*, vol. 129, no. 1–2, pp. 152–165, 2011.
- [20] S. Zheng, B. S. Wu, C. R. Thorne, and A. Simon, "Morphological evolution of the North Fork Toutle River following the eruption of Mount St. Helens, Washington," *Geomorphology*, vol. 208, pp. 102–116, 2014.
- [21] A. D. Howard, "Equilibrium and time scales in geomorphology: application to sand-bed alluvial streams," *Earth Surface Processes & Landforms*, vol. 7, no. 4, pp. 303–325, 1982.

- [22] B. Yu and M. G. Wolman, "Some dynamic aspects of river geometry," *Water Resources Research*, vol. 23, no. 3, pp. 501–509, 1987.
- [23] C. Leon, P. Y. Julien, and D. C. Baird, "Case study: equivalent widths of the middle Rio Grande, New Mexico," *Journal of Hydraulic Engineering*, vol. 135, no. 4, pp. 306–315, 2009.
- [24] Y. Ma, H. Q. Huang, G. C. Nanson, Y. Li, and W. Yao, "Channel adjustments in response to the operation of large dams: the upper reach of the lower Yellow River," *Geomorphology*, vol. 147–148, pp. 35–48, 2012.
- [25] E. Pasche and G. Rouvé, "Overbank flow with vegetatively roughened flood plains," *Journal of Hydraulic Engineering*, vol. 111, no. 9, pp. 1262–1278, 1985.
- [26] S. E. Darby and C. R. Thorne, "Predicting stage-discharge curves in channels with bank vegetation," *Journal of Hydraulic Engineering*, vol. 122, no. 10, pp. 583–586, 1996.
- [27] E. Mosselman, "Morphological modeling of rivers with erodible banks," *Hydrological Processes*, vol. 12, no. 8, pp. 1357–1370, 1998.
- [28] S. E. Darby, "Effect of riparian vegetation on flow resistance and flood potential," *Journal of Hydraulic Engineering*, vol. 125, no. 5, pp. 443–454, 1999.
- [29] N. Rütther and N. R. B. Olsen, "Three-dimensional modeling of sediment transport in a narrow 90° channel bend," *Journal of Hydraulic Engineering*, vol. 131, no. 10, pp. 917–920, 2005.
- [30] T. Helmiö, "Unsteady 1D flow model of compound channel with vegetated floodplains," *Journal of Hydrology*, vol. 269, no. 1–2, pp. 89–99, 2002.
- [31] G. Wang, J. Xia, and B. Wu, "Numerical simulation of longitudinal and lateral channel deformations in the braided reach of the Lower Yellow River," *Journal of Hydraulic Engineering*, vol. 134, no. 8, pp. 1064–1078, 2008.
- [32] J. Xia, B. Wu, G. Wang, and Y. Wang, "Estimation of bankfull discharge in the Lower Yellow River using different approaches," *Geomorphology*, vol. 117, no. 1–2, pp. 66–77, 2010.
- [33] D. Jia, X. Shao, H. Wang, and G. Zhou, "Three-dimensional modeling of bank erosion and morphological changes in the Shishou bend of the middle Yangtze River," *Advances in Water Resources*, vol. 33, no. 3, pp. 348–360, 2010.
- [34] Z.-H. Sun, Y.-T. Li, Y. Huang, and K.-C. Gao, "Fluvial process of sandbars and shoals in branching channels of the middle Yangtze River," *Journal of Hydraulic Engineering*, vol. 42, no. 12, pp. 1398–1406, 2011.
- [35] D. Motta, J. D. Abad, E. J. Langendoen, and M. H. Garcia, "A simplified 2D model for meander migration with physically-based bank evolution," *Geomorphology*, vol. 163–164, pp. 10–25, 2012.
- [36] K. Asahi, Y. Shimizu, J. Nelson, and G. Parker, "Numerical simulation of river meandering with self-evolving banks," *Journal of Geophysical Research: Earth Surface*, vol. 118, no. 4, pp. 2208–2229, 2013.
- [37] B. Wu, G. Wang, J. Ma, and R. Zhang, "Case study: river training and its effects on fluvial processes in the Lower Yellow River, China," *Journal of Hydraulic Engineering*, vol. 131, no. 2, pp. 85–96, 2005.
- [38] Z. X. Xu, K. Takeuchi, and H. Ishidaira, "Monotonic trend and step changes in Japanese precipitation," *Journal of Hydrology*, vol. 279, no. 1–4, pp. 144–150, 2003.
- [39] D. S. Wilks, *Statistical Methods in the Atmospheric Sciences*, Academic Press, Oxford, UK, 3rd edition, 2011.
- [40] J. M. Hooke, "River channel adjustment to meander cutoffs on the River Bollin and River Dane, northwest England," *Geomorphology*, vol. 14, no. 3, pp. 235–253, 1995.
- [41] A. Simon and C. R. Thorne, "Channel adjustment of an unstable coarse-grained stream: opposing trends of boundary and critical shear stress, and the applicability of extremal hypotheses," *Earth Surface Processes & Landforms*, vol. 21, no. 2, pp. 155–180, 1996.
- [42] G. A. Richard, *Quantification and prediction of lateral channel adjustments downstream from Cochiti Dam [Ph.D. thesis]*, Colorado State University, Rio Grande, NM, USA, 2001.
- [43] G. V. Wilkerson and G. Parker, "Physical basis for quasi-universal relationships describing bankfull hydraulic geometry of sand-bed rivers," *Journal of Hydraulic Engineering*, vol. 137, no. 7, pp. 739–753, 2011.
- [44] W. K. Annable, C. C. Watson, and P. J. Thompson, "Quasi-equilibrium conditions of urban gravel-bed stream channels in southern Ontario, Canada," *River Research and Applications*, vol. 28, no. 3, pp. 302–325, 2012.
- [45] C. H. Hu, *Complex Channel Response and Variation of 13 Flow and Sediment Processes of the Yellow River*, Science Press, Beijing, China, 1st edition, 2005.
- [46] W. Zhang, G. Lu, and X. Pan, "The analysis and discussion of sediment transport capacity formula," *Applied Mechanics and Materials*, vol. 188, pp. 259–263, 2012.
- [47] E. D. Andrews, "Effective and bankfull discharges of streams in the Yampa River basin, Colorado and Wyoming," *Journal of Hydrology*, vol. 46, no. 3–4, pp. 311–330, 1980.

## Research Article

# River Flow Estimation from Upstream Flow Records Using Support Vector Machines

Halil Karahan,<sup>1</sup> Serdar Iplikci,<sup>2</sup> Mutlu Yasar,<sup>1</sup> and Gurhan Gurarslan<sup>1</sup>

<sup>1</sup> Department of Civil Engineering, Faculty of Engineering, Pamukkale University, 20070 Denizli, Turkey

<sup>2</sup> Department of Electrical and Electronics Engineering, Faculty of Engineering, Pamukkale University, 20070 Denizli, Turkey

Correspondence should be addressed to Halil Karahan; [hkarahan@pau.edu.tr](mailto:hkarahan@pau.edu.tr)

Received 28 January 2014; Revised 22 May 2014; Accepted 6 June 2014; Published 30 June 2014

Academic Editor: Guohe Huang

Copyright © 2014 Halil Karahan et al. This is an open access article distributed under the Creative Commons Attribution License, which permits unrestricted use, distribution, and reproduction in any medium, provided the original work is properly cited.

A novel architecture for flood routing model has been proposed and its efficiency is validated on several problems by employing support vector machines. The architecture is designed by including the inputs and observed and calculated outflows from the previous time step output. Whole observed data have been used for determining the model parameters in the heuristic methods given in the literature, which constitutes the major disadvantage of the existing approaches. Moreover, using the whole data for training may lead to overtraining problem that causes overfitting of estimations and data. Therefore, in this study, 60–90% of the data are randomly selected for training and then the remaining data are used for validation. In order to take the effects of the measurement errors into consideration, the data are corrupted by some additive noise. The results show that the proposed architecture improves the model performance under noisy and missing data conditions and that support vector machines can be powerful alternative in flood routing modeling.

## 1. Introduction

Flood routing is important in the design of flood protection measures in order to estimate how the proposed measures will affect the behavior of flood waves in rivers so that adequate protection and economic solutions can be found [1]. Flood routing models may be classified as either hydrologic or hydraulic. The hydraulic models solve the Saint-Venant equations by using a numerical method such as finite difference or finite element methods. A great deal of studies based on hydraulic models was developed by various researchers for flood routing [2–8]. These models require the measurement of flow depth and discharges. If detailed topographical surveys of channel cross-sections and roughness at close intervals are not available, hydraulic models are not suitable to serve the purpose of flood routing. In this case, hydrologic models may be used because they can cope with sparse spatial data [9].

Hydrologic models are based on the storage continuity equation and another equation which usually expresses the storage volume as a linear or nonlinear function of inflow and outflow discharges. The Muskingum method is the

most widely used hydrologic flood routing method owing to its simplicity [10]. Many researchers made studies on the parameter estimation of Muskingum flood routing models [11–14]. Performances of the Muskingum models depend on the selection of the appropriate storage equation and the optimal parameter estimation of these models. Even if the parameters of storage equation are determined as optimum, every flood event may not be adequately represented. In particular, this problem occurs in a flood event containing more than one peak and/or having substantially lateral flow.

In order to overcome this problem, data-driven flood routing models based on support vector machines (SVM) need to be developed. SVM is based on statistical learning theory and structural risk minimization principle and can solve any regression problems without getting stuck into local minima. They achieve the global solution by transforming the regression problem into a quadratic programming (QP) problem and then solving it by a QP solver. Finding global solution and possessing higher generalization capability constitute the major advantages of the SVM algorithms over other regression techniques [15]. In the last decade, SVM-based algorithms have been developed very rapidly and have

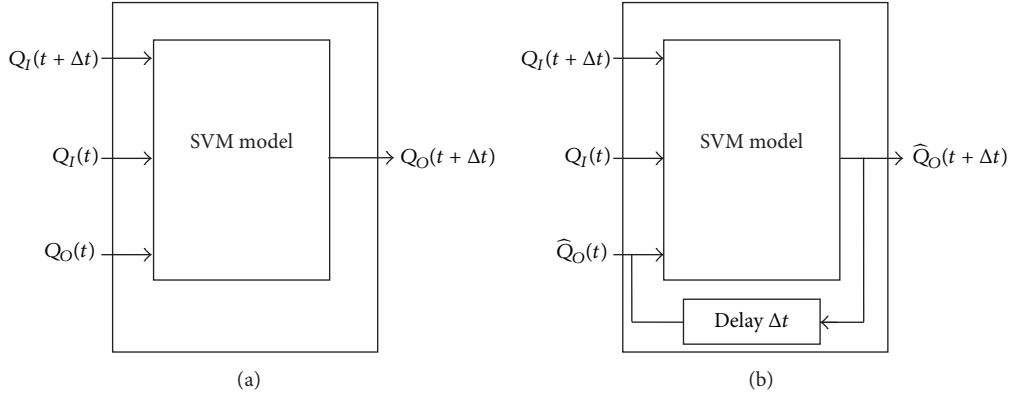


FIGURE 1: (a) Training phase and (b) prediction phase.

been applied to many areas [16, 17]. In particular, the SVM have been used for modeling and prediction purposes for solving some problems in the hydrology area of research and application [18–29].

The fact that the whole observed data has been used for determining the model parameters in the abovementioned heuristic methods constitutes the major disadvantage of these approaches. This may lead to overtraining problem that degrades generalization capability [34]. In order to prevent overtraining, some part of the data is used for training and the remaining part is spared for validation. Thus, in this study, 60–90% of the data are randomly selected for training (for determining model parameters) and then the remaining unseen data are used for validation. Therefore, in this study, novel model architecture has been proposed and its efficiency is validated on several problems. This is organized as follows.

In the next section, first, the proposed training and prediction procedures are introduced and then the training algorithm is explained in detail for SVM in the following subsection. In Section 3, the three numerical applications are investigated to show the efficiency of the proposed method by comparing SVM to other methods when all data are used for training and also to each other when only some portion of the data is used for training. The simulation results are discussed in Section 4.

## 2. Model Development

In this study, we have employed SVM in flood routing modeling for prediction of its future behavior. For this purpose, as can be seen in Figure 1(a), an SVM model of the flood routing is obtained in the training phase by using a training set  $T$  as given by

$$T = \{Q_I(t + k\Delta t), Q_I(t + (k-1)\Delta t), Q_O(t + (k-1)\Delta t); Q_O(t + k\Delta t)\}_{k=1}^{k=N}, \quad (1)$$

where  $Q_I(t)$  and  $Q_O(t)$  are the measured input and output flow rates at time  $t$ , respectively,  $\Delta t$  is the time interval between the successive measurements, and  $N$  is the number of training data. For sake of the simplicity, the data set  $T$  can be represented more compactly as  $T = \{\mathbf{x}_k; y(k)\}_{k=1}^{k=N}$ , where

$\mathbf{x}_k \in X \subseteq \mathfrak{R}^3$  is the  $k$ th input data point in the input space and  $y(k) \in Y \subseteq \mathfrak{R}$  is the corresponding output value; that is,

$$\mathbf{x}_k [Q_I(t + k\Delta t), Q_I(t + (k-1)\Delta t), Q_O(t + (k-1)\Delta t)]^T; \quad y(k) = Q_O(t + k\Delta t). \quad (2)$$

In the modeling phase, to obtain a model that represents the relationship between the input and output data points is desired. The training data set  $T$  is to be used to obtain an approximate model of the flood. Once the SVM model of the flood routing is obtained, then its future behavior can be predicted by the mechanism depicted in Figure 1(b), where the predicted output of the model is delayed by  $\Delta t$  and then fed back to the model itself as the third input thereby making the model more realistic to predict the flood.

In this section, the  $\varepsilon$ -SVR algorithm, SVM regression algorithm used in this study, is described briefly. The primal form of an SVM regression model is given by (3), which is linear in a higher dimensional feature space  $F$ .

Consider

$$\hat{y}(\mathbf{x}_i) = \langle \mathbf{w}, \Phi(\mathbf{x}_i) \rangle + b, \quad (3)$$

where  $\mathbf{w}$  is a vector in the feature space  $F$ ,  $\Phi(\cdot)$  is a mapping from the input space to the feature space,  $b$  is the bias term, and  $\langle \cdot \rangle$  is the inner product operation in the feature space. The SVM regression algorithm looks upon the regression problem as an optimization problem in dual space, where the model is given by

$$\hat{y}(\mathbf{x}_i) = \sum_{j=1}^N \alpha_j K(\mathbf{x}_i, \mathbf{x}_j) + b, \quad (4)$$

where  $\alpha_j$ 's are the coefficients of each training data point and  $K(\mathbf{x}_i, \mathbf{x}_j)$  is a kernel function. The kernel function handles the inner product in the feature space; that is,  $K(\mathbf{x}_i, \mathbf{x}_j) = \langle \Phi(\mathbf{x}_i), \Phi(\mathbf{x}_j) \rangle$ , and hence the explicit form of  $\Phi(\mathbf{x})$  does not need to be known. In this study, we have used the radial basis kernel function given by

$$K(\mathbf{x}_i, \mathbf{x}_j) = K_{ij} = \exp\left(-\frac{\|\mathbf{x}_i - \mathbf{x}_j\|^2}{2\sigma^2}\right), \quad (5)$$

TABLE 1: Comparison of the observed and computed outflows for Wilson data.

Time (h)	Input (cms)	Output (cms)	NLMM-L [30]	VPWFDM-L [31]	FIS [32]	SVM
0	22	22	22	22	22.0	22.00
6	23	21	21.71	20.66	20.9	20.93
12	35	21	22.02	21.5	21.0	20.98
18	71	26	26.08	25.79	26.0	25.92
24	103	34	33.51	33.71	34.0	34.04
30	111	44	42.83	44.65	44.0	43.97
36	109	55	55.44	54.37	57.1	55.04
42	100	66	66.67	65.72	66.2	65.96
48	86	75	75.77	75.78	75.0	75.06
54	71	82	82.12	82.55	82.0	81.93
60	59	85	84.78	84.65	85.4	84.95
66	47	84	83.42	84.07	84.0	84.08
72	39	80	79.44	79.36	80.0	79.93
78	32	73	72.48	72.67	73.0	72.92
84	28	64	64.08	63.75	64.0	64.02
90	24	54	54.58	54.53	54.0	54.04
96	22	44	45.22	44.87	44.0	43.96
102	21	36	36.34	36.24	35.9	36.04
108	20	30	29.21	29.5	29.9	29.96
114	19	25	24.21	24.56	25.3	25.04
120	19	22	20.96	21.31	21.7	21.96
126	18	19	19.41	19.39	19.1	19.04
SSE			9.823	5.178	4.830	0.056

where  $\|\cdot\|$  is the Euclidean norm and  $\sigma$  is the width parameter. In the model (4), a training point  $\mathbf{x}_j$  corresponding to a nonzero  $\alpha_j$  value is referred to as the *support vector*. The  $\varepsilon$ -SVR algorithm employs Vapnik's  $\varepsilon$ -insensitive loss function  $L(\varepsilon, y, \hat{y})$  given by

$$L(\varepsilon, y, \hat{y}) = \begin{cases} 0 & y - \hat{y} \leq \varepsilon \\ y - \hat{y} & y - \hat{y} > \varepsilon \end{cases} \quad (6)$$

and formulates the primal form of the regression problem as follows:

$$\min_{\mathbf{w}, b, \xi, \xi^*} P_\varepsilon = \frac{1}{2} \|\mathbf{w}\|^2 + C \sum_{i=1}^N (\xi_i + \xi_i^*), \quad (7)$$

subject to the constraints

$$\begin{aligned} y(\mathbf{x}_i) - \langle \mathbf{w}, \Phi(\mathbf{x}_i) \rangle - b &\leq \varepsilon + \xi_i, \quad i = 1, \dots, N \\ \langle \mathbf{w}, \Phi(\mathbf{x}_i) \rangle + b - y(\mathbf{x}_i) &\leq \varepsilon + \xi_i^*, \quad i = 1, \dots, N \\ \xi_i, \xi_i^* &\geq 0, \quad i = 1, \dots, N, \end{aligned} \quad (8)$$

where  $\xi_i$ 's and  $\xi_i^*$ 's are slack variables,  $\varepsilon$  is the upper value of tolerable error for the output, and  $C$  is a regularization parameter that provides a compromise between the model complexity and the degree of tolerance to the errors larger

than  $\varepsilon$ . Dual form of the optimization problem becomes a quadratic programming (QP) problem as follows:

$$\begin{aligned} \min_{\beta, \beta^*} D_\varepsilon = & \frac{1}{2} \sum_{i=1}^N \sum_{j=1}^N K_{ij} (\beta_i - \beta_i^*) (\beta_j - \beta_j^*) + \varepsilon \sum_{i=1}^N (\beta_i + \beta_i^*) \\ & - \sum_{i=1}^N y(\mathbf{x}_i) (\beta_i - \beta_i^*), \end{aligned} \quad (9)$$

subject to the constraints

$$0 \leq \beta_i, \beta_i^* \leq C, \quad \sum_{i=1}^N (\beta_i - \beta_i^*) = 0, \quad i = 1, \dots, N. \quad (10)$$

Solution of the QP problem gives the optimum values of  $\beta_i$ 's and  $\beta_i^*$ 's. The value of  $b$  in the model is determined as follows: the condition  $y(\mathbf{x}_i) - \hat{y}(\mathbf{x}_i) = \varepsilon$  is satisfied for each support vector  $\mathbf{x}_i$  for which the condition  $0 \leq \beta_i - \beta_i^* \leq C$  holds. If  $\alpha_j$  is defined to be the new coefficient of  $\mathbf{x}_j$  for  $j = 1, \dots, N$  as  $\alpha_j = \beta_j - \beta_j^*$ , then we obtain an SVM model as given by (4). Furthermore, if the support vectors are considered only, then the model becomes

$$\hat{y}(\mathbf{x}_i) = \sum_{\substack{j=1 \\ j \in \text{SV}}}^{\#\text{SV}} \alpha_j K(\mathbf{x}_i, \mathbf{x}_j) + b, \quad (11)$$

TABLE 2: Comparison of the observed and routed outflows for Viessman and Lewis data.

Time (h)	Input (cms)	Output (cms)	NLMM-L [30]	VPWFDM-L [31]	SVM
0	166.2	118.4	166.2	118.40	118.40
1	263.6	197.4	166.2	182.23	198.71
2	365.3	214.1	263.25	262.43	215.39
3	580.5	402.1	346.87	362.43	403.06
4	594.7	518.2	505.25	496.97	519.25
5	662.6	523.9	563.12	559.30	526.01
6	920.3	603.1	620.77	633.91	604.67
7	1568.8	829.7	773.8	803.13	831.03
8	1775.5	1124.2	1109.49	1150.33	1122.98
9	1489.5	1379	1381.64	1417.85	1377.61
10	1223.3	1509.3	1460.43	1433.22	1508.11
11	713.6	1379	1389.1	1345.15	1378.08
12	645.6	1050.6	1133.57	1115.25	1049.46
13	1166.7	1013.7	890.74	968.99	1012.38
14	1427.2	1013.7	982.97	994.50	1012.35
15	1282.8	1013.7	1167.97	1022.09	1014.47
16	1098.7	1209.1	1236.21	1216.84	1207.94
17	764.6	1248.8	1192.89	1231.67	1246.96
18	458.7	1002.4	1019.78	1023.80	1000.48
19	351.1	713.6	743.04	689.20	714.04
20	288.8	464.4	501.27	473.12	466.09
21	228.8	325.6	345.06	351.18	327.39
22	170.2	265.6	245.18	266.89	266.12
23	143	222.6	168.87	194.24	224.38
			73399.33	26185	43.37

where #SV stands for the number of support vectors in the model [19, 35] The SVM model is sparse in the sense that the whole training data are represented by only support vectors. The parameters of  $\epsilon$ -SVR are the maximum tolerable error  $\epsilon$  at the output, the regularization parameter  $C$ , the number of training patterns  $N$ , and the width parameter  $\sigma$ . The major advantage of the  $\epsilon$ -SVR algorithm is that it allows for the determination of the maximum total training error beforehand by choosing a proper  $\epsilon$  value.

### 3. Numerical Applications

In this study, we have tested modeling and prediction performance of the proposed SVM structure on three different flood problems. For each problem, we have gathered some artificial and real-world data for modeling purposes. In this comparative work, we have split our comparisons into two cases. In Case I, in order to have a basis for fair comparisons to other methods, all of the gathered data are used for only training of SVM structure. In Case II, only some portions,  $\mu$ , of the data are used for training, while remaining data are spared for validation and then the SVM approach is compared to other models given in the literature. For both cases in the training phase, all variables in each data set are

normalized to the interval  $[0, 1]$  and then an appropriate data set for training is formed. Afterwards, SVM model is obtained to give least possible training plus validation errors.

*3.1. Application to Wilson Data [36].* Data sets reported by Wilson are known to present a nonlinear relationship between weighted discharge and storage and used extensively in the literature as a benchmark problem. The number of data in this example is 22. The comparison of the SVM to other methods with respect to the prediction performances for Example 1 is given in Table 1.

The Wilson flood data were modeled by Karahan et al. (2014) using a nonlinear Muskingum model incorporating lateral flow (NLMM-L) and SSE value was found as 9.823. Chu (2009) presented the combined application of fuzzy inference system (FIS) and Muskingum model in flood routing. Chu (2009) found the SSE value as 4.830. More recently, Karahan et al. (2014) have proposed a variable-parameter nonlinear Muskingum model incorporating lateral flow with a weighted finite difference method [VPWFDM-L] and applied this model to Wilson data. Karahan et al. (2014) have reported the SSE value as 5.178. When the SVM model is employed for the same flood data, the SSE value has been found as 0.056, which is much better than that of other methods.

TABLE 3: Comparison of the observed and routed outflows for the River Wyre data.

Time (h)	Input (cms)	Output (cms)	LMM-L [33]	NLMM-L [30]	SVM
0	2.6	8.3	8.3	8.3	8.300
1	4.2	9	8.2	8.51	9.092
2	12.3	9.9	8.1	8.79	10.020
3	25.4	10.2	12.7	10.94	10.338
4	24.1	18.9	27.9	20.28	19.063
5	20.3	35.9	39.9	37.54	35.980
6	23.3	51.8	45.7	49.07	51.815
7	27.7	59.4	52.2	55.11	59.327
8	27.7	63.3	61.4	62.5	63.279
9	26.9	69.6	68.9	71.44	69.482
10	24.8	76.7	74.7	78.03	76.649
11	26.9	82	77.2	82.07	82.051
12	33.7	85.3	79.8	83.72	85.234
13	33.9	89	87.8	87.43	88.901
14	27.8	94.6	95.5	95.49	94.514
15	20.8	98.8	97.7	100.88	98.683
16	15.6	98	94.4	99.29	97.902
17	11.9	91.8	87.9	92.06	91.728
18	9.5	82.3	79.8	82.22	82.217
19	7.8	72	71.5	71.75	72.086
20	6.5	61.9	63.6	61.91	61.824
21	5.8	53	56.1	53.12	53.068
22	5	45.6	49.6	45.47	45.560
23	4.8	39.2	43.7	39.14	39.259
24	4.5	33.8	38.8	33.76	33.764
25	4.1	29.3	34.6	29.55	29.363
26	3.7	26.2	30.9	26.12	26.085
27	3.4	23.5	27.7	23.2	23.496
28	3.2	21.2	24.8	20.67	21.289
29	2.9	19.2	22.3	18.52	19.367
30	2.8	17.7	20.1	16.71	17.747
31	2.6	16.4	18.2	15.12	16.527
SSE			468.840	53.708	0.253

3.2. *Application to Viessman and Lewis Data [37]*. This example is based on inflow and outflow hydrographs exhibiting linear characteristics and presents a relatively difficult prediction problem for flood routing, where there exist two successively active floods. The number of data in this example is 24.

Table 2 shows the comparison results numerically. It is obviously seen that the SVM method outperforms others in prediction of the flood dynamics, which can be attributed to the proposed training and prediction structures and also the generalization potentials of SVM approach.

As can be seen from Table 2, the SSE values are obtained as 73399.33 for the NLMM-L model, 26185 for the VPWFDML model, and 43.37 for the SVM model, respectively. It is observed from the results of Table 3 that the SSE value (0.253) obtained by the SVM model for the River Wyre data is better than those obtained when the LMM-L and NLMM-L models are used.

3.3. *Application to River Wyre [33]*. For the River Wyre data, the flood volume between the inflow and the outflow sections is 25 km, along which there are lateral flows that considerably contribute to the flood [33]. Moreover, the input hydrograph has multiple peaks. The number of data in this example is 32.

In the literature, the River Wyre flood data were first modeled by O'Donnell (1985) using a linear Muskingum model incorporating lateral flow (LMM-L) and the SSE value was found as 468.840. Recently, Karahan et al. (2014) have applied NLMM-L model to River Wyre flood data and have reported the SSE value as 53.708. It is observed from the results that the SSE value (0.253) obtained by the SVM model for the River Wyre data is better than those obtained when the LMM-L and NLMM-L models are used.

3.4. *Verification of Model Robustness*. In Sections 3.1–3.3, the SVM models have been obtained by using whole data and then compared to other methods in the literature. The

TABLE 4: Average SSE values of the SVM approach for Wilson data, Viessman and Lewis data, and River Wyre data.

Data	$\mu$	$\delta = 0$	$\delta = 0.01$	$\delta = 0.05$	$\delta = 0.10$
Wilson	0.9	1.389	1.627	2.013	2.691
	0.8	3.486	4.120	4.160	7.738
	0.7	7.284	8.473	8.835	10.818
	0.6	12.540	14.872	17.878	21.755
Viessman and Lewis	0.9	12460.720	14446.716	18456.445	21172.915
	0.8	34631.312	48888.423	50163.966	58837.181
	0.7	83005.647	84387.246	112145.221	100247.301
	0.6	124339.197	124324.518	118768.183	131235.761
River Wyre	0.9	5.760	9.895	11.922	7.788
	0.8	218.236	55.846	70.096	289.540
	0.7	291.692	161.367	133.620	363.987
	0.6	331.883	271.468	239.053	440.319

results have shown that there is good agreement between the predicted and measured outflows for the three examples under investigation. However, it is possible that there may be some erroneous and/or missing measurements in practical applications. In order to test the performance of the proposed SVM model under such conditions, input data have been corrupted by additive uniformly distributed noise with zero mean. The noisy data are obtained as [38, 39]

$$Q_I^*(t) = Q_I(t) + \lambda\delta Q_I(t), \quad (12)$$

where  $Q_I(t)$  and  $Q_I^*(t)$  stand for the noiseless and noisy input flow rates at time  $t$ , respectively,  $\lambda$  represents the measurements errors that are distributed uniformly between  $-1$  and  $1$ , and  $\delta$  is a noise level scalar between  $0.0$  and  $0.1$ . In this study, various noise level conditions, namely,  $0.01$ ,  $0.05$ , and  $0.10$ , are considered and also it is assumed that some portions (10 to 40 percent) of the data are missing in order to investigate the effects of the missing data on the model performance. In order to get more reliable results, the tests have been performed at least 100 times for each case and then their average SSE values have been given in Table 4.

As can be seen from Table 4, only  $\mu$  portion of data is used for training, while its remaining part is spared for validation. The test data are selected randomly out of the whole data set. It is observed from numerical results that the SVM method provides excellent prediction performance when there is no measurement noise ( $\delta = 0$ ) and the nearly whole data are used ( $\mu = 0.9$ ). On the other hand, as the level of the measurement noise and the portion of the missing data are increased, the model performance decreases expectedly. Still, in the worst case ( $\delta = 0.1$  and  $\mu = 0.6$ ) the proposed SVM method provides acceptable performance.

## 4. Conclusions

In this study, a novel architecture for flood routing model has been proposed and its efficiency is validated on three different flood routing problems by employing SVM approach. Proposed model is designed including the inputs and observed and calculated outflows from the previous time step output,

thereby making the model more realistic. The SVM approach has been implemented to capture the dynamics of the investigated floods from the observed data. In this study, higher generalization capabilities have motivated us to employ the SVM structure. After completing the learning phase, the model has been performed to predict the routing outflows. The proposed model has also been compared to the different models in the literature.

The simulation results have revealed that when combined with the powerful modeling tools, such as SVM, the proposed architecture exhibits excellent modeling and prediction performances for flood routing problems under investigation. The results have also demonstrated that the proposed model provides better prediction performance than the ones existing in the literature when whole data are used for training. Furthermore, SVM approach has been employed when only some portions (60–90%) of the data are used for training, and it has been observed that SVM maintains its prediction performance up to an acceptable level even if only 60% of the data are used for training under noisy condition. Consequently, the proposed model possesses higher applicability potential in forecasting outflows with different inflow patterns and thus it can be employed for solving flood routing problems.

## Conflict of Interests

The authors declare that there is no conflict of interests regarding the publication of this paper.

## References

- [1] V. P. Singh and R. C. McCann, "Some notes on Muskingum method of flood routing," *Journal of Hydrology*, vol. 48, no. 3–4, pp. 343–361, 1980.
- [2] M. Amein, "An implicit method for natural flood routing," *Water Resources Research*, vol. 4, no. 4, pp. 719–726, 1968.
- [3] R. A. Baltzer and C. Lai, "Computer simulation of unsteady flows in waterway," *Journal of Hydraulic Division*, vol. 94, no. 4, pp. 1083–1117, 1968.

- [4] M. Amein and C. S. Fang, "Implicit flood routing in natural channels," *Journal of Hydraulic Research*, vol. 96, no. 12, pp. 2481–2500, 1970.
- [5] M. Amein and L. H. Chu, "Implicit numerical modeling of unsteady flows," *Journal of Hydraulic Division*, vol. 101, no. 6, pp. 717–731, 1975.
- [6] M. B. Abbott and J. A. Cunge, *Engineering Applications of Computational Hydraulics*, Marshfield, Pitman, NJ, USA, 1982.
- [7] U.S. Army Corps of Engineering (USACE), *HEC-RAS River Analysis System Hydraulic Reference Manual (Version 3.1)*, USACE-HEC, Davis, Calif, USA, 2002.
- [8] Danish Hydrological Institute (DHI), *User's Manual and Technical References for MIKE II (Version 2003b)*, Danish Hydrological Institute (DHI), Hørsholm, Denmark, 2003.
- [9] H. Karahan, G. Gurarslan, and Z. W. Geem, "Parameter estimation of the nonlinear muskingum flood routing model using a hybrid harmony search algorithm," *Journal of Hydrologic Engineering*, vol. 18, no. 3, pp. 352–360, 2013.
- [10] H. Karahan, "Predicting Muskingum flood routing parameters using spreadsheets," *Computer Applications in Engineering Education*, vol. 20, no. 2, pp. 280–286, 2012.
- [11] A. Aldama, "Least-squares parameter estimation for Muskingum flood routing," *Journal of Hydraulic Engineering*, vol. 116, no. 4, pp. 580–586, 1990.
- [12] A. Das, "Parameter estimation for Muskingum models," *Journal of Irrigation and Drainage Engineering*, vol. 130, no. 2, pp. 140–147, 2004.
- [13] S. Mohan, "Parameter estimation of nonlinear Muskingum models using genetic algorithm," *Journal of Hydraulic Engineering*, vol. 123, no. 2, pp. 137–142, 1997.
- [14] J. H. Kim, Z. W. Geem, and E. S. Kim, "Parameter estimation of the nonlinear Muskingum model using harmony search," *Journal of the American Water Resources Association*, vol. 37, no. 5, pp. 1131–1138, 2001.
- [15] V. N. Vapnik, *Statistical Learning Theory*, Adaptive and Learning Systems for Signal Processing, Communications, and Control, Wiley- Interscience, New York, NY, USA, 1998.
- [16] N. Cristianini and J. S. Taylor, *An Introduction to Support Vector Machines and Other Kernel-Based Learning Methods*, Cambridge University Press, New York, NY, USA, 2000.
- [17] B. Schölkopf, C. J. C. Burges, and A. J. Smola, *Advances in Kernel Methods: Support Vector Learning*, MIT Press, Cambridge, Mass, USA, 1999.
- [18] M. Behzad, K. Asghari, M. Eazi, and M. Palhang, "Generalization performance of support vector machines and neural networks in runoff modeling," *Expert Systems with Applications*, vol. 36, no. 4, pp. 7624–7629, 2009.
- [19] X. Zhang, R. Srinivasan, and M. van Liew, "Approximating SWAT model using artificial neural network and support vector machine," *Journal of the American Water Resources Association*, vol. 45, no. 2, pp. 460–474, 2009.
- [20] G. F. Lin, Y. C. Chou, and M. C. Wu, "Typhoon flood forecasting using integrated two-stage support vector machine approach," *Journal of Hydrology*, vol. 486, pp. 334–342, 2013.
- [21] E. K. Kakaei Lafdani, A. M. Moghaddam Nia, and A. Ahmadi, "Daily suspended sediment load prediction using artificial neural networks and support vector machines," *Journal of Hydrology*, vol. 478, pp. 50–62, 2013.
- [22] Z.B. Yu, D. Liu, H.S. Lu, L. Xiang, and Y. H. Zhu, "A multi-layer soil moisture data assimilation using and ensemble particle filter," *Journal of Hydrology*, vol. 475, pp. 53–64, 2012.
- [23] O. Kisi, "Modeling discharge-suspended sediment relationship using least square support vector machine," *Journal of Hydrology*, vol. 456–457, pp. 110–120, 2012.
- [24] O. Kisi and M. Cimen, "A wavelet-support vector machine conjunction model for monthly streamflow forecasting," *Journal of Hydrology*, vol. 399, no. 1–2, pp. 132–140, 2011.
- [25] H. Yoon, S. C. Jun, Y. Hyun, G. O. Bae, and K.K. Lee, "A comparative study of artificial neural networks and support vector machines for predicting groundwater levels in a coastal aquifer," *Journal of Hydrology*, vol. 396, pp. 128–138, 2011.
- [26] S. T. Chen, P. S. Yu, and Y. H. Tang, "Statistical downscaling of daily precipitation using support vector machines and multivariate analysis," *Journal of Hydrology*, vol. 385, no. 1–4, pp. 13–22, 2010.
- [27] G.-F. Lin, G.-R. Chen, P.-Y. Huang, and Y.-C. Chou, "Support vector machine-based models for hourly reservoir inflow forecasting during typhoon-warning periods," *Journal of Hydrology*, vol. 372, no. 1–4, pp. 17–29, 2009.
- [28] S. Tripathi, V. V. Srinivas, and R. S. Nanjundiah, "Downscaling of precipitation for climate change scenarios: a support vector machine approach," *Journal of Hydrology*, vol. 330, no. 3–4, pp. 621–640, 2006.
- [29] T. Asefa, M. Kemblowski, M. McKee, and A. Khalil, "Multi-time scale stream flow predictions: the support vector machines approach," *Journal of Hydrology*, vol. 318, no. 1–4, pp. 7–16, 2006.
- [30] H. Karahan, G. Gurarslan, and Z. W. Geem, "A new nonlinear muskingum flood routing model incorporating lateral flow," *Engineering Optimization. In press*, 2014.
- [31] H. Karahan, "Discussion of "improved nonlinear Muskingum model with variable exponent parameter";" *Journal of Hydrologic Engineering*, 2014.
- [32] H.-J. Chu, "The Muskingum flood routing model using a neuro-fuzzy approach," *KSCE Journal of Civil Engineering*, vol. 13, no. 5, pp. 371–376, 2009.
- [33] T. O'Donnell, "A direct three-parameter Muskingum procedure incorporating lateral inflow," *Hydrological Sciences Journal*, vol. 30, no. 4, pp. 479–496, 1985.
- [34] H. R. Maier and G. C. Dandy, "Neural networks for the prediction and forecasting of water resources variables: a review of modelling issues and applications," *Environmental Modelling & Software*, vol. 15, no. 1, pp. 101–124, 2000.
- [35] A. J. Smola and B. Schölkopf, "A tutorial on support vector regression," *NeuroCOLT Tech. Rep. NC-TR-98-030*, Royal Holloway College, University of London, 1998.
- [36] E. M. Wilson, *Engineering Hydrology*, MacMillan Education, Hampshire, UK, 1974.
- [37] W. Viessman Jr. and G. L. Lewis, *Introduction to Hydrology*, Pearson Education Inc, Upper Saddle River, NJ, USA, 2003.
- [38] H. Karahan and M. T. Ayvaz, "Simultaneous parameter identification of a heterogeneous aquifer system using artificial neural networks," *Hydrogeology Journal*, vol. 16, no. 5, pp. 817–827, 2008.
- [39] G. Gurarslan, *Identification of groundwater contaminant source locations and release histories by using differential evolution algorithm [Ph. D. thesis]*, Department of Civil Engineering, Pamukkale University, Denizli, Turkey, 2011, (Turkish).

## Research Article

# Mathematical Modeling and Simulation of SWRO Process Based on Simultaneous Method

**Aipeng Jiang, Qiang Ding, Jian Wang, Shu Jiangzhou, Wen Cheng, and Changxin Xing**

*School of Automation, Hangzhou Dianzi University, Hangzhou, Zhejiang 310018, China*

Correspondence should be addressed to Aipeng Jiang; [jiangaipeng@gmail.com](mailto:jiangaipeng@gmail.com)

Received 30 January 2014; Revised 23 May 2014; Accepted 28 May 2014; Published 23 June 2014

Academic Editor: X. S. Qin

Copyright © 2014 Aipeng Jiang et al. This is an open access article distributed under the Creative Commons Attribution License, which permits unrestricted use, distribution, and reproduction in any medium, provided the original work is properly cited.

Reverse osmosis (RO) technique is one of the most efficient ways for seawater desalination to solve the shortage of freshwater. For prediction and analysis of the performance of seawater reverse osmosis (SWRO) process, an accurate and detailed model based on the solution-diffusion and mass transfer theory is established. Since the accurate formulation of the model includes many differential equations and strong nonlinear equations (differential and algebraic equations, DAEs), to solve the problem efficiently, the simultaneous method through orthogonal collocation on finite elements and large scale solver were used to obtain the solutions. The model was fully discretized into NLP (nonlinear programming) with large scale variables and equations, and then the NLP was solved by large scale solver of IPOPT. Validation of the formulated model and solution method is verified by case study on a SWRO plant. Then simulation and analysis are carried out to demonstrate the performance of reverse osmosis process; operational conditions such as feed pressure and feed flow rate as well as feed temperature are also analyzed. This work is of significant meaning for the detailed understanding of RO process and future energy saving through operational optimization.

## 1. Introduction

China, which has the largest population in the world and is called the world's factory, has a much more serious problem of freshwater shortage. This problem is expected to worsen in the whole world with the growth of industrialization, as well as climate change [1–3]. Seawater desalination based on RO (reverse osmosis) membrane technique is one of the most promising ways to obtain freshwater, especially in the coastal regions and islands. More than 40% market shares of seawater desalination based on RO technique was occupied worldwide in the past decade [4]. Reverse osmosis (RO) is also a membrane technology driven by high pressure and is used to separate salt and water of the same order of molecular size. High pressure is applied on the feed side of the membrane to overcome the osmotic pressure and cause transport of the solvent from feed to permeate side. Among the membrane modules, spiral-wound RO occupies the largest market share because of its relative ease of cleaning, fabrication technology, and very large surface area per unit volume [5, 6]. The general process of SWRO can be found in the specialized literature [7, 8]. To achieve a high recovery in a single stage, several

spiral-wound elements in series, held in a cylindrical pressure vessel, are usually used in seawater desalination applications. Generally a reverse osmosis desalination unit is composed of dozens of cylindrical pressure vessels, and several units with a permeate water storage tank were used as the key part of a seawater desalination plant.

The feed pressure as well as other parameters such as operational temperature and properties of the membrane has significant effect on the performance of SWRO process. It is quite important to understand the mechanism of SWRO process and improve the performance and reduce the energy consumption. For this reason, based on solution-diffusion model and film theory, the model of RO process was researched, found, analyzed, and used to optimize the operation of SWRO plant [9, 10].

Libotean and Khayet established the performance prediction model based on data-driven method such as artificial neural networks [11, 12]. Since modeling based on rigid first principle can reveal more information, Senthilmurugan et al. [9] applied the solution-diffusion model modified with the concentration polarization theory for analyzing the

operation and performance of RO systems. Abbas analyzed and simulated an industrial medium-scale brackish water reverse osmosis plant with semirigorous model, and then he used it to analyze the optimal operation of RO system [13]. Geraldès considered both the investment cost and operation cost of SWRO system and provided the differential equations of the RO process with distributed method [14]. Then, to avoid computing difficulties, he simplified the simulation process and solved his optimal problem with simple difference equations. Sundaramoorthy et al. build more complex analytical model of spiral wound reverse osmosis modules, based on complex model parameters estimation; the model is computed based on sequential method [15]. To get more accurate results, more modeling and simulation of reverse osmosis system are carried out with CFD technique [16–18]. But since these models are not founded with simultaneous method, computing efficiency for simulation and optimization cannot be guaranteed for online application.

In this paper, to achieve accurate prediction of RO process performance and to accelerate the computing efficiency for real time simulation, the mathematical modeling is carried out based on rigid first principle, then simultaneous method within which the differential variables are fully discretized by finite element collocation. The mathematical model is verified and then simulation under different conditions will be discussed.

## 2. Mathematical Modeling of Spiral-Wound RO Process

The performance of SWRO plants is quite sensitive to the quality of the feed water and plant operating conditions. Based on solution-diffusion model and film theory and according to the schematic diagram of the SWRO process shown in Figure 2, more accurate membrane transport equations of steady-state in the form of distributed parameters can be derived.

For the RO membrane, the overall fluid and solute mass balance equations are

$$\begin{aligned} Q_p &= Q_f - Q_r \\ Q_f C_f &= Q_r C_r + Q_p C_p \\ Q_p &= n_l W \int_0^L J_v dz. \end{aligned} \quad (1)$$

Here subscripts  $f$ ,  $r$ , and  $p$  refer to the feed, reject (brine), and permeate (product) streams.  $Q$  and  $C$  refer to the flow rate and salt concentration, respectively. The local water flux and salt flux can be calculated from the Kimura-Sourirajan solution-diffusion mass transport relations.  $n_l$ ,  $W$ , and  $L$  express the number of leaves and the width and length of the RO module, respectively. The solution-diffusion model is assumed to be valid for the transport of solvent and solute through the membrane. According to this model, solvent flux

$J_v$  and solute flux  $J_s$  through membrane are expressed by the following equations:

$$\begin{aligned} J_v &= A_w (P_f - P_d - P_p - \Delta\pi) \\ J_s &= B_s (C_m - C_b). \end{aligned} \quad (2)$$

Let

$$\begin{aligned} P_b &= P_f - P_d, \\ \Delta P &= (P_b - P_p). \end{aligned} \quad (3)$$

Then

$$J_v = A_w (\Delta P - \Delta\pi), \quad (4)$$

where  $A_w$  is the solvent transport parameter,  $P_f$  is the feed pressure,  $P_d$  is the pressure drop along a RO spiral-wound module,  $P_b$  is the pressure along the channel of spiral-wound module, and  $P_p$  is the pressure of permeate side, which in general is assumed as environment pressure.  $\Delta\pi$  is the pressure loss of osmosis pressure.  $B_s$  is the solute transport parameter,  $C_m$  and  $C_{sp}$  are solute concentration at the membrane surface on the feed side and solute concentration on the permeate side, respectively, and  $C_p$  is the value of  $C_b$  at the end of module. That means  $C_p = C_b(L)$ .  $A_w$  and  $B_s$  are sensitive with operational temperature and related factors; the relationship is expressed as follows:

$$\begin{aligned} A_w &= A_{w0} \exp\left(\alpha_1 \frac{T - 273}{273} - \alpha_2 (P_f - P_d)\right) \\ B_s &= B_{s0} \exp\left(\beta_1 \frac{T - 273}{273}\right), \end{aligned} \quad (5)$$

where  $A_{w0}$  and  $B_{s0}$  are intrinsic transport parameter in standard condition and  $\alpha_1$ ,  $\alpha_2$ , and  $\beta_1$  are constant parameters for transport.  $T$  represents operational temperature with unit of kelvin degree. The osmotic pressure is nearly linearly related to concentration by the equation

$$\Delta\pi = RT (C_m - C_p), \quad (6)$$

where  $R$  is the gas law constant.

Solution of the above equations requires knowledge of the RO process specification and parameters as well as the solute concentration of  $C_m$  at the membrane wall, which is quite different from the bulk concentration  $C_b$  due to the CP (concentration polarization) phenomenon. Through steady-state material balance around the boundary layer and CP theory, the following simple expression is developed:

$$\phi = \frac{C_m - C_p}{C_b - C_p} = \exp\left(\frac{J_v}{k_c}\right). \quad (7)$$

The bulk concentration  $C_b$  and solvent transports  $J_v$  vary along the membrane channel. The computation of the mass transfer coefficient  $k_c$  is as follows [19]:

$$\text{Sh} = \frac{k_c d_e}{D_{AB}} = 0.065 \text{Re}^{0.875} \text{Sc}^{0.25}, \quad (8)$$

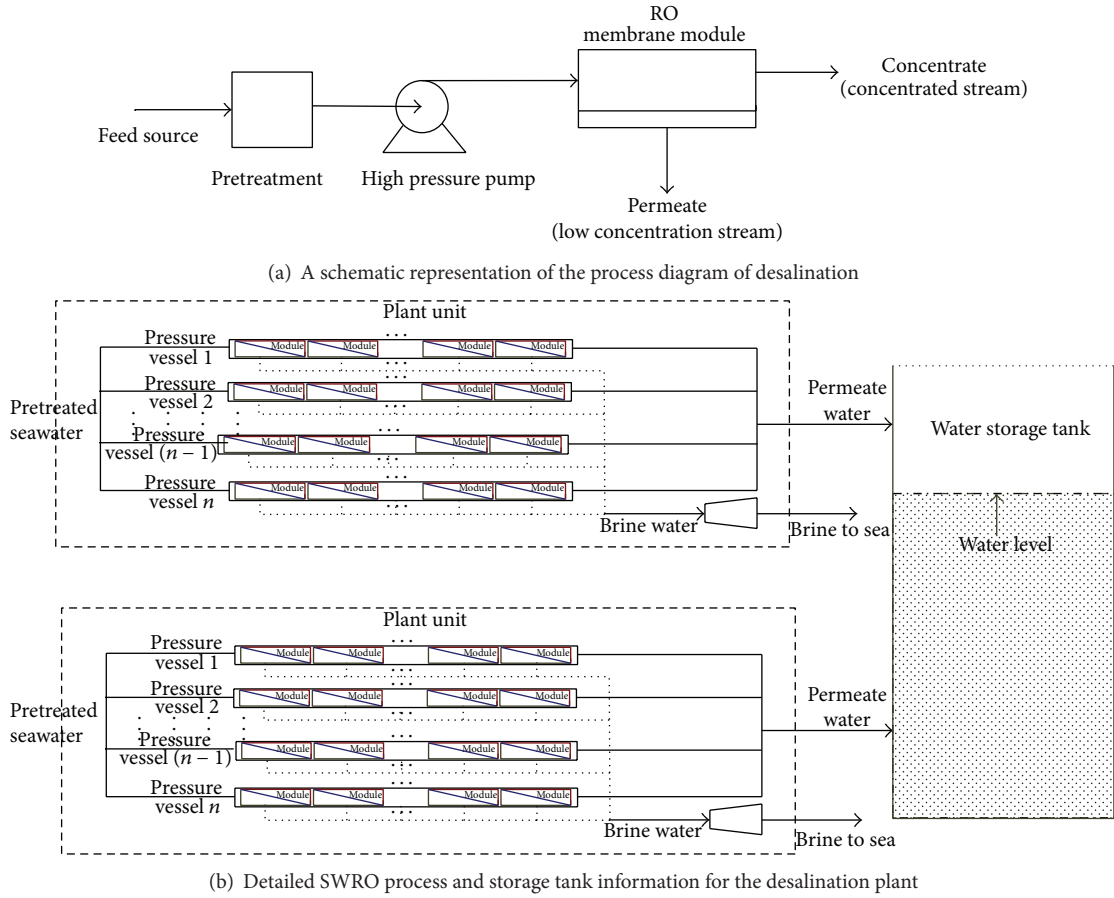


FIGURE 1: Detailed schematic diagram of RO process and water storage process.

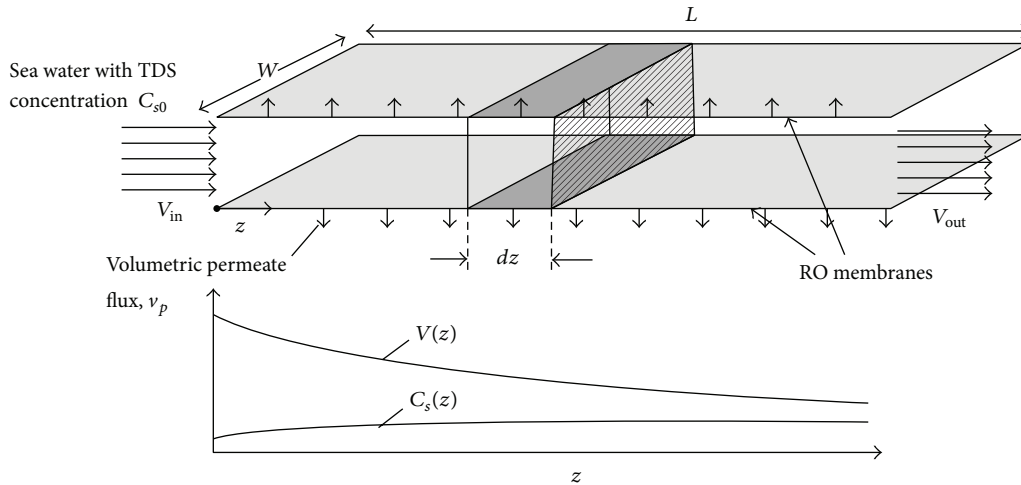


FIGURE 2: Scheme of the rectangular channel model of spiral wound module feed channel.

where

$$Re = \frac{\rho V d_e}{\mu}$$

$$Sc = \frac{\mu}{(\rho D_{AB})}$$

$\rho$  is the density of permeate water,  $d_e$  is hydraulic diameter of the feed spacer channel,  $\mu$  is kinematic viscosity, and  $D_{AB}$  is dynamic viscosity; it can be calculated by the regression equation

$$(9) \quad D_{AB} = 6.725 \times 10^{-6} \cdot \exp\left(0.1546 \times 10^{-3} C_b - \frac{2513}{273.15 + T}\right) \quad (10)$$

The relationship between  $Jv$  and  $J_s$  is

$$J_s = JvC_p. \quad (11)$$

According to Figure 2, the pressure loss along the RO channel can be formulated as

$$\frac{dP_d}{dz} = -\lambda \frac{\rho}{d_e} \frac{V^2}{2}, \quad (12)$$

where

$$\lambda = 6.23K_\lambda \text{Re}^{-0.3}. \quad (13)$$

$K_\lambda$  is the empirical parameter. Since the pressure along RO  $P_b = P_f - P_d$ , so

$$\frac{dP_b}{dz} = -\frac{dP_d}{dz} = \lambda \frac{\rho}{d_e} \frac{V^2}{2}, \quad (14)$$

at  $z = 0$ ,  $P_b = P_f$ , at  $z = L$ ,  $P_b = P_r$ .

$V$  is axial velocity in feed channel and satisfies

$$\frac{dV}{dz} = -\frac{2Jv}{h_{sp}}$$

$$\text{at } z = 0, \quad V = V_f = \frac{Q_f}{n_e W h_{sp}} \quad (15)$$

$$\text{at } z = L, \quad V = V_r = \frac{Q_r}{n_e W h_{sp}}.$$

$h_{sp}$  is height of the feed spacer channel.

The bulk concentration  $C_b$  varies along the membrane channel and can be given as

$$\frac{dC_b}{dz} = \frac{2Jv}{h_{sp}V} (C_b - C_p), \quad (16)$$

and at  $z = 0$ ,  $C_b = C_f$ ; at  $z = L$ ,  $C_b = C_r$ .

From the solution of the above equations,  $Q_p$  and  $C_p$  at given operational conditions and specification of membrane can be obtained, from which the water recovery rate  $\text{Rec}$  and specific energy consumption  $\text{SEC}$  can be calculated by the equations

$$\text{Rec} = \frac{Q_p}{Q_f} \quad (17)$$

$$\text{SEC} = \frac{(P_f Q_f / \varepsilon_p - P_r Q_r \varepsilon_{ef})}{Q_p}. \quad (18)$$

Salt passage and salt rejection coefficient are also two important parameters reflecting the performance of the RO process. They are formulated as the following equations:

$$\text{Sp} = \frac{C_p}{C_f} \times 100\% \quad (19)$$

$$\text{Ry} = \frac{(C_f - C_p)}{C_f} \times 100\%, \quad (20)$$

where  $\varepsilon_p$  and  $\varepsilon_{pf}$  are the mechanical efficiency and energy recovery efficiency, respectively.

Equations (1)–(20) explain the detailed reverse osmosis process with spiral-wound membrane module. If the operational variables, such as feed flow rate and feed pressure, are fixed, the permeate quality and related performance can be obtained by the solution of the equations. Otherwise, the operational variables and related parameters can be calculated by (1)–(20) under certain constraints. The constraints listed in (21) include requirement of equipment safety, water quality, and parameter of CP:

$$\begin{aligned} P_{flo} &\leq P_f \leq P_{fup} \\ Q_{flo} &\leq Q_f \leq Q_{fup} \\ C_{plo} &\leq C_p \leq C_{pup} \\ T_{lo} &\leq T \leq T_{up} \\ \phi &\leq \phi_{\max} \\ H_{t\min} &\leq H_t \leq H_{t\max}. \end{aligned} \quad (21)$$

### 3. Discretization and the Solution Method

Since (1)–(20) include a set of strong nonlinear equations and even DAEs (differential and algebraic equations) and since there are more constraints than those of the equation mentioned above, it is fairly tough to solve this kind of problem efficiently with high accuracy [20–22]. Here the DAEs (1)–(21) are converted into the form of NLP (non-linear programming) through simultaneous approach by approximating state and control profiles with a family of polynomials on finite elements (shown as Figure 3) [20, 23]. These polynomials can be represented as power series, such as orthogonal polynomials, or in Lagrange form. Here the following monomial basis representation for the differential profile was selected, which is popular for Runge-Kutta discretizations [23]:

$$z(t) = z_{i-1} + h_i \sum_{q=1}^K \Omega_q \left( \frac{t - t_{i-1}}{h_i} \right) \frac{dz}{dt_{i,q}}. \quad (22)$$

Here  $z_{i-1}$  is the value of the differential variable at the beginning of element  $i$ ,  $h_i$  is the length of element  $i$ ,  $dz/dt_{i,q}$  denotes the value of its first derivative in element  $i$  at the collocation point  $q$ , and  $\Omega_q$  is a polynomial of order  $K$ , satisfying

$$\Omega_q(0) = 0, \quad q = 1, \dots, K \quad (23)$$

$$\Omega'_q(\rho_r) = \delta_{q,r}, \quad q = 1, \dots, K,$$

where  $\rho_r$  is the location of the  $r$ th collocation point within each element. Continuity of the differential profile is enforced by

$$z_i = z_{i-1} + h_i \sum_{q=1}^K \Omega_q(1) \frac{dz}{dt_{i,q}}. \quad (24)$$

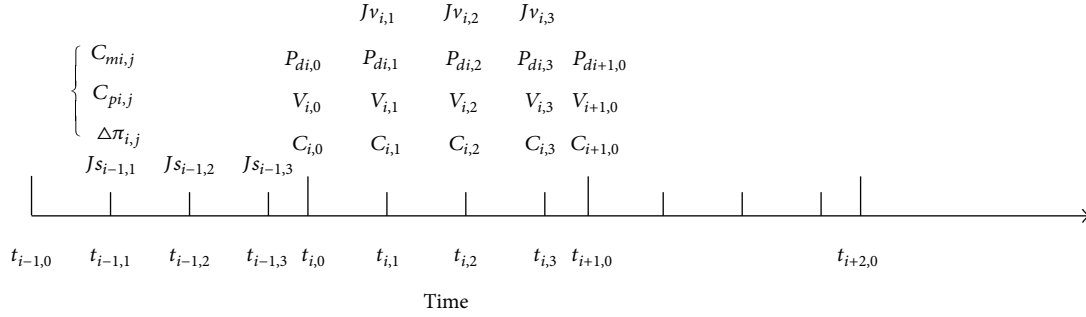


FIGURE 3: Discretization by collocation on finite element.

Based on a number of studies of Larry group [20, 24–26], Radau collocation points were selected in this study because they allow constraints to be set at the end of each element and to stabilize the system more efficiently if high index DAEs are present. In addition, the control and algebraic profile are approximated using a Lagrange basis representation which takes the following form:

$$y(t) = \sum_{q=1}^K \psi_q \left( \frac{t - t_{i-1}}{h_i} \right) y_{i,q} \quad (25)$$

$$u(t) = \sum_{q=1}^K \psi_q \left( \frac{t - t_{i-1}}{h_i} \right) u_{i,q}.$$

Here  $y_{i,q}$  and  $u_{i,q}$  represent the values of the algebraic and control variables, respectively, in element  $i$  at collocation point  $q$ ,  $t$  is the value satisfying  $t_{i-1} \leq t \leq t_i$ , and  $\Psi_q$  is the Lagrange polynomial of degree  $K$  satisfying

$$\psi_q(t) = \prod_{r=1}^K \frac{(t - t^r)}{(t^q - t^r)} = \prod_{r=1}^K \frac{(t - t^r)/h_i}{(t^q - t^r)/h_i} = \prod_{r=1}^K \frac{(t - t^r)/h_i}{(\rho^q - \rho^r)}$$

$$\psi_q(\rho_r) = \delta_{q,r}, \quad q, r = 1, \dots, K. \quad (26)$$

And, at collocation points,

$$\psi_q(t^r) = \delta_{q,r} = \begin{cases} 1, & q = r \\ 0, & q \neq r \end{cases} \quad (q, r = 1, \dots, K). \quad (27)$$

The differential variables are required to be continuous throughout the time (or space) horizon, while the control and algebraic variables are allowed to have discontinuities at the boundaries of the elements.

Through the simultaneous method DAEs of (1)–(21) were transformed into NLP problem. Some state variables in (1)–(21) can be discretized as flow variables:  $P_{di,j}$ ,  $V_{i,j}$ ,  $C_{bi,j}$ ,  $Z_{i,j}$ ,  $C_{bi,0}$ ,  $V_{i,0}$ ,  $P_{di,0}$ ,  $Z_{i,0}$ , and  $Jv_{i,j}$ ,  $Js_{i,j}$ ,  $\lambda_{i,j}$ ,  $Sc_{i,j}$ ,  $Re_{i,j}$ ,  $k_{ci,j}$ ,  $C_{mi,j}$ ,  $\Delta\pi_{i,j}$ . Operational variables  $Q_f$ ,  $P_f$  and other environmental variables such as  $T_f$  and  $C_f$  are not discretized because they

are operational variables and feed condition variables. The equations are expressed in the following form:

$$A_w(i, j) = A_{w0} \exp \left( \alpha_1 \frac{T - 273}{273} - \alpha_2 (P_f - P_d(i, j)) \right)$$

$$B_s = B_{s0} \exp \left( \alpha_2 \frac{T - 273}{273} \right)$$

$$Jv_{i,j} = A_w (P_f - P_{di,j} - \Delta\pi_{i,j})$$

$$Js_{i,j} = B_w (C_{mi,j} - C_{pi,j})$$

$$C_{pi,j} = \frac{Js_{i,j}}{Jv_{i,j}}$$

$$\Delta\pi_{i,j} = RT (C_{mi,j} - C_{pi,j})$$

$$C_{mi,j} = \left[ (C_{bi,j} - C_{pi,j}) \exp \left( \frac{Jv_{i,j}}{k_{ci,j}} \right) \right] + C_{pi,j}$$

$$k_{ci,j} = 0.065 Re_{i,j}^{0.875} Sc_{i,j}^{0.25} \frac{d_e}{D_{AB}}$$

$$Sc_{i,j} = \frac{\mu_{i,j}}{(\rho D_{AB})}$$

$$\lambda_{i,j} = 6.23 K_\lambda Re_{i,j}^{-0.3}. \quad (28)$$

ODE formulations are

$$Re_{i,j} = \frac{\rho V_{i,j} d_e}{\mu_{i,j}}$$

$$\frac{dV_{i,j}}{dx} = - \frac{2Jv_{i,j}}{h_{sp}}$$

$$\frac{dC_{bi,j}}{dx} = 2Jv_{i,j} \frac{(C_{bi,j} - C_{pi,j})}{(h_{sp} \times V_{i,j})} \quad (29)$$

$$\frac{dP_{di,j}}{dx} = \frac{\lambda_{i,j} \rho}{d_e} \times \frac{(V_{i,j}^2)}{2}.$$

Collocation equations are

$$\begin{aligned} C_{bi,j} &= C_{bi,0} + h_i \sum_{k=1}^{ncp} \Omega_k(\rho_j) \frac{dC_b}{dx_{i,k}} \\ V_{i,j} &= V_{bi,0} + h_i \sum_{k=1}^{ncp} \Omega_k(\rho_j) \frac{dV}{dx_{i,j}} \\ P_{di,j} &= P_{di,0} + h_i \sum_{k=1}^{ncp} \Omega_k(\rho_j) \frac{dP_d}{dx_{i,j}}. \end{aligned} \quad (30)$$

Continuity equations are

$$\begin{aligned} C_{bi,0} &= C_{bi-1,0} + h_{i-1} \sum_{k=1}^{ncp} \Omega_k(1) \frac{dC_b}{dx_{i-1,k}} \\ V_{i,0} &= V_{i-1,0} + h_{i-1} \sum_{k=1}^{ncp} \Omega_k(1) \frac{dV_d}{dx_{i-1,k}} \\ P_{di,0} &= P_{di-1,0} + h_{i-1} \sum_{k=1}^{ncp} \Omega_k(1) \frac{dP_d}{dx_{i-1,k}}. \end{aligned} \quad (31)$$

Initial conditions are

$$\begin{aligned} C_{b1,0} &= C_f \\ V_{1,0} &= V_f \\ P_{d1,0} &= 0. \end{aligned} \quad (32)$$

Here  $0 \leq x_i^j \leq L$ ,  $i = 1 \dots 100$   $j = 1 \dots K$ .

Figure 3 gives the detailed discretization process and distribution of discretized variables. Since the NLP problem is formulated with large scale equations and variables through discretization of the original model, it can be solved by large scale NLP solvers such as IPOPT. If all the operational variables (feed pressure and feed flow rate) are fixed, the solution of the problem results in the simulation of the RO process; profiles of key performance parameters as well as detailed status variables can be obtained, which is helpful for us to understand the mechanism and the whole process.

#### 4. Model Simulation and Analysis Based on Seawater Desalination Plant

Based on the mathematical model and collocation method on finite element, the solution of the problem will yield the profiles of key performance parameters as well as the distribution of state variables. To verify the validity of the established model, data of a real seawater desalination plant is studied and then used for the simulation and analysis. The main process of the plant is the same as Figure 1. SW30HR-380 membrane modules were selected in series in the pressure vessel, and 55 pressure vessels were used to form two RO process units. Some conditional parameters are listed in Table 1.

Field data of a RO process are used for model verification and parameter identification. The key performance

TABLE 1: Feed condition of the seawater plant.

Feed concentration (kg/m <sup>3</sup> )	30
Feed temperature (°C)	25
Feed pressure (Bar)	59
Feed PH	5–8
Density $\rho$ (kg/m <sup>3</sup> )	1000 (at 0°C)
Kinematic viscosity (kg/m/s)	$1.02e - 6$ (at 0°C)

TABLE 2: Comparison of the actual performance with those from ROSA9.0 and our model.

Item	Rec (%)	Ry (%)
Field data	41.6	99.37
ROSA9.0	42.7	99.58
Model	42.1	99.52

parameters such as water recovery rate and salt rejection are compared to indicate the accuracy of the model. Comparison of the field data with those obtained from established models and ROSA9.0 is listed in Table 2. ROSA is a powerful software package developed by Dow Chemical Company to help design the RO process system [27]. As can be seen from Table 2, the overall results obtained from the established model are in good agreement with those obtained from both ROSA and the field data. Though the water recovery ratio and salt reject are lower than our model and that of ROSA9.0, the relative error is quite small. So the established model can be well used for the simulation and analysis of the seawater RO process. Since the established model was affected by feed temperature obviously, the properties and correction factor are also compared with the real data or the data from literature [13].

Figures 4, 5, and 6 are the comparison results between model value and real value; it can be seen that these property parameters agree with the real data with relatively high accuracy. The RO process model is fairly robust at the temperature range from 0°C to 60°C.

Based on the collocation method on finite element, simulation results are yielded through the solution of the discrete model. Simulation results are shown in Figures 7, 8, 9, 10, 11, 12, 13, 14, 15, and 16. From these figures it can be seen that the velocity of solvent, permeate flux, and concentration polarization in modules decrease nonlinearly along the length of membrane. The reason is that the feed flow is separated as two parts, and the pressure difference between the two sides decreases quickly. The osmosis pressure increase is the main factor for the decrease of pressure difference, which is shown in Figure 9. It also can be seen that the decrease of CP along the length of membrane is relatively small, and the rejection coefficient is higher than 99.4% along the length of membrane; the decrease is fairly small and the simulation value is almost the same as the real value. Figure 11 shows the relationship of feed TDS and permeate TDS; as the feed TDS increase linearly, the permeate TDS increase nonlinearly.

From (18), the value SEC is affected by the energy recovery efficiency  $\varepsilon_{pf}$  and the mechanical efficiency  $\varepsilon_p$ . Here they are

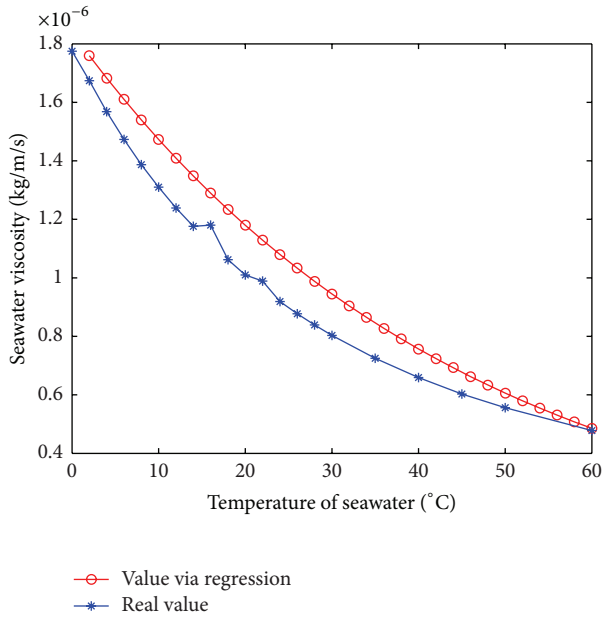


FIGURE 4: Value of seawater viscosity along temperature.

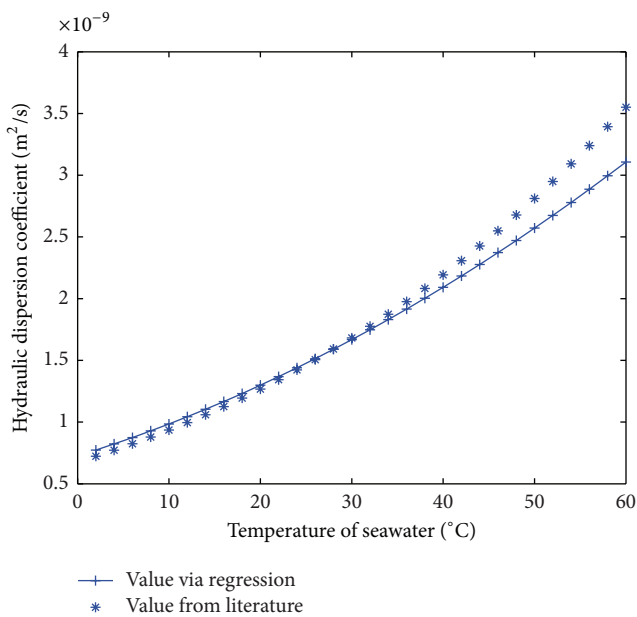


FIGURE 5: Comparison of DAB with literature.

set as 0.85 and 0.65, respectively. At the given feed condition of Table 1, calculation result shows that about 4.373 kw-h electricity energy should be consumed to produce one cubic meter freshwater. From Figure 16 it can be found that the value of SEC decreases at initial time when the feed pressure increases; then the SEC increases again as the pressure increases continually; there is a minimizing value as the feed pressure increases from about 30 bars to 90 bars. This means that through improving the operational condition, significant energy saving can be achieved.

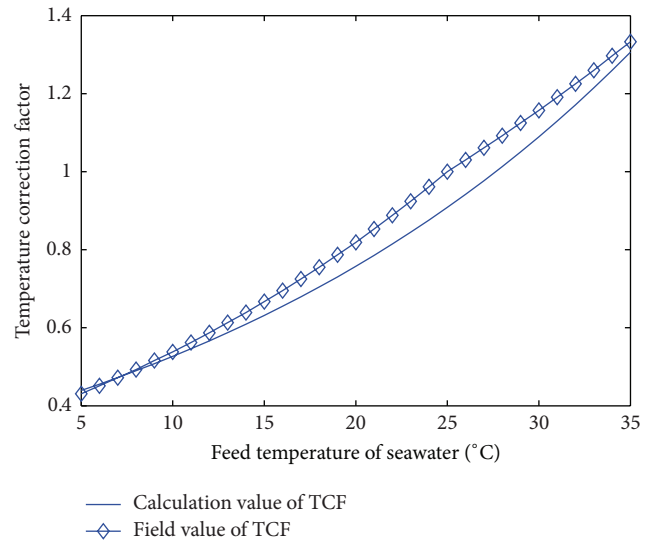


FIGURE 6: Comparison of TCF curve along temperature.

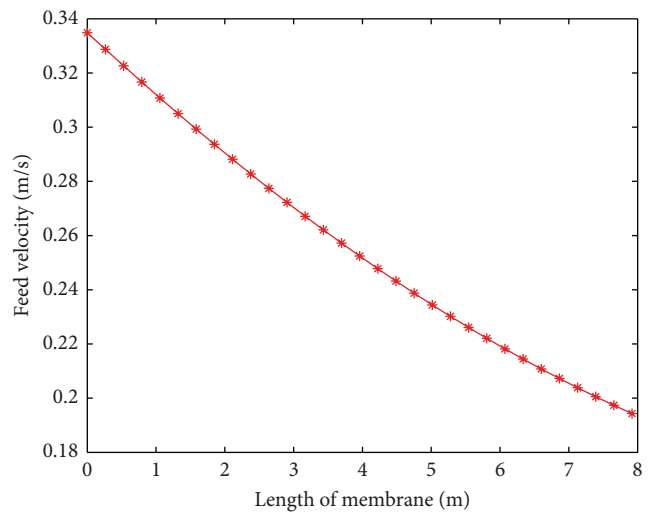


FIGURE 7: Flow velocity along the length of membrane.

Based on the well-established model, profiles of the relationship between feed conditions and key performance parameters can be obtained, which are listed in Figures 12–16. From Figure 12 it can be seen that Rec (water recovery ratio) increases quickly and almost linearly with the increase of feed pressure, because the increase of feed pressure can cause the increase of permeate flux  $J_v$ . The other parameter of salt reject increases nonlinearly and slowly with the increase of feed pressure; at the feed pressure of 59 bar, the salt reject is more than 99.5%. From Figure 13 it can be seen that Rec reduces quickly as the feed flow rate increases, while the  $R_y$  has the positive relationship with the feed flow rate; this is because of the fact that velocity in the feed channel has positive linear relationship with feed flow rate. And when the feed flow rate increases, the velocity of feed channel increases correspondingly, but the residence time of seawater in the channel will be largely decreased; there

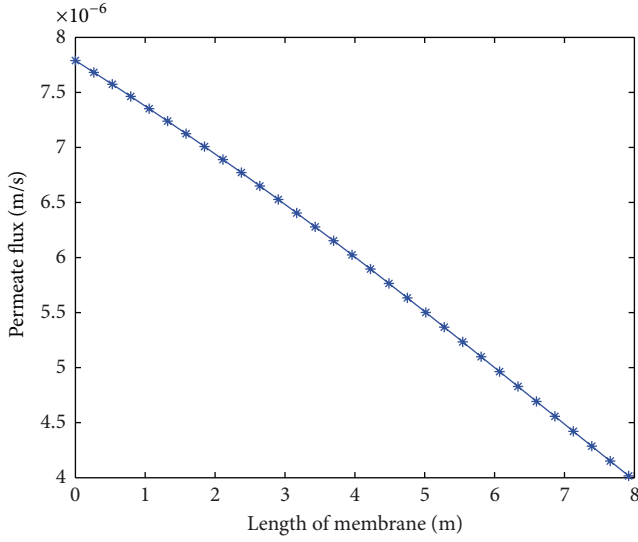
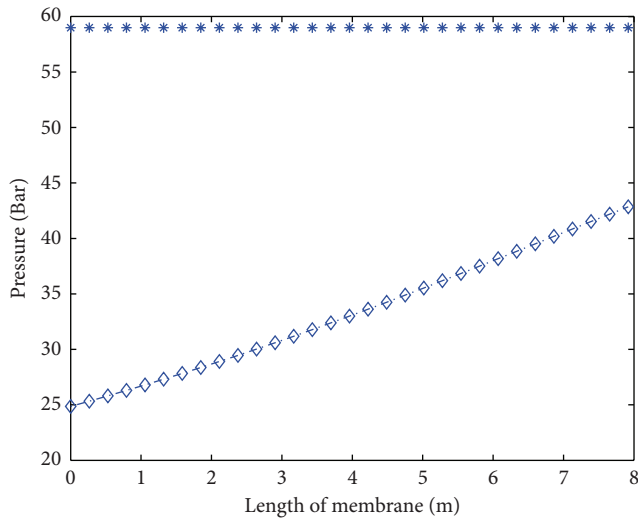


FIGURE 8: Permeate flux along the length of membrane.



—\*— Feed pressure  
 -◇- Osmosis pressure

FIGURE 9: Osmosis pressure along the membrane.

is also not enough time for salt to be transported to the permeate water side, which results in the reduction of Rec. From Figure 14, it can be seen that, as the feed concentration  $C_f$  increases, the water recovery and salt reject decrease substantially; this is explained by the needing of much more transmembrane osmotic pressure and more difficulty to resist the diffusion of brine. The effect of temperature on the RO process performance is shown in Figure 15, from which it can be seen that, with the increase of feed temperature, Rec increases substantially, but the Ry decreases accordingly. This can be explained by the increase of transport parameters  $A_w$  and  $B_s$  and the corresponding increase of permeate flux and solute flux.

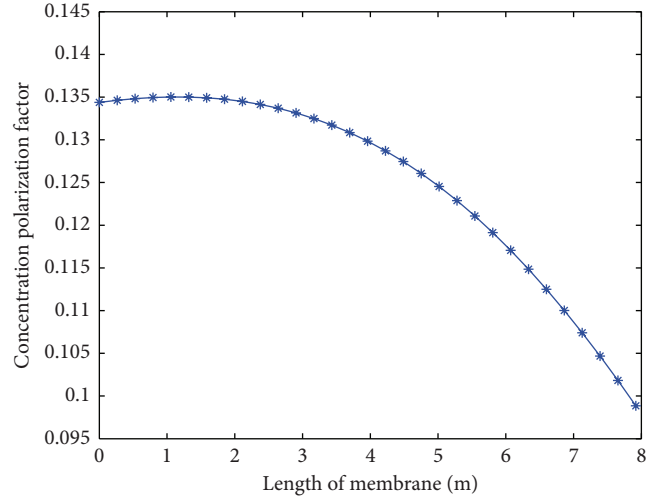


FIGURE 10: Concentration polarization along membrane.

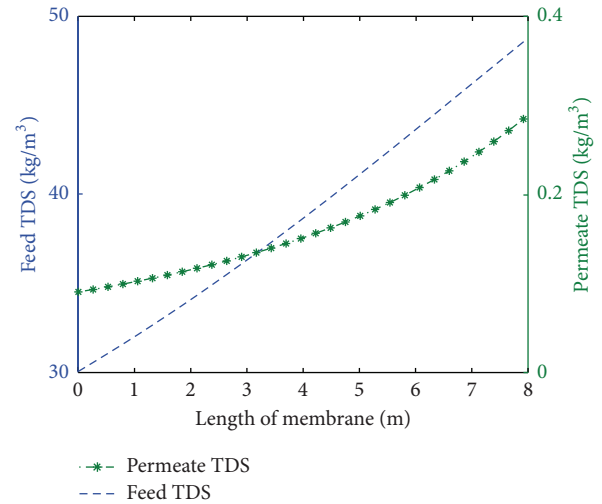


FIGURE 11: Values of feed TDS and permeate TDS along membrane.

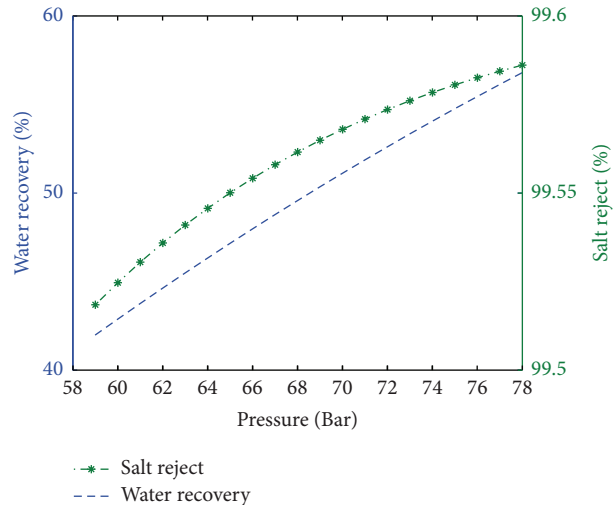


FIGURE 12: Rec and Ry as the function of feed pressure.

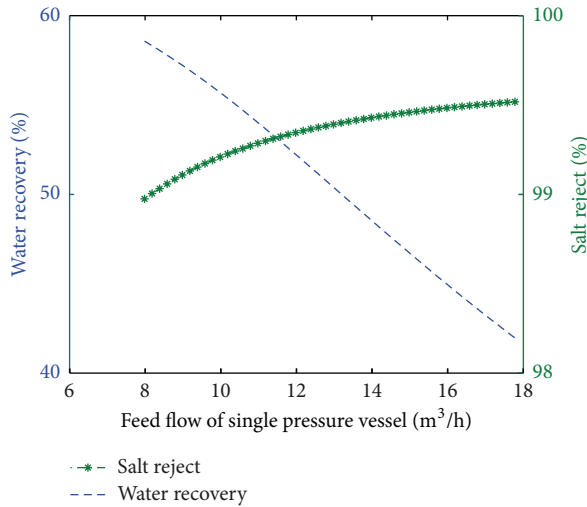


FIGURE 13: Rec and Ry as the function of feed flow rate.

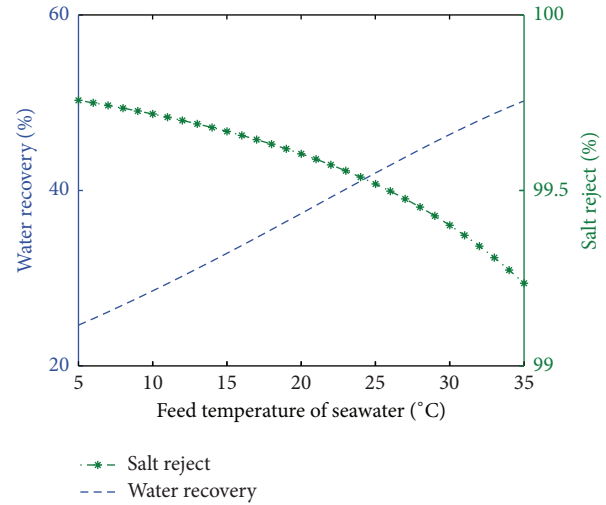


FIGURE 15: Rec and Ry as the function feed temperature.

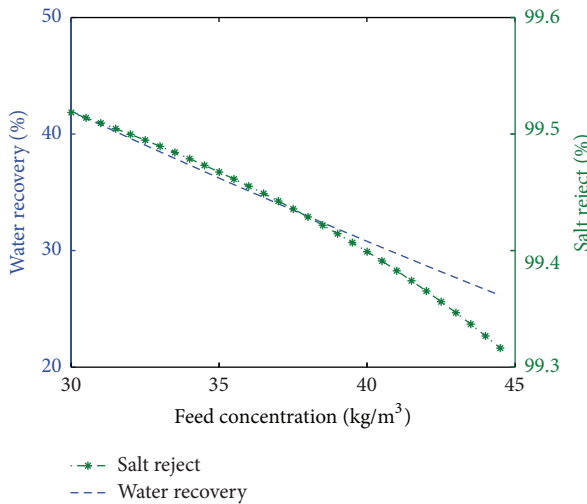


FIGURE 14: Rec and Ry as the function of feed concentration.

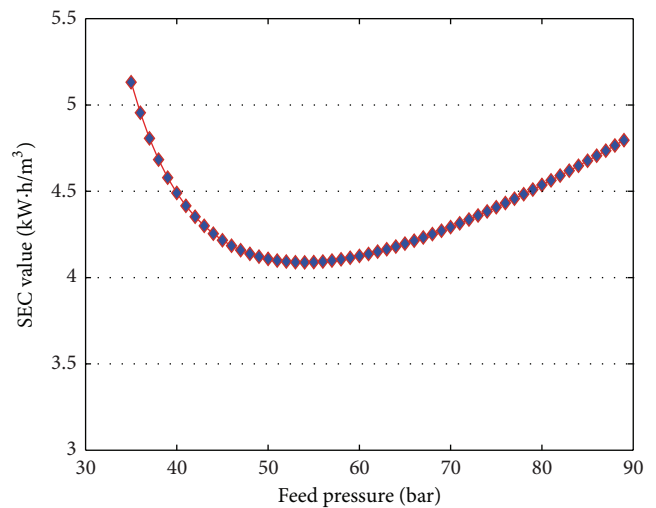


FIGURE 16: Sec value change curve along the feed pressure.

## 5. Conclusion

In this paper, based on the solution-diffusion and mass transfer theory, a spiral-wound SWRO process model is established. The model is expressed by DAEs (differential and algebraic equations) of (1)–(21) with some inequality and equality constraints of equipment and water quality. To solve the tough problem with high efficiency and accuracy, orthogonal collocation on finite element is proposed to transform the problem into NLP. All the state variables and intermediate variables are discretized and (1)–(21) are transferred into (28)–(32). Then IPOPT solver under GAMS platform is used for the efficient solution. And the efficient solution yields detailed simulation results related to operational variables and key performance. Profiles of feed pressure, feed concentration, and feed velocity along feed channel are investigated as well as relationship of water

recovery with temperature and feed pressure. SEC, which is the key performance parameter of energy consumption, is also calculated. The minimizing value in the middle curve shows that, through improving the operational condition, significant energy saving can be achieved. Factors including the feed conditions and operational temperature are also analyzed. All the work is helpful to further understand the mechanism of SWRO process, and shows the significant potential for energy saving through optimal operation.

## Nomenclature

$\alpha_1, \alpha_2, \beta_1$ : Constant parameters  
 $A_w$ : Membrane water permeability  
 ( $\text{m s}^{-1} \text{Pa}^{-1}$ )

$A_{w0}$ : Intrinsic membrane water permeability ( $\text{m s}^{-1} \text{Pa}^{-1}$ )  
 $B_s$ : Membrane TDS permeability (m/s)  
 $B_{s0}$ : Intrinsic membrane TDS permeability (m/s)  
 $C_f$ : Feed salt concentration ( $\text{kg/m}^3$ )  
 $C_r$ : Brine concentration ( $\text{kg/m}^3$ )  
 $C_p$ : Permeate concentration ( $\text{kg/m}^3$ )  
 $C_{sp}$ : Bulk concentration along feed channel ( $\text{kg/m}^3$ )  
 $C_m$ : Salt concentration on the membrane surface ( $\text{kg/m}^3$ )  
 $d_e$ : Hydraulic diameter of the feed spacer channel (m)  
 $D_{AB}$ : Dynamic viscosity ( $\text{m}^2/\text{s}$ )  
 $h_i$ : The length of the  $i$ th finite element  
 $h_{sp}$ : Height of the feed spacer channel  
 $J_v$ : Solvent flux  
 $J_s$ : Solute flux  
 $K_\lambda$ : Empirical parameter  
 $k_c$ : Mass transfer coefficient (m/s)  
 $L$ : Length of the RO module (m)  
 $n_l$ : Number of leaf in RO module  
 $P_f$ : Feed pressure (bar)  
 $P_d$ : Pressure drop along RO spiral wound module (bar)  
 $P_p$ : Pressure in permeate side (bar)  
 $P_b$ : Pressure along feed channel (bar)  
 $P_r$ : Brine pressure (bar)  
 $Q_f$ : Feed flow rate ( $\text{m}^3/\text{h}$ )  
 $Q_r$ : Brine flow rate ( $\text{m}^3/\text{h}$ )  
 $Q_p$ : Permeate flow rate ( $\text{m}^3/\text{h}$ )  
 $R$ : Gas law constant  
 $Re$ : Reynolds number (dimensionless)  
 $Sc$ : Schmidt number (dimensionless)  
 $Sh$ : Sherwood number (dimensionless)  
 $T$ : Operational temperature (K)  
 $V$ : Axial velocity in feed channel (m/s)  
 $W$ : Width of the RO module (m)  
 $Rec$ : Water recovery ratio (%)  
 $SEC$ : Specific energy consumption ( $\text{kw}\cdot\text{h}/\text{m}^3$ )  
 $Sp$ : Salt passage coefficient (%)  
 $Ry$ : Salt rejection coefficient (%)  
 $y_{i,q}$ : Values of algebraic variables in element  $i$  at collocation point  $q$   
 $u_{i,q}$ : Values of control variables in element  $i$  at collocation point  $q$   
 $z(t)$ : Differential variable  
 $z_{i-1}$ : Value of the differential variable at the beginning of element  $i$ .

### Greek Symbols

$\Delta\pi$ : Pressure loss of osmosis pressure (bar)  
 $\rho$ : Density of permeate water ( $\text{kg}/\text{m}^3$ )  
 $\mu$ : Kinematic viscosity ( $\text{kg m}^{-1} \text{s}^{-1}$ )  
 $\lambda$ : Friction factor  
 $\varepsilon_p$ : Mechanical efficiency of high pressure pump

$\varepsilon_{pf}$ : Energy recovery efficiency  
 $\Omega_q(t)$ : Polynomial of order  $K$   
 $\Psi_q(t)$ : Lagrange polynomial of degree  $K$ .

### Subscripts

$b$ : Bulk  
 $f$ : Module feed channel  
 $m$ : Membrane surface  
 $p$ : Permeate side  
 $s$ : Salt.

### Conflict of Interests

The authors declare that there is no conflict of interests regarding the publication of this paper.

### Acknowledgments

This work was supported by the National Natural Science foundation of China (nos. 60904058; 61374142), the National Key Technology Research and Development Program (2009BAB47B06), and the Natural Science Foundation of Zhejiang (LY12F03001). The authors would like to extend their sincere thanks to Dr. Yijun He from Shanghai Jiao Tong University for many helpful discussions.

### References

- [1] F. H. Butt, F. Rahman, and U. Baduruthamal, "Hollow fine fiber vs. spiral-wound reverse osmosis desalination membranes part 2: membrane autopsy," *Desalination*, vol. 109, no. 1, pp. 83–94, 1997.
- [2] M. A. Shannon, P. W. Bohn, M. Elimelech, J. G. Georgiadis, B. J. Marias, and A. M. Mayes, "Science and technology for water purification in the coming decades," *Nature*, vol. 452, no. 7185, pp. 301–310, 2008.
- [3] S. Gray, R. Semiat, M. Duke, A. Rahardianto, and Y. Cohen, "Seawater use and desalination technology," in *Treatise on Water Science*, P. Wilderer, Ed., pp. 73–109, Academic Press, Oxford, UK, 2011.
- [4] K. Wangnick, *IDA Worldwide Desalting Plants Inventory*, Report no. 17, Wangnick Consulting GmbH, Gnarrenburg, Germany, 2002.
- [5] B. Van der Bruggen and C. Vandecasteele, "Distillation vs. membrane filtration: overview of process evolutions in seawater desalination," *Desalination*, vol. 143, no. 3, pp. 207–218, 2002.
- [6] S. Ebrahim and M. Abdel-Jawad, "Economics of seawater desalination by reverse osmosis," *Desalination*, vol. 99, no. 1, pp. 39–55, 1994.
- [7] O. K. Buros, *The ABCs of Desalting*, International Desalination Association, Topsfield, Mass, USA, 2000.
- [8] A. Gambier, A. Krasnik, and E. Badreddin, "Dynamic modeling of a simple reverse osmosis desalination plant for advanced control purposes," in *Proceedings of the American Control Conference (ACC '07)*, New York, NY, USA, July 2007.
- [9] S. Senthilmurugan, A. Ahluwalia, and S. K. Gupta, "Modeling of a spiral-wound module and estimation of model parameters using numerical techniques," *Desalination*, vol. 173, no. 3, pp. 269–286, 2005.

- [10] J. Marriott and E. Sørensen, "A general approach to modelling membrane modules," *Chemical Engineering Science*, vol. 58, no. 22, pp. 4975–4990, 2003.
- [11] D. M. Libotean, *Modeling the reverse osmosis processes performance using artificial neural networks [Ph.D. thesis]*, University of California, Los Angeles, Calif, USA, 2007.
- [12] M. Khayet, C. Cojocaru, and M. Essalhi, "Artificial neural network modeling and response surface methodology of desalination by reverse osmosis," *Journal of Membrane Science*, vol. 368, no. 1-2, pp. 202–214, 2011.
- [13] A. Abbas, "Simulation and analysis of an industrial water desalination plant," *Chemical Engineering and Processing: Process Intensification*, vol. 44, no. 9, pp. 999–1004, 2005.
- [14] V. Geraldes, N. E. Pereira, and M. N. de Pinho, "Simulation and optimization of medium-sized seawater reverse osmosis processes with spiral-wound modules," *Industrial & Engineering Chemistry Research*, vol. 44, no. 6, pp. 1897–1905, 2005.
- [15] S. Sundaramoorthy, G. Srinivasan, and D. V. R. Murthy, "An analytical model for spiral wound reverse osmosis membrane modules: part I—model development and parameter estimation," *Desalination*, vol. 280, no. 1-3, pp. 403–411, 2011.
- [16] A. Sagiv and R. Semiat, "Finite element analysis of forward osmosis process using NaCl solutions," *Journal of Membrane Science*, vol. 379, no. 1-2, pp. 86–96, 2011.
- [17] V. V. Tarabara and M. R. Wiesner, "Computational fluid dynamics modeling of the flow in a laboratory membrane filtration cell operated at low recoveries," *Chemical Engineering Science*, vol. 58, no. 1, pp. 239–246, 2003.
- [18] A. Alexiadis, D. E. Wiley, A. Vishnoi, R. H. K. Lee, D. F. Fletcher, and J. Bao, "CFD modelling of reverse osmosis membrane flow and validation with experimental results," *Desalination*, vol. 217, no. 1-3, pp. 242–250, 2007.
- [19] G. Schock and A. Miquel, "Mass transfer and pressure loss in spiral wound modules," *Desalination*, vol. 64, pp. 339–352, 1987.
- [20] L. T. Biegler, "An overview of simultaneous strategies for dynamic optimization," *Chemical Engineering and Processing: Process Intensification*, vol. 46, no. 11, pp. 1043–1053, 2007.
- [21] J. V. Villadsen and W. E. Stewar, "Solution of boundary-value problems by orthogonal collocation," *Chemical Engineering Science*, vol. 22, no. 1967, pp. 1483–1502, 1967.
- [22] B. A. Finlayson, *Nonlinear Analysis in Chemical Engineering*, McGraw-Hill, New York, NY, USA, 1980.
- [23] L. T. Biegler, *Nonlinear Programming: Concepts, Algorithms and Applications to Chemical Processes*, Society for Industrial and Applied Mathematics, Cambridge University Press, Pittsburgh, Pa, USA, 2010.
- [24] M. Bartl, P. Li, and L. T. Biegler, "Improvement of state profile accuracy in nonlinear dynamic optimization with the quasi-sequential approach," *AIChE Journal*, vol. 57, no. 8, pp. 2185–2197, 2011.
- [25] A. Cervantes and L. T. Biegler, "Large-scale DAE optimization using a simultaneous NLP formulation," *AIChE Journal*, vol. 44, no. 5, pp. 1038–1050, 1998.
- [26] L. T. Biegler, A. M. Cervantes, and A. Wächter, "Advances in simultaneous strategies for dynamic process optimization," *Chemical Engineering Science*, vol. 57, no. 4, pp. 575–593, 2002.
- [27] [http://www.dowwaterandprocess.com/en/resources/rosa\\_system\\_design\\_software](http://www.dowwaterandprocess.com/en/resources/rosa_system_design_software).

## Research Article

# Water Demand Forecast in the Baiyangdian Basin with the Extensive and Low-Carbon Economic Modes

T. L. Qin, D. H. Yan, G. Wang, and J. Yin

Water Resources Department, China Institute of Water Resources and Hydropower Research, Beijing 100038, China

Correspondence should be addressed to D. H. Yan; denghuay@gmail.com

Received 13 December 2013; Revised 28 April 2014; Accepted 5 May 2014; Published 5 June 2014

Academic Editor: Yuefei Huang

Copyright © 2014 T. L. Qin et al. This is an open access article distributed under the Creative Commons Attribution License, which permits unrestricted use, distribution, and reproduction in any medium, provided the original work is properly cited.

The extensive and low-carbon economic modes were constructed on the basis of population, urbanization level, economic growth rate, industrial structure, industrial scale, and ecoenvironmental water requirement. The objective of this paper is to quantitatively analyze effects of these two economic modes on regional water demand. Productive and domestic water demands were both derived by their scale and quota. Ecological water calculation involves the water within stream, wetland, and cities and towns. Total water demand of the research region was obtained based on the above three aspects. The research method was applied in the Baiyangdian basin. Results showed that total water demand with the extensive economic mode would increase by 1.27 billion m<sup>3</sup>, 1.53 billion m<sup>3</sup>, and 2.16 billion m<sup>3</sup> in 2015, 2020, and 2030, respectively, compared with that with low-carbon mode.

## 1. Introduction

Affected by climate change and economic-social development, water resource problems such as excess water, water shortage in quantity and quality, aggravation of hydroecological and hydroenvironmental system, disorder of hydrosedimentary system, low water efficiency, and unsustainable water resource management which has been discussed by Wang [1] have become more diverse and serious. These problems have led to water resource crisis and intensified the relationship between water supply and water demand.

Water demand forecast has gained more attention in water-deficient areas due to the increasing water requirement of rapid economic development. It is not only the basis of national economic and social development plans, water resource plans, and operation plans of hydraulic projects and water management, but also the equilibrium point between social-economic system and ecoenvironmental system, as discussed elsewhere [2, 3]. Different economic development modes should be taken into consideration of the water demand forecast of different level years in the future for targets of economic and social development, energy conservation and pollution reduction, and water resources protection. It becomes a key technique for rational allocation of water resources towards the low-carbon development

mode, rational deployment of water resources based on macroeconomic structure, and ecology-oriented reasonable deployment of water resources, as discussed elsewhere [4–7].

Research of water demand abroad began at the 1st evaluation of national water resources in USA in 1968. Water use structure in most developed countries such as EU and US has changed into sustainable mode steadily. Forecast method of water demand is becoming mature. Gistau et al. established pattern recognition model to forecast short-term domestic and industrial water demand [8, 9]. Zhou et al. applied time series method in the city of Melbourne to forecast daily urban water demand [10]. Mays established logarithmic and semilogarithmic regression model relating water demand and relative factors for the media-long term and applied it to Texas of USA [11]. Adamowski established peak daily water demand forecast modeling using artificial neural networks [12]. Yasar et al. forecast water demand of Adana city of Turkey using stepwise multiple nonlinear regression analysis model [13].

In China, water demand forecast began when the 1st evaluation of national water resources started in 1980. Zhong et al. constructed comprehensive prediction method based on the general formula, integrating advantages of some common methods [14]. Zhang et al. forecast domestic water demand of Beijing with multiple-linear regression model [15]. Lv et al. established practical dynamic model of urban water

TABLE 1: Comparison of two factors of two economic modes.

Item	Extensive economic mode	Low-carbon economic mode
Economic growth rate	Rate of 2010	Optimal economic growth rate
Industrial structure	Structure of 2010	Optimal structure
Water use quota	Quota of 2010	Decreasing water quota in accordance with Twelfth Five-Year Plan of Water Conservancy
Water use structure	Status of 2010	Adjusting the structure of water use in accordance with the optimal industrial one
Natural ecological water demand	No consideration	Considering reasonable ecological flow requirement within the stream and wetland ecological water demand

consumption [16]. Zhang et al. established projection pursuit model of water demand prediction based on IEA which solved high dimension, nonlinear, nonnormal problems, and so forth [17].

Research advances above show that the developments of mathematical methods and computer simulation technique promote water demand forecast methods. There are three types of forecast methods, including trend analysis, time series, and numerical simulation. Some methods are in common use at present, such as pattern recognition model, regression model, comprehensive prediction method based on the general formula, practical dynamic model to predict water consumption, grey system method, projection pursuit means, and artificial neural networks [18–24].

These above means are produced and applied to water demand forecast in different basins. However, they lack effect analysis of low-carbon economic development mode on water consumption and comparison of water demand forecast between varied economic modes. Economic development mode of China is being changed into green, low-carbon, and sustainable mode so that water demand forecast has to consider its effect on regions and different water users.

The purpose of this paper is to analyze effect of extensive and low-carbon economic development mode on total regional water demand and different water users. In the former mode, many kinds of resources are consumed to keep rapid economic growth but there exists unreasonable structure of industries and water use, resulting in the occupancy of ecological water demand, excessive water consumption by economic-social system, large energy consumption, and carbon emission. The content of carbon dioxide in the atmosphere could increase, which could intensify regional climate change. In the latter mode, total water consumption, energy consumption, and carbon emissions are all reduced by decreasing quota of water use and optimizing the structure of industries, water use, and energy consumption and considering reasonable water demand of ecosystems. This mode can promote the construction of low-carbon society and mitigate climate change. Key factors of the two modes are detailed in Table 1.

## 2. Materials and Methods

**2.1. Study Area.** The Baiyangdian basin is located in the middle of the North China Plain and Haihe River basin.

Its geographic coordinates are roughly  $E113^{\circ}40' \sim E116^{\circ}48'$  and  $N38^{\circ}10' \sim N40^{\circ}03'$ . The basin covers an area of about  $34878.25 \text{ km}^2$ .

Rivers stretch through Shanxi province, Hebei province, and Beijing municipality. The inflow is mainly from upstream rivers including Juma River, Zhong-yishui River, Baigou River, Puhe River, Caohe River, Qingshui River, Tanghe River, Zhulong River, and Cihe River. Through Zaolinzhuang conjunction, these rivers flow into Zhaowang New Channel and then converge into Dongdian of Baiyangdian wetland. After that they flow into Xiaobai River in the lower reach and then flows into Haihe River through Duliujian River, as discussed by Bai and Ning [25], shown in Figure 1.

Annual average precipitation volume of the basin is 1.902 billion  $\text{m}^3$ , 70%–80% of which falls in the flood season from June to September, as discussed by Wang and Xu [27].

Total amount of water consumption was about 4.65 billion  $\text{m}^3$  in 2010, of which productive, domestic, and ecoenvironmental water consumption were, respectively, 4.05 billion  $\text{m}^3$ , 0.47 billion  $\text{m}^3$ , and 0.13 billion  $\text{m}^3$ . Gross domestic product (GDP) was about 460.26 billion RMB in the same year, of which the growth rate was greater than 10%. Economic development and population growth brought about high water consumption. There are series of ecoenvironmental problems in the basin, including water resource shortage, groundwater overexploitation, ecological water being taken possession, occupied ecological land, and deteriorated water quality.

**2.2. Basic Data.** Water demand forecast involves six types of data, consisting of socioeconomic development, water resource, scale and quota of water consumption, water use indexes, and hydrological observation data. Details and sources are listed in Table 2.

**2.3. Forest Method.** Water demand forecast of research region includes productive, domestic, and ecological part. Details are listed in Table 3. The two former parts and ecological demand for cities and towns were derived by multiplying scale by quota. The technical framework of this paper is detailed in Figure 2.

In respect of production water demand, based on the historical data of GDP, optimal economic growth rate and GDP were obtained with Cobb-Douglas production function

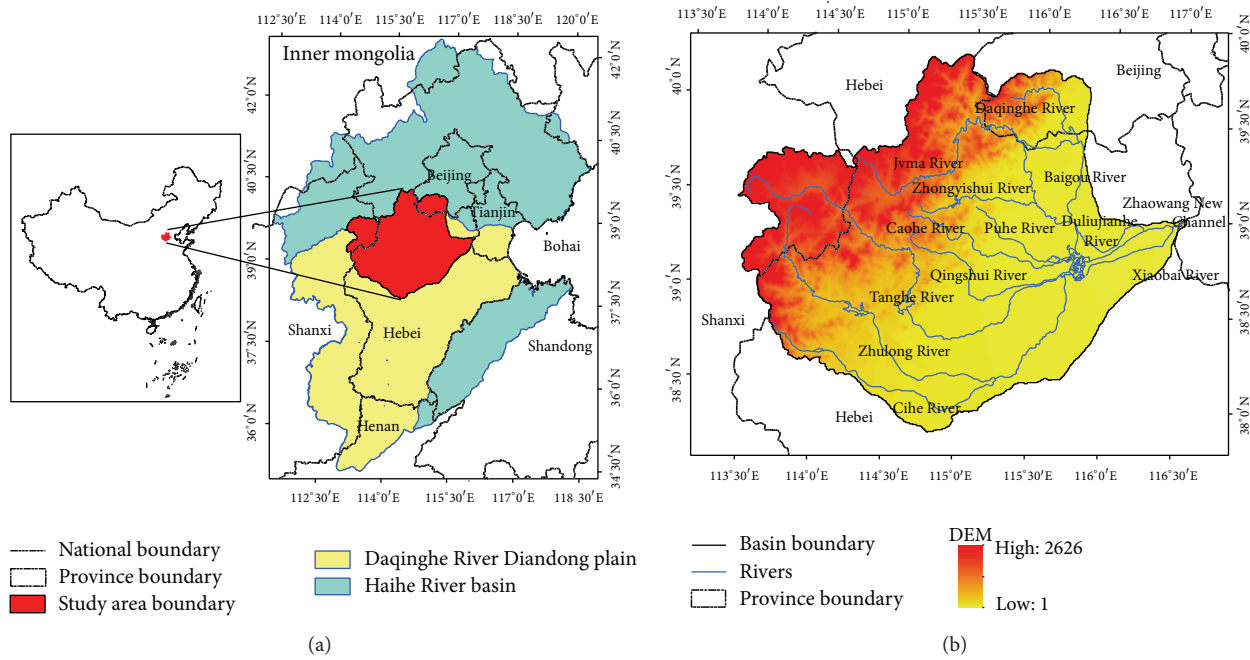


FIGURE 1: (a) Location of research area; (b) river net and digital elevation distribution [26].

TABLE 2: Basic data of water demand forecast.

Data type	Details	Major source
Socioeconomic development	Population, urbanization level, GDP, industrial structure, and investment in fixed assets	Statistical yearbook of Beijing municipality, Hebei province, and Shanxi province during 2005–2010
Water resource amount	Water consumption	Water resources bulletin and attached list during 2001–2010
Water-consumption scale	Irrigation area, forestland area, fish pond area, the number of livestock and poultry, and green land area of cities	Statistical yearbook of Beijing municipality, Hebei province, and Shanxi province during 2005–2010
Water-consumption quota	Irrigation quota, water-consumption quota of animal husbandry and fishery, and water-consumption quota of secondary and tertiary industry	Water conservancy yearbook during 2005–2010 and Twelfth Five-Year Plan of Beijing municipality, Hebei province, and Shanxi province
Water-consumption index	Water efficiency of irrigation and cannels	Water conservancy yearbook of Beijing municipality, Hebei province, and Shanxi province during 2005–2010
Hydrological data	Daily flow discharge	Hydrological yearbook during 1956–2000

TABLE 3: Major departments of productive, domestic, and ecological water users.

Water users	Major divisions
Productive users	
Primary industry	Agriculture, forestry, animal husbandry, and fishery
Secondary industry	General industry and construction
Tertiary industry	Other industries except for the primary and secondary industry, including service, banking, insurance, transportation, medical treatment, and education
Domestic users	Residents of cities and villages
Ecological users	Natural and artificial ecosystem

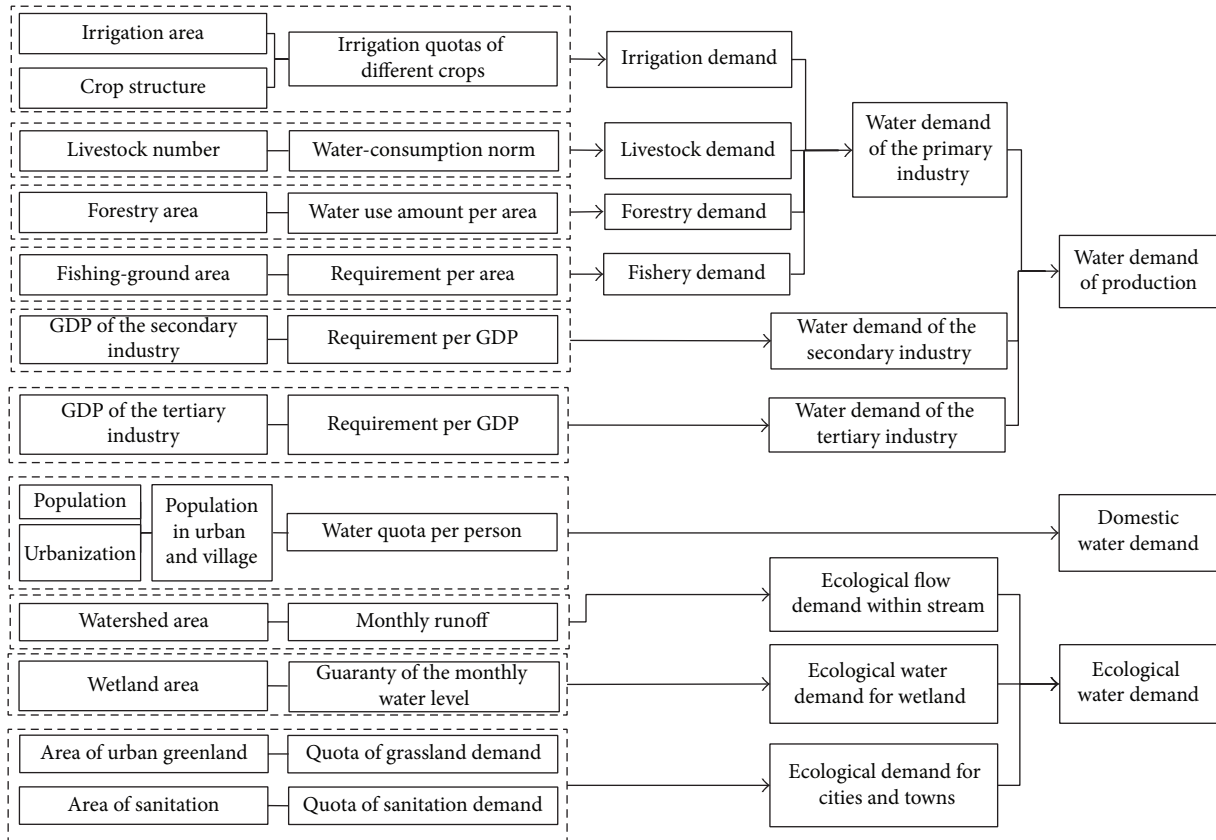


FIGURE 2: Technical framework of water demand. Remark: the left is “scale” and the right “quota” in the box with dotted line.

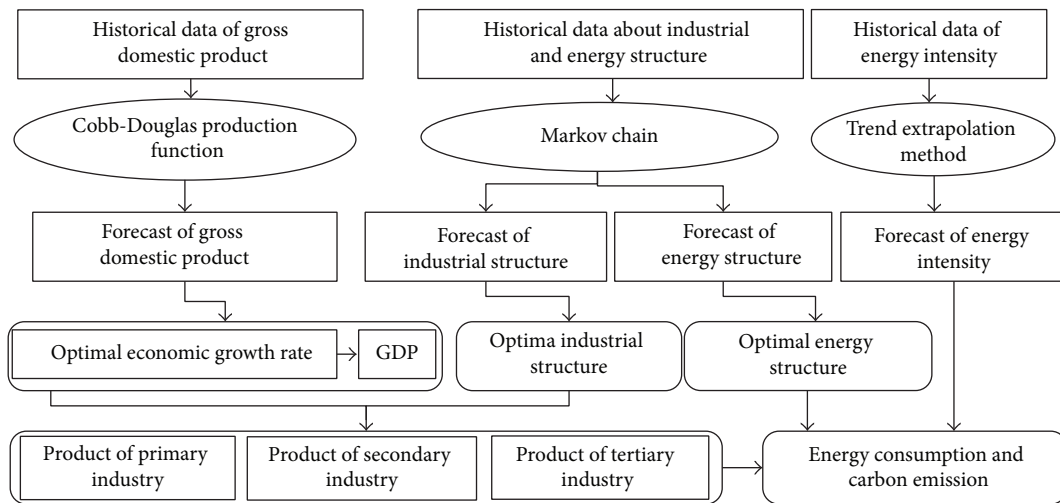


FIGURE 3: Method of forecasting GDP and carbon emission with the low-carbon mode.

which had the lowest total energy consumption. Optimal industrial structure and water use one were derived with Markov chain. The product of primary industry, secondary industry, and tertiary industry is, respectively, obtained based on forecasted results of optimal GDP and industrial structure. Then, the water demand scale of secondary industry and tertiary industry can be derived. Energy intensity was

forecast with linear trend extrapolation method. Total energy consumption and carbon emissions were both derived based on these factors. Relationship of the above forecast methods is shown in Figure 3.

In respect of domestic water demand, population was forecast with the rate of natural population increase and urbanization level with linear trend extrapolation method.

TABLE 4: Net irrigation quotas of different kinds of crops in different areas of basin; unit: mm.

Region	Wheat	Summer corn	Spring corn	Cotton	Fruit	Vegetable	Miscellaneous cereals
Mountainous region	218	56	99	—	225	306	28
Hilly region	218	113	98	—	225	303	—
Plain region	191	112	—	117	225	261	—

In respect of water demand of natural ecosystem, ecological flow demand within stream was forecast based on the monthly runoff of major hydrostation and ecological water demand of wetland was forecast based on the monthly water level for different guaranties.

2.4. Forecast of Population and Urbanization

2.4.1. Population. The rate of natural population increase was considered in population forecast, while mechanical growth rate was not considered in this paper because of its uncertainty. Regional population was forecasted with the following formula:

$$P = P_0(1 + k)^t, \tag{1}$$

where  $P$  and  $P_0$  are the total population of planning level year and status year, respectively,  $t$  is the number of planning level years, and  $k$  is the natural increase rate during planning years.

2.4.2. Urbanization Level. Urbanization level is an important index weighing regional economic development. Trend extrapolation method was adopted to forecast it based on urbanization evolution during 2000–2010. Forecast methods of the two above factors are suitable for both extensive and low-carbon economic modes.

2.5. Economic Index

2.5.1. Economic Growth Rate. Economic growth rate of extensive economic mode was the same as that of 2010. In low-carbon economic mode, Cobb-Douglas productive function model was adopted to forecast and optimize economic growth rate. Then, GDP was obtained.

This model relates optimal economic growth rate with low energy consumption, meeting the target of low-carbon mode. Moon and Sonn established Cobb-Douglas productive function model to research the relationship between economic growth and energy consumption [28]. It is as follows:

$$Y(t) = (A_0 e^{vt})^{1/\alpha} \tau(t)^{(1-\alpha)/\alpha} (\omega N_0 e^{nt})^{\gamma/\alpha} K(t), \quad 0 < A_0 < 1. \tag{2}$$

Zhu et al. integrated employment rate and scientific technology factor into this function to improve it [29]. Then, improved optimal steady economic growth rate is as follows:

$$g(t) = \left( n - \frac{\rho}{\delta} \right) + \frac{1}{\delta} (\varepsilon - \theta) (A_0 e^{vt})^{1/\alpha} \tau(t)^{(1-\alpha)} (\omega(t) N_0 e^{nt})^{\gamma/\alpha}, \tag{3}$$

where  $\tau(t)$  is energy intensity of the year  $t$ , which is ton of standard coal equivalent per 10 thousand RMB of GDP;  $L(t)$  is the labor population of the year  $t$ ;  $N_0$  is the total population of the initial year;  $\omega(t)$  is the labor force participation rate, the same as employment rate;  $n$  is the annual average rate of population growth;  $\alpha$  is the capital output elastic coefficient;  $\gamma$  is the labor output elastic coefficient;  $v$  is the growth rate of total factor productivity;  $\delta$  is the risk aversion coefficient;  $\rho$  is the rate of time preference;  $\varepsilon$  is error term;  $\varepsilon = 1 - \delta$ .

2.5.2. Industrial Structure. The ratio of the primary, secondary, and tertiary industry was forecast with Markov chain. Its result was used in low-carbon mode, while structure of 2010 was used in extensive mode.

2.6. The Forecast of Production Water Demand

2.6.1. The Primary Industry. Irrigation water demand is affected by precipitation, cultivated land, crop structure, irrigation area, and efficiency. In this paper, the point is economic development and agricultural planting so precipitation forecast is not considered temporally.

In the low-carbon economic mode, gross irrigation water requirement of the 2015 level year was forecast based on cultivated land area, crop structure, irrigation quotas of different crops, and water use efficiency of irrigation requested by Twelfth Five-Year Plan. The above factors related to irrigation were the same as those of 2010 except for cultivated land area with the extensive economic mode. However, in the low-carbon mode, they were forecast with methods as follows.

Change rates of cultivated land area in 2015, 2020, and 2030 were forecast with trend extrapolation method on the basis of the status land area and the request of Twelfth Five-Year Plan. The results showed that change rates of Beijing municipality, Hebei province, and Shanxi province were  $-4.8\%$ ,  $+1.4\%$ , and  $+1.48\%$ , respectively.

Net irrigation quotas of different crops were referred to those set in *Technique routine of high efficient water use of Hebei province* and *Local standard of water use of Hebei province (DB13)*, shown in Table 4. Irrigation quotas of Beijing Municipality and Shanxi province were similar as those of Hebei province because data collection was too difficult.

Water efficiency of irrigation of Beijing municipality is required to reach up 53% and of Hebei province 74% in 2015. There is no request for Shanxi province.

Water requirement of livestock was forecast based on livestock number and water consumption norm. In low-carbon economic mode, daily water requirements of large

TABLE 5: Forecast result of livestock amount for the whole basin; unit: 10 thousand.

Year	Large livestock	Small livestock	Poultry
2015	76	591	5964
2020	63	557	4369
2030	77	599	6180

livestock, small livestock, and poultry were  $0.1 \text{ m}^3$ ,  $0.025 \text{ m}^3$ , and  $0.001 \text{ m}^3$ , respectively, according to *local standard of water use of Hebei province (DB13)*. In extensive economic mode, this quota was the same as that of 2010. Amount of livestock was forecast with trend extrapolation method using historical data during 2000–2010, shown in Table 5. It is improved according to the requirements in the Twelfth Five-Year Plan. The result was used in two economic modes.

The result showed that the amount of livestock would be controlled in 2015 but would increase in 2030 due to scientific cultivation technology and people's diet. Forestry water demand was forecast based on the area and water use amount per area. Gross demand of forestry was derived with efficiency of water supply system. Growth rate of forestry area of Beijing municipality, Hebei province, and Shanxi province would be 8%, 1%, and 0.5%, respectively, according to the demand of the Twelfth Five-Year Plan. As a result, the area of Baiyangdian basin would be 55457 ha, 58177 ha, and 68427 ha in 2015, 2020, and 2030. The data is for both extensive and low-carbon economic modes.

Fishery demand was forecasted based on the area of fishing ground and water requirement per hectare. Because of the shortage of historical data of water use amount per fishing-ground area in Beijing municipality and Shanxi province, their quotas were forecasted with trend extrapolation method on the basis of historical sequence in Hebei province during 2000–2010. Gross quota of the whole basin would be 10.7 thousand  $\text{m}^3$ , 11.4 thousand  $\text{m}^3$ , and 9.2 thousand  $\text{m}^3$  per hectare in 2015, 2020, and 2030, respectively. With trend extrapolation method based on historical sequence during 2000–2010, the area of fishing ground would be 5115.6 ha, 5112.6 ha, and 5106.7 ha in 2015, 2020, and 2030, respectively.

In view of the two parameters mentioned above and efficiency of water supply system, gross water demand of fishery was obtained. In the extensive mode, efficiency of water supply system was the same as that of 2010; in the low-carbon mode, it was set according to the request of Twelfth Five-Year Plan.

**2.6.2. The Secondary and Tertiary Industry.** Water demand of the secondary and tertiary industry was forecasted based on GDP, status and planning industry quota, efficiency of water supply system, and utilization ratio of recycled water.

GDP of the secondary and tertiary industry was forecasted based on industrial structure and optimal economic growth rate, which is shown in Table 6.

Water consumption of the whole basin was  $22.8 \text{ m}^3$  per 10 thousand GDP in 2010, which was adopted in the extensive mode. According to Twelfth Five-Year Plan, this index of Beijing municipality and Shanxi province would decrease by

TABLE 6: GDP of the secondary and tertiary industry for the low-carbon mode; unit: billion RMB.

Type	2015	2020	2030
The secondary industry	301.87	428.54	751.89
The tertiary industry	230.09	335.95	612.97

TABLE 7: Estimation of key parameters.

Parameter	Value	<i>t</i> -test value	Significance level
$A_0$	1.666	4.495	0.002
$v$	0.009	2.582	0.033
$\alpha$	0.487	6.015	0.000
$\gamma$	0.099	0.571	0.586

15%, 30%, and 16.3%, respectively, so that the whole basin would decrease by 25%. It was adopted in the low-carbon mode.

The rate of treated sewage and reclaimed wastewater would increase to 85% and 15% according to Twelfth Five-Year Plan of National Municipal Wastewater Treatment and Reclaimed Wastewater Facility Construction.

**2.7. Domestic Water Demand.** Domestic water demand was forecasted through multiplying population by water quota per person based on population, urbanization level, the quota of domestic water use, and efficiency of water supply system. The last parameter was the same as that from Twelfth Five-Year Plan for the low-carbon mode, while it was the same as status data of 2010 in the extensive mode.

Natural population growth rates of Beijing municipality, Hebei province, and Shanxi province should not be bigger than 7.2‰, 7.13‰, and 6.5‰, which were specified by Twelfth Five-Year Plan. According to forecast result of natural growth rate, population of the whole basin would be 14.79 million, 14.91 million, and 15.01 million in 2015, 2020, and 2030.

Results showed that urbanization level would rise up to 55.13%, 59.72%, and 63.59% in 2015, 2020, and 2030. Net quota of domestic water use for each people was forecast with trend extrapolation method on the basis of historical sequence of domestic water use and population during 2001–2010. Net quota of cities would be 54.4 L/d, 49.2 L/d, and 46.8 L/d, while net rural quota would be 56.6 L/d, 57.5 L/d, and 57.9 L/d.

**2.8. Ecological Water Demand.** Ecological water users include natural system and artificial system. The former one involves ecological flow requirement within the stream and wetland ecological water demand and the latter one involves water demand in green land of cities and towns. This part was also considered in the low-carbon mode.

**2.8.1. Ecological Flow Demand within Stream.** Considering both calculation requirement and present data, ecological flow demand within stream equaled the maximum value between 90% of flow frequency and average runoff of the

TABLE 8: Optimal economic growth rate and energy consumption with different economic modes.

Year	Extensive mode		Low-carbon mode	
	Energy consumption (Mtce)	Economic growth rate (%)	Energy consumption (Mtce)	Optimal economic growth rate (%)
2015	99.1	12.3	74.6	8.2
2020	176.99	12.3	91.6	6.9
2030	564.58	12.3	119.9	5.2

driest period. Ecological flow demand within stream of lack-data watershed was converted with area compared to the one having data. That was because hydrological stations with observation data were all in the upstream and there was no main stream in Baiyangdian basin.

2.8.2. *Ecological Water Demand for Wetland.* Ecological water demand for Baiyangdian wetland was forecasted to protect the wetland and brought into full play its ecoenvironmental and social-economic effect. Considering factors such as protection targets, protection scale, constituents of ecosystem, and trophic structure of Baiyangdian wetland, ecological water demand for wetland was assessed under different schemes.

2.8.3. *Ecological Demand for Cities and Towns.* This part involves grassland and sanitation. Relevant quota was set according to Twelfth Five-Year Plan of Water Resource. Based on status water use of Haihe River basin and Integrated Plan of Water Resource in Hebei, quotas of grassland and sanitation are 3000 m<sup>3</sup> and 900 m<sup>3</sup> per hectare. The ratio of green land in Beijing municipality, Hebei province, and Shanxi province is requested to be 57%, 35%, and 36% in 2015, respectively.

### 3. Results and Discussion

3.1. *Population and Urbanization Level.* Results showed that the population of Baiyangdian basin would be 14.79, 14.91, and 1.51 million persons and urbanization level would be 55.1%, 59.7%, and 63.6% in 2015, 2020, and 2030.

3.2. *Economic Growth and Energy Consumption.* Linear regression analysis was used to derive key parameters of Cobb-Douglas productive function model of Baiyangdian basin with SPSS, shown in Table 7.

Results demonstrated that equation fitting rate  $R^2$  was equal to 0.995 and significance levels of  $A_0$ ,  $v$ , and  $\alpha$  were under that of 5% except  $\gamma$  which was not significantly related to economic growth rate. As a result, the labor force participation rate was not involved in this model and the function is changed as follows:

$$g(t) = -\frac{1}{\delta} \left[ \rho - (\varepsilon - \theta\tau(t)) (A_0 e^{vt})^{1/\alpha} \tau(t)^{(1-\alpha)} \right]. \quad (4)$$

That may be caused by short sequence of historical data. Penetration rate of carbon emission reduction and energy saving technology can be integrated into the model if possible in the future.

TABLE 9: Water demand of the primary, secondary, and tertiary industry at the different planning levels (0.1 billion m<sup>3</sup>).

Type	Status level			Planning level		
	2015	2020	2030	2015	2020	2030
Agriculture	32.12	32.72	33.05	19.81	20.1	20.39
Forestry	2.04	2.52	3.85	1.77	2.18	3.33
Livestock	1.62	1.4	1.65	0.9	0.78	0.91
Fishery	0.55	0.58	0.47	0.47	0.51	0.41
Primary industry	36.32	37.22	39.03	22.95	23.56	25.05
Secondary industry	6.89	9.78	17.20	2.98	4.23	7.42
Tertiary industry	2.45	3.58	6.54	1.06	1.55	2.82

Optimized economic growth rate simulated from the function model should conform to the actual growth rate so this could be a constraint condition for the regulation of  $\delta$  and  $\rho$ . Thus we got  $\delta = 8.903$  and  $\rho = -0.829$ .

Based on the estimation of the above parameters, optimal economic growth rate and energy consumption were derived for the low-carbon economic mode, shown in Table 8.

3.3. *Water Demand of Production.* Water demand of the primary industry accounts for more than 60% of the total demand of production. However, rapid development of the secondary and tertiary industry leads to the low weight of the primary industry. Results showed that no matter whether the water use was maintained in the current situation or according to the Twelfth Five-Year Plan, gross water demand of the primary industry would decrease, while the secondary and tertiary industry would increase, which is shown in Table 9.

3.4. *Domestic Water Demand.* According to the result, with the increase of urbanization, water demand of cities would have an increasing trend and that of villages would have a decreasing trend, which is shown in Table 10. Due to the increasing water efficiency of cities and decreasing quota of each person, the increase rate of domestic water demand would slow down in the future.

#### 3.5. Ecological Water Demand

3.5.1. *Ecological Water Demand within Stream.* Monthly water demand within stream was derived with the principle of no river blanking based on natural monthly data of Wang Kuai, Xidayang, Zijinguan, Angezhuang, Zhang Fang, and Hengshanling hydrological station. Results are shown in Table 11.

TABLE 10: Domestic water demand of the basin in the different planning level year; unit: 0.1 billion m<sup>3</sup>.

Status						Plan					
2015		2020		2030		2015		2020		2030	
City	Village	City	Village	City	Village	City	Village	City	Village	City	Village
2.27	2.37	2.40	2.16	2.54	1.80	1.97	2.05	2.08	1.87	2.20	1.56

TABLE 11: Monthly water demand of typical hydrological station in the basin; unit: 10 thousand m<sup>3</sup>.

Hydrological station	Wang Kuai	Xidayang	Zijinguan	Angezhuang	Zhang Fang	Hengshanling
River name	Zhulong River	Ci River	Juma River	Zhongyishui River	Juma River	Ci River
Monthly runoff of 90% frequency	0	419	589	0	718	0.00
Average annual value	530	1019	935	20	1544	47
Monthly water demand	530	419	589	20	718	47

TABLE 12: Annual ecological water demand of different rivers in the basin (0.1 billion m<sup>3</sup>).

River	Juma River	Zhongyishui River	Pu River, Cao River, and Qingshui River	Tang River	Sha River	Ci River	Whole basin
Amount of ecological water demand within stream	0.86	0.02	0.06	0.50	0.64	0.06	2.14

Both Zi-jinguan and Zhang-fang hydrological station are in the Jvma river. As a result, their maximum was chosen as the monthly water demand of the river. There is a lack of observation data of Pu River, Cao River, and Qingshui River. Their annual water demand was converted through comparing area of them to that of Zhong-yishui river. Annual ecological water demand of main rivers in the upstream was derived and that of the whole basin was 0.214 billion m<sup>3</sup>, shown in Table 12. It would be 0.136 billion m<sup>3</sup> only if the monthly runoff of 90% frequency was considered.

Monthly forecast of ecological water demand within stream was not completed because of incomplete data of precipitation, runoff and evaporation, and no match on spatial and temporal scale. If enough regional data is got, dynamic analysis will be done.

3.5.2. *Ecological Water Demand of Baiyangdian Wetland.* 65% and 75% guaranties of the monthly water level are suitable for bulrush production, fishery production, diversion and storage of floods, and keeping the habit of target species, the great reed warbler, as discussed by Zhao [30]. Corresponding annual water demand of wetland is 0.472 and 0.389 billion m<sup>3</sup>. The latter was more suitable for this paper considering the cost of water supply.

3.5.3. *Ecological Demand for Cities and Towns.* Forecast results of ecological demand for cities and towns are shown in Table 13.

3.6. *Total Water Demand.* Total water demand was derived based on the above results and it was demonstrated that it would increase by 1.269, 1.529, and 2.163 billion m<sup>3</sup> in 2015,

TABLE 13: Ecological demand for cities and towns in the basin (10 thousand m<sup>3</sup>).

Status			Plan		
2015	2020	2030	2015	2020	2030
15040.77	17883.16	25885.25	12533.98	14902.63	21571.04

2020, and 2030 with the extensive economic mode compared to that of low-carbon mode, shown in Table 14.

#### 4. Conclusions

Taking Baiyangdian basin as the example, this paper constructed the extensive and low-carbon economic mode and quantitatively analyzed their effects on regional water demand. Results showed that total water demand with the extensive mode would increase by 1.27 billion m<sup>3</sup>, 1.53 billion m<sup>3</sup>, and 2.16 billion m<sup>3</sup> in 2015, 2020, and 2030, respectively, compared with that of low-carbon economic mode.

Low-carbon economic mode has optimal economic growth rate. It can not only be in accordance with the target of carbon emission reduction, but also control productive and domestic water demand and meet the requirement of ecological system. Results of Baiyangdian basin can provide data for water resource plan, target of ecoenvironmental conservancy plan, and water resource allocation of intake area of south-to-north project.

Some aspects of this research have to be improved, including forecast of economic growth rate, irrigation, and ecological water demand within stream if enough data is collected.

TABLE 14: Total water demand of the basin with the extensive and low-carbon economic mode (0.1 billion m<sup>3</sup>).

Year	Productive water demand		Domestic water demand		Ecological water demand		Total water demand	
	Extensive	Low-carbon	Extensive	Low-carbon	Extensive	Low-carbon	Extensive	Low-carbon
2015	45.66	26.98	4.64	4.02	1.50	8.11	51.80	39.11
2020	50.58	29.34	4.56	3.95	1.79	8.35	56.93	41.64
2030	62.77	35.29	4.34	3.76	2.59	9.02	69.70	48.07

## Conflict of Interests

The authors declare that there is no conflict of interests regarding the publication of this paper.

## Acknowledgments

The paper was supported by the Project of Influence Mechanism of Climate Change on Water Cycle in Huang-Huai-Hai River Area and Water Resources Security Evaluation (2010CB951102) of the National Program on Key Basic Research Project (973 Program) and the General Program of the National Natural Science Foundation of China (Grant no. 51279207).

## References

- [1] H. Wang, D.-H. Yan, Y.-W. Jia, D.-L. Hu, and L.-H. Wang, "Subject system of modern hydrology and water resources and research frontiers and hot issues," *Advances in Water Science*, vol. 21, no. 4, pp. 479–489, 2010.
- [2] M. Salman and W. Mualla, "Water demand management in Syria: centralized and decentralized views," *Water Policy*, vol. 10, no. 6, pp. 549–562, 2008.
- [3] R. M. Saleth, "Water scarcity and climatic change in India: the need for water demand and supply management," *Hydrological Sciences Journal*, vol. 56, no. 4, pp. 671–686, 2011.
- [4] D.-H. Yan, T.-L. Qin, P. Zhang, and Z.-Q. Xing, "Study on water resources rational deployment framework based on the low-carbon development mode," *Journal of Hydraulic Engineering*, vol. 41, no. 8, pp. 970–976, 2010.
- [5] D.-H. Yan, T.-L. Qin, W.-H. Xiao, and D.-X. Li, "Study on the model of water resources rational deployment for the low-carbon development mode," *Journal of Hydraulic Engineering*, vol. 43, no. 5, pp. 586–593, 2012.
- [6] X.-R. Huang, X.-H. Zhang, Y.-S. Pei, and C. Liang, "Rational deployment of water resources in Ningxia Autonomous Region based on rationalization of macroeconomic structure," *Journal of Hydraulic Engineering*, vol. 37, no. 3, pp. 371–375, 2006.
- [7] D.-H. Yan, H. Wang, S.-Y. Yang, and Z. Huo, "Ecology-oriented reasonable deployment of water resources and giving priority to protection of wetland," *Journal of Hydraulic Engineering*, vol. 39, no. 10, pp. 1241–1247, 2008.
- [8] R. G. Gistau, "Dem and forecasting in water supply systems," in *Water Supply Systems: State of the Art and Future Trends*, E. Cabrera and F. Martinez, Eds., pp. 56–64, Computational Mechanics Publications, Southampton, UK, 1993.
- [9] S. Leonid and F. Mordechai, "Forecasting hourly water demand of pattern approach," *Water Supply*, vol. 4, no. 5, pp. 168–172, 2003.
- [10] S. L. Zhou, T. A. McMahon, A. Walton, and J. Lewis, "Forecasting daily urban water demand: a case study of Melbourne," *Journal of Hydrology*, vol. 236, no. 3-4, pp. 153–164, 2000.
- [11] L. W. Mays, "Water demand forecasting," in *Hydrosystem Engineering and Management*, pp. 24–32, 1992.
- [12] J. F. Adamowski, "Peak daily water demand forecast modeling using artificial neural networks," *Journal of Water Resources Planning and Management*, vol. 134, no. 2, pp. 119–128, 2008.
- [13] A. Yasar, M. Bilgili, and E. Simsek, "Water demand forecasting based on stepwise multiple nonlinear regression analysis," *Arabian Journal for Science & Engineering*, vol. 37, no. 8, pp. 2333–2341, 2012.
- [14] P. A. Zhong, X. Y. Chen, and K. Chen, "Synthetic prediction method for industrial water demand," *Journal of Hohai University*, vol. 29, no. 4, pp. 67–71, 2001.
- [15] Y. J. Zhang, Q. S. Liu, C. M. Feng et al., "Linear multiple regression for domestic water demand forecasting in Beijing," *Water & Wastewater Engineering*, vol. 29, no. 4, pp. 26–28, 2003.
- [16] M. Lv, H. B. Zhao, H. W. Li et al., "Combined practical dynamic modeling prediction hourly water consumption," *Water & Wastewater Engineering*, vol. 14, no. 1, pp. 9–11, 1998.
- [17] Z. Ling, C. Xiao-Hong, and L. Qing-Er, "PP model of water demand prediction based on IEA," *Journal of Irrigation and Drainage*, vol. 27, no. 1, pp. 73–76, 2008.
- [18] R. G. Gistau, "Demand forecasting in water supply systems," in *Water Supply Systems: State of the Art and Future Trends*, E. Cabrera and F. Martinez, Eds., pp. 56–64, Computational Mechanics Publications, Southampton, UK, 1993.
- [19] A. Ibrahim, A. Abdelhamid, K. Yasir, and E. Ali, "A probabilistic forecast of water demand for a tourist and desalination dependent city: case of Mecca, Saudi Arabia," *Desalination*, vol. 294, pp. 53–59, 2012.
- [20] C. Qi and N.-B. Chang, "System dynamics modeling for municipal water demand estimation in an urban region under uncertain economic impacts," *Journal of Environmental Management*, vol. 92, no. 6, pp. 1628–1641, 2011.
- [21] M. M. Mohamed and A. Al-Mualla, "Water demand forecasting in Umm Al-Quwain using the constant rate model," *Desalination*, vol. 259, no. 1-3, pp. 161–168, 2010.
- [22] M. Lv, H. B. Zhao, L. Hongwei et al., "Combined practical dynamic modelling predicting hourly water consumption," *China Water Supply and Drainage*, vol. 14, no. 1, pp. 9–11, 1998.
- [23] C. C. Zhang, Y. B. Cui, and C. H. Hu, "Study on water demand forecast methods," *Meteorological and Environmental Sciences*, vol. 32, no. 1, pp. 1–4, 2009.
- [24] W. Li and Z. Huicheng, "Urban water demand forecasting based on HP filter and fuzzy neural network," *Journal of Hydroinformatics*, vol. 12, no. 2, pp. 172–184, 2010.
- [25] D. B. Bai and Z. P. Ning, "Discussion on causes of dry lake of Baiyangdian wetland," *China Flood and Drought Control*, vol. 2, pp. 46–62, 2007.

- [26] T. L. Qin, D. H. Yan, H. Wang et al., "Rational allocation of water resource towards the low-carbon development mode in Baiyangdian Basin," in *Proceedings of the IAHR World Congress*, 2013.
- [27] J. Wang and Z. X. Xu, "Long-term trend and the sustainability of air temperature and precipitation in the Baiyangdian Basin," *Resources Science*, vol. 31, no. 9, pp. 1498–1505, 2009.
- [28] Y.-S. Moon and Y.-H. Sonn, "Productive energy consumption and economic growth: an endogenous growth model and its empirical application," *Resource and Energy Economics*, vol. 18, no. 2, pp. 189–200, 1996.
- [29] Y. Zhu, Z. Wang, L. Pang, L. Wang, and X. Zou, "Simulation on China's economy and prediction on energy consumption and carbon emission under optimal growth path," *Acta Geographica Sinica*, vol. 64, no. 8, pp. 935–944, 2009.
- [30] Z. X. Zhao, *Coupling Mechanism of Eco-Hydrological Processes and Integrated Regulation in Baiyangdian Wetland*, Tianjin University, 2012.

## Research Article

# A Conjunction Method of Wavelet Transform-Particle Swarm Optimization-Support Vector Machine for Streamflow Forecasting

Fanping Zhang, Huichao Dai, and Deshan Tang

College of Water Conservancy and Hydropower Engineering, Hohai University, Nanjing 210098, China

Correspondence should be addressed to Huichao Dai; [dai.huichao@263.net](mailto:dai.huichao@263.net)

Received 21 January 2014; Revised 27 April 2014; Accepted 27 April 2014; Published 22 May 2014

Academic Editor: Y. P. Li

Copyright © 2014 Fanping Zhang et al. This is an open access article distributed under the Creative Commons Attribution License, which permits unrestricted use, distribution, and reproduction in any medium, provided the original work is properly cited.

Streamflow forecasting has an important role in water resource management and reservoir operation. Support vector machine (SVM) is an appropriate and suitable method for streamflow prediction due to its best versatility, robustness, and effectiveness. In this study, a wavelet transform particle swarm optimization support vector machine (WT-PSO-SVM) model is proposed and applied for streamflow time series prediction. Firstly, the streamflow time series were decomposed into various details ( $D_s$ ) and an approximation ( $A_3$ ) at three resolution levels ( $2^1-2^2-2^3$ ) using Daubechies (db3) discrete wavelet. Correlation coefficients between each  $D$  subtime series and original monthly streamflow time series are calculated.  $D_s$  components with high correlation coefficients ( $D_3$ ) are added to the approximation ( $A_3$ ) as the input values of the SVM model. Secondly, the PSO is employed to select the optimal parameters,  $C$ ,  $\epsilon$ , and  $\sigma$ , of the SVM model. Finally, the WT-PSO-SVM models are trained and tested by the monthly streamflow time series of Tangnaihai Station located in Yellow River upper stream from January 1956 to December 2008. The test results indicate that the WT-PSO-SVM approach provide a superior alternative to the single SVM model for forecasting monthly streamflow in situations without formulating models for internal structure of the watershed.

## 1. Introduction

The accuracy of streamflow forecasting is a key factor for reservoir operation and water resource management. However, streamflow is one of the most complex and difficult elements of the hydrological cycle due to the complexity of the atmospheric process. The elements affecting streamflow forecasting precision include catchment, geomorphologic and climate characteristics, and so forth [1]. The process of streamflow is extremely complex due to the influence of these variables and their combinations. Therefore, there are many forecasting techniques that have been proposed for streamflow forecasting [2–4].

Among them, the most popular and widely known statistical method used in time series forecasting is autoregressive integrated moving average (ARIMA) model due to its superiority of forecasting capabilities and richness of information on time-related changes [5]. Several studies have shown that ARIMA can be trusted as a reliable model in water

resources time series analysis [6]. For example, Lee and Tong [7] proposed a hybrid model for nonlinear time series forecasting by combining ARIMA and genetic programming and demonstrated the effectiveness of the proposed forecasting model. But the ARIMA models are a class of linear model and thus only suitable for capturing linear features of data time series [8]. In recent years, gray model, artificial neural network (ANN), and support vector machine (SVM) have been frequently used to predict the nonlinear time series and achieved good results [9–11]. For instance, Kişi [12] used three different ANN techniques, namely, feed forward neural networks, generalized regression neural networks and, radial basis ANN in one-month-ahead streamflow forecasting. However, there are some disadvantages of ANN due to its network structure, which is hard to determine and usually established using a trial-and-error approach [13].

Support vector machines (SVM) were suggested by Vapnik [14] as one of the soft computational techniques and are widely used for classification and regression based on

statistical learning theory (SLT). The basic idea of SVM for regression is to introduce a kernel function, map the input data into a high-dimensional feature space by a nonlinear mapping, and then perform linear regression in the feature space [5]. Currently, SVM were frequently applied in a number of different fields, such as fault diagnosis [16], pattern recognition [17], and classification [18]. In the hydrology context, SVM has been successfully applied to forecast the flood stage [19–21], to predict future water levels in Lake Erie [22], and to forecast discharges [23, 24]. Previous studies have indicated that SVM is an effective method for streamflow forecasting [5, 23–25].

More recently, the conjunction model of wavelet and SVM has drawn increasing interest and has displayed advantages over a single SVM model in terms of prediction accuracy. Wavelet analysis (WA) is an advanced method proposed by Morlet et al. [26] in signal processing and has attracted much attention due to its ability to reveal simultaneously both spectral and temporal information within one signal [27]. The application of WA in the areas of hydrology and water resource research mainly includes these aspects: identification of hydrologic series deterministic components such as trend, periods, and change points [28–31]; wavelet denoising in hydrologic series [30, 31]; and hydrologic series simulation and prediction based on wavelet [27, 32, 33]. Wavelet analysis can be used to decompose an observed time series (such as streamflow time series) into various components so that the new time series can be used as inputs for SVM models [34].

SVM implements the principle of structure risk minimization in place of experiential risk minimization, which makes it have excellent generalization ability in the situation of small sample. However, the practicability of SVM is affected by the difficulty of selecting appropriate SVM parameters [35]. At present, the most common parameters selection method for SVM is the cross validation method but it is time-consuming [36]. Recently, some intelligent algorithms have been applied for parameters selecting. Compared with cross validation, genetic algorithm (GA) is less time-consuming and can obtain the optimal solution well, but the operation of genetic algorithm is difficult with the steps of choosing, crossover, and mutation for different optimal problems [37]. As a new global optimizing algorithm, particle swarm optimization (PSO), proposed by Kennedy and Eberhart in 1995, is based on swarm intelligent by generating a random decision variable set called “particles” [35]. PSO is a versatile algorithm and can be used to solve different optimizing problems. In recent years, because of the best global searching ability and the simple implementing procedure, PSO has been successfully applied for function optimization [38], data mining [39], and other engineering optimization problems [15, 40] and achieved good results. Therefore, the PSO can be applied to optimize the parameters of SVM model for streamflow forecasting in this paper.

This paper is organized as follows. Section 2 introduces the principle theory of wavelet analysis, parameter selection method of SVM models based on PSO, and SVM regression forecasting model. The study area and streamflow time series analysis are introduced in Section 3. The forecasting results of the conjunction model with the real streamflow time series

data sets from Tangnaihai hydrology station in China are analyzed in Section 4. Finally, the conclusion is presented in Section 5.

## 2. Methodology

**2.1. Support Vector Machine (SVM).** The basic idea of SVM for regression is to introduce a kernel function, map the input data into a high-dimensional feature space by a nonlinear mapping, and then perform linear regression in the feature space [5]. Supposing that there is a training dataset  $D = \{(\mathbf{x}_1, \mathbf{y}_1), (\mathbf{x}_2, \mathbf{y}_2), \dots, (\mathbf{x}_n, \mathbf{y}_n)\} \in R^p \times R$ ,  $\mathbf{x}$  is the input vector,  $\mathbf{y}$  is the expected output,  $n$  is the number of data, and  $p$  is the total number of data patterns. By nonlinear mapping function  $\Phi$ ,  $\mathbf{x}$  is mapped into a feature space in which a linear estimate function is defined as

$$\mathbf{y} = f(\mathbf{x}, \boldsymbol{\omega}) = \langle \boldsymbol{\omega}, \Phi(\mathbf{x}) \rangle + b; \quad \boldsymbol{\omega}, \mathbf{x} \in R^p, \quad b \in R, \quad (1)$$

where  $\Phi(\mathbf{x})$  represents the high-dimensional feature spaces, which is nonlinearly mapped from the input space  $\mathbf{x}$ ;  $\boldsymbol{\omega}$  and  $b$  are coefficients that have to be estimated from the input data. By introducing the slack variables  $\xi$  and  $\xi^*$  and following the regularization theory, parameters  $\boldsymbol{\omega}$  and  $b$  are estimated by minimizing the cost function

$$\min J(\boldsymbol{\omega}, \xi) = \frac{1}{2} \|\boldsymbol{\omega}\|^2 + C \sum_{i=1}^n (\xi_i + \xi_i^*) \quad (2)$$

subject to the constraints:

$$\begin{aligned} y_i - \langle \boldsymbol{\omega}, \mathbf{x}_i \rangle - b &\leq \varepsilon + \xi_i \\ \langle \boldsymbol{\omega}, \mathbf{x}_i \rangle + b - y_i &\leq \varepsilon + \xi_i^* \\ \xi_i, \xi_i^* &\geq 0. \end{aligned} \quad (3)$$

The first term  $(1/2)\|\boldsymbol{\omega}\|^2$  is weight vector norm;  $C$  is referred to as the regularized constraint determining the tradeoff between the empirical error and the regularized term; and  $\varepsilon$  is the insensitive loss function.

By using Lagrange multiplier techniques, the minimization of (2) leads to the following dual-optimization problem:

$$\begin{aligned} \max \quad W(\alpha_i, \alpha_i^*) &= -\frac{1}{2} \sum_{i=1}^n \sum_{j=1}^n [(\alpha_i - \alpha_i^*)(\alpha_j - \alpha_j^*)K(\mathbf{x}_i, \mathbf{x}_j)] \\ &\quad - \varepsilon \sum_{i=1}^n (\alpha_i + \alpha_i^*) + \sum_{i=1}^n y_i (\alpha_i - \alpha_i^*) \\ \text{s.t.} \quad \sum_{i=1}^n (\alpha_i - \alpha_i^*) &= 0; \quad \alpha_i, \alpha_i^* \in [0, C], \end{aligned} \quad (4)$$

where  $(\alpha_i^*, \alpha_i)$  are coefficients determined by training and  $K(\mathbf{x}_i, \mathbf{x}_j)$  is the kernel function which can be expressed as inner product:

$$K(\mathbf{x}_i, \mathbf{x}) = \Phi(\mathbf{x}_i)^T \Phi(\mathbf{x}). \quad (5)$$

The decision function takes the form

$$f(x) = \sum_{i=1}^n (\alpha_i^* - \alpha_i) K(\mathbf{x}, \mathbf{x}_i) + b. \quad (6)$$

The selection of an appropriate kernel function plays an important role in SVM regression since the kernel function defines the feature space. Gaussian radial basis function kernel has received significant attention from the machine learning community. Gaussian radial basis function (RBF) kernel is defined as

$$K(\mathbf{x}, \mathbf{x}_i) = \exp\left(\frac{-\|\mathbf{x} - \mathbf{x}_i\|^2}{2\sigma^2}\right). \quad (7)$$

Here  $\sigma$  is the kernel parameter.

**2.2. Wavelet Analysis.** In wavelet analysis, the signals are analyzed in both the time and the frequency domain by decomposing the original signals in different frequency bands using wavelet functions. The wavelet transform (WT) uses the scalable windowing technique for analyzing local variation in the time series [41]. WT provides useful decompositions of original time series, so that wavelet-transformed data improve the ability of a forecasting model by capturing useful information on various resolution levels [42]. The time series data are preprocessed using wavelet transformation techniques to obtain decomposed wavelet coefficients that are used as inputs in the forecasting models.

The basic objective of WT is to achieve a complete timescale representation of localized and transient phenomena occurring at different timescales [4, 43]. The continuous wavelet transform is defined as the sum over all time of the signal multiplied by scale and shifted versions of wavelet function  $\psi$ :

$$W(a, b) = \frac{1}{\sqrt{a}} \int_{-\infty}^{+\infty} f(x) \psi\left(\frac{x-b}{a}\right) dx, \quad (8)$$

where  $a$  is a scale parameter;  $b$  is a position parameter; and  $\psi$  corresponds to the complex conjugate. The coefficient plots of the continuous wavelet transform are precisely the timescale view of the signal. However, calculating wavelet coefficients at every possible scale is time-consuming and generates large amount of information. Thus, the use of the continuous wavelet transform for forecasting is not practically possible.

In hydrology, observed hydrologic series are often expressed as discrete series, so the discrete wavelet transform is usually employed to decompose a hydrologic series into a set of coefficients and subsignals under different scales, and then guide other time series analyses [44]. The DWT is defined as the following form:

$$f(t) = \sum C_{j_0,k} \phi_{j_0,k}(t) + \sum_{j>j_0} \sum \omega_{j,k} 2^{j/2} \psi(2^j t - k), \quad (9)$$

where  $j$  is the dilation or level index,  $k$  is the translation or scaling index, and  $\phi_{j_0,k}$  is a scaling function of coarse scale coefficients.  $C_{j_0,k}$ ,  $\omega_{j,k}$ , is the scaling function of detailed

(fine scale) coefficients and all functions of  $\psi(2^j t - k)$  are orthonormal.

The original time series are decomposed into various details ( $D_s$ ) and an approximation ( $A_s$ ) at different resolution levels using DWT. The approximations are the high-scale, low frequency components of the signal and the details are the low-scale, high frequency components. Normally, the low frequency component of the signal ( $A$ ) is the most important part which demonstrates the signal identity [45]. The choice of wavelet type is an important issue. The Daubechies wavelets are one of the widely used in wavelet family, which are written dbN, where db is the ‘‘surname’’ and  $N$  is the order of the wavelet [46]. Daubechies wavelets exhibit good tradeoff between parsimony and information richness [34], so in this study the Daubechies wavelets were employed as the mother wavelet to decompose the time series.

### 2.3. Parameters Selection of SVM Based on PSO

**2.3.1. The Principle of PSO.** PSO, deriving from the research for the movement of organisms in a bird flocking or fish schooling, performs searches using a population (called swarm) of individuals (called particles) that are updated from iteration to iteration [47, 48]. An equation (velocity update) controls the swarm in moving around the search space seeking the optimum state. In each iteration, the algorithm saves the local optimum and compares it with the global (best yet) optimum values. Definitely the criteria for being chosen as an optimum state depend on the fitness of the objective function. Candidate solutions (decision variables) of any particle calculate and remember its own fitness. The position of any particle accelerated towards the global best position by using (10) and (11) [49]. In any search step  $t$ , the  $i$ th particle is used to update its candidate solution's current position  $x_{i,j}(t)$  by using local best  $p_{i,j}(t)$  and best  $p_{g,j}(t)$  position achieved yet. Consider the following:

$$v_{i,j}(t+1) = \omega v_{i,j}(t) + c_1 r_1 [p_{i,j} - x_{i,j}(t)] + c_2 r_2 [p_{g,j} - x_{i,j}(t)] \quad (10)$$

$$x_{i,j}(t+1) = x_{i,j}(t) + v_{i,j}(t+1), \quad j = 1, 2, \dots, d, \quad (11)$$

where  $v_{i,j}$  is velocity measures for particles;  $\omega$  is inertial weight controlling velocity direction;  $c_1$  and  $c_2$  are acceleration coefficients;  $r_1$  and  $r_2$  are random numbers uniformly distributed between [0, 1].  $x_{i,j}$  is the position of any particle.

**2.3.2. Parameters Selection of SVM Based on PSO.** In the SVM regression model, three parameters, namely,  $C$ ,  $\varepsilon$ , and  $\sigma$ , should be identified before forecasting. Therefore, PSO algorithm is used for optimizing the SVM parameters. The process of optimizing the SVM parameters with PSO is presented in Figure 1 and the steps are described as follows [47].

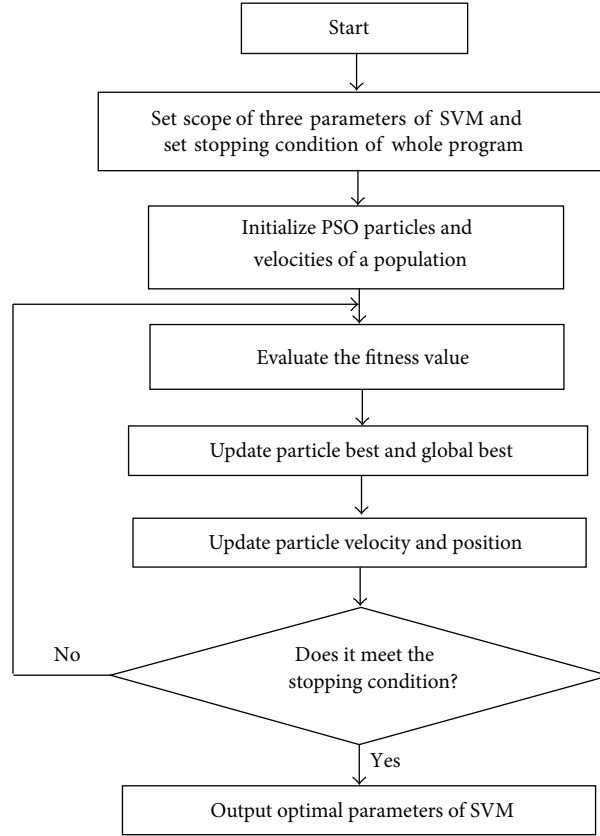


FIGURE 1: The process of optimizing the SVM parameters with PSO.

*Step 1. Initialization:* consider randomly initial particles and velocities of a population (every particle contains three variables, namely,  $C$ ,  $\varepsilon$ , and  $\sigma$ ).

*Step 2. Fitness evaluation:* the fitness function of PSO is shown as follows:

$$\text{fitness} = \eta_{\text{MAPE}} = \frac{1}{m} \sum_{i=1}^m \frac{|y_i - \hat{y}_i|}{y_i}, \quad (12)$$

where  $\eta_{\text{MAPE}}$  is the mean absolute percentage error;  $y_i$  is the actual value and  $\hat{y}_i$  is the predicted value; and  $m$  is the number of subsets. The solution with a smaller  $\eta_{\text{MAPE}}$  has a smaller fitness value.

*Step 3. Update global and personal best according to fitness evaluation results.*

*Step 4. Calculation of velocity:* particle flies toward a new position by calculating the velocity of position change. Velocity of each particle is calculated by (10).

*Step 5. Update position value:* each particle moves to its next position according to (11).

*Step 6. Termination:* repeat the same procedures from Step 2 to Step 5 until stopping conditions are satisfied.

**2.4. Model Evaluation.** It is essential to evaluate the performance of the models by employing appropriate methods. In

this study, the performance of the models is evaluated by the indexes of the correlation coefficients ( $R$ ), root mean squared error (RMSE), mean absolute error (MAE), and mean absolute relative error (MARE). These indexes are respectively defined as follows.

Correlation coefficients ( $R$ ):

$$R = \frac{\sum_{i=1}^n (y_i - \bar{y}_i)(\hat{y}_i - \bar{\hat{y}}_i)}{\sqrt{\sum_{i=1}^n (y_i - \bar{y}_i)^2 \sum_{i=1}^n (\hat{y}_i - \bar{\hat{y}}_i)^2}}. \quad (13)$$

Root mean squared error (RMSE):

$$\text{RMSE} = \sqrt{\frac{1}{n} \sum_{i=1}^n (y_i - \hat{y}_i)^2}. \quad (14)$$

Mean absolute error (MAE):

$$\text{MAE} = \frac{1}{n} \sum_{i=1}^n |y_i - \hat{y}_i|. \quad (15)$$

Mean absolute relative error (MARE):

$$\text{MARE} = \frac{1}{n} \sum_{i=1}^n \left| \frac{y_i - \hat{y}_i}{y_i} \right|; \quad (16)$$

where  $y_i$  stands for the observed data and  $\hat{y}_i$  stands for the forecasting data.  $n$  is number of the data.

### 3. Study Area and Data Analysis

In this study, we examined the data obtained from the monthly streamflow of the Tangnaihai Hydrological station located at the upper catchment of the Yellow River in Qinghai Province of China. Tangnaihai Hydrological station is the upstream hydrological station of Longyang Gorge Reservoir which is the largest regulating reservoir in the upper catchment of the Yellow River, so there are few human impacts disordering streamflow regular. Location of Tangnaihai Hydrological station is shown in Figure 2. The Yellow River catchment covers an area of 95,000 km<sup>2</sup>.

The monthly streamflow time series of Tangnaihai Hydrological station, consisting of 636 monthly records (January 1956 to December 2008), are used in this study. The dataset was split up into two parts: training and testing, where the first dataset consisting of 536 monthly records (January 1956 to August 2000) was used for training, while the final dataset contains 100 monthly records (September 2000 to December 2008). Training data were used exclusively for model development and testing data were used to measure the performance of the model on untrained data. The testing set was also used to evaluate the forecasting ability of the model and to compare the proposed model with others.

### 4. Results Analysis

*4.1. Wavelet Decomposition of Streamflow Time Series.* The WT-PSO-SVM model structure is shown in Figure 3. For the SVM model inputs, the original time series are decomposed into subseries with an approximation ( $A_s$ ) with low frequency and details ( $D_1, D_2, \dots, D_s$ ) with high frequency by Daubechies DWT algorithm.

The optimal decomposition level of the streamflow time series in wavelet analysis plays an important role in preserving the information and reducing the distortion of the datasets [4]. The number of decomposition levels controls the streamflow approximation in the data. The general rule for the appropriate decomposition levels is that the largest levels should be shorter than the size of the testing data [50].

In this case, the largest scales were chosen as three for the Tangnaihai station streamflow time series. Therefore, the flow data sets are decomposed into various details ( $D_s$ ) and an approximation ( $A_3$ ) at three resolution levels ( $2^1-2^2-2^3$ ) using db3 DWT shown in Figure 4. The new decomposed subseries present variations of the original time series on different periods. MATLAB codes were developed using its library functions to perform wavelet decomposition of the time series data. The correlation coefficients between each  $D$  subtime series and original monthly streamflow time series are given in Table 1 for the Tangnaihai station. In the table, the  $D_{t-1}$  and  $Q_t$  denote the  $D$  subtime series at time  $t-1$  and measured streamflow at time  $t$ , respectively. These correlation values provide information for the determination of effective wavelet components on streamflow. It can be seen from Table 1 that the  $D_3$  has the highest correlation ( $R = 0.259$ ) among  $D_s$ . The average correlation between  $A$  and  $Q_t$  is 0.363. According to the correlation analysis between  $D_s$  and the original current streamflow data, the effective component

TABLE 1: The correlation coefficients between subtime series and original streamflow data.

Discrete wavelet components	Correlations			
	$D_{t-1}$ and $Q_t$	$D_{t-2}$ and $Q_t$	$D_{t-3}$ and $Q_t$	Average
$D_1$	0.103	-0.003	0.105	0.070
$D_2$	-0.081	0.084	0.328	0.164
$D_3$	-0.023	0.295	0.459	0.259
$A$	0.211	0.390	0.488	0.363

( $D_3$ ) is selected. Then, the new series obtained by adding the effective  $D_3$  and approximation component are used as an input combination to the SVM model.

*4.2. Parameters Selection of SVM Based on PSO.* In this study, RBF is employed as kernel function of SVM forecasting model, so three parameters, namely, balance parameter  $C$ , insensitive parameter  $\epsilon$ , and kernel function, parameter  $\sigma$  should be selected. Some researchers have shown that different kernel functions have little impact on performance, but kernel function parameter  $\sigma$  is a key factor affecting performance of SVM. Among three parameters,  $\sigma$  precisely defines structure of highly dimensional space, so it controls complexity of ultimate solution;  $C$  determines complexity of model and punishment level of fitting deviation;  $\epsilon$  indicates forecasting model's expectation on estimating functions' error of sample data, and the larger  $\epsilon$ , the less support vector number and more sparse solution expression. But large  $\epsilon$  can also reduce accuracy of SVM forecasting model.

For monthly streamflow time series  $X = \{x_1, x_2, \dots, x_N\}$ , the flow data at time  $i+p$  is predicted based on the previous flow data. The general expression is shown as follows:

$$x_{i+p} = f(x_{i+1}, x_{i+2}, \dots, x_{i+p-1}), \quad (17)$$

where  $f$  is a nonlinear function indicating relationship of monthly streamflow time series;  $x_i$  is streamflow data at time  $i$ ,  $i = 1, 2, \dots, N$ ; and  $p$  is the forecasting step (month), which is set as 3 in this paper.  $N-p$  monthly streamflow time series data sets are used for training and testing SVM forecasting model. The particle swarm optimization is employed to optimize the best parameters set ( $\sigma, C, \epsilon$ ) of SVM model [51].

For the Tangnaihai station, three input combinations based on preceding monthly streamflows are evaluated to estimate current streamflow value. The input combinations evaluated in the study are as follows: (i)  $Q_{t-1}, Q_{t-2}$ , and  $Q_{t-3}$ ; (ii)  $Q_{t-1}(A), Q_{t-2}(A)$ , and  $Q_{t-3}(A)$ ; (iii)  $Q_{t-1}(A+D_3), Q_{t-2}(A+D_3)$ , and  $Q_{t-3}(A+D_3)$ . In all cases, the output is the discharge  $Q_t$  for the current month.

In the training stage, firstly the parameters  $\sigma, C$ , and  $\epsilon$  of SVM model are optimized by PSO, the validation error is measured by (12), and the adjusted parameters with minimum validation error are selected as the most appropriate parameters which are provided in Table 2. Then, the optimal parameters are utilized to train SVM and WSVM models.

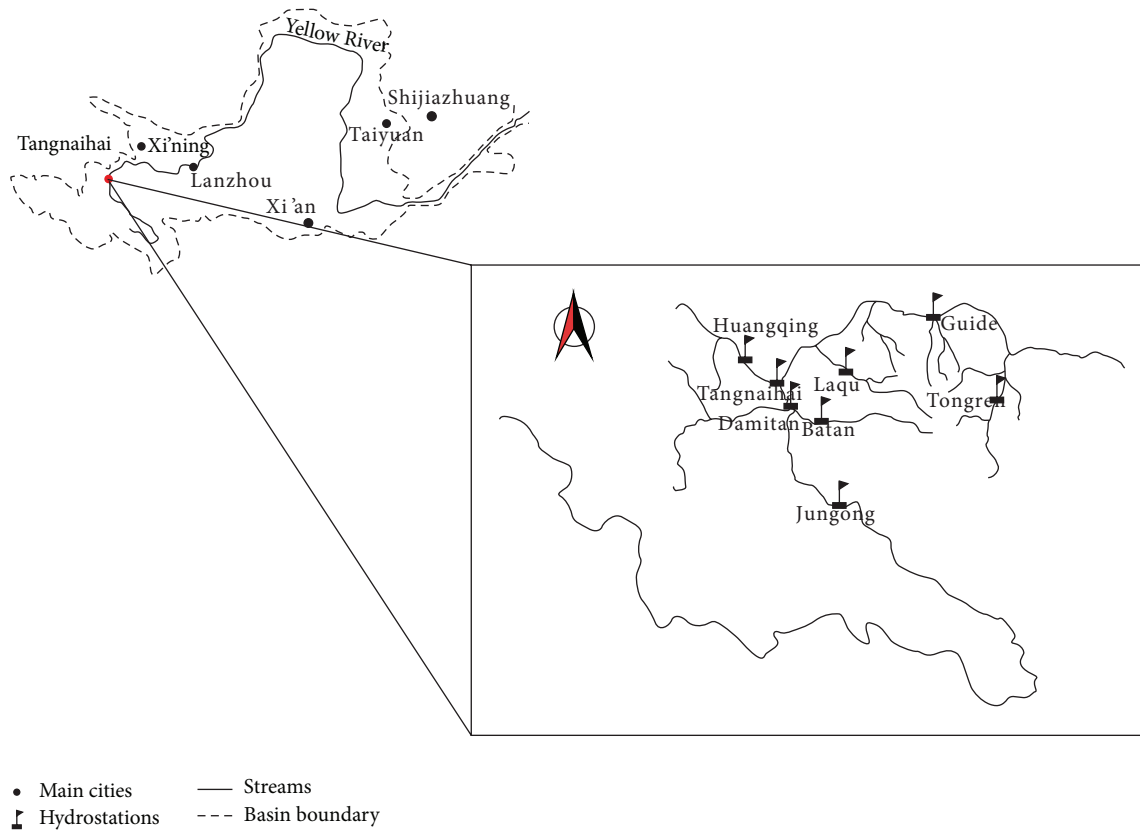


FIGURE 2: Location map of Yellow River and Tangnaihai station.

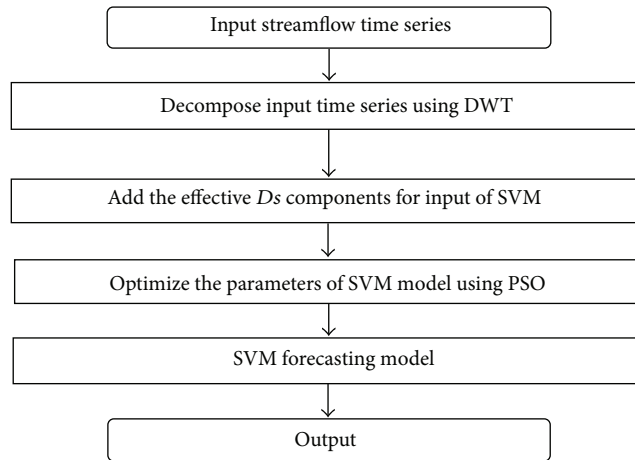


FIGURE 3: The WA-LSSVM-PSO model structure.

TABLE 2: Optimal parameters of SVM and WSVM models.

Model	Input variables	Output	Parameters		
			$\sigma$	$C$	$\varepsilon$
(i) SVM	(i) $Q_{t-1}, Q_{t-2},$ and $Q_{t-3}$		0.90156	2.3149	0.01
(ii) WSVM <sub>1</sub>	(ii) $Q_{t-1}(A), Q_{t-2}(A),$ and $Q_{t-3}(A)$	$Q_t$	0.01	46.8765	0.01
(iii) WSVM <sub>2</sub>	(iii) $Q_{t-1}(A + D_3), Q_{t-2}(A + D_3),$ and $Q_{t-3}(A + D_3)$		28.4876	6.0929	0.01

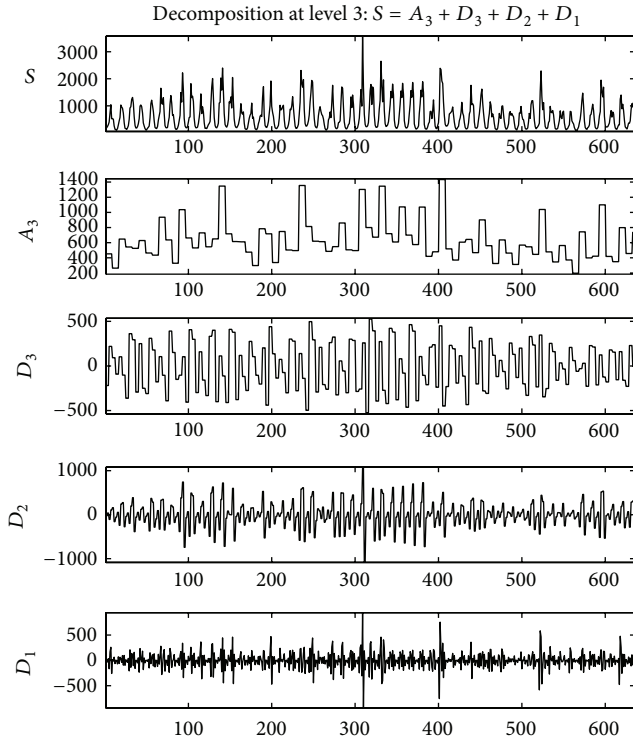


FIGURE 4: Decomposed wavelet subtime series components ( $D_s$ ) of runoff data of Tangnaihai station.

Before the training process begins, data normalization is often performed. Runoff time series data was normalized in the range  $[0, 1]$  by the following equation:

$$y_i = \frac{x_i - x_{\min}}{x_{\max} - x_{\min}}, \quad (18)$$

where  $y_i$  represents the normalized data, while  $x_i$  is the actual observation value and  $x_{\max}$ ,  $x_{\min}$ , respectively, represent the maximum and minimum value among the actual observation values.

**4.3. Streamflow Forecasting Based on WT-PSO-SVM.** As shown in Table 2, the optimal parameters for SVM (input model (i)) and WSVM (input models (ii) and (iii)) models are  $\sigma_1 = 0.90156$ ,  $C_1 = 2.3149$ , and  $\varepsilon_1 = 0.01$ ;  $\sigma_2 = 0.01$ ,  $C_2 = 46.8765$ , and  $\varepsilon_2 = 0.01$ ; and  $\sigma_3 = 28.4876$ ,  $C_3 = 6.0929$ , and  $\varepsilon_3 = 0.01$ . The optimal parameters are used to examine the accuracy of the SVM and WSVM forecasting models with the testing data sets. Table 3 shows the performance results obtained in the training and testing periods of the SVM and WSVM models for Tangnaihai station.

Results obtained from the three models for 3-month-advance flow forecasting at Tangnaihai station are presented in Table 3. Performance of the three models was compared by evaluating indexes of  $R$ , RMSE, MAE, and MARE. It is observed that the forecasting accuracy of the WSVM<sub>2</sub> model was much better than that of corresponding SVM and WSVM<sub>1</sub> models. Comparing the forecasting results of SVM and WSVM<sub>1</sub>, the  $R$ , RMSE, MAE, and MARE in

the testing period were 0.768–0.613, 317.035–331.420 ( $\text{m}^3/\text{s}$ ), 247.480–256.368 ( $\text{m}^3/\text{s}$ ), and 17.81–23.49 (%), respectively. It is observed that SVM is more superior than WSVM<sub>1</sub> because some useful details ( $D_s$ ) of original streamflow series were eliminated in the model WSVM<sub>1</sub>. Comparing the forecasting results of SVM and WSVM<sub>2</sub>, the values of  $R$ , RMSE, MAE, and MARE in the testing period were 0.768–0.806, 317.035–243.268, 247.480–173.20, and 17.81–11.52, respectively. It is obvious from Table 3 and Figure 5 that the WSVM<sub>2</sub> performs better than the SVM model. These results indicated that  $D_3$  was an effective component for the runoff series and the  $D_1$  and  $D_2$  were the noise that should be eliminated before streamflow forecasting. Wavelet transform is a necessary process of data preprocessing for improving predicting accuracy.

## 5. Conclusion

This study developed a WT-PSO-SVM hybrid model to forecast monthly streamflow. The WT-PSO-SVM model was obtained by combining three methods, discrete wavelet transform-particle swarm optimization, and support vector machine regression. The combined model integrated the advantages of best versatility, robustness and effectiveness of SVM, the best global searching ability and the simple implementing procedure of PSO for parameter selection, and the ability of WT to reveal simultaneously both spectral and temporal information within one signal. This hybrid approach was successfully applied to simulate streamflow time series of Tangnaihai Hydrology station in the Yellow River.

The streamflow time series were decomposed into various details ( $D_s$ ) and an approximation ( $A_3$ ) at three resolution levels ( $2^1$ - $2^2$ - $2^3$ ) by using db3 DWT of the wavelet function of Daubechies 3 (db3). The correlation coefficients between each  $D$  subtime series and original monthly streamflow time series were calculated.  $D_s(D_3)$  components with high correlation coefficients ( $R = 0.259$ ) were added to the approximation ( $A$ ) as the input values of SVM model. The input combinations evaluated in the study are as follows: (i)  $Q_{t-1}$ ,  $Q_{t-2}$ , and  $Q_{t-3}$ ; (ii)  $Q_{t-1}(A)$ ,  $Q_{t-2}(A)$ , and  $Q_{t-3}(A)$ ; (iii)  $Q_{t-1}(A + D_3)$ ,  $Q_{t-2}(A + D_3)$ , and  $Q_{t-3}(A + D_3)$ . The PSO was employed to select the optimal parameters,  $C$ ,  $\varepsilon$ , and  $\sigma$ , of the three input models which were used to test the accuracy of the SVM model. Three different input combinations of SVM predicting results indicated that the discrete wavelet transform can significantly increase the accuracy of the SVM model in forecasting monthly streamflow. In addition, particle swarm optimization can determine suitable parameters to forecast streamflow as well. Predicting accuracy was evaluated by indexes of  $R$ , RMSE, MAE, and MARE. At the Tangnaihai station, the best predictions belong to WSVM<sub>2</sub> model. WSVM<sub>2</sub> model increased the prediction  $R$  by 0.038 and 0.193 with respect to the SVM and WSVM<sub>1</sub> models and reduced MARE by 6.29% and 11.97%, respectively, in the testing period. These results indicated that  $D_3$  was an effective component for the runoff series and the  $D_1$  and  $D_2$  were the noise that should be eliminated before streamflow forecasting. Wavelet transform

TABLE 3: Forecasting performance indexes of SVM and WSVM models in Tangnaihai station.

Model	Training				Testing			
	R	RMSE (m <sup>3</sup> /s)	MAE (m <sup>3</sup> /s)	MARE (%)	R	RMSE (m <sup>3</sup> /s)	MAE (m <sup>3</sup> /s)	MARE (%)
(i) SVM	0.853	287.315	196.524	14.33	0.768	317.035	247.480	17.81
(ii) WSVM <sub>1</sub>	0.548	306.554	217.883	18.24	0.613	331.420	256.368	23.49
(iii) WSVM <sub>2</sub>	0.808	201.784	141.730	7.46	0.806	243.268	173.20	11.52

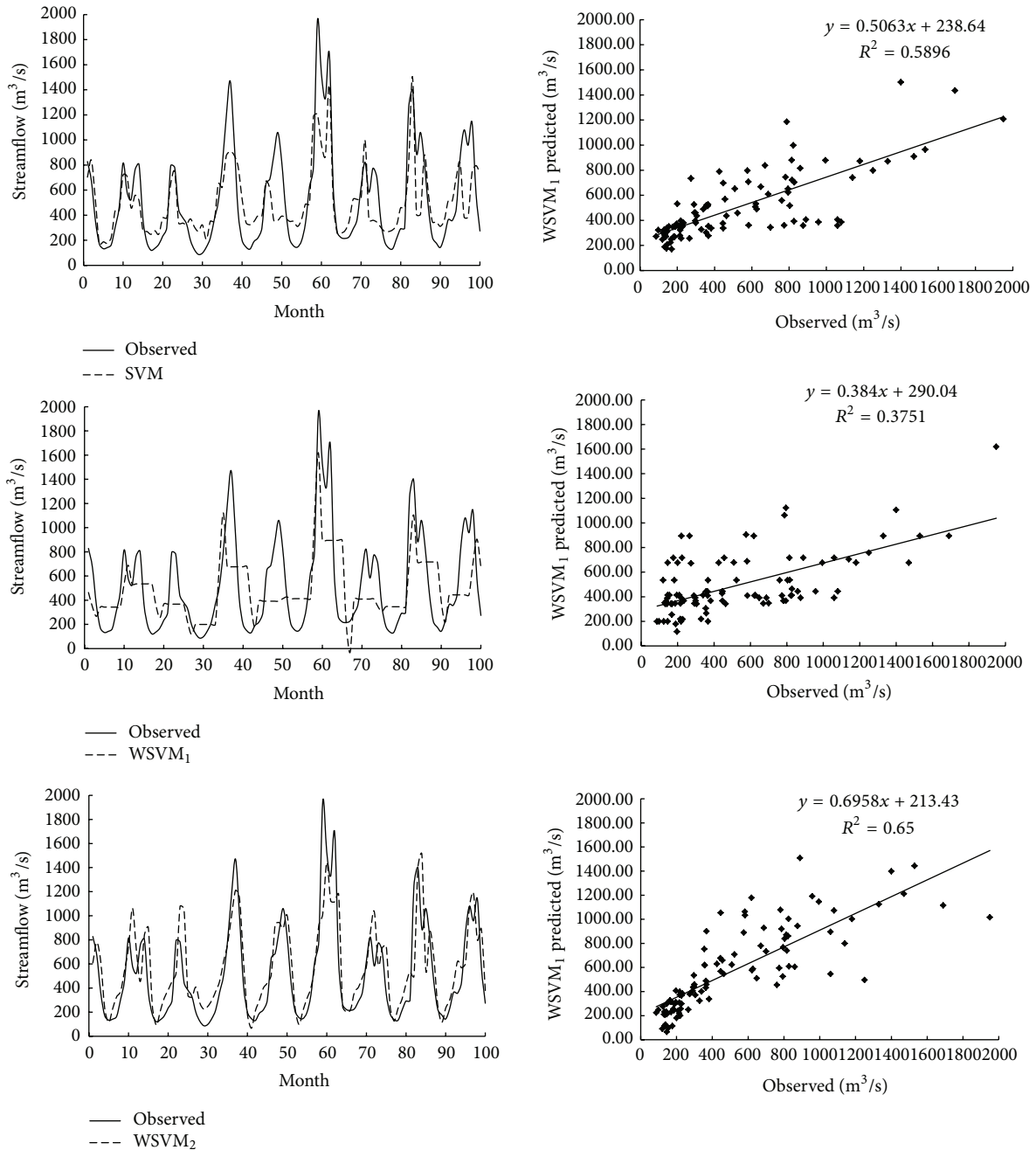


FIGURE 5: Predicted and observed streamflow in the testing period by SVM, WSVM<sub>1</sub>, and WSVM<sub>2</sub>.

is a necessary process of data preprocessing for improving predicting accuracy. The test results indicated that PSO-WT-SVM approach provides a superior alternative to the single SVM model for forecasting monthly streamflow in situations, without formulating models for the internal structure of the watershed.

## Conflict of Interests

The authors declare that there is no conflict of interests regarding the publication of this paper.

## Acknowledgments

This work was supported by the National Key Basic Research Program of China (973 Program) (2012CB417006), the National Science Fund for Distinguished Young Scholars (Grant no. 50925932), National Natural Science Foundation of China (Grant no. 50979050), and the College Graduate Research and Innovation Projects of Jiangsu Province of China (Grant no. 2013B20414). The authors wish to thank the Yellow River Conservancy Commission for providing the requisite meteorological data.

## References

- [1] A. Jain and A. M. Kumar, "Hybrid neural network models for hydrologic time series forecasting," *Applied Soft Computing Journal*, vol. 7, no. 2, pp. 585–592, 2007.
- [2] O. Kisi and M. Cimen, "A wavelet-support vector machine conjunction model for monthly streamflow forecasting," *Journal of Hydrology*, vol. 399, no. 1-2, pp. 132–140, 2011.
- [3] J. Adamowski and K. Sun, "Development of a coupled wavelet transform and neural network method for flow forecasting of non-perennial rivers in semi-arid watersheds," *Journal of Hydrology*, vol. 390, no. 1-2, pp. 85–91, 2010.
- [4] N. Pramanik, R. K. Panda, and A. Singh, "Daily river flow forecasting using wavelet ANN hybrid models," *Journal of Hydroinformatics*, vol. 13, no. 1, pp. 49–63, 2011.
- [5] A. Shabri and Suhartono, "Streamflow forecasting using least-squares support vector machines," *Hydrological Sciences Journal*, vol. 57, no. 7, pp. 1275–1293, 2012.
- [6] J. Adamowski and C. Karapataki, "Comparison of multivariate regression and artificial neural networks for peak urban water-demand forecasting: evaluation of different ANN learning algorithms," *Journal of Hydrologic Engineering*, vol. 15, no. 10, pp. 729–743, 2010.
- [7] Y.-S. Lee and L.-I. Tong, "Forecasting time series using a methodology based on autoregressive integrated moving average and genetic programming," *Knowledge-Based Systems*, vol. 24, no. 1, pp. 66–72, 2011.
- [8] P. G. Zhang, "Time series forecasting using a hybrid ARIMA and neural network model," *Neurocomputing*, vol. 50, pp. 159–175, 2003.
- [9] H. V. Trivedi and J. K. Singh, "Application of grey system theory in the development of a runoff prediction model," *Biosystems Engineering*, vol. 92, no. 4, pp. 521–526, 2005.
- [10] N. Vivekanandan, "Prediction of annual runoff using artificial neural network and regression approaches," *Mausam*, vol. 62, no. 1, pp. 11–20, 2011.
- [11] G. Yu, J. Yang, and Z. Xia, "The prediction model of chaotic series based on support vector machine and its application to runoff," *Advanced Materials Research*, vol. 255–260, pp. 3594–3599, 2011.
- [12] Ö. Kişi, "River flow forecasting and estimation using different artificial neural network techniques," *Hydrology Research*, vol. 39, no. 1, pp. 27–40, 2008.
- [13] Ö. Kişi, "River flow modeling using artificial neural networks," *Journal of Hydrologic Engineering*, vol. 9, no. 1, pp. 60–63, 2004.
- [14] V. Vapnik, "The nature of statistical learning theory," *Data Mining and Knowledge Discovery*, vol. 6, pp. 1–47, 1995.
- [15] M. H. Afshar, "Large scale reservoir operation by constrained particle swarm optimization algorithms," *Journal of Hydro-Environment Research*, vol. 6, no. 1, pp. 75–87, 2012.
- [16] A. Widodo and B.-S. Yang, "Support vector machine in machine condition monitoring and fault diagnosis," *Mechanical Systems and Signal Processing*, vol. 21, no. 6, pp. 2560–2574, 2007.
- [17] M. Zhu, K. Fu, X. Huang, S. Wu, and W. Jin, "A novel recognition approach for radar emitter signals based on on-line independent support vector machines," *Advances in Computer Science and Its Applications*, vol. 2, no. 3, pp. 390–396, 2013.
- [18] E. Carrizosa and D. Romero Morales, "Supervised classification and mathematical optimization," *Computers & Operations Research*, vol. 40, no. 1, pp. 150–165, 2013.
- [19] D. Han, L. Chan, and N. Zhu, "Flood forecasting using support vector machines," *Journal of Hydroinformatics*, vol. 9, no. 4, pp. 267–276, 2007.
- [20] P.-S. Yu, S.-T. Chen, and I.-F. Chang, "Support vector regression for real-time flood stage forecasting," *Journal of Hydrology*, vol. 328, no. 3-4, pp. 704–716, 2006.
- [21] C. Sivapragasam and S.-Y. Liong, "Flow categorization model for improving forecasting," *Nordic Hydrology*, vol. 36, no. 1, pp. 37–48, 2005.
- [22] M. S. Khan and P. Coulibaly, "Application of support vector machine in lake water level prediction," *Journal of Hydrologic Engineering*, vol. 11, no. 3, pp. 199–205, 2006.
- [23] J.-Y. Lin, C.-T. Cheng, and K.-W. Chau, "Using support vector machines for long-term discharge prediction," *Hydrological Sciences Journal*, vol. 51, no. 4, pp. 599–612, 2006.
- [24] W.-C. Wang, K.-W. Chau, C.-T. Cheng, and L. Qiu, "A comparison of performance of several artificial intelligence methods for forecasting monthly discharge time series," *Journal of Hydrology*, vol. 374, no. 3-4, pp. 294–306, 2009.
- [25] T. Asefa, M. Kemblowski, M. McKee, and A. Khalil, "Multi-time scale stream flow predictions: the support vector machines approach," *Journal of Hydrology*, vol. 318, no. 1-4, pp. 7–16, 2006.
- [26] J. Morlet, G. Arens, E. Fourgeau, and D. Glard, "Wave propagation and sampling theory—part I: complex signal and scattering in multilayered media," *Geophysics*, vol. 47, no. 2, pp. 203–221, 1982.
- [27] V. Nourani, M. T. Alami, and M. H. Aminfar, "A combined neural-wavelet model for prediction of Ligvanchai watershed precipitation," *Engineering Applications of Artificial Intelligence*, vol. 22, no. 3, pp. 466–472, 2009.
- [28] L. C. Smith, D. L. Turcotte, and B. L. Isacks, "Stream flow characterization and feature detection using a discrete wavelet transform," *Hydrological Processes*, vol. 12, no. 2, pp. 233–249, 1998.
- [29] T. Partal and M. Küçük, "Long-term trend analysis using discrete wavelet components of annual precipitations measurements in Marmara region (Turkey)," *Physics and Chemistry of the Earth*, vol. 31, no. 18, pp. 1189–1200, 2006.

- [30] Y.-F. Sang, D. Wang, J.-C. Wu, Q.-P. Zhu, and L. Wang, "The relation between periods' identification and noises in hydrologic series data," *Journal of Hydrology*, vol. 368, no. 1-4, pp. 165–177, 2009.
- [31] Y.-F. Sang, D. Wang, J.-C. Wu, Q.-P. Zhu, and L. Wang, "Entropy-based wavelet de-noising method for time series analysis," *Entropy*, vol. 11, no. 4, pp. 1123–1147, 2009.
- [32] T. Partal and Ö. Kişi, "Wavelet and neuro-fuzzy conjunction model for precipitation forecasting," *Journal of Hydrology*, vol. 342, no. 1-2, pp. 199–212, 2007.
- [33] L. Karthikeyan and D. Nagesh Kumar, "Predictability of non-stationary time series using wavelet and EMD based ARMA models," *Journal of Hydrology*, vol. 502, pp. 103–119, 2013.
- [34] D. Benaouda, F. Murtagh, J.-L. Starck, and O. Renaud, "Wavelet-based nonlinear multiscale decomposition model for electricity load forecasting," *Neurocomputing*, vol. 70, no. 1-3, pp. 139–154, 2006.
- [35] S.-W. Lin, K.-C. Ying, S.-C. Chen, and Z.-J. Lee, "Particle swarm optimization for parameter determination and feature selection of support vector machines," *Expert Systems with Applications*, vol. 35, no. 4, pp. 1817–1824, 2008.
- [36] X. Li, S.-D. Yang, and J.-X. Qi, "New support vector machine optimized by improved particle swarm optimization and its application," *Journal of Central South University of Technology*, vol. 13, no. 5, pp. 568–572, 2006.
- [37] P.-F. Pai and W.-C. Hong, "Forecasting regional electricity load based on recurrent support vector machines with genetic algorithms," *Electric Power Systems Research*, vol. 74, no. 3, pp. 417–425, 2005.
- [38] R. Brits, A. P. Engelbrecht, and F. van den Bergh, "Locating multiple optima using particle swarm optimization," *Applied Mathematics and Computation*, vol. 189, no. 2, pp. 1859–1883, 2007.
- [39] K. Sarath and V. Ravi, "Association rule mining using binary particle swarm optimization," *Engineering Applications of Artificial Intelligence*, vol. 26, no. 8, pp. 1832–1840, 2013.
- [40] L. Ostadrahimi, M. A. Mariño, and A. Afshar, "Multi-reservoir operation rules: multi-swarm PSO-based optimization approach," *Water Resources Management*, vol. 26, no. 2, pp. 407–427, 2012.
- [41] H. Abghari, H. Ahmadi, S. Besharat, and V. Rezaverdinejad, "Prediction of daily pan evaporation using wavelet neural networks," *Water Resources Management*, vol. 26, no. 12, pp. 3639–3652, 2012.
- [42] Y. Chen, B. Yang, and J. Dong, "Time-series prediction using a local linear wavelet neural network," *Neurocomputing*, vol. 69, no. 4-6, pp. 449–465, 2006.
- [43] D. Labat, R. Ababou, and A. Mangin, "Rainfall-runoff relations for karstic springs. Part II: continuous wavelet and discrete orthogonal multiresolution analyses," *Journal of Hydrology*, vol. 238, no. 3-4, pp. 149–178, 2000.
- [44] Y. F. Sang, "A practical guide to discrete wavelet decomposition of hydrologic time series," *Water Resources Management*, vol. 26, no. 11, pp. 3345–3365, 2012.
- [45] R. V. Ramana, B. Krishna, S. Kumar, and N. Pandey, "Monthly rainfall prediction using wavelet neural network analysis," *Water Resources Management*, vol. 27, no. 10, pp. 3697–3711, 2013.
- [46] S. Wei, H. Yang, J. Song, K. Abbaspour, and Z. Xu, "A wavelet-neural network hybrid modelling approach for estimating and predicting river monthly flows," *Hydrological Sciences Journal*, vol. 58, no. 2, pp. 374–389, 2013.
- [47] S.-W. Fei, M.-J. Wang, Y.-B. Miao, J. Tu, and C.-L. Liu, "Particle swarm optimization-based support vector machine for forecasting dissolved gases content in power transformer oil," *Energy Conversion and Management*, vol. 50, no. 6, pp. 1604–1609, 2009.
- [48] W. Pedrycz, B. J. Park, and N. J. Pizzi, "Identifying core sets of discriminatory features using particle swarm optimization," *Expert Systems with Applications*, vol. 36, no. 3, pp. 4610–4616, 2009.
- [49] Q. Wu, "A hybrid-forecasting model based on Gaussian support vector machine and chaotic particle swarm optimization," *Expert Systems with Applications*, vol. 37, no. 3, pp. 2388–2394, 2010.
- [50] C. L. Wu, K. W. Chau, and Y. S. Li, "Methods to improve neural network performance in daily flows prediction," *Journal of Hydrology*, vol. 372, no. 1-4, pp. 80–93, 2009.
- [51] Y.-B. Li, N. Zhang, and C.-B. Li, "Support vector machine forecasting method improved by chaotic particle swarm optimization and its application," *Journal of Central South University of Technology*, vol. 16, no. 3, pp. 478–481, 2009.

## Research Article

# Identification of Contamination Control Strategy for Fluid Power System Using an Inexact Chance-Constrained Integer Program

Y. Q. Huang, S. L. Nie, and H. Ji

*College of Mechanical Engineering and Applied Electronics Technology, Beijing University of Technology, Beijing 100124, China*

Correspondence should be addressed to S. L. Nie; [niesonglin@tom.com](mailto:niesonglin@tom.com)

Received 27 October 2013; Accepted 2 January 2014; Published 12 May 2014

Academic Editor: Yuefei Huang

Copyright © 2014 Y. Q. Huang et al. This is an open access article distributed under the Creative Commons Attribution License, which permits unrestricted use, distribution, and reproduction in any medium, provided the original work is properly cited.

An inexact chance-constrained integer programming (ICIP) method is developed for planning contamination control of fluid power system (FPS). The ICIP is derived by incorporating chance-constrained programming (CCP) within an interval mixed integer linear programming (IMILP) framework, such that uncertainties presented in terms of probability distributions and discrete intervals can be handled. It can also help examine the reliability of satisfying (or risk of violating) system constraints under uncertainty. The developed method is applied to a case of contamination control planning for one typical FPS. Interval solutions associated with risk levels of constraint violation are obtained. They can be used for generating decision alternatives and thus help designers identify desired strategies under various environmental, economic, and system reliability constraints. Generally, willingness to take a higher risk of constraint violation will guarantee a lower system cost; a strong desire to acquire a lower risk will run into a higher system cost. Thus, the method provides not only decision variable solutions presented as stable intervals but also the associated risk levels in violating the system constraints. It can therefore support an in-depth analysis of the tradeoff between system cost and system-failure risk.

## 1. Introduction

Contamination has long been recognized as one of the major causes of components' wear, work-failure, and related downtime of fluid power system (FPS). Although a number of studies were undertaken for dealing with the contamination problems in the FPS [1–7], they focused on the contaminant sensitivity analysis for single system component, the ingress estimation of contaminant particle, and the online monitoring of cleanliness level. They had difficulties in reflecting the filtration systems from the perspective of the whole FPS as well as analyzing the economic effects of system maintenance.

Actually, in contamination control of FPS, uncertainties may exist in related costs and impact factors such as the contaminant-ingress/generation rate, component's contaminant-sensitivity, and filter's contaminant-holding capacity. These complexities may be further multiplied by not only interactions among uncertain components, but also

their associations with economic penalties if major contamination accidents occur. It is thus desirable to develop effective optimization methods for reflecting the inherent complexities and uncertainties as well as effective management measures for mitigating the effect of contamination in FPS. Nie et al. developed several inexact optimization methods for addressing uncertainties and nonlinearities in the contamination control and filter management strategies of the fluid power systems [8–11]. For example, Nie et al. developed an interval-parameter integer nonlinear programming method to deal with the uncertainties in the contamination control of FPS, where the uncertainties have been presented into interval numbers [8]. Nie et al. developed an interval-fuzzy quadratic programming method for planning contamination control of the fluid power systems under uncertainty, which incorporated techniques of interval-parameter programming (IPP) and fuzzy quadratic programming within a general framework to handle uncertainties expressed in terms of interval values and fuzzy sets; multiple control variables were

adopted to tackle independent uncertainties in the model's right-hand side, and fuzzy quadratic terms were used to minimize the variation of satisfaction degrees among the constraints [9]. Nie et al. proposed an independent variables controlled interval-fuzzy nonlinear programming method for the assessment of filter allocation and replacement strategies in FPS under uncertainty; by introducing independent control variables and L-R fuzzy numbers into the interval nonlinear programming model framework, the developed method can address the independent characteristics of constraints uncertainty [10]. Nie et al. advanced an interval-fuzzy chance-constrained integer programming (IFCIP) approach for dealing with uncertainties presented in terms of fuzzy sets, intervals, and random variables [11].

Stochastic mathematical programming (SMP) can deal with uncertainties based on the probability theory, in which probabilistic information for a limited number of uncertain parameters can be incorporated within the optimization framework. The SMP methods are effective when the left-hand-side coefficients are deterministic while the right-hand-side coefficients are uncertain but with known probability distributions [12]. The SMP methods include chance-constrained programming, two-stage stochastic programming, and multistage stochastic programming (abbreviated as CCP, TSP, and MSP). CCP can effectively reflect the reliability of satisfying (or risk of violating) system constraints under uncertainty [13, 14]. In fact, CCP does not require that all of the constraints be totally satisfied. Instead, they can be satisfied in a proportion of cases with given probabilities [15–18]. There have been many applications of CCP methods to environmental management problems [19–24]. Huang advanced two fuzzy chance-constrained programming methods for capital budgeting and investment problems that are involved in fuzzy-random parameters [25, 26]; Li et al. proposed a multistage fuzzy chance-constrained programming approach for dealing with uncertainties expressed as fuzzy sets and probabilities in water resources management systems [17]. Although the CCP can deal with uncertainties presented as probability distributions, linear constraints in the CCP can only reflect the case when the left-hand-side coefficient is deterministic, while the set of feasible constraints becomes much more complicated or numerous if both left- and right-hand sides are both random variables [21, 27–30]. However, the CCP is effective in reflecting probability distributions of the constraints' right-hand sides but not so much for independent uncertainties of the left-hand-side coefficients in each constraint or the objective function; moreover, the quality of many uncertainties is often not good enough to be presented as probability distributions [21]. These difficulties may affect practical applicability of the CCP method.

Interval-parameter programming (IPP) is an alternative for handling uncertainties presented as interval numbers in the model's left- and/or right-hand sides as well as those that cannot be quantified as membership or distribution functions [31]. IPP can be transformed into two deterministic submodels, which correspond to upper- and lower-bounds of the desired objective function value. However, an IPP model may become infeasible when its right-hand-side parameters are highly uncertain [32]. In fact, in the contamination control

process of FPS, many parameters may appear uncertain and their interrelationships are complicated, such as fluid flow, filtration ratio, contaminant ingress rate, contaminant generation rate, component tolerance level, filter costs, and system maintenance fees. These uncertainties can be quantified as probability density functions (PDFs), while the others may exist as discrete intervals. For example, an engineering designer/manager may know that the contaminant-generation-rate in a FPS fluctuates within a certain interval, but he/she may find it difficult to state its reliable probability distribution [33]. Therefore, one potential approach for better accounting for the uncertainties, as well as the relevant system reliabilities, is to incorporate the CCP into the interval mixed integer linear programming (IMILP) framework. This would then lead to an inexact chance-constrained integer programming (ICIP) method.

As an extension of the previous works, this study aims to develop such an inexact chance-constrained integer programming (ICIP) method for contamination control and filter management under uncertainty. This method will incorporate techniques of interval, integer, and chance-constrained programming within a general framework to reflect a variety of uncertainties existing in the system parameters. It can also help examine the reliability of satisfying (or risk of violating) system constraints under uncertainty and thus quantify the cost of violating the constraints under varied risk levels. The method will then be applied to a case of contamination control planning for FPS. The results can be used for generating a range of decision alternatives under various system conditions and thus helping FPS managers to identify desired contamination control policies.

## 2. Methodology

*2.1. Interval Integer Programming.* According to Huang et al. [34], an interval mixed integer linear programming (IMILP) problem can be expressed as follows:

$$\begin{aligned} & \text{Minimize} && f^\pm = C^\pm X^\pm \\ & \text{Subject to:} && A^\pm X^\pm \leq B^\pm \\ & && X^\pm \geq 0, \end{aligned} \quad (1)$$

where  $A^\pm \in \{R^\pm\}^{m \times n}$ ,  $B^\pm \in \{R^\pm\}^{m \times 1}$ ,  $C^\pm \in \{R^\pm\}^{1 \times n}$ ,  $X^\pm \in \{R^\pm\}^{n \times 1}$ ,  $R^\pm$  denotes a set of interval numbers,  $f^\pm$  refers to an interval objective function, and the decision variables ( $X^\pm$ ) can be sorted into two categories: continuous and binary. The IMILP model can be transformed into two deterministic submodels corresponding to upper- and lower-bounds of the objective function value [34]. By solving the two submodels, interval solutions can be obtained.

*2.2. Chance-Constrained Programming.* In a real-world contamination control problem, randomness in other right-hand-side parameters, such as component contamination sensitivities and contaminant-holding capacities, also needs to be reflected. For example, the contaminant-holding capacity may be fixed with a level of probability, which represents

the admissible risk of violating the uncertain capacity constraint. However, the interval mathematical programming method has difficulties in reflecting uncertainties expressed as probabilistic distributions. Chance-constrained programming (CCP) method can be used for dealing with the above type of uncertainty and analyzing the risk of violating the uncertain constraints [14]. In CCP, it is required that the constraints should be satisfied under given probabilities [15, 19–24, 35, 36]. Consider a general probabilistic stochastic linear problem as follows:

$$\begin{aligned} \text{Min} \quad & C(t) X \\ \text{Subject to:} \quad & A(t) X \leq B(t) \\ & X \geq 0, \end{aligned} \quad (2)$$

where  $X$  is a vector of decision variables and  $A(t)$ ,  $B(t)$ , and  $C(t)$  are sets with random elements defined on a probability space  $T$ ,  $t \in T$  [14, 30]. The CCP approach solves the above model by converting it into a deterministic version through (i) fixing a certain level of probability  $p_i$  ( $p_i \in [0, 1]$ ) for uncertain constraint  $i$ , which represents the admissible risk of violating constraint  $i$ , and (ii) imposing the condition that the constraint should be satisfied with at least a probability level of  $1 - p_i$ . The feasible solution set is thus subject to the following constraints [21, 37]:

$$\begin{aligned} \text{Pr} [\{A_i(t) X \leq b_i(t)\}] \\ \geq 1 - q_i, \quad A_i(t) \in A(t), \quad i = 1, 2, \dots, m. \end{aligned} \quad (3)$$

Constraint (3) is generally nonlinear, and the set of feasible constraints is convex only for some particular distributions and certain levels of  $p_i$ , such as the cases when (i)  $a_{ij}$  are deterministic and  $b_i$  are random (for all  $p_i$  values); (ii)  $a_{ij}$  and  $b_i$  are discrete random coefficient, with  $p_i \geq \max_{r=1,2,\dots,R}(1-q_r)$ , where  $q_r$  is the probability associated with realization  $r$ ; or (iii)  $a_{ij}$  and  $b_i$  have Gaussian distributions, with  $p_i \geq 0.5$  [27]. When elements of  $a_{ij}$  are deterministic and  $b_i(t)$  are random, constraint (3) can be converted into a linear one as follows:

$$A_i(t) X \leq b_i(t)^{p_i}, \quad \forall i, \quad (4)$$

where  $b_i(t)^{p_i} = F_i^{-1}(p_i)$ , given the cumulative distribution function (CDF) of  $b_i$  (i.e.,  $F_i(b_i)$ ) and the probability of violating constraint  $i$  (i.e.,  $p_i$ ). The problem with constraint (4) is that linear constraints can only reflect the case when the left-hand-side coefficients ( $A$ ) are deterministic. If both left- and right-hand sides ( $A$  and  $B$ ) are uncertain, the set of feasible constraints may become more complicated [21, 27–30]. To reflect randomness of the objective function in IIP model, an “equivalent” deterministic objective is usually defined in the CCP approach. There are four main options: (i) optimization of mean value, (ii) minimization of variance or other dispersion parameters, (iii) minimization of risks, and (iv) maximization of the fractile (or Kataoka’s problem). However, these considerations may be unable to effectively handle independent uncertainties in  $c_j$  and communicate them into the constraints.

One potential approach for better accounting for multiple uncertainties that exist in both left- and right-hand sides (of the constraints) as well as objective-function coefficients (i.e.,  $A$ ,  $B$ , and  $C$ ) is to incorporate the CCP within the above IMILP framework, where intervals and probability distributions could be reflected. This leads to an interval chance-constrained integer programming (ICIP) model as follows:

$$\begin{aligned} \text{Maximize} \quad & \lambda^\pm \\ \text{Subject to:} \quad & C^\pm X^\pm \leq f^+ - \lambda^\pm (f^+ - f^-) \\ & A_i^\pm(t) X^\pm \leq b_i(t)^{q_i^\pm} \quad \forall i, \quad i = 1, 2, \dots, m; \\ & A_i^\pm(t) \in A^\pm(t) \\ & x_j^\pm \geq 0, \quad x_j^\pm \in X^\pm; \quad j = 1, 2, \dots, n_1 \\ & 0 \leq \lambda^\pm \leq 1, \end{aligned} \quad (5)$$

where  $\lambda^\pm$  is a control variable, representing the degree of satisfaction for fuzzy decision. Figure 1 shows the framework of the ICIP. It is indicated that the ICIP integrates techniques of interval sets, integer and chance-constrained within a general framework. Each technique has its unique contribution in enhancing the model’s capacities for tackling uncertainties and dynamics. The ICIP can thus deal with uncertainties described as discrete intervals sets and their combinations. Based on an interactive algorithm, interval solutions associated with levels of system-failure risk can be obtained through solving two submodels sequentially. The solutions are useful in generating desired decision alternatives with the relationships among system cost, satisfaction degree, and constraint-violation risk being quantified.

### 3. Case Study

**3.1. Statement of Problem.** Since the fluid power system can inevitably be contaminated by large amounts of contaminants, filters have to be adopted to mitigate the contamination level and thus guarantee the critical hydraulic components not being polluted and/or destroyed. The major functions of filters are to remove contaminant particles and thus keep the system contamination at a safe level (i.e., lower than the tolerance levels of various system components). Assume that four types of filters (suction, pressure, return, and bypass filters) would be installed in the study system. The detailed nomenclatures for the variables and parameters are provided in the appendix. The binary variables (i.e., decision variables,  $F_k$  and  $A_{kn}$ ) can be employed to identify (i) whether or not particular filter needs to be installed and (ii) whether or not the existing filter needs to be replaced. For example, if filter  $k$  exists then  $F_k = 1$ ; otherwise  $F_k = 0$ ; similarly, if filter  $k$  needs to be replaced in period, then  $A_{kn} = 1$ ; otherwise  $A_{kn} = 0$ .

Additionally, the filter fineness plays a crucial role in ensuring the reliability and service life of pump in the FPS. The management of filters is of importance during the operation of FPS. Installing new filters and/or replacing the existing filters frequently may lead to an increased operation

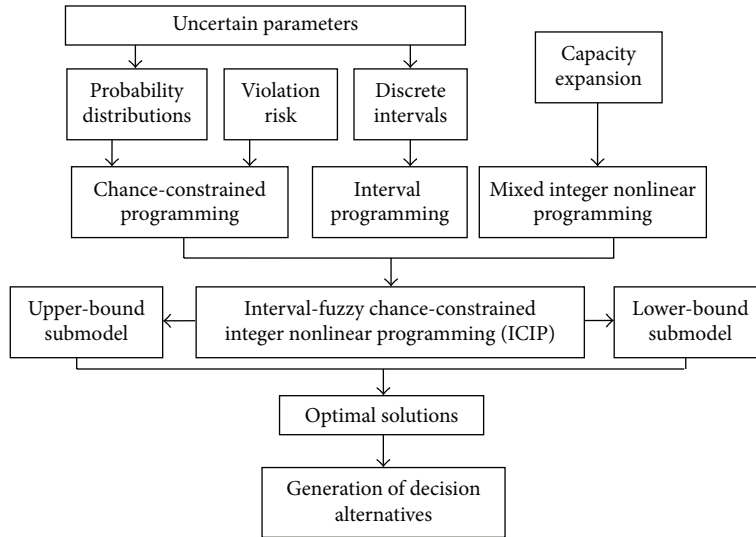


FIGURE 1: Framework of the ICIP model.

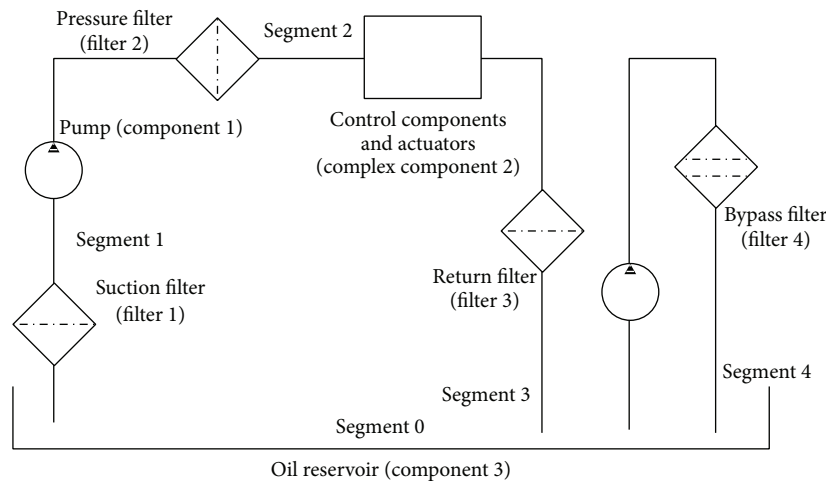


FIGURE 2: Typical hydraulic system with bypass filtration system.

cost. However, misact in installing filters and/or prolonging the replacement period of the filters may pose serious contamination threats on the FPS. Several factors such as operation cost, replacement period, system performance, service life of pump, and fineness of filters may be complex and conflicted with each other. Therefore, it is desirable to select filter fineness and plan the replacement period of filters properly and to identify how to choose suitable filters (including filter housing and filter element) and/or when to replace the existing filters at an appropriate time which would make a tradeoff between operation cost and system-failure risk.

Consider a problem wherein a decision maker is responsible for the selection, installation, and replacement of filters in a FPS with a bypass filtration circuit. Figure 2 presents such a FPS, which includes an oil reservoir, a hydraulic pump, a suction filter, a pressure filter, a return filter, a bypass filter and several control components, and an actuator. To simplify

the formal deduction of model these control components and actuator are regarded to be a complex component here.

Several assumptions are made when formulating the model, which includes the following. (1) Contaminants are evenly distributed in each segment of the fluid power system and the contamination level in any segment will not vary within a working period of filter; (2) filtration ratio of the filter is constant at any time for a given particle parameter range; (3) the other components after those filters cannot remove the contaminant particles; (4) the flow rate is assumed to be constant and the effect of system pressure and flow on the filtration efficiency is negligible; (5) all of the contaminants are considered spherical when calculating their granular mass; (6) the settling effect of the contaminants in the oil reservoir is negligible; (7) the effect of cavitation on the performance of hydraulic components due to the flow resistance of the filters is negligible; (8) the replacement of oil is out of consideration in this study.

3.2. *Model Formulation.* In such a typical hydraulic system (as shown in Figure 2), contaminant mainly comes from both outside environment and inside hydraulic components. Since the contamination ingress rate (CIR) plays an important part in removing contaminant, a further research should be conducted concerning more details about CIR. It is known that CIR is not a constant during the operation of the system. At the threshold of the system running, the value of CIR is at the top and starts to decrease with an increased speed because of intense friction. Gradually, the friction surfaces become smoother and thus the reducing rate of the speed slows down and finally ends up with zero, which means that the CIR keeps being a constant.

In the CCP, the required level of probability represents the admissible risk of violating the constraints [14, 21]. Thus, the CCP can be incorporated into the concept of IIP into a general framework to deal with uncertainties in the contaminant-holding capacity of filters and component contaminant sensitivity. Based on the preceding research [8], a chance-constrained programming (CCP) model (A) can be formulated as follows:

$$\begin{aligned} \text{Minimize } F_{\text{cost}} &= \sum_{k=1}^4 B_k F_k \\ &+ \sum_{k=1}^4 \sum_{n=1}^N (ER_k + WM_k + LM_k) A_{kn} \end{aligned} \quad (6a)$$

subject to

$$\Pr \{NF_{1nm} \leq S_{1nm}\} \geq 1 - p_i, \quad \forall n, m, \quad (6b)$$

$$\Pr \{NF_{2nm} \leq S_{2nm}\} \geq 1 - p_i, \quad \forall n, m, \quad (6c)$$

$$\begin{aligned} \Pr \left\{ \sum_{n=1}^t \sum_{m=1}^M F_1 \times NF_{0nm} \times \left(1 - \frac{1}{\beta_{1m}}\right) QT \right. \\ \left. \times \left[ \frac{4\rho\pi}{3} \times \left(\frac{D_m}{2}\right)^3 \right] \leq \sum_{n=1}^t A_{1n} C_1 \times 10^{15} \right\} \\ \geq 1 - p_i, \quad \forall t = 1, 2, \dots, N, \end{aligned} \quad (6d)$$

$$\begin{aligned} \Pr \left\{ \sum_{n=1}^t \sum_{m=1}^M F_2 \left( NF_{1nm} + \frac{R_{1(n-1)m}}{Q} \right) \right. \\ \left. \times \left(1 - \frac{1}{\beta_{2m}}\right) QT \left[ \frac{4\rho\pi}{3} \times \left(\frac{D_m}{2}\right)^3 \right] \right. \\ \left. \leq \sum_{n=1}^t A_{2n} C_2 \times 10^{15} \right\} \\ \geq 1 - p_i, \quad \forall t = 1, 2, \dots, N, \end{aligned} \quad (6e)$$

$$\begin{aligned} \Pr \left\{ \sum_{n=1}^t \sum_{m=1}^M F_3 \left( NF_{2nm} + \frac{R_{2(n-1)m}}{Q} \right) \right. \\ \left. \times \left(1 - \frac{1}{\beta_{3m}}\right) QT \left[ \frac{4\rho\pi}{3} \times \left(\frac{D_m}{2}\right)^3 \right] \right. \\ \left. \leq \sum_{n=1}^t A_{3n} C_3 \times 10^{15} \right\} \\ \geq 1 - p_i, \quad \forall t = 1, 2, \dots, N, \end{aligned} \quad (6f)$$

$$\begin{aligned} \Pr \left\{ \sum_{n=1}^t \sum_{m=1}^M F_4 \left( NF_{3nm} + \frac{R_{3(n-1)m}}{Q} \right) \right. \\ \left. \times \left(1 - \frac{1}{\beta_{4m}}\right) QT \left[ \frac{4\rho\pi}{3} \times \left(\frac{D_m}{2}\right)^3 \right] \right. \\ \left. \leq \sum_{n=1}^t A_{4n} C_4 \times 10^{15} \right\} \\ \geq 1 - p_i, \quad \forall t = 1, 2, \dots, N, \end{aligned} \quad (6g)$$

$$\begin{aligned} NF_{0(n+1)m} &= (NF_{3nm} - NF_{0nm}) \frac{QT}{V} \\ &+ \frac{R_{3nm}T}{V} + NF_{0nm} + (NF_{4nm} - NF_{3nm}) \frac{Q_b T}{V}, \end{aligned} \quad (6h)$$

$$F_k = \begin{cases} 1 & \text{if filter needs to be installed} \\ 0 & \text{otherwise,} \end{cases} \quad \forall k, \quad (6i)$$

$$A_{kn} = \begin{cases} 1 & \text{if filter needs to be replaced} \\ 0 & \text{otherwise,} \end{cases} \quad \forall k, n, \quad (6j)$$

$$A_{kn} \leq F_k \quad \forall k, n. \quad (6k)$$

The chance constraints can be converted into deterministic and linear ones through (1) fixing a certain level of probability  $p_i$ ,  $p_i \in [0, 1]$ , for constraint  $i$ , and (2) imposing the condition that constraint  $i$  is satisfied with at least a probability of  $1 - p_i$  [15, 21]. Thus, the chance constraints  $[\Pr(A_i x \leq b_i) \geq 1 - p_i]$  can be specified into

$$A_i X \leq b_i^{p_i}, \quad \forall i, \quad (7)$$

where  $b_i^{p_i} = F_i^{-1}(p_i)$ , given the cumulative distribution function (CDF) of  $b_i$  (i.e.,  $F_i(b_i)$ ) and the probability of

violating constraint  $i$  (i.e.,  $p_i$ ). Consequently, the above CCP model can be converted into a linear model (B) as follows:

$$\begin{aligned} \text{Minimize } F_{\text{cost}} = & \sum_{k=1}^4 B_k F_k \\ & + \sum_{k=1}^4 \sum_{n=1}^N (ER_k + WM_k + LM_k) A_{kn} \end{aligned} \quad (8a)$$

subject to

$$NF_{1nm} \leq S_{1nm}^{(pi)}, \quad \forall n, m, \quad (8b)$$

$$NF_{2nm} \leq S_{2nm}^{(pi)}, \quad \forall n, m, \quad (8c)$$

$$\begin{aligned} \sum_{n=1}^t \sum_{m=1}^M F_1 \times NF_{0nm} \left(1 - \frac{1}{\beta_{1m}}\right) QT \\ \times \left[ \frac{4\rho\pi}{3} \times \left(\frac{D_m}{2}\right)^3 \right] \end{aligned} \quad (8d)$$

$$\leq \sum_{n=1}^t A_{1n} C_1^{(pi)} \times 10^{15}, \quad \forall t = 1, 2, \dots, N,$$

$$\begin{aligned} \sum_{n=1}^t \sum_{m=1}^M F_2 \left( NF_{1nm} + \frac{R_{1(n-1)m}}{Q} \right) \left(1 - \frac{1}{\beta_{2m}}\right) QT \\ \times \left[ \frac{4\rho\pi}{3} \times \left(\frac{D_m}{2}\right)^3 \right] \end{aligned} \quad (8e)$$

$$\leq \sum_{n=1}^t A_{2n} C_2^{(pi)} \times 10^{15}, \quad \forall t = 1, 2, \dots, N,$$

$$\begin{aligned} \sum_{n=1}^t \sum_{m=1}^M F_3 \left( NF_{2nm} + \frac{R_{2(n-1)m}}{Q} \right) \left(1 - \frac{1}{\beta_{3m}}\right) QT \\ \times \left[ \frac{4\rho\pi}{3} \times \left(\frac{D_m}{2}\right)^3 \right] \end{aligned} \quad (8f)$$

$$\leq \sum_{n=1}^t A_{3n} C_3^{(pi)} \times 10^{15}, \quad \forall t = 1, 2, \dots, N,$$

$$\begin{aligned} \sum_{n=1}^t \sum_{m=1}^M F_4 \left( NF_{3nm} + \frac{R_{3(n-1)m}}{Q} \right) \left(1 - \frac{1}{\beta_{4m}}\right) QT \\ \times \left[ \frac{4\rho\pi}{3} \times \left(\frac{D_m}{2}\right)^3 \right] \end{aligned} \quad (8g)$$

$$\leq \sum_{n=1}^t A_{4n} C_4^{(pi)} \times 10^{15} \quad \forall t = 1, 2, \dots, N,$$

$$\begin{aligned} NF_{0(n+1)m} = (NF_{3nm} - NF_{0nm}) \frac{QT}{V} + \frac{R_{3nm}T}{V} \\ + NF_{0nm} + (NF_{4nm} - NF_{3nm}) \frac{Q_b T}{V}, \end{aligned} \quad (8h)$$

$$F_k = \begin{cases} 1 & \text{if filter needs to be installed} \\ 0 & \text{otherwise,} \end{cases} \quad \forall k, \quad (8i)$$

$$A_{kn} = \begin{cases} 1 & \text{if filter needs to be replaced} \\ 0 & \text{otherwise,} \end{cases} \quad (8j)$$

$$A_{kn} \leq F_k, \quad \forall k, n. \quad (8k)$$

The above CCP model can handle all right-hand-side uncertainties expressed as probability distributions. However, the linear constraints only correspond to cases when the left-hand-side coefficients are deterministic. Although the CCP approach can deal with left-hand-side uncertainties presented as probability density functions, three limitations exist: (1) the resulting nonlinear model would be associated with a number of difficulties in global-optimization acquisition; (2) it is unable to handle independent uncertainties in objective coefficients [38]; (3) for many practical problems, the quality of information that can be obtained for these uncertainties is mostly not good enough to be presented as probability distributions. Thus, for uncertainties in left-hand-side parameters (e.g., contamination level and component contamination sensitivity and contaminant retaining capacity), an extended consideration would be the introduction of interval parameters into the model (C). This leads to an inexact chance-constrained integer programming (ICIP) model as follows:

$$\begin{aligned} \text{Minimize } F_{\text{cost}}^\pm = \sum_{k=1}^4 B_k^\pm F_k^\pm \\ + \sum_{k=1}^4 \sum_{n=1}^N (ER_k^\pm + WM_k^\pm + LM_k^\pm) A_{kn}^\pm \end{aligned} \quad (9a)$$

subject to

$$NF_{1nm}^\pm \leq S_{1nm}^{(pi)\pm}, \quad \forall n, m, \quad (9b)$$

$$NF_{2nm}^\pm \leq S_{2nm}^{(pi)\pm}, \quad \forall n, m, \quad (9c)$$

$$\begin{aligned} \sum_{n=1}^t \sum_{m=1}^M F_1 \times NF_{0nm}^\pm \left(1 - \frac{1}{\beta_{1m}}\right) QT \\ \times \left[ \frac{4\rho\pi}{3} \times \left(\frac{D_m}{2}\right)^3 \right] \end{aligned} \quad (9d)$$

$$\leq \sum_{n=1}^t A_{1n}^\pm C_1^{(pi)\pm} \times 10^{15}, \quad \forall t = 1, 2, \dots, N,$$

$$\sum_{n=1}^t \sum_{m=1}^M F_2 \left( NF_{1nm}^\pm + \frac{R_{1(n-1)m}^\pm}{Q} \right) \left( 1 - \frac{1}{\beta_{2m}} \right) QT \times \left[ \frac{4\rho\pi}{3} \times \left( \frac{D_m}{2} \right)^3 \right] \leq \sum_{n=1}^t A_{2n}^\pm C_2^{(pi)\pm} \times 10^{15}, \quad \forall t = 1, 2, \dots, N, \tag{9e}$$

$$\sum_{n=1}^t \sum_{m=1}^M F_3 \left( NF_{2nm}^\pm + \frac{R_{2(n-1)m}^\pm}{Q} \right) \left( 1 - \frac{1}{\beta_{3m}} \right) QT \times \left[ \frac{4\rho\pi}{3} \times \left( \frac{D_m}{2} \right)^3 \right] \tag{9f}$$

$$\leq \sum_{n=1}^t A_{3n}^\pm C_3^{(pi)\pm} \times 10^{15}, \quad \forall t = 1, 2, \dots, N,$$

$$\sum_{n=1}^t \sum_{m=1}^M F_4 \left( NF_{3nm}^\pm + \frac{R_{3(n-1)m}^\pm}{Q} \right) \left( 1 - \frac{1}{\beta_{4m}} \right) QT \times \left[ \frac{4\rho\pi}{3} \times \left( \frac{D_m}{2} \right)^3 \right] \tag{9g}$$

$$\leq \sum_{n=1}^t A_{4n}^\pm C_4^{(pi)\pm} \times 10^{15}, \quad \forall t = 1, 2, \dots, N,$$

$$NF_{0(n+1)m}^\pm = (NF_{3nm}^\pm - NF_{0nm}^\pm) \frac{QT}{V} + \frac{R_{3nm}^\pm T}{V} + NF_{0nm}^\pm + (NF_{4nm}^\pm - NF_{3nm}^\pm) \frac{Q_b T}{V}, \tag{9h}$$

$$F_k = \begin{cases} 1 & \text{if filter needs to be installed} \\ 0 & \text{otherwise,} \end{cases} \tag{9i}$$

$$\forall k,$$

$$A_{kn}^\pm = \begin{cases} 1 & \text{if filter needs to be replaced} \\ 0 & \text{otherwise,} \end{cases} \tag{9j}$$

$$\forall k, n, \tag{9k}$$

$$A_{kn}^\pm \leq F_k, \quad \forall k, n,$$

where  $F_{\text{cost}}^\pm$ ,  $B_k^\pm$ ,  $ER_k^\pm$ ,  $WM_k^\pm$ ,  $LM_k^\pm$ ,  $A_{kn}^\pm$ ,  $C_i^{(qi)\pm}$ ,  $S_{inm}^{(qi)\pm}$ ,  $NF_{inm}^\pm$ , and  $R_{inm}^\pm$  are interval parameters and variables; the “-” and “+” superscripts represent lower- and upper-bounds of the parameters, respectively. This ICIP model can be transformed into two deterministic submodels that correspond to the

lower- and upper-bounds of the desired objective. Interval solutions, which are feasible and stable in the given decision space, can then be obtained by solving the two submodels sequentially [34]. According to Huang [21], the submodel corresponding to the lower-bound objective ( $F_{\text{cost}}^-$ ) can be firstly formulated as follows:

$$\text{Minimize } F_{\text{cost}}^- = \sum_{k=1}^4 B_k^- F_k^- + \sum_{k=1}^4 \sum_{n=1}^N (ER_k^- + WM_k^- + LM_k^-) A_{kn}^- \tag{10a}$$

subject to

$$NF_{1nm}^- \leq S_{1nm}^{(pi)-}, \quad \forall n, m, \tag{10b}$$

$$NF_{2nm}^- \leq S_{2nm}^{(pi)-}, \quad \forall n, m, \tag{10c}$$

$$\sum_{n=1}^t \sum_{m=1}^M F_1 \times NF_{0nm}^- \left( 1 - \frac{1}{\beta_{1m}} \right) QT \times \left[ \frac{4\rho\pi}{3} \times \left( \frac{D_m}{2} \right)^3 \right] \tag{10d}$$

$$\leq \sum_{n=1}^t A_{1n}^- C_1^{(pi)-} \times 10^{15}, \quad \forall t = 1, 2, \dots, N,$$

$$\sum_{n=1}^t \sum_{m=1}^M F_2 \left( NF_{1nm}^- + \frac{R_{1(n-1)m}^-}{Q} \right) \left( 1 - \frac{1}{\beta_{2m}} \right) QT \times \left[ \frac{4\rho\pi}{3} \times \left( \frac{D_m}{2} \right)^3 \right] \tag{10e}$$

$$\leq \sum_{n=1}^t A_{2n}^- C_2^{(pi)-} \times 10^{15}, \quad \forall t = 1, 2, \dots, N,$$

$$\sum_{n=1}^t \sum_{m=1}^M F_3 \left( NF_{2nm}^- + \frac{R_{2(n-1)m}^-}{Q} \right) \left( 1 - \frac{1}{\beta_{3m}} \right) QT \times \left[ \frac{4\rho\pi}{3} \times \left( \frac{D_m}{2} \right)^3 \right] \tag{10f}$$

$$\leq \sum_{n=1}^t A_{3n}^- C_3^{(pi)-} \times 10^{15}, \quad \forall t = 1, 2, \dots, N,$$

$$\sum_{n=1}^t \sum_{m=1}^M F_4 \left( NF_{3nm}^- + \frac{R_{3(n-1)m}^-}{Q} \right) \left( 1 - \frac{1}{\beta_{4m}} \right) QT \times \left[ \frac{4\rho\pi}{3} \times \left( \frac{D_m}{2} \right)^3 \right] \tag{10g}$$

$$\leq \sum_{n=1}^t A_{4n}^- C_4^{(pi)-} \times 10^{15}, \quad \forall t = 1, 2, \dots, N,$$

$$NF_{0(n+1)m}^- = (NF_{3nm}^- - NF_{0nm}^-) \frac{QT}{V} + \frac{R_{3nm}^- T}{V} + NF_{0nm}^- + (NF_{4nm}^- - NF_{3nm}^-) \frac{Q_b T}{V}, \quad (10h)$$

$$F_k = \begin{cases} 1 & \text{if filter needs to be installed} \\ 0 & \text{otherwise,} \end{cases} \quad (10i)$$

$$\forall k,$$

$$A_{kn}^- = \begin{cases} 1 & \text{if filter needs to be replaced} \\ 0 & \text{otherwise,} \end{cases} \quad (10j)$$

$$\forall k, n,$$

$$A_{kn}^- \leq F_k, \quad \forall k, n. \quad (10k)$$

Correspondingly, the submodel corresponding to the upper-bound objective ( $F_{\text{cost}}^+$ ) can be formulated as follows:

$$\begin{aligned} \text{Minimize } F_{\text{cost}}^+ &= \sum_{k=1}^4 B_k^+ F_k^+ \\ &+ \sum_{k=1}^4 \sum_{n=1}^N (ER_k^+ + WM_k^+ + LM_k^+) A_{kn}^+ \end{aligned} \quad (11a)$$

subject to

$$NF_{1mm}^+ \leq S_{1mm}^{(pi)+}, \quad \forall n, m, \quad (11b)$$

$$NF_{2mm}^+ \leq S_{2mm}^{(pi)+}, \quad \forall n, m, \quad (11c)$$

$$\begin{aligned} \sum_{n=1}^t \sum_{m=1}^M F_1 \times NF_{0nm}^+ \left(1 - \frac{1}{\beta_{1m}}\right) QT \\ \times \left[ \frac{4\rho\pi}{3} \times \left(\frac{D_m}{2}\right)^3 \right] \end{aligned} \quad (11d)$$

$$\leq \sum_{n=1}^t A_{1n}^+ C_1^{(pi)+} \times 10^{15}, \quad \forall t = 1, 2, \dots, N,$$

$$\begin{aligned} \sum_{n=1}^t \sum_{m=1}^M F_2 \left( NF_{1mm}^+ + \frac{R_{1(n-1)m}^+}{Q} \right) \left(1 - \frac{1}{\beta_{2m}}\right) QT \\ \times \left[ \frac{4\rho\pi}{3} \times \left(\frac{D_m}{2}\right)^3 \right] \end{aligned} \quad (11e)$$

$$\leq \sum_{n=1}^t A_{2n}^+ C_2^{(pi)+} \times 10^{15}, \quad \forall t = 1, 2, \dots, N,$$

$$\begin{aligned} \sum_{n=1}^t \sum_{m=1}^M F_3 \left( NF_{2mm}^+ + \frac{R_{2(n-1)m}^+}{Q} \right) \left(1 - \frac{1}{\beta_{3m}}\right) QT \\ \times \left[ \frac{4\rho\pi}{3} \times \left(\frac{D_m}{2}\right)^3 \right] \end{aligned} \quad (11f)$$

$$\leq \sum_{n=1}^t A_{3n}^+ C_3^{(pi)+} \times 10^{15}, \quad \forall t = 1, 2, \dots, N,$$

$$\begin{aligned} \sum_{n=1}^t \sum_{m=1}^M F_4 \left( NF_{3mm}^+ + \frac{R_{3(n-1)m}^+}{Q} \right) \left(1 - \frac{1}{\beta_{4m}}\right) QT \\ \times \left[ \frac{4\rho\pi}{3} \times \left(\frac{D_m}{2}\right)^3 \right] \end{aligned} \quad (11g)$$

$$\leq \sum_{n=1}^t A_{4n}^+ C_4^{(pi)+} \times 10^{15}, \quad \forall t = 1, 2, \dots, N,$$

$$\begin{aligned} NF_{0(n+1)m}^+ &= (NF_{3nm}^+ - NF_{0nm}^+) \frac{QT}{V} + \frac{R_{3nm}^+ T}{V} \\ &+ NF_{0nm}^+ + (NF_{4nm}^+ - NF_{3nm}^+) \frac{Q_b T}{V}, \end{aligned} \quad (11h)$$

$$F_k = \begin{cases} 1 & \text{if filter needs to be installed} \\ 0 & \text{otherwise,} \end{cases} \quad (11i)$$

$$\forall k,$$

$$A_{kn}^+ = \begin{cases} 1 & \text{if filter needs to be replaced} \\ 0 & \text{otherwise,} \end{cases} \quad (11j)$$

$$\forall k, n,$$

$$A_{kn}^+ \leq F_k, \quad \forall k, n. \quad (11k)$$

The above solutions provide stable intervals for the objective function value and the decision variables under different levels of risk in violating the constraints. They can be easily interpreted for generating multiple decision alternatives. The detailed solution process can be summarized as follows.

*Step 1.* Acquire distribution information for the system constraints (e.g., contaminant retaining capacity and contamination sensitivity of filters).

*Step 2.* Formulate ICIP model.

*Step 3.* Transform ICIP model into two submodels, where the submodel corresponding to  $F_{\text{cost}}^-$  should be firstly solved (to obtain the most optimistic decision option within the decision space) since the objective is to minimize  $F_{\text{cost}}^\pm$ .

*Step 4.* Formulate  $F_{\text{cost}}^-$  submodel, including the objective function and the relevant constraints.

*Step 5.* Solve the  $F_{\text{cost}}^-$  submodel and obtain  $F_{\text{cost-opt}}^-$  under different  $q_i$  levels.

Step 6. Formulate  $F_{\text{cost}}^+$  submodel, including the objective function and the relevant constraints.

Step 7. Solve the  $F_{\text{cost}}^+$  submodel and obtain  $F_{\text{cost-opt}}^+$  under different  $q_i$  levels.

Step 8. Calculate  $F_{\text{opt}}^\pm = [F_{\text{cost-opt}}^-, F_{\text{cost-opt}}^+]$  under each given  $q_i$  level.

Step 9. Stop.

3.3. *Data Collection.* Consider a case wherein a manager is responsible for designing and managing a hydraulic system (as shown in Figure 2). The problem to be resolved is how to keep contamination level by allocating various filters with a minimal sum of capital to achieve a maximal system safe. The planning time period is one year. The flow rate is approximately 100 L/min, the maximal pressure is around 35 MPa, and the fluid volume of the reservoir is about 1300 L. Table 1 shows seven different practical combinations under each scenario at low, medium, and high ingress/generation level. Table 2 presents the diameter intervals of contaminant particles (according to piecewise linearization approach), average diameters, and its corresponding initial contamination levels and contamination tolerance levels which are listed under four probability distributions. The initial contamination level of the suction line is considered to meet the cleanliness class requirement of NAS 1638 Level 7~9 [8]. It is indicated that the contaminant ingress/generation rates and the tolerance levels of the main hydraulic components are both expressed as interval values.

In addition, the average density of contaminant particles ( $\rho$ ) is approximately  $0.5 \times 10^3 \text{ kg/m}^3$ . Table 3 provides the types and performance parameters of the filters. It is indicated that each filter possesses its own contaminant retaining capacities that are various among four different probability distributions. The cost for installing/maintaining/replacing filters and the economic losses denoted by their corresponding mean values due to maintaining/replacing filters are presented in Table 4 [8, 35].

According to NAS 1638 contamination level, the contaminant ingress/generation rates of hydraulic components are divided into low, medium, and high levels. Table 5 presents the distributions of different contaminant ingress/generation levels corresponding to different particle diameters (low level corresponding to NAS 1638 Level 1~4, medium level corresponding to Level 5~7, and high level corresponding to Level 8~10). Interactive relationships exist among a variety of impact factors and contamination-related processes, and many parameters in the studied system are uncertain. Therefore, the developed ICIP method is supposed to tackle this type of contamination control management problem.

3.4. *Result Analysis.* The above models can be solved through software package LINGO. Representative outcomes (as shown in Tables 6 to 8) are explicated to demonstrate important findings. Since it is a one-year plan, an estimated

TABLE 1: Practicable filter combinations.

Filter	Scenario						
	1	2	3	4	5	6	7
$F_1$	0	0	0	1	1	1	1
$F_2$	0	1	1	0	0	1	1
$F_3$	1	0	1	0	1	0	1
$F_4$	1	0	0	1	1	0	0
Code	0011	0100	0110	1001	1011	1100	1110

replacement period was offered according to final contamination level of the hydraulic oil when the actual replacement period is longer than one year.

Tables 6(a)–6(d) show results at low ingress/generation level. Optimized system costs correspond with four probabilities. That is because none of those filters call for any replacement with four probabilities. Optimized system costs have achieved the bottom values, which means they cannot be lower any more, but there are still some tiny differences among results with four different probabilities. Take Scenario 1, for example; four results are [376.3, 382.2], [376.5, 382.8], [377.3, 385.3], and [392.5, 404.0] days corresponding to four probabilities. The solutions indicate that the system costs would decrease with  $p_i$ , where  $p_i = 0.10, 0.15, 0.20, 0.30$  ( $i = 1, 2, 3, 4$ ), respectively. The replacement periods would become longer as  $p_i$  increases ( $p_1 < p_2 < p_3 < p_4$ ). In fact, an increased  $p_i$  means more relaxed constraints, such as contaminant retaining capacity of filters and component contaminant sensitivity, and thus a raised risk in violating the two constrains.

Tables 7(a)–7(d) show results at medium ingress/generation level. It is obvious that these results are interrupted by occasionally some bad results, the values of which do not agree with normal tendency. For example, the results under Scenario 2 are [178, 187], [166, 357.7], [175, 358.1], and [87, 360.8] days. The general trend is that replacement periods go up as  $p_i$  increases except that 178 days with  $p_i$  distribution is not on the track. However, the data still represents the principle perfectly. The same phenomenon also appears under other scenarios.

Tables 8(a)–8(d) show results at high ingress/generation level. Since the contamination/generation level is high, any change in  $p_i$  would yield different contaminant retaining capacities of filters and component contaminant sensitivities and thus obviously result in different system costs. Under a probability level of  $p_i = p_1 = 0$ , the violation of the system cost and replacement period would be zero. The system costs under Scenarios 1, 2, 3, 5, 6, and 7 are RMB ¥ [44500, 50150], [59000, 67400], [49950, 56550], [41600, 46850], [38250, 39750], and [42250, 47800], respectively. Under a significance level of  $p_i = p_2$ , the system costs under Scenarios 1, 2, 3, 5, 6, and 7 are RMB ¥ [52150, 59150], [50750, 57950], [45000, 51350], [50600, 55100], [36350, 35700], and [40600, 43200], respectively. The costs are a little lower than those under the probability of  $p_i$  due to a slightly increased risk. Then  $p_i$  rises up to  $p_3$  and the corresponding costs go down accordingly. Under a probability level of  $p_i = p_3$ , the system costs under Scenarios 1, 2, 3, 5, 6, and 7 are RMB ¥ [49450, 58000],

TABLE 2: Particle diameters, initial contamination, and contamination tolerance levels.

Contaminant particle divisions	1	2	3	4	5	6	7	8	9
Range of diameters ( $\mu\text{m}$ )	0~5	5~10	10~15	15~20	20~25	25~30	30~50	50~100	100~
Initial contamination level $N_{01m}^{\pm}$ (number of particles/mL)	[1000, 1500]	[300, 500]	[150, 250]	[60, 100]	[30, 50]	[10, 15]	[6, 10]	[2.5, 4.0]	[0.5, 0.8]
Contamination tolerance level $S_{1nm}^{\pm}$ (number of particles/mL)									
$q_1$	[4000, 6000]	[1200, 2000]	[600, 1000]	[250, 400]	[140, 230]	[50, 67]	[30, 43]	[12, 17]	[5, 7]
$q_2$	[4300, 6300]	[1300, 2100]	[680, 1080]	[300, 460]	[120, 200]	[40, 60]	[25, 40]	[10, 15]	[4, 6]
$q_3$	[4600, 6500]	[1500, 2200]	[720, 1200]	[350, 530]	[160, 260]	[60, 71]	[35, 45]	[14, 19]	[6, 8]
$q_4$	[8000, 12000]	[2400, 4000]	[1200, 2000]	[500, 800]	[240, 400]	[80, 120]	[50, 80]	[20, 30]	[8, 12]
Contamination tolerance level $S_{2nm}^{\pm}$ (number of particles/mL)									
$q_1$	[2000, 3000]	[600, 1000]	[300, 500]	[120, 200]	[60, 100]	[20, 30]	[12, 20]	[5, 8]	[2, 3]
$q_2$	[2100, 3100]	[700, 1200]	[380, 560]	[150, 210]	[70, 105]	[30, 35]	[16, 23]	[7, 10]	[3, 4]
$q_3$	[2200, 3200]	[800, 1280]	[450, 630]	[180, 220]	[80, 110]	[40, 40]	[20, 26]	[9, 12]	[4, 5]
$q_4$	[4000, 6000]	[1200, 2000]	[600, 1000]	[240, 400]	[120, 200]	[40, 60]	[24, 40]	[10, 16]	[4, 6]

TABLE 3: Type and performance parameters of filters.

Filters	Type of filters	Fineness of filters ( $\mu\text{m}$ )	Rated flow (L/min)	Maximum pressure (MPa)	Contaminant-holding capability $C_k$ (g)			
					$p_1$	$p_2$	$p_3$	$p_4$
Suction filter	AS 150-01	100	200	Low	[100, 120]	[105, 125]	[110, 130]	[200, 240]
Pressure filter	HD 414-56	10	210	35	[50, 60]	[60, 71]	[65, 75]	[100, 120]
Return filter	E 211-58	20	210	Low	[70, 85]	[72, 86]	[80, 90]	[140, 170]
Bypass filter	FNA 016-553	1E	16	0.4	[65, 80]	[67, 82]	[72, 86]	[130, 160]

TABLE 4: Cost data.

Filters	Price of filters $B_k$ (RMB ¥)	Replacement expenditure $E_k$ (RMB ¥)	Wage of maintenance worker $M_k$ (RMB ¥) per time	Downtime cost $P_k$ (RMB ¥) per time
Suction filter	[1000, 1300]	[500, 600]	50	200
Pressure filter	[8000, 9500]	[1100, 1400]	50	200
Return filter	[2000, 2500]	[900, 1100]	50	200
Bypass filter	9000	1300	50	200

TABLE 5: Initial contaminant ingestion/generation rates of hydraulic components.

Contaminant particle divisions	1	2	3	4	5	6	7	8	9
Low level ( $\times 10^3$ number of particles/min)									
$R_{1nm}^{\pm}$	[25, 35]	[7, 8]	[2.5, 3.5]	[0.7, 1.6]	[0.55, 0.65]	[0.18, 0.3]	[0.07, 0.15]	[0.03, 0.09]	[0.017, 0.025]
$R_{2nm}^{\pm}$	[100, 400]	[28, 32]	[10, 14]	[2.8, 6.4]	[2.2, 2.6]	[0.72, 1.14]	[0.28, 0.6]	[0.12, 0.36]	[0.068, 0.1]
$R_{3nm}^{\pm}$	[50, 70]	[14, 16]	[5, 7]	[1.4, 3.2]	[1.1, 1.3]	[0.36, 0.52]	[0.14, 0.2]	[0.06, 0.18]	[0.034, 0.05]
Medium level ( $\times 10^4$ number of particles/min)									
$R_{1nm}^{\pm}$	[33, 36]	[9, 13]	[3, 7]	[1, 3]	[0.5, 1.5]	[0.2, 0.45]	[0.1, 0.25]	[0.08, 0.11]	[0.007, 0.027]
$R_{2nm}^{\pm}$	[132, 144]	[36, 52]	[12, 28]	[4, 12]	[2, 6]	[0.8, 1.8]	[0.4, 1]	[0.32, 0.44]	[0.028, 0.108]
$R_{3nm}^{\pm}$	[66, 72]	[18, 26]	[6, 14]	[2, 6]	[1, 3]	[0.4, 0.9]	[0.2, 0.5]	[0.16, 0.22]	[0.014, 0.054]
High level ( $\times 10^4$ number of particles/min)									
$R_{1nm}^{\pm}$	[255, 270]	[85, 100]	[40, 50]	[10, 20]	[7.5, 8.5]	[2.5, 3.5]	[1, 2]	[0.5, 1]	[0.1, 0.2]
$R_{2nm}^{\pm}$	[1020, 1080]	[340, 400]	[160, 200]	[40, 80]	[30, 32]	[10, 14]	[4, 8]	[2, 4]	[0.4, 0.8]
$R_{3nm}^{\pm}$	[510, 540]	[170, 200]	[80, 100]	[20, 40]	[15, 16]	[5, 7]	[2, 4]	[1, 2]	[0.2, 0.4]

TABLE 6: (a) Results for optimized system cost and filter-replacement period under low ingresson/generation rate (8 hours per day) (when  $p_1 = 0.10$ ). (b) Results for optimized system cost and filter-replacement period under low ingresson/generation rate (8 hours per day) (when  $p_2 = 0.15$ ). (c) Results for optimized system cost and filter-replacement period under low ingresson/generation rate (8 hours per day) (when  $p_3 = 0.20$ ). (d) Results for optimized system cost and filter-replacement period under low ingresson/generation rate (8 hours per day) (when  $p_4 = 0.30$ ).

(a)				
Scenario	Optimized system cost (RMB ¥)	Replacement period of filter element (days)		
		$k = 1$	$k = 2$	$k = 3$
1	[2000, 2500]	—	—	[376.3, 382.2]
2	[8000, 9500]	—	[385.8, 398.8]	—
3	[10000, 12000]	—	[413, 433.5]	[403, 419.1]
4	[1000, 1300]	[366.6, 367.2]	—	—
5	[3000, 3800]	[384.1, 390.6]	—	[379.2, 385.7]
6	[9000, 10800]	[379.9, 385.2]	[415.2.8, 415]	—
7	[11000, 13300]	[399.1, 409.2]	[425.0, 446.9]	[404.7, 420.1]

(b)				
Scenario	Optimized system cost (RMB ¥)	Replacement period of filter element (days)		
		$k = 1$	$k = 2$	$k = 3$
1	[2000, 2500]	—	—	[376.5, 382.8]
2	[8000, 9500]	—	[392.4, 408.4]	—
3	[10000, 12000]	—	[424.03.1, 449.4]	[404.5.0, 420.8]
4	[1000, 1300]	[366.7, 367.3]	—	—
5	[3000, 3800]	[384.9, 391.9]	—	[379.5, 386.4]
6	[9000, 10800]	[380.6, 386.3]	[409.6, 426.3]	—
7	[11000, 13300]	[400.6, 411.5]	[437.1, 464.4]	[405.2, 421.8]

(c)				
Scenario	Optimized system cost (RMB ¥)	Replacement period of filter element (days)		
		$k = 1$	$k = 2$	$k = 3$
1	[2000, 2500]	—	—	[377.3, 385.3]
2	[8000, 9500]	—	[394.8, 413.2]	—
3	[10000, 12000]	—	[428.0.0, 457.3]	[406.7.5, 427.8]
4	[1000, 1300]	[366.8, 367.5]	—	—
5	[3000, 3800]	[385.8, 393.2]	—	[380.3, 389.2]
6	[9000, 10800]	[381.3, 387.4]	[412.4, 431.8]	—
7	[11000, 13300]	[402.1, 413.8]	[441.5, 473.2]	[407.5, 428.9]

(d)				
Scenario	Optimized system cost (RMB ¥)	Replacement period of filter element (days)		
		$k = 1$	$k = 2$	$k = 3$
1	[2000, 2500]	—	—	[392.5, 404.0]
2	[8000, 9500]	—	[422.0, 446.6]	—
3	[10000, 12000]	—	[472.8.0, 512.8]	[450.6.7, 480.0]
4	[1000, 1300]	[368.6, 367.7]	—	—
5	[3000, 3800]	[404.3, 395.9]	—	[397.7, 410.2]
6	[9000, 10800]	[397.3, 389.7]	[444.2, 470.7]	—
7	[11000, 13300]	[435.0, 418.4]	[491.2, 534.6]	[452.1, 482.0]

TABLE 7: (a) Results for optimized system cost and filter-replacement period under medium ingress/generation rate (8 hours per day) (when  $p_1 = 0.10$ ). (b) Results for optimized system cost and filter-replacement period under medium ingress/generation rate (8 hours per day) (when  $p_2 = 0.15$ ). (c) Results for optimized system cost and filter-replacement period under medium ingress/generation rate (8 hours per day) (when  $p_3 = 0.20$ ). (d) Results for optimized system cost and filter-replacement period under medium ingress/generation rate (8 hours per day) (when  $p_4 = 0.30$ ).

(a)				
Scenario	Optimized system cost (RMB ¥)	Replacement period of filter element (days)		
		$k = 1$	$k = 2$	$k = 3$
1	[5200, 6600]	—	—	[361.3, 362.9]
2	[14450, 14750]	—	[178, 187]	—
3	[15000, 15000]	—	[358.1, 362.3]	[192, 244]
4	[2150, 2500]	[178, 187]	—	—
5	[5150, 6450]	[365.4, 366.4]	—	[362.1, 363.7]
6	[12450, 13300]	[128, 274]	[147, 253]	—
7	[14650, 14650]	[194, 367.5]	[363.1, 366.8]	[232, 361.2]

(b)				
Scenario	Optimized system cost (RMB ¥)	Replacement period of filter element (days)		
		$k = 1$	$k = 2$	$k = 3$
1	[5200, 6600]	—	—	[67, 256]
2	[12800, 13400]	—	[166, 357.7]	—
3	[15000, 15000]	—	[241, 250]	[247, 364.2]
4	[2150, 2500]	[231, 364.9]	—	—
5	[5150, 6450]	[174, 186]	—	[362.1, 363.7]
6	[10800, 11100]	[364.3, 365.1]	[151, 365.5]	—
7	[14650, 14650]	[230, 367.6]	[239, 364.0]	[124, 364.2]

(c)				
Scenario	Optimized system cost (RMB ¥)	Replacement period of filter element (days)		
		$k = 1$	$k = 2$	$k = 3$
1	[3850, 5450]	—	—	[70, 142]
2	[12800, 13400]	—	[175, 358.1]	—
3	[15000, 15000]	—	[127, 364.2]	[361.4, 364.7]
4	[2150, 2500]	[202, 364.9]	—	—
5	[5150, 6450]	[186, 365.5]	—	[91, 363.9]
6	[10800, 11100]	[364.3, 365.2]	[159, 366.0]	—
7	[14650, 14650]	[365.9, 367.8]	[260, 368.9]	[130, 265]

(d)				
Scenario	Optimized system cost (RMB ¥)	Replacement period of filter element (days)		
		$k = 1$	$k = 2$	$k = 3$
1	[3850, 4300]	—	—	[362.5, 364.6]
2	[11150, 10700]	—	[187, 360.8]	—
3	[12000, 12500]	—	[244, 369.0]	[187, 364.9]
4	[1750, 2150]	[187, 364.9]	—	—
5	[3800, 4150]	[366.7, 366.8]	—	[363.4, 365.6]
6	[10800, 10350]	[365.1, 365.4]	[364.6, 369.1]	—
7	[12150, 13300]	[246, 368.2]	[373.8, 367.7]	[364.3, 369.1]

TABLE 8: (a) Results for optimized system cost and filter-replacement period under high ingresson/generation rate (8 hours per day) (when  $p_1 = 0.10$ ). (b) Results for optimized system cost and filter-replacement period under high ingresson/generation rate (8 hours per day) (when  $p_2 = 0.15$ ). (c) Results for optimized system cost and filter-replacement period under high ingresson/generation rate (8 hours per day) (when  $p_3 = 0.20$ ). (d) Results for optimized system cost and filter-replacement period under high ingresson/generation rate (8 hours per day) (when  $p_4 = 0.30$ ).

(a)					
Scenario	Optimized system cost (RMB ¥)	Replacement period of filter element (days)			
		$k = 1$	$k = 2$	$k = 3$	$k = 4$
1	[53500, 59150]	—	—	[12, 17]	[98, 105]
2	[59000, 67400]		[7, 9]		
3	[49950, 56550]		[17, 47]	[26, 27]	
4	—	—			—
5	[50600, 55850]	[71, 110]		[16, 22]	[107, 114]
6	[38250, 39750]	[19, 88]	[19, 46]		
7	[42250, 47800]	[24, 33]	[17, 47]	[27, 70]	

(b)					
Scenario	Optimized system cost (RMB ¥)	Replacement period of filter element (days)			
		$k = 1$	$k = 2$	$k = 3$	$k = 4$
1	[52150, 59150]	—	—	[12, 18]	[101, 108]
2	[50750, 57950]		[22, 22]		
3	[45000, 51350]		[7, 17]	[48, 69]	
4	—	—			—
5	[50600, 55100]	[74, 115]		[16, 23]	[110, 117]
6	[36350, 35700]	[26, 65]	[13, 22]		
7	[40600, 43200]	[32, 88]	[17, 269]	[42, 49]	

(c)					
Scenario	Optimized system cost (RMB ¥)	Replacement period of filter element (days)			
		$k = 1$	$k = 2$	$k = 3$	$k = 4$
1	[49450, 58000]	—	—	[13, 20]	[105, 116]
2	[47450, 55250]		[16, 58]		
3	[42000, 50000]		[34, 80]	[34, 75]	
4	—	—			—
5	[46350, 53950]	[77, 121]		[17, 25]	[115, 126]
6	[35000, 34950]	[14, 61]	[46, 67]		
7	[38400, 43200]	[18, 54]	[34, 46]	[92, 136]	

(d)					
Scenario	Optimized system cost (RMB ¥)	Replacement period of filter element (days)			
		$k = 1$	$k = 2$	$k = 3$	$k = 4$
1	[35500, 38800]	—	—	[24, 34]	[196, 209]
2	[34250, 37700]		[13, 18]		
3	[30300, 32700]		[47, 65]	[27, 192]	
4	[54850, 59100]	[40, 44]			[16, 21]
5	[35850, 36700]	[132, 142]		[31, 44]	[214, 227]
6	[24200, 23700]	[65, 112]	[22, 37]		
7	[26700, 28450]	[33, 71]	[47, 65]	[97, 187]	

, [42000, 50000], [46350, 53950], [35000, 34950], and [38400, 43200], respectively. Under a probability level of  $p_i = p_4$ , the system risks the most while the costs of the system prominently fall. The system costs under seven scenarios are RMB ¥ [35500, 38800], [34250, 37700], [30300, 32700], [54850, 59100], [35850, 36700], [24200, 23700], and [26700, 28450], respectively.

Figure 3 presents outcomes for system optimal cost of all scenarios under low contaminant ingress/generation rates. When contaminant ingress/generation rate is low, the system maintenance cost achieves the optimal one. Accordingly, results under four probabilities denote the general trend and some tiny differences among results with different probabilities. Obviously, the system shows good characteristic of resisting violation.

Figure 4 presents outcomes for system optimal cost of all scenarios under medium contaminant ingress/generation rates under four probabilities. Take scenario 001, for example; the cost under probability  $p_1$  is 0 less than that under probability  $p_2$ ; the cost under probability  $p_2$  is [1150, 1350] less than that under probability  $p_3$ ; the cost under probability  $p_3$  is RMB ¥ [0, 1150] less than that under probability  $p_4$ . All the increments are small which means the system is good at resisting risk. Take scenario 010, for example; the cost under probability  $p_1$  is RMB ¥ [1350, 1650] less than that under probability  $p_2$ ; the cost under probability  $p_2$  is 0 less than that under probability  $p_3$ ; the cost under probability  $p_3$  is RMB ¥ [2100, 2250] less than that under probability  $p_4$ . Small increments show good risk-resisting ability. Take scenario 011, for example; the cost under probability  $p_1$  is 0 less than that under probability  $p_2$ ; the cost under probability  $p_2$  is 0 less than that under probability  $p_3$ ; the cost under probability  $p_3$  is RMB ¥ [2500, 3000] less than that under probability  $p_4$ . Environment violation has little influence on cost change. Take scenario 100, for example; the cost under probability  $p_1$  is 0 less than that under probability  $p_2$ ; the cost under probability  $p_2$  is 0 less than that under probability  $p_3$ ; the cost under probability  $p_3$  is RMB ¥ [350, 400] less than that under probability  $p_4$ . Under scenario 101, the cost under probability  $p_1$  is 0 less than that under probability  $p_2$ ; the cost under probability  $p_2$  is 0 less than that under probability  $p_3$ ; the cost under probability  $p_3$  is RMB ¥ [1350, 2300] less than that under probability  $p_4$ . Under scenario 110, the cost under probability  $p_1$  is RMB ¥ [1650, 2200] less than that under probability  $p_2$ ; the cost under probability  $p_2$  is 0 less than that under probability  $p_3$ ; the cost under probability  $p_3$  is RMB ¥ [300, 450] less than that under probability  $p_4$ . Under scenario 111, the cost under probability  $p_1$  is 0 less than that under probability  $p_2$ ; the cost under probability  $p_2$  is 0 less than that under probability  $p_3$ ; the cost under probability  $p_3$  is RMB ¥ [1350, 2500] less than that under probability  $p_4$ .

Figure 5 presents outcomes for system optimal cost of all scenarios under high contaminant ingress/generation rates under four probabilities. Take scenario 001, for example; the cost under probability  $p_1$  is RMB ¥ [0, 1350] less than that under probability  $p_2$ ; the cost under probability  $p_2$  is RMB ¥ [-5100, 2700] less than that under probability  $p_3$ ; the cost under probability  $p_3$  is [13950, 25450] less than that under probability  $p_4$ . All the increments are large which means the

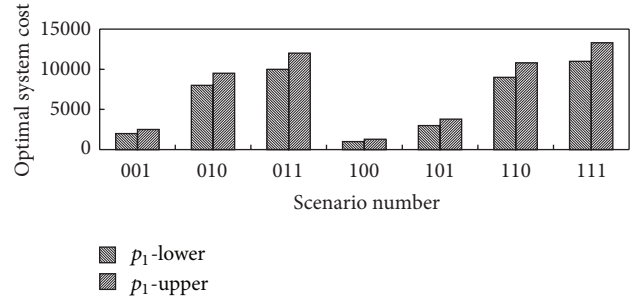


FIGURE 3: Optimal costs under low contaminant ingress/generation level.

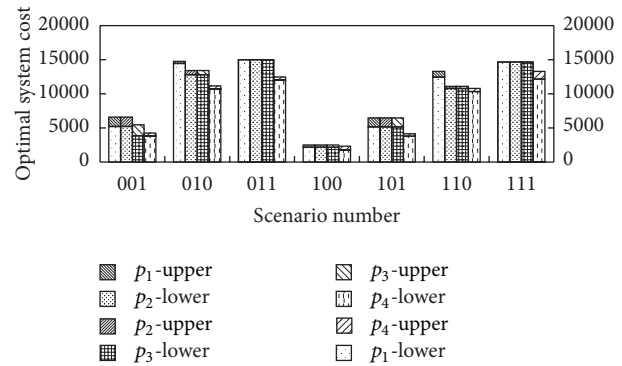


FIGURE 4: Optimal costs under medium contaminant ingress/generation level.

system is bad at resisting risk. Take scenario 010, for example; the cost under probability  $p_1$  is RMB ¥ [8250, 9450] less than that under probability  $p_2$ ; the cost under probability  $p_2$  is RMB ¥ [3300, 2700] less than that under probability  $p_3$ ; the cost under probability  $p_3$  is RMB ¥ [13200, 17550] less than that under probability  $p_4$ . Small increments show bad risk-resisting ability. Take scenario 011, for example; the cost under probability  $p_1$  is RMB ¥ [50, 5200] less than that under probability  $p_2$ ; the cost under probability  $p_2$  is RMB ¥ [1350, 3000] less than that under probability  $p_3$ ; the cost under probability  $p_3$  is RMB ¥ [11700, 17300] less than that under probability  $p_4$ . Environment violation has great influence on cost changes. Results under scenario 100 are infeasible except for that under probability  $p_4$  because of severe violation. Under scenario 101, the cost under probability  $p_1$  is [0, 750] less than that under probability  $p_2$ ; the cost under probability  $p_2$  is RMB ¥ [1150, 4250] less than that under probability  $p_3$ ; the cost under probability  $p_3$  is RMB ¥ [10500, 17250] less than that under probability  $p_4$ . Under scenario 110, the cost under probability  $p_1$  is RMB ¥ [2550, 3400] less than that under probability  $p_2$ ; the cost under probability  $p_2$  is RMB ¥ [750, 1350] less than that under probability  $p_3$ ; the cost under probability  $p_3$  is RMB ¥ [10800, 11250] less than that under probability  $p_4$ . Under scenario 111, the cost under probability  $p_1$  is RMB ¥ [1650, 4600] less than that under probability  $p_2$ ; the cost under probability  $p_2$  is RMB ¥ [0, 2200] less than that under probability  $p_3$ ; the cost under probability  $p_3$  is RMB ¥ [11700, 14750] less than that under probability  $p_4$ . Generally

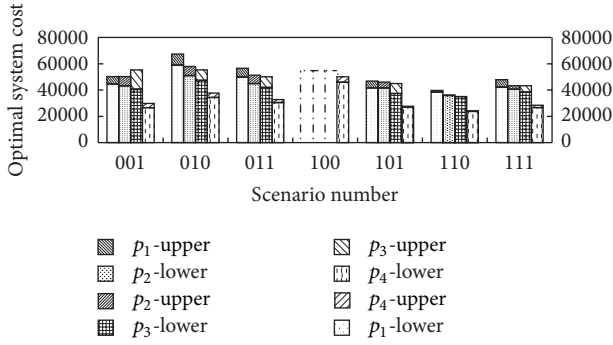


FIGURE 5: Optimal costs under high contaminant ingress/generation level.

speaking, when contamination ingress/generation rate is high, the hydraulic system is more vulnerable to any violation from environment.

The  $p_i$  levels represent a set of probabilities at which the constraints will be violated (i.e., the admissible risk of violating the constraints). Thus, the relation between  $F^\pm$  and  $p_i$  would demonstrate a tradeoff between system cost and constraint-violation risk. An increased  $p_i$  means a raised risk of constraint violation and, at the same time, it will lead to a decreased strictness for the constraints and thus a decreased system cost. Such a decreased cost, however, would be linked to a potentially increased threat of component failure and thus a raised risk of constraint violation. Figures 3, 4, 5, 6, 7, 8, 9, 10, and 11 indicate that, as the actual values of the decision variables vary within their two bounds, the expected system cost will change correspondingly between  $F_{\text{cost-opt}}^-$  and  $F_{\text{cost-opt}}^+$  with different reliability levels. Decisions at a lower  $p_i$  level would lead to an increased reliability in fulfilling the system requirements but with a higher cost; in comparison, decisions at a higher  $p_i$  level would result in a lower cost, but the risk of violating the constraints would be increased. These demonstrate a tradeoff between the filter maintenance cost and the system-failure risk due to the dual uncertainties that exist in various system components (i.e., interval and probabilistic information). In practice, planning with a higher system cost may guarantee that hydraulic system requirements and economic budget are met with higher system reliability; however, when the plan aims towards a lower system cost, these requirements may not be adequately met because of higher system risk.

**3.5. Discussion.** Solutions of the inexact chance-constrained integer linear programming (ICIP) model (Tables 6(a), 7(a), and 8(a)) provide two extremes of the expected system cost. In practice, decisions for a lower cost may correspond to advantageous system conditions (e.g., lower contaminated ingress/generation rate), while those with a higher cost correspond to more demanding conditions. In comparison with the interval-fuzzy chance-constrained integer programming (IFCIP) method, the ICIP does not integrate the fuzzy programming within a general framework. Accordingly, the

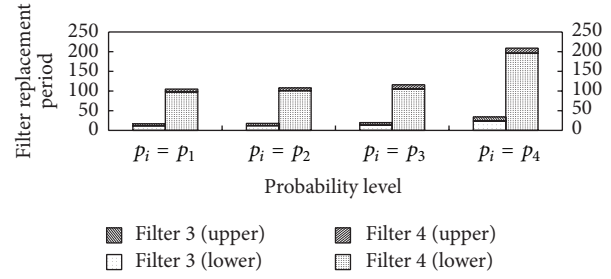


FIGURE 6: Filter replacement periods for Scenario 1 under high contaminant ingress/generation level.

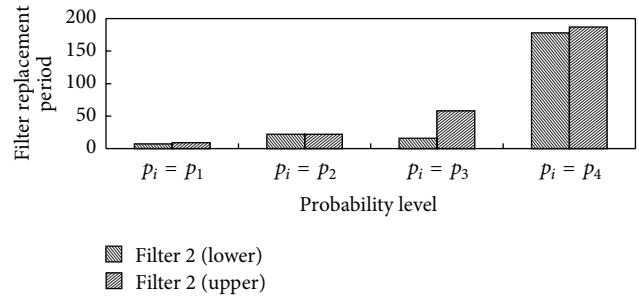


FIGURE 7: Filter replacement periods for Scenario 2 under high contaminant ingress/generation level.

analytical approaches have many differences between the two methods.

The interval-parameter two-stage stochastic nonlinear programming (ITSNP) is a hybrid methodology of inexact optimization and two-stage stochastic programming. Thus, the method has some advantages over other approaches, such as the following. (a) It can deal with uncertainties that exist in FPS through generating scenarios of its future events; these scenarios correspond to different effects of varying filter-allocations on the economic objective. (b) It can reflect the dynamics of system uncertainties and decision processes under different scenarios. In comparison with the ICIP, the ITSNP has the following limitations: (i) it can only generate one interval solution without information about the risk of violating the capacity constraints; (ii) the system cost obtained through the ITSNP model is generally higher than those through the ICIP method (under a range of  $p_i$  levels) since no relaxation on capacity constraints is allowed in the ITSNP [39]. Generally, without the chance constraints, the ITSNP is unable to support in-depth analysis of the tradeoff between system cost and system-failure risk. It may potentially result in system failure and thus increased system costs. The problem can be solved through a chance-constrained linear programming method by letting all left-hand-side interval coefficients (including the cost coefficients) in the ICIP model be equal to their midvalues. The system costs from the solutions of chance-constrained linear programming (CLP) lie within the ICIP solution intervals, demonstrating the stability of the ICIP solutions. With the CLP, only one deterministic solution corresponding to each  $p_i$  level is generated, since the model's left-hand-side

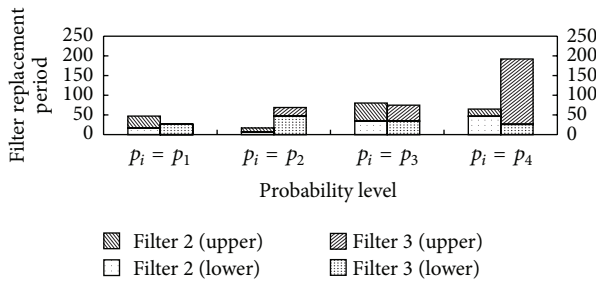


FIGURE 8: Filter replacement periods for Scenario 3 under high contaminant ingress/generation level.

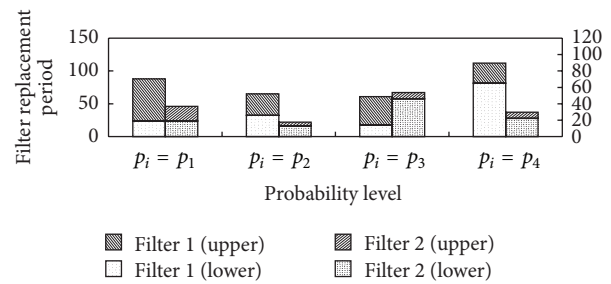


FIGURE 10: Filter replacement periods for Scenario 6 under high contaminant ingress/generation level.

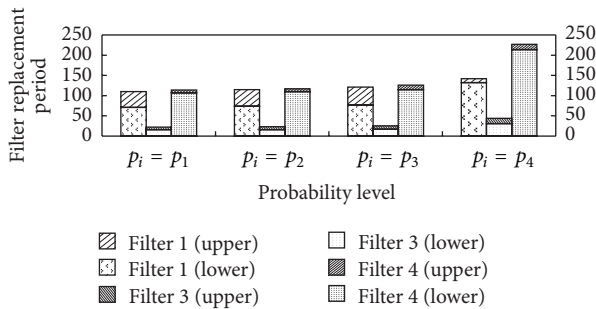


FIGURE 9: Filter replacement periods for Scenario 5 under high contaminant ingress/generation level.

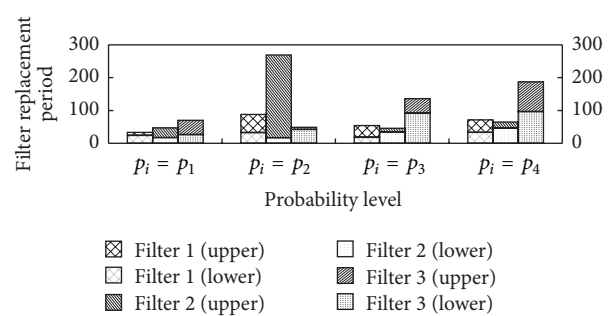


FIGURE 11: Filter replacement periods for Scenario 7 under high contaminant ingress/generation level.

coefficients are all assumed to be deterministic. However, the sensitivity analysis can only provide an individual response to variations of the uncertain inputs and, thus, can hardly reflect interactions among various uncertain parameters. Therefore, in comparison with the CLP, the ICIP method can incorporate more uncertain information within its modeling framework. The obtained interval solutions under different risk levels of violating the capacity constraints can be used to generate decision alternatives and help hydraulic system managers to identify desired policies under various condition, economic, and system-reliability constraints.

#### 4. Conclusions

An inexact chance-constrained integer programming (ICIP) method has been developed for contaminant control for hydraulic system. The method improves upon the existing interval-integer and chance-constrained programming approaches by allowing uncertainties presented as both probability distributions and discrete intervals to be effectively incorporated within the optimization framework. Moreover, it can help examine the reliability of satisfying (or risk of violating) system constraints under uncertainty.

The developed method has been applied to a case of hydraulic system operation. Violations for capacity constraints are allowed under a range of significance levels. Interval solutions associated with different risk levels of constraint violation have been obtained. They were used for generating decision alternatives and thus help waste managers to identify

desired policies under various environmental, economic, and system-reliability constraints.

The ICIP can incorporate more uncertain information within its modeling framework. It can reflect economic penalties as corrective measures or recourse against any infeasibilities arising due to a particular realization of uncertainty. Thus, the method provides not only decision variable solutions presented as stable intervals but also the associated risk levels in violating the system constraints. It can therefore support an in-depth analysis of the tradeoff between system cost and system-failure risk.

Although this study is the first attempt for contamination control of hydraulic system through developing the ICIP approach, the results suggest that this integrated technique is applicable to other hydraulic contamination control problems that involve uncertainties presented in multiple formats.

#### Nomenclature

- “-”/“+”: Superscripts represent lower- and upper-bounds of the interval parameters, respectively
- $\beta_{km}$ : Filtration ratio of filter  $k$  for a given particle diameter range  $m$  ( $k = 1$  for the suction filter,  $k = 2$  for the pressure filter,  $k = 3$  for the return filter, and  $k = 4$  for the bypass filter)
- $\rho$ : Average density of contaminants ( $\text{kg}/\text{m}^3$ )
- $\lambda^\pm$ : Degree of satisfaction for the fuzzy objective and/or constraints

- $A_{kn}$ : Binary decision variable, if filter  $k$  needs to be replaced in period  $n$ , then  $A_{kn} = 1$ ; otherwise  $A_{kn} = 0$
- $B_k$ : Purchase price of filter  $k$  (RMB ¥,  $k = 1, 2, 3$ )
- $C_k$ : Characteristic parameter of filters which is obtained from the diagram of filtration efficiency (if filter with fineness code  $k$  is selected as a suction filter then  $c_1 = c_{1k}$ ; if filter with fineness code  $l$  is selected as a pressure filter then  $c_2 = c_{2l}$ ; if filter with fineness code  $u$  is selected as a suction filter then  $c_3 = c_{3u}$ )
- $C_{1k}$ : Contaminant-holding capacity of suction filter with fineness code  $k$  (g)
- $C_{2l}$ : Contaminant-holding capacity of pressure filter with fineness code  $l$  (g)
- $C_{3u}$ : Contaminant-holding capacity of return filter with fineness code  $u$  (g)
- $C_4$ : Contaminant-holding capacity of bypass filter (g)
- $C_k^{(q_i)}$ : Cumulative function of the contaminant-holding capacity of filter  $k$  (g) with the probability  $q_i$  of violating constraint  $i$  and  $k = 1, 2, 3, 4$
- $C_k$ : Contaminant-holding capacity of filter  $k$  (g,  $k = 1, 2, 3, 4$ )
- $D_m$ : Average diameter of particle diameter range  $m$  ( $\mu\text{m}$ )
- $ER_k$ : Expenditure for replacement of filter element  $k$  (RMB ¥)
- $F_{\text{cost}}$ : Total cost of the filtration system (RMB ¥)
- $F_{\text{cost-opt}}$ : Optimal objective function values of the total cost of the filtration system (RMB ¥)
- $F_k$ : Binary variable, if filter  $k$  exists then  $F_k = 1$ ; otherwise  $F_k = 0$ ;  $k = 1, 2, 3, 4$
- $LM_k$ : Economic loss due to downtime caused by maintenance of filter element  $k$  (RMB ¥)
- $m$ : Sequential number of a given particle diameter range,  $m = 1, 2, \dots, M$
- $M$ : Maximum sequential number of a given particle diameter range
- $n$ : Working period number of filter,  $n = 1, 2, \dots, N$
- $N$ : Maximum period number during a planning horizon
- $NF_{imm}$ : Contamination level in segment  $i$  and period  $n$  for a given particle diameter range  $m$  ( $i = 0$  for the suction line,  $i = 1$  for the pump inlet,  $i = 2$  for the inlet of the complex component, and  $i = 3$  for the return line) (number of particles/mL)
- $NF_{0mm}^{\pm}$ : An initial contamination level in segment 0 and period  $n$  for a given particle diameter range  $m$
- $R_{kx_i}$ : Contaminant ingress and generation rates of contaminant particle diameter larger than  $x_i$  in segment  $k$  (number of particles/min;  $k = 1$  for the pump,  $k = 2$  for the complex component, and  $k = 3$  for the oil reservoir)
- $\text{Pr}(x)$ : Probability function
- $p_i$ : Probability  $p_i$  of violating constraint  $i$
- $Q$ : Flow rate through the main circuit (mL/min)
- $Q_b$ : Flow rate of the bypass system (mL/min)
- $R_{jnm}$ : Contaminant ingress/generation rate of component  $j$  in period  $n$  for a given particle diameter range  $m$  (number of particles/min)
- $S_{jnm}^{(q_i)}$ : Cumulative function of contaminant tolerance level of component  $j$  in period  $n$  for a given particle diameter range  $m$  ( $j = 1$  for the pump,  $j = 2$  for control components and actuators) with the probability  $q_i$  of violating constraint  $i$
- $S_{jnm}$ : Contaminant tolerance level of component  $j$  ( $j = 1, 2$ ) in period  $n$  for a given particle diameter range  $m$  (number of particles/mL)
- $T$ : Circulation time in which the fluid flows through the whole hydraulic system (min)
- $V$ : Fluid volume in the oil reservoir (mL)
- $WM_k$ : Worker wage spent on maintaining filter  $k$  (RMB ¥) and/or constraint degree of satisfaction for the fuzzy objective and/or constraint.

## Conflict of Interests

The authors declare that there is no conflict of interests regarding the publication of this paper.

## Acknowledgments

The authors would like to thank the Natural Science Foundations of China (nos. 51075007 and 51375018), National High-Tech R&D (863) Program (no. 2012AA091103), and The Importation and Development of High-Caliber Talents Project of Beijing Municipal Institutions (CIT&TCD 20130316) for funding this research. The authors would like to thank the anonymous reviewers for their insightful comments and suggestions that were very helpful for improving the paper.

## References

- [1] R. H. Frith and W. Scott, "Control of solids contamination in hydraulic systems—an overview," *Wear*, vol. 165, no. 1, pp. 69–74, 1993.
- [2] C. D. David, "Keeping hydraulic fluid clean," *Plant Engineering*, vol. 51, no. 3, pp. 86–88, 1997.
- [3] B. Poeth, "Proactive maintenance," *Fluid Power Journal*, vol. 12, no. 1, pp. 28–30, 2005.
- [4] S. L. Nie, G. H. Huang, Y. Q. Zhu, Z. Y. Li, and Y. P. Li, "SEWHAPM: development of a water hydraulic axial piston motor for underwater tool systems," *Journal of Mechanical Engineering Science*, vol. 219, no. 7, pp. 639–656, 2005.
- [5] S. L. Nie, G. H. Huang, and Y. P. Li, "Tribological study on hydrostatic slipper bearing with annular orifice damper for

- water hydraulic axial piston motor," *Tribology International*, vol. 39, no. 11, pp. 1342–1354, 2006.
- [6] S. L. Nie, G. H. Huang, Y. P. Li, Y. S. Yang, and Y. Q. Zhu, "Research on low cavitation in water hydraulic two-stage throttle poppet valve," *Journal of Process Mechanical Engineering*, vol. 220, no. 3, pp. 167–179, 2006.
- [7] C. Y. Yao and J. Y. Zhao, "Application of silting principle to on-line monitoring oil contamination in hydraulic system," *China Mechanical Engineering*, vol. 17, no. 2, pp. 112–124, 2006.
- [8] S. L. Nie, Y. P. Li, X. Y. Shi, G. H. Huang, and B. Hu, "An IPINP model for the assessment of filter allocation and replacement strategies in a hydraulic contamination control system under uncertainty," *Journal of Mechanical Engineering Science*, vol. 223, no. 4, pp. 999–1015, 2009.
- [9] S. L. Nie, Z. Hu, Y. P. Li, and G. H. Huang, "Non-linear programming for filter management in a fluid power system with uncertainty," *Journal of Power and Energy*, vol. 224, no. 2, pp. 185–201, 2010.
- [10] S. L. Nie, Y. P. Li, Z. B. Xiong, G. H. Huang, and B. Hu, "IFQP: a hybrid optimization method for filter management in fluid power systems under uncertainty," *Engineering Optimization*, vol. 42, no. 1, pp. 45–68, 2010.
- [11] S. L. Nie, Y. L. Zheng, Y. P. Li, S. Peng, and G. H. Huang, "IFCIP: an integrated optimization method for planning filters in fluid power systems under uncertainty," *Engineering Optimization*, vol. 43, no. 3, pp. 329–348, 2011.
- [12] I. M. Stancu-Minasian, "Overview of different approaches for solving stochastic programming problems with multiple objective functions," in *Stochastic Versus Fuzzy Approaches to Multiobjective Mathematical Programming under Uncertainty*, pp. 71–101, Kluwer Academic, Dordrecht, The Netherlands, 1990.
- [13] A. Charnes and W. W. Cooper, "Chance-constrained programming," *Management Science*, vol. 6, no. 1, pp. 73–79, 1959.
- [14] A. Charnes and W. W. Cooper, "Response to 'decision problems under risk and chance constrained programming: dilemmas in the transitions,'" *Management Science*, vol. 29, no. 6, pp. 750–753, 1983.
- [15] D. P. Loucks, J. R. Stedinger, and D. A. Haith, *Water Resource Systems Planning and Analysis*, Prentice-Hall, Englewood Cliffs, NJ, USA, 1981.
- [16] Y. P. Li, G. H. Huang, S. L. Nie, and X. S. Qin, "ITCLP: an inexact two-stage chance-constrained program for planning waste management systems," *Resources, Conservation and Recycling*, vol. 49, no. 3, pp. 284–307, 2007.
- [17] Y. P. Li, G. H. Huang, S. L. Nie, and L. Liu, "Inexact multistage stochastic integer programming for water resources management under uncertainty," *Journal of Environmental Management*, vol. 88, no. 1, pp. 93–107, 2008.
- [18] B. Liu, *Theory and Practice of Uncertain Programming*, Springer, Berlin, Germany, 2nd edition, 2009.
- [19] J. H. Ellis, E. A. McBean, and G. J. Farquhar, "Chance-constrained/stochastic linear programming model for acid rain abatement—I. Complete colinearity and noncolinearity," *Atmospheric Environment*, vol. 19, no. 6, pp. 925–937, 1985.
- [20] J. H. Ellis, E. A. McBean, and G. J. Farquhar, "Chance-constrained/stochastic linear programming model for acid rain abatement—II. Limited colinearity," *Atmospheric Environment*, vol. 20, no. 3, pp. 501–511, 1986.
- [21] G. H. Huang, "A hybrid inexact-stochastic water management model," *European Journal of Operational Research*, vol. 107, no. 1, pp. 137–158, 1998.
- [22] G. H. Huang, N. Sae-Lim, L. Liu, and Z. Chen, "An interval-parameter fuzzy-stochastic programming approach for municipal solid waste management and planning," *Environmental Modeling & Assessment*, vol. 6, no. 4, pp. 271–283, 2001.
- [23] L. Liu, G. H. Huang, Y. Liu, G. A. Fuller, and G. M. Zeng, "A fuzzy-stochastic robust programming model for regional air quality management under uncertainty," *Engineering Optimization*, vol. 35, no. 2, pp. 177–199, 2003.
- [24] D. R. Morgan, J. W. Eheart, and A. J. Valocchi, "Aquifer remediation design under uncertainty using a new chance constrained programming technique," *Water Resources Research*, vol. 29, no. 3, pp. 551–568, 1993.
- [25] X. Huang, "Chance-constrained programming models for capital budgeting with NPV as fuzzy parameters," *Journal of Computational and Applied Mathematics*, vol. 198, no. 1, pp. 149–159, 2007.
- [26] X. Huang, "Optimal project selection with random fuzzy parameters," *International Journal of Production Economics*, vol. 106, no. 2, pp. 513–522, 2007.
- [27] M. Roubens and J. Teghem Jr., "Comparison of methodologies for fuzzy and stochastic multi-objective programming," *Fuzzy Sets and Systems*, vol. 42, no. 1, pp. 119–132, 1991.
- [28] T. Watanabe and H. Ellis, "A joint chance-constrained programming model with row dependence," *European Journal of Operational Research*, vol. 77, no. 2, pp. 325–343, 1994.
- [29] Y. Zare and A. Daneshmand, "A linear approximation method for solving a special class of the chance constrained programming problem," *European Journal of Operational Research*, vol. 80, no. 1, pp. 213–225, 1995.
- [30] G. Infanger and D. P. Morton, "Cut sharing for multistage stochastic linear programs with interstage dependency," *Mathematical Programming B*, vol. 75, no. 2, pp. 241–251, 1996.
- [31] Y. R. Fan and G. H. Huang, "A robust two-step method for solving interval linear programming problems within an environmental management context," *Journal of Environmental Informatics*, vol. 19, no. 1, pp. 1–12, 2012.
- [32] G. H. Huang, B. W. Baetz, and G. G. Patry, "A grey fuzzy linear programming approach for municipal solid waste management planning under uncertainty," *Civil Engineering Systems*, vol. 10, no. 2, pp. 123–146, 1993.
- [33] Z. X. Xia, *Contamination Control of Hydraulic System*, China Machine Press, Beijing, China, 1992, (Chinese).
- [34] G. H. Huang, B. W. Baetz, and G. G. Patry, "Grey integer programming: an application to waste management planning under uncertainty," *European Journal of Operational Research*, vol. 83, no. 3, pp. 594–620, 1995.
- [35] D. Norvelle, "Cleaning up clutter in fluid analysis," *Machine Design*, vol. 69, no. 11, pp. 48–52, 1997.
- [36] N. C. P. Edirisinghe, E. I. Patterson, and N. Saadouli, "Capacity planning model for a multipurpose water reservoir with target-priority operation," *Annals of Operations Research*, vol. 100, no. 1–4, pp. 273–303, 2000.
- [37] Y. P. Li, G. H. Huang, S. L. Nie, and Y. F. Huang, "IFTSIP: interval fuzzy two-stage stochastic mixed-integer linear programming: a case study for environmental management and planning," *Civil*

*Engineering and Environmental Systems*, vol. 23, no. 2, pp. 73–99, 2006.

- [38] J. R. Birge and F. V. Louveaux, “A multicut algorithm for two-stage stochastic linear programs,” *European Journal of Operational Research*, vol. 34, no. 3, pp. 384–392, 1988.
- [39] S. Peng, *Research on application of two-stage stochastic, chance-constrained and fuzzy-parameter optimization in contamination control for hydraulic systems [Ph.D.dissertation]*, University of Science and Technology, Huazhong, China, 2009, (Chinese).

## Research Article

# Accurate Simulation of Contaminant Transport Using High-Order Compact Finite Difference Schemes

**Gurhan Gurarslan**

*Department of Civil Engineering, Faculty of Engineering, Pamukkale University, 20070 Pamukkale, Denizli, Turkey*

Correspondence should be addressed to Gurhan Gurarslan; gurarslan@pau.edu.tr

Received 24 January 2014; Revised 27 March 2014; Accepted 10 April 2014; Published 29 April 2014

Academic Editor: Yuefei Huang

Copyright © 2014 Gurhan Gurarslan. This is an open access article distributed under the Creative Commons Attribution License, which permits unrestricted use, distribution, and reproduction in any medium, provided the original work is properly cited.

Numerical simulation of advective-dispersive contaminant transport is carried out by using high-order compact finite difference schemes combined with second-order MacCormack and fourth-order Runge-Kutta schemes. Both of the two schemes have accuracy of sixth-order in space. A sixth-order MacCormack scheme is proposed for the first time within this study. For the aim of demonstrating efficiency and high-order accuracy of the current methods, some numerical experiments have been done. The schemes are implemented to solve two test problems with known exact solutions. It has been exhibited that the methods are capable of succeeding high accuracy and efficiency with minimal computational effort, by comparisons of the computed results with exact solutions.

## 1. Introduction

Transport of sediments and contaminants has long been one of the great concerns to hydraulic and environmental engineers. Sediment particles in alluvial rivers are subject to random and complex movement. Understanding the transport of sediment particles is of fundamental and practical importance to hydraulic engineering. Accurate simulation of suspended sediment transport is essential for water quality management, environmental impact assessment, and design of hydraulic structures. Among others, the advection-dispersion equation is crucial to the simulation of suspended sediment transport, contaminant transport in groundwater, and water quality in rivers. Therefore, improving the efficiency and accuracy of numerical schemes for the advection-dispersion equation has been a focus of research [1]. The analytical solutions of advection-dispersion equation can be obtained for limited number of initial and boundary conditions making some simplifying assumptions. But, the usage of analytical solutions in field applications is rather limited because ideal conditions could not generally be satisfied.

Remarkable research studies have been conducted in order to solve advection-dispersion equation numerically like method of characteristic with Galerkin method [2],

finite difference method [3–5], high-order finite element techniques [6], high-order finite difference methods [7–20], green element method [21], cubic B-spline [22], cubic B-spline differential quadrature method [23], method of characteristics integrated with splines [24–26], Galerkin method with cubic B-splines [27], Taylor collocation and Taylor-Galerkin methods [28], B-spline finite element method [29], least squares finite element method (FEMLSF and FEMQSF) [30], lattice Boltzmann method [31], Taylor-Galerkin B-spline finite element method [32], and meshless method [33, 34].

Widely used discretization scheme for the numerical solution of hyperbolic partial differential equations is the MacCormack (MC) scheme [35] which is an explicit and two step predictor-corrector schemes. MC scheme is equivalent to the Lax-Wendroff scheme regarding linear equations. MC scheme does not give diffusive errors in the solution while first-order upwind scheme does. This procedure provides the reasonably accurate results and needs less CPU time. Several advantages of the MC scheme make the method a popular choice in computational hydraulics problems. Firstly, the scheme is a shock-capturing technique with second-order accuracy both in time and space. Secondly, the inclusion of the source terms is relatively simple. Thirdly, implementing it in an explicit time-marching algorithm is convenient [36]. This scheme has been successfully applied to unsteady open

channel flows [37–40], overland flows [41], and contaminant transport [12, 42–44]. To be able to solve many problems accurately, using high-order numerical methods is necessary. The idea of using MC schemes with compact finite difference schemes was suggested for the first time by Hixon and Turkel [45]. In the corresponding study, two different fourth-order compact MC schemes were suggested. However in this study, a sixth-order compact MacCormack scheme (MC-CD6) which is structurally different than Hixon and Turkel schemes was proposed. MC-CD6 is applied to the contaminant transport problem in this study for the first time. Another scheme used in this study is RK4-CD6 scheme which is formed by combining a fourth-order Runge-Kutta (RK4) scheme and a sixth-order compact finite difference scheme (CD6) in space. This scheme was applied to the solution for one-dimensional contamination transport problem by Gurarlan et al. [19]. Gurarlan et al. [19] has declared that the RK4-CD6 scheme is very accurate solution approach in solving one-dimensional contaminant transport equation for low and moderate Peclet numbers, that is,  $Pe \leq 5$ . Using the related scheme for two-dimensional contaminant transport problem took place within this study for the first time. Examples of both one- and two-dimensional advection-dispersion problems will be used to investigate accuracy of the RK4-CD6 and MC-CD6 scheme. Numerical results obtained from these examples will be compared to available analytical and/or numerical results existing in the literature.

## 2. Governing Equation

Two-dimensional advection-dispersion equation in the conservative form is given as follows:

$$\frac{\partial C}{\partial t} = \frac{\partial}{\partial x} \left( D_x \frac{\partial C}{\partial x} \right) + \frac{\partial}{\partial y} \left( D_y \frac{\partial C}{\partial y} \right) - \frac{\partial}{\partial x} (UC) - \frac{\partial}{\partial y} (VC), \quad (1)$$

where  $C$  is concentration of a tracer without deposition or degradation;  $x$  and  $y$  are space coordinates;  $U$  and  $V$  are depth-averaged horizontal fluid velocity components in  $x$ - and  $y$ -direction, respectively;  $D_x$  and  $D_y$  are dispersion coefficients in  $x$ - and  $y$ -direction, respectively; and  $t$  is time. In case of applying classical finite difference schemes as a solution, fundamental difficulty is encountered with arises from the advection term which causes oscillations in solution [1]. Sixth-order compact finite-difference schemes are enhanced to overcome this existing problem. For approximating time derivative, MacCormack and Runge-Kutta schemes are used.

## 3. Compact Finite Difference Schemes

In this section, compact schemes whose solution and various order derivatives are assumed as unknowns are introduced. An implicit equation including implicit derivatives and functions helps us to solve the derivatives at grid points. Two essential properties of compact schemes can be expressed as high spectral accuracy and relatively compact stencils which correlate the derivatives with function. Compact high-order schemes are closer to spectral methods and they maintain the

freedom to retain accuracy in complex geometries, as well. Details about derivation of compact finite difference schemes can be obtained from [46, 47].

**3.1. Spatial Discretization.** Compact finite difference schemes are used to evaluate spatial derivatives. For any scalar point-wise value  $C$ , the derivatives of  $C$  are reached by solving a linear equation system. For derivation of such a formula, great amount of work has been done [46]. When two-dimensional problem is considered, one needs to approximate both partial derivatives in  $x$  and  $y$ . The approximation is automatically carried out by using an equal number of grid points in both directions. If  $y$  value is fixed, approximation of all partial derivatives with respect to  $x$  is done by using the compact scheme. If  $x$  value is fixed, approximation of all partial derivatives with respect to  $y$  is done.

The formulation of first derivative with respect to  $x$  at internal nodes can be expressed as follows [48]:

$$\sum_{i=-1}^1 a_{i+k} C'_{i+k} = \frac{1}{\Delta x} \sum_{i=-2}^2 b_{i+k} C_{i+k}, \quad (2)$$

where  $a_{i\pm 1} = 20 \pm 5\alpha$ ,  $a_i = 60$ ,  $b_{i\pm 2} = \pm 5/3 + 5\alpha/6$ ,  $b_{i\pm 1} = \pm 140/3 + 20\alpha/3$ ,  $b_i = -15\alpha$ , and  $\Delta x$  is grid size in  $x$ -direction. If  $\alpha < 0$ , the scheme is fifth-order compact upwind scheme; if  $\alpha = 0$ , it is reduced to sixth-order central compact scheme. The suggested value for  $\alpha$  is  $\alpha = -1$ , and the corresponding fifth-order compact upwind scheme is [48]

$$\begin{aligned} & \frac{5}{12} C'_{i-1} + C'_i + \frac{3}{12} C'_{i+1} \\ &= \frac{1}{\Delta x} \left( -\frac{1}{24} C_{i-2} - \frac{8}{9} C_{i-1} + \frac{1}{4} C_i + \frac{2}{3} C_{i+1} + \frac{1}{72} C_{i+2} \right). \end{aligned} \quad (3)$$

The formulation of second derivative with respect to  $x$  at internal nodes can be expressed as follows [46]:

$$\begin{aligned} & \frac{2}{11} C''_{i-1} + C''_i + \frac{2}{11} C''_{i+1} \\ &= \frac{12}{11} \frac{C_{i+1} - 2C_i + C_{i-1}}{\Delta x^2} + \frac{3}{11} \frac{C_{i+2} - 2C_i + C_{i-2}}{4\Delta x^2}. \end{aligned} \quad (4)$$

Regarding the nodes close to boundary, approximation formulae of derivatives of nonperiodic problems can be derived by evaluating one-sided schemes. One can find further details about derivations for the first- and second-order derivatives in [46]. The derived formulae at boundary points are given as follows.

The third-order formulae at boundary point 1

$$C'_1 + 2C'_2 = \frac{1}{\Delta x} \left( -\frac{5}{2} C_1 + 2C_2 + \frac{1}{2} C_3 \right), \quad (5a)$$

$$C''_1 + 11C''_2 = \frac{1}{\Delta x^2} (13C_1 - 27C_2 + 15C_3 - C_4). \quad (5b)$$

The fourth-order formulae at boundary points 2 and  $N-1$

$$\frac{1}{4}C'_{i-1} + C'_i + \frac{1}{4}C'_{i+1} = \frac{3}{2} \left( \frac{C_{i+1} - C_{i-1}}{2\Delta x} \right), \quad (6a)$$

$$\frac{1}{10}C''_{i-1} + C''_i + \frac{1}{10}C''_{i+1} = \frac{6}{5} \left( \frac{C_{i+1} - 2C_i + C_{i-1}}{\Delta x^2} \right). \quad (6b)$$

The third-order formulae at boundary point  $N$ ,

$$2C'_{N-1} + C'_N = \frac{1}{\Delta x} \left( \frac{5}{2}C_N - 2C_{N-1} - \frac{1}{2}C_{N-2} \right), \quad (7a)$$

$$11C''_N + C''_{N-1} = \frac{1}{\Delta x^2} (13C_N - 27C_{N-1} + 15C_{N-2} - C_{N-3}). \quad (7b)$$

Using formulae given above will result in following matrix equation:

$$\mathbf{AC}' = \mathbf{BC}, \quad (8a)$$

$$\mathbf{DC}'' = \mathbf{EC}, \quad (8b)$$

where  $\mathbf{C} = (c_1, \dots, c_N)^T$ , for all fixed  $y$ . Here,  $N$  resembles the number of grid points in each direction. Similarly, the formulae for  $y$ -direction at boundary and internal points can be derived readily with all fixed  $x$ .

**3.2. Temporal Discretization.** In order to solve advection-dispersion equation, MC and RK4 schemes are used. Utility of the compact finite difference method to (1) gives rise to the following differential equation in time:

$$\frac{d\mathbf{C}}{dt} = L(\mathbf{C}), \quad (9)$$

where  $L$  indicates a spatial differential operator. Compact finite difference formulae are used to approximate the spatial derivatives. Using the compact finite difference formulae enables us to obtain each spatial derivative on the right hand side of (9) and semidiscrete Equation (9) has been solved by the help of MC and RK4 schemes. Solution domain is discretized as to be equally spaced grids for numerical solutions of the problem with the taken boundary and initial conditions using the current scheme.

**3.2.1. MacCormack Scheme.** MC scheme is a second-order accurate explicit scheme in both time and space, and composed of predictor and corrector steps. For approximating first-order spatial derivatives, first-order backward finite difference formula is used in the predictor step and first-order forward finite difference formula is being used in the corrector step. For approximating second-order spatial derivatives, second-order central finite difference formula is being used in both steps. The semidiscrete Equation (9)

is solved by using MC scheme through the operations as follows:

$$\mathbf{C}^{(p)} = \mathbf{C}^n + \Delta t L(\mathbf{C}^n), \quad (10a)$$

$$\mathbf{C}^{n+1} = \mathbf{C}^n + 0.5\Delta t (L(\mathbf{C}^n) + L(\mathbf{C}^{(p)})). \quad (10b)$$

In this study, for approximating first-order spatial derivatives, fifth-order backward compact finite difference formula is used in predictor step and fifth-order forward compact finite difference formula is used in the corrector step. For resolving second-order spatial derivatives, sixth-order central compact difference equations are used in both steps. An accurate finite difference scheme (MC-CD6) which is sixth-order in space and second-order in time is obtained.

**3.2.2. Runge-Kutta Scheme.** Another time-integration scheme which was used in this study is RK4 scheme. In this scheme, a sixth-order central compact finite difference formula is used for approximating first-, and second-order spatial derivatives. Steps of RK4 scheme are given below:

$$\mathbf{C}^{(1)} = \mathbf{C}^n + \frac{1}{2}\Delta t L(\mathbf{C}^n), \quad (11a)$$

$$\mathbf{C}^{(2)} = \mathbf{C}^n + \frac{1}{2}\Delta t L(\mathbf{C}^{(1)}), \quad (11b)$$

$$\mathbf{C}^{(3)} = \mathbf{C}^n + \Delta t L(\mathbf{C}^{(2)}), \quad (11c)$$

$$\begin{aligned} \mathbf{C}^{n+1} = & \mathbf{C}^n + \frac{1}{6}\Delta t \\ & \times [L(\mathbf{C}^n) + 2L(\mathbf{C}^{(1)}) + 2L(\mathbf{C}^{(2)}) + L(\mathbf{C}^{(3)})]. \end{aligned} \quad (11d)$$

## 4. Numerical Applications

To be able to demonstrate behavior and capability of the present schemes, computational experiments were performed in this section. Checking accuracy of the methods was achieved by applying current methods for different grid size and time step values. Some codes produced in MATLAB 7.0 enabled us to carry out all computations.

*Example 1.* For solving the advection-dispersion equation, a straight prismatic channel in which the water flows at constant velocity  $U$  was used. Channel length was taken as  $L = 100$  m and the channel is divided into intervals of constant length  $\Delta x = 1$  m. It is assumed in this example that flow velocity and dispersion coefficients are to be  $U = 0.01$  m/s and  $D = 0.002$  m<sup>2</sup>/s. These circumstances lead to the propagation of a steep front, that is, simultaneously subjected to the dispersion. Analytical solution of the advection-dispersion equation is given below [49]:

$$C(x, t) = \frac{1}{2} \operatorname{erfc} \left( \frac{x - Ut}{\sqrt{4Dt}} \right) + \frac{1}{2} \exp \left( \frac{Ux}{D} \right) \operatorname{erfc} \left( \frac{x + Ut}{\sqrt{4Dt}} \right). \quad (12)$$

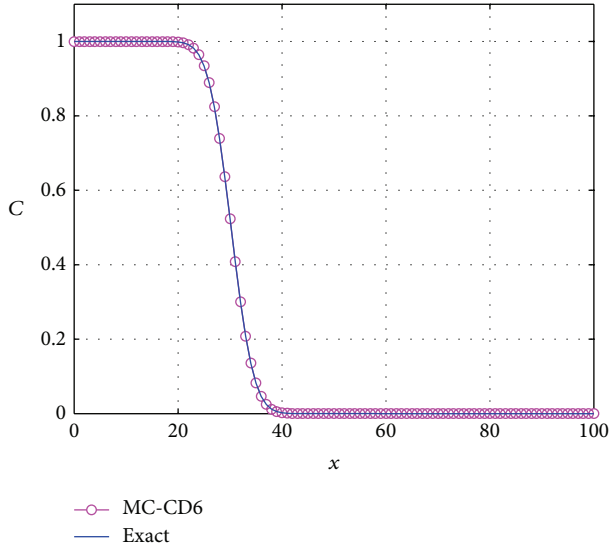


FIGURE 1: Comparison of the exact solution and the numerical solution obtained with MC-CD6 scheme for  $t = 3000$  s.

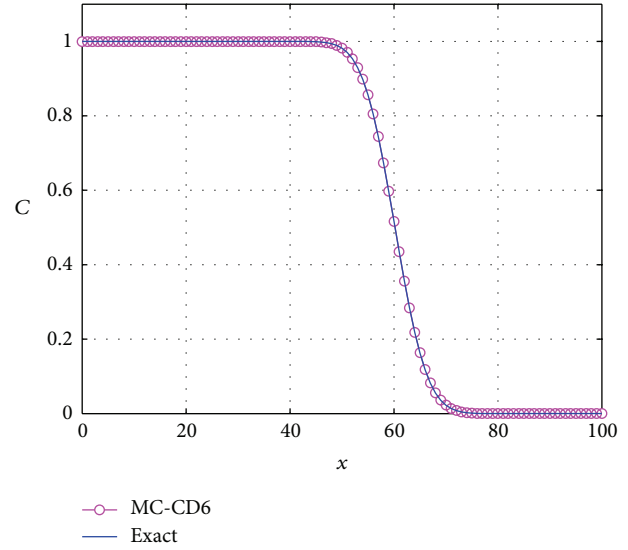


FIGURE 2: Comparison of the exact solution and the numerical solution obtained with MC-CD6 scheme for  $t = 6000$  s.

At the boundaries, the following conditions are used:

$$C(0, t) = 1, \quad (13a)$$

$$\frac{\partial C}{\partial x}(L, t) = 0. \quad (13b)$$

Initial conditions can be taken from exact solution. Table 1 exhibits the comparison between numerical solutions and exact solution. Table 1 apparently shows that solutions obtained for  $t = 3000$  s with FEMLSF [30] and FEMQSF [30] do not sufficiently converge, for  $\Delta t = 60$  s. It is proven by this status that selected time step of these methods is larger than what it needs to be. Because of the fact that solution for  $\Delta t = 60$  s is not accurate enough, calculations have been done for situations of  $\Delta t = 10$  s and  $\Delta t = 1$  s, and corresponding results were compared with FEMLSF, FEMQSF, and RK4-CD6 [19]. As the results of the schemes for  $\Delta t = 10$  s are considered on acceptable level, the results obtained by MC-CD6 and RK4-CD6 schemes for  $\Delta t = 1$  s are same with exact solution. Errors of these two schemes ( $L_2$  norm error and  $L_\infty$  norm error) are quite close to each other. As seen again in Table 1, the CPU time required for MC-CD6 scheme is less with respect to RK4-CD6 scheme. Thus, both RK4-CD6 and MC-CD6 schemes can be safely used in solving one-dimensional contaminant transport problems.

Figures 1 and 2 show comparison of exact solution and the numerical solution obtained by using MC-CD6 scheme for  $t = 3000$  s and  $t = 6000$  s ( $\Delta x = 1$  m,  $\Delta t = 1$  s). Figures 1 and 2 prove that there arises an excellent agreement between MC-CD6 and exact solutions.

*Example 2.* Let (1) for,  $U = V = 0.8$  and domain  $0 < x, y < 2$  evaluated with initial condition presented below,

$$C(x, y, 0) = \exp\left(-\frac{(x-0.5)^2}{D_x} - \frac{(y-0.5)^2}{D_y}\right). \quad (14)$$

The exact solution is given by [16] and the appropriate boundary conditions can easily be obtained from the exact solution. Consider

$$C(x, y, t) = \frac{1}{1+4t} \exp\left(-\frac{(x-Ut-0.5)^2}{D_x(1+4t)} - \frac{(y-Vt-0.5)^2}{D_y(1+4t)}\right). \quad (15)$$

Initial condition which is a Gaussian pulse and having a pulse height of 1 is centered at (0.5, 0.5). Figures 3 and 4 exhibit initial pulse and the pulse at  $t = 1.25$  obtained through the RK4-CD6 scheme. After a time period of 1.25 sec, Gaussian pulse moves to a position centered at (1.5, 1.5) with a pulse height of 1/6. Parameters are taken as  $\Delta x = \Delta y = h = 0.025$ ,  $D_x = D_y = 0.01$ , and  $t = 1.25$  in Table 2.  $\Delta t$  value is taken as 0.00625 in order to obtain average absolute and  $L_\infty$  errors. Table 2 apparently exhibits that the errors obtained by using the RK4-CD6 are far smaller when it is compared to the literature. CPU time values required for RK4-CD6 and MC-CD6 schemes are found as 13.98 sec and 6.90 sec, respectively. Although MC-CD6 scheme requires less CPU time than RK4-CD6 scheme, it is apparently seen in Table 2 that MC-CD6 does not produce more accurate results than RK4-CD6. When  $\Delta t = 0.000625$  is chosen, the value of average |error| is obtained as  $2.60e - 07$  and  $L_\infty$  error is obtained as  $7.91e - 05$  with MC-CD6. But in this case, CPU time required for MC-CD6 scheme is calculated as 65.40 sec.

TABLE 1: Comparison between numerical solutions and the exact solution.

$x$	FEMLSF [30]	FEMQSF [30]	Exact [19]	RK4-CD6 [19]		MC-CD6	
				$\Delta t = 10$ s	$\Delta t = 1$ s	$\Delta t = 10$ s	$\Delta t = 1$ s
0	1.000	1.000	1.000	1.000	1.000	1.000	1.000
18	1.000	1.000	1.000	1.000	1.000	1.000	1.000
19	1.000	1.000	0.999	0.999	0.999	0.999	0.999
20	0.999	1.000	0.998	0.998	0.998	0.998	0.998
21	0.997	0.999	0.996	0.996	0.996	0.996	0.996
22	0.993	0.996	0.991	0.992	0.991	0.991	0.991
23	0.985	0.989	0.982	0.982	0.982	0.982	0.982
24	0.970	0.974	0.964	0.965	0.964	0.965	0.964
25	0.943	0.946	0.934	0.936	0.935	0.936	0.935
26	0.902	0.900	0.889	0.891	0.889	0.891	0.889
27	0.842	0.832	0.823	0.827	0.824	0.827	0.824
28	0.763	0.743	0.738	0.743	0.739	0.743	0.739
29	0.666	0.638	0.636	0.641	0.637	0.642	0.637
30	0.556	0.524	0.523	0.528	0.523	0.529	0.523
31	0.442	0.411	0.408	0.413	0.408	0.414	0.408
32	0.332	0.306	0.301	0.306	0.301	0.306	0.301
33	0.235	0.218	0.208	0.212	0.208	0.213	0.208
34	0.156	0.147	0.135	0.138	0.135	0.138	0.135
35	0.096	0.095	0.082	0.084	0.082	0.084	0.082
36	0.055	0.058	0.046	0.048	0.047	0.048	0.047
37	0.030	0.034	0.024	0.025	0.025	0.025	0.025
38	0.015	0.019	0.012	0.012	0.012	0.012	0.012
39	0.007	0.010	0.005	0.006	0.005	0.006	0.005
40	0.003	0.005	0.002	0.002	0.002	0.002	0.002
41	0.001	0.003	0.001	0.001	0.001	0.001	0.001
42	0.000	0.001	0.000	0.000	0.000	0.000	0.000
CPU time (s)				0.13	0.86	0.12	0.76
$L_2$ norm error				0.0142	0.0017	0.0148	0.0017
$L_\infty$ norm error				0.0055	0.0008	0.0060	0.0008

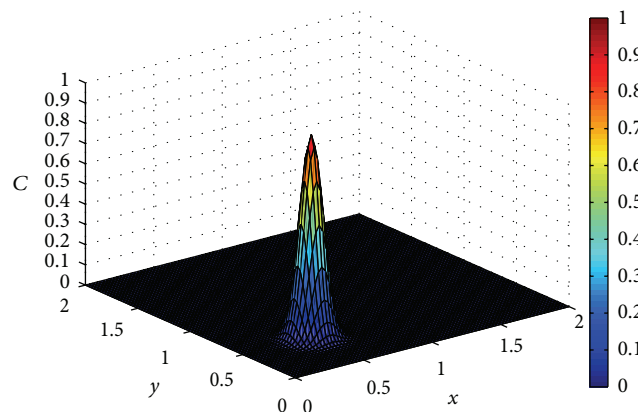


FIGURE 3: Initial Gaussian pulse of Example 2.

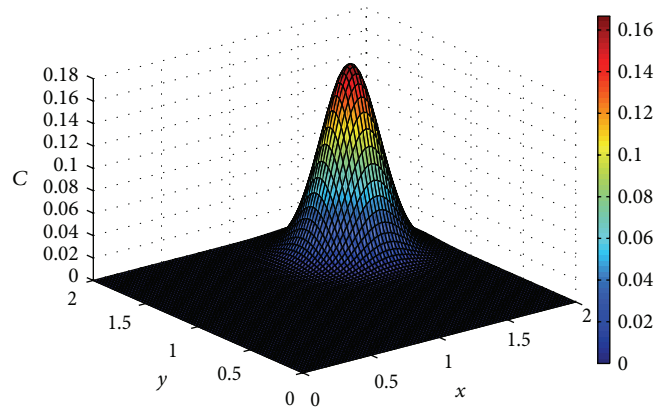


FIGURE 4: The RK4-CD6 solution of Example 2 with  $\Delta t = 0.0125$ ,  $h = 0.025$ ,  $D_x = D_y = 0.01$ , and  $t = 1.25$  for  $0 < x, y < 2$ .

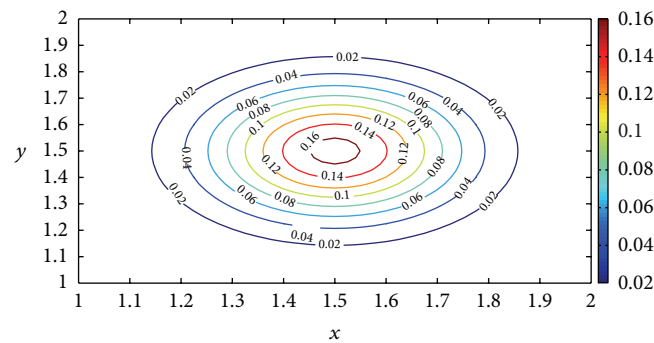


FIGURE 5: Contour lines of the RK4-CD6 solution and absolute errors in the domain  $1 < x, y < 2$  with  $\Delta t = 0.0125$ ,  $h = 0.025$ ,  $D_x = D_y = 0.01$ , and  $t = 1.25$ .

TABLE 2: Comparison of average absolute and maximum absolute errors with the literature.

Method	Average [Error]	$L_\infty$ errors
Kalita et al. [16]	$1.60E - 05$	$4.45E - 04$
Karaa and Zhang [17]	$9.22E - 06$	$2.50E - 04$
Tian and Ge [18]	$9.66E - 06$	$2.66E - 04$
PR-ADI [20]	$3.11E - 04$	$7.78E - 03$
Noye and Tan [20]	$1.97E - 05$	$6.51E - 04$
MC-CD6	$2.60E - 05$	$7.92E - 03$
RK4-CD6	$2.24E - 08$	$1.65E - 05$

TABLE 3: Pulse height values of Example 2 for various values of  $\Delta t$  with  $h = 0.025$ ,  $D_x = D_y = 0.01$ , and  $t = 1.25$ .

Method	$\Delta t$	Pulse height
(9,5) scheme [16]	0.00625	0.202492
	0.00025	0.167553
	0.00010	0.166852
(5,9) scheme [16]	0.00625	0.144447
	0.00010	0.165983
	0.00005	0.166210
(9,9) scheme [16]	0.0125	0.166863
	0.00625	0.166540
	0.00010	0.166656
MC-CD6	0.0125	0.165131
	0.00625	0.166293
RK4-CD6	0.00010	0.166667
	0.0125	0.166669
Analytical	0.00625	0.166667
	0.00010	0.166667

Therefore, using RK4-CD6 scheme is suggested for solution of two-dimensional contaminant transport problems.

Table 3 presents the pulse height values obtained for the parameters  $\Delta x = \Delta y = h = 0.025$ ,  $D_x = D_y = 0.01$ , and  $t = 1.25$  by using various time steps. Kalita et al. [16] have used three different compact schemes in their studies. Obtained results are compared with results of (9,5), (5,9), and (9,5) schemes of Kalita et al. [16]. Table 3 proves that pulse height values of the RK4-CD6 scheme is more accurate than the results of the (5,9), (9,5), and (9,9) schemes, despite the fact that the results of MC-CD6 scheme are accurate at acceptable level. Figure 5 shows contour lines of the RK4-CD6 solutions

in the domain  $1 < x, y < 2$  with the parameters  $\Delta t = 0.0125$ ,  $h = 0.025$ ,  $D_x = D_y = 0.01$ , and  $t = 1.25$ .

## 5. Conclusions

Throughout this study, high-order compact finite difference schemes composed of second-order MacCormack and fourth-order Runge-Kutta time integration schemes have been used to be able to perform numerical simulation of one- and two-dimensional advective-dispersive contaminant transport. For demonstrating efficiency and high-order accuracy of the current methods, numerical experiments have been done. Then, the schemes are implemented for solving two test problems which have known exact solutions. It has been shown that the used methods are capable of succeeding high accuracy and efficiency with minimal computational effort, supported by comparisons of the computed results with exact solutions.

In solution for one-dimensional contaminant transport problem, it was seen that the error values obtained with RK4-CD6 and MC-CD6 schemes and the required CPU time values are close to each other. Whereas in solution for two-dimensional contaminant transport problem, it was observed that RK4-CD6 scheme is stable for great  $\Delta t$  values and produces better results than MC-CD6 scheme. When  $\Delta t$  value is decreased, it was determined that MC-CD6 scheme gives fine results but required CPU time value considerably increases. RK4-CD6 scheme has produced better results than the studies given in literature in solution for both one- and two-dimensional contaminant transport problem. The proposed schemes produce convergent approximations for the contaminant transport problems having low and moderate Pe number. Obtaining the solutions for contaminant transport problem in higher Peclet numbers by using compact upwind schemes was left to further studies.

## Conflict of Interests

The author declares that there is no conflict of interests regarding the publication of this paper.

## References

- [1] C. Man and C. W. Tsai, "A higher-order predictor-corrector scheme for two-dimensional advection-diffusion equation," *International Journal for Numerical Methods in Fluids*, vol. 56, no. 4, pp. 401–418, 2008.
- [2] R. Szymkiewicz, "Solution of the advection-diffusion equation using the spline function and finite elements," *Communications in Numerical Methods in Engineering*, vol. 9, no. 3, pp. 197–206, 1993.
- [3] H. Karahan, "Implicit finite difference techniques for the advection-diffusion equation using spreadsheets," *Advances in Engineering Software*, vol. 37, no. 9, pp. 601–608, 2006.
- [4] H. Karahan, "Unconditional stable explicit finite difference technique for the advection-diffusion equation using spreadsheets," *Advances in Engineering Software*, vol. 38, no. 2, pp. 80–86, 2007.
- [5] H. Karahan, "Solution of weighted finite difference techniques with the advection-diffusion equation using spreadsheets," *Computer Applications in Engineering Education*, vol. 16, no. 2, pp. 147–156, 2008.
- [6] H. S. Price, J. C. Cavendish, and R. S. Varga, "Numerical methods of higher-order accuracy for diffusion-convection equations," *Society of Petroleum Engineers*, vol. 8, no. 3, pp. 293–303, 1968.
- [7] K. W. Morton, "Stability of finite difference approximations to a diffusion-convection equation," *International Journal for Numerical Methods in Engineering*, vol. 15, no. 5, pp. 677–683, 1980.
- [8] H. Karahan, "A third-order upwind scheme for the advection-diffusion equation using spreadsheets," *Advances in Engineering Software*, vol. 38, no. 10, pp. 688–697, 2007.
- [9] Y. Chen and R. A. Falconer, "Advection-diffusion modelling using the modified QUICK scheme," *International Journal for Numerical Methods in Fluids*, vol. 15, no. 10, pp. 1171–1196, 1992.
- [10] M. Dehghan, "Weighted finite difference techniques for the one-dimensional advection-diffusion equation," *Applied Mathematics and Computation*, vol. 147, no. 2, pp. 307–319, 2004.
- [11] M. Dehghan and A. Mohebbi, "High-order compact boundary value method for the solution of unsteady convection-diffusion problems," *Mathematics and Computers in Simulation*, vol. 79, no. 3, pp. 683–699, 2008.
- [12] G. Gürarşlan and H. Karahan, "Numerical solution of advection-diffusion equation using a high-order MacCormack scheme," in *Proceedings of the 6th National Hydrology Congress*, Denizli, Turkey, September 2011.
- [13] M. Sari, G. Gürarşlan, and A. Zeytinođlu, "High-order finite difference schemes for solving the advection-diffusion equation," *Mathematical and Computational Applications*, vol. 15, no. 3, pp. 449–460, 2010.
- [14] A. Mohebbi and M. Dehghan, "High-order compact solution of the one-dimensional heat and advection-diffusion equations," *Applied Mathematical Modelling*, vol. 34, no. 10, pp. 3071–3084, 2010.
- [15] A. A. Mohamad, "Spatially fourth-order-accurate scheme for unsteady-convection problems," *Numerical Heat Transfer B: Fundamentals*, vol. 31, no. 3, pp. 373–385, 1997.
- [16] J. C. Kalita, D. C. Dalal, and A. K. Dass, "A class of higher order compact schemes for the unsteady two-dimensional convection-diffusion equation with variable convection coefficients," *International Journal for Numerical Methods in Fluids*, vol. 38, no. 12, pp. 1111–1131, 2002.
- [17] S. Karaa and J. Zhang, "High order ADI method for solving unsteady convection-diffusion problems," *Journal of Computational Physics*, vol. 198, no. 1, pp. 1–9, 2004.
- [18] Z. F. Tian and Y. B. Ge, "A fourth-order compact ADI method for solving two-dimensional unsteady convection-diffusion problems," *Journal of Computational and Applied Mathematics*, vol. 198, no. 1, pp. 268–286, 2007.
- [19] G. Gürarşlan, H. Karahan, D. Alkaya, M. Sari, and M. Yasar, "Numerical solution of advection-diffusion equation using a sixth-order compact finite difference method," *Mathematical Problems in Engineering*, vol. 2013, Article ID 672936, 7 pages, 2013.
- [20] B. J. Noye and H. H. Tan, "Finite difference methods for solving the two-dimensional advection-diffusion equation," *International Journal for Numerical Methods in Fluids*, vol. 9, no. 1, pp. 75–98, 1989.
- [21] A. E. Taigbenu and O. O. Onyejekwe, "Transient 1D transport equation simulated by a mixed green element formulation," *International Journal for Numerical Methods in Fluids*, vol. 25, no. 4, pp. 437–454, 1997.

- [22] R. C. Mittal and R. K. Jain, "Numerical solution of convection-diffusion equation using cubic B-splines collocation methods with Neumann's boundary conditions," *International Journal of Applied Mathematics and Computation*, vol. 4, no. 2, pp. 115–127, 2012.
- [23] A. Korkmaz and I. Dag, "Cubic B-spline differential quadrature methods for the advection-diffusion equation," *International Journal of Numerical Methods for Heat & Fluid Flow*, vol. 22, no. 8, pp. 1021–1036, 2012.
- [24] F. M. Holly Jr. and A. Preissmann, "Accurate calculation of transport in two dimensions," *Journal of Hydraulic Division*, vol. 103, no. 11, pp. 1259–1277, 1977.
- [25] T.-L. Tsai, J.-C. Yang, and L.-H. Huang, "Characteristics method using cubic-spline interpolation for advection-diffusion equation," *Journal of Hydraulic Engineering*, vol. 130, no. 6, pp. 580–585, 2004.
- [26] T.-L. Tsai, S.-W. Chiang, and J.-C. Yang, "Examination of characteristics method with cubic interpolation for advection-diffusion equation," *Computers & Fluids*, vol. 35, no. 10, pp. 1217–1227, 2006.
- [27] L. R. T. Gardner and I. Dag, "A numerical solution of the advection-diffusion equation using B-spline finite element," in *Proceedings of the International AMSE Conference "Systems Analysis, Control & Design"*, vol. 1, pp. 109–116, Lyon, France, July 1994.
- [28] I. Dag, A. Canivar, and A. Sahin, "Taylor-Galerkin method for advection-diffusion equation," *Kybernetes*, vol. 40, no. 5-6, pp. 762–777, 2011.
- [29] S. Dhawan, S. Kapoor, and S. Kumar, "Numerical method for advection diffusion equation using FEM and B-splines," *Journal of Computational Science*, vol. 3, no. 5, pp. 429–437, 2012.
- [30] I. Dag, D. Irk, and M. Tombul, "Least-squares finite element method for the advection-diffusion equation," *Applied Mathematics and Computation*, vol. 173, no. 1, pp. 554–565, 2006.
- [31] B. Servan-Camas and F. T.-C. Tsai, "Lattice Boltzmann method with two relaxation times for advection-diffusion equation: third order analysis and stability analysis," *Advances in Water Resources*, vol. 31, no. 8, pp. 1113–1126, 2008.
- [32] M. K. Kadalbajoo and P. Arora, "Taylor-Galerkin B-spline finite element method for the one-dimensional advection-diffusion equation," *Numerical Methods for Partial Differential Equations*, vol. 26, no. 5, pp. 1206–1223, 2010.
- [33] M. Zerroukat, K. Djidjeli, and A. Charafi, "Explicit and implicit meshless methods for linear advection-diffusion-type partial differential equations," *International Journal for Numerical Methods in Engineering*, vol. 48, no. 1, pp. 19–35, 2000.
- [34] J. Li, Y. Chen, and D. Pepper, "Radial basis function method for 1-D and 2-D groundwater contaminant transport modeling," *Computational Mechanics*, vol. 32, no. 1-2, pp. 10–15, 2003.
- [35] R. W. MacCormack, "The effect of viscosity in hypervelocity impact cratering," AIAA Paper 69-354, 1969.
- [36] M.-H. Tseng, "Kinematic wave computation using an efficient implicit method," *Journal of Hydroinformatics*, vol. 12, no. 3, pp. 329–338, 2010.
- [37] R. J. Fennema and M. H. Chaudhry, "Explicit numerical schemes for unsteady free-surface flows with shocks," *Water Resources Research*, vol. 22, no. 13, pp. 1923–1930, 1986.
- [38] R. J. Fennema and M. H. Chaudhry, "Simulation of one-dimensional dam-break flows," *Journal of Hydraulic Research*, vol. 25, no. 1, pp. 41–51, 1987.
- [39] D. C. Dammuler, S. M. Bhallamudi, and M. H. Chaudhry, "Modeling of unsteady flow in curved channel," *Journal of Hydraulic Engineering*, vol. 115, no. 11, pp. 1479–1495, 1989.
- [40] P. K. Mohapatra and M. H. Chaudhry, "Numerical solution of Boussinesq equations to simulate dam-break flows," *Journal of Hydraulic Engineering*, vol. 130, no. 2, pp. 156–159, 2004.
- [41] C. M. Kazezyilmaz-Alhan, M. A. Medina Jr., and P. Rao, "On numerical modeling of overland flow," *Applied Mathematics and Computation*, vol. 166, no. 3, pp. 724–740, 2005.
- [42] P. Rao and M. A. Medina Jr., "A multiple domain algorithm for modeling one-dimensional transient contaminant transport flows," *Applied Mathematics and Computation*, vol. 167, no. 1, pp. 1–15, 2005.
- [43] P. Rao and M. A. Medina Jr., "A multiple domain algorithm for modeling two dimensional contaminant transport flows," *Applied Mathematics and Computation*, vol. 174, no. 1, pp. 117–133, 2006.
- [44] P. Verma, K. S. H. Prasad, and C. S. P. Ojha, "MacCormack scheme based numerical solution of advection-dispersion equation," *ISH Journal of Hydraulic Engineering*, vol. 12, no. 1, pp. 27–38, 2006.
- [45] R. Hixon and E. Turkel, "Compact implicit MacCormack-type schemes with high accuracy," *Journal of Computational Physics*, vol. 158, no. 1, pp. 51–70, 2000.
- [46] S. K. Lele, "Compact finite difference schemes with spectral-like resolution," *Journal of Computational Physics*, vol. 103, no. 1, pp. 16–42, 1992.
- [47] T. K. Sengupta, *Fundamentals of Computational Fluid Dynamics*, Universities Press, Hyderabad, India, 2004.
- [48] X. Zhong, "High-order finite-difference schemes for numerical simulation of hypersonic boundary-layer transition," *Journal of Computational Physics*, vol. 144, no. 2, pp. 662–709, 1998.
- [49] R. Szymkiewicz, *Numerical Modeling in Open Channel Hydraulics*, Springer, Amsterdam, The Netherlands, 2010.

## Research Article

# Numerical Simulation of Flow and Suspended Sediment Transport in the Distributary Channel Networks

Wei Zhang,<sup>1,2</sup> Qiong Jia,<sup>2</sup> and Xiaowen Chen<sup>3</sup>

<sup>1</sup> State Key Laboratory of Hydrology-Water Resources and Hydraulic Engineering, Hohai University, Nanjing 210098, China

<sup>2</sup> College of Harbor, Coastal and Offshore Engineering, Hohai University, Nanjing 210098, China

<sup>3</sup> Guangdong Provincial Bureau of Xijiang River Basin Administration, Zhuhai 519090, China

Correspondence should be addressed to Wei Zhang; zhangweihhu@126.com

Received 24 November 2013; Accepted 17 March 2014; Published 13 April 2014

Academic Editor: Y. P. Li

Copyright © 2014 Wei Zhang et al. This is an open access article distributed under the Creative Commons Attribution License, which permits unrestricted use, distribution, and reproduction in any medium, provided the original work is properly cited.

Flow and suspended sediment transport in distributary channel networks play an important role in the evolution of deltas and estuaries, as well as the coastal environment. In this study, a 1D flow and suspended sediment transport model is presented to simulate the hydrodynamics and suspended sediment transport in the distributary channel networks. The governing equations for river flow are the Saint-Venant equations and for suspended sediment transport are the nonequilibrium transport equations. The procedure of solving the governing equations is firstly to get the matrix form of the water level and suspended sediment concentration at all connected junctions by utilizing the transformation of the governing equations of the single channel. Secondly, the water level and suspended sediment concentration at all junctions can be obtained by solving these irregular sparse matrix equations. Finally, the water level, discharge, and suspended sediment concentration at each river section can be calculated. The presented 1D flow and suspended sediment transport model has been applied to the Pearl River networks and can reproduce water levels, discharges, and suspended sediment concentration with good accuracy, indicating this that model can be used to simulate the hydrodynamics and suspended sediment concentration in the distributary channel networks.

## 1. Introduction

Distributary channels are very common in the delta area, among which many junctions connect individual channel together to form the river networks system. Channel junctions not only play a crucial role in dividing the river discharge over distributary channels but also govern the distribution of the river sediment transportation in the form of suspended sediment. Since flow and suspended sediment transport in the distributary channels are not only highly related to the evolution of deltas and estuaries but are also related to the environment issue, it is important to understand hydrodynamics and suspended sediment transport in the distributary channels system. The 1D numerical model as an important tool has been widely used to simulate flow and sediment transport over river networks because it can accurately represent complex river network geometries and complex structures like weirs, barrages, and dams [1].

In the late 1970's, Thomas and Prashum [2] formulated the Hydraulic Engineering Center (HEC-6) model in a rectilinear coordinate and described it by using finite-difference schemes. This model was introduced for sediment movement under steady flows in gravel-bed rivers. Then, Karim and Kennedy [3] and Karim [4] developed the Iowa ALLUVIAL (IALLUVIAL) model on the basis of a rectilinear coordinate system and the Saint-Venant flow equations in a quasisteady flow. The obvious difference between IALLUVIAL model and the HEC-6 model is that the HEC-6 solves the differential conservation equation of energy instead of the momentum equation. There are many unsteady flow models (e.g., Chang [5], Molinas and Yang [6], Holly and Rahuel [7], and Runkel and Broshears [8]), which have been developed and applied to river networks and other situations where the unsteady flow prevails over the steady one. Different from rectilinear coordinate, Chang [5] used a curvilinear coordinate system to solve the

governing equations of his model FLUVIAL 11. The model accounts for the presence of secondary currents in a curved channel by adjusting the magnitude of the streamwise velocity. Furthermore, Molinas and Yang [6] implemented the theory of minimum stream power to determine the optimum channel width and geometry for a given set of hydraulic and sediment conditions. But the OTIS (one-dimensional transport with inflow and storage) [8] modified the 1D advection diffusion equation with additional terms to account for lateral inflow, first-order decay, sorption of nonconservative solutes, and transient storage of these solutes. Moreover, considering unsteady flow conditions that occur over transcritical flow stream, Papanicolaou et al. [9] developed steep stream sediment transport 1D model (3STID) model which is capable of capturing hydraulic jumps and simulating supercritical flows; therefore, it is applicable to flows over step-pool sequences in mountain streams. Han [10] firstly provided a method for nonequilibrium transport of nonuniform suspended load. Van Niekerk et al. [11] simulate deposition and erosion in alluvial channels. Rahuel et al. [12] developed a model to simulate the unsteady water and sediment movement in alluvial rivers. Wu et al. [13] further refined this model to simulate the nonequilibrium transport of nonuniform total load in in the distributary channel networks. Fang et al. [14] presented a one-dimensional numerical model for unsteady flow and nonuniform sediment transport in alluvial rivers. The model calculated the unsteady flow in open channels using the Preissmann implicit method and the Thomas algorithm.

Most of the 1D models, however, are widely used to simulate the basic parameters, including the velocity, water level, bed elevation, and suspended sediment transport, in a single channel. Actually, 1D models can also be used to investigate hydrodynamics and sediment transport in distributary channel networks with complex planimetric structure and dynamics [15, 16]. Hence, model representation of network connections and river reach geometry has been heretofore defined by modelers to meet the needs of individual hydraulic and hydrologic models (Liu and Hodges) [17]. So far, river network systems used to be simulated by 1D model, described by Saint-Venant equations, and then solved together with other common 1D rivers. With this kind of models, it takes special experience and much work to divide and simplify the computation domains (Zhang et al.) [18]. What is more, compared with the traditional models, because of their low data, central processor unit (CPU) requirements, and simplicity of use, the presented 1D flow and suspended sediment model is very efficient and can be used in river engineering for long-term predictions of river morphological development. Therefore, the objective of this paper is to (1) develop a junction-control method for water level and suspended sediment concentration to simulate unsteady flow and suspended sediment transport over distributary channel networks and to (2) apply this model to the Pearl River networks to check the applicability of this model.

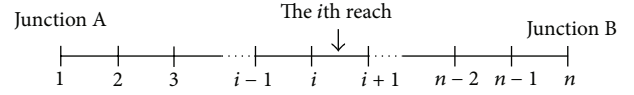


FIGURE 1: Illustration of the flow on grid and network domains.

## 2. Mathematical Model and Numerical Approach

**2.1. Governing Equations.** The hydrodynamic module of 1D model is based on the well-known Saint-Venant equations of the mass and momentum conservation. Consider

$$\begin{aligned} \frac{\partial Q}{\partial x} + B \frac{\partial Z}{\partial t} &= q, \\ \frac{\partial Q}{\partial t} + 2u \frac{\partial Q}{\partial x} + (gA - Bu^2) \frac{\partial Z}{\partial x} - u^2 \frac{\partial A}{\partial x} + g \frac{n^2 |u| Q}{R^{4/3}} &= 0. \end{aligned} \quad (1)$$

Suspended sediment model is based on the nonequilibrium transport equation. The continuity equation of suspended load can be expressed as

$$\frac{\partial (AS)}{\partial t} + \frac{\partial (QS)}{\partial x} = -\alpha B \omega (S - S_*). \quad (2)$$

The formula for sediment carrying capacity can be expressed as

$$S_* = K \left( \frac{u^3}{gR\omega} \right)^m, \quad (3)$$

where  $x$  and  $t$  are spatial and temporal axes,  $Q$  is flow discharge,  $A$  is flow area,  $q$  is the lateral flow,  $g$  is gravitational acceleration,  $R$  is the hydraulic radius, and  $Z$  is water surface elevation,  $B$  is water surface width,  $u$  is water velocity,  $n$  is Manning roughness coefficient,  $S$  is sediment concentration,  $\alpha$  is adjustment coefficient for a cross-section,  $\omega$  is fall velocity of sediment particles,  $S_*$  is averaged sediment carrying capacity, and  $K$  and  $m$  are the coefficients of sediment carrying capacity.

### 2.2. Solution for Flow Equations

**2.2.1. The Finite-Difference Equations.** The finite-difference equations are obtained by using Preissmann's four-point implicit difference scheme (Figure 1). Consider

$$\begin{aligned} C_i Z_i^{n+1} + C_i Z_{i+1}^{n+1} - Q_i^{n+1} + Q_{i+1}^{n+1} &= D_i, \\ E_i Q_i^{n+1} + G_i Q_{i+1}^{n+1} - F_i Z_i^{n+1} + F_i Z_{i+1}^{n+1} &= H_i, \end{aligned} \quad (4)$$

where  $C_i$ ,  $D_i$ ,  $E_i$ ,  $G_i$ ,  $F_i$ , and  $H_i$  are the coefficients of the difference equations as below:

$$\begin{aligned} C_i &= B_{wi+1/2}^n \frac{\Delta x_i}{2\theta\Delta t}, \\ B_{wi+1/2}^n &= 0.5 [B_{wi}^n + B_{wi+1}^n], \\ D_i &= \frac{(1-\theta)}{\theta} (Q_i^n - Q_{i+1}^n) + C_i (Z_i^n + Z_{i+1}^n) + q_i \frac{\Delta x_i}{\theta}, \\ E_i &= \frac{\Delta x_i}{2\theta\Delta t} - 2u_{i+1/2}^n + \frac{g\Delta x_i}{2\theta} \left( \frac{n^2 |u|}{R^{4/3}} \right)_i^n, \\ F_i &= (gA - Bu^2)_{i+1/2}^n = gA_{i+1/2}^n - B_{i+1/2}^n \cdot u_{i+1/2}^{2n}, \\ G_i &= \frac{\Delta x_i}{2\theta\Delta t} + 2u_{i+1/2}^n + \frac{g\Delta x_i}{2\theta} \left( \frac{n^2 |u|}{R^{4/3}} \right)_{i+1}^n, \\ H_i &= \frac{\Delta x_i}{2\theta\Delta t} (Q_i^n + Q_{i+1}^n) + \frac{2(1-\theta)}{\theta} u_{i+1/2}^n (Q_i^n - Q_{i+1}^n) \\ &\quad + \frac{(1-\theta)}{\theta} (gA - Bu^2)_{i+1/2}^n (Z_i^n - Z_{i+1}^n) \\ &\quad + \frac{\Delta x_i}{\theta} \left( u^2 \frac{\partial A}{\partial x} \right)_{i+1/2}^n, \end{aligned} \quad (5)$$

where  $\theta$  ( $0.5 \leq \theta \leq 1$ ) is the weighting coefficient and

$$\left( u^2 \frac{\partial A}{\partial x} \right)_{i+1/2}^n = (u_{i+1/2}^n)^2 \frac{A_{i+1}^n - A_i^n}{\Delta x_i}. \quad (6)$$

**2.2.2. Supplementary Equation at Junctions.** The hydraulic conditions at river networks junctions are reasonably assumed to satisfy two additional conditions: the quality conservation and energy conservation conditions. The quality conservation condition, which is also called discharge connection condition, means that the discharge changes are assumed to be equal to the shortage variation of discharge at a certain junction. Consider

$$\sum_{i=1}^m Q_i = Q_I^{n+(1/2)} - Q_O^{n+(1/2)} = \frac{(\Omega_k^{n+1} - \Omega_k^n)}{\Delta t}, \quad (7)$$

where  $k$  is the junction number,  $m$  is the number of incoming (outflow) rivers at the  $k$ th junction,  $Q_i$  is the discharge of the  $i$ th river course,  $\Omega_k$  is the storage of the  $k$ th junction,  $Q_I$  is the incoming discharge, and  $Q_O$  is the outflow discharge.

The equation of energy conservation can be approximated using the following kinematic compatibility condition [19]:

$$Z_{in,k} = Z_{out,k} = H_k, \quad (8)$$

where  $Z_{in,k}$  and  $Z_{out,k}$  represent the water level of any of the incoming and outflowing rivers at the  $i$ th junction, respectively, and  $H_k$  is the water level at the  $i$ th junction.

Finally, the finite-difference approximation of the continuity equation around the junction can be written as follows:

$$\frac{H_k^{n+1} - H_k^n}{\Delta t} A_j = Q_I^{n+(1/2)} - Q_O^{n+(1/2)}, \quad (9)$$

where  $A_j$  is the cross-section area of each junction.

The values for water level can be calculated at each junction by successively applying the double sweep Thomas algorithm.

For each river section, based on the finite-difference equation (4), the equation of each subsection can be eliminated autocorrelation; then (4), can be rewritten in the following form:

$$Q_i = \alpha_i + \beta_i Z_i + \gamma_i Z_{n+1} \quad (i = n, \dots, 2, 1), \quad (10)$$

$$Q_{i+1} = \xi_{i+1} + \zeta_{i+1} Z_{i+1} + \eta_{i+1} Z_1 \quad (i = 1, 2, \dots, n), \quad (11)$$

where the coefficients in (10) are defined as follows:

$$\begin{aligned} \alpha_n &= \frac{H_n - G_n D_n}{E_n + G_n}, & \beta_n &= \frac{G_n C_n + F_n}{E_n + G_n}, \\ \gamma_n &= \frac{G_n C_n - F_n}{E_n + G_n}, \\ \alpha_i &= \frac{Y_1 (H_i - G_i \alpha_{i+1}) - Y_2 (D_i - \alpha_{i+1})}{Y_1 E_i + Y_2}, \\ \beta_i &= \frac{Y_2 C_i + Y_1 F_i}{Y_1 E_i + Y_2}, \\ \gamma_i &= \frac{\gamma_{i+1} (Y_2 - Y_1 G_i)}{Y_1 E_i + Y_2}, \end{aligned} \quad (12)$$

$(i = n - 1, \dots, 1),$

where

$$Y_1 = C_i + \beta_{i+1}, Y_2 = G_i \beta_{i+1} + F_i. \quad (13)$$

The coefficients in (11) are defined as follows:

$$\begin{aligned} \xi_n &= \frac{E_1 D_1 + H_1}{E_1 + G_1}, & \zeta_n &= -\frac{C_1 E_1 + F_1}{E_1 + G_1}, \\ \eta_n &= -\frac{C_1 E_1 - F_1}{E_1 + G_1}, \\ \xi_{i+1} &= \frac{Y_2 (D_i + \xi_i) + Y_1 (H_i - E_i \xi_i)}{Y_2 + Y_1 G_i}, \\ \zeta_{i+1} &= -\frac{Y_2 C_i + Y_1 F_i}{Y_2 + Y_1 G_i}, \\ \eta_{i+1} &= \frac{\eta_i (Y_2 - Y_1 E_i)}{Y_2 + Y_1 G_i}, \end{aligned} \quad (14)$$

$$(i = 2, 3, \dots, n).$$

$$Y_1 = \zeta_i - G_i, \quad Y_2 = E_i \zeta_i - F_i.$$

Subsequently, the relationship between the river sections and the junction can be deduced from a single river channel by using the formula (10) and (11) as follows:

$$Q_1 = \alpha_1 + \beta_1 Z_1 + \gamma_1 Z_{n+1}, \quad (15)$$

$$Q_{n+1} = \xi_{n+1} + \zeta_{n+1} Z_{n+1} + \eta_{n+1} Z_1.$$

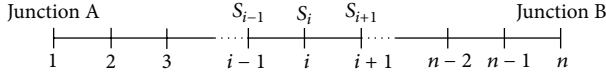


FIGURE 2: Illustration of the suspended sediment on grid and network domains.

Substituting (15) at each junction into (7), water levels at junctions of river networks can be expressed as a matrix form:

$$f_i(Z_1, Z_2, \dots, Z_i, \dots, Z_M) = 0 \quad (i = 1, 2, \dots, M), \quad (16)$$

where  $M$  is the total number of junction of the river networks.

Finally, the water level and discharge at each river section of the river networks can be calculated.

### 2.3. Solution for Suspended Sediment Transport Equations

**2.3.1. The Finite-Difference Equations.** For suspended sediment transport, the upwind finite-difference scheme and Preissmann's four-point implicit difference scheme are adopted (Figure 2). According to the flow direction, the difference equations of the governing equation (2) can be expressed as follows.

(i) For the downflow,

$$\begin{aligned} A \frac{\partial S}{\partial t} &= \bar{A}_{i-1/2} \frac{S_i^{n+1} + S_{i-1}^{n+1} - S_i^n - S_{i-1}^n}{2\Delta t}, \\ Q \frac{\partial S}{\partial x} &= \bar{Q}_{i-1/2} \frac{\theta(S_i^{n+1} - S_{i-1}^{n+1}) + (1-\theta)(S_i^n - S_{i-1}^n)}{\Delta x_{i-1}}, \\ -\alpha B \omega (S - S_*) &= -\frac{1}{2} \alpha_i^{n+1} B_i^{n+1} \omega_i^{n+1} (S_i^{n+1} - S_{*i}^{n+1}) \\ &\quad - \frac{1}{2} \alpha_{i-1}^{n+1} B_{i-1}^{n+1} \omega_{i-1}^{n+1} (S_{i-1}^{n+1} - S_{*i-1}^{n+1}), \end{aligned} \quad (17)$$

where

$$\begin{aligned} \bar{A}_{i-1/2} &= \frac{1}{2} (A_i^{n+1} + A_{i-1}^{n+1}), \\ \bar{Q}_{i-1/2} &= \frac{1}{2} (Q_i^{n+1} + Q_{i-1}^{n+1}). \end{aligned} \quad (18)$$

The irregular matrix equations are written as

$$\alpha \alpha_i S_{i-1}^{n+1} + \beta \beta_i S_i^{n+1} = DD_i, \quad (19)$$

where

$$\begin{aligned} \alpha \alpha_i &= \frac{\bar{A}_{i-1/2}}{2\Delta t} - \frac{\bar{Q}_{i-1/2} \theta}{\Delta x_{i-1}} + \frac{1}{2} \alpha_{i-1}^{n+1} B_{i-1}^{n+1} \omega_{i-1}^{n+1}, \\ \beta \beta_i &= \frac{\bar{A}_{i-1/2}}{2\Delta t} + \frac{\bar{Q}_{i-1/2} \theta}{\Delta x_{i-1}} + \frac{1}{2} \alpha_i^{n+1} B_i^{n+1} \omega_i^{n+1}, \\ DD_i &= \frac{\bar{A}_{i-(1/2)}}{2\Delta t} (S_i^n + S_{i-1}^n) - \frac{\bar{Q}_{i-1/2} (1-\theta)}{\Delta x_{i-1}} (S_i^n - S_{i-1}^n) \\ &\quad + \frac{1}{2} \alpha_i^{n+1} B_i^{n+1} \omega_i^{n+1} S_{*i}^{n+1} + \frac{1}{2} \alpha_{i-1}^{n+1} B_{i-1}^{n+1} \omega_{i-1}^{n+1} S_{*i-1}^{n+1}. \end{aligned} \quad (20)$$

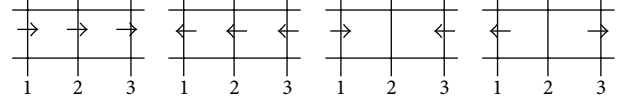


FIGURE 3: The four types of the flow at a single river channel. The types are as follows: downflow, upflow, faced-flow, and depart-flow, from the left to the right.

(ii) For the upflow,

$$\begin{aligned} A \frac{\partial S}{\partial t} &= \bar{A}_{i+1/2} \frac{S_i^{n+1} + S_{i+1}^{n+1} - S_i^n - S_{i+1}^n}{2\Delta t}, \\ Q \frac{\partial S}{\partial x} &= \bar{Q}_{i+1/2} \frac{\theta(S_{i+1}^{n+1} - S_i^{n+1}) + (1-\theta)(S_{i+1}^n - S_i^n)}{\Delta x_i}, \\ -\alpha B \omega (S - S_*) &= -\frac{1}{2} \alpha_i^{n+1} B_i^{n+1} \omega_i^{n+1} (S_i^{n+1} - S_{*i}^{n+1}) \\ &\quad - \frac{1}{2} \alpha_{i+1}^{n+1} B_{i+1}^{n+1} \omega_{i+1}^{n+1} (S_{i+1}^{n+1} - S_{*i+1}^{n+1}), \end{aligned} \quad (21)$$

where

$$\begin{aligned} \bar{A}_{i+1/2} &= \frac{1}{2} (A_i^{n+1} + A_{i+1}^{n+1}), \\ \bar{Q}_{i+1/2} &= \frac{1}{2} (Q_i^{n+1} + Q_{i+1}^{n+1}). \end{aligned} \quad (22)$$

The irregular matrix equations are written as

$$\beta \beta_i S_i^{n+1} + rr_i S_{i+1}^{n+1} = DD_i, \quad (23)$$

where

$$\begin{aligned} \beta \beta_i &= \frac{\bar{A}_{i+1/2}}{2\Delta t} - \frac{\bar{Q}_{i+1/2} \theta}{\Delta x_i} + \frac{1}{2} \alpha_i^{n+1} B_i^{n+1} \omega_i^{n+1}, \\ rr_i &= \frac{\bar{A}_{i+1/2}}{2\Delta t} + \frac{\bar{Q}_{i+1/2}}{\Delta x_i} + \frac{1}{2} \alpha_{i+1}^{n+1} B_{i+1}^{n+1} \omega_{i+1}^{n+1}, \\ DD_i &= \frac{\bar{A}_{i+1/2}}{2\Delta t} (S_i^n + S_{i+1}^n) - \frac{\bar{Q}_{i+1/2} (1-\theta)}{\Delta x_i} (S_{i+1}^n - S_i^n) \\ &\quad + \frac{1}{2} \alpha_i^{n+1} B_i^{n+1} \omega_i^{n+1} S_{*i}^{n+1} + \frac{1}{2} \alpha_{i+1}^{n+1} B_{i+1}^{n+1} \omega_{i+1}^{n+1} S_{*i+1}^{n+1}, \end{aligned} \quad (24)$$

where  $\alpha \alpha_i$ ,  $\beta \beta_i$ ,  $\gamma \gamma_i$ , and  $DD_i$  are as the known coefficients of the equations.

**2.3.2. Solution Algorithm for a Single River.** In the tidal channel, the flow direction changes with tidal level fluctuation. The flow types of a single channel can be classified as four types (Figure 3): (a) downflow,  $Q_s \geq 0$ ,  $Q_e \geq 0$ ; (b) upflow,  $Q_s < 0$ ,  $Q_e < 0$ ; (c) faced-flow,  $Q_s \geq 0$ ,  $Q_e < 0$ ; and (d) depart-flow,  $Q_s < 0$ ,  $Q_e \geq 0$ .

For the downflow, it is single direction flow. If the sediment concentration at the upboundary junction ( $S_{i+1}^{n+1}$ )

is known, the suspended sediment concentration at each junction can be obtained by the following formula:

$$S_i^{n+1} = P_i + R_i S_1^{n+1} \quad (i = 1, 2, \dots, n+1), \quad (25)$$

where  $P_i$ ,  $R_i$  are the coefficients, and they can be gotten by (19), (25), and written as

$$\begin{aligned} P_1 &= 0, & R_1 &= 1, \\ P_i \frac{DD_i - \alpha\alpha_i P_{i-1}}{\beta\beta_i}, & & R_i &= -\frac{\alpha\alpha_i R_{i-1}}{\beta\beta_i} \end{aligned} \quad (26)$$

$(i = 2, 3, \dots, n+1).$

For the upflow, it is also single direction flow. If the sediment concentration at the downboundary junction ( $S_{n+1}^{n+1}$ ) is known, the sediment concentration at each junction can be obtained by the following formula:

$$S_i^{n+1} = P_i + R_i S_{n+1}^{n+1} \quad (i = 1, 2, \dots, n+1), \quad (27)$$

where  $P_i$ ,  $R_i$  are the coefficients, and they can be gotten by (23), (27), and written as

$$\begin{aligned} P_{n+1} &= 0, & R_{n+1} &= 1, \\ P_i \frac{DD_i - \gamma\gamma_i P_{i+1}}{\beta\beta_i}, & & R_i &= -\frac{\gamma\gamma_i R_{i+1}}{\beta\beta_i} \end{aligned} \quad (28)$$

$(i = n, \dots, 2, 1).$

For the faced-flow, it is double direction flow. The single river can be divided into two single direction flow river segments. If the sediment concentrations at the up and down boundary junctions ( $S_1^{n+1}$ ,  $S_{n+1}^{n+1}$ ) are known, the suspended sediment concentration at each junction can be obtained by the formulas (25) and (27).

For the depart-flow, it is another double direction flow. First, the position of the stagnant point ( $Q_k = 0$ ) must be determined, the suspended sediment concentration at the stagnant point ( $S_1^{n+1}$ ) may be obtained by the transport equation, and then the single river can be divided into two single direction flow river segments which boundary is the stagnant point; finally, the suspended sediment concentration at each junction can be obtained by the formulas (25), (27). The position of the stagnant point is presented as the following formula:

$$\Delta x_{mk} = \frac{|Q_m|}{|Q_m| + Q_l} \Delta x_{ml}. \quad (29)$$

And the suspended sediment concentration at the stagnant point is

$$S_k^{n+1} = \frac{A_k^n}{A_k^{n+1}} S_k^n \exp\left(-\frac{\alpha_k^{n+1} B_k^{n+1} \omega_k^{n+1}}{A_k^{n+1}} \Delta t\right). \quad (30)$$

This paper also presents a junction-control method for suspended sediment in river networks.

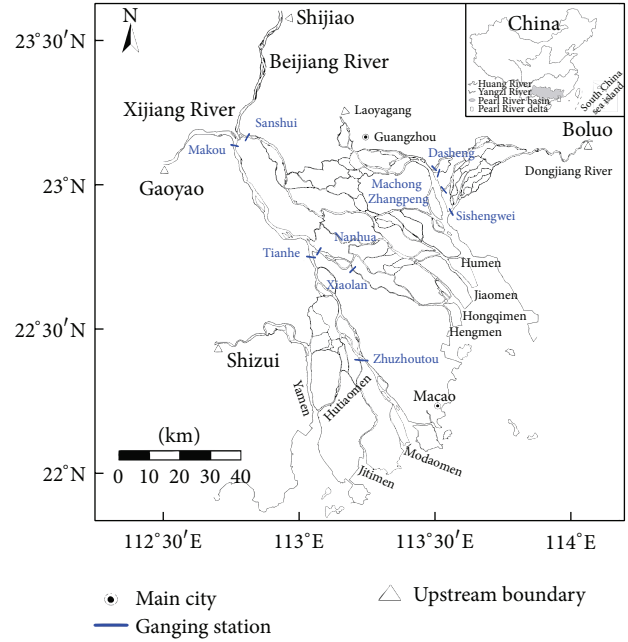


FIGURE 4: Map of the Pearl River networks and sampling stations.

Assuming that the erosion and deposition at the junction are small, the suspended sediment mass conservation equation is written as

$$\sum Q_{in} S_{in} = \sum Q_{out} S_{out} \quad (S_{out} = S_j), \quad (31)$$

where  $S_j$  is sediment concentration at junctions.

Utilizing (25) and (27), the relation formula of sediment concentration between upjunction ( $i = 1$ ) and downjunction ( $i = n+1$ ) is obtained, and the control equations for all junctions' sediment concentration can be written in matrix notation as

$$F_j (S_1, S_2, \dots, S_M) = 0 \quad j = 1, 2, \dots, M. \quad (32)$$

Solving (31), the suspended sediment concentration at all river junctions can be gotten. Finally, by solving the single river equations (25) and (27), suspended sediment concentration at all channel sections of the distributary channel networks can be calculated.

**2.4. Modeling Setup.** The river networks in the Pearl River Delta (PRD) (Figure 4) are selected to check the applicability of the 1D flow and suspended sediment model. The river network in the PRD is considered as one of the world's most complicated river networks, with the density of channel length per unit at 0.68–1.07 km/km<sup>2</sup>. The area of the Pearl River networks cover approximately 9750 km<sup>2</sup>, with a total length of over 1600 km and a coastline extending over 450 km from east to west. The Pearl River networks drain three main tributaries, Dongjiang River, Beijiang River, and Xijiang River, pass through this complex river network, and finally flow into the South China Sea through eight subestuaries that are separately called Humen, Jiaomen, Hongqimen, Hengmen, Modaomen, Jitimen, Hutiaomen, and Yamen.

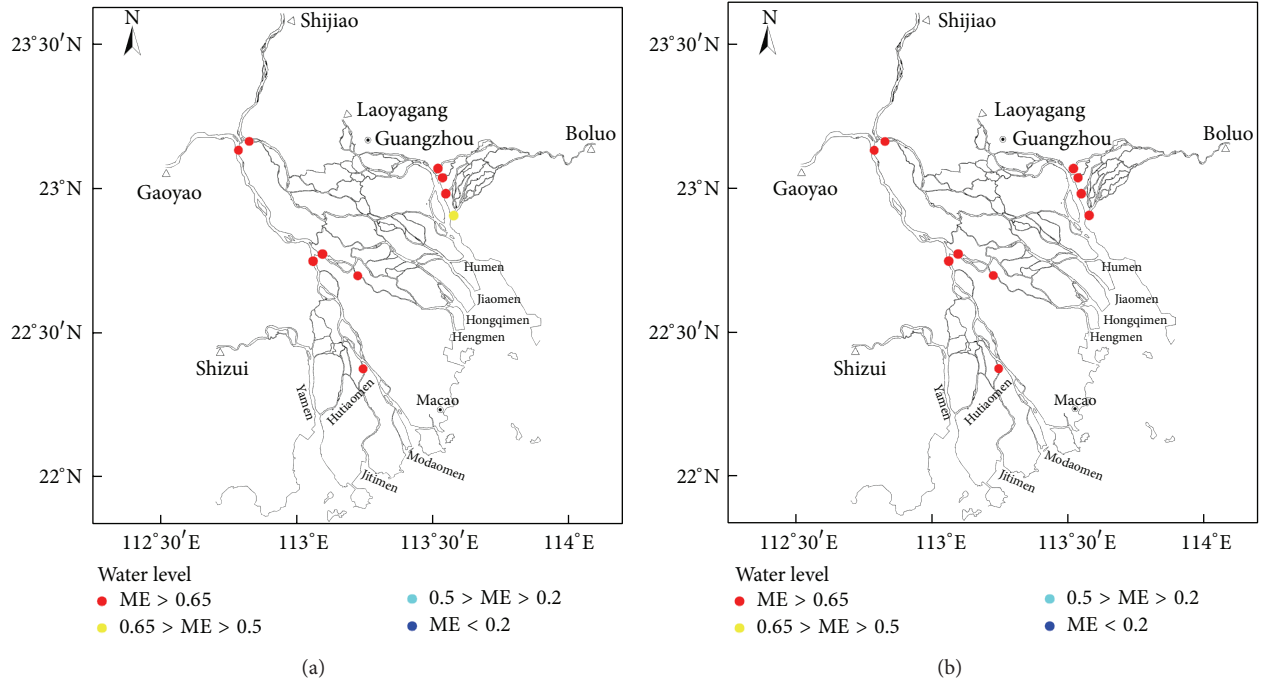


FIGURE 5: (a) The calibration of water levels from July 18 to July 19, 1998. (b) The validation of water levels from February 7 to February 16, 2001.

The Pearl River network is simplified as 328 single river channels, 13 boundary rivers, 5108 computational river sections with the interval varying from 0.2 to 3.0 km, and 216 river channel junctions. Upstream boundary conditions are given by discharge and suspended sediment concentration at the five upstream boundary junctions (Shizui, Gaoyao, Shijiao, Laoyangang, and Boluo). Tidal level fluctuation and suspended sediment concentration at the downstream outlets are used as downstream boundary conditions. The Manning coefficients in the Pearl rivers are taken to be 0.01–0.05.  $K$  and  $m$ ; the coefficients of sediment carrying capacity are taken to be 0.005 and 0.92. The value of adjustment coefficient for a cross-section  $\alpha$  is 0.25 (when deposition) or 1.0 (when erosion). Computations are performed using a time step of 1 minute.

### 3. Results and Discussion

The distributary channel networks model has been extensively calibrated with respect to the field measurements to optimize the representation of the water level, discharge, and suspended sediment concentration over the study area. The field measurement data in 1998 and 2001 are used for calibration and validation, respectively. The Nash-Sutcliffe model efficiency (ME) which is the ratio of model error to variability in observational data is employed in this paper to evaluate the performance of the distributary channel networks model. Consider

$$ME = 1 - \frac{\sum (D - M)^2}{\sum (D - \bar{D})^2}, \quad (33)$$

where  $D$  are the observational data,  $\bar{D}$  is the mean of the observational data, and  $M$  is the corresponding model estimate. In the squaring of the error, a good fit receives a high score and a poor fit receives a low score. Performance levels are categorized as follows:  $ME > 0.65$  is excellent,  $0.5-0.65$  is very good,  $0.2-0.5$  is good, and  $ME < 0.2$  is poor [20]. The calibration and verification of water level, discharge, and suspended sediment concentration are shown in Figures 5 to 7.

The calibration result shows that the majority of the ME values for water levels over the Pearl River networks is over 0.65, indicating that the numerical model of the distributary channel networks can accurately simulate water level in the river networks (Figure 5(a)). The water level is further verified by comparing the model results and measured value from February 7 to February 16, 2001 (Figure 5(b)). The comparison revealed that the simulated water level and distribution over the main branches matched excellently with the observed value and the ME value of almost all stations, which are greater than 0.65.

In terms of water discharge (Figure 6(a)), the modeled flow discharges follow the observations reasonably well, and the ME values are over 0.65 at 8 stations, showing an excellent skill. It can be noticed that there are two stations with efficiencies below 0.65, which are probably due to the let-out discharges of the reservoir nearby during the simulation period. The verification results also show a very good agreement in the discharge distribution over the Pearl River networks (Figure 6(b)). Based on the agreement in water level and discharge between the simulated and the measured throughout the distributary river networks, it is reasonable to

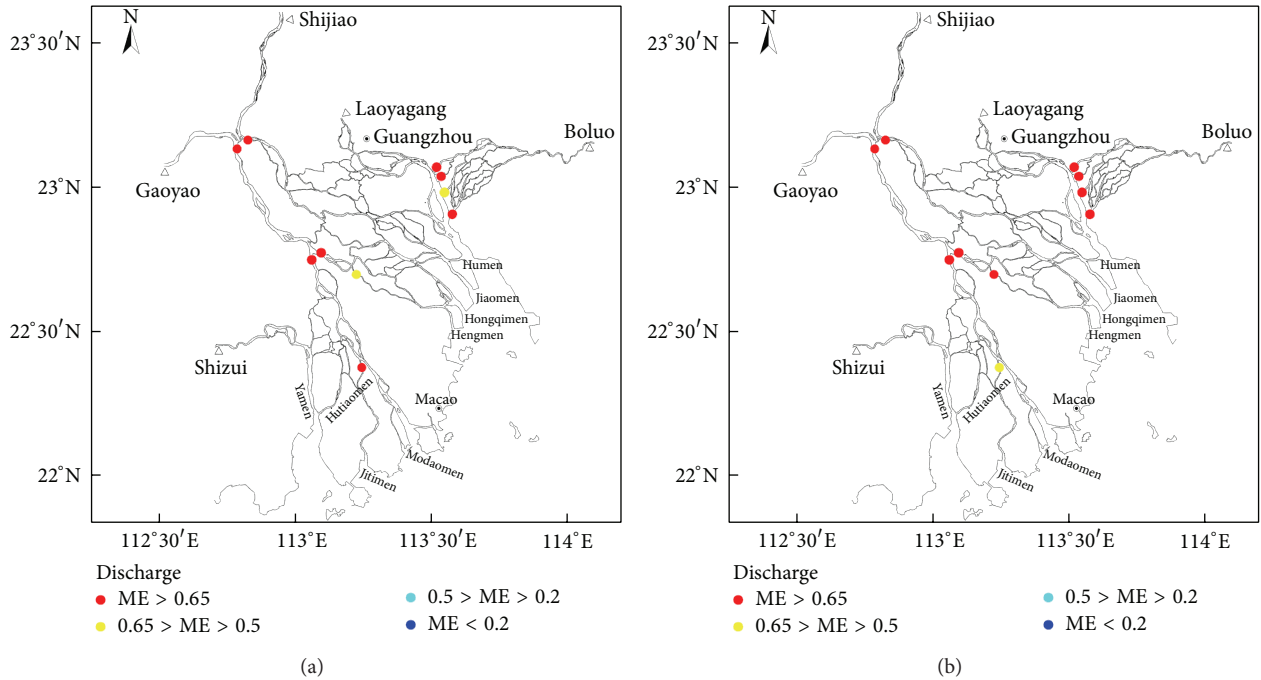


FIGURE 6: (a) The calibration of discharges from July 18 to July 19, 1998. (b) The validation of discharges from February 7 to February 16, 2001.

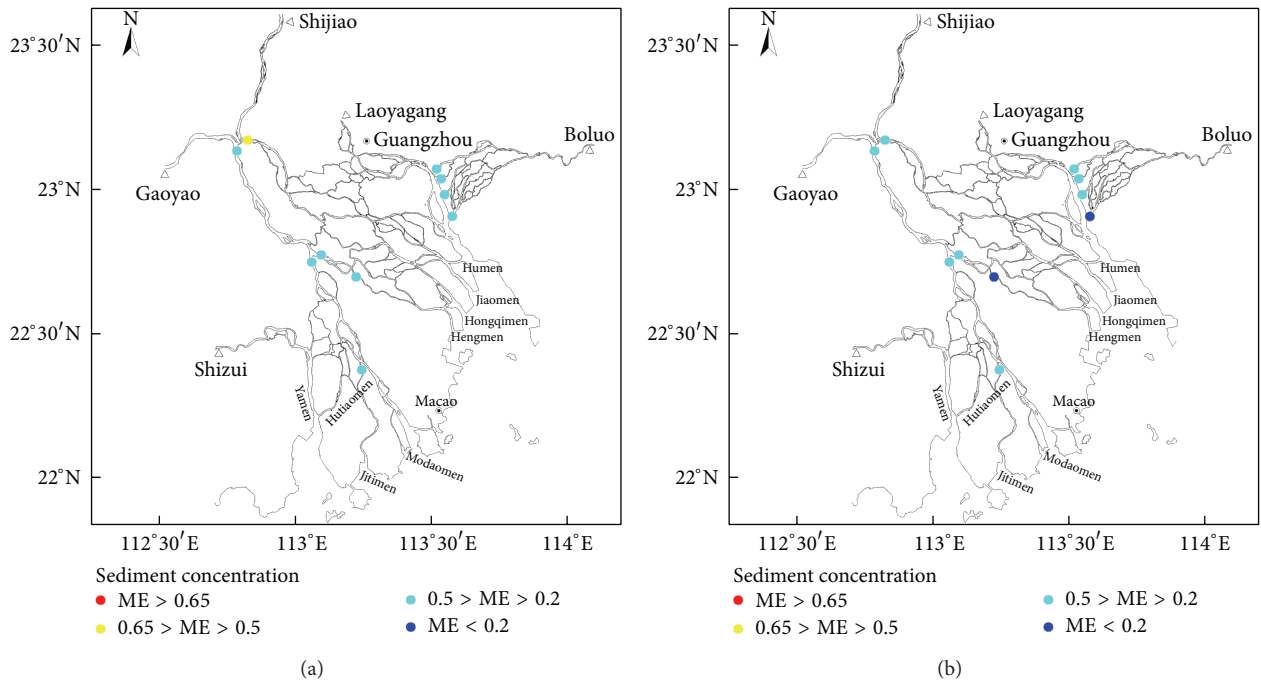


FIGURE 7: (a) The calibration of suspended sediment concentration from July 18 to July 19, 1998. (b) The validation of suspended sediment concentration from February 7 to 16, 2001.

conclude that the distributary channel networks model can simulate hydrodynamics process well in the river networks system.

Figures 7(a) and 7(b) show the results of calibration and validation of the suspended sediment concentration in the Pearl River networks. It can be noticed that the simulated

suspended sediment concentration in the Pearl River network still seem to be in a good agreement with the observed data, although the simulated results do not perform quite as well as water level and the discharge. The calibration results show that among the 10 stations observed, Sanshui station has ME value between 0.5 and 0.65, implying a very good skill, and

nine stations have scores between 0.2 and 0.5, showing a good skill. The verification results show two stations with scores less than 0.2 accounting for 20% of the total number of stations with poor skills. Generally speaking, most of the stations have ME value for simulation sediment transport between 0.2 and 0.5 for both the wet and dry seasons.

There are some potential reasons for errors between the simulated and observed suspended sediment concentration. Firstly, the bathymetry of the Pearl River network changes dramatically due to the intensive sand excavation during the last three decades. Therefore, the asynchronous of hydrographic and bathymetry measurement may directly lead to the inaccuracy of the simulation results. Actually, the field hydrographic measurements took place in 1998 and 2001, but the bathymetry survey happened in 1999 in our model. The asynchronous of hydrographic and bathymetry measurement should be one of the main reasons for the simulation errors. Secondly, large domain simulation needs more data and parameters, especially in suspended sediment transport simulation. However, some parameters of the suspended sediment, such as the diameter of the sediment, are regarded as relatively uniform distribution over the Pearl River network due to the limit of the data, which definitely lead to errors when simulating sediment transport. In general, the modeled results can be considered acceptable for simulating the flow and suspended sediment transport in the distributary channel networks.

#### 4. Conclusion

A 1D hydrodynamics and suspended sediment model is developed for simulating the flow and sediment transport in the distributary channel networks. Firstly, by utilizing the finite-difference equations of the single river, as well as the mass and energy conservation at junctions, the equations of water level at junctions can be transformed to the irregular sparse matrix equations. Water level and discharge at each channel section of a certain channel then can be obtained by the governing equations of the single channel. Assuming that the the erosion and deposition at the junctions are small, the nonequilibrium transport equation for suspended sediment can also be written in a matrix form. Solving the irregular sparse matrix equations, suspended sediment concentration can also be obtained at all junctions. Finally, the suspended sediment concentration at each river section in river networks can be calculated.

The distributary channel networks model was applied to the Pearl River networks, one of the most complicated river networks in the world, to check the performance of the model. The model was extensively calibrated and validated against field measurements to provide an accurate representation of water level and discharge, as well as suspended sediment transport in the Pearl River networks. The calibrated and validated results show that the distributary channel networks model display an excellent performance in simulating water level and discharge. Although the performance in simulating suspended sediment concentration is not as excellent as that of water level and discharge, the model

is still good enough to simulate the suspended sediment transport in the distributary channel networks model.

#### Conflict of Interests

The authors declare that there is no conflict of interests regarding the publication of this paper.

#### Acknowledgments

This research was financially supported by Commonwealth Program of Chinese Ministry of Water Resources (Project number: 201301072), the Natural Science Foundation of China (NSFC, Project number: 41376094), Joint Research Projects NSFC-NWO (Project number: 51061130545), and Program for Excellent Innovative Talents of Hohai University.

#### References

- [1] D. J. Twigt, E. D. de Goede, F. Zijl, D. Schwanenberg, and A. Y. W. Chiu, "Coupled 1D-3D hydrodynamic modelling, with application to the Pearl River Delta," *Ocean Dynamics*, vol. 59, no. 6, pp. 1077–1093, 2009.
- [2] W. A. Thomas and A. I. Prashum, "Mathematical model of scour and deposition," *Journal of the Hydraulics Division*, vol. 110, no. 11, pp. 1613–1641, 1977.
- [3] M. F. Karim and J. F. Kennedy, "IALLUVIAL: a commuter based flow and sediment routing for alluvial streams and its application to the Missouri River," Report No. 250, Iowa Institute of Hydraulic Research, University of Iowa, Iowa City, Iowa, USA, 1982.
- [4] M. F. Karim, "IALLUVIAL: analysis of sediment continuity and application to the Missouri River," Report No. 292, Iowa Institute of Hydraulic Research, University of Iowa, Iowa City, Iowa, USA, 1985.
- [5] H. H. Chang, "Modeling of river channel changes," *Journal of Hydraulic Engineering*, vol. 110, no. 2, pp. 157–172, 1984.
- [6] A. Molinas and J. C. Yang, *Computer Program User's Manual for GSTARS*, U.S. Department of Interior, Bureau of Reclamation, Engineering Research Center, Washington, DC, USA, 1986.
- [7] F. M. Holly and J. L. Rahuel, "New numerical/physical framework for mobile-bed modelling—part I: numerical and physical principles," *Journal of Hydraulic Research*, vol. 28, no. 4, pp. 401–416, 1990.
- [8] R. L. Runkel and R. E. Broshears, "OTIS: one-dimensional transport with inflow and storage: a solute transport model for small streams," CADSWES Technical Report 91-01, University of Colorado, Boulder, Colo, USA, 1991.
- [9] A. N. Papanicolaou, A. Bdour, and E. Wicklein, "One-dimensional hydrodynamic/sediment transport model applicable to steep mountain streams," *Journal of Hydraulic Research*, vol. 42, no. 4, pp. 357–375, 2004.
- [10] Q. W. Han, "A study on the non-equilibrium transportation of suspended load," in *Proceedings of the 1st International Symposium on River Sedimentation*, Beijing, China, 1980.
- [11] A. van Niekerk, K. R. Vogel, R. L. Slingerland, and J. S. Bridge, "Routing of heterogeneous sediments over movable bed: model development," *Journal of Hydraulic Engineering*, vol. 118, no. 2, pp. 246–262, 1992.

- [12] J. L. Rahuel, F. M. Holly, J. P. Chollet, P. J. Belleudy, and G. Yang, "Modeling of riverbed evolution for bedload sediment mixtures," *Journal of Hydraulic Engineering*, vol. 115, no. 11, pp. 1521–1542, 1989.
- [13] W. Wu, D. A. Vieira, and S. S. Y. Wang, "One-dimensional numerical model for nonuniform sediment transport under unsteady flows in channel networks," *Journal of Hydraulic Engineering*, vol. 130, no. 9, pp. 914–923, 2004.
- [14] H. W. Fang, M. H. Chen, and Q. H. Chen, "One-dimensional numerical simulation of non-uniform sediment transport under unsteady flows," *International Journal of Sediment Research*, vol. 23, no. 4, pp. 316–328, 2008.
- [15] P. E. Ashmore, "Laboratory modelling of gravel braided stream morphology," *Earth Surface Processes and Landforms*, vol. 7, no. 3, pp. 201–225, 1982.
- [16] P. E. Ashmore, "How do gravel-bed rivers braid?" *Canadian Journal of Earth Sciences*, vol. 28, no. 3, pp. 326–341, 1991.
- [17] F. Liu and B. R. Hodges, "Applying microprocessor analysis methods to river network modelling," *Environmental Modelling and Software*, vol. 52, pp. 234–252, 2014.
- [18] X. B. Zhang, D. C. Hu, and M. Wang, "A 2-D hydrodynamic model for the river, lake and network system in the Jingjiang reach on the unstructured quadrangles," *Journal of Hydrodynamics*, vol. 22, no. 3, pp. 419–429, 2010.
- [19] A. O. Akan and B. C. Yen, "Diffusion-wave flood routing in channel networks," *Journal of the Hydraulics Division*, vol. 107, no. 16299, pp. 719–732, 1981.
- [20] J. I. Allen, P. J. Somerfield, and F. J. Gilbert, "Quantifying uncertainty in high-resolution coupled hydrodynamic-ecosystem models," *Journal of Marine Systems*, vol. 64, no. 1–4, pp. 3–14, 2007.

## Research Article

# Calculation of the Instream Ecological Flow of the Wei River Based on Hydrological Variation

Shengzhi Huang, Jianxia Chang, Qiang Huang, Yimin Wang, and Yutong Chen

State Key Laboratory Base of Eco-Hydraulic Engineering in Arid Area, Xi'an University of Technology, Xi'an 710048, China

Correspondence should be addressed to Jianxia Chang; [chxiang@xaut.edu.cn](mailto:chxiang@xaut.edu.cn)

Received 10 October 2013; Revised 14 February 2014; Accepted 6 March 2014; Published 2 April 2014

Academic Editor: Y. P. Li

Copyright © 2014 Shengzhi Huang et al. This is an open access article distributed under the Creative Commons Attribution License, which permits unrestricted use, distribution, and reproduction in any medium, provided the original work is properly cited.

It is of great significance for the watershed management department to reasonably allocate water resources and ensure the sustainable development of river ecosystems. The greatly important issue is to accurately calculate instream ecological flow. In order to precisely compute instream ecological flow, flow variation is taken into account in this study. Moreover, the heuristic segmentation algorithm that is suitable to detect the mutation points of flow series is employed to identify the change points. Besides, based on the law of tolerance and ecological adaptation theory, the maximum instream ecological flow is calculated, which is the highest frequency of the monthly flow based on the GEV distribution and very suitable for healthy development of the river ecosystems. Furthermore, in order to guarantee the sustainable development of river ecosystems under some bad circumstances, minimum instream ecological flow is calculated by a modified Tennant method which is improved by replacing the average flow with the highest frequency of flow. Since the modified Tennant method is more suitable to reflect the law of flow, it has physical significance, and the calculation results are more reasonable.

## 1. Introduction

As known, river ecosystems play a significant role in watershed ecosystems, whose primary functions are purification, water storage, landscape, shipping, maintaining biodiversity, offering habitats for aquatic animals, and so on [1, 2]. Recently, the river ecosystems however are deteriorated under the background of climate change and increasingly intensified human activities (e.g., the construction of water conservancy project, conservation of water and soil, agricultural practices, etc.). As a result, the ecological chain is heavily destroyed, and a large number of species are decreasing on a large scale, some even die out. The core problem is that the flow in the river cannot satisfy the requirement of the ecological sustainable development due to unreasonable utilization of water resources and the neglect of the ecological flow. Therefore, the key step to improve river ecosystems is to reasonably calculate the instream ecological flow.

To date, about two hundred methods in the world have been introduced in the calculation of instream ecological flow [3–7]. Yang et al. [8] have used the improved Tennant method to calculate the instream ecological flow for the Irtysh

River. Chen et al. [9] have used the morphological methods which are based on the hydrological and morphological characteristics of river to compute ecological flow of the Liao Basin in China. Gippel and Stewardson [6] have used the wetted perimeter method to define the minimum environment flow. Dong et al. [10] have applied the monthly guarantee rate method to estimating the ecological water requirements for typical areas in the Huaihe Basin. Nevertheless, few of them have considered the hydrological variation when calculating the instream ecological flow. In fact, the runoff variations have occurred in many regions due to climate change and increasingly intensified human activities. The inflection point of the hydrological series causes the consistency of the entire hydrological series to be broken, and the overall distributions of the sample before and after the inflection point are different. Thus, it is not scientific and reasonable to compute instream ecological flow without considering hydrological variation which has changed the local ecological balance. It is thought that the local ecosystem has adapted to the hydrological status before hydrological variations. The river ecosystems before the change points of the hydrological series are better and healthier than those

after them. Therefore, the instream ecological flow calculated based on the data before the hydrological variations is a more reasonable ecological water requirement. For this reason, it is necessary to take hydrological variations into account when the instream ecological flow is computed, which will help to reveal different influence factors on the instream ecological flow. Wei River, the biggest first grade tributary of the Yellow River in China, is located in the middle reach of the Yellow River. The Wei River Basin is an important region for China, especially for the establishment of the Guanzhong-Tianshui Economic Zone, which will rapidly promote the economic development in the entire western region. However, during the recent decades, the runoff in the Wei River Basin has a significantly decreasing trend caused by climate change and human activities, and the flow is seriously polluted, which results in severe ecological damages and will greatly restrict the economic and social development of the basin and will even affect the national economic development strategy. Therefore, it is of significant importance to calculate the instream ecological flow in the Wei River for the local watershed management department to reasonably allocate water resources, which will help to promote the recovery of the local river ecosystems.

Considering the seriousness of the river ecosystems damages in the Wei River Basin, many attempts have been made to estimate the instream ecological flow, thus improving the ecological conditions [11, 12]. Pang et al. [11] have introduced a method considering not only the self-purification but also the flow demand for the aquatic animals' habitat to calculate the ecological base flow of the Wei River in Shaanxi province. Wang et al. [12] have used an approach based on water quality control target to estimate the lowest environmental water demands in the Wei River. However, to the best of our knowledge, none of them have considered the hydrological variations before computing the instream ecological flow, which is of significant importance to reasonably estimate the optimal instream ecological flow. Therefore, the hydrological variations are taken into consideration in this study.

Many traditional methods (e.g., Slide  $F$  test, Slide  $t$ -test, Mann-Kendall test methods, etc.) were applied to detect inflection point in the field of hydrology. However, all those methods are based on the assumption that the hydrological data are stationary and linear. Conversely, they are nonstationary and nonlinear. Therefore, some deviations will occur if the conventional methods are employed to identify change points. Whereas the heuristic segmentation algorithm first proposed by Bernaola-Galván et al. [13] is used to tackle this problem successfully, which is based on the thought of sliding  $t$ -test and modified to detect the mean change point of nonlinear and nonstationary time series. Compared with the traditional methods, the heuristic segmentation algorithm can divide a nonstationary time series with some stationary subseries that have various physical backgrounds. Thus, this approach is employed in this research to detect the change point of runoff series.

Furthermore, motivated by Song et al. [14], who has pointed out that living beings adapt to the high frequency of environmental factors after long-term natural selection;

the highest frequency of the runoff is regarded as the optimal instream ecological flow in this study. However, it is worth mentioning that the calculated optimal instream ecological values may be greatly higher than the monthly average flow after runoff variation due to the increasingly decreasing runoff at present. Therefore, the flow at present cannot meet the optimal instream ecological requirements. In view of reality and operability, the modified Tennant method is employed to compute the minimum instream ecological flow based on the calculated optimal instream ecological flow [3]. Thus, the main objectives of this study are (1) to detect the annual runoff change points in the Wei River Basin based on heuristic segmentation algorithm and (2) to reasonably estimate the maximum and minimum instream ecological monthly flow based on the highest frequency of monthly runoff and Tennant method.

## 2. Study Area and Data

*2.1. Introduction of the Wei River Basin.* The Wei River Basin, as shown in Figure 1, is selected in this study. The Wei River is the largest tributary of the Yellow River, which lies between  $103.5^{\circ}\text{E}$ – $110.5^{\circ}\text{E}$  and  $33.5^{\circ}\text{N}$ – $37.5^{\circ}\text{N}$ , covering a total area of  $1.35 \times 10^5 \text{ km}^2$ . Located in the continental monsoon climate zone, the Wei River Basin is characterized by relative abundant precipitation and generally high temperatures in summer but by rare precipitation and very low temperatures in winter. The annual precipitation of the Wei River Basin is about 559 mm [15]. At the same time, the rainfall has a large seasonal variation that during flood season (from June to September) generally accounts for approximately 60% of the total annual rainfall. The annual rainfall also varies greatly due to the unstable features of the intensity, duration, and influencing area of the subtropical high pressure belt over the northern Pacific. For instance, the annual rainfall is more than 800 mm in wet years, whilst it is less than 370 mm in drought years, which is likely to result in highly frequent droughts and floods in the Wei River Basin. Topographically, the altitude decreases from the highest northwest mountainous area to the lowest Guanzhong Plain in the southeast and southern portion of the basin. The Guanzhong Plain is designated as a state key economic development zone, which will greatly promote the economic development of surrounding area. Therefore, the economic development of Guanzhong Plain will directly affect the sustainable development of economy and society in the basin. However, in recent decades, the runoff of the basin has a remarkable decreasing trend caused by the climate changes and human activities. According to Xiao et al., 2012 [16], with regards to Linjiacun station, the runoff during 1980–1990 and 1991–2000 was reduced by 52% and 42% compared with that during 1950–1959, respectively. Furthermore, the flow of the Wei River is seriously polluted on a large scale, leading to severe ecological damages, which will greatly restrict the economic and social development of this basin and will even affect national economic development strategy. For this reason, it is necessary for the local watershed management department to accurately calculate the instream ecological flow in the Wei

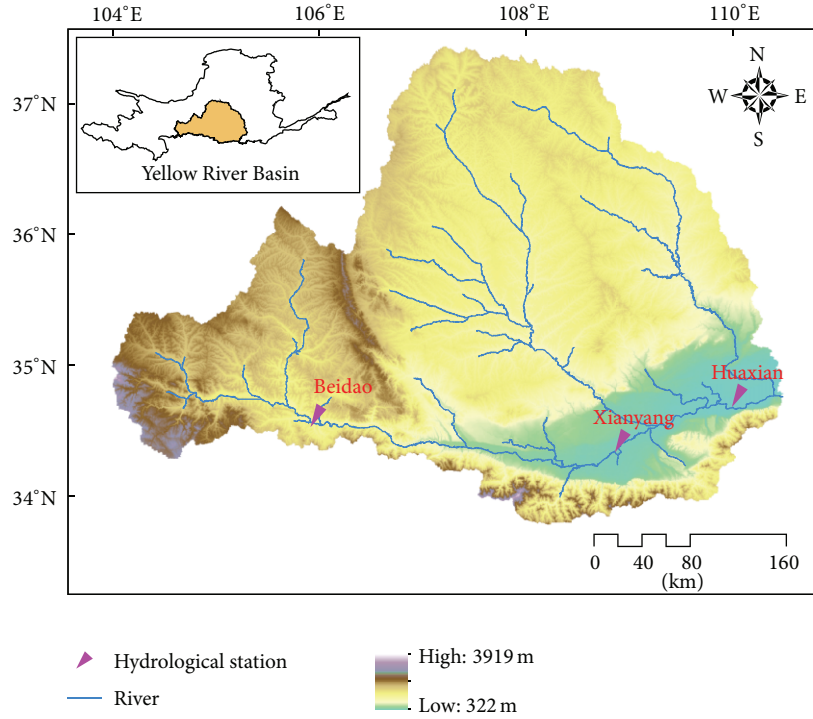


FIGURE 1: Location of Wei River and hydrological station in Yellow River Basin.

River, which will help to reasonably allocate water resources and promote the recovery of the local river ecosystems.

**2.2. Study Data.** Daily runoff data from Beidao, Xianyang, and Huaxian hydrological stations on the upper, middle, and lower reaches, respectively, of the Wei River is employed in this study. Amongst the three hydrological stations, the Beidao station has daily runoff data covering January 1, 1956–December 31, 2010, the Xianyang station has daily runoff data covering January 1, 1960–December 31, 2006, and the Huaxian station has daily runoff data covering January 1, 1919–December 31, 2011. The monthly and annual data is calculated by the daily data from the hydrological stations. The data is acquired from the hydrologic manual and strictly controlled during their release. The Huaxian hydrological station has some missing data of several days, which is reconstructed by calculating the average value of its neighboring days at the same station. In our opinions, the missing data reconstructed approach has little effect on the study. In addition, the double-mass curve method is used to check the consistency of the data, and the results indicate that all the daily meteorological data used in the paper are consistent.

### 3. Methodology

**3.1. Heuristic Segmentation Method.** In order to divide a nonstationary time series into several stationary segments, a sliding pointer is moved step-by-step from left to right along the time series [13]. The average of the subset of the series to the left of the pointer  $\mu_1$  and to the right  $\mu_2$  is calculated.

For two Gaussian distributed random series, the difference between the averages of the two series  $\mu_1$  and  $\mu_2$  under the statistical significance is estimated by Student's  $t$ -test statistic as follows:

$$t = \left| \frac{\mu_1 - \mu_2}{S_D} \right|, \quad (1)$$

where

$$S_D = \left( \frac{(N_1 - 1)s_1^2 + (N_2 - 1)s_2^2}{N_1 + N_2 - 2} \right)^{1/2} \left( \frac{1}{N_1} + \frac{1}{N_2} \right)^{1/2} \quad (2)$$

denotes the pooled variance,  $S_1$  and  $S_2$  stand for the standard deviations of the two series, and  $N_1$  and  $N_2$  are the number of points from the two series. Moving the pointer along the given time series step-by-step, then statistic  $t$  is calculated to estimate the difference between the averages of the right-side and left-side time series. Larger  $t$  denotes that the average values of the two time series tend to be more significantly different. The largest  $t$  value is regarded as a good candidate for the cut point. Then, the statistical significance  $P(t_{\max})$  is computed. It is worth mentioning that  $P(t_{\max})$  is not the standard Student's  $t$ -test since the series are not independent and cannot be obtained in a closed analytical form; therefore  $P(t_{\max})$  is approximately calculated as follows:

$$P(t_{\max}) \approx \left\{ 1 - I_{[\nu/(\nu+t_{\max}^2)]}(\delta\nu, \delta) \right\}^\eta, \quad (3)$$

where  $\eta = 4.19 \ln N - 11.54$  and  $\delta = 0.40$  are acquired from Monte Carlo simulations,  $N$  denotes the number of the time series to be cut,  $\nu = N - 2$ , and  $I_x(a, b)$  represents

the incomplete beta function. If the difference in average is not statistically significant, for instance, if  $P(t_{\max})$  value is less than a threshold (normally set to 0.95), this time series is not divided. Conversely, the time series is divided into two segments whose averages are significantly different. If the time series is split, the iteration of the above procedure on each new segment continues until the acquired significance value is less than the threshold, or the length of the acquired segments is less than presupposed minimum segment length  $\ell_0$ .

**3.2. Law of Tolerance.** The growth and development of biology follows the laws of tolerance [17–19]. The law of tolerance is that there are biological minimum and maximum limits of various factors affecting the growth and development of biology. When the ecological factor is not between the upper and lower limitations, the biology will be degenerated and even die. Amongst many environmental factors, the factors which are close to or beyond the biological tolerance limitation and limit the development of biology are called the restriction factors. For a river ecosystem, flow, water flow rate, water level, water quality, and so on are its important ecological factors, and all of them are the function of flow. Therefore, flow is closely related to the limiting factors of river ecological system, which is also a greatly important limiting factor of river ecological system.

**3.3. Ecological Adaptation Theory.** The number of biology changes following the variation of a certain ecological factors, when the biological number reaches the maximum value, the corresponding ecological factor value is the optimal value for this species. Under the optimal environment, the number of this species is highest and the growth rate is fastest. Whereas the ecological factor deviates the optimal value and beyond the biological tolerance limitation, this species will stop growing and the number will reduce. Long-term natural selection makes creatures adapt to the higher frequency of environmental factors [14]. Therefore, the highest frequency of flow is regarded as the optimal instream ecological flow.

### 3.4. Calculation of Instream Ecological Flow

**3.4.1. Kolmogorov-Smirnov (K-S) Test.** The K-S test considers the null hypothesis that the cumulative distribution function (CDF) of a target distribution, represented by  $F(x)$ , is similar to the CDF of a reference distribution,  $R(x)$ . Thus, the K-S test is possible to judge whether the two distributions have the same CDFs [20].

When using a two-sample K-S test, the distance  $D$  between two empirical distribution functions  $F_{N_1}(x)$  and  $R_{N_2}(x)$  is computed as

$$D = \sup_{-\infty < x < \infty} |F_{N_1}(x) - R_{N_2}(x)|, \quad (4)$$

where  $N_1$  and  $N_2$  denote the number of data points in the first and second sample, respectively. Let

$$N = \frac{N_1 N_2}{N_1 + N_2}. \quad (5)$$

Then

$$p(\sqrt{ND} > \lambda) \doteq \sum_{i=1}^{+\infty} (-1)^{i-1} e^{-2i^2 \lambda^2}. \quad (6)$$

The null hypothesis that the two distributions are similar is rejected at significance level  $\alpha$ , if  $D^* = \sqrt{ND}$  is more than the corresponding critical value. The approximate  $P$  value  $p(D)$ , that is termed the similarity probability in the vibration signal-processing literature, can be calculated by (6).

If the two distributions are similar ( $D \rightarrow 0$ ), then the similarity probability  $p(D)$  approximates 1. Otherwise, the similarity probability  $p(D)$  approximates 0.

**3.4.2. Calculation of the Optimal Instream Ecological Flow.** If there are change points of the hydrological series, the series before the change point is extremely different from that after the change point and the entire series is not inconsistent. It is thought that the local ecosystem has adapted to the hydrological status before hydrological variations, but the hydrological variations have changed the local ecological balance. Therefore, it is essential to use the hydrological series before hydrological variations to calculate the optimal instream ecological flow.

Based on the relationship between environmental factors and population, the highest frequency of flow is most suitable for river ecosystems. Since the flow of each month at the same station is different, the calculated highest frequency of flow for each month is regarded as the optimal instream ecological flow of the corresponding month; then the optimal instream ecological flow of different month in a year is calculated. In order to select the most suitable probability distribution function, Kolmogorov-Smirnov (K-S) method is employed to compute the test probability of monthly average flow [21]. Through calculating the test probability of each month at every station and comparing the fitting effect, the result indicates that GEV distribution is most suitable for the instream month average flow.

The GEV probability density function is expressed as follows:

$$f(x) = \frac{1}{\sigma} + (x)^{\xi+1} e^{-t(x)}, \quad (7)$$

$$t(x) = \begin{cases} \left(1 + \xi \frac{x - \mu}{\sigma}\right)^{-1/\xi} & \xi \neq 0 \\ e^{-(x-\mu)/w} & \xi = 0, \end{cases} \quad (8)$$

where  $\sigma$  is scale parameter, which affects distribution scale;  $\xi$  is shape parameter, which influences the distribution tail;  $\mu$  is position parameter, which affects the distribution in a horizontal position.  $L$ -moment method is employed to estimate the parameter of GEV distribution [22]. The observed variable  $X$  is in ascending order.  $X_j$  represents the  $j$ th value

in the series; then the  $L$ -distance of the first three order  $l_1, l_2, l_3$  and  $L$ -coefficient of skew  $t_3$  is expressed as follows:

$$\begin{aligned}
 l_1 &= n^{-1} \sum_{j=1}^n X_j, \\
 l_2 &= 2n^{-1} \sum_{j=2}^n \frac{(j-1)}{(n-1)} x_j - l_1, \\
 l_3 &= 6n^{-1} \sum_{j=3}^n \frac{(j-1)(j-2)}{(n-1)(n-2)} x_j - 6n^{-1} \sum_{j=2}^n \frac{(j-1)}{(n-1)} x_j + l_1, \\
 t_3 &= \frac{l_3}{l_2}.
 \end{aligned}
 \tag{9}$$

According to formula (9), the parameter of GEV distribution can be estimated as follows:

$$\begin{aligned}
 \xi &\approx - \left[ 7.859 \left( \frac{2}{3+t_3} - \frac{\log 3}{\log 2} \right) + 2.955 \left( \frac{2}{3+t_3} - \frac{\log 3}{\log 2} \right)^2 \right], \\
 \sigma &= \frac{l_2 \xi}{(1-2^{-\xi}) \Gamma(1+\xi)}, \\
 \mu &= l_1 + \frac{\sigma [\Gamma(1+\xi) - 1]}{\xi},
 \end{aligned}
 \tag{10}$$

where  $\Gamma(1+\xi)$  denotes gamma function.

Through the most valuable analysis of formula (7), the highest frequency of flow is calculated as follows:

$$x = \frac{\sigma}{\xi} [(\xi + 1)^{-\xi} - 1] + \mu,
 \tag{11}$$

where  $x$  denotes the optimal instream ecological flow of every month.

**3.4.3. Calculation of the Minimum Instream Ecological Flow.** Since the monthly average flow before variation is higher than that after variation, it is very difficult to provide the optimal instream ecological flow due to the increasing water demand for the economic and social development. For this reason, the optimal instream ecological flow can be regarded as the maximum instream ecological flow. However, recently, the flow in the Wei River has a significantly decreasing trend, it is very difficult for the flow at present to satisfy the maximum instream ecological flow. Considering the reality and operability, the minimum instream ecological flow can be calculated by a modified Tennant method. In terms of the traditional Tennant method, the formula calculating the instream ecological flow is as follows:

$$W_t = \sum_{i=1}^{12} M_i N_i,
 \tag{12}$$

where  $W_t$  denote the instream ecological flow,  $M_i$  are the average flow of the  $i$ th month in a year, and  $N_i$  represents

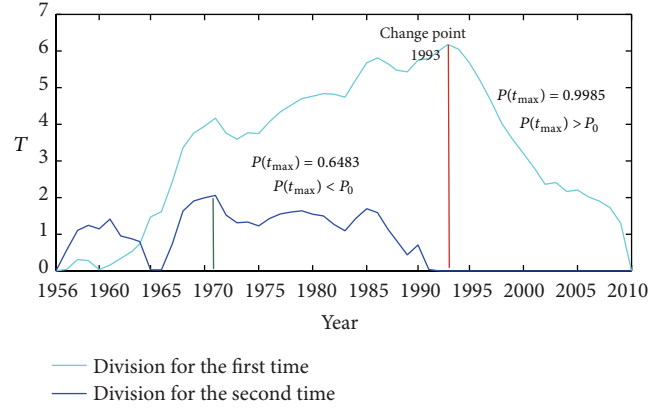


FIGURE 2: Segmentations and change points of annual runoff at Beidao station.

the recommended base flow percentage of the corresponding  $i$ th month. Based on Tennant method, the monthly average flow is replaced by the calculated optimal instream ecological flow which can be better suitable to reflect the law of the monthly runoff. From October to March, the minimum instream ecological flow is computed by the corresponding optimal instream ecological flow multiplied by 0.2; from April to September, the minimum instream ecological flow is computed by the corresponding optimal instream ecological flow multiplied by 0.4. The minimum instream ecological flow is used when the flow is insufficient, while the maximum instream ecological flow is employed when the runoff is abundant.

## 4. Results

### 4.1. The Change Points of the Runoff at Each Hydrological Station

**4.1.1. The Change Points of the Runoff at Beidao Station.** Since the annual runoff in the Wei River Basin has nonlinear and nonstationary characteristics, therefore, the heuristic segmentation method introduced in Section 3 is employed to detect the change points of the annual runoff. The threshold  $P_0$  is set to 0.95 and  $\ell_0$  is set to 25. The segmentations and change points of annual runoff at Beidao station are exhibited in Figure 2. During the first iteration and segmentation process, a change point (1993) is identified due to its  $P(t_{\max}) = 0.9985 > P_0$ . During the second iteration and segmentation, no change points are detected due to its  $P(t_{\max}) = 0.6483 < P_0$ . When the second iteration finishes, the segmentation process ends due to the length of the segments that is less than  $\ell_0$ .

**4.1.2. The Change Points of the Runoff at Xianyang Station.** As in the same procedure as above, the threshold  $P_0$  is set to 0.95 and  $\ell_0$  is set to 25. The segmentations and change points of annual runoff at Xianyang station are presented in Figure 3. During the first iteration and segmentation process, a change point (1994) is detected due to its  $P(t_{\max}) = 0.9996 >$

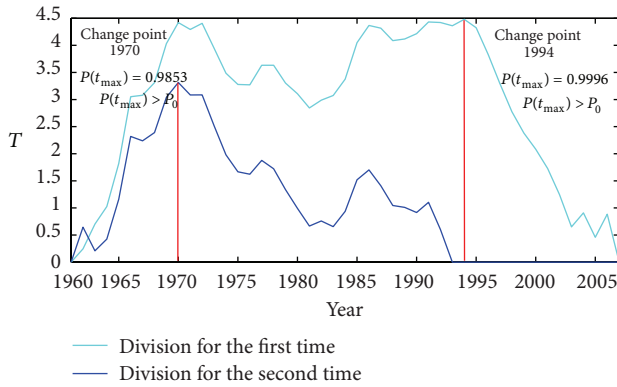


FIGURE 3: Segmentations and change points of annual runoff at Xianyang station.

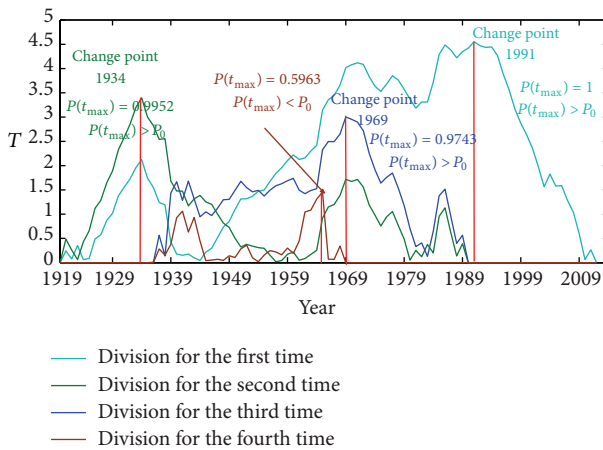


FIGURE 4: Segmentations and change points of annual runoff at Huaxian station.

$P_0$ . During the second iteration and segmentation, another change point (1970) is found due to its  $P(t_{\max}) = 0.9853 > P_0$ . When the second iteration finishes, the segmentation process ends due to the length of the segments that is less than  $\ell_0$ .

4.1.3. *The Change Points of the Runoff at Huaxian Station.*

Similarly, the threshold  $P_0$  is set to 0.95 and  $\ell_0$  is set to 25. The segmentations and change points of annual runoff at Huaxian station is shown in Figure 4. During the first iteration and segmentation process, a change point (1991) is detected due to its  $P(t_{\max}) = 1 > P_0$ . During the second iteration and segmentation, another change point (1934) is found due to its  $P(t_{\max}) = 0.9952 > P_0$ . During the third iteration and segmentation process, another change point (1969) is identified due to its  $P(t_{\max}) = 0.9743 > P_0$ .

During the fourth iteration and segmentation process, no change points are found due to its  $P(t_{\max}) = 0.5963 < P_0$ . When the fourth iteration finishes, the segmentation process ends due to the length of the segments that is less than  $\ell_0$ .

Therefore, for the Beidao station, only one change point of annual runoff is identified. As regards to the Xianyang station, two change points was detected. With regards to the

Huaxian station, three change points are found. In view of the length of flow series and the degree of variation, the annual runoff covering 1919–1991 at Huaxian station is regarded as the series before variation, and the annual runoff during 1992–2011 is regarded as the series after variation; the annual runoff covering 1960–1994 at Xianyang station is regarded as the series before variation, and the annual runoff during 1995–2006 is regarded as the series after variation; the annual runoff covering 1956–1993 at Huaxian station is regarded as the series before variation, and the annual runoff during 1994–2010 is regarded as the series after variation.

4.2. *The Calculation Results of the Optimal Instream Ecological Flow.*

As introduced in Section 3, the optimal (maximum) instream ecological flow is the highest frequency of monthly flow based on the GEV distribution before runoff variation. The  $L$ -moment method is used to estimate the parameter of GEV distribution, and the highest frequency of flow is computed according to formulas (11); then the corresponding instream ecological flow of every month at each station is calculated; the calculation results are presented in Table 1.

It can be easily observed from Table 1 that the maximum instream ecological flow from January to August at Beidao and Huaxian stations is increasing, whilst that from September to December is decreasing. Similarly, the maximum instream ecological flow at Xianyang station is increasing from January to September and decreasing from October to December. In general, the maximum instream ecological flow at Huaxian station is largest. Compared with the calculation results of Tennant method [3], most of the calculated maximum instream ecological flow of every month at each station are at the best level. The main reason is that the monthly runoff in this river is greatly decreasing and the monthly average flow after the variation is less than that before the variation. The frequency of monthly flow satisfying the maximum instream ecological flow in the Wei River is shown in Table 2. It can be obviously seen that the frequency of monthly flow satisfying the maximum instream ecological flow before the flow variation is extremely larger than that after the flow variation, especially for the Beidao station; the frequency of half of the months after variation is zero, implying that the river ecosystem is subject to severe damage after the flow variation. Comparatively, most of the frequencies of the three stations before the flow variation are larger than 40%. The underlying cause of this phenomenon is increasingly intensifying human activities. The growing population and increasing economy result in a great reduction of runoff. With regards to Beidao station, the development of agriculture and animal husbandry need a lot of water, whilst regarding Xianyang and Huaxian stations, water demand in households and economic development have a very large proportion. Additionally, amongst the three hydrological stations, the frequency of monthly flow satisfying the maximum instream ecological flow at Xianyang station in nonflood season is lowest. The primary reason lies in the large number of water demand for economic and agricultural development. The Xianyang station is located in the Guanzhong Plain, and many industrial parks lie in the

TABLE 1: The maximum instream ecological flow at three stations.

Month	Hydrological stations		
	Beidao ( $10^8 \text{ m}^3$ )	Xianyang ( $10^8 \text{ m}^3$ )	Huaxian ( $10^8 \text{ m}^3$ )
January	0.3693	1.4157	2.214
February	0.4164	1.2969	2.2344
March	0.6508	1.4179	2.9864
April	0.7763	1.6253	3.1216
May	1.1252	2.1386	4.2134
June	1.124	2.6713	4.8661
July	2.2039	3.2768	11.616
August	2.3685	4.9855	13.4456
September	2.2127	10.0234	11.3155
October	1.8079	8.6294	8.5133
November	0.8667	4.1154	4.3768
December	0.469	2.0948	2.7472

area above the station. Thus, during the nonflood period, a lot of water is used for industrial manufacture, thereby leading to less flow failing to satisfy the ecological demand.

In theory, the maximum instream ecological flow is most suitable for the healthy development of the river ecosystem in this basin, when the flow is sufficient; the maximum instream ecological flow can be used as the instream ecological water requirements to provide during high flow year. However, since the monthly flow has a significant decreasing trend caused by climate change and the increasingly intensified human activities, in practice, it is difficult for the flow at present to satisfy the optimal (maximum) instream ecological flow. Therefore, it is necessary to calculate the minimum instream ecological flow when the flow is insufficient, which can be used to ensure the sustainable development of the river ecosystems under the bad circumstance.

*4.3. The Calculation Results of the Minimum Instream Ecological Flow.* According to Section 3, the minimum instream ecological flow is calculated by a modified Tennant method, which is based on the Tennant method and replaced by the monthly average flow with the calculated maximum instream ecological flow. The calculation results of the Tennant method and the modified Tennant approach are exhibited in Table 3.

For Beidao station, the minimum instream ecological flow calculated by the modified Tennant method is always larger than that computed by Tennant method, but the difference between them is small. For Xianyang station, all the minimum instream ecological flows calculated by the modified Tennant method are larger than that calculated by Tennant method except the minimum instream ecological flow of April and May. For Huaxian station, the minimum instream ecological flow of April, May, September, and October computed by the modified Tennant method is less than that calculated by Tennant method. In general, the minimum instream ecological flow calculated by the modified Tennant method is slightly larger than that computed by Tennant method. Since the modified Tennant method is based on the highest frequency of monthly flow and has physical significance, therefore the minimum instream ecological

flow calculated by the modified Tennant method is more reasonable than that calculated by Tennant method.

## 5. Discussion

It is worth mentioning that  $P_0$  and  $\ell_0$  are two important parameters for the heuristic segmentation method to identify the change points. The magnitudes of  $P_0$  and  $\ell_0$  will directly affect the identification of the mutation points and further influence the calculated maximum and minimum instream ecological flow. The threshold  $P_0$  is set to 0.95 and  $\ell_0$  is set to 25, which is determined by empirical analysis and subjective to some extent.

The results show that the decreasing runoff in the Wei River Basin is affected by human activities and climate change, and the human activities are the most primary driving factor. There are two primary change points of annual runoff in the Wei River, which are the early the 1970s and the middle 1990s, respectively.

Firstly, the causes of the first change point are analyzed. As known, the soil conservation measures in the Wei River Basin were carried out in the 1950s and expanded on a large scale after the early 1970s, which will obviously reduce the runoff. Besides, the Wei River Basin is in the continental monsoon climate zone of China and influenced by the West Pacific Subtropical high pressure system. In 1972, the weakness of this system in combination with development of an El Niño event caused substantial atmospheric circulation and climate anomalies in China [23], resulting in a sharp reduction in rainfall in the basin, which contributes to the mutation point identified in that year. Furthermore, there are many reservoirs and irrigation canals completed in the early 1970s (e.g., the Yangmaowan reservoir and Fengcun reservoir are completed in 1970, the Dayu reservoir and Shimen reservoir are constructed in 1972 and the Baojixia canal completed in 1971), which will highly reduce the runoff and induce the change point.

Lastly, the causes of the second inflection point are analyzed. National economic water consumption sectors in the Wei River Basin in the 1990s have remarkably increased, especially in domestic and industrial water use. The total national economy water consumption is 4.3 billion  $\text{m}^3$ , which is increased by 52.6% compared to the time period before 1990s, directly resulting in the decreasing runoff. Moreover, according to Zhang [15], a third ENSO event occurred in 1994, when the West Pacific Subtropical high pressure system was strong, which resulted in an extreme drop in rainfall in the basin, contributing to a 42.4% reduction in average annual runoff.

As there are change points of the runoff series in the Wei River and the variation has broken the ecological balance before the flow variation, it is necessary to take the variation into account when calculating the instream ecological flow. It is worth noting that the instream ecological flow considered about the variation tends to be larger than that without considering the variation due to the decreasing flow.

TABLE 2: The frequency of monthly flow satisfying the maximum instream ecological flow in the Wei River.

Month	Beidao station		Xianyang station		Huaxian station	
	BFV (%)	AFV (%)	BFV (%)	AFV (%)	BFV (%)	AFV (%)
January	46	0	28	0	40	5
February	52	0	33	7	44	9
March	51	0	58	14	41	14
April	35	0	64	14	55	27
May	46	0	73	28	51	27
June	35	7	48	7	41	14
July	41	7	70	28	40	14
August	35	4	42	14	35	9
September	38	4	36	7	48	18
October	46	11	27	14	45	32
November	33	4	24	7	56	27
December	38	0	27	0	40	14

Note: BFV denotes before flow variation and AFV denotes after flow variation.

TABLE 3: The minimum instream ecological flow of the Wei River.

Month	Beidao station		Xianyang station		Huaxian station	
	MTM	TM	MTM	TM	MTM	TM
January	0.0739	0.06227	0.2831	0.2074	0.4428	0.3807
February	0.0833	0.069	0.2594	0.19586	0.4469	0.3851
March	0.1302	0.1013	0.2836	0.2691	0.5973	0.5248
April	0.3105	0.2200	0.6501	0.9618	1.2487	1.5203
May	0.4501	0.3272	0.8554	1.3871	1.6854	2.0202
June	0.4496	0.3783	1.0685	0.9779	1.9464	1.7816
July	0.8816	0.6755	1.3107	2.0110	4.6464	4.0136
August	0.9474	0.7178	1.9942	1.7417	5.3782	4.5461
September	0.8851	0.6641	4.0094	2.9904	4.5262	5.1085
October	0.3616	0.2930	1.7259	1.2367	1.7027	1.9978
November	0.1733	0.1296	0.8231	0.5693	0.8754	0.9926
December	0.0938	0.0694	0.4190	0.2713	0.5494	0.4949

Note: MTM denotes the modified Tennant method and TM denotes Tennant method.

## 6. Conclusion

Recently, the Wei River Basin has witnessed a severe destruction of river ecosystems. The key way to solve this problem is to reasonably allocate water resources and ensure the basic requirement water of river ecosystem. The core problem is to accurately calculate instream ecological flow. Under the background of climate change and increasing identified human activities, there are some change points of the runoff series in the Wei River. In order to reasonably compute the instream ecological flow, the variation is taken into consideration in this study. The heuristic segmentation algorithm is employed to identify the change points due to the nonlinear and nonstationary flow series, which is difficult for the traditional statistical test to accurately detect the change points. The diagnosis results suggest that the runoff of Beidao station has a change point (1991); the runoff of Xianyang

station has two change points (1970 and 1994); the runoff of Huaxian station has three change points (1934, 1969 and 1991).

Based on the law of tolerance and ecological adaptation theory, the optimal (maximum) instream ecological flow is calculated in this study, which is the highest frequency of the monthly flow from the GEV distribution. Since the monthly flow before the variation is larger than that after the variation, the optimal instream ecological flow is difficult to provide due to the decreasing runoff. In order to guarantee the sustainable development of river ecosystems under some bad circumstances, the minimum instream ecological flow is calculated by a modified Tennant method which is improved by replacing the average flow with the highest frequency of flow based on the GEV distribution. Since the modified Tennant method is more suitable to reflect the law of flow, it has physical significance, and the calculation results are more reasonable. The maximum and minimum instream

ecological flow is a greatly important reference for protection and restoration of the river ecosystems in the Wei River Basin.

### Conflict of Interests

The authors declare that there is no conflict of interests regarding the publication of this paper.

### Acknowledgments

This research was supported by the National Major Fundamental Research Program (2011CB403306), the National Natural Fund Major Research Plan (51190093), and the National Science Foundation of China (51179148, 51179149). Sincere gratitude is extended to the editor and anonymous reviewers for their professional comments and corrections, which greatly improved the presentation of the paper.

### References

- [1] Z.-R. Dong, "Diversity of river morphology and diversity of bio-communities," *Journal of Hydraulic Engineering*, vol. 48, no. 11, pp. 1–6, 2003 (Chinese).
- [2] J. Gao, Y. Gao, G. Zhao, and G. Hörmann, "Minimum ecological water depth of a typical stream in Taihu Lake Basin, China," *Quaternary International*, vol. 226, no. 1-2, pp. 136–142, 2010.
- [3] D. L. Tennant, "Instream flow regimens for fish, wildlife, recreation, and related environmental resources," in *Proceedings of Symposium and Special Conference on Instream Flow Needs II*, J. F. Osborn and C. H. Allman, Eds., pp. 359–373, American Fisheries Society, Bethesda, Md, USA, 1976.
- [4] X. Xia, Z. Yang, and Y. Wu, "Incorporating eco-environmental water requirements in integrated evaluation of water quality and quantity—a study for the Yellow River," *Water Resources Management*, vol. 23, no. 6, pp. 1067–1079, 2009.
- [5] N. D. Gordon, T. A. McMahon, and B. L. Finlayson, *Stream Hydrology: An Introduction for Ecologists*, John Wiley & Sons, New York, NY, USA, 2nd edition, 2004.
- [6] C. J. Gippel and M. J. Stewardson, "Use of wetted perimeter in defining minimum environmental flows," *River Research and Applications*, vol. 14, no. 1, pp. 53–67, 1998.
- [7] S. Liu, X. Mo, J. Xia et al., "Uncertainty analysis in estimating the minimum ecological instream flow requirements via wetted perimeter method: curvature technique or slope technique," *Acta Geographica Sinica*, vol. 61, no. 3, pp. 273–281, 2006.
- [8] F. Yang, Z. Xia, L. Yu, and L. Guo, "Calculation and analysis of the instream ecological flow for the Irtysh River," *Procedia Engineering*, vol. 28, pp. 438–441, 2012.
- [9] M. Chen, G. Wang, H. Feng, and L. Wang, "The calculation of river ecological flow for the Liao basin in China," *Procedia Engineering*, vol. 28, pp. 715–722, 2012.
- [10] X. Dong, P. Du, Q. Tong, and J. Chen, "Ecological water requirement estimates for typical areas in the huaihe basin," *Tsinghua Science and Technology*, vol. 13, no. 2, pp. 243–248, 2008.
- [11] B. Pang, Z. X. Xu, and W. Wu, "Estimation of the ecological base flow of Wei River in Shaanxi province," *Procedia Environmental Sciences*, vol. 13, pp. 1559–1568, 2012.
- [12] X. Q. Wang, Z. F. Yang, and C. M. Liu, "Method of resolving the lowest environmental water demands in river course (II)—application," *Acta Scientiae Circumstantiae*, vol. 21, no. 5, pp. 549–552, 2001.
- [13] P. Bernaola-Galván, F. C. Ivanov, L. A. Nunes Amaral, and H. E. Stanley, "Scale invariance in the nonstationarity of human heart rate," *Physical Review Letters*, vol. 87, no. 16, Article ID 168105, 4 pages, 2001.
- [14] L.-L. Song, G.-H. Lu, and L. Liu, "Estimation of instream flow based on hydrological indexes," *Journal of Hydraulic Engineering*, vol. 37, no. 11, pp. 1336–1341, 2006.
- [15] H. L. Zhang, Y. Chen, and G. X. Ren, "The characteristics of precipitation variation of Weihe River Basin in Shaanxi Province during recent 50 years," *Agricultural Research in the Arid Areas*, vol. 26, pp. 236–240, 2008.
- [16] J. Xiao, J. G. Luo, J. Xie, and C. Chen, "Analysis on interannual and annual variation trend of runoff in the main stream of Weihe River," *Yellow River*, vol. 34, no. 11, pp. 32–36, 2012 (Chinese).
- [17] Ü. Niinemets and F. Valladares, "Environmental tolerance," in *Encyclopedia of Ecology*, S. E. Jørgensen and B. D. Fath, Eds., pp. 1370–1376, Elsevier, Oxford, UK, 2008.
- [18] V. E. Shelford, "Some concepts of bioecology," *Ecological Society of America*, vol. 12, no. 3, pp. 455–467, 1931.
- [19] A. Mackenzie, A. S. Ball, and S. R. Virdee, *Instant Notes in Ecology*, Instant Notes Series, BIOS Scientific Publishers, London, UK, 2nd edition, 2001.
- [20] X. Wang and V. Makis, "Autoregressive model-based gear shaft fault diagnosis using the Kolmogorov-Smirnov test," *Journal of Sound and Vibration*, vol. 327, no. 3-5, pp. 413–423, 2009.
- [21] F. J. Messey, "The Kolmogorov-Smirnov test for goodness of fit," *Journal of the American Statistical Association*, vol. 46, no. 253, 1951.
- [22] J. R. M. Hosking, "L-moments: analysis and estimation of distributions using linear combinations of order statistics," *Journal of the Royal Statistical Society. Series B. Methodological*, vol. 52, no. 1, pp. 105–124, 1990.
- [23] Z. X. Bao, J. Y. Zhang, and G. Q. Wang, "Attribution for decreasing streamflow of the Haihe River basin, northern China: climate variability or human activities," *Journal of Hydrology*, vol. 407, pp. 117–129, 2012.

## Research Article

# Monthly Optimal Reservoirs Operation for Multicrop Deficit Irrigation under Fuzzy Stochastic Uncertainties

Liudong Zhang,<sup>1,2</sup> Ping Guo,<sup>1</sup> Shiqi Fang,<sup>1</sup> and Mo Li<sup>1</sup>

<sup>1</sup> Centre for Agricultural Water Research in China, China Agricultural University, Number 17 Qinghua East Road, Haidian, Beijing 100083, China

<sup>2</sup> College of Water Conservancy, Yunnan Agricultural University, Kunming 650201, China

Correspondence should be addressed to Ping Guo; guop@cau.edu.cn

Received 11 December 2013; Accepted 6 February 2014; Published 18 March 2014

Academic Editor: Y. P. Li

Copyright © 2014 Liudong Zhang et al. This is an open access article distributed under the Creative Commons Attribution License, which permits unrestricted use, distribution, and reproduction in any medium, provided the original work is properly cited.

An uncertain monthly reservoirs operation and multicrop deficit irrigation model was proposed under conjunctive use of underground and surface water for water resources optimization management. The objective is to maximize the total crop yield of the entire irrigation districts. Meanwhile, ecological water remained for the downstream demand. Because of the shortage of water resources, the monthly crop water production function was adopted for multiperiod deficit irrigation management. The model reflects the characteristics of water resources repetitive transformation in typical inland rivers irrigation system. The model was used as an example for water resources optimization management in Shiyang River Basin, China. Uncertainties in reservoir management shown as fuzzy probability were treated through chance-constraint parameter for decision makers. Necessity of dominance (*ND*) was used to analyse the advantages of the method. The optimization results including reservoirs real-time operation policy, deficit irrigation management, and the available water resource allocation could be used to provide decision support for local irrigation management. Besides, the strategies obtained could help with the risk analysis of reservoirs operation stochastically.

## 1. Introduction

Shortage of water resources is a critical constraint for agricultural production in arid and semiarid regions. Because of the changing environment, agricultural water supply is facing the unpredictable challenge. Ashofteh et al. estimated that water demand volume in the future (2026–2039) would increase 16%, while the average long-term annual volume of runoff would decrease 0.7% [1]. To meet the challenge, reservoirs operation (RO) is important and particularly difficult [2].

Reservoirs operation plays an important role for arid and semiarid areas, especially, when the competition between agricultural and ecological water demand is intense. Agricultural water is critical for food productivity, while ecological water is important to regional sustainable development. Reservoirs operation problems concerned with maximization of irrigation benefits have been emphasized by many researchers since the 1970s [3]. Typical reservoirs operation method was dynamic programming [3–5]. Vedula and Mujumdar [6] integrated the reservoir release and irrigation

allocation by using dynamic programming, but they took rainfall and potential evapotranspiration as deterministic inputs. Furthermore, Vedula and Kumar [7] overcome the shortcomings considering the rainfall and inflow as stochastic parameters.

But when the irrigation water is limited to ecological water, the situation is more complicated. Unfortunately, the previous studies mainly focused on irrigation water management. Mujumdar and Ramesh [8] developed a real-time dynamic programming model for optimal crops water allocation and reservoir release, but the framework of the model is deterministic. Moradi-Jalal et al. [2] considered annual crops irrigation water for monthly reservoirs operation and optimal crop pattern. But their research did not consider the relationship between water and crops.

Optimal water allocation for irrigation district is an important issue which has received considerable attention in previous researches. Evers et al. [9] integrated hydrologic model (*PRMS*) and crop growth simulation model (*EPIC*)

for reservoir management options. Dos Santos Teixeira [5] developed a forward dynamic programming (FDP) model for real-time reservoirs operation of irrigation districts. Georgiou and Papamichail [10] aimed to determine optimal irrigation allocation and cropping pattern for multicrops. Prasad et al. 2012 [11] developed a real-time reservoir release decision. Among these studies, crop yield was critical data for decision objective. There were two ways to determine crop yield: (1) estimated by average production per unit area or per cube water [12] and (2) calculated through water production function [6, 11, 13].

However, in real-world problem the source of water could be groundwater and surface (reservoir) water. Then the problem becomes more complicated to identify the most efficient strategies for the whole system. Reichard [14] applied a stochastic simulation optimization model for Santa Clara-Callcguas Basin surface water-groundwater management. Vedula et al. [13] optimized multicrop water allocation for a reservoir-canal-aquifer system considering intraseasonal period. As discussed above, previous researchers just considered two issues among reservoirs operation, irrigation district, ecological water requirement, and surface water-groundwater conjunctive use. To approach the real situation, an integrated water allocation model related to these issues was considered.

Another difficulty in the whole system was the uncertainties, including natural factors and human triggers. Uncertainties in reservoir and irrigation system caused by river inflows and crops requirement had been discussed from different aspects [1, 15–18]. Karamouz and Vasiliadis [15] forecasted the stream flows by Bayesian stochastic dynamic programming (BSDP) with different conditional probabilities. Teegavarapu and Simonovic [16] handled the imprecise loss function for short time reservoirs operation under fuzzy environment. Seifi and Hipel [19] presented a stochastic model to deal with the stochasticity of inflows under multiple inflow scenarios. Chang et al. [18] combined grey system with fuzzy stochastic dynamic programming. Although uncertainty was considered, the reliability of satisfying (or risk of violating) cannot be reflected. Then Azaiez et al. [20] applied chance constraint to explain the potential benefits of groundwater saving.

But these methods cannot handle dual uncertainties presented as linkage between fuzzy and probability distribution. To handle this problem, Guo and Huang [21] developed a two-stage fuzzy chance-constraint programming for water resources management. In a similar fashion, if adequate samples of historic reservoir inflow date were obtained, then different reservoir inflow levels distributed as randomness distribution. If the total reservoir release water cannot be met, chance-constraint programming can be applied to obtain the expected net benefits [22]. Nevertheless, in the progress of RO, alternations were made by decision makers with different goals; probabilities of different inflow levels could not exactly reflect randomness of inflows alone [23]. Thus, the probabilities may own the fuzzy information based on the decision maker's judgment, leading to fuzzy stochastic characteristic.

In this paper, an optimization model for deficient irrigation water allocation under uncertainties was developed.

The model is combined with ground-surface water joint-use model, monthly reservoirs operation model, and multicrop irrigation model. Fuzzy stochastic characteristic was represented as fuzzy probability, reflecting the risk of reservoir release water and necessity of dominance (ND) was considered to illustrate it. Reservoir water and groundwater were integrated as interactive resources for both irrigation districts and ecological water. Irrigation water was calculated through Jensen model under deficit irrigation condition.

## 2. Model Formulation

The available water resources mainly come from the mountainous runoff in typical inland area of China. According to the characters of water resources of inland river system, as shown in Figure 1, the watershed can be divided into two parts, runoff formation and disappear areas. Accumulated water flows into mountainous river for water utilization in the plain region. Several reservoirs located mainly in the mountain river and some of the water was used for irrigation, but the rest leaked in the piedmont plain as groundwater recharge. Groundwater was pumped for agricultural irrigation once more and the surplus water needs to meet the ecological water demand of downstream meanwhile. The water resources transformation process leads to efficient water development pattern and the water recycle is improved. However excessive development scale and unreasonable allocation of water resources can cause the overextraction of groundwater and deterioration of the environment.

At present, maximum utilization of water resources is very important because of the shortage of water resources. To optimize water resources considering exploitation and replenishment balance of groundwater for upstream and downstream users, the current study was used to simulate multiperiod reservoirs operation and multicrop irrigation optimization. The objective is to maximize the total crop yields of the entire irrigation districts.

This model can be written as follows and the meanings of parameters are listed in the Nomenclature section. All of variables are nonnegative:

$$\begin{aligned} \text{Max } F = & \sum_{k=1}^K \sum_{n=1}^N \left[ Y_{\max}^n \prod_{t=1}^T \left( \frac{ET_t^{k,n}}{ET_{t \max}^n} \right)^{\lambda_t^n} \times A^{k,n} \right] \\ & + \sum_{i=1}^I \sum_{n=1}^N \left[ Y_{\max}^n \prod_{t=1}^T \left( \frac{ET_t^{i,n}}{ET_{t \max}^n} \right)^{\lambda_t^n} \times A^{i,n} \right]. \end{aligned} \quad (1)$$

The expected crop yields are estimated by deficit irrigation crop water production function. The water production function can be used to tackle the irrigation management. We divide the crop planting stages into monthly periods. The crop's monthly water consumption is the decision variable in the model. The deficit irrigation Jensen model [24] is introduced to reflect crop yields linked to sensitivity of water shortage. Sufficient water requirement of crop can lead to maximum crop yields, and water deficit in different stages may reduce the actual crop production in different degrees.

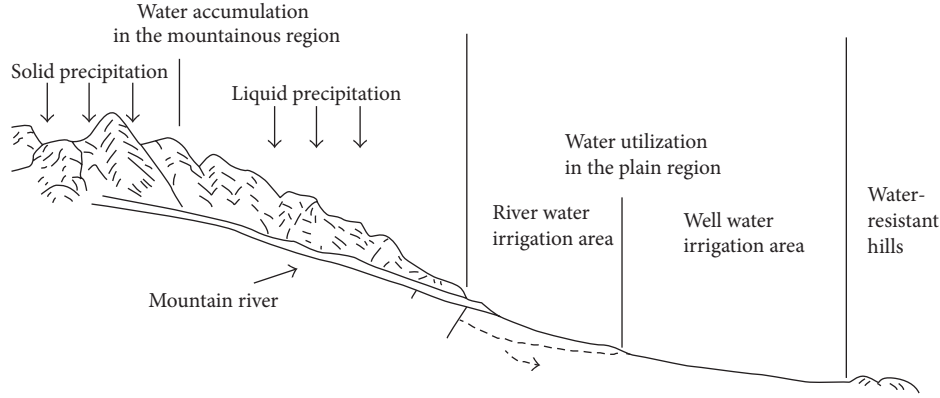


FIGURE 1: The relationship of water resources transformation in arid inland area.

Subject to: Avoiding large water deficit during the period of crop water consumption and not exceeding maximum evapotranspiration constraints,

$$\begin{aligned} 0.6ET_{t \max}^n &\leq ET_t^{k,n} \leq ET_{t \max}^n, \\ 0.6ET_{t \max}^n &\leq ET_t^{i,n} \leq ET_{t \max}^n. \end{aligned} \quad (2)$$

Considering the balance equation of the reservoirs located in the mountain pass of the rivers,

$$V_t^k = V_{t-1}^k + I_t^k - R_t^k - O_t^k - E_t^k. \quad (3)$$

Reservoirs overflow constraint is expressed as follows. In each planning time period, accumulated water in the mountainous region flows into the reservoirs. Part of the water is utilized for the irrigation district. If the available storage of reservoir at the end of time period exceeds total effective capacity, the overflow happens. The 0-1 type integer variables are introduced into the model to decide the overflow of the reservoir, 1 for overflow from reservoir occurring and 0 for not occurring.  $M$  is a fixed bigger number:

$$\begin{aligned} b_t^k &\leq \frac{V_t^k}{C^k}, \\ O_t^k - b_t^k \times M &\leq 0. \end{aligned} \quad (4)$$

Reservoir capacity constraint: the available storage of reservoir is less than the effective capacity of reservoir:

$$V_t^k \leq C^k. \quad (5)$$

In real-world practical problem, we allow proper violations. The constraint is considered as uncertain inputs. A risk of violating may lead to higher benefit and more reasonable management strategy. It is often difficult to define the precise boundary of the constraint due to the fuzzy decision. With reference to Guo and Huang [21], the constraint is shown by the following:

$$\Pr(V_t^k \leq C^k) \geq \bar{\delta}^k. \quad (6)$$

Then, we have

$$\tilde{I}V_t^k \leq C^{k(\bar{p}_k)}, \quad (7)$$

where  $C^{k(\bar{p}_k)} = F_k^{-1}(\bar{p}_k)$  is given the cumulative distribution function of  $C^k$  and the probability of violating constraint  $k(\bar{p}_k)$ .  $\bar{\delta}^k$  is fuzzy tolerance measures ( $0 \leq \bar{\delta}^k \leq 1$ ,  $k = 1, 2, \dots, K$ ), and  $\bar{\delta}^k = 1 - \bar{p}_k$ .

Assume that the fuzzy coefficients are considered trapezoidal fuzzy sets. Thus,  $\tilde{I} = (\underline{1}, 1, \bar{1}) = (0.8, 1.0, 1.2)$ , indicating that the risk level of the reservoir storage is represented as fuzzy uncertainty. When the lower bound of the coefficient is calculated, reservoir storage water was at a high risk level:

$$\begin{aligned} \bar{p}_k &= (\underline{p}_k, p_{k0}, \bar{p}_k) = (1 - \bar{\delta}^k, 1 - \delta^{k0}, 1 - \underline{\delta}^k), \\ \bar{p}_k &= (1 - 0.95, 1 - 0.8, 1 - 0.6) = (0.05, 0.2, 0.4). \end{aligned} \quad (8)$$

It meant that the risk level of the reservoir allowable release water distributed as fuzzy stochastic uncertainty. Utilizing  $\alpha$ -cut technique, fuzzy parameter under each  $\alpha$ -cut level can be included within a closed interval. And it is expressed as necessity of dominance (ND) solutions. Consider

$$((1 - \alpha)\underline{1} + \alpha)V_t^k \leq C^{k((1-\alpha)\underline{p}_k + \alpha p_{k0})}, \quad (9)$$

$$(0.8 + 0.2\alpha)V_t^k \leq C^{k((1-\alpha)0.05 + \alpha 0.2)}. \quad (10)$$

In order to ensure sustainable utilization of reservoir, the available storage of reservoir at the ending time period is requested not to be less than the beginning time period:

$$V_n^k - V_0^k \geq 0 \quad k = 1, 2, \dots, K. \quad (11)$$

Water consumption in the irrigation district consists of agricultural water and nonagricultural water including domestic and industrial water. According to the irrigation district population, livestock, and industrial production, nonagricultural water including water conveyance loss can be estimated.

Multiplying water withdrawal for agriculture by utilization coefficient of irrigation water is irrigation water requirement:

$$\begin{aligned} R_t^k &= AW_t^k + DW_t^k, \\ IR_t^k &= AW_t^k \cdot \eta^k. \end{aligned} \quad (12)$$

By combining the rainfall with water consumption of crops in river irrigation district during growing stages net irrigation water requirement is calculated as follows:

$$IR_t^k = \sum_{n=1}^N (ET_t^{k,n} - P_t^{k,n}) \times A^{k,n}. \quad (13)$$

Subtracting seepage and evaporation loss reservoirs overflow flows into the downstream. According to the measuring data, the river water loss is large in river irrigation district:

$$O_t^k = RL_t^k + RO_t^k. \quad (14)$$

The available water resource is utilized firstly in river irrigation district and water conveyance loss is unavailable, such as seepage and evaporation. Meanwhile seepage loss supplies groundwater to well irrigation district. Recharge of groundwater can be written as

$$GO_t = \sum_{k=1}^K (\alpha E_t^k + \beta RL_t^k + \gamma AW_t^k (1 - \eta^k)) + GI_t. \quad (15)$$

Groundwater exploitation is not taken in river irrigation district. The recharge of groundwater comes from reservoir seepage, river seepage, irrigation seepage, and the lateral groundwater inflow from mountains.  $\alpha$ ,  $\beta$ ,  $\gamma$  are groundwater recharge coefficients, respectively. In well irrigation district, groundwater can be regarded as an entire underground reservoir. Through conjunctive use of underground and surface water, the underground water reservoir is mainly supplied from surface water. Groundwater quantity balance can be shown as follows:

$$\begin{aligned} VG_t &= VG_{t-1} + GO_t \\ &+ \omega \sum_{k=1}^K RO_t^k + \sum_{i=1}^I [\gamma' AW_t^i (1 - \eta^i)] \\ &- \sum_{i=1}^I R_t^i - GWD_t - GWO_t. \end{aligned} \quad (16)$$

$\omega$ ,  $\gamma'$  are groundwater recharge coefficients of rivers and agricultural irrigation in well irrigation district.

Similarly, the groundwater is pumped for agricultural and nonagricultural purpose in well irrigation district. Net irrigation water requirement is calculated as follows:

$$\begin{aligned} R_t^i &= AW_t^i + DW_t^i, \\ IR_t^i &= AW_t^i \cdot \eta^i, \\ IR_t^i &= \sum_{n=1}^N (ET_t^{i,n} - P_t^{i,n}) \times A^{i,n}. \end{aligned} \quad (17)$$

In order to ensure the reasonable exploitation of groundwater, annual exploitation does not exceed allowable amount of groundwater:

$$R_t^i \leq R_{\max}^i. \quad (18)$$

After the allocation of water resources in plain region, the rest of the water consists of two parts: the surplus water of rivers and groundwater. Excess underground water overflows for downstream as springs. The surplus water of rivers is written as follows:

$$RO_t' = (1 - \varepsilon) \sum_{k=1}^K RO_t^k. \quad (19)$$

$\varepsilon$  is river loss coefficient in well irrigation district. The demand of downstream should be satisfied. So the surplus water should be more than the minimum ecological water demand:

$$RO_t' + GWD_t \geq W_{\min}. \quad (20)$$

The model reflects the characteristics of water resources repetitive transformation in typical inland rivers irrigation system. Multiperiod reservoirs operation and multicrop irrigation optimization is reflected under water allocation and conjunctive use of ground and surface water.

### 3. Case Study

Shiyang River Basin (101°41' ~104°16'E, 36°29' ~39°27'N) is located in arid and semiarid region in Gansu province, northwest of China, which is a typical inland river basin in Hexi Corridor with an annual precipitation of 150–300 mm and potential evaporation of 1200–2000 mm. Water resources in the basin are scarce and have been overused so that a series of ecological environment problems occurred. As shown in Figure 2, the watershed can be divided into three separate river systems according to hydrogeological units: Dajing River, six rivers, and Xida River. In the six rivers system, there are two main basins, Wuwei and Minqin basins. Wuwei Basin was selected as the study area to illustrate the monthly reservoirs operation for multicrop irrigation optimization model under dual uncertainties.

The major water supply of the study area originates from the southern part of the Qilian Mountain and there are six tributaries of the Shiyang River, that is, the Gulang, Huangyang, Zamu, Jinta, Xiyang, and Donghe rivers. Some reservoirs are built to regulate water resources in the mountain pass of the rivers except Zamu River. There are six river irrigation districts corresponding to the six rivers, respectively: Gulang (GL), Huangyang (HY), Zamu (ZM), Jinta (JT), Xiyang (XY), and Donghe (DH) irrigation districts which are located in the south of Wuwei Basin. The available water resource is utilized in river irrigation districts and flows into the northern well irrigation districts. There are four well irrigation districts in the north of the basin: Qingyuan (QY), Jingyang (JY), Yongchang (YC), and Qinghe (QH) irrigation districts. The surplus water resources flow into the downstream Minqin Basin.

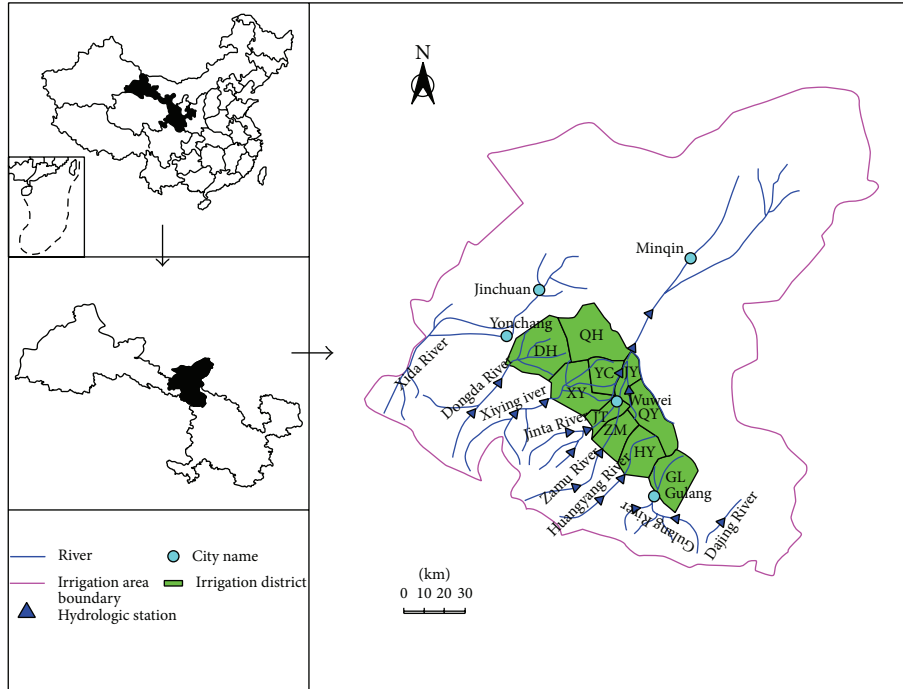


FIGURE 2: The study area.

The dynamic transformation of water resources in river basin complicates the water cycle process. The extensive agriculture development and improper water resources allocation lead to environmental deterioration. The research of Shiyang River Basin water resources transformation was significant to provide decision support for local irrigation managements and agricultural producers.

Because of lower precipitation and higher evaporation, runoff generation is different in Wuwei Basin. The basic water demand of crop growth may not be met. Mountainous runoff is the main source for the crop irrigation. Figure 3 shows the comparison of precipitation and reference crop evapotranspiration ( $ET_0$ ).  $ET_0$  is only related to local meteorological conditions.  $ET_0$  and crop coefficients will be adapted to estimate crop water requirement which is the foundation of irrigation water management. Long-term average annual precipitation is 176 mm while long-term average annual  $ET_0$  is 1008 mm: however, crop water requirement is larger than  $ET_0$ .

As mentioned above, mountainous runoff allocation is a critical factor for entire irrigation districts benefits. Runoff statistical study is used to analyze the data from 1955 to 2009 and the six rivers monthly runoff of 2000 ( $P = 50\%$ ) as shown in Table 1 is selected as the model inflow data.

The reservoirs total effective storages in the mountainous pass of rivers are 14520, 56440, 16260, 24000, and 80000  $\times 10^3 m^3$  corresponding to Gulang, Huangyang, Jinta, Xiyang, and Donghe. The annual losses of the reservoirs are approximately 900, 3300, 1000, 3300, and 2400  $\times 10^3 m^3$ , respectively. In the model, the reservoir is not built on Zamu river, when  $k = 4$ ,  $V_t^k$  and  $E_t^k$  is equal to zero. Beside irrigation district water withdrawal the mountainous runoff flows into

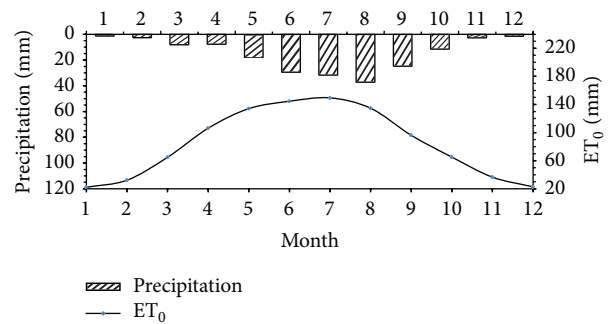


FIGURE 3: The comparison of precipitation and  $ET_0$  of the study area.

the downstream river. The balance equation is rewritten as follows:

$$I_t^k = R_t^k + O_t^k \tag{21}$$

Irrigation district water withdrawal covers agricultural and nonagricultural purposes, and crop irrigation water is the majority of the agricultural water. The main planting crops in these irrigation districts are wheat, maize, potato, flax, and melon. Growing periods of main crops last from March to September. Irrigated crop area of each irrigation district is shown in Table 2.

The present irrigation method is a traditional model that manages surface irrigation to meet the high yield crop irrigation water requirement which leads to unreasonable water allocation between upstream and downstream users. Because of the scarcity of water resources, deficit irrigation is necessary in the study area. The Jensen model has been

TABLE 1: The monthly runoff of the six rivers in 2000 ( $P = 50\%$ ).

River index	Monthly runoff (m <sup>3</sup> /s)											
	Jan.	Feb.	Mar.	Apr.	May	Jun.	Jul.	Aug.	Sep.	Oct.	Nov.	Dec.
Gulang	0.52	0.88	0.97	1.81	3.09	2.25	3.12	5.06	5.05	2.74	1.83	1.13
Huangyang	1.46	1.29	1.90	2.84	3.05	5.05	2.46	9.95	9.88	2.97	1.86	1.90
Zamu	0.93	0.73	1.99	4.59	8.05	14.60	8.83	17.10	16.20	7.64	3.16	2.08
Jinta	0.54	0.38	0.61	1.07	2.99	13.30	7.84	10.60	6.89	2.46	0.90	1.01
Xiyang	1.38	1.08	2.57	4.94	11.70	19.30	18.10	25.00	21.20	7.25	3.27	2.79
Donghe	3.78	3.80	4.47	6.08	10.32	17.41	15.41	18.55	14.30	6.93	5.03	3.86

TABLE 2: The irrigated crop area of each irrigation district.

Irrigation district index	Irrigated crop area (hm <sup>2</sup> )				
	Wheat	Maize	Potato	Flax	Melon
GL	4242.41	1288.71	1523.88	206.95	103.47
HY	8047.64	2444.63	2890.73	392.57	196.28
ZM	6804.69	2067.06	2444.26	331.94	165.97
JT	4714.45	1432.11	1693.44	229.97	114.99
XY	13526.99	4109.09	4858.92	659.85	329.93
DH	12303.28	3737.36	4419.36	600.16	300.08
QY	5357.88	1627.56	1924.56	261.36	130.68
JY	3689.18	1120.66	1325.16	179.96	89.98
YC	5039.17	1530.75	1810.08	245.81	122.91
QH	6037.39	1833.97	2168.64	294.51	147.25

more widely adopted for deficit irrigation water production function which is a crop production stage water consumption model and can be used to calculate staged irrigation water. Crop yield calculation method by Jensen model has the following expression:

$$Y = Y_{\max} \prod_{i=1}^n \left( \frac{ET_i}{ET_{mi}} \right)^{\lambda_i} \quad (22)$$

$\lambda_i$  is sensitivity index of crop to water deficit.  $ET_i$  and  $ET_{mi}$  are staged actual evapotranspiration and maximum evapotranspiration.  $Y_{\max}$  is maximum crop yield under sufficient irrigation water condition and it can be obtained by water production function in the whole stages. The previous researchers have provided a large number of experimental data and fitted water production function to estimate  $Y_{\max}$ , which usually is shown as the following:

$$Y = a_1 + b_1 ET + c_1 ET^2 \quad (23)$$

$a_1, b_1, c_1$  are empirical coefficients fixed by experimental data. The calculation results of  $Y_{\max}$  are 8097.82, 11219.43, 26978.29, 2268.16, and 3057.46 kg/hm<sup>2</sup> corresponding to the main crop.

For reservoirs operation and irrigation management, crop sensitivity to water deficit in irrigation interval is more effective than in growth stage. Kipkorir and Raes [25] have applied Jensen model in irrigation interval. Tsakiris [26] provides a method of estimating crop sensitivity to water deficiency at given time intervals. However, relevant study

is not reported in the study area. The Jensen model is fitted in monthly interval in keeping up with the optimization model as shown in Table 3. Effective rainfall in example year is 5.7 mm, 0 mm, 62 mm, 9.3 mm, 33.3 mm, and 18.6 mm corresponding to the period from April to September.

Annual nonagricultural water consumption in the model is estimated through the irrigation district population, livestock, and industrial production which are shown in Table 4.

Parameter determination is important for the optimization results. According to *Comprehensive Planning of Shiyang River Basin (2007)*, utilization coefficient of irrigation water of river irrigation area is 0.65 in Gulang irrigation district, 0.58 in Xiyang irrigation district, and 0.54 in Huangyang, Zamu, Jinta, and Donghe irrigation districts; utilization coefficient of irrigation water of well irrigation area is 0.6.

The water of each tributary flows together into Shiyang River minus evaporation and leakage loss. River flow in northern Wuwei Basin is low due to severe leakage. According to the investigation, we take 0.667 for the value of leakage rate.

Complement between the surface water and underground water is obvious in the basin.

Groundwater is not pumped in southern Wuwei Basin. Considering the underground aquifer as a whole groundwater reservoir, sources of its supply are reservoir seepage, river seepage, irrigation seepage, and the lateral groundwater inflow. Under low rainfall and deep groundwater level, groundwater is scarcely recharged by the rainfall according to Ma et al. [27]. Rainfall seepage is ignored in the model.

TABLE 3: The fitted value of  $ET_m$  (mm) and  $\lambda$ .

Crop index		Month						
		Mar.	Apr.	May.	Jun.	Jul.	Aug.	Sep.
Wheat	$ET_m$	23.54	119.29	176.03	219.21	153.23	0.00	0.00
	$\lambda$	0.06	0.07	0.15	0.08	0.01	0.00	0.00
Maize	$ET_m$	0.00	27.82	70.76	112.55	171.92	129.06	23.03
	$\lambda$	0.00	0.04	0.12	0.20	0.31	0.22	0.03
Potato	$ET_m$	0.00	16.87	61.56	129.22	118.91	101.47	11.32
	$\lambda$	0.00	0.01	0.03	0.07	0.06	0.05	0.00
Flax	$ET_m$	0.00	18.49	105.02	150.06	146.19	77.90	0.00
	$\lambda$	0.00	0.12	0.27	0.36	0.35	0.09	0.00
Melon	$ET_m$	0.00	0.00	51.85	62.84	125.85	68.48	21.65
	$\lambda$	0.00	0.00	0.06	0.07	0.15	0.08	0.01

TABLE 4: Nonagricultural water of irrigation districts ( $10^6 m^3$ ).

Irrigation district index	GL	HY	ZM	JT	XY	DH	QY	JY	YC	QH
Nonagricultural water	7.74	9.30	16.71	8.39	6.20	1.53	4.49	4.86	7.07	3.03

The quantity of groundwater supply is calculated by recharged coefficients. Qu et al. [28] estimate reservoir seepage and river seepage recharged coefficients as 0.85 and irrigation seepage as 0.8.

Calculation results of Yao et al. [29] show that the lateral groundwater inflow is  $136 \times 10^6 m^3$  and the lateral groundwater outflow is  $254 \times 10^6 m^3$ .

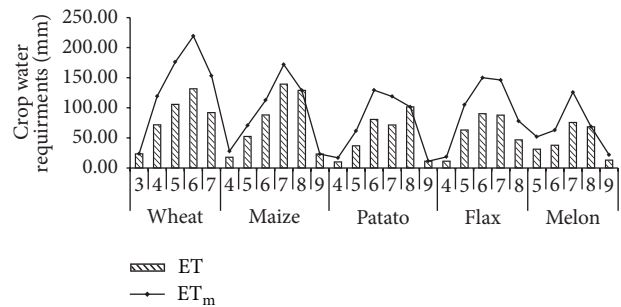
To ensure reasonable water allocation between upstream and downstream users, according to local planning, the available groundwater mining is controlled below  $319 \times 10^6 m^3$  and minimum downstream water requirement is not less than  $218 \times 10^6 m^3$  under local planning requirements.

### 4. Results Analysis

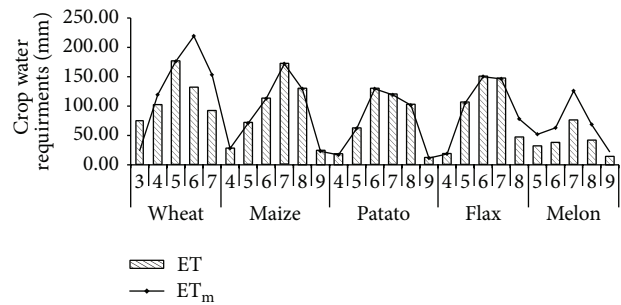
**4.1. Multicrop Deficit Irrigation Management.** Deficit irrigation could result in the lower crop yields and reduce the net benefits of the irrigation district. However, it is unavoidable because of water resources shortage. The relation between sensitivity of water deficit and crop water use efficiency was studied through the use of Jensen model.

According to the calculation results of optimal decision-making model, deficit irrigation proportions of the five crops in the whole growth stage in river irrigation district are 0.61, 0.84, 0.71, 0.60, and 0.68, respectively, and in well irrigation district the values are 0.76, 1.00, 1.00, 0.94, and 0.60. It indicates that deficit irrigation should be adopted primarily in river irrigation district.

The optimization model can reach crop water requirement in each irrigation interval. As shown in Figure 4, the priority deficit irrigation crops are melon and wheat in well irrigation district.  $ET$  is monthly optimal crop water requirements and  $ET_m$  is monthly potential crop water requirements. The results can provide multiperiod deficit irrigation management for the agricultural producers.



(a) Optimal crop water requirements in river irrigation



(b) Optimal crop water requirements in well irrigation

FIGURE 4: Results of crop deficit irrigation management.

**4.2. Monthly Reservoirs Operation.** In the monthly multicrop irrigation system, water resource is mainly obtained from the mountain river. Reservoirs regulation is significant for the water utilization. Reservoirs release and overflow management can be determined by the model. The nonagricultural water demand of each irrigation district among time periods is even, but the primary part of agriculture water demand depends on the crop area and growing periods of crop.

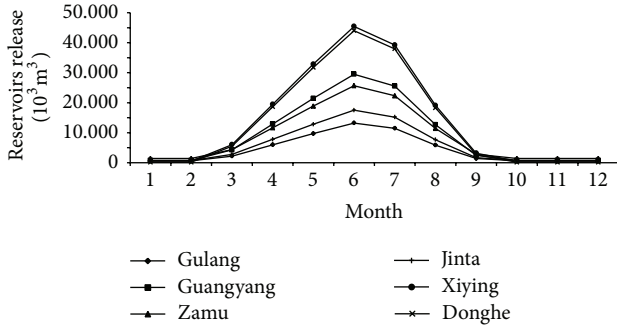


FIGURE 5: Real-time multireservoirs release.

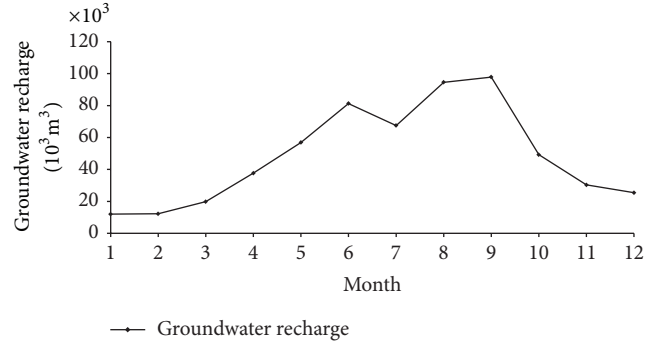


FIGURE 7: Monthly groundwater recharge in the basin.

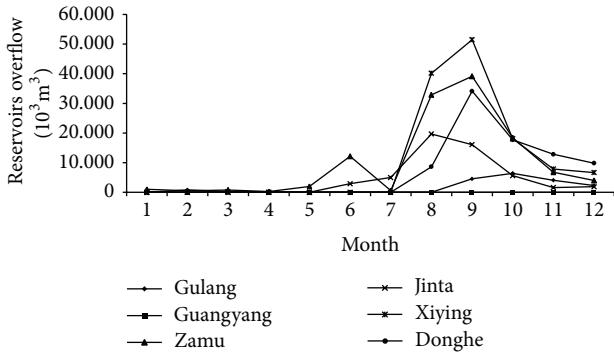


FIGURE 6: Real-time reservoirs overflow.

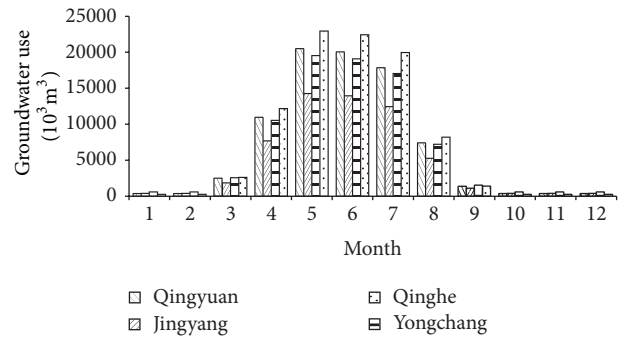


FIGURE 8: Monthly groundwater use in well irrigation district.

Total annual runoff of the six rivers is  $1145.9 \times 10^6 \text{ m}^3$  and real-time multireservoirs release can be shown in Figure 5. Agricultural water consumption takes most rates in water consumption structure. The maximum water demand occurs in June. Water withdrawal is closely related to irrigation area of each reservoir water-supply zone. The total annual water withdrawal from reservoir is  $665.74 \times 10^6 \text{ m}^3$ .

To avoid the occurrence of shortage and overflow at the same time period, overflow would not happen unless the reservoir is full storage. Figure 6 shows the real-time reservoirs overflow. Overflow occurred in the period from August to October when irrigation water demand decreased and monthly runoff was still high. The annual reservoirs overflow is  $154.51 \times 10^6 \text{ m}^3$ . It indicates that mountainous runoff is utilized by river irrigation district. The maximum annual overflow is from Xiyang Reservoir with  $124.24 \times 10^6 \text{ m}^3$ , and the minimum overflow is from Huangyang Reservoir with  $0.21 \times 10^6 \text{ m}^3$ .

**4.3. Recharge Relationship between Surface Water and Underground Water.** Wuwei Basin is a typical inland river basin; conjunctive use of surface water and underground water is necessary to the arid irrigation area. To be more efficient in the groundwater management, managers should try to realize recharge relationship between surface water and underground water and determine the available underground water.

In the model, underground water is pumped in the well irrigation district and supply from reservoir seepage,

river seepage, irrigation seepage, and the lateral groundwater inflow in the southern basin. Figure 7 shows the monthly groundwater recharge of the basin.

As a result of conjunctive use of surface water and groundwater optimization model, the groundwater use in each well irrigation district can be listed in Figure 8, in order to provide decision support for local irrigation management. The major groundwater exploitation is from April to August. Groundwater quantity balance is considered in the model. Groundwater exploitation is less than groundwater recharge, and annual exploitation does not exceed allowable amount of groundwater.

**4.4. Fuzzy Stochastic Uncertainty.** In real-world practical problem, reservoir capacity is not considered as strictly determinate numbers, and the failure of the constraint is allowed. So the chance-constraint programming is considered to analyse the uncertain constraint of the failure of the limitation of the total reservoir capacity. Proper violation under different risks is studied in the model, which provides selectable management strategies for the decision makers. Necessity of dominance (ND) solutions under three  $\alpha$ -cut levels are calculated.

As shown in Figure 9, the lower  $\alpha$ -cut level leads to higher total crop yield. It means that reservoir capacity constraint is loose under lower  $\alpha$ -cut level and higher violation risk leads to larger system benefit.

In this model, the right hand of the reservoir capacity constraint is allowed to change under the given probabilities.

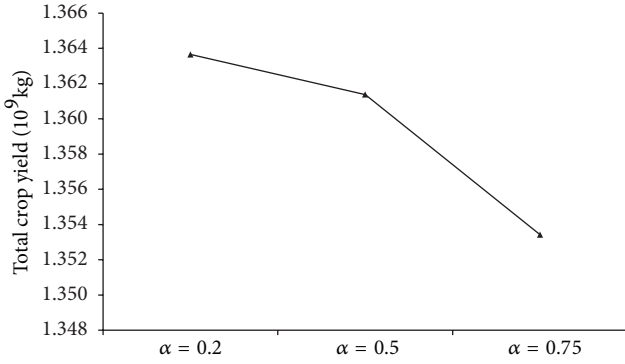


FIGURE 9: Total crop yield of the entire irrigation districts under different  $\alpha$ -cut levels.

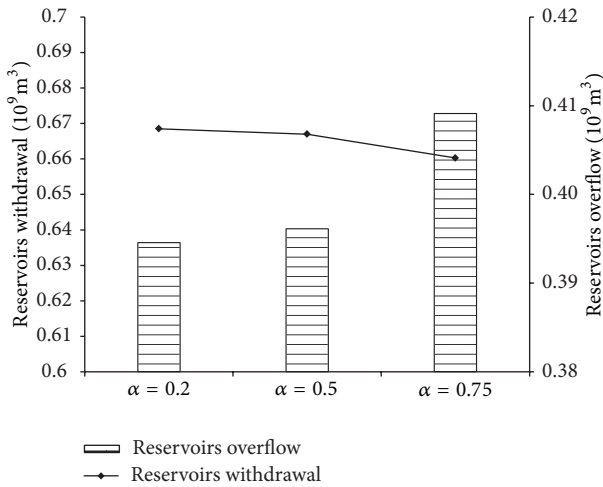


FIGURE 10: Reservoirs withdrawal and overflow under different  $\alpha$ -cut levels.

As shown in Figure 10, water supply from reservoirs is  $0.668 \times 10^9$  m<sup>3</sup> ( $\alpha = 0.2$ ) and the corresponding figure is  $0.660 \times 10^9$  m<sup>3</sup> ( $\alpha = 0.75$ ), while water overflow from reservoirs experiences the opposite change.

### 5. Conclusions

In this study, a multicrop irrigation water resources optimization model based on Jensen water production function model for real-time reservoirs operation is proposed. The objective of the model is to achieve the maximum benefit of irrigation areas, considering water stress level of crops and the dynamic characteristic in the irrigation water resources optimal allocation system. The proposed model can provide decision makers with different irrigation water optimal staged allocation schedules (conjunctive of surface water and groundwater) of upstream and downstream and agricultural and nonagricultural water resources, and so forth.

Considering the uncertainties of irrigation water resources management system, fuzzy chance-constraint programming is introduced to the developed model. Necessity of dominance (ND) is adopted to solve fuzzy

chance-constraint program, with the membership function of both fuzzy parameters and probabilities being a triangular fuzzy membership function in this study.

The developed model has been applied to Shiyang River Basin, China, to demonstrate the applicability of the developed model. The limited water resources supply, that is, monthly runoff and effective precipitation, the conjunctive use of surface water and groundwater, and the ecological water demand of downstream are considered. As a result, the irrigation water resources optimal allocation schedules for multiple crops of multiple periods of reservoirs operation under different  $\alpha$ -cut levels are obtained and analyzed. Such results are valuable for local irrigation managements and agricultural producers. Further study will focus on field measurement experiments of some parameters, for example, utilization coefficient of irrigation water, seepage recharged coefficients, and river leakage rate to make the developed model have more practical value.

### Nomenclature

- $A^{k,n}$ : Irrigated crop area
- $b_t^k$ : 0-1 type integer variables to decide the overflow of the reservoir
- $C^k$ : Effective capacity of reservoir
- $E_t^k$ : Reservoir losses
- $ET_t^{k,n}$ : Actual crop evapotranspiration
- $ET_{t,max}^n$ : Potential maximum crop evapotranspiration
- $\lambda_t^n$ : Sensitive index of the crop to water stress during the stage
- $F$ : Expected crop yields of the entire irrigation districts
- $GI_t$ : Lateral groundwater inflow from mountains
- $GO_t$ : Recharge of groundwater from river irrigation district
- $GWD_t$ : Groundwater supplementary amount for downstream
- $GWO_t$ : Lateral groundwater outflow from well irrigation district
- $i$ : Well irrigation district index
- $I_t^k$ : Inflow to the reservoir in time period  $t$
- $IR_t^k$ : Net irrigation water requirement
- $AW_t^k$ : Agricultural water requirement in river irrigation district
- $AW_t^i$ : Agricultural water requirement in well irrigation district
- $DW_t^k$ : Nonagricultural water requirement in river irrigation district
- $DW_t^i$ : Agricultural water requirement in well irrigation district
- $k$ : River irrigation district index
- $n$ : Crop index
- $O_t^k$ : Reservoir overflow
- $P_t^{k,n}$ : Effective precipitation
- $R_{max}$ : Annual allowable amount of groundwater

$W_{\min}$ : Annual downstream minimum ecological water demand  
 $R_t^k$ : Water consumption in the irrigation district  
 $RL_t^k$ : Loss of river  
 $RO_t^k$ : Remaining flow of the rivers  
 $t$ : Time period index  
 $V_{t-1}^k$ : Reservoir storage at the beginning of time period  $t$   
 $V_t^k$ : Reservoir storage at the end of time period  $t$   
 $Y_{\max}^n$ : Crop maximum yield of crop  $n$  under the condition of full irrigation method  
 $VG_t$ : Storage capacity of groundwater  
 $\eta^k$ : Utilization coefficient of irrigation water.

### Conflict of Interests

The authors declare that there is no conflict of interests regarding the publication of this paper.

### Acknowledgments

The research was sponsored by the National Natural Science Foundation of China (nos. 41271536 and 51321001) and National High Technology Research and Development Program of China (863 Program) (nO. 2013AA102904).

### References

- [1] P. S. Ashofteh, O. B. Haddad, and M. A. Mariño, "Climate change impact on reservoir performance indexes in agricultural water supply," *Journal of Irrigation and Drainage Engineering*, vol. 139, no. 2, pp. 85–97, 2012.
- [2] M. Moradi-Jalal, O. Bozorg Haddad, B. W. Karney, and M. A. Mariño, "Reservoir operation in assigning optimal multi-crop irrigation areas," *Agricultural Water Management*, vol. 90, no. 1-2, pp. 149–159, 2007.
- [3] W. S. Butcher, "Stochastic dynamic programming for optimum reservoir operation," *Water Resources Bulletin*, vol. 7, no. 1, pp. 115–123, 1971.
- [4] J. R. Stedinger, B. F. Sule, and D. P. Loucks, "Stochastic dynamic programming models for reservoir operation optimization," *Water Resources Research*, vol. 20, no. 11, pp. 1499–1505, 1984.
- [5] A. Dos Santos Teixeira and M. A. Mariño, "Coupled reservoir operation-irrigation scheduling by dynamic programming," *Journal of Irrigation and Drainage Engineering*, vol. 128, no. 2, pp. 63–73, 2002.
- [6] S. Vedula and P. P. Mujumdar, "Optimal reservoir operation for irrigation of multiple crops," *Water Resources Research*, vol. 28, no. 1, pp. 1–9, 1992.
- [7] S. Vedula and D. N. Kumar, "An integrated model for optimal reservoir operation for irrigation of multiple crops," *Water Resources Research*, vol. 32, no. 4, pp. 1101–1108, 1996.
- [8] P. P. Mujumdar and T. S. V. Ramesh, "Real-time reservoir operation for irrigation," *Water Resources Research*, vol. 33, no. 5, pp. 1157–1164, 1997.
- [9] A. Evers, R. Elliott, and E. Stevens, "Integrated decision making for reservoir, irrigation, and crop management," *Agricultural Systems*, vol. 58, no. 4, pp. 529–554, 1998.
- [10] P. E. Georgiou and D. M. Papamichail, "Optimization model of an irrigation reservoir for water allocation and crop planning under various weather conditions," *Irrigation Science*, vol. 26, no. 6, pp. 487–504, 2008.
- [11] A. S. Prasad, N. Umamahesh, and G. Viswanath, "Short-term real-time reservoir operation for irrigation," *Journal of Water Resources Planning and Management*, vol. 139, no. 2, pp. 149–158, 2012.
- [12] A. Afshar, M. A. Marino, and A. Abrishamchi, "Reservoir planning for irrigation district," *Journal of Water Resources Planning and Management*, vol. 117, no. 1, pp. 74–85, 1991.
- [13] S. Vedula, P. P. Mujumdar, and G. Chandra Sekhar, "Conjunctive use modeling for multicrop irrigation," *Agricultural Water Management*, vol. 73, no. 3, pp. 193–221, 2005.
- [14] E. G. Reichard, "Groundwater-surface water management with stochastic surface water supplies: a simulation optimization approach," *Water Resources Research*, vol. 31, no. 11, pp. 2845–2865, 1995.
- [15] M. Karamouz and H. V. Vasiliadis, "Bayesian stochastic optimization of reservoir operation using uncertain forecasts," *Water Resources Research*, vol. 28, no. 5, pp. 1221–1232, 1992.
- [16] R. S. V. Teegavarapu and S. P. Simonovic, "Modeling uncertainty in reservoir loss functions using fuzzy sets," *Water Resources Research*, vol. 35, no. 9, pp. 2815–2823, 1999.
- [17] X. Li, S. Guo, P. Liu, and G. Chen, "Dynamic control of flood limited water level for reservoir operation by considering inflow uncertainty," *Journal of Hydrology*, vol. 391, no. 1-2, pp. 124–132, 2010.
- [18] F.-J. Chang, S.-C. Hui, and Y.-C. Chen, "Reservoir operation using grey fuzzy stochastic dynamic programming," *Hydrological Processes*, vol. 16, no. 12, pp. 2395–2408, 2002.
- [19] A. Seifi and K. W. Hipel, "Interior-point method for reservoir operation with stochastic inflows," *Journal of Water Resources Planning and Management*, vol. 127, no. 1, pp. 48–57, 2001.
- [20] M. N. Azaiez, M. Hariga, and I. Al-Harkan, "A chance-constrained multi-period model for a special multi-reservoir system," *Computers and Operations Research*, vol. 32, no. 5, pp. 1337–1351, 2005.
- [21] P. Guo and G. H. Huang, "Two-stage fuzzy chance-constrained programming: application to water resources management under dual uncertainties," *Stochastic Environmental Research and Risk Assessment*, vol. 23, no. 3, pp. 349–359, 2009.
- [22] A. J. Askew, "Chance—constrained dynamic programming and the optimization of water resource systems," *Water Resources Research*, vol. 10, no. 6, pp. 1099–1106, 1974.
- [23] D. Z. Fu, Y. P. Li, and G. H. Huang, "A factorial-based dynamic analysis method for reservoir operation under fuzzy-stochastic uncertainties," *Water Resources Management*, vol. 27, no. 13, pp. 4591–4610, 2013.
- [24] M. E. Jensen, "Water consumption by agricultural plants," *Water Deficits and Plant Growth*, vol. 2, pp. 1–22, 1968.
- [25] E. C. Kipkorir and D. Raes, "Transformation of yield response factor into Jensen's sensitivity index," *Irrigation and Drainage Systems*, vol. 16, no. 1, pp. 47–52, 2002.
- [26] G. P. Tsakiris, "A method for applying crop sensitivity factors in irrigation scheduling," *Agricultural Water Management*, vol. 5, no. 4, pp. 335–343, 1982.

- [27] J. Ma, Z. Ding, W. M. Edmunds, J. B. Gates, and T. Huang, "Limits to recharge of groundwater from Tibetan plateau to the Gobi desert, implications for water management in the mountain front," *Journal of Hydrology*, vol. 364, no. 1-2, pp. 128–141, 2009.
- [28] Y. Qu, S. Ma, and W. Qu, "water resources transformation and development and use model in the arid area of northwest china," *Journal of Desert Research*, vol. 18, no. 4, pp. 299–307, 1988.
- [29] L. Yao, S. Feng, X. Mao, Z. Huo, S. Kang, and D. A. Barry, "Coupled effects of canal lining and multi-layered soil structure on canal seepage and soil water dynamics," *Journal of Hydrology*, vol. 430-431, pp. 91–102, 2012.

## Research Article

# Spatial and Temporal Variation of Annual Precipitation in a River of the Loess Plateau in China

**Cui Shen and Huang Qiang**

*State Key Laboratory of Eco-Hydraulic Engineering in Shaanxi, School of Water Resources and Hydropower, Xi'an University of Technology, Xi'an 710048, China*

Correspondence should be addressed to Huang Qiang; [wresh@mail.xaut.edu.cn](mailto:wresh@mail.xaut.edu.cn)

Received 9 October 2013; Accepted 20 December 2013; Published 19 February 2014

Academic Editor: G. H. Huang

Copyright © 2014 C. Shen and H. Qiang. This is an open access article distributed under the Creative Commons Attribution License, which permits unrestricted use, distribution, and reproduction in any medium, provided the original work is properly cited.

Empirical orthogonal function (EOF) decomposition and geostatistical (semivariogram) analysis are used to analyze the spatial and temporal patterns of annual precipitation in the Weihe basin based on the data from 1960 to 2011 at 30 national meteorological stations within and surrounding the Weihe basin area of the Loess Plateau in China. Then the Mann-Kendall method is used to discriminate the variation points of precipitation series at each station. The results show that, during the study period, there was an overall reduction in annual precipitation across the basin and there were two spatial patterns: increase in the northwest, decrease in southeast and increase in the west, decrease in east. Variation points in the annual precipitation series at each meteorological station in the basin were detected, and they occur earliest in the southeast and downstream, then progressively later in the northwest and upstream areas. These variations were most frequent during the 1970s and 1980s. The findings have significant implications for the variations research of runoff in the basin and formulate robust strategies to adapt to climate change and mitigate its effects.

## 1. Introduction

Climate change is causing increasing concerns globally. Precipitation is a key climatic parameter that strongly affects runoff and diverse hydrological variables. Thus, knowledge of precipitation patterns is essential for characterizing past and present climate changes, predicting future changes, and evaluating their effects. Several studies have shown that annual precipitation in China is declining [1, 2], while the frequency of extreme weather events is increasing [3]. The changes in precipitation are closely related to changes in runoff and thus are affecting ecosystems and restricting socioeconomic development [4]. In the Weihe basin, located in the eastern part of northwest China, there are fragile ecosystems and frequent natural disasters. Thus, analysis of the spatial and temporal variation in precipitation in the basin is essential for understanding changes in runoff and the associated socioeconomic and ecological impact in the region and for formulating robust, cost-effective strategies to adapt to and mitigate the effects of climate change.

## 2. Study Area

Weihe River of the Loess Plateau in China originates in the north of Niaoshu mountain in Weiyuan county of Gansu province, emptying into the Yellow River at Tongguan county of Shaanxi province, which has a drainage area of 135000 km<sup>2</sup> and flows 818 km eastwards through 84 counties and three provinces across the guanzhong basin [5]. The Weihe basin spans longitude and latitude ranges of 103.5° ~110.5° E and 5° ~37.5° N, respectively, and the two main tributaries are the rivers Jinghe and Beiluohe [6]. The southeast part of the basin is located in the continental monsoon zone, while the northwest part is in the transitional zone between arid and humid regions, controlled by West Pacific subtropical high and Mongolia High, the basin is drought in spring, rainy hot in summer but drought frequent, dry cold in autumn and winter [7]. There are major annual variations in precipitation, which is concentrated in July to October, when about 65% of annual precipitation occurs [8]. The average temperature is -1° to -3°C in the coldest month (January) and 23° ~26°C in the warmest month (July) [9].

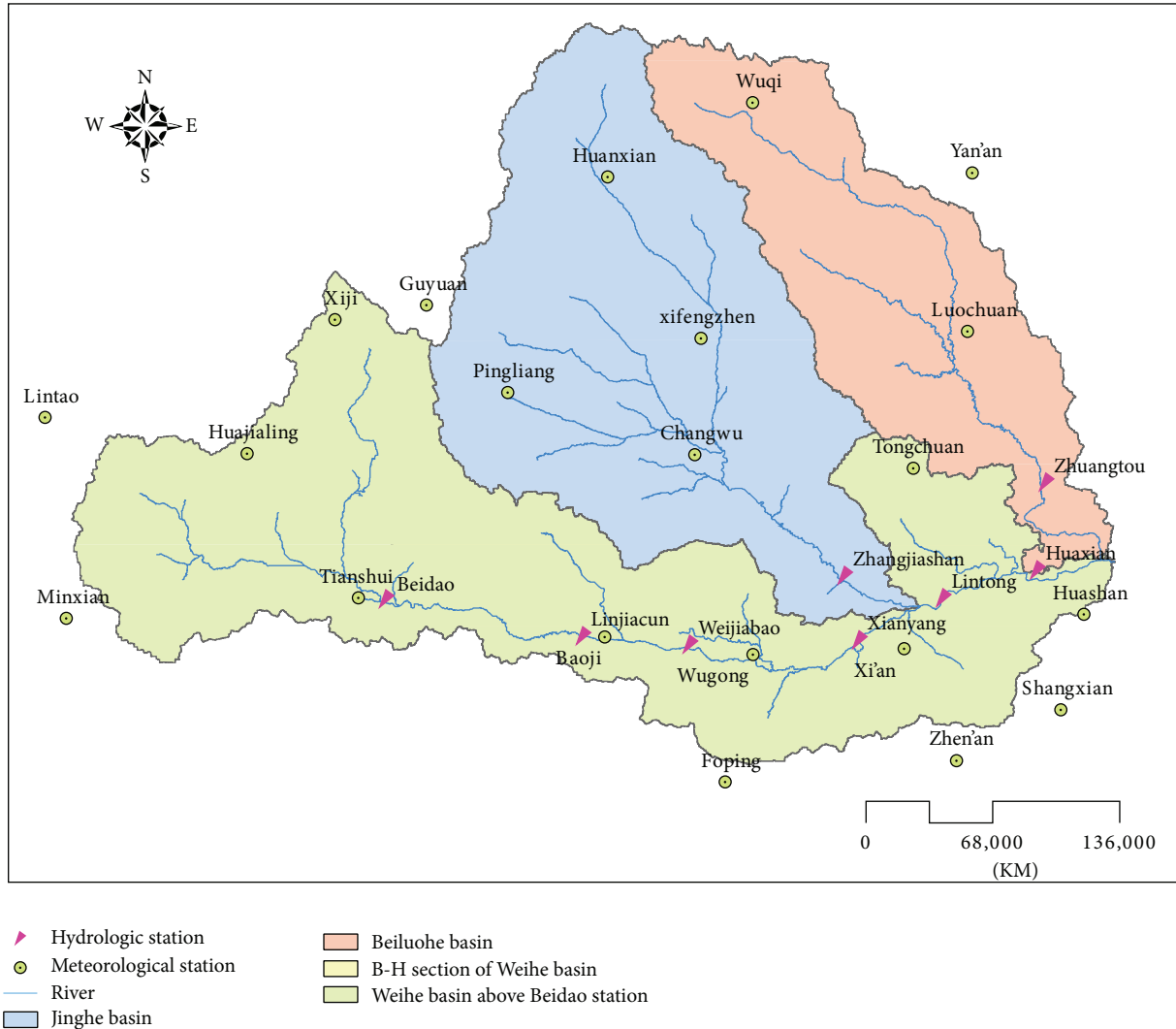


FIGURE 1: Map of the Weihe basin showing the four subbasins and locations of hydrological and meteorological stations.

Climate changes have had marked effects in the Weihe basin. Thus, we have examined changes in annual precipitation in the basin, from 1960 to 2011, in order to elucidate their spatial and temporal patterns, thereby facilitating attempts to formulate effective mitigation strategies. For the purposes of the study, the Weihe basin is divided into four subbasins with distinct hydrological characteristics and control stations: the basin above Beidao station, Jinghe basin, Beiluohe basin, and the Beidao to Huaxian section of the Weihe mainstream. A map showing the areas covered by these subbasins and locations of hydrological and meteorological stations is presented in Figure 1.

### 3. Data Sources and Methodology

**3.1. Data Sources.** The annual precipitation data used in this paper are recorded from 1960 to 2011 at 30 National Standard Stations in the Weihe basin and the surrounding

area obtained from the China Meteorological Data Sharing Service System (<http://cdc.cma.gov.cn/home.do>).

**3.2. Methodology.** First we calculate means in annual precipitation in the Weihe basin by statistical methods and determine trends by regression analysis. Then we use empirical orthogonal function (EOF) decomposition and geostatistical analysis method to analyze spatial and temporal patterns associated with precipitation. Eigenvectors obtained from EOF decomposition are then multiplied by trend vectors in the matrix of the precipitation series to obtain eigenvector fields, thus describing the spatial trends in annual precipitation. Finally, we use the Mann-Kendall (M-K) method to identify variation points in the precipitation series for each station, thereby comprehensively describing the temporal and spatial patterns of annual precipitation in each of the subbasins.

**3.2.1. Regression Analysis.** Regression analysis is applied to analyze the correlation of two variables, which determines relative direction and intensity. In this study, regression analysis is used to get the linear regression of precipitation and time, and the equation is as follows:

$$P = aT + b, \quad (1)$$

where  $P$  is the precipitation,  $T$  is the time, and  $a$  and  $b$  are parameters. If the unit of  $T$  is the year, usually  $a$  is the changing trend of annual precipitation.

**3.2.2. Empirical Orthogonal Function Decomposition.** EOF decomposition involves decomposition of a matrix  $\mathbf{X}$  of data describing the distribution of a variable in both space and time into a spatial function  $\mathbf{V}$  and time function  $\mathbf{T}$  as shown in

$$\mathbf{X} = \mathbf{V}\mathbf{T},$$

$$\mathbf{X} = \begin{bmatrix} x_{11} & \cdots & x_{1j} & \cdots & x_{1n} \\ \vdots & & \vdots & & \vdots \\ x_{i1} & \cdots & x_{ij} & \cdots & x_{in} \\ \vdots & & \vdots & & \vdots \\ x_{m1} & \cdots & x_{mj} & \cdots & x_{mn} \end{bmatrix}, \quad (2)$$

where  $m$  and  $n$  are points in space and time, respectively, and  $x_{ij}$  is the value of the variable at point  $i$  and time  $j$  (here, annual precipitation at station  $i$  in year  $j$ ).

If  $\mathbf{V}$  and  $\mathbf{T}$  are orthogonal,

$$\sum_{i=1}^m v_{ik}v_{il} = 1, \quad \text{when } k = l, \quad (3)$$

$$\sum_{j=1}^n t_{kj}t_{lj} = 0, \quad \text{when } k \neq l.$$

If  $\mathbf{X}$  is an anomaly matrix (reference), multiplying the equation  $\mathbf{X} = \mathbf{V}\mathbf{T}$  by  $\mathbf{X}^T$  gives

$$\mathbf{X}\mathbf{X}^T = \mathbf{V}\mathbf{T}\mathbf{X}^T = \mathbf{V}\mathbf{T}\mathbf{T}^T\mathbf{V}^T = \mathbf{V}\mathbf{\Lambda}\mathbf{V}, \quad (4)$$

where  $\mathbf{\Lambda}$  is a diagonal matrix composed of eigenvalues  $\lambda_i$  of matrix  $\mathbf{X}\mathbf{X}^T$  and

$$\mathbf{T}\mathbf{T}^T = \mathbf{\Lambda}. \quad (5)$$

Due to the characteristics of the eigenvectors,  $\mathbf{V}^T\mathbf{V}$  is a unit matrix, meeting the requirements of orthogonality. Thus, the spatial function matrix  $\mathbf{V}$  can be calculated from eigenvectors of the matrix  $\mathbf{X}\mathbf{X}^T$ .

Here, we multiply the spatial function matrix  $\mathbf{V}$  of annual precipitation in the Weihe basin by the trend vector  $\mathbf{D} = \{d_1, d_2, \dots, d_m\}$ , composed of trends in annual precipitation recorded at each station ( $\mathbf{V}_d = \mathbf{D}\mathbf{V}$ ), thus describing the spatial trends of annual precipitation in the basin.

EOF decomposition was first established in 1902 [10]. It decomposes elements of a set of space-time data into

two functions, one dependent only on time and another dependent only on space, to analyze the spatial structure of element fields [11]. Thus, EOF decomposition is commonly used to analyze spatial and temporal variations in meteorological elements. In contrast, principal component analysis (PCA) is mainly used to find a few independent vectors in a dataset to reduce its dimensionality, thereby simplifying data handling and interpretation. However, the operational steps are basically the same, when the original variables are anomaly data or standardized anomaly data [12]. Hence, we can use the PCA module of SPSS (statistical product and service solution) software for EOF decomposition [13].

EOF decomposition and several variants thereof have been widely applied for analyzing spatial changes in meteorological elements. Notably, EOF decomposition has been used to analyze drought occurrence in both time and space in Korea [14]. It has also been applied to establish contributions of annual evaporation, annual precipitation, and both warm- and cold-season precipitation to the annual runoff of rivers in an arid zone to obtain quantitative estimates of the effects of climatic factors on reconstructions of annual runoff series in an ungauged area [15]. A data-interpolating empirical orthogonal function (DINEOF) has been used to analyze distributions of sea surface temperatures in a study demonstrating that DINEOF decomposition can be highly effective, even when very high proportions of data are missing [16]. In addition, rotated empirical orthogonal function (REOF) decomposition has been applied to analyze space-time patterns of groundwater fluctuations in the Choshui River alluvial fan, Taiwan, based on monthly observations of piezometric heads from 66 wells during the period 1997–2002 [17].

**3.2.3. Mann-Kendall Variation Analysis.** The Mann-Kendall test has been widely used for identifying trends in time-series data because it is nonparametric and thus suitable for handling data that are not normally distributed, and it is not sensitive to interference from a few outliers. The Mann-Kendall test can also be used for variation diagnosis, and the calculation method is as follows.

For a time series  $X = \{x_1, x_2, \dots, x_n\}$ , the Mann-Kendall test statistic  $D_\tau$  is given by the following model:

$$D_\tau = \sum_{i=1}^{\tau} R_i \quad (\tau = 2, 3, \dots, i), \quad (6)$$

where

$$R_i = \begin{cases} +1, & x_i > x_j \\ 0, & x_i \leq x_j \end{cases} \quad (j = 1, 2, \dots, i). \quad (7)$$

The sequential statistic  $UF_\tau$  (in which  $UF_1 = 0$ ) is calculated by is

$$UF_\tau = \frac{|D_\tau - E(D_\tau)|}{\sqrt{V(D_\tau)}}, \quad (8)$$

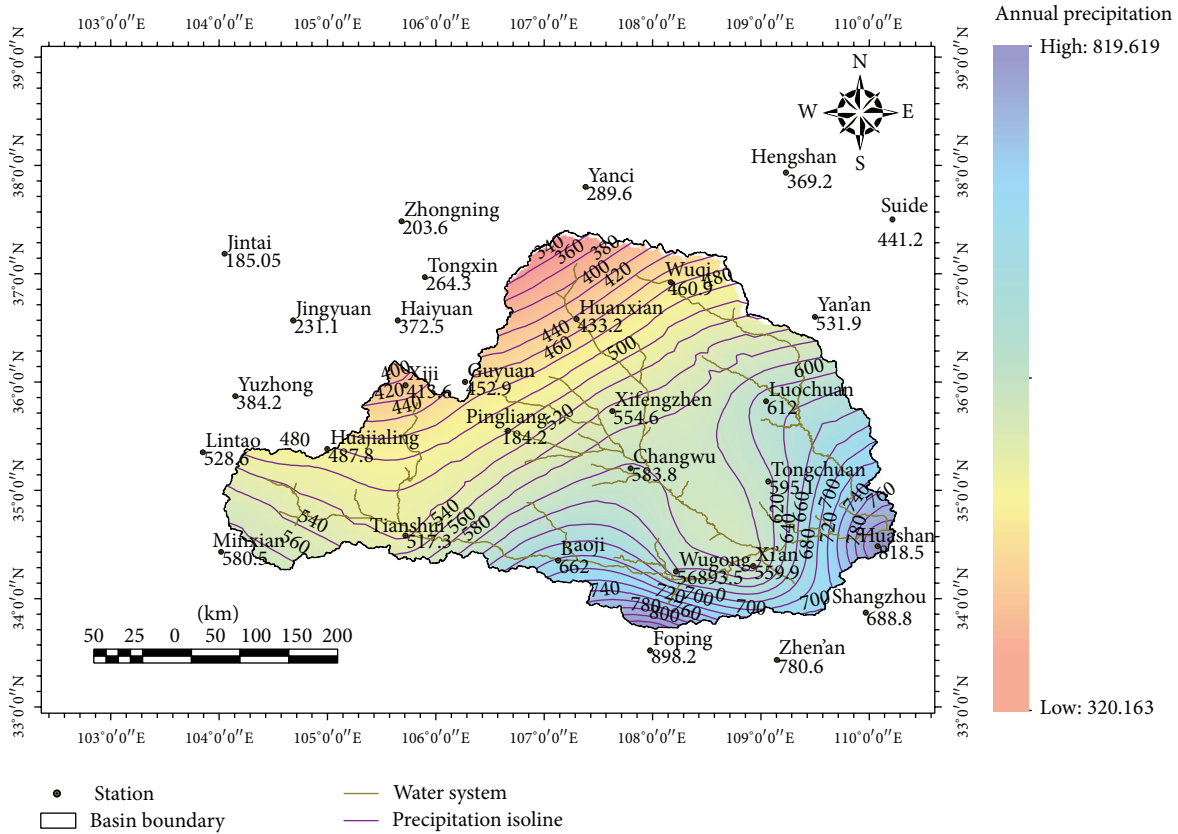


FIGURE 2: Isohyets showing mean annual precipitation in the Weihe basin.

where  $E(D_\tau)$  and  $V(D_\tau)$  are the mean and variance of the series, given, respectively, by

$$E(D_\tau) = \frac{\tau(\tau - 1)}{4}, \tag{9}$$

$$V(D_\tau) = \frac{\tau(\tau - 1)(2\tau + 5)}{72}.$$

Then repeat the calculation with the inversion series  $X' = \{x_n, x_{n-1}, \dots, x_1\}$ , and let  $UB_\tau = -UF_\tau$ , ( $\tau = n, n - 1, \dots, 1$ ). Define the significant level  $\alpha$ , and find out the critical value  $\pm U_{(1-\alpha)/2}$ . If the curves of  $UF_\tau$  and  $UB_\tau$  intersect and the intersections are between the critical line (in this study, the significant level  $\alpha$  is 0.95, and the critical line is  $\pm U_{0.05/2} = \pm 1.96$ ), the time of curve intersections is the starting time of the variation.

Originally published in 1945 [18], it was initially only used to detect trends in sequences. However, subsequent modifications have enabled its use for detecting variation points in various trends [19], and it has been applied in reversed sequence to detect variation points in trends in climate data time series [20]. Since then the method has been widely used to diagnose variation points in hydrological and meteorological data sequences [21, 22]. Notably, the M-K method has been used to determine whether there were positive or negative trends in seven meteorological variables (and if so their significance) recorded at 12 weather stations in

Serbia during 1980–2010 [23]. A modified form of the method has also been used to test scaling effects [24], and four variants have been applied to determine trends in selected streamflow statistics from Indiana [25]. In addition, a procedure for calculating exact distributions of the M-K trend test statistic for persistent data with an arbitrary correlation structure has been presented [26], and the test has been used to detect directions and magnitudes of changes in monotonic trends in annual and seasonal precipitation over time in annual precipitation in Madhya Pradesh, India [27]. Here, we applied the M-K test to detect trends variation points in the time series of the data obtained from the 30 stations in the Weihe basin (Figure 1).

## 4. Results

**4.1. Spatial Patterns of Annual Precipitation in the Weihe Basin.** Means and trends in annual precipitation in the Weihe basin from 1960 to 2011 are shown in Figures 2 and 3. The mean annual precipitation at each station changed greatly. Spatially, it declined from the southeast to northwest. Mean annual precipitation in the basin amounted to 580 mm, with a maximum exceeding 800 mm at Huashan and Zhen'an area and a minimum of 340 mm in the northwest. The annual precipitation trend at each station was negative, except at Xi'an where it increased by 0.123 mm/a. The mean trend

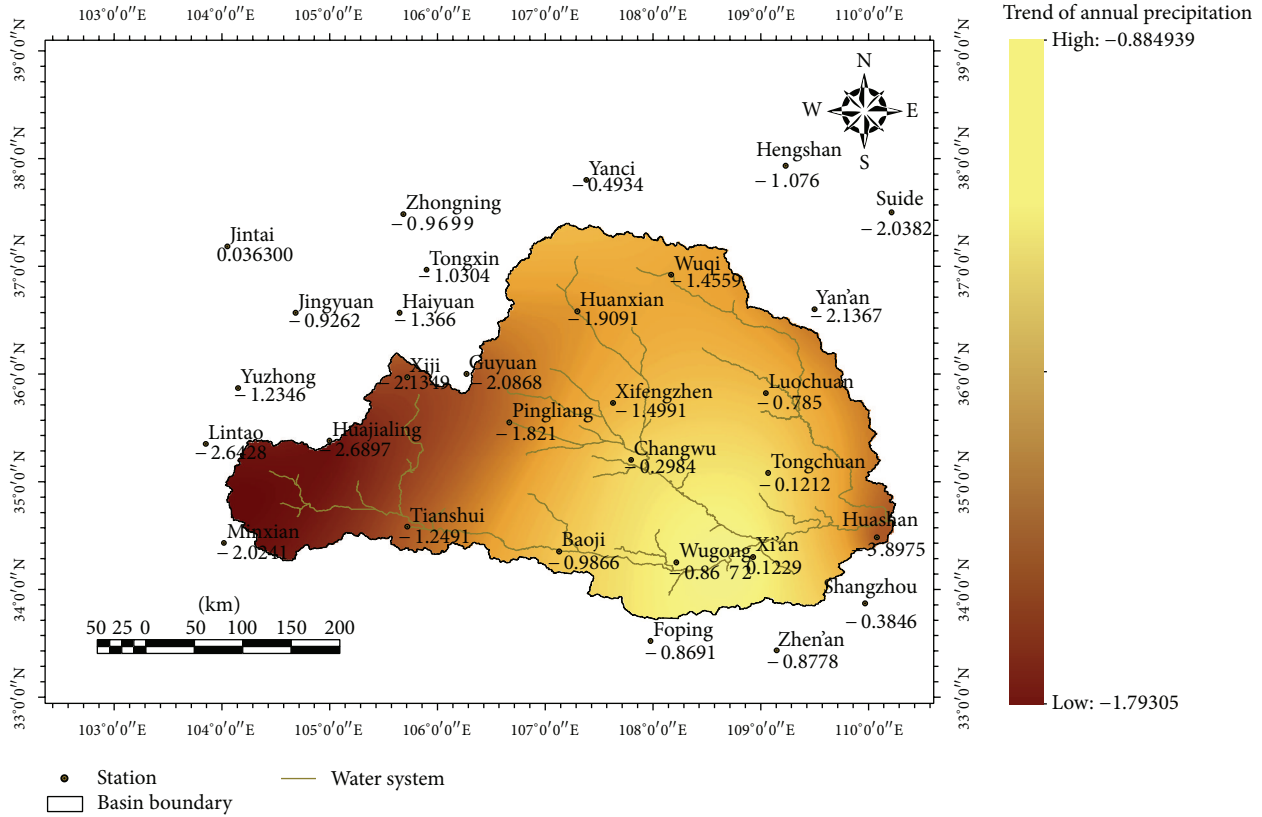


FIGURE 3: Annual precipitation trends in the Weihe basin.

TABLE 1: Eigenvalues and their contributions to the variance of annual precipitation in the Weihe basin obtained from EOF decomposition.

Component	Initial eigenvalues			Extraction sums of squared loadings		
	Eigenvalues $\lambda_i$	Proportion of variation (%)	Cumulative proportion of variation (%)	Eigenvalues $\lambda_i$	Proportion of variation (%)	Cumulative proportion of variation (%)
1	13.648	45.494	45.494	13.648	45.494	45.494
2	5.363	17.875	63.369	5.363	17.875	63.369
3	1.997	6.658	70.027	1.997	6.658	70.027
4	1.404	4.681	74.708			
5	1.196	3.985	78.693			
6	0.912	3.039	81.732			
7	0.685	2.285	84.017			
8	0.634	2.113	86.130			
9	0.506	1.686	87.816			
10	0.422	1.408	89.224			

Extraction method: principal component analysis.

across the basin was  $-1.662$  mm/a, clearly showing that annual precipitation declined and that this trend was most pronounced in upstream areas.

4.2. EOF Decomposition of Annual Precipitation in the Weihe Basin. The precipitation data analyzed herein originated from the Weihe basin and the surrounding 30 national standard stations during the period 1960–2011. From this

data, we derived the normalized anomaly matrix  $X$  for annual precipitation. Empirical orthogonal function (run in SPSS) was used to calculate the eigenvalues of the covariance matrix of  $X$  and the amount of variation that each principal component explained, as shown in Table 1.

Eigenvalues for the covariance matrix of the Weihe basin annual precipitation matrix and their contributions to variance (specific and cumulative), obtained by empirical

orthogonal function (using SPSS software), are shown in Table 1. The precipitation field rapidly converged; the first principal component (PC) accounted for almost half (45.5%) of the variation in annual precipitation, and the first three components (all of which had eigenvalues exceeding 1) for 70.0% of the variation. Thus, the first three PCs and eigenvectors describe the spatial distribution of annual precipitation in the Weihe basin quite well.

Eigenvectors of the covariance matrix cannot be directly obtained from the SPSS output but can be obtained by dividing the  $i$  vectors of the matrix by the square roots of the corresponding eigenvalues. The vector corresponding to the largest eigenvalue is eigenvector 1, with progressively small eigenvalues associated with subsequent eigenvectors (2, 3, 4, etc.). The first three eigenvectors obtained from the EOF decomposition of the annual precipitation in the Weihe basin dataset are shown in Table 2.

The first three eigenvectors obtained from the EOF analysis provide an approximate description of the precipitation values. If their values are consistently positive or negative, there is a consistent precipitation trend, and the area with the largest absolute value is the center of the variable field. In contrast, if the eigenvector values fluctuate between positive and negative, the trend is nonuniform.

We used the Geostatistical Analyst module of ArcGIS to undertake a semivariogram analysis of the first three eigenvectors and thus, to obtain the spatial variability parameters shown in Table 3. We then used Kriging interpolation to draw a map of each eigenvector field.

As can be seen from Table 3, the azimuth angles of eigenvectors 1, 2, and 3 are  $4.7^\circ$ ,  $65.5^\circ$ , and  $309.6^\circ$ , approximately south to north, east-northeast to west-southwest, and northwest to southeast orientations, respectively. All the eigenvectors have a small Nugget value, indicating that the precipitation measurement error is small. Indeed, the Nugget of eigenvector 2 is zero, indicating that the measurement error for precipitation in this eigenvector field can be ignored. The partial sill of eigenvector 1 is significantly lower than that of the other eigenvectors, indicating that it reflects smaller-scale variations. The Weihe basin spans about  $7^\circ$  longitude and  $4^\circ$  latitude. Thus, since the major ranges in the eigenvectors are  $6.29^\circ$  latitude and longitude, the variability of precipitation changes with distance across the basin.

#### 4.3. Variation Diagnosis of Annual Rainfall in the Weihe Basin.

The Weihe basin is divided into four subbasins, with differing hydrological characteristics, and controlled by different hydrological stations. The areas covered by the subbasins and locations of hydrological and meteorological stations are shown in Figure 1. The M-K method was used to discriminate variation points in the trends in the annual precipitation series recorded at each station during 1960–2011, and the results are shown in Table 4.

## 5. Analysis and Discussion of Results

5.1. Analysis of Spatial Variation of Annual Precipitation in the Weihe Basin. As shown in Table 2, all components of

TABLE 2: Eigenvectors obtained by EOF decomposition of the annual precipitation in the Weihe basin dataset.

	Eigenvectors		
	Eigenvector 1 $V_1$	Eigenvector 2 $V_2$	Eigenvector 3 $V_3$
Lintao	0.190	-0.137	-0.291
Huajialing	0.190	-0.043	-0.383
Wuqi	0.196	-0.157	0.112
Guyuan	0.224	-0.082	-0.086
Huanxia	0.210	-0.140	0.086
Yan'an	0.208	0.011	0.251
Xiji	0.192	-0.131	-0.308
Pingliang	-0.070	0.045	-0.019
Xifengzhen	0.222	0.104	0.067
Changwu	0.204	0.201	0.058
Luochuan	0.200	0.139	0.179
Tongchua	0.154	0.248	0.168
Minxian	0.202	0.001	-0.271
Tianshui	0.204	0.057	-0.241
Baoji	0.167	0.287	-0.021
Wugong	0.180	0.273	-0.010
Xi'an	0.158	0.277	0.051
Huashan	0.163	0.215	-0.100
Foping	0.177	0.218	0.009
Zhen'an	0.157	0.245	0.042
Shangzhou	0.167	0.223	-0.021
Jingtai	0.119	-0.198	0.272
Jingyuan	0.167	-0.250	-0.084
Yuzhong	0.178	-0.156	-0.281
Zhongning	0.182	-0.206	0.127
Yanci	0.170	-0.200	0.250
Hengshan	0.183	-0.120	0.240
Suide	0.175	-0.108	0.260
Haiyuan	0.199	-0.231	0.004
Tongxin	0.192	-0.221	0.072

TABLE 3: Spatial variability parameters of eigenvectors of annual precipitation in the Weihe basin.

	Eigenvectors		
	Eigenvector 1 $V_1$	Eigenvector 2 $V_2$	Eigenvector 3 $V_3$
Azimuth angle ( $^\circ$ )	4.7	65.5	309.6
Nugget ( $C_0$ )	0.0012685	0	0.0013054
Partial sill ( $C$ )	0.0014968	0.41084	0.044187
Major range ( $^\circ$ latitude and longitude)	6.28911	6.28911	6.28911

eigenvector 1 are positive, except the data from Pingliang station, indicating that precipitation in the Weihe basin had high spatial consistency during the study period. The downward

TABLE 4: Variation points in annual precipitation trends in the Weihe basin.

Subbasins	Meteorological stations	Variation points				
		1960–1969	1970–1979	1980–1989	1990–1999	2000–2011
Weihe basin above Beidao station	Tianshui		1971	1983, 1985		2002
	Minxian			1986, 1988		2006
	Huajialing			1986		
	Lintao			1986, 1987		2003, 2006, 2008
	Xiji					2005
Jinghe basin	Huanxian		1970			2002
	Guyuan		1972	1986	1996	
	Pingliang		1971, 1977	1980–1985*	1990	
	Xifengzhen		1972, 1979			
	Changwu		1978, 1979	1983, 1985		
Beiluohe basin	Wuqi		1971–1974*	1981, 1983, 1986–1995*, 1998		2000, 2003, 2007
	Yan'an		1972–1975* 1978, 1979	1982		
	Luochuan		1970, 1976			
Beidao to Huaxian section of Weihe mainstream	Baoji	1969	1971, 1974, 1976, 1978	1980, 1982		
	Wugong	1961, 1964–1970*				
	Xi'an	1962, 1965				
	Tongchuan		1976	1983, 1985		
	Zhen'an		1972, 1975			
	Foping	1966, 1968	1973, 1977, 1979	1986, 1988		
	Shangxian	1960, 1963	1971, 1975	1984		
Huanshan			1986			

Extraction method: Mann-Kendall method. \* indicates that variation occurred frequently during the indicated period.

trend of annual precipitation shows that annual precipitation in the basin declined in the region, and this consistent trend accounts for 45.5% of the variance. The basin covers parts of the continental monsoon zone and transitional zone between arid and humid regions of northwest China. The overall consistency and decline represented by eigenvector 1 are the main spatial features of precipitation patterns in the Weihe basin during the study period.

The eigenvector 2 values obtained from EOF decomposition of the annual precipitation data are shown in Figure 4. The values can be divided by a line passing roughly from Yan'an through Pingliang to Tianshui, into positive and negative anomaly areas covering the southeastern parts of the Weihe basin (with the most-positive anomaly center in Baoji) and northwestern parts (with the most-negative anomaly center in Wu Qi), respectively. These results confirm that the annual precipitation in the basin has a clear northwest-southeast pattern.

Combining the eigenvalues with the trends in annual precipitation recorded at each of the stations gives the eigenvector 2 trend values (Figure 5), which show that precipitation declined in the southeast and increased in the northwest. The decline was most pronounced at the downstream station Huashan.

The eigenvector 3 values have a clear eastwest pattern (Figure 6), with a negative anomaly area covering upstream parts of the basin and a positive anomaly center located in the Luochuan region, north of Shaanxi. These findings show that, in addition to the consistent overall pattern and northwest-southeast precipitation patterns, there is a clear eastwest pattern. In combination with the precipitation trends at the 30 stations, the results clearly show that annual precipitation declined in northern Shaanxi and increased in the upstream areas (Figure 7).

To summarize, there were three spatial patterns of annual precipitation in the Weihe basin during the study period: (1) consistent overall decline, (2) declined in the southeast and increased in the northwest, (3) declined in northern Shaanxi and increased in the upstream areas.

*5.2. Analysis of Annual Precipitation Variation in the Weihe Basin.* The results summarized in Table 4 show that variation points occurred in trends of the annual precipitation sequence recorded at every meteorological station in the Weihe basin, but their timings differed in the following manner.

- (1) The timing of variation points has clear spatial characteristics, with gradual progressions from southeast

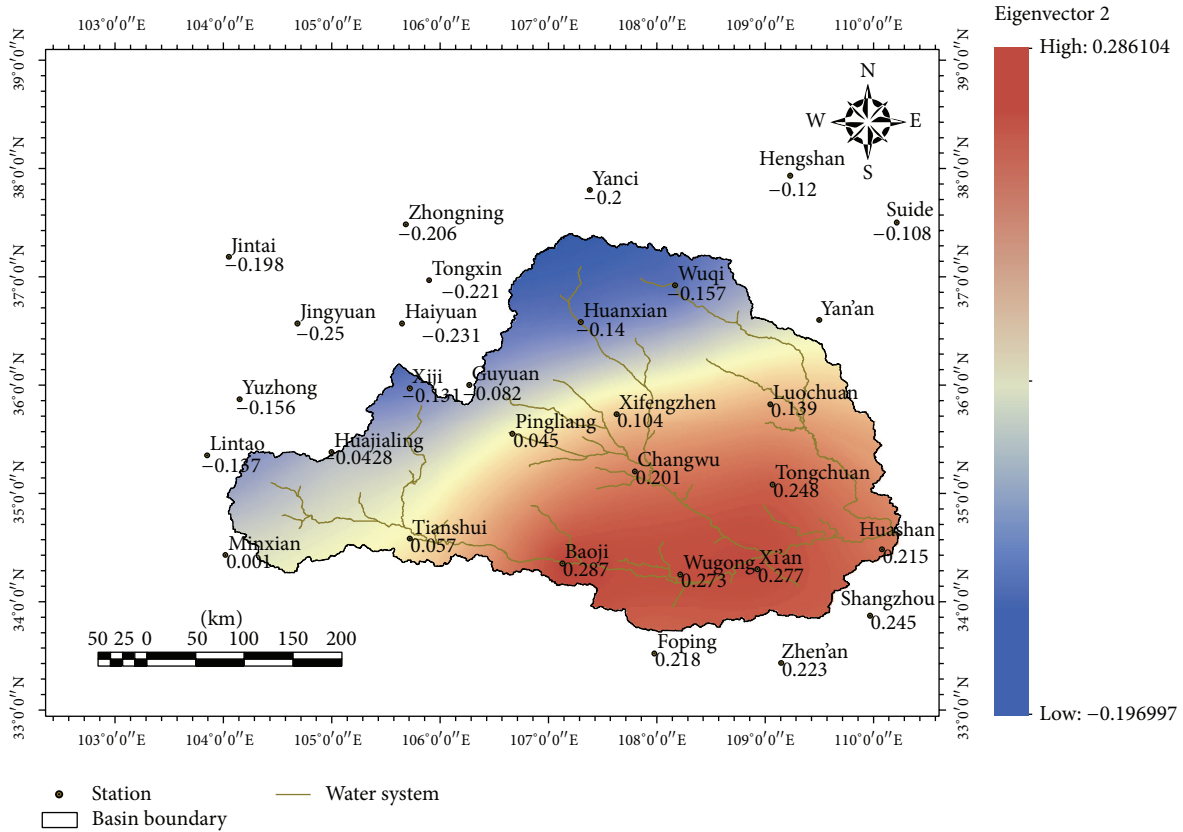


FIGURE 4: The eigenvector 2 values for annual precipitation in the Weihe basin.

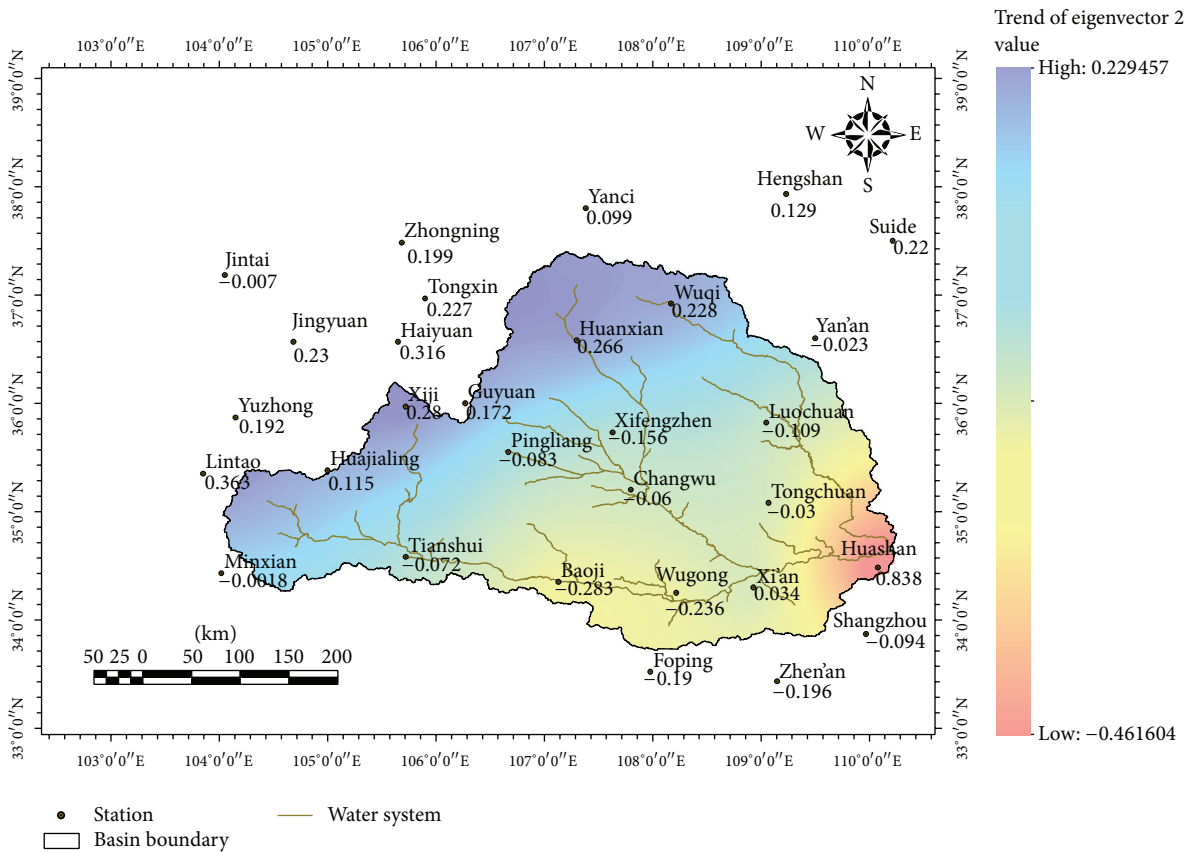


FIGURE 5: The eigenvector 2 trend field for annual precipitation in the Weihe basin.

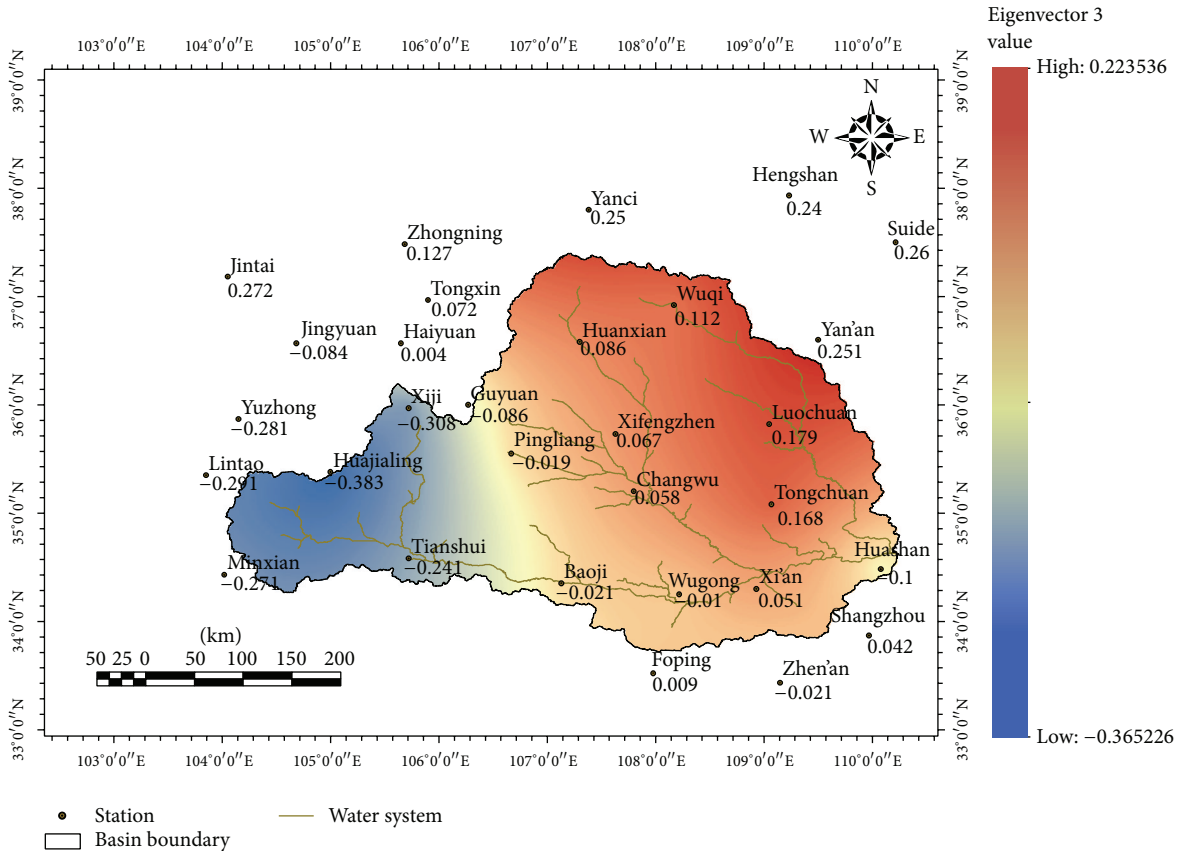


FIGURE 6: The eigenvector 3 values for annual precipitation in the Weihe basin.

to northwest and downstream to upstream. The first variation points occurred in the early 1960s at the Shangxian, Wugong, and Xi'an stations in the Beidao to Huaxian section of the Weihe mainstream, and later in the late 1960s and early 1970s, other stations variation occurred in this section. In the Jinghe and Beiluohe basins the first variation occurred in the early 1970s. In the Weihe basin above Beidao station and variation occurred most recently, in the mid- and late 1980s, except at Tianshui station (1971).

- (2) Variation points in the trends of annual precipitation in the basin above Beidao station were concentrated in the 1980s, while they covered longer periods of the 1970s and 1980s in other subbasins. These results indicate that precipitation variation points occurred frequently during the 1970s to 1980s in each subbasin.
- (3) After the 1990s, the frequency and scope of precipitation variation declined. No variation points in the 1990s were detected except at Guyuan, Pingliang, and Wuqi stations. After the 1990s, there were no variation points in the annual precipitation sequences recorded in the Beidao to Huaxian section of the Weihe mainstream, Jinghe basin, or Beiluohe basin. These results show that, after an active period of precipitation variation in 1970s and 1980s, the annual

precipitation sequence in the Weihe basin was relatively stable. Thus, during the study period there were shifts in precipitation from one stable state to another after disturbance.

- (4) From 2000 to 2011, further changes in annual precipitation occurred in the basin above the Beidao station and at the most northern stations of the basin (Huanxian and Wuqi). These variations were clearly regional, concentrated in the northwest of the Weihe River basin and the source areas of the rivers Jinghe and Beiluohe. Due to the limited length of the time series, it is not possible to distinguish whether these variations were due to small-scale regional variations, or represent initial stages of wide-ranging variation across the whole basin, or were the result of lingering temporal and spatial effects of the basin-wide variation that occurred in the 1970s and 1980s.
- (5) The variation in annual precipitation in the Weihe basin propagated from the southeast to the northwest. This is consistent with the orientation of the eigenvector 2 field of annual precipitation obtained from EOF decomposition and the spatial pattern of mean annual precipitation in the basin. The factors causing these patterns are not clear from the data presented here but will be addressed in future studies.

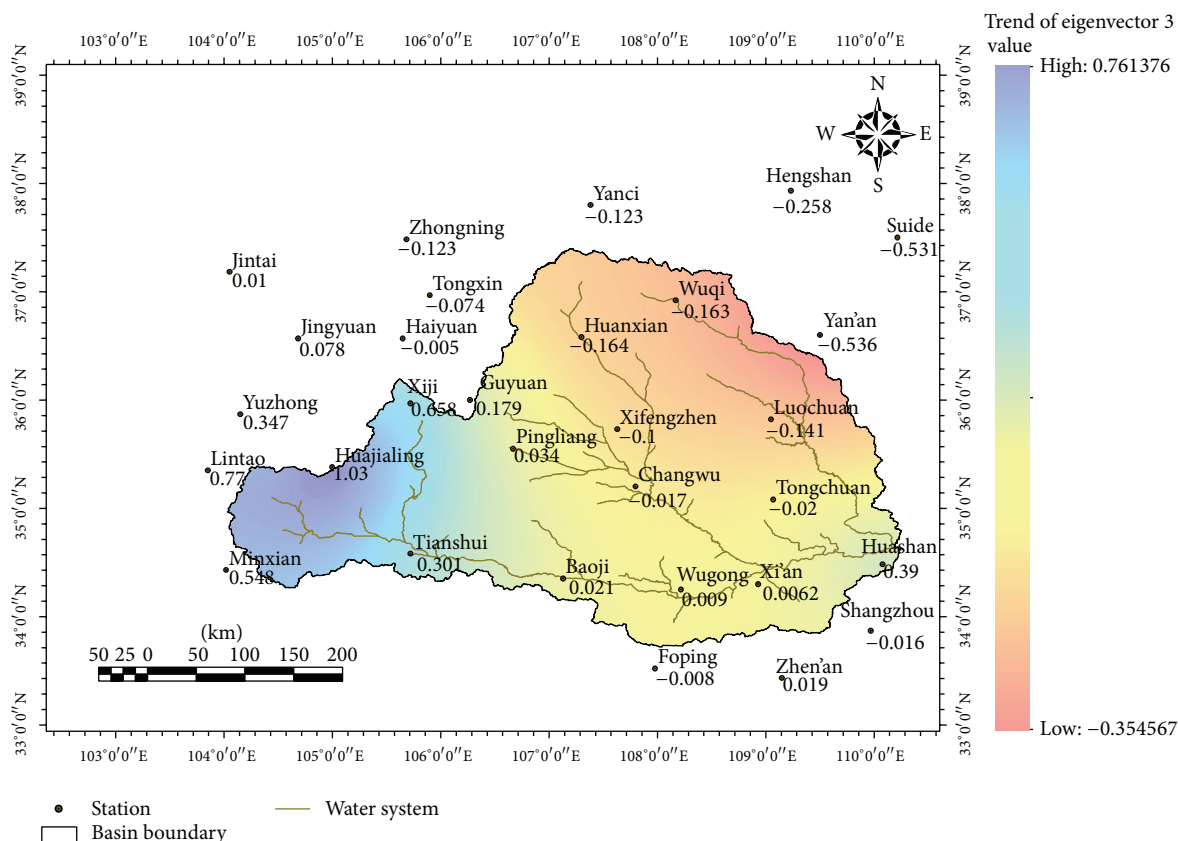


FIGURE 7: The eigenvector 3 trend field for annual precipitation in the Weihe basin.

## 6. Conclusions

We have analyzed spatial and temporal patterns of annual precipitation in the Weihe basin using data recorded from 1960 to 2011 at 30 National Standard Stations in the basin and surrounding area, by applying empirical orthogonal function decomposition in combination with geostatistical (semivariogram) analysis, then using the Mann-Kendall method to discriminate variation points in the precipitation series recorded at each station.

- (1) The main spatial patterns of annual precipitation in the Weihe Basin during the study period were a consistent overall decline, which was strongest in the northwest and progressively weaker from northwest to southwest and from west to east. The consistent overall decline accounted for 45.5% of the total variation.
- (2) Variation points were detected in the annual precipitation sequences recorded at all the meteorological stations in the basin, but their timing had clear spatial patterns, starting gradually later from the southeast to the northwest and downstream to upstream. In the 1970s and 1980s they occurred frequently in each subbasin.

- (3) After the 1990s, following the active period of precipitation variation in the 1970s and 1980s, the frequency and scope of precipitation variations declined. Thus, during the study period there were shifts in precipitation from one stable state to another after disturbance.

## Conflict of Interests

The authors declare that there is no conflict of interests regarding the publication of this paper.

## Acknowledgments

This work was financially supported by the Natural Science Foundation of China (Grant nos. 51190093, 51179148, and 51179149), the National Key Basic Research 973 of China (Grant no. 2012CB417003), and the MWR Welfare Sector Funds (Grant nos. 201101043, 201101049). Constructive comments from reviewers of a previous version of the paper are gratefully acknowledged.

## References

- [1] H. Zhang, Y. Chen, G. Ren et al., "The characteristics of precipitation variation of Weihe River Basin in Shaanxi Province

- during recent 50 years,” *Agricultural Research in the Arid Areas*, vol. 26, no. 04, pp. 236–241, 2008.
- [2] K. Che and J. Jian, “A study of climate variability in Zedang during 1960–1999,” *Meteorological Monthly*, vol. 26, no. 1, pp. 54–56, 2000.
- [3] Y. Ding, G. Ren, G. Shi et al., “National assessment report of climate change (I): climate change in China and its future trend,” *Advances in Climate Change Research*, vol. 2, no. 1, pp. 3–8, 2006.
- [4] Y. He, F. Wang, X. Mu et al., “Temporal and spatial characteristics of temperature and precipitation in Weihe River basin,” *Bulletin of Soil and Water Conservation*, vol. 32, no. 4, pp. 102–105, 2012.
- [5] Y.-X. Zhang, F. Wang, and X.-M. Mu, “Research of quantitative relations between Geographical environment factor and water and sediment in the Weihe River basin,” *Journal of Northwest A & F University, (Natural Science Edition)*, vol. 37, no. 1, pp. 61–65, 2009.
- [6] C. Jiang, F. Wang, and X. Mu, “Effect of climate change on net primary productivity (NPP) of natural vegetation in Wei river basin (II). NPP of natural vegetation in Wei river basin,” *Journal of Arid Land Resources and Environment*, vol. 27, no. 5, pp. 53–57, 2013.
- [7] Y. Zhang, “Hydrologic feature analysis for Weihe basin in Shaanxi province,” *Northwest Water Resources & Water Engineering*, no. 2, pp. 62–64, 2002.
- [8] G. Wang and Y. Wang, “Analysis on causes of runoff and sediment variation in Weihe basin based on hydrological model,” *Journal of Soil Water Conservation*, no. 4, pp. 22–25, 2000.
- [9] W. He and Z. Xu, “Spatial and temporal characteristics of the long-term trend for temperature and pan evaporation in the Wei River Basin,” *Journal of Beijing Normal University (Natural Science)*, vol. 42, no. 1, pp. 102–106, 2006.
- [10] K. Pearson, “On lines and planes of closest fit to system of points in space,” *Philosophical Magazine*, vol. 6, no. 2, pp. 559–572, 1902.
- [11] D.-X. Cui and W.-Y. Liu, “Application of empirical orthogonal function resolution to analysis of crustal vertical deformation field,” *Earthquake*, vol. 20, no. 3, pp. 82–86, 2000.
- [12] T. Liu and H. Zhang, “Compared with principal component analysis and empirical orthogonal function decomposition,” *Statistics and Decision*, vol. 340, no. 16, pp. 159–162, 2011.
- [13] H. Lin and W. Zhang, “Similarities and differences of principal component analysis and factor analysis and SPSS software,” *Statistics Research*, no. 3, pp. 65–69, 2005.
- [14] D. H. Kim, C. Yoo, and T.-W. Kim, “Application of spatial EOF and multivariate time series model for evaluating agricultural drought vulnerability in Korea,” *Advances in Water Resources*, vol. 34, no. 3, pp. 340–350, 2011.
- [15] N. S. Loboda, A. V. Glushkov, and V. N. Khokhlov, “Using meteorological data for reconstruction of annual runoff series over an ungauged area: empirical orthogonal function approach to Moldova-Southwest Ukraine region,” *Atmospheric Research*, vol. 77, no. 1–4, pp. 100–113, 2005.
- [16] D. Sirjacobs, A. Alvera-Azcárate, A. Barth et al., “Cloud filling of ocean colour and sea surface temperature remote sensing products over the Southern North Sea by the Data Interpolating Empirical Orthogonal Functions methodology,” *Journal of Sea Research*, vol. 65, no. 1, pp. 114–130, 2011.
- [17] H.-L. Yu and H.-J. Chu, “Understanding space-time patterns of groundwater system by empirical orthogonal functions: a case study in the Choshui River alluvial fan, Taiwan,” *Journal of Hydrology*, vol. 381, no. 3–4, pp. 239–247, 2010.
- [18] H. B. Mann, “Nonparametric tests against trend,” *Econometrica*, vol. 13, pp. 245–259, 1945.
- [19] R. Snyers, “Sur La Determination de la stabilite des series climatologiques,” in *Proceedings of the UNESCO-WMO Symposium of Changes of Climate*, vol. 20 of *Uneseo Arid Zone Research Series*, pp. 37–44, Unesco, Paris, France, 1963.
- [20] C. Goossens and A. Berger, “Annual and seasonal climatic variations over the northern hemisphere and Europe during the last century,” *Annales Geophysicae B*, vol. 4, no. 4, pp. 385–400, 1986.
- [21] C. Fu and Q. Wang, “The definition and detection of the abrupt climatic change,” *Chinese Journal of Atmospheric Sciences*, vol. 16, no. 4, pp. 482–493, 1992.
- [22] P. Xie, G. Chen, D. Li et al., “Hydrological variation integrated diagnosis method and application research,” *Hydroelectric Energy*, vol. 23, no. 2, pp. 11–14, 2005.
- [23] M. Gocic and S. Trajkovic, “Analysis of changes in meteorological variables using Mann-Kendall and Sen’s slope estimator statistical tests in Serbia,” *Global and Planetary Change*, vol. 100, pp. 172–182, 2013.
- [24] K. H. Hamed, “Trend detection in hydrologic data: the Mann-Kendall trend test under the scaling hypothesis,” *Journal of Hydrology*, vol. 349, no. 3–4, pp. 350–363, 2008.
- [25] S. Kumar, V. Merwade, J. Kam, and K. Thurner, “Streamflow trends in Indiana: effects of long term persistence, precipitation and subsurface drains,” *Journal of Hydrology*, vol. 374, no. 1–2, pp. 171–183, 2009.
- [26] K. H. Hamed, “Exact distribution of the Mann-Kendall trend test statistic for persistent data,” *Journal of Hydrology*, vol. 365, no. 1–2, pp. 86–94, 2009.
- [27] D. Duhan and A. Pandey, “Statistical analysis of long term spatial and temporal trends of precipitation during 1901–2002 at Madhya Pradesh, India,” *Atmospheric Research*, vol. 122, pp. 136–149, 2013.

## Research Article

# A Physically Based Runoff Model Analysis of the Querétaro River Basin

**Carlos Javier Villa Alvarado,<sup>1</sup> Eladio Delgadillo-Ruiz,<sup>1</sup> Carlos Alberto Mastachi-Loza,<sup>2</sup> Enrique González-Sosa,<sup>1</sup> and Ramos Salinas Norma Maricela<sup>3</sup>**

<sup>1</sup> *División de Estudios de Posgrado, Facultad de Ingeniería, Universidad Autónoma de Querétaro, Cerro de las Campanas S/N Centro, 76000 Querétaro, QRO, Mexico*

<sup>2</sup> *Centro Interamericano de Recursos del Agua (CIRA), Facultad de Ingeniería, Cerro de Coatepec CU, 50110 Toluca, MEX, C.P., Mexico*

<sup>3</sup> *División de Estudios de Posgrado, Facultad de Contabilidad y Administración, Universidad Autónoma de Querétaro, Cerro de las Campanas S/N Centro, 76000 Querétaro, QRO, Mexico*

Correspondence should be addressed to Carlos Javier Villa Alvarado; [cjvillaa@yahoo.com](mailto:cjvillaa@yahoo.com)

Received 19 August 2013; Revised 25 November 2013; Accepted 25 November 2013; Published 16 February 2014

Academic Editor: Y. P. Li

Copyright © 2014 Carlos Javier Villa Alvarado et al. This is an open access article distributed under the Creative Commons Attribution License, which permits unrestricted use, distribution, and reproduction in any medium, provided the original work is properly cited.

Today the knowledge of physical parameters of a basin is essential to know adequately the rainfall-runoff process; it is well known that the specific characteristics of each basin such as temperature, geographical location, and elevation above sea level affect the maximum discharge and the basin time response. In this paper a physically based model has been applied, to analyze water balance by evaluating the volume rainfall-runoff using SHETRAN and hydrometric data measurements in 2003. The results have been compared with five ETp different methodologies in the Querétaro river basin in central Mexico. With these results the main effort of the authorities should be directed to better control of land-use changes and to working permanently in the analysis of the related parameters, which will have a similar behavior to changes currently being introduced and presented in observed values in this basin. This methodology can be a strong base for sustainable water management in a basin, the prognosis and effect of land-use changes, and availability of water and also can be used to determine application of known basin parameters, basically depending on land-use, land-use changes, and climatological database to determine the water balance in a basin.

## 1. Introduction

The main problems in the world are associated with the quantity and quality of existing data [1], which represent more time of process and uncertainty in the obtained results. Moreover the government policies are limited in making growing plans for urban centers and do not consider a scheme of penalties when variables as land-use are not respected because there is no knowledge of the effect of changes in the basin's hydrology. As mentioned in Amini et al. [2], in which a dendritic watershed system is used to determine the conditions of a watershed affected by land-use changes, they do not consider the full quantity of precipitation in one observed year or the effect of antecedent soil moisture.

In Mitsuda and Ito [3], different factors that affect the response of the basin are listed such as the land-use changes, the landowners activities, and the poor political strategies that increase the climate change effects [4], biodiversity alteration, and changes in biogeochemical and hydrological cycle; however they assume that natural and environmental factors are based only in the slope that is one of many variables that should be studied in a hydrologic basin, where the main interest is related to environmental topics as mentioned in Su and Christensen, 2013 [5].

In Mendoza et al. [6], the implications for land-use and land cover changes are soil erosion and degradation that disturbs the ecosystem capability to provide the natural benefits such as superficial and underground water retention;

nevertheless it is considered a distributed model that considers the runoff as a function of biophysical characteristics and not based on the physical basin variables. With the product of this research, as mentioned in Li and Huang, 2012 [7], a linkage can be applied among environmental regulations and economic implications with the use of informatics tools; finally through numerical modeling and applied research an environmental linkage can be carried out that involves the law and the economic implications [7].

In many places there are problems associated with the quantity and quality of existing dataset, representing time and uncertainty of the data. Moreover, government policies are limited in making decisions growing plans for urban centers and do not present a scheme of penalties when the laws on land-use changes are not respected.

As mentioned in Ewen [8], the physically based models are used to determine the water flow in the surface, underground, and environment. Surface and underground processes are widely explained in Birkinshaw and Bathurst [9] wherein SHETRAN is used as a distributed hydrologic model.

The importance of this model in water balance is related to the places in the world where quantity and quality of measurement stations are poor with lack of data in most of cases. The insufficient quantity of climate datasets is the main problem to solve to make decisions for annual water use management in this basin and its use.

The results suggest that the use of SHETRAN in water balance in the Querétaro river basin has the advantage that it depends on the knowledge of physic parameters of the basin and can be applied in unmeasured basins when the stations are damaged or do not have resources to implement a system of hydrometric monitoring.

## 2. Material and Methods

**2.1. Location.** The Querétaro river basin area is 2,707.74 square kilometers, located in central Mexico, 200 km to the northwest of Mexico City (Figure 1). Its coordinates are UTM-WGS84\_14N  $x(E) = 358,380$ ;  $y(N) = 2'282,700$ ; 1,800 meters above sea level (masl). The basin drains to the Ameche hydrometric station (1,787 masl), 20 kilometers west of Querétaro city. The annual rainfall rate is 55 centimeters per year, mean annual temperature is 18.7°C, and mean annual potential evaporation is 2,050–2,200 mm. This basin is close to the Continental Divide of the Americas and drains to Lake Chapala in the state of Jalisco, 450 km to the west of Querétaro city.

The total rainfall registered in climate stations in 2003 (Table 1) represents twice the average annual volume. As mentioned in Nayak and Mandal [13] and Mahmood et al., [14], these effects can be attributed to the phenomenon of global warming so that the high rainfall events should be analyzed in shorter time periods to determine the response of basin to these changes [15].

**2.2. Basin.** The last years there has been an increase in urban land-use changes, principally in east, west, and northwest of the basin, due to topographic natural conditions and industrial-commercial activity increasing. Because of this

recent increase in land-use changes, the basin is subject to floods more frequently.

In this basin there is no methodology to determine the water balance based on the characteristics of the region, so that different formulas are applied based on existing regulations [16], which can be implemented in a better way if the physical parameters of the basin are considered, due to the poor level of hydrometric data quality; nevertheless actually these data are used to determine the water balance. A physically based method can be applied calculating the runoff by using the precipitation and land-use conditions. At the same time the margin of uncertainty that can be very sensitive in low availability of water resources in the basin must be continuously evaluated.

**2.3. Digital Terrain Model.** A digital terrain model (DTM) was obtained from INEGI (Instituto Nacional de Estadística y Geografía, México) topographic maps (INEGI, 2010), at a scale of 1:50,000. The data was processed with ArcMap 3D\_Analyst to define the catchment [17], using

$$Z(x) = m(x) + '(x) + '' , \quad (1)$$

where  $Z(x)$  is the value of the elevation in the position  $x$ ,  $m(x)$  is the function that describes the dataset,  $'(x)$  is the stochastic local variation in the dataset after the  $m(x)$  variation, and  $''$  is the no tendencies variability dataset (noise). When the dataset has no tendencies  $m(x) = 0$ , then

$$E[Z(x) - Z(x+h)] = 0, \quad (2)$$

where  $h$  is the distance among the evaluated points and the variogram  $\gamma(h)$  as follows:

$$\text{Var}[Z(x) - Z(x+h)] = E\{[Z(x) - Z(x+h)]^2\} = 2\gamma(h). \quad (3)$$

Figure 1 shows the resulting digital terrain model.

**2.4. Runoff and Rivers.** In this basin there are three main rivers (Figures 2 and 2(a)): Arenal river (from north to south), Pueblito river (from south to north), and Querétaro river at the center of the basin (from east to west), which all converge close to the Querétaro-Guanajuato state border. All of them flow across the Querétaro city urban area, where in recent years repetitive flooding has been observed. On the one hand the risk of flooding damage to population affects public services, economic activities, and social activities. On the other hand, the water deficit occurs for most of the year and in dry years the total rainfall is less than 450 mm [11].

**2.5. Satellite Images.** A Landsat TM Satellite geotiff 30 × 30 meters image (September 2003) was used to generate the grid used in the hydrological model. This image was classified with ArcMap 5.4.3 (red, green and blue) bands a reflectance of  $R = C2$ ,  $G = C3$ ,  $B = C1$ . The resulting image was aggregated to obtain a 2.1 × 2.1-kilometer grid model. A classification method supervised was used with in situ interpretation and land-use. Satellite data was obtained from

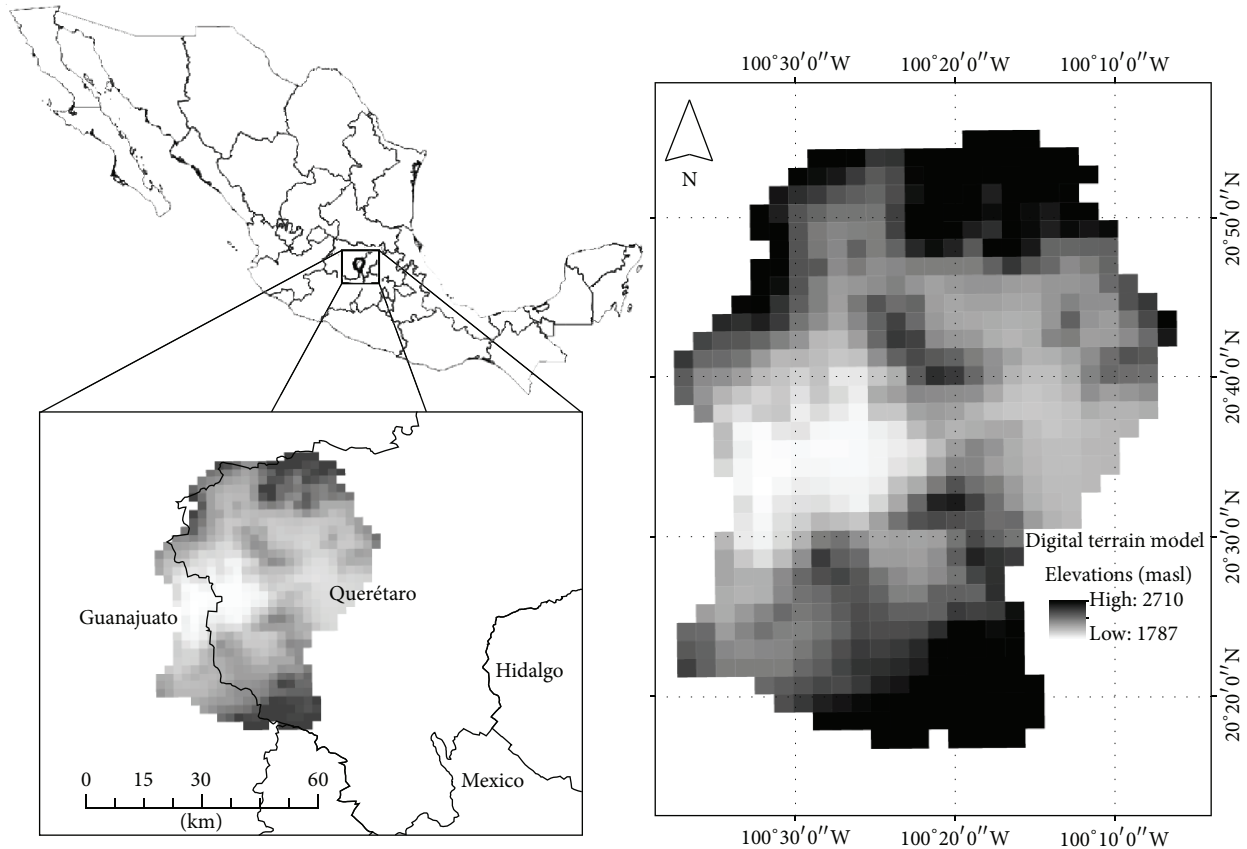


FIGURE 1: Central Mexico: Querétaro river basin. In the middle of Guanajuato and Querétaro State. SHETRAN terrain model values were aggregated to a 2,100 m mesh. At north (2,710) and south (2,610) are the major elevations above the sea level.

the United States Geological Survey (USGS) and was used to reduce the landscape and land-use cover uncertainty [18] in this basin in natural and urban areas. As a result of the satellite image analysis, the forest represents 20%, arable land 65%, water bodies 1%, and urban paved surfaces 14% (Figure 2).

**2.6. Land-Use and Interception.** In semiarid areas of Mexico, matorral intercepts from 1.9% to 7.7% of gross rainfall [19], deciduous trees from 9% to 20%, and coniferous trees from 20% to 48% [12]. In urban areas, rainfall is intercepted by buildings and vegetation. Buildings intercept rainfall on rooftops and laterally on wall surfaces, modifying the hydrological response peak time [20]. Canopy shrub and grass saturation was estimated at 1.5 mm using the linear relationship between throughfall and stemflow, compared to forest saturation, which was observed at 5.0 mm [12].

The edge effects present in isolated tree canopies might increase evaporation from wet canopies [21, 22]. Urban vegetation occurs as individuals or parklands, and therefore area-based interception percentages are smaller than reported for natural forests, grass, and possibly agroforests [12, 23–25]. Klaassen et al. [26] affirm that proximity to the forest edge affects both the interception storage capacity and the rate of evaporation of intercepted water, which cancel each other.

**2.7. Soil.** In Querétaro river basin the following different soils exist: litosol, vertisol, fluvisol, phaeozem, chernozem, castañozem, and yermosol (Figure 3 and Table 3), according to World Reference Base for Soil Resources of the Food and Agriculture Organization (FAO), where clay, loam, and sand are the principal elements found in the basin. The maximum depth layer is found at 5 m with a rock basement detected, located at the north of the basin. Vertisol is located in the center of the basin, litosol at the south, north, and east, and phaeozem in the upper areas coinciding with the watershed mainly at the north and south; other soils are small area of fluvisol (north), chernozem (south) in Huimilpan municipality, and yermosol and castañozem.

**2.8. Precipitation.** In this region the main rainfall volume occurs in summer (June to September), but the weather stations usually have breakdowns, resulting in incomplete databases that usually are filled by calculating missing values; to determine the mean precipitation 80 rainfall years have been analyzed. As a result dry years are considered between 257 and 550 mm/year.

The maximum rainfall volume occurs between 5,850 and 6,800 hours, but May 2003 (3,700) and June (4,500) showed an increase in volume annual rainfall. The maximum event corresponds to 68 mm (24-hour rainfall register). The 100 cm

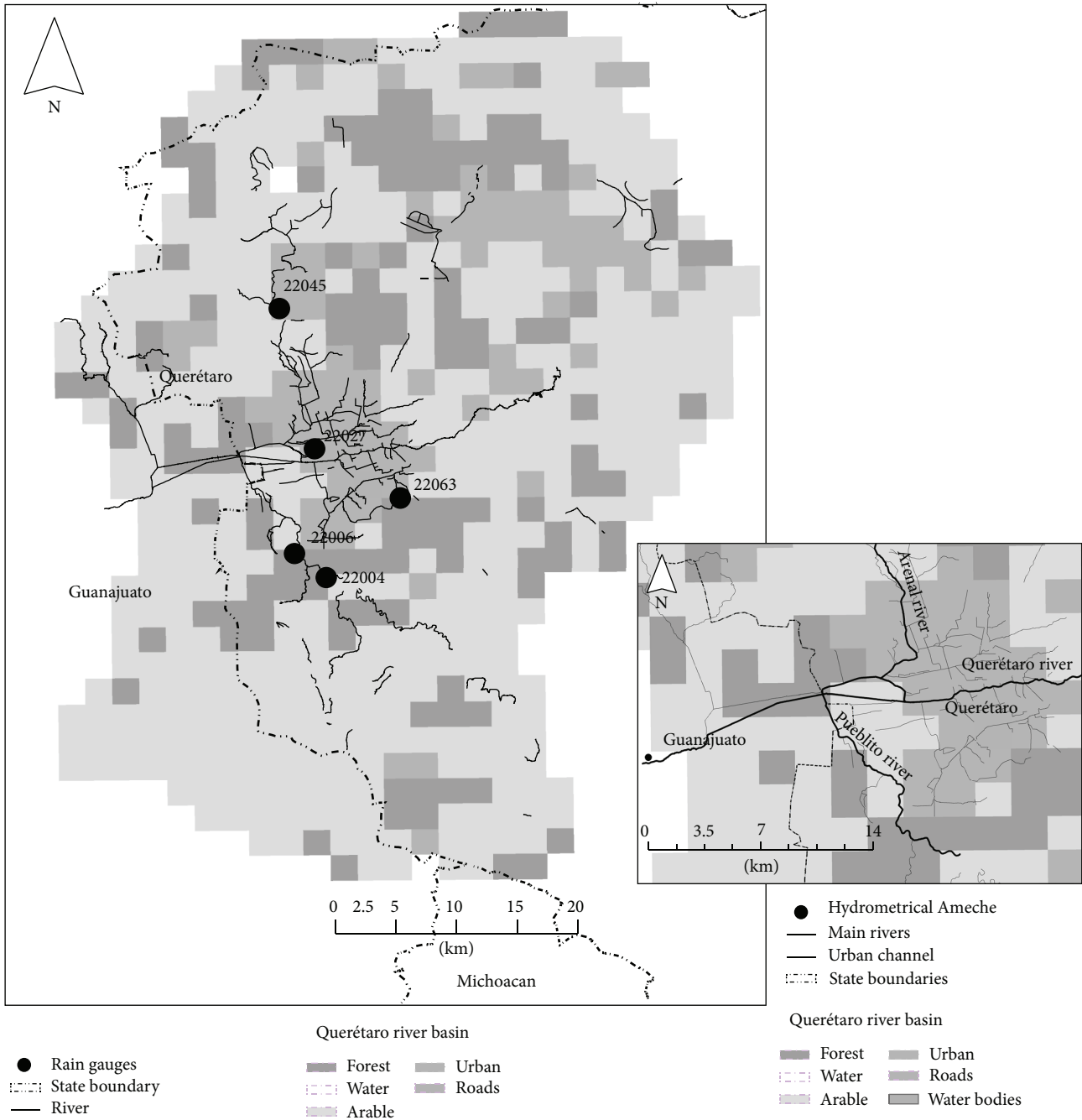


FIGURE 2: (a) Climate stations and land-use in Querétaro river catchment. Land-use: 65% correspond to arable land (grass, arable land and shrub), urbanized and paved surfaces 14% (mainly at the center of the basin; 1,870 masl) and forest and water 21% (at north and south, in the higher elevations). In (a), Querétaro (32.73 km), Pueblito (16.29 km) and Arenal (11.76 km) main rivers and flow direction are shown.

registered precipitation is considered in this paper to evaluate the basin model calibration and runoff total volume. The spatial rainfall analysis was made with daily precipitation records, using for this 5 climate stations which were visited to evaluate if they comply with the World Meteorological Organization (WMO) principally related to obstructions at surroundings [27].

The rainfall applied in the basin was the daily data obtained from the government climate stations in data

station: 22027 (Carrillo), 22045 (Juriquilla), El Batán (22004), 22006 (Pueblito), and 22063 (Querétaro). The climate stations details and location are shown in Table 1 and Figure 2.

### 3. Theory

A SHETRAN grid soil column model [15] is used to determine superficial and subsuperficial water interchanges

TABLE 1: Climate stations: the 2003 total rainfall measured is shown. The maximum difference found in altitude is 85 m, where the minimum is Carrillo (1,800 masl) and the highest is Juriquilla (1,885 masl).

Name	ID	Locality	Municipality	Latitude <sup>a</sup>	Longitude <sup>a</sup>	Altitude (masl)	Total 2003 rainfall <sup>b</sup> (mm)
El Batan	22004	El Batan	Corregidora	20°30'17.33''	100°25'27.08''	1881	1,119.50
El Pueblito	22006	El Pueblito	Corregidora	20°32'17.92''	100°26'25.55''	1826	1,079.00
Carrillo	22027	Querétaro	Querétaro	20°36'12.60''	100°25'55.49''	1800	994.80
Juriquilla	22045	Juriquilla	Querétaro	20°43'04.99''	100°27'34.00''	1885	904.20
Querétaro	22063	Querétaro	Querétaro	20°33'48.42''	100°22'09.88''	1813	934.20
						Mean	1,006.34 <sup>c</sup>

<sup>a</sup>Geographical coordinate system (WGS-84. 14 north).

<sup>b</sup>Total annual measured values in the climate station.

<sup>c</sup>Annual mean precipitation in Querétaro is 550 mm-year<sup>-1</sup>.

[28]. Evaporation is calculated with the Penman-Monteith equation [29]:

$$E_p = \frac{R_n \Delta + (\rho C_p \delta_e / r_a)}{\lambda (\Delta + \gamma)},$$

$$\gamma = \frac{P C_p}{\sigma \lambda},$$

$$LE = \frac{\Delta (R_n - G) + \rho C_p ((e_s - e) / r_a)}{\Delta + \gamma^*},$$

$$\gamma^* = \gamma \left( 1 + \frac{r_c}{r_h} \right),$$
(4)

where  $E_p$  is potential evapotranspiration,  $R_n$  is net radiation,  $\Delta$  is rate of increase with temperature of the saturation vapor pressure of water at air temperature,  $\rho$  is density of air,  $\delta_e$  is vapor pressure deficit of the air,  $r_a$  is aerodynamic resistance to transport of water vapor from the canopy to a plane 2 m above it,  $\lambda$  is latent heat of vaporization of water,  $\gamma$  is psychrometric constant,  $P$  is atmospheric pressure, and  $\sigma$  is ratio of density of water vapor to density of air ( $\sigma \approx 0.622$ ).

$C_p$  is specific heat of air at constant pressure,  $LE$  is latent heat flux ( $Wm^{-2}$ ),  $R_n$  is net radiation ( $Wm^{-2}$ ),  $G$  is soil heat flux ( $Wm^{-2}$ ),  $\rho$  is air density ( $kgm^{-3}$ ),  $C_p$  is specific heat of dry air  $Jkg^{-1} (^{\circ}C^{-1})$ ,  $e_s$  is the saturation vapor pressure (kPa),  $e$  is actual vapor pressure of the air (kPa), and  $r_h$  is aerodynamic resistance to turbulent heat ( $sm^{-1}$ ). Canopy resistance  $r_c$  is bulk surface resistance that describes the resistance to flow of water vapor from inside the leaf, vegetation canopy, or soil to outside.

The surface calculated with stomatal resistance,  $r_s$ , and leaf area index are

$$r_c = 2 \frac{r_s}{L_t},$$

$$r_h = \frac{\ln((z-d)/z_M) \ln((z-d)/z_h)}{k^2 U_z}.$$
(5)

$z$  is height above the ground surface for the wind speed measurement (m),  $d$  displacement (m),  $z_M$  roughness coefficient transference bending (m),  $z_h$  assumed roughness length

governing the transfer of sensible heat from the surface,  $k$  von Karman constant diffusive turbulence, and  $U_z$  wind velocity at  $z$  in  $ms^{-1}$ .

3.1. *ETp Methods.* The Thornthwaite [30] method is one of the most applied methods to determine a basin's water balance and thus originally was described:

$$P = I + AET + OF + \Delta SM + \Delta GWS, \quad (6)$$

where  $P$  is the total precipitation,  $I$  is the interception,  $AET$  is the evapotranspiration,  $OF$  is the overland flow,  $\Delta SM$  is the soil moisture storage change, and  $\Delta GWS$  is the groundwater ponding changes.  $P$ ,  $I$ , and  $AET$  are the main water balance variables that consider changes in soil moisture and groundwater storage changes.

In SHETRAN, the ET ratio, actual evaporation (AE), and potential evaporation (ETp) are the main parameters that increase or decrease the calculated annual runoff volume in the basin discharge and therefore it is necessary to calculate the ETp considering the database old weather stations, in which the temperature is one of the most important variables.

Five different methodologies have been analyzed to determine ET values to calculate and compare the total discharge and runoff volume: Thornthwaite and Papadakis (monthly data, M), Blaney and Criddle, Hargreaves, and Hamon (daily data, D). These methods are briefly explained.

Originally, the Thornthwaite method [30] was developed with rainfall-runoff data applied to different basins. Results were an empirical relationship between ETp, air temperature that involves the vapor flux, and heat balance:

$$ETp = 16 \left( \frac{10T}{I} \right)^a, \quad (7)$$

where

$$I = \sum_1^{12} i,$$

$$a = (675 * 10^{-9} I^3) - (771 * 10^{-7} I^2) + (1792 * 10^{-5} I) + 0.49239,$$
(8)

$$i = \left( \frac{T}{5} \right)^{1.514}.$$

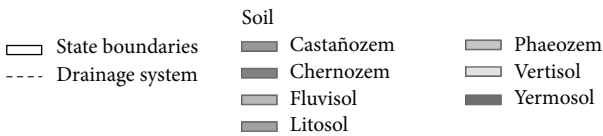
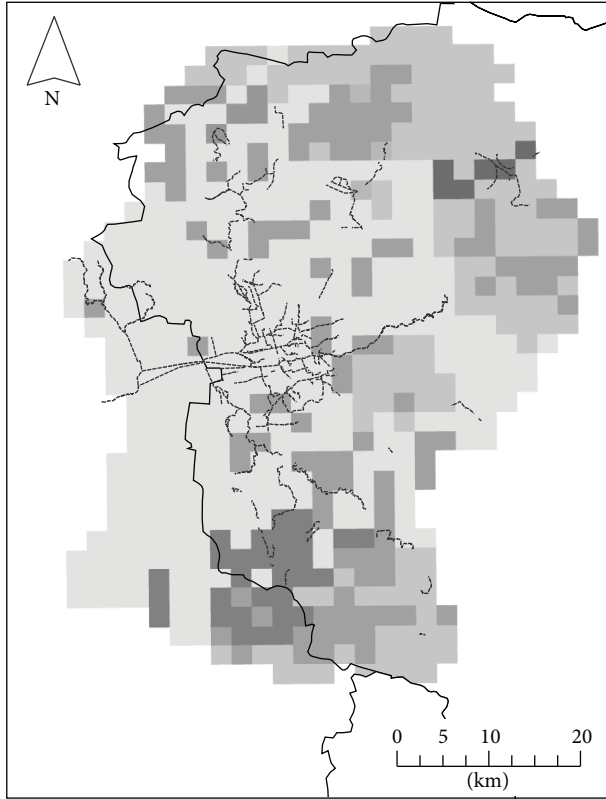


FIGURE 3: SHETRAN soils in the Querétaro river basin (mesh resolution: 2,100 meters). The existing soil composition in this basin is *vertisol* (52%), *phaeozem* (23%), *litosol* (18%), and *fluvisol*, *castañozem*, *chernozem*, and *yermosol* (7%). *Vertisol* principally at the center of the basin, at *phaeozem* north and south, and *litosol* found at the center, northwest, and southwest.

The Papadaky's method is based on saturated vapor deficit ( $e^0 - e$ ), relative humidity, and temperature. The potential ET was proposed in cases where the climate database is not complete. In this method, Papadaky's [31] proposed that:

$$ETp = 5.625 (e^0 (t_{max}) - e^0 (t_{min} - 2)), \quad (9)$$

where the vapor pressure at saturation,  $e^0$ , can be calculated with Bossen's relationship using average temperature ( $t_{med}$ ) in °C as follows:

$$e^0 = 33.8639 \left[ (0.00738 * t_{med} + 0.8072)^8 - 0.000019 * (1.8 * t_{med} + 48) + 0.001316 \right]. \quad (10)$$

The Hargreaves method [32] is often used to evaluate potential ETp using temperature and solar radiation. The relationship is known as follows:

$$ETp = 0.0023 (t_{med} + 17.78) * R_0 * (t_{max} - t_{min})^{0.5}, \quad (11)$$

where  $R_0$  (also known as  $R_a$ ) is the extraterrestrial solar radiation as a function of latitude. In Querétaro (México) this value is north 21°.

The Blaney and Criddle method [33] is used in arid and semiarid regions to calculate ETp for periods of one month or greater. It is commonly used to estimate reference crop evapotranspiration in soil with water deficit using the temperature variable as follows:

$$ETp = p * [(0.46 * T_{med}) + 8.13], \quad (12)$$

where  $p = 100 * (\text{daylight hours per day/daylight hours per year})$ .

The Hamon method is applied mainly in places where there are no reliable climate databases. Thornthwaite developed an empirical method with mean temperature data and average daylight hours. Different authors found similarities between the empirical Thornthwaite relationship and saturated vapor pressure. The Hamon relationship is

$$ETp = 29.8 * D * \frac{e_a(T_{med})}{T_{med} + 273.2}. \quad (13)$$

An average of 10 hours ( $D$  value) is applied; saturated vapor is thus calculated:

$$e_a(T_{med}) = 0.611 \exp\left(\frac{17.3T_{med}}{T_{med} + 237.3}\right). \quad (14)$$

**3.2. Hydrological Model.** SHETRAN is a physically based distributed hydrological model for water and sediment flow in basins. This model includes the Gash model [34] and Rutter model [35, 36] applying their rainfall interception model to vegetation and to different land-uses as well as to ETp phenomena. This software uses variables as vapor-transpiration components for variable saturated subsurface flow interception, overland flow through the numerical solution of the Saint-Venant equations, and interactions between surface and subsurface waters with the Richards equation; the mass and momentum are solved with differential equations in a three-dimensional finite difference grid [37]. The different applications of this tool have been demonstrated to represent water flow, land-use changes, soils production erosion, transport effect simulation [38], and contaminant transport by runoff in Birkinshaw and Ewen [39].

The SHETRAN platform is based on a vertical column model representation dividing the basin into finite difference cells where upper cells are the superficial and subsuperficial water. At the end of column is the confined groundwater. The superficial layers are the vegetation and soil; over this layer are canopy and other interceptors. This tool is physically based because it allows solving the physically based equations of momentum and mass-energy conservation. Hence the parameters have physical meaning and allow evaluating the field measurements across the partial spatially distributed results.

In the Querétaro river basin the different vegetation layers have been included with experimental results parameters [12]. The physically based model allows the change in forest cover to be modeled by changing the vegetation parameter

TABLE 2: Land-use SHETRAN parameter values in the Querétaro river basin. AE/PE is the relationship for actual and potential evaporation. Values of canopy storage capacity, leaf area index, and maximum routing depth are based on Guevara-Escobar et al., 2000 [10], Mastachi-Loza et al., 2010 [11], and Guevara-Escobar et al., 2007 [12].

Type	Vegetation type	Canopy storage capacity (mm)	Leaf area index	Max routing depth (m)	Total area (%)	AE/PE at field capacity <sup>a</sup>
1	Deciduous forest	5.0	6	1.5	21.00	1.10
2	Grass	1.5	6	1	20.00	1.10
3	Arable	1.5	4	0.8	45.00	1.05
4	Urban	0	0.3	0.5	13.50	1.00
5	Urban streets	0	0.3	0.5	0.50	1.00

<sup>a</sup>Final calibrated value.

values to represent the forest and urban centers condition. In this model a  $2,100 \times 2,100$  m vegetation types mesh is used, composed as in Table 2.

Runoff is solved by Saint-Venant equations which describe the one-dimensional flux of the wide wave and steady regime as follows

Continuity equation (mass water conservation) is as follows:

$$\frac{\partial Q}{\partial x} + \frac{\partial A}{\partial t} = q. \quad (15)$$

Momentum conservation is as follows:

$$\frac{\partial Q}{\partial t} + \frac{\partial (\alpha (Q^2/A))}{\partial x} + gA \frac{\partial h}{\partial x} + \frac{gQ|Q|}{C^2 AR} = 0, \quad (16)$$

where  $t$  is time,  $x$  is measured distance along the channel (m),  $Q$  is discharge ( $\text{m}^3\text{s}^{-1}$ ),  $A$  is hydraulic area ( $\text{m}^2$ ),  $q$  is tributary outflow ( $\text{m}^3\text{s}^{-1}$ ),  $h$  is channel depth (m),  $C$  is Chezy coefficient ( $\text{m}^{0.5}\text{s}^{-1}$ ),  $R$  is ratio hydraulic (m), and  $\alpha$  is correction factor.

**3.3. Model Calibration.** The results of calibration are shown in Figure 6, which shows the observed precipitation in millimeters and the total runoff observed in one year (8,760 hours). The Nash-Sutcliffe model efficiency coefficient is used to assess the predictive power of hydrological models; this method is defined as follows:

$$E = 1 - \frac{\sum_{t=1}^T (Q_o^t - Q_m^t)^2}{\sum_{t=1}^T (Q_o^t - \bar{Q}_o)^2}, \quad (17)$$

where  $Q_o$  is the observed discharge,  $Q_m$  is modeled discharge, and  $t$  is time. The Nash-Sutcliffe model was used to compare the results.

Once the reference model represents the existing conditions in the basin, the different ETp methodologies have been introduced to the model with the results shown in Figure 7. The result shows variability of the response of the basin applying the five different ETp methods.

## 4. Results Analysis

Model calibration of 2003 (Figure 6: model calibration) has been carried out by using the Nash-Sutcliffe efficiency factor

( $E = 90.25\%$ ) that represents the approximation of the method of calibration basin. The hydrometric data compared with those observed have differences attributable to the size of the basin, detention, or extractions.

The obtained values of calibrated model were used to implement ETp results obtained from each method used. In Table 3 (soil parameters) parameters used for the Querétaro river basin for different coverage and calibration for AE/PE ratio value are listed.

From the calculated daily (D) and monthly (M) methods it can be appreciated that Hamon (D) and Thornthwaite (M) methods have water volume of 5.15 and 3.82 times the SHETRAN calculated volume whereas in the Blaney (D), Hargreaves (D), and Papadakys (M) methods the calculated volume is 31.10%, 37.92%, and 46.83% (68.97%, 59.12%, and 56.98% less) of the total, respectively (Table 4). According to these results obtained the Papadakys method has the best similarity with the reference model but does not have significant differences with Blaney and Hargreaves results.

According to the results presented, methods that have an overestimation of runoff volumes (compared with SHETRAN model results) are Hamon and Thornthwaite (315.66% and 218.46%); Blaney, Hargreaves, and Papadakys (31.09%, 37.92%, and 46.82%) represent a smaller runoff volume. None of the shown methods has values close to the observed values in the hydrometric station.

The Blaney method presents greater discharge values compared to the other methods in the representation of the ETp, where it is observed that small rainfall (10 mm accumulated in 24 hours) is intercepted by vegetation; the total volume in the year (Figures 4(b) and 5(b)) has values of 147.14 mm (Blaney) and 191.53 (Hamon). Rainfall higher than 25 mm accumulated in 24 hours represents the runoff observed in the basin outlet.

The 8,760 hours of modeling are shown in Figure 4 in which the evaporation ranges are among 195.26 and 307.67 mm accumulated (Figures 4(a) and 5(a)); soil evaporation (Figures 4(c) and 5(c)) has values ranging from 110.67 (Hamon) to 120.09 (Blaney) mm per year and the total cumulative transpiration (Figures 4(d) and 5(d)) is 862.12 mm (Thornthwaite) and 973.07 mm (Papadakys). The results represent an approach to values that official sources have not been available in the basin and can be obtained through measurements and instrumentation. This means that disaggregating the results in each of the different parameters

TABLE 3: SHETRAN soil parameters applied to model.

Soil category	Soil layer	Soil type	Depth at base of layer (m)	Saturated water content	Residual water content	Saturated conductivity (m/day)	Van Genuchten-Alpha ( $\text{cm}^{-1}$ ) <sup>a</sup>	Van Genuchten- $n$ <sup>b</sup>
1	1	Silt loam (10% sand : 10% clay)	1	0.452	0.093	0.163	$5.15E - 03$	1.681
2	1	Loamy sand (85% sand : 6% clay)	1	0.370	0.075	0.467	$1.99E - 02$	1.793
3	1	Sandy silt loam (35% sand : 10% clay)	1	0.434	0.086	0.317	$8.38E - 03$	1.587
3	2	Silty clay loam (10% sand : 27% clay)	2	0.507	0.144	0.036	$7.24E - 03$	1.608
3	3	Bedrock	5	0.200	0.030	0.100	$3.00E - 02$	1.900
4	1	Clay loam (35% sand : 27% clay)	1	0.489	0.153	0.055	$9.23E - 03$	1.657
6	1	Sandy clay (52% sand : 40% clay)	1	0.499	0.233	0.029	$1.07E - 02$	1.879
7	1	Silty clay (10% sand : 40% clay)	1	0.529	0.212	0.019	$6.54E - 03$	1.531
8	1	Sandy loam (65% sand : 10% clay)	1	0.412	0.098	0.622	$1.44E - 02$	1.736

<sup>a</sup>Van Genuchten exponent  $\alpha$  for soil moisture content-tension curve in  $\text{cm}^{-1}$ .

<sup>b</sup>Van Genuchten exponent  $n$  for soil moisture content-tension curve.

TABLE 4: SHETRAN peak discharge and volume calculated data. Significant differences are observed from daily (D) and monthly (M) methods where Thornthwaite and Hamon overestimate volume; on the other hand Blaney, Hargreaves, and Papadakys underestimate the calculated total volume (31.10%, 37.92%, and 46.83%, resp.).

ETp method	SHETRAN	Blaney (D)	Hamon (D)	Hargreaves (D)	Papadakys (M)	Thornthwaite (M)
Volume $\times 1000 \text{ m}^3$	76,273.78	23,667.24	393,299.12	31,176.94	32,809.94	291,799.56
Peak discharge ( $\text{m}^3 \text{ s}^{-1}$ )	60.58	18.84	191.24	22.97	28.37	132.35
Peak discharge percent	—	-68.90%	315.68%	-62.08%	-53.17%	218.47%
Total volume percent	—	-68.97%	515.64%	-59.12%	-56.98%	382.57%

of the basin allows a better understanding of the processes that are involved in the water balance including dry-wet transitions.

## 5. Discussion

In this paper a digital terrain model was implemented in which the concentration of runoff is observed in the upstream to the lower parts of the basin, so the ETp phenomenon considers the location and concentration of flows in the lowlands, streams, and surface runways with elevations ranging from 1,787 masl to 2,710 masl.

Different variables have been used that are involved in the hydrological cycle. The most important are land-use, canopy storage capacity, leaf area index, routing depth, actual-potential evaporation relationship (Table 2), depth at base of layer, saturated water content, residual water content, saturated conductivity, and Van Genuchten parameters (Table 3). The variables have been recovered from past investigations in the basin but must be evaluated in order to have more and better results. The obtained parameters

allow having a knowledge of the different variables used and they can help authorities to determine penalties or rewards to users that affect or contribute to its preservation. With this model the runoff volume is permanently determined with the climatological data or if they do not exist, they can be inferred from the model calculation.

The rainfall-runoff results from 2003 shows that for the basin conditions the SHETRAN model results represent the hydrological phenomena of the Querétaro river basin. Calibration parameters of the relationship AE/PE are shown in Table 2.

These values indicate that the losses in the basin are significant due to the detention of the basin, as well as the water volume losses of water extractions for agricultural and cattle uses.

Once the model has been calibrated, five different ETp methods analysis is made. The runoff maximum volume was obtained by the Thornthwaite and Hamon methods, while the methods results with smaller runoff volume were Blaney, Papadakys, and Hargreaves compared with the model calibrated.

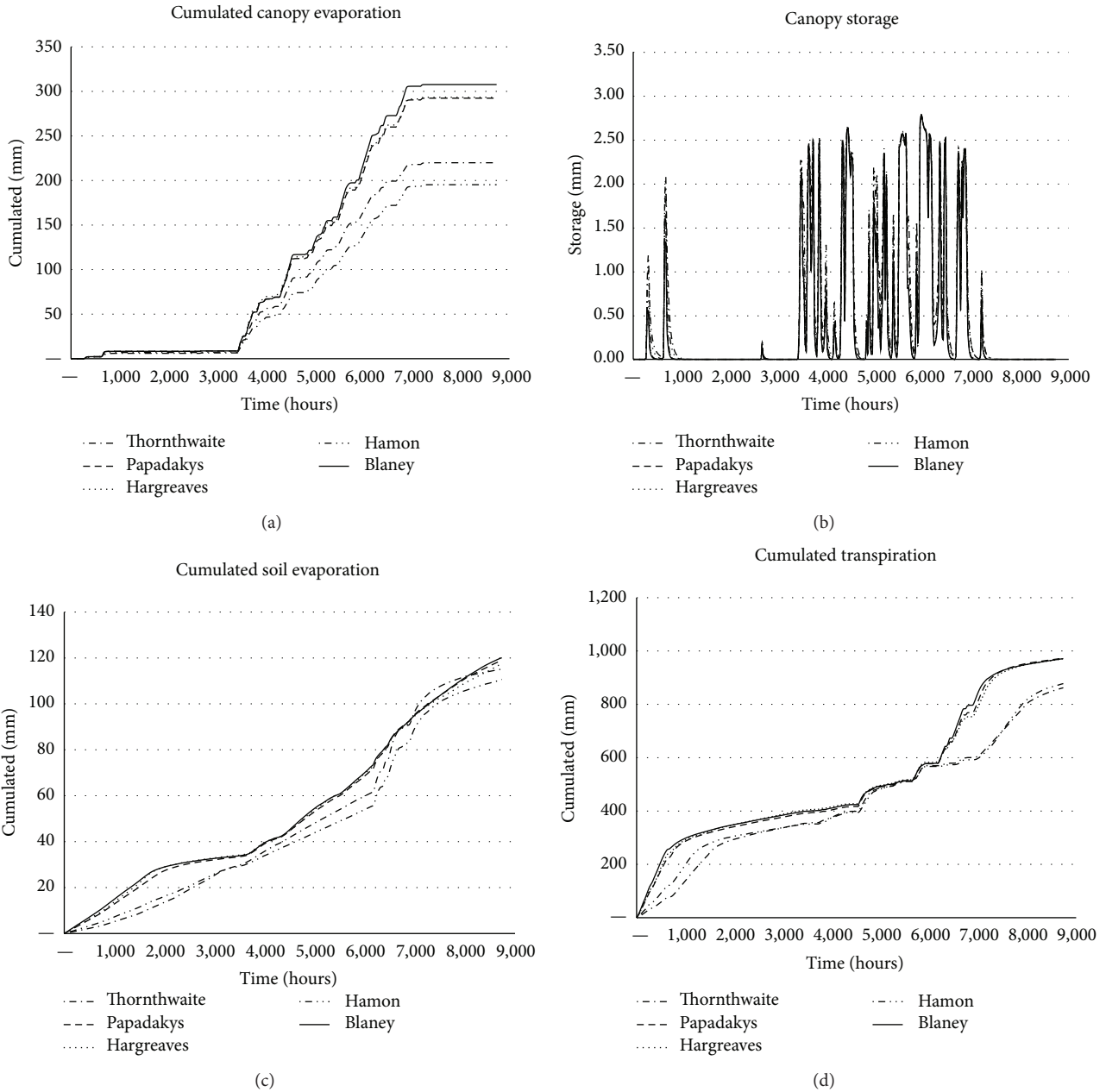


FIGURE 4: Cumulated and calculated values for canopy storage, transpiration, evaporation, and soil evaporation.

The results for the different methods show that the source of information based on variables such as saturated vapor deficit, relative humidity, temperature, solar radiation, and saturated vapor affects calculated volume, so care must be taken in evaluating and selecting the ETp method because the results may not be reliable. It is recommended to have extensive knowledge of the physical conditions of the basin, so that parameters such as AE/PE and the Strickler coefficient represent the phenomenon.

This tool allows an initial scheme for the regulation applied to the variables involved in the hydrologic cycle and carries out government programs of the environment

preservation with economic activities, with the results of physically based numerical models.

## 6. Conclusions

Knowledge of the hydrological parameters of a watershed is intended to enable authorities to carry out actions related to the rational use of resources and the preservation of hydrologic historical conditions as rainfall and runoff, and thus it is possible to regulate and restrict land-uses according to the effects on natural resources. In this paper data from the weather stations of the basin for a full year of observations

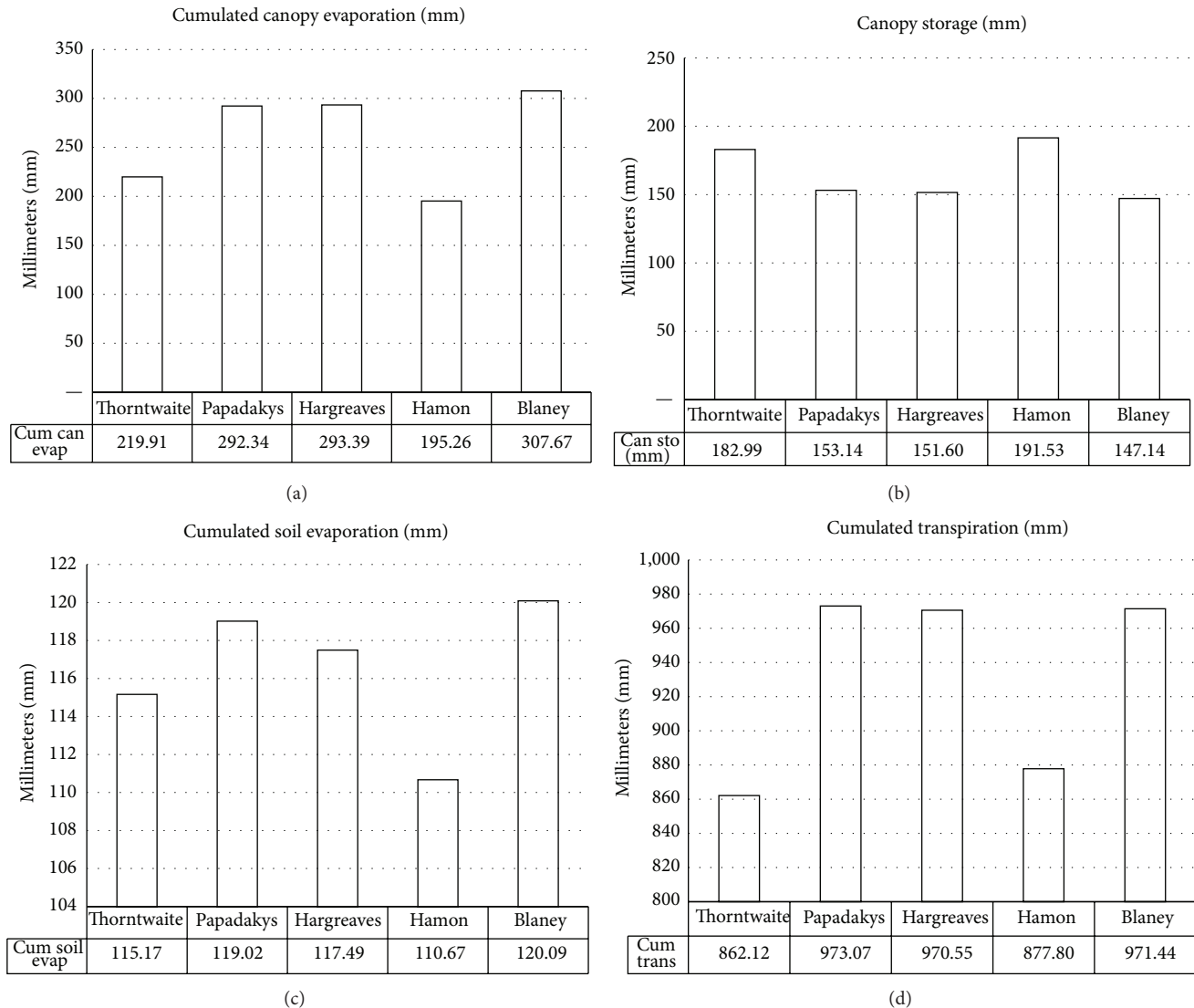


FIGURE 5: The different total calculated values are shown to the main variables of the five ET methods shown.

have been used, which has made it possible to determine the conditions of evaporation in dry weather periods and rain season which is a short part of the year.

The main limitations in this model are the fact that it has been applied to 2003 database that is the most complete year and is based on a basin of 2,700 square kilometers so that the methodology can be applied with different basins size. An advantage of using this model to calculate flow in ungagged basins is that once a hydrometric system is implemented, the climate data can be introduced according to the time-step observed as minutes or hours of accumulated rainfall.

This research in North America represents semiarid conditions; the methodological differences in the evaluated methods determine the total evaporation variation values for ETp methods of 1 (daily) and 30 days (monthly). Climatological information represents the rainfall in this basin; the urban area is located at the center of the basin, so that the results

suggest that urban area affects the calculated hydrograph shape and particularly the observed peak discharge.

The main objective of this methodology is to infer results based on a physically based model on watersheds where there is missing data or no data and that has parameters obtained from research, so that it can be applied to determine the amount of water available from rainfall-runoff processes in places where the total rainfall volume is low and the continuous changes in the components of vegetation, soil, and superficial drainage system demonstrate the lack of analysis tools to predict the increase in runoff volumes, given the continuous land-use changes.

According to the results, there is a big difference in the basin's runoff volume and peak discharge, calculated by different ETp methods, and therefore the application of each method for purposes of water balance should be considered to avoid wrong calculated values.

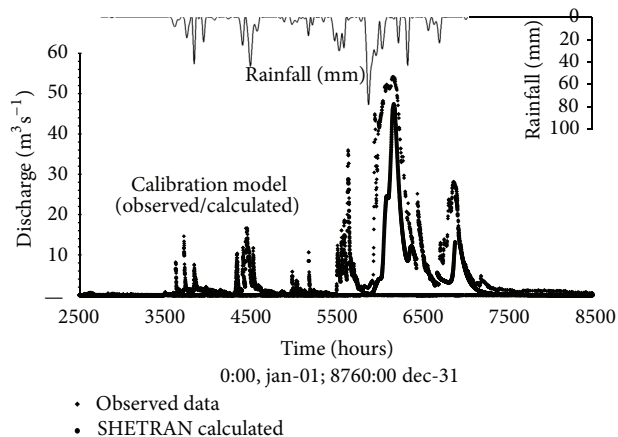


FIGURE 6: Model calibration: hydrometrical station discharge data, measured at the catchment outlet, and calculated SHETRAN discharge. In the ordinate axis the 2003 year hours are shown (0 hours is January 1st; 0:00 and 8,760 hours are December 31st, 24:00).

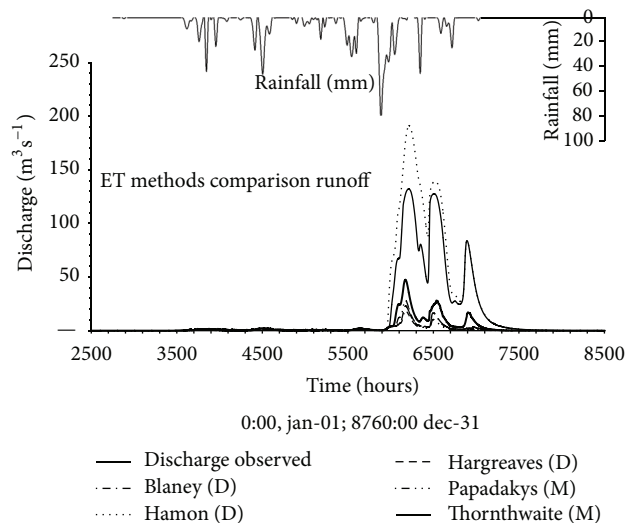


FIGURE 7: SHETRAN model using different ET methods. Observed discharge data in Ameche hydrometrical station are shown.

The obtained data show the differences between the methods used; however it is too important to pay special attention to the existing data in the basin, as there are variables that are very important in obtaining better results, such as the basin's size, quantity and quality of the weather stations data, the water bodies within the watershed, and operating policies. The proposed method allows collecting the different parameters of a watershed; however for the best results better measurements are needed in continuous periods which can be validated to identify significant basin alterations.

### Conflict of Interests

In this research the results using SHETRAN are shown, applied in the Querétaro river basin, in order to propose a

physically based methodology for water balance analysis in this catchment. With the obtained results five methodologies used in basins have been evaluated where data are scarce. The results suggest that all methodologies have differences between calculated and observed data. In Mexico the government agency of regulations on water issues is Comisión Nacional del Agua (CONAGUA), which can use the scientific contribution developed by research centers and universities. The results are intended to show the shortcomings of traditional methods in the calculation, but this does not affect the point of view of the authorities because all the methods are compared on the same analysis. Therefore the authors declare that there is no conflict of interests regarding the publication of this paper.

### Acknowledgments

The authors want to thank the Program of Water Resources and Environmental Engineering of Civil Engineering School (Universidad Autónoma de Querétaro), the CIAQ General Director Dr. Alfonso Gutierrez Lopez, 2012 Mexico Hydraulic Awarded Researcher, for reading comments, SIIG Engineering Consultancy finance support, and Research Fund CONACyT-CONAGUA 2010-2 (148159) from Modelo de Gestión y Administración de los Usos del Agua de la Cuenca del Rio Querétaro.

### References

- [1] F. A. Deviney Jr, D. E. Brown, and K. C. Rice, "Evaluation of bayesian estimation of a hidden continuous-time Markov chain model with application to threshold violation in water-quality indicators," *Journal of Environmental Informatics*, vol. 19, no. 2, pp. 70–78, 2012.
- [2] A. Amini, T. M. Ali, A. H. B. Ghazali, A. A. Aziz, and S. M. Akib, "Impacts of land-use change on streamflows in the damansara watershed, Malaysia," *Arabian Journal for Science and Engineering*, vol. 36, no. 5, pp. 713–720, 2011.
- [3] Y. Mitsuda and S. Ito, "A review of spatial-explicit factors determining spatial distribution of land use/land-use change," *Landscape and Ecological Engineering*, vol. 7, no. 1, pp. 117–125, 2011.
- [4] Y. P. Lin, N. M. Hong, P. J. Wu, and C. J. Lin, "Modeling and assessing land-use and hydrological processes to future land-use and climate change scenarios in watershed land-use planning," *Environmental Geology*, vol. 53, no. 3, pp. 623–634, 2007.
- [5] L. Y. Su, P. Christensen, and J. L. Liu, "Comparative study of water resource management and policies for ecosystems in China and Denmark," *Journal of Environmental Informatics*, vol. 21, no. 1, pp. 72–83, 2013.
- [6] M. E. Mendoza, G. Bocco, E. López-Granados, and M. Bravo Espinoza, "Hydrological implications of land use and land cover change: spatial analytical approach at regional scale in the closed basin of the Cuitzeo Lake, Michoacan, Mexico," *Singapore Journal of Tropical Geography*, vol. 31, no. 2, pp. 197–214, 2010.
- [7] Y. P. Li and G. H. Huang, "A recourse-based nonlinear programming model for stream water quality management," *Stochastic Environmental Research and Risk Assessment*, vol. 26, no. 2, pp. 207–223, 2012.

- [8] J. Ewen, *SHETRAN User Manual for Version 5*, WRSRL.2001.1, Water Resource Systems Research Laboratory, School of Civil Engineering and Geosciences, University of Newcastle, Newcastle upon Tyne, UK, 2001.
- [9] S. J. Birkinshaw and J. C. Bathurst, "Model study of the relationship between sediment yield and river basin area," *Earth Surface Processes and Landforms*, vol. 31, no. 6, pp. 750–761, 2006.
- [10] A. Guevara-Escobar, W. R. N. Edwards, R. H. Morton, P. D. Kemp, and A. D. Mackay, "Tree water use and rainfall partitioning in a mature poplar-pasture system," *Tree Physiology*, vol. 20, no. 2, pp. 97–106, 2000.
- [11] C. Mastachi-Loza, E. González-Sosa, R. Becerril-Piña, and I. Braud, "Interception loss by mesquite (*Prosopis laevigata*) and huisache (*Acacia farnesiana*) in the semiarid region of central Mexico," *Technology and Water Sciences*, vol. 1, no. 1, pp. 89–106, 2010.
- [12] A. Guevara-Escobar, E. González-Sosa, C. Véliz-Chávez, E. Ventura-Ramos, and M. Ramos-Salinas, "Rainfall interception and distribution patterns of gross precipitation around an isolated *Ficus benjamina* tree in an urban area," *Journal of Hydrology*, vol. 333, no. 2–4, pp. 532–541, 2007.
- [13] S. S. Nayak and M. M. Mandal, "Impact of land-use and land-cover changes on temperature trends over Western India," *Current Science*, vol. 102, no. 8, pp. 1166–1173, 2012.
- [14] R. Mahmood, R. Pielke, K. Hubbard et al., "Impacts of land use/land cover change on climate and future research priorities," *Bulletin of the American Meteorological Society*, vol. 91, no. 1, pp. 37–46, 2010.
- [15] S. J. Birkinshaw, P. James, and J. Ewen, "Graphical user interface for rapid set-up of SHETRAN physically-based river catchment model," *Environmental Modelling and Software*, vol. 25, no. 4, pp. 609–610, 2010.
- [16] Diario Oficial de la Federación de México, "Secretaría de Medio Ambiente y Recursos Naturales," Norma Oficial Mexicana NOM-011-CNA-2000, 2002, <http://www.conagua.gob.mx/CONAGUA07/Contenido/Documentos/N11.pdf>.
- [17] P. A. Burrough, *Principles of Geographical Information Systems for Land Resources Assessment*, Monographs on Soil and Resources Survey, no. 12, Oxford University Press, 1986.
- [18] B. De Foy, L. T. Molina, and M. J. Molina, "Satellite-derived land surface parameters for mesoscale modelling of the Mexico City basin," *Atmospheric Chemistry and Physics*, vol. 6, no. 5, pp. 1315–1330, 2006.
- [19] D. E. Carlyle-Moses, "Throughfall, stemflow, and canopy interception loss fluxes in a semi-arid Sierra Madre Oriental matorral community," *Journal of Arid Environments*, vol. 58, no. 2, pp. 181–202, 2004.
- [20] B. Blocken and J. Carmeliet, "A review of wind-driven rain research in building science," *Journal of Wind Engineering and Industrial Aerodynamics*, vol. 92, no. 13, pp. 1079–1130, 2004.
- [21] A. W. L. Veen, W. Klaassen, B. Kruijt, and R. W. A. Hutjes, "Forest edges and the soil-vegetation-atmosphere interaction at the landscape scale: the state of affairs," *Progress in Physical Geography*, vol. 20, no. 3, pp. 292–310, 1996.
- [22] G. D. Russell, C. P. Hawkins, and M. P. O'Neill, "The role of GIS in selecting sites for riparian restoration based on hydrology and land use," *Restoration Ecology*, vol. 5, no. 4, pp. 56–68, 1997.
- [23] N. A. Jackson, "Measured and modelled rainfall interception loss from an agroforestry system in Kenya," *Agricultural and Forest Meteorology*, vol. 100, no. 4, pp. 323–336, 2000.
- [24] Q. Xiao, E. McPherson, L. Ustin, M. Grismer, and J. Simpson, "Winter rainfall interception by two mature open-grown trees in Davis, California," *Hydrological Processes*, vol. 14, no. 4, pp. 763–784, 2000.
- [25] T. S. David, J. H. C. Gash, F. Valente, J. S. Pereira, M. I. Ferreira, and J. S. David, "Rainfall interception by an isolated evergreen oak tree in a Mediterranean savannah," *Hydrological Processes*, vol. 20, no. 13, pp. 2713–2726, 2006.
- [26] W. Klaassen, H. J. M. Lankreijer, and A. W. L. Veen, "Rainfall interception near a forest edge," *Journal of Hydrology*, vol. 185, no. 1–4, pp. 349–361, 1996.
- [27] Z. Xiefei, Y. Hao, Z. Ling, C. Wen, and W. Yong, "International meteorological and hydrological training and its evaluation at WMO RTC Nanjing," *Procedia Environmental Sciences*, vol. 12, pp. 1122–1128, 2012.
- [28] D. Tongway and N. Hindley, "Assessing and monitoring desertification with soil indicators," in *Rangeland Desertification*, S. Archer and O. Arnalds, Eds., Kluwer Academic Publishers, Dordrecht, The Netherlands, 2000.
- [29] K. G. McNaughton and P. G. Jarvis, "Using the Penman-Monteith equation predictively," *Agricultural Water Management*, vol. 8, no. 1–3, pp. 263–278, 1984.
- [30] C. W. Thornthwaite, "An approach toward a rational classification of climate," *Geographical Review*, vol. 38, pp. 55–94, 1948.
- [31] J. Papadakys, *Climatic Tables for the World*, Selbstverl. d. Verf., Buenos Aires, Argentina, 1961.
- [32] G. H. Hargreaves and Z. A. Samani, *Reference Crop Evapotranspiration from Ambient Air Temperature*, American Society of Agricultural Engineers, 1985.
- [33] H. F. Blaney and W. D. Criddle, *Determining Water Requirements in Irrigated Areas from Climatological and Irrigation Data*, Department of Agriculture, Soil Conservation Service, 1950.
- [34] J. H. C. Gash, "An analytical model of rainfall interception by forests," *Quarterly Journal of the Royal Meteorological Society*, vol. 105, pp. 43–45, 1979.
- [35] A. J. Rutter, K. A. Kershaw, P. C. Robins, and A. J. Morton, "A predictive model of rainfall interception in forests. I: derivation of the model from observations in a plantation of Corsican pine," *Agricultural Meteorology*, vol. 9, pp. 367–384, 1971.
- [36] A. J. Rutter and A. J. Morton, "A predictive model of rainfall interception in forest. Sensitivity of the model to stand and parameters and meteorological variables," *Journal of Applied Ecology*, vol. 14, no. 2, pp. 567–588, 1977.
- [37] J. Ewen, G. Parkin, and P. E. O'Connell, "SHETRAN: distributed river basin flow and transport modeling system," *Journal of Hydrologic Engineering*, vol. 5, no. 3, pp. 250–258, 2000.
- [38] B. T. Lukey, J. C. Bathurst, R. A. Hiley, and J. Ewen, "System design: Sediment erosion and transport," SHETRAN V3.4 manual, Appendix B.2, 1995.
- [39] S. J. Birkinshaw and J. Ewen, "Modelling nitrate transport in the Slapton Wood catchment using SHETRAN," *Journal of Hydrology*, vol. 230, no. 1–2, pp. 18–33, 2000.

## Research Article

# Study on Spacing Threshold of Nonsubmerged Spur Dikes with Alternate Layout

Xiaomeng Cao,<sup>1</sup> Zhenghua Gu,<sup>1</sup> and Hongwu Tang<sup>2</sup>

<sup>1</sup> College of Civil Engineering and Architecture, Zhejiang University, Hangzhou 310058, China

<sup>2</sup> State Key Laboratory of Hydrology-Water Resources and Hydraulic Engineering, Hohai University, Nanjing 210098, China

Correspondence should be addressed to Zhenghua Gu; wise@zju.edu.cn

Received 21 September 2013; Accepted 19 November 2013

Academic Editor: Y. P. Li

Copyright © 2013 Xiaomeng Cao et al. This is an open access article distributed under the Creative Commons Attribution License, which permits unrestricted use, distribution, and reproduction in any medium, provided the original work is properly cited.

This paper investigated the spacing threshold of nonsubmerged spur dikes with alternate layout to classify the impact scale of spur dikes. A mathematical model was built based on standard  $k$ - $\epsilon$  model, finite volume method (FVM), and rigid lid assumption and was verified by experimental data. According to dimensional analysis, three indices, that is,  $F_r$  (Froude number),  $B/b$  (channel width to dike length), and  $B/h$  (channel width to water depth), were identified as the influencing factors on the spacing threshold, based on which fifteen sets of conditions were simulated. The calculation results indicate that  $B/h$  is the most influencing parameter on  $S_c/b$  (spacing threshold to dike length), followed by  $B/b$  and  $F_r$ . A dimensionless empirical formula of spacing threshold is fitted by multivariate regression. The results of four sets of additional conditions illustrate that the generalization of empirical formula is satisfactory and the precision of interpolation is higher than that of extrapolation. Furthermore, the spacing threshold of alternate spur dikes is generally smaller than ipsilateral spur dikes.

## 1. Introduction

Spur dikes are one of the most widely used structures in hydraulic engineering. They are introduced in rivers for channel regulation, flood prevention, and river diversion [1–3]. After the construction of spur dike, the original channel becomes narrow and the flow characteristics in the vicinity of spur dike are changed. In actual projects, spur dike exerts influence on river system usually in the form of groups [4, 5]. These spur dikes (or groups) interact with each other in a certain range, beyond which they are independent [6]. They can be classified as large-scale and small-scale groups according to their interaction strength. When dikes have interaction with each other and play a role as whole, their combination can be considered as a spur dike group in small-scale, whereas a spur dike group in large-scale is comprised of single spur dikes or spur dike groups in small-scale with the long distance and few influence between each other [7, 8]. The past research of spur dikes has mainly been focused on the effects of small-scale spur dike groups on local river ways, but rarely on the overall impact of large-scale spur

dike groups on river systems [9–12]. However, the latter has vital significance to maintain river health, sustainable development and utilization of river systems, and integrated management of river basins [13–15]. Therefore, it is necessary to firstly find the cut-off point between small-scale and large-scale groups. On this matter, several scholars have proposed the concepts of spur dike's recovery length or uninfluenced distance [6, 9, 16], but so far, they did not obtain a clear conclusion. In our past research, the concept of spacing threshold has been proposed and used on nonsubmerged spur dikes with ipsilateral layout and same length [8]. In bank protection projects, however, alternate spur dikes arranged on both sides of the river are very common. Due to asymmetry, there are obvious differences in flow characteristics between alternate spur dikes and ipsilateral spur dikes [17]. Hence, it is necessary to conduct further investigations on the spacing threshold of alternate spur dikes.

In the current work, flume experiments considering nonsubmerged spur dikes with ipsilateral and alternate layout were conducted firstly. Then, a numerical model which depends on the standard  $k$ - $\epsilon$  model, the finite volume method

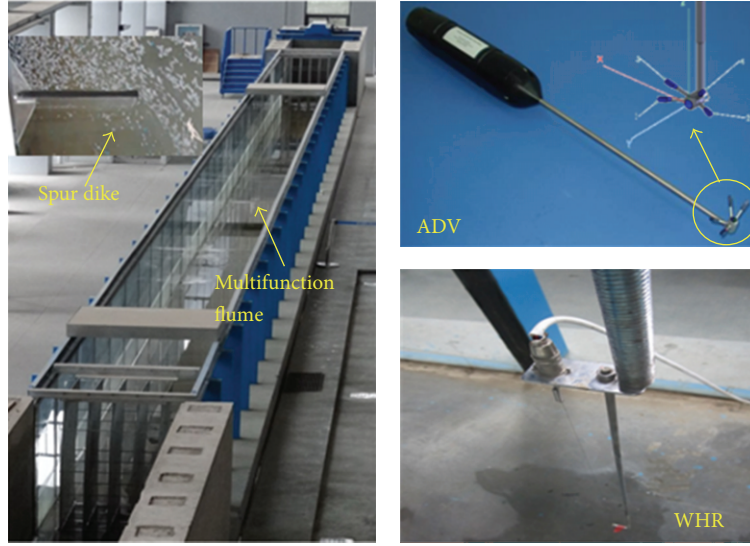


FIGURE 1: Multifunction flume and measuring instruments.

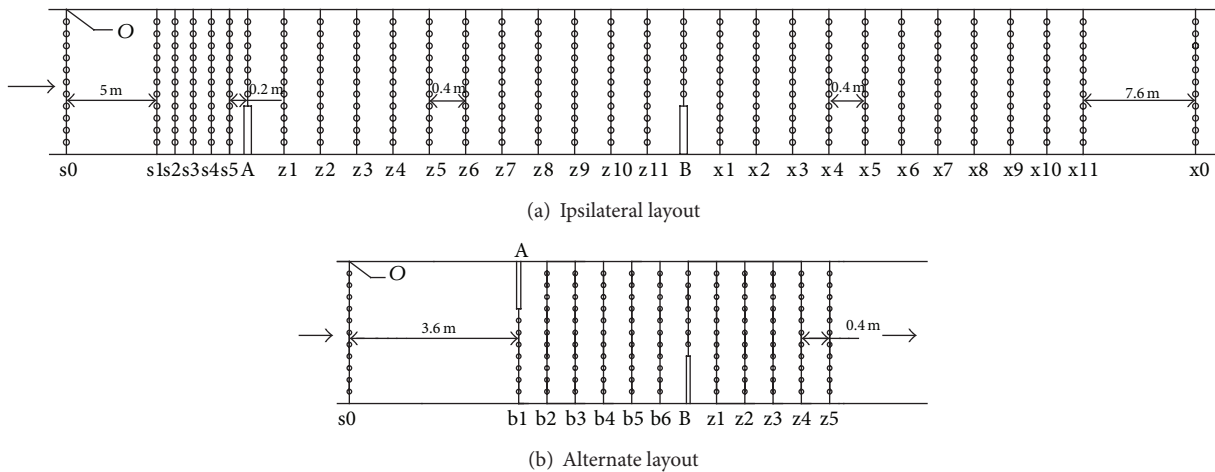


FIGURE 2: Spur dike layouts, monitoring cross sections, and monitoring points.

(FVM), and the rigid lid assumption was verified by observed data and employed to investigate the spacing threshold of alternate spur dikes.

## 2. Materials and Methods

**2.1. Flume Experiments.** The multifunction flume used in this study is 50 m long, 1.2 m wide, and 1.4 m deep, with a concrete floor and two toughened glass sidewalls. It is located in Jiangong, Test Hall of Zhejiang University, China, as shown in Figure 1. The longitudinal slope of the flume is zero. The spur dikes are made of plexiglass being 1.6 cm thick and 40 cm high, which are installed on the vertical walls of flume by slots. A three-dimensional ADV (Acoustic Doppler Velocimeter) probe is employed to measure the underlying velocity field, and WHR (wave height recorder) is utilized for bathymetry.

They are both shown in Figure 1. There are two kinds of the layouts of spur dikes (namely, ipsilateral and alternate) shown in Figure 2. The spur dikes 1, 2 and the inlet are placed at sections A, B, and s0, respectively. In the ipsilateral layout (Figure 2(a)), the flow velocity is recorded at 5 cross sections on the upstream of spur dike 1 with equal interval of 0.2 m, 11 (z1–z11) between spur dike 1 and spur dike 2 with equal interval of 0.4 m, and 11 (x1–x11) on the downstream of spur dike 2 with equal interval of 0.4 m. The outlet is placed at section x0 with 7.6 m from section x11. There are totally 31 monitoring cross sections with 341 points in the whole test region. In the alternate layout (Figure 2(b)), there are 10 cross sections (b2–z4) between b1 and z5 with equal interval of 0.4 m. The original coordinate is set at the point O at the bottom of flume as shown in Figure 2. The direction along the mainstream is X, along the water depth is Y, and along the axis of spur dike is Z.

TABLE 1: Verification conditions.

No.	Category	Flow rate $Q$ (m <sup>3</sup> /s)	Dike length $B$ (m)	Water depth $h$ (m)	Dike spacing $s$ (m)
v1	Ipsilateral	0.0416	0.4	0.15	4.8
v2	Alternate	0.0603	0.4	0.3	2.4

## 2.2. Numerical Model

**2.2.1. Model Construction and Boundary Conditions.** The commercial computational fluid dynamics (CFD) code, FLUENT, is chosen to build the numerical model. Several auxiliary surfaces are added to divide the calculation area into regular blocks. Hexahedral structured meshes are adopted and refined in the vicinity of spur dikes. In our past research [18], three turbulence models, that is, the standard  $k$ - $\epsilon$  model, the Reynolds stress model (RSM), and the large eddy simulation (LES) model, were used to simulate the flow field of nonsubmerged spur dikes. In each model, the free surface boundary was implemented by two approaches, that is, the rigid lid assumption and the volume of fluid (VOF) method. The results showed that the standard  $k$ - $\epsilon$  model combined with the rigid lid assumption was most efficient among all the combinations and it is used in this study.

The pressure-based solver in FLUENT is used. The hydraulic diameter  $D_H$  and the turbulence intensity  $I$  are selected as turbulence parameters, expressed in (1) and (2), respectively [19]:

$$D_H = \frac{2A}{C}, \quad (1)$$

$$I = 0.16(R_e)^{-1/8}, \quad (2)$$

where  $A$  is the cross section area;  $C$  is the wetted perimeter;  $R_e$  is the Reynolds number associated with  $D_H$ .

The pressure-velocity coupling is achieved by SIMPLIC (semi-implicit method for pressure-linked equations consistent). The body force weighted method is used for pressure discretization and the first-order upwind method for the discrete format of momentum, turbulent kinetic energy, and turbulent dissipation rate. For boundary conditions, the mass-flow-inlet is used for approaching flow at the inlet, the outflow at the outlet, no-slip walls for the vertical and bottom faces of flume and dike bodies, and standard wall functions for the solution of  $k$ ,  $\epsilon$  near walls. The rigid lid assumption takes the free surface as constant, and the top face of water body is assumed to be symmetric. Compared with the wall treatment method, the tangential velocity on the free surface may not be zero.

**2.2.2. Model Verification.** To verify the numerical model, two sets of experimental conditions, that is, ipsilateral (v1) and alternate (v2), listed in Table 1 are chosen. s5, z1, z6, z11, x1, and x0 cross sections are selected for ipsilateral spur dikes and b1, b4, B, and z3 for alternative spur dikes. Since the velocities of mainstream ( $X$  direction) are dominant and the velocities in  $Y$  and  $Z$  directions are very small, only the velocities in  $X$  direction ( $u$ ) are verified. Figure 3 compares the observed

and computed velocity in  $X$  direction along  $Z$  on a horizontal plane under v1 and v2 conditions. It is clearly revealed that the computed velocities agree well with the observed under both conditions. Therefore, the numerical model is accurate and can be used for the following analyses.

**2.3. Dimensional Analysis.** Since the spur dike flow is regarded as fully turbulent, viscous effects (i.e., Reynolds number effects) can be neglected [20]. The dike thickness is 0.016 m, which is insignificant for dike spacing. Hence, the dimensional analysis suggests the following functional relationship for the spacing threshold ( $S_c$ ) of nonsubmerged double spur dikes with alternate layout and same length in straight rectangular channel:

$$S_c = f(\rho, g, Q, h, b, B), \quad (3)$$

where  $B$  is channel width;  $b$  is dike length;  $Q$  is the flow rate of approaching flow;  $h$  is water depth. According to  $\pi$  theorem,  $\rho$ ,  $g$ , and  $h$  are selected as the basic parameters. Dimensionless equations are further deduced in

$$\frac{S_c}{b} = f\left(F_r, \frac{B}{h}, \frac{B}{b}\right), \quad (4)$$

$$F_r = \frac{Q}{Bh\sqrt{gh}}.$$

Based on (4), 15 conditions, listed in Table 2, are simulated. In c1 to c5,  $Q$  is varied in five steps from 0.0336 m<sup>3</sup>/s to 0.2352 m<sup>3</sup>/s leading to a variable  $F_r$  ranging from 0.1 to 0.7 with constant  $B/h = 6$  and  $B/b = 6$ . In c6 to c10,  $B/b$  is varied from 2.4 to 12 with constant  $F_r = 0.2$  and  $B/h = 6$ . In c11 to c15,  $B/h$  is varied from 2 to 12 with constant  $F_r = 0.2$  and  $B/b = 6$ . To exclude the interference of channel length on the spur dike field, the length of numerical flume is taken as 100 m after several trials.

## 3. Results and Discussion

**3.1. Spacing Thresholds.** In our past research [8], we have proposed the definition of spacing threshold of nonsubmerged double spur dikes with ipsilateral layout and same length in straight rectangular channel, that is, the spacing when lateral distributions of velocities at adjacent two spur dike sections become coincided. For simplicity, the depth-averaged velocity ( $\bar{u}$ ) near adjacent two spur dike tips can be used as an alternative criterion [8, 18]. For alternate spur dikes, the threshold value should be redefined as the spacing when the lateral distribution of velocities at adjacent two spur dike sections becomes just coincided in reverse direction, while the criterion for the ipsilateral spur dikes

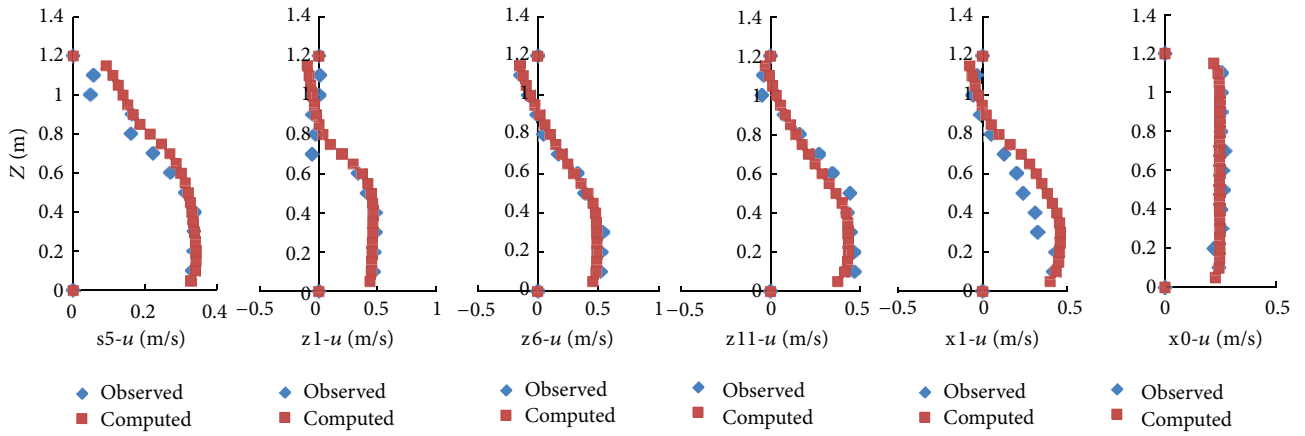
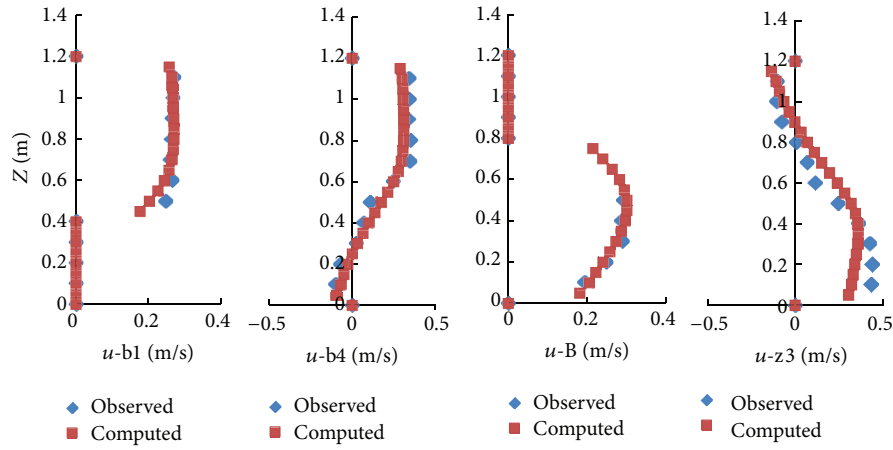
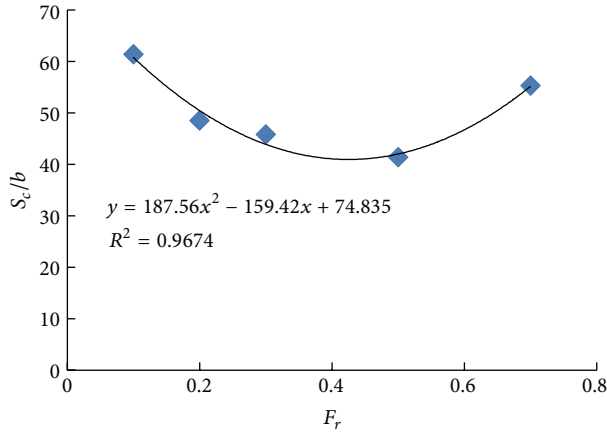
(a)  $v_1$  at horizontal plane  $Y = 0.16$  m(b)  $v_2$  at horizontal plane  $Y = 0.09$  mFIGURE 3: Comparison of  $u$  between observed and computed values.

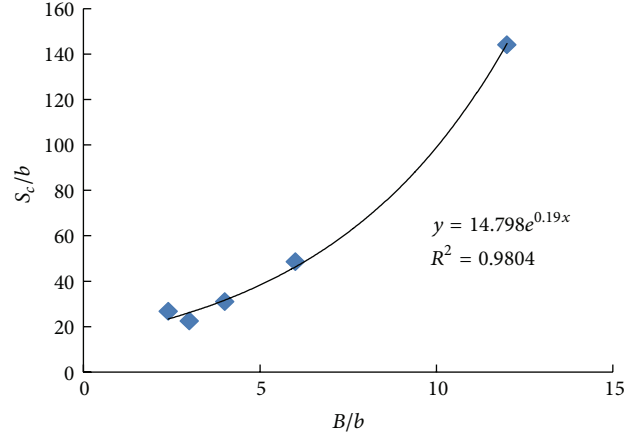
TABLE 2: Simulation conditions.

No.	$B$ (m)	$b$ (m)	$h$ (m)	$Q$ ( $\text{m}^3/\text{s}$ )	$F_r$	$B/h$	$B/b$
c1	1.2	0.2	0.2	0.0336	0.1	6	6
c2	1.2	0.2	0.2	0.0672	0.2	6	6
c3	1.2	0.2	0.2	0.1008	0.3	6	6
c4	1.2	0.2	0.2	0.168	0.5	6	6
c5	1.2	0.2	0.2	0.2352	0.7	6	6
c6	1.2	0.5	0.2	0.0672	0.2	6	2.4
c7	1.2	0.4	0.2	0.0672	0.2	6	3
c8	1.2	0.3	0.2	0.0672	0.2	6	4
c9	1.2	0.2	0.2	0.0672	0.2	6	6
c10	1.2	0.1	0.2	0.0672	0.2	6	12
c11	0.6	0.1	0.3	0.0618	0.2	2	6
c12	1.2	0.2	0.3	0.1235	0.2	4	6
c13	1.2	0.2	0.2	0.0672	0.2	6	6
c14	1.8	0.3	0.2	0.1009	0.2	9	6
c15	2.4	0.4	0.2	0.1345	0.2	12	6

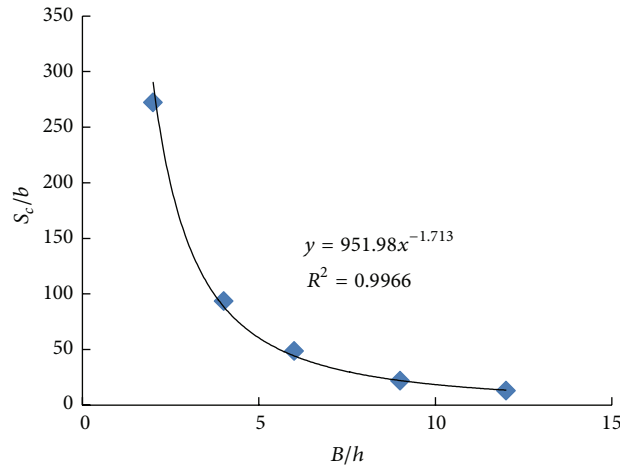
Note: c2, c9 and c13 are identical.



(a)  $S_c/b \sim F_r$  ( $B/h = 6$  and  $B/b = 6$ )



(b)  $S_c/b \sim B/b$  ( $F_r = 2$  and  $B/h = 6$ )



(c)  $S_c/b \sim B/h$  ( $F_r = 2$  and  $B/b = 6$ )

FIGURE 4: Variation of  $S_c/b$  with  $F_r$ ,  $B/b$  and  $B/h$ .

is still applicable. After the flow passes a spur dike, the disturbance reduces gradually but does not disappear. It is assumed that, when the velocity difference  $\Delta u$  reaches  $ku_0$  ( $k$  is a constant and less than 1 and here is 0.01), the velocities at spur dike 2 are considered recovered [21]. Spur dike 1 is placed at  $X = 26$  m and the spacing thresholds are searched by changing the location of spur dike 2. Table 3 lists the spacing threshold  $S_c$  and dimensionless parameter  $S_c/b$  of c1–c15.

**3.2. Multivariate Dimensionless Regression.** According to the data in Table 3, the variations of  $S_c/b$  with  $F_r$ ,  $B/b$  and  $B/h$  are shown in Figures 4(a), 4(b), and 4(c), respectively. It is clear that when  $B/h$  and  $B/b$  are maintained,  $S_c/b$  decreases first and then increases as  $F_r$  increases, and the minimum of  $S_c/b$  arises at around  $F_r = 0.4$ . The relationship between  $S_c/b$  and  $F_r$  is a quadratic function with an upward opening. When  $F_r$  and  $B/h$  are fixed,  $S_c/b$  increases monotonically as  $B/b$  increases, and the increase rate of  $S_c/b$  is firstly slow and then rapid. The relationship between  $S_c/b$  and  $B/b$  is approximately an exponential function. When  $F_r$  and  $B/b$  are

TABLE 3: Spacing thresholds of c1–c15.

No.	$S_c$ (m)	$S_c/b$
c1	12.273	61.365
c2	9.699	48.495
c3	9.154	45.770
c4	8.271	41.355
c5	11.056	55.280
c6	13.330	26.660
c7	8.982	22.455
c8	9.280	30.933
c9	9.699	48.495
c10	14.402	144.020
c11	27.214	272.140
c12	18.667	93.335
c13	9.699	48.495
c14	6.545	21.817
c15	5.059	12.648

TABLE 4: Testing conditions.

No.	$B$ (m)	$b$ (m)	$h$ (m)	$Q$ (m <sup>3</sup> /s)	$F_r$	$B/h$	$B/b$
t1	1	0.2	0.25	0.1566	0.4	4	5
t2	1.5	0.15	0.2	0.1051	0.25	7.5	10
t3	3	0.75	0.2	0.7564	0.9	15	4
t4	3	0.2	0.3	0.1235	0.08	10	15

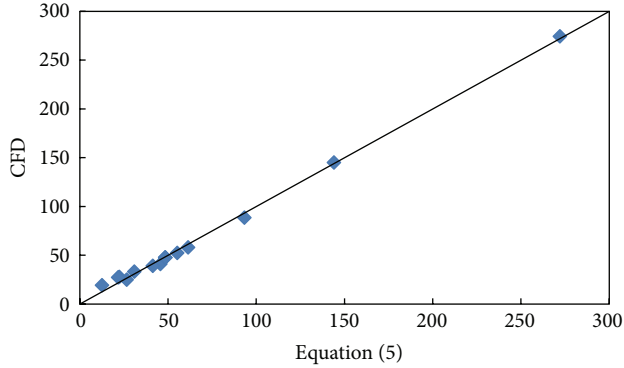


FIGURE 5: Results of the regression analysis.

maintained,  $S_c/b$  decreases monotonically as  $B/h$  increases, and when  $B/h$  is smaller than 5, the falling speed of  $S_c/b$  is very fast, and then it becomes smooth. The relationship between  $S_c/b$  and  $B/h$  follows a power function. In addition, it also appears that among the three influencing factors,  $B/h$  is the most influencing parameter on  $S_c/b$ , followed by  $B/b$  and  $F_r$ . Therefore, controlling the water depth in channel and designing the reasonable length of spur dikes can change the recovery distance of spur dike flow effectively.

The results of Figure 4 are regressed by the statistical analysis software SPSS, and the dimensionless empirical formula of the spacing threshold of nonsubmerged double spur dikes with alternate layout and same length is obtained as

$$\frac{S_c}{b} = 187.5F_r^2 - 159.4F_r + 14.64e^{0.19B/b} + 875.75\left(\frac{B}{h}\right)^{-1.71} - 14.69. \quad (5)$$

Figure 5 shows the comparison of the calculation results of  $S_c/b$  between CFD and (5) under c1–c15. A good agreement indicates that the fitting effect of empirical formula is satisfactory. To further test the accuracy of (5) applied to other conditions, four sets of new numerical simulations (t1–t4) listed in Table 4 are conducted by using the same model. Conditions t1 and t2 are the interpolation of c1–c15 while t3 and t4 are extrapolated. Table 5 lists the comparison of the calculation results of  $S_c$  between CFD and (5) under t1–t4. It can be seen that the relative error (RE) of the four conditions is less than 10%, which shows that the calculation accuracy of (5) for other conditions is satisfactory. Meantime, the RE of interpolation conditions is less than that of extrapolated

TABLE 5: Comparisons of  $S_c$  between CFD and (5) under t1–t4.

No.	CFD (m)	Equation (5) (m)	RE (%)
t1	13.868	14.245	2.72
t2	12.605	12.448	-1.25
t3	18.566	16.783	-9.60
t4	48.785	51.212	4.98

conditions, which reveals that the dimensionless empirical formula is more accurate for the interpolation conditions.

The dimensionless empirical formula of the spacing threshold of nonsubmerged double spur dikes with ipsilateral layout and same length is expressed in [8]

$$\frac{S_c}{b} = 143.15F_r^2 - 94.39F_r + 14.13\frac{B}{b} + 278.02\left(\frac{B}{h}\right)^{-0.53} - 79.38. \quad (6)$$

Figure 6 compares the empirical formulas (5) and (6) from univariate analyses. The variation tendencies of  $S_c/b$  with each influencing factor under the two types of spur dike layouts are similar, and  $S_c$  of alternate spur dikes are mostly smaller than those of ipsilateral spur dikes, which indicates that the flow passing alternate spur dikes is easier to recover.

The empirical formula obtained in this paper can be used to determine the impact scale of spur dikes in straight and rectangular channel. Meanwhile, the empirical formula can be used to find the recovery section of velocities at the downstream of spur dike, and it can be also used for solving the local head loss of spur dike [16]. In addition, the empirical formula lays a foundation for the research of cumulative effect of large-scale spur dikes on the river system. However, due to the assumptions used in the paper, it has inevitable application limitations. Specifically, it is required that the shape of the two spur dikes be straight without head slope, the angle between spur dike axis and flow direction of the two spur dikes be 90°, and the size of the two spur dikes be the same. The channel must be straight and rectangular with zero bottom slope. It should be noted that most of the limitations can be overcome by adding corresponding parameters to the empirical formula based on additional simulations. In the future, these works will be done to perfect the empirical formula and broaden its applicability.

#### 4. Conclusions

A numerical model combining the standard  $k$ - $\epsilon$  model, FVM, and rigid lid assumption has been built in this study to

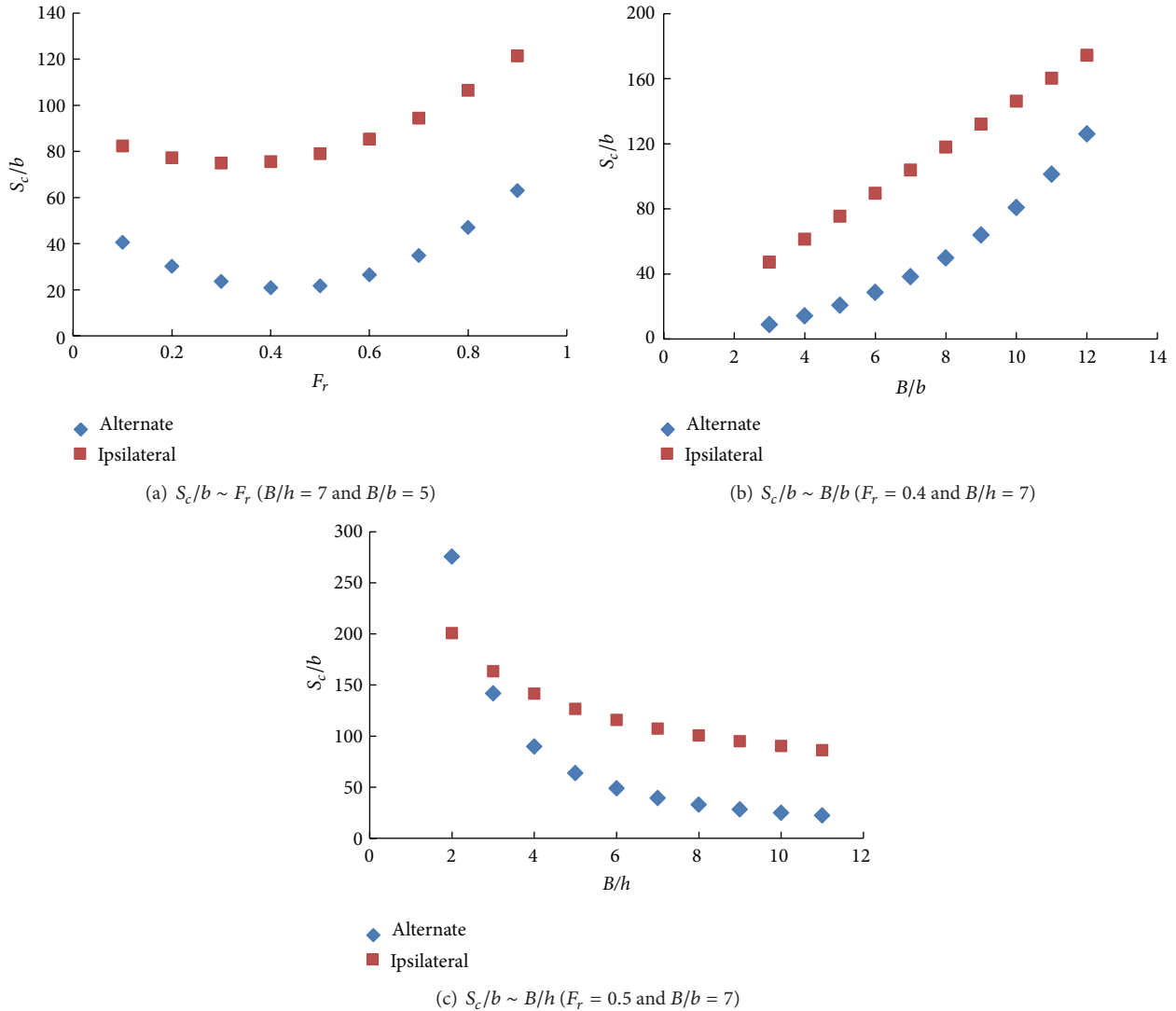


FIGURE 6: Comparison of empirical formulas between alternate spur dikes and ipsilateral spur dikes.

investigate the spacing threshold of nonsubmerged double spur dikes with alternate layout and same length in straight rectangular channel. The main conclusions are as follows.

- (1) The three influencing factors of  $S_c/b$ , that is,  $F_r$ ,  $B/b$  and  $B/h$ , are obtained by the dimensional analysis, and  $B/h$  is the most influencing parameter on  $S_c/b$ , followed by  $B/b$  and  $F_r$ .
- (2) The dimensionless empirical formula of spacing threshold is obtained via multivariate regression analysis, and its accuracy is satisfactory.
- (3) Compared with the spur dikes with ipsilateral layout, the spacing thresholds of alternate spur dikes are mostly smaller under the same conditions.
- (4) The empirical formula proposed in this paper lays down a foundation for the research of cumulative impact of spur dikes and other river structures, for example, bridge, levee, wing-dike, navigational dam, and so forth, on river systems.

### Acknowledgments

The study is supported by the National Natural Science Foundation of China (50909085, 51125034, and 51279046), the Department of Water Resources of Zhejiang Province (RC1106), and the Ministry of Water Resources of China (201101027).

### References

- [1] T. Ohmoto, R. Hirakawa, and N. Koreeda, "Effects of water surface oscillation on turbulent flow in an open channel with a series of spur dikes," in *Proceedings of the Hydraulic Measurements and Experimental Methods*, pp. 1–10, August 2002.
- [2] J. G. Duan, L. He, X. Fu, and Q. Wang, "Mean flow and turbulence around experimental spur dike," *Advances in Water Resources*, vol. 32, no. 12, pp. 1717–1725, 2009.
- [3] X. Zhang, P. Wang, and C. Yang, "Experimental study on flow turbulence distribution around a spur dike with different structure," in *Proceedings of the International Conference on*

*Modern Hydraulic Engineering (CMHE '12)*, vol. 28, pp. 772–775, Chongqing, China, March 2012.

- [4] R. A. Kuhnle, Y. Jia, and C. V. Alonso, “Measured and simulated flow near a submerged spur dike,” *Journal of Hydraulic Engineering*, vol. 134, no. 7, pp. 916–924, 2008.
- [5] A. Y. Ha, G. D. Li, L. Yang, and G. Chen, “Local flow field and scour near the water intake project between spur dikes,” *Journal of Basic Science and Engineering*, vol. 20, no. 4, pp. 602–611, 2012 (Chinese).
- [6] Q. Ying and Z. B. Jiao, *Hydraulics of Spur Dike*, Ocean Press, Beijing, China, 2004 (Chinese).
- [7] X. D. Xu, *Study on flow characteristics and impact scale of non-submerged orthogonal double spur dikes [M.S. thesis]*, Zhejiang University, Zhejiang, China, 2013 (Chinese).
- [8] Z. H. Gu, X. M. Cao, H. W. Tang, and X. D. Xu, “Investigation on spacing threshold of non-submerged double spur dikes with ipsilateral layout and same length”.
- [9] F. T. Chang and W. Feng, “Experiment at investigation of reasonable spacing among spur dikes,” *Journal of Hohai University*, vol. 20, no. 4, pp. 7–14, 1992 (Chinese).
- [10] W. Volker, A. S. Scott, and H. J. Gerhard, “Experiments on mass exchange between groin fields and main stream in rivers,” *Journal of Hydraulic Engineering*, vol. 134, no. 2, pp. 173–183, 2008.
- [11] X. G. Gao, H. F. Liu, G. F. Hua, and Z. Wang, “Rational spacing characters of double permeable spur,” *Journal of Shihezi University*, vol. 28, no. 5, pp. 614–617, 2010 (Chinese).
- [12] M. Vaghefi, M. Ghodsian, and S. Neyshabouri, “Experimental study on scour around a T-shaped spur dike in a channel bend,” *Journal of Hydraulic Engineering*, vol. 138, no. 5, pp. 471–474, 2012.
- [13] N. Pinter, A. A. Jemberie, J. W. F. Remo, R. A. Heine, and B. S. Ickes, “Cumulative impacts of river engineering, Mississippi and lower Missouri Rivers,” *River Research and Applications*, vol. 26, no. 5, pp. 546–571, 2010.
- [14] A. S. Mahiny and K. C. Clarke, “Simulating hydrologic impacts of urban growth using SLEUTH, multi criteria evaluation and runoff modeling,” *Journal of Environmental Informatics*, vol. 22, no. 1, pp. 27–38, 2013.
- [15] Y. Yang and H. Chen, “Assessing impacts of flow regulation on trophic interactions in a wetland ecosystem,” *Journal of Environmental Informatics*, vol. 21, no. 1, pp. 63–67, 2013.
- [16] P. J. Yue, W. S. Li, and X. G. Yang, “Length of whirlpool flow behind dikes,” *Journal of Waterway and Harbor*, vol. 2, pp. 3–9, 1999 (Chinese).
- [17] Y. Z. Feng and F. T. Chang, “Interaction between alternate groins in water flow,” *Journal of Hohai University*, vol. 24, no. 1, pp. 70–76, 1996 (Chinese).
- [18] Z. H. Gu, X. M. Cao, and W. Z. Jane Lu, “Appropriate CFD models for simulating flow around spur dike group”.
- [19] A. Karvinen and H. Ahlstedt, “Computation of turbulence models in case of three-dimensional diffuser,” in *Proceedings of the Open Source CFD International Conference*, 2008.
- [20] H. Azinfar and J. A. Kells, “Backwater prediction due to the blockage caused by a single, submerged spur dike in an open channel,” *Journal of Hydraulic Engineering*, vol. 134, no. 8, pp. 1153–1157, 2008.
- [21] Q. Ying, “Flow pattern near the submerged spur dike,” *Journal of Hohai University*, vol. 23, no. 4, pp. 62–68, 1995 (Chinese).

## Research Article

# Mathematical Modeling for Water Quality Management under Interval and Fuzzy Uncertainties

J. Liu, Y. P. Li, and G. H. Huang

MOE Key Laboratory of Regional Energy Systems Optimization, Resources and Environmental Research Academy, North China Electric Power University, Beijing 102206, China

Correspondence should be addressed to Y. P. Li; [yongping.li33@gmail.com](mailto:yongping.li33@gmail.com)

Received 4 October 2013; Accepted 29 November 2013

Academic Editor: X. S. Qin

Copyright © 2013 J. Liu et al. This is an open access article distributed under the Creative Commons Attribution License, which permits unrestricted use, distribution, and reproduction in any medium, provided the original work is properly cited.

In this study, an interval fuzzy credibility-constrained programming (IFCP) method is developed for river water quality management. IFCP is derived from incorporating techniques of fuzzy credibility-constrained programming (FCP) and interval-parameter programming (IPP) within a general optimization framework. IFCP is capable of tackling uncertainties presented as interval numbers and possibility distributions as well as analyzing the reliability of satisfying (or the risk of violating) system's constraints. A real-world case for water quality management planning of the Xiangxi River in the Three Gorges Reservoir Region (which faces severe water quality problems due to pollution from point and nonpoint sources) is then conducted for demonstrating the applicability of the developed method. The results demonstrate that high biological oxygen demand (BOD) discharge is observed at the Baishahe chemical plant and Gufu wastewater treatment plant. For nonpoint sources, crop farming generates large amounts of total phosphorus (TP) and total nitrogen (TN). The results are helpful for managers in not only making decisions of effluent discharges from point and nonpoint sources but also gaining insight into the tradeoff between system benefit and environmental requirement.

## 1. Introduction

Water is one of the most essential constituents for the human life, which is crucial to various socioeconomic issues such as industrial production, agricultural activity, environmental protection, and regional sustainability. In recent years, especially in China, degradation of water quality due to point and nonpoint source pollutions has become one of the most pressing environmental concerns. According to the 2010 Report on Water Environmental Quality of China, approximately 33.8% of the monitored river water (204 rivers with 409 monitoring stations) is in the worst two categories of water quality classification system (i.e., no longer fishable and of questionable agricultural value); around 53.8% of the assessed lakes and reservoirs are subject to different degrees of eutrophication [1]. Under such a circumstance, water quality management is an essential task for preserving valuable water resources and facilitating sustainable socioeconomic development in watershed systems [2]. In fact, water quality planning efforts are complicated with a variety of uncertainties, which may be derived from the random characteristics

of natural processes (i.e., precipitation and climate change) and stream conditions (i.e., stream flow, water supply, and point/nonpoint source pollution), the errors in estimated modeling parameters, and the vagueness of system objectives and constraints. In general, the system objectives are often associated with a number of socioeconomic and ecological factors such as economic return, environmental protection, and ecological sustainability, while the constraints are related to pollutant discharges, soil losses, resources availabilities, environmental requirements, and policy regulations. Moreover, these uncertainties may be further amplified by not only interactions among various uncertain and dynamic impact factors, but also their associations with economic implications of violated environmental requirements [3].

Fuzzy mathematic programming (FMP), based on fuzzy sets theory, can facilitate the analysis of system associated with uncertainties being derived from vagueness or fuzziness [4]. FMP method is suitable for situation when the uncertainties cannot be expressed as probability density functions (PDFs), such that adoption of fuzzy membership

functions becomes an attractive alternative [5]. Previously, a number of FMP methods were developed for water quality management [5–15]. For example, Julien [6] investigated the application of a fuzzy possibilistic programming to address imprecise parameters which were represented by possibility distributions in water quality decision-making problems. Mujumdar and Sasikumar [8] formulated a fuzzy flexible optimization model for dealing with the system's fuzzy goal and constraints in a water quality management problem. Nie et al. [12] proposed a fuzzy robust optimization model for water quality management of an agricultural system to deal with uncertainties expressed as fuzzy membership functions in both left- and right-hand-side coefficients (of the model's constraints). Maeda et al. [13] employed a fuzzy flexible optimization model which involved fuzzy set theory to express vagueness in constraints and objectives in river water quality management problems. Liu et al. [15] developed a two-stage fuzzy robust programming model for water quality management to address fuzzy parameters which were represented by possibility distributions in the left- and right-hand sides of the constraints.

Generally, FMP methods can be classified into three categories in view of the forms of uncertainties: (i) fuzzy flexible programming, (ii) robust programming, and (iii) fuzzy possibilistic programming. In detail, fuzzy flexible programming can deal with decision problems under fuzzy goal and constraints; however, it has difficulties in tackling ambiguous coefficients of the objective function and constraints. Robust programming improves upon fuzzy flexible programming by allowing fuzzy parameters in the constraints to be represented by possibility distributions. However, the main limitations of this method remain in its difficulties in tackling uncertainties in a nonfuzzy decision space. In fuzzy possibilistic programming, fuzzy parameters that are regarded as possibility distributions are introduced into the modeling frameworks. It can handle ambiguous coefficients in the left- and right-hand sides of the constraints and in the objective function.

Fuzzy credibility-constrained programming (FCP) is a computationally efficient fuzzy possibilistic programming approach that relies on mathematical concepts (i.e., the expected value of a fuzzy number and the credibility measure) and can support different kinds of fuzzy members such as triangular and trapezoidal forms as well as enabling the decision maker to satisfy some constraints in at least some given confidence levels [16]. When the credibility value of a fuzzy event reaches 1, the fuzzy event will certainly occur; when the credibility value of a fuzzy event reaches 0, the fuzzy event will not occur. For example, with respect to water quality management, if the allowable total phosphorus (TP) discharges are 7.0, 7.6, and 8.2 kg/day, and the amount of actual discharge may be 7.8 kg/day, then the credibility degree of the event, wherein the total phosphorus discharge can satisfy the river's self-purification capacity, would be 0.33; the credibility degree of its complement event (water pollution occur) would be 0.67. No feature of fuzzy sets would be missing by using credibility measure [16, 17]. However, the main limitation of FCP lies within its deterministic coefficients for the objective function, leading to potential

losses of valuable uncertain information; besides, when many uncertain parameters are expressed as fuzzy sets, interactions among these uncertainties may lead to serious complexities, particularly for large-scale practical problems [18]. In fact, in water quality management problems, uncertainty is an inherent component of any economic analysis, particularly those (e.g., effluent trading programs) associated with environmental policy and project appraisal [19]. For example, one major characteristic of nonpoint source pollution that differs from point source pollution is imperfect knowledge about pollutant loadings; the crop productivity and cost benefit coefficients are easier to be presented as intervals than by membership functions. Interval-parameter programming (IPP) is an alternative for handling uncertainties in the model's left- and/or right-hand sides as well as those that cannot be quantified as membership or distribution functions, since interval numbers are acceptable as its uncertain inputs [20].

Therefore, the objective of this study is to develop an inexact fuzzy credibility-constrained programming (IFCP) method for water quality management, through coupling fuzzy credibility-constrained programming (FCP) with interval-parameter programming (IPP). The main advantage of IFCP is that it can effectively handle uncertain parameters expressed as both fuzzy sets and interval values in the objective function and constraints. IFCP would not lead to serious complexities in its solution process, and it is applicable to large-scale practical problems. Then, the developed IFCP method is applied to a real-world case of water quality management of the Xiangxi River, which faces severe water quality problems due to point and nonpoint source pollution. The results obtained can help decision makers to generate alternatives for industrial production scale, water supply, cropped area, livestock husbandry size, and manure/fertilizer application rate, with consideration of river water quality management.

The paper will be organized as follows: Section 2 describes the development process of the IFCP; Section 3 provides a case study of river water quality management; Section 4 presents result analysis and discussion; Section 5 draws some conclusions and extensions.

## 2. Methodology

When coefficients in the constraints are ambiguous and can be expressed as possibility distributions, the problem can be formulated as a fuzzy credibility-constrained programming (FCP) model as follows:

$$\text{Max } f = \sum_{j=1}^n c_j x_j, \quad (1a)$$

subject to:

$$\text{Cr} \left\{ \sum_{j=1}^n a_{ij} x_j \leq \tilde{b}_i \right\} \geq \lambda_i, \quad (1b)$$

$$x_j \geq 0, \quad i = 1, 2, \dots, n, \quad (1c)$$

where  $x = (x_1, x_2, \dots, x_n)$  is a vector of nonfuzzy decision variables,  $c_j$  are benefit coefficients,  $a_{ij}$  are technical coefficients, and  $\bar{b}_i$  are right-hand-side coefficients. Some or all of these coefficients can be fuzzy numbers. Cr is the credibility measure which is firstly proposed and was widely used in many research areas [16]. Let  $\xi$  be a fuzzy variable with membership function  $\mu$ , and let  $r$  be real numbers. The credibility measure can be defined as follows [17]:

$$\text{Cr} \{ \xi \leq r \} = \frac{1}{2} \left( \sup_{x \leq r} \mu(x) + 1 - \sup_{x > r} \mu(x) \right). \quad (2)$$

Noteworthy, since  $\text{Pos} \{ \xi \leq r \} = \sup_{x \leq r} \mu(x)$  and  $\text{Nec} \{ \xi \leq r \} = 1 - \sup_{x > r} \mu(x)$ , the credibility measure can be defined as follows:

$$\text{Cr} \{ \xi \leq r \} = \frac{1}{2} (\text{Pos} \{ \xi \leq r \} + \text{Nec} \{ \xi \leq r \}). \quad (3)$$

Similar to the probability measure,

$$\text{Cr} \{ \xi \leq r \} + \text{Cr} \{ \xi > r \} = 1. \quad (4)$$

Consider a triangular fuzzy variable since it is the most popular possibility distribution, the fuzzy variable  $\xi$  fully determined by the triplet  $(\underline{t}, t, \bar{t})$  of crisp numbers with  $\underline{t} < t < \bar{t}$  whose membership function is given by

$$\mu(r) = \begin{cases} \frac{r - \underline{t}}{t - \underline{t}}, & \text{if } \underline{t} \leq r \leq t, \\ \frac{r - \bar{t}}{t - \bar{t}}, & \text{if } t \leq r \leq \bar{t}, \\ 0, & \text{otherwise.} \end{cases} \quad (5)$$

Based on this membership function, credibility of  $r \leq \xi$  can be expressed by

$$\text{Cr} \{ r \leq \xi \} = \begin{cases} 1, & \text{if } r \leq \underline{t}, \\ \frac{2t - \underline{t} - r}{2(t - \underline{t})}, & \text{if } \underline{t} \leq r \leq t, \\ \frac{r - \bar{t}}{2(t - \bar{t})}, & \text{if } t \leq r \leq \bar{t}, \\ 0, & \text{if } r \geq \bar{t}. \end{cases} \quad (6)$$

The inverse function of the credibility measure is  $\text{Cr}^{-1}(\lambda) = r$ , when  $\text{Cr}(r \leq \xi) = \lambda$ . Normally, it is assumed that a significant credibility level should be greater than 0.5. Therefore, (6) can be written as

$$\text{Cr} \{ r \leq \xi \} = \frac{2t - \underline{t} - r}{2(t - \underline{t})} \geq \lambda. \quad (7)$$

Then, (7) can be transformed into a deterministic constraint as follows:

$$r \leq t + (1 - 2\lambda)(t - \underline{t}). \quad (8)$$

The fuzzy credibility-constrained programming (FCP) model can be formulated as follows:

$$\text{Max } f = \sum_{j=1}^n c_j x_j, \quad (9a)$$

subject to

$$\sum_{j=1}^n a_{ij} x_j \leq b_i + (1 - 2\lambda_i)(b_i - \underline{b}_i), \quad (9b)$$

$$x_j \geq 0, \quad i = 1, 2, \dots, n. \quad (9c)$$

Obviously, model (9a), (9b), and (9c) can effectively deal with uncertainties in the right-hand sides presented as fuzzy sets when coefficients in the left-hand sides and in the objective function are deterministic. However, in real-world optimization problems, uncertainties may exist in both left- and right-hand sides (of the constraints) as well as objective-function coefficients; moreover, the quality of information that can be obtained is mostly not satisfactory enough to be presented as fuzzy membership functions [2]. For example, economic return, pollutant discharge, and resources availability are easier to be expressed as intervals than membership functions [21]. Since interval-parameter programming (IPP) is useful for addressing uncertainties expressed as interval values in modeling parameters, it can be integrated into the FCP model to deal with uncertainties presented in fuzzy and interval formats. Then, an interval fuzzy credibility-constrained programming (IFCP) can be formulated as follows:

$$\text{Max } f^\pm = \sum_{j=1}^n c_j^\pm x_j^\pm, \quad (10a)$$

subject to

$$\sum_{j=1}^n a_{ij}^\pm x_j^\pm \leq b_i + (1 - 2\lambda_i^\pm)(b_i - \underline{b}_i), \quad (10b)$$

$$x_j^\pm \geq 0, \quad i = 1, 2, \dots, n, \quad (10c)$$

where the “-” and “+” superscripts represent the lower- and upper-bounds of interval parameters/variables, respectively. Then, a two-step solution method is proposed for facilitating computations of the IFCP model. The first submodel can be formulated as follows:

$$\text{Max } f^+ = \sum_{j=1}^{k_1} c_j^+ x_j^+ + \sum_{j=k_1+1}^n c_j^+ x_j^-, \quad (11a)$$

subject to

$$\sum_{j=1}^{k_1} |a_{ij}|^- \text{Sign}(a_{ij}^-) x_j^+ + \sum_{j=k_1+1}^n |a_{ij}|^+ \text{Sign}(a_{ij}^+) x_j^- \quad (11b)$$

$$\leq b_i + (1 - 2\lambda_i^-) (b_i - \underline{b}_i), \quad \forall i = 1, 2, \dots, m,$$

$$x_j^+ \geq 0, \quad j = 1, 2, \dots, k_1, \quad (11c)$$

$$x_j^- \geq 0, \quad j = k_1 + 1, \dots, n, \quad (11d)$$

where  $c_j^+$  ( $j = 1, 2, \dots, k_1$ )  $> 0$ ;  $c_j^+$  ( $j = k_1 + 1, k_2 + 1, \dots, n$ )  $< 0$ ;  $\text{Sign}(a_{ij}^\pm) = -1$  when  $a_{ij}^\pm < 0$ ;  $\text{Sign}(a_{ij}^\pm) = 1$  when  $a_{ij}^\pm > 0$ ;  $\lambda_i^-$  is the lower bound of the credibility level value. The optimal solutions of the first submodel would be  $x_{j\text{opt}}^+$  ( $j = 1, 2, \dots, k_1$ ) and  $x_{j\text{opt}}^-$  ( $j = k_1 + 1, k_2 + 1, \dots, n$ ). In the second step, the submodel corresponding to  $f^-$  can be formulated:

$$\text{Max } f^- = \sum_{j=1}^{k_1} c_j^- x_j^- + \sum_{j=k_1+1}^n c_j^+ x_j^+, \quad (12a)$$

subject to

$$\sum_{j=1}^{k_1} |a_{ij}|^+ \text{Sign}(a_{ij}^+) x_j^- + \sum_{j=k_1+1}^n |a_{ij}|^- \text{Sign}(a_{ij}^-) x_j^+ \quad (12b)$$

$$\leq b_i + (1 - 2\lambda_i^+) (b_i - \underline{b}_i), \quad \forall i = 1, 2, \dots, m,$$

$$0 \leq x_j^- \leq x_{j\text{opt}}^+, \quad j = 1, 2, \dots, k_1, \quad (12c)$$

$$x_j^+ \geq x_{j\text{opt}}^-, \quad j = k_1 + 1, \dots, n. \quad (12d)$$

The optimal solutions of model (11a), (11b), (11c), and (11d) would be  $x_{j\text{opt}}^-$  ( $j = 1, 2, \dots, k_1$ ) and  $x_{j\text{opt}}^+$  ( $j = k_1 + 1, k_2 + 1, \dots, n$ ) can be obtained. Through integrating the solutions of the two submodels, the solution for the objective-function value and decision variables can be obtained as follows:

$$f_{\text{opt}}^\pm = [f_{\text{opt}}^-, f_{\text{opt}}^+], \quad (13a)$$

$$x_{j\text{opt}}^\pm = [x_{j\text{opt}}^-, x_{j\text{opt}}^+]. \quad (13b)$$

### 3. Case Study

The Xiangxi River (which ranges in longitude from  $110^\circ 25'$  to  $111^\circ 06'$  E and in latitude from  $30^\circ 57'$  to  $31^\circ 34'$  N) is located at 40 km upstream of the Three Gorges Reservoir [22]. It

is 94 km long with a catchment area of 3099 km<sup>2</sup>, and its elevation generally ranges from 154 m to 3000 m. It is located in the subtropical continental monsoon climate zone, with an annual temperature of 15.6°C (from 1961 to 2004) and the long-term annual mean runoff depth of 688 mm [23]. Moreover, it is one of the rainiest centers in the west of Hubei province, with an average annual precipitation ranges from 900 mm to 1200 mm. The temporal precipitation of this basin is uneven, which varies largely among different seasons. For example, more than 41% precipitation occurs in June to August, and the rainfall in the spring, autumn, and winter seasons occupy 28%, 26%, and 5% of the total precipitation per year, respectively. There are plenty of mineral resources (i.e., phosphate ore, coal, pyrite, and granite), where the reserve of phosphorite is among the top three in China, which reaches 357 million t (i.e., tonne) [1]. Relying on these advantages, the number of phosphorus mining companies and related chemical plants are increasing along the banks of the Xiangxi River. Besides, multiple crops such as rice, maize, wheat, citrus, tea, potato, and vegetable are cultivated in the catchment since the land-use patterns are diverse, and the tillable area land is approximately 294.5 km<sup>2</sup>. In addition, pig, ox, sheep, and domestic fowl are the main live stocks in animal husbandry. The main pattern is scattered livestock breeding instead of large-scale standardized breeding.

Currently, water quality problems due to point and nonpoint source pollution discharges become more and more challenging in this catchment. Main point sources include five chemical plants (i.e., GF, BSH, PYK, LCP, and XJLY), six phosphorus mining companies (i.e., XL, XH, XC, GP, JJW, and SJS), and four wastewater treatment plants (WTPs) (i.e., Gufu, Nanyang, Gaoyang, and Xiakou), while four agricultural zones (AZ1 to AZ4) are the main nonpoint sources due to the application of manure/fertilizer. These point and nonpoint sources scatter along a length of about 51 km river stretch which is segmented into five reaches, and the reaches are marked as I to V. The main water quality problems include (i) the immoderate discharge of high-concentration phosphorus-containing wastewater and industrial soil wastes (i.e., chemical wastes, slags, and tailings) far exceed what can be decomposed by self-purification (according to the field investigation, 23.89 t of phosphorus enters downstream of the Xiangxi River); (ii) high potential for generating soil erosion and surface runoff due to the special geography and heavy rainfall (i.e., the average erosion modulus reaches 6,488 t/(km<sup>2</sup>·a) in Xiangshan County in this catchment); (iii) large amounts of nutrient pollutants (in terms of phosphorus and nitrogen) in livestock wastewater and wastes (from pig, ox, sheep, and domestic fowl breeding) are drained into the river by direct discharge or in rainfall. In such a circumstance, decision makers should seek to develop a sound pollution control plan to ameliorate the current situation of the water environment since it is infeasible and technical impossible to ensure zero emission of pollutants.

In this study, the planning horizon is one year. Moreover, since some crops should be grown in dry season, while some other crops should be cultivated in wet season, two periods are chosen to cover the planning horizon. The first period

is from June to October (i.e., dry season), and the second period is from November to May of the next year (i.e., wet season). The objective is to maximize the net system benefit subject to the environmental requirements under uncertainty over the planning horizon. Policies in terms of the related human activities (i.e., industrial, municipal, and agricultural activities) and the pollutant discharges (from fifteen point and four nonpoint sources) are critical for ensuring a maximum system benefit and a safe water quality [24]. Based on field investigations and related literatures, biological oxygen demand (BOD), total nitrogen (TN), and total phosphorus (TP) are selected as water quality indicators [1, 25]. To develop the local economy in a sustainable manner, pollutant discharge should be controlled by setting the thresholds for TP, TN, and BOD discharge in each reach [26]. However, human-induced imprecision in acquiring these thresholds (i.e., lack of available data and biased judgment) make it more complicate.

On the other hand, uncertainties in the study system include the following: (a) cost of wastewater treatment, manure, and fertilizer purchase are associated with many uncertain factors, which are expressed as interval numbers (e.g., an interval of [30, 35] RMB¥/t is denoted as cost of manure purchase of AZI in dry season); (b) the BOD and TP treatment efficiencies of wastewater in WTPs and chemical plants are related to operating conditions of the treatment facilities, which cannot be obtained as deterministic numbers (e.g., an interval of [0.89, 0.92] is denoted as treatment efficiencies of wastewater in Xiaokou WTP); (c) nonpoint source losses of nitrogen and phosphorus from agricultural zones fluctuate dynamically due to variability in soil erosion (corresponding to solid-phase nitrogen) and surface runoff (corresponding to dissolved nitrogen) (e.g., average soil loss from AZI planted with citrus in dry season would be [20.49, 22.82] t/ha), and runoff from AZI planted with citrus in dry season would be [78.07, 96.50] mm); (d) the amount of fertilizer and manure applications may vary with the soil fertility to meet the nutrient demands of each crop (i.e., nitrogen and phosphorus); (e) energy and digestible protein demands of human and animals are determined by crops' yield (e.g., yield of citrus planted in AZI during dry season would be [10.3, 12.6] t/ha). Therefore, based on the IFCP method developed in Section 2, the study problem can be formulated as:

$$\begin{aligned} \text{Max } f^\pm = & \sum_{i=1}^5 \sum_{t=1}^2 L_t \cdot BC_{it}^\pm \cdot PLC_{it}^\pm + \sum_{s=1}^4 \sum_{t=1}^2 L_t \cdot BW_{st}^\pm \cdot QW_{st}^\pm \\ & + \sum_{p=1}^6 \sum_{t=1}^2 L_t \cdot BP_{pt}^\pm \cdot PLM_{pt}^\pm \\ & + \sum_{r=1}^4 BL_r^\pm \cdot NL_r^\pm + \sum_{j=1}^4 \sum_{k=1}^9 \sum_{t=1}^2 CY_{jkt}^\pm \cdot BA_{jkt}^\pm \cdot PA_{jkt}^\pm \\ & - \sum_{j=1}^4 \sum_{k=1}^9 \sum_{t=1}^2 CM_{jt}^\pm \cdot AM_{jkt}^\pm \end{aligned}$$

$$\begin{aligned} & - \sum_{j=1}^4 \sum_{k=1}^9 \sum_{t=1}^2 CF_{jt}^\pm \cdot AF_{jkt}^\pm \\ & - \sum_{i=1}^5 \sum_{t=1}^2 L_t \cdot PLC_{it}^\pm \cdot WC_{it}^\pm \cdot CC_{it}^\pm \\ & - \sum_{s=1}^4 \sum_{t=1}^2 L_t \cdot QW_{st}^\pm \cdot GT_{st}^\pm \cdot CT_{st}^\pm \\ & - \sum_{j=1}^4 \sum_{k=1}^9 \sum_{t=1}^2 PA_{jkt}^\pm \cdot IQ_{jkt}^\pm \cdot WSP_t^\pm \\ & - \sum_{i=1}^5 \sum_{t=1}^2 L_t \cdot PLC_{it}^\pm \cdot FW_{it}^\pm \cdot WSP_t^\pm \\ & - \sum_{s=1}^4 \sum_{t=1}^2 L_t \cdot QW_{st}^\pm \cdot WSP_t^\pm, \end{aligned} \quad (14a)$$

subject to

(1) wastewater treatment capacity constraints:

$$QW_{st}^\pm \cdot GT_{st}^\pm \leq TPC_{st}^\pm \quad (14b)$$

$$WC_{it}^\pm \cdot PLC_{it}^\pm \leq TPD_{it}^\pm, \quad (14c)$$

(2) BOD discharge constraints:

$$\text{Cr} \left\{ PLC_{it}^\pm \cdot WC_{it}^\pm \cdot IC_{it}^\pm \cdot (1 - \eta_{BOD,it}^\pm) \leq \widetilde{ABC}_{it}^\pm \right\} \geq \lambda^\pm \quad (14d)$$

$$\text{Cr} \left\{ QW_{st}^\pm \cdot GT_{st}^\pm \cdot BM_{st}^\pm \cdot (1 - \eta_{BOD,st}^\pm) \leq \widetilde{ABW}_{st}^\pm \right\} \geq \lambda^\pm, \quad (14e)$$

(3) nitrogen discharge constraints:

$$\text{Cr} \left\{ \left( L_t \cdot \sum_{r=1}^4 AML_{rt}^\pm \cdot NL_r^\pm + L_t \right. \right.$$

$$\left. \cdot AMH_t^\pm \cdot RP_t^\pm - \sum_{j=1}^4 \sum_{k=1}^9 AM_{jkt}^\pm \right) \quad (14f)$$

$$\left. \cdot MS_t^\pm \cdot \varepsilon_{NM}^\pm + L_t \cdot RP_t^\pm \cdot ACW_t^\pm \cdot DNR_t^\pm \leq \widetilde{ANL}_t^\pm \right\} \geq \lambda^\pm$$

$$\sum_{k=1}^9 (NS_{jk}^\pm \cdot SL_{jkt}^\pm + RF_{jkt}^\pm \cdot DN_{jkt}^\pm) \cdot PA_{jkt}^\pm \quad (14g)$$

$$\leq MNL_{jt}^\pm \cdot TA_{jt}^\pm,$$

(4) phosphorus discharge constraints:

$$\text{Cr} \left\{ \text{PLC}_{it}^{\pm} \cdot [\text{WC}_{it}^{\pm} \cdot \text{PCR}_{it}^{\pm} \cdot (1 - \eta_{TP,it}^{\pm}) + \text{ASC}_{it}^{\pm} \cdot \text{SLR}_{it}^{\pm} \cdot \text{PSC}_{it}^{\pm}] \leq \widetilde{\text{APC}_{it}^{\pm}} \right\} \geq \lambda^{\pm} \quad (14h)$$

$$\text{Cr} \left\{ \left( L_t \cdot \sum_{r=1}^4 \text{AML}_{rt}^{\pm} \cdot \text{NL}_r^{\pm} + L_t \cdot \text{AMH}_t^{\pm} \cdot \text{RP}_t^{\pm} - \sum_{j=1}^4 \sum_{k=1}^9 \text{AM}_{jkt}^{\pm} \right) \cdot \text{MS}_t^{\pm} \cdot \varepsilon_{PM}^{\pm} + L_t \cdot \text{RP}_t^{\pm} \cdot \text{ACW}_t^{\pm} \cdot \text{DPR}_t^{\pm} \leq \widetilde{\text{APL}_t^{\pm}} \right\} \geq \lambda^{\pm}, \quad (14i)$$

$$\text{Cr} \left\{ \text{QW}_{st}^{\pm} \cdot \text{GT}_{st}^{\pm} \cdot \text{PCM}_{st}^{\pm} \cdot (1 - \eta_{TP,st}^{\pm}) \leq \widetilde{\text{APW}_{st}^{\pm}} \right\} \geq \lambda^{\pm} \quad (14j)$$

$$\text{Cr} \left\{ \text{PLM}_{pt}^{\pm} \cdot \text{WPM}_{pt}^{\pm} \cdot \text{MWC}_{pt}^{\pm} \cdot (1 - \theta_{pt}^{\pm}) + \text{PLM}_{pt}^{\pm} \cdot \text{ASM}_{pt}^{\pm} \cdot \text{PCS}_{pt}^{\pm} \cdot \text{SLW}_{pt}^{\pm} \leq \widetilde{\text{APM}_{pt}^{\pm}} \right\} \geq \lambda^{\pm}, \quad (14k)$$

$$\sum_{k=1}^9 (\text{PS}_{jk}^{\pm} \cdot \text{SL}_{jkt}^{\pm} + \text{RF}_{jkt}^{\pm} \cdot \text{DP}_{jkt}^{\pm}) \cdot \text{PA}_{jkt}^{\pm} \leq \text{MPL}_{jt}^{\pm} \cdot \text{TA}_{jt}^{\pm}, \quad (14l)$$

(5) soil loss constraints:

$$\sum_{k=1}^9 \text{SL}_{jkt}^{\pm} \cdot \text{PA}_{jkt}^{\pm} \leq \text{MSL}_{jt}^{\pm} \cdot \text{TA}_{jt}^{\pm}, \quad (14m)$$

(6) fertilizer and manure constraints:

$$(1 - \text{NVF}_t^{\pm}) \cdot \varepsilon_{NF}^{\pm} \cdot \text{AF}_{jkt}^{\pm} + (1 - \text{NVM}_t^{\pm}) \cdot \varepsilon_{NM}^{\pm} \cdot \text{AM}_{jkt}^{\pm} - \text{NR}_{jkt}^{\pm} \cdot \text{PA}_{jkt}^{\pm} \geq 0, \quad (14n)$$

$$\varepsilon_{PF}^{\pm} \cdot \text{AF}_{jkt}^{\pm} + \varepsilon_{PM}^{\pm} \cdot \text{AM}_{jkt}^{\pm} - \text{PR}_{jkt}^{\pm} \cdot \text{PA}_{jkt}^{\pm} \geq 0, \quad (14o)$$

$$\sum_{k=1}^9 (\varepsilon_{NF}^{\pm} \cdot \text{AF}_{jkt}^{\pm} + \varepsilon_{NM}^{\pm} \cdot \text{AM}_{jkt}^{\pm} - \text{NR}_{jkt}^{\pm} \cdot \text{PA}_{jkt}^{\pm}) \leq \text{MNI}_{jt}^{\pm} \cdot \text{TA}_{jt}^{\pm}, \quad (14p)$$

$$\sum_{k=1}^9 (\varepsilon_{PF}^{\pm} \cdot \text{AF}_{jkt}^{\pm} + \varepsilon_{PM}^{\pm} \cdot \text{AM}_{jkt}^{\pm} - \text{PR}_{jkt}^{\pm} \cdot \text{PA}_{jkt}^{\pm}) \leq \text{MPL}_{jt}^{\pm} \cdot \text{TA}_{jt}^{\pm}, \quad (14q)$$

$$L_t \cdot \sum_{r=1}^4 \text{AML}_{rt}^{\pm} \cdot \text{NL}_r^{\pm} + L_t \cdot \text{AMH}_t^{\pm} \cdot \text{RP}_t^{\pm} - \sum_{j=1}^4 \sum_{k=1}^9 \text{AM}_{jkt}^{\pm} \geq 0, \quad (14r)$$

(7) energy and digestible protein constraints:

$$\sum_{j=1}^4 \sum_{k=1}^9 \sum_{t=1}^2 \text{CY}_{jkt}^{\pm} \cdot \text{PA}_{jkt}^{\pm} \cdot \text{NEC}_k^{\pm} - \sum_{r=1}^4 \text{ERL}_r^{\pm} \cdot \text{NL}_r^{\pm} - \sum_{t=1}^2 \text{ERH}_t^{\pm} \cdot \text{RP}_t^{\pm} \geq 0, \quad (14s)$$

$$\sum_{j=1}^4 \sum_{k=1}^9 \sum_{t=1}^2 \text{CY}_{jkt}^{\pm} \cdot \text{PA}_{jkt}^{\pm} \cdot \text{DPC}_k^{\pm} - \sum_{r=1}^4 \text{DRL}_r^{\pm} \cdot \text{NL}_r^{\pm} - \sum_{t=1}^2 \text{DRH}_t^{\pm} \cdot \text{RP}_t^{\pm} \geq 0, \quad (14t)$$

(8) production scale constraints:

$$\text{PLC}_{i,\min} \leq \text{PLC}_{it}^{\pm} \leq \text{PLC}_{i,\max}, \quad (14u)$$

$$\text{NL}_{r,\min} \leq \text{NL}_r^{\pm} \leq \text{NL}_{r,\max}, \quad (14v)$$

$$\text{QW}_{s,\min} \leq \text{QW}_{st}^{\pm} \leq \text{QW}_{s,\max}, \quad (14w)$$

$$\text{PLM}_{p,\min} \leq \text{PLM}_{pt}^{\pm} \leq \text{PLM}_{p,\max}, \quad (14x)$$

(9) total yield of crops:

$$\sum_{j=1}^4 \text{CY}_{jkt}^{\pm} \cdot \text{PA}_{jkt}^{\pm} \geq \text{MCY}_{kt}^{\pm}, \quad (14y)$$

(10) planning area constraints:

$$\sum_{k=1}^9 \text{PA}_{jkt}^{\pm} \leq \text{TA}_{jt}^{\pm}, \quad (14z)$$

(11) nonnegative constraints:

$$\text{PLC}_{it}^{\pm}, \text{PA}_{jkt}^{\pm}, \text{NL}_r^{\pm}, \text{QW}_{st}^{\pm}, \text{PLM}_{pt}^{\pm}, \text{AM}_{jkt}^{\pm}, \text{AF}_{jkt}^{\pm} \geq 0, \quad (14aa)$$

where  $i$ : chemical plant;  $i = 1$  Gufu (GF);  $i = 2$  Baishahe (BSH);  $i = 3$  Pingyikou (PYK);  $i = 4$  Liucaopo (LCP);  $i = 5$  Xiangjinlianying (XJLY);  $j$ : agricultural zone;  $j = 1, \dots, 4$ ;  $k$ : main crop;  $k = 1$  citrus;  $k = 2$  tea;  $k = 3$  wheat;  $k = 4$  potato;  $k = 5$  rapeseed;  $k = 6$  alpine rice;  $k = 7$  second rice;  $k = 8$  maize;  $k = 9$  vegetables;  $p$ : phosphorus mining company;  $p = 1$  Xinglong (XL);  $p = 2$  Xinghe (XH);  $p = 3$

TABLE 1: Net benefits from each production.

	Period	
	$t = 1$	$t = 2$
Net benefits from chemical plant (RMB¥/t)		
GF	[718.6, 834.5]	[743.75, 876.2]
BSH	[1291.5, 1499.7]	[1336.7, 1574.8]
PYK	[743.0, 862.8]	[769.0, 905.9]
LCP	[1324.2, 1537.5]	[1370.6, 1614.4]
XJLY	[1524.4, 1770.0]	[1578.7, 1858.5]
Net benefits from water supply (RMB¥/m <sup>3</sup> )		
Gufu	[39.1, 42.1]	[43.4, 47.7]
Nanyang	[29.0, 31.2]	[32.2, 35.4]
Gaoyang	[35.3, 38.0]	[39.2, 43.1]
Xiakou	[32.1, 34.6]	[35.7, 39.3]
Net benefits from phosphorus mining company (RMB¥/t)		
XL (Xinglong, $p = 1$ )	[150, 173]	[147, 180]
XH (Xinghe, $p = 2$ )	[126, 145]	[130, 156]
XC (Xingchang, $p = 3$ )	[135, 155]	[135, 162]
GP (Geping, $p = 4$ )	[144, 166]	[150, 180]
JJW (Jiangjiawan, $p = 5$ )	[137, 158]	[141, 169]
SJS (Shenjiashan, $p = 6$ )	[140, 164]	[145, 175]

Xingchang (XC);  $p = 4$  Geping (GP);  $p = 5$  Jiangjiawan (JJW);  $p = 6$  Shenjiashan (SJS);  $r$ : livestock;  $r = 1$  pig;  $r = 2$  ox;  $r = 3$  sheep;  $r = 4$  domestic fowls;  $s$ : town;  $s = 1$  Gufu;  $s = 2$  Nanyang;  $s = 3$  Gaoyang;  $s = 4$  Xiakou;  $t$ : time period;  $t = 1$  dry season;  $t = 2$  wet season;  $L_t$ : length of period (day);  $BC_{it}^{\pm}$ : net benefit from chemical plant  $i$  during period  $t$  (RMB¥/t);  $PLC_{it}^{\pm}$ : production level of chemical plant  $i$  during period  $t$  (t/day);  $BW_{st}^{\pm}$ : benefit from water supply to municipal uses (RMB¥/m<sup>3</sup>);  $QW_{st}^{\pm}$ : quantity of water supply to town  $s$  in period  $t$  (m<sup>3</sup>/day);  $BP_{pt}^{\pm}$ : average benefit for per unit phosphate ore (RMB¥/t);  $PLM_{pt}^{\pm}$ : production level of phosphorus mining company  $p$  during period  $t$  (t/day);  $BL_r^{\pm}$ : average benefit from livestock  $r$  (RMB¥/unit);  $NL_r^{\pm}$ : number of livestock  $r$  in the study area (unit);  $CY_{jkt}^{\pm}$ : yield of crop  $k$  planted in agricultural zone  $j$  during period  $t$  (t/ha);  $BA_{jkt}^{\pm}$ : average benefit of agricultural product (RMB¥/t);  $PA_{jkt}^{\pm}$ : planting area of crop  $k$  in agricultural zone  $j$  during period  $t$  (ha);  $CM_{jt}^{\pm}$ : cost of manure collection/disposal in agricultural zone  $j$  during period  $t$  (RMB¥/t);  $CF_{jt}^{\pm}$ : cost of purchasing fertilizer in agricultural zone  $j$  during period  $t$  (RMB¥/t);  $AM_{jkt}^{\pm}$ : amount of manure applied to agricultural zone  $j$  with crop  $k$  during period  $t$  (t);  $AF_{jkt}^{\pm}$ : amount of fertilizer applied to agricultural zone  $j$  with crop  $k$  during period  $t$  (t);  $WC_{it}^{\pm}$ : wastewater generation rate of chemical plant  $i$  during period  $t$  (m<sup>3</sup>/t);  $CC_{it}^{\pm}$ : wastewater treatment cost of chemical plant  $i$  during period  $t$  (RMB¥/m<sup>3</sup>);  $GT_{st}^{\pm}$ : wastewater discharge amount at town  $s$  during period  $t$  (m<sup>3</sup>/m<sup>3</sup>);  $CT_{st}^{\pm}$ : cost of municipal wastewater treatment (RMB¥/m<sup>3</sup>);  $IQ_{jkt}^{\pm}$ : irrigation quota for crop  $k$  in zone  $j$  during period  $t$  (m<sup>3</sup>/ha);  $WSP_t^{\pm}$ : water supply price (RMB¥/m<sup>3</sup>);  $FW_{it}^{\pm}$ : water consumption of per

unit production of chemical plant  $i$  during period  $t$  (m<sup>3</sup>/t);  $IC_{it}^{\pm}$ : BOD concentration of raw wastewater from chemical plant  $i$  in period  $t$  (kg/m<sup>3</sup>);  $\eta_{BOD,it}^{\pm}$ : BOD treatment efficiency in chemical plant  $i$  during period  $t$  (%);  $\widetilde{ABC}_{it}^{\pm}$ : allowable BOD discharge for chemical plant  $i$  in period  $t$  (kg/day);  $BM_{st}^{\pm}$ : BOD concentration of municipal wastewater at town  $s$  during period  $t$  (kg/m<sup>3</sup>);  $\eta_{BOD,st}^{\pm}$ : BOD treatment efficiency of WTPs at town  $s$  during period  $t$  (%);  $\widetilde{ABW}_{st}^{\pm}$ : allowable BOD discharge for WTPs at town  $s$  during period  $t$  (kg/day);  $NS_{jk}^{\pm}$ : nitrogen content of soil in agricultural zone  $j$  planted with crop  $k$  (%);  $SL_{jkt}^{\pm}$ : average soil loss from agricultural zone  $j$  planted with crop  $k$  in period  $t$  (t/ha);  $RF_{jkt}^{\pm}$ : runoff from agricultural zone  $j$  with crop  $k$  in period  $t$  (mm);  $DN_{jkt}^{\pm}$ : dissolved nitrogen concentration in the runoff from agricultural zone  $j$  planted with crop  $k$  in period  $t$  (mg/L);  $MNL_{jt}^{\pm}$ : maximum allowable nitrogen loss in agricultural zone  $j$  during period  $t$  (t/ha);  $TA_{jt}^{\pm}$ : tillable area of agricultural zone  $j$  during period  $t$  (ha);  $AML_r^{\pm}$ : amount of manure generated by livestock  $r$  [t/(unit-day<sup>-1</sup>)];  $AMH_t^{\pm}$ : amount of manure generated by humans [t/(unit-day<sup>-1</sup>)];  $RP_t^{\pm}$ : total rural population in the study area during period  $t$  (unit);  $MS_t^{\pm}$ : manure loss rate in period  $t$  (%);  $ACW_t^{\pm}$ : wastewater generation of per capita water consumption during period  $t$  [m<sup>3</sup>/(unit-day<sup>-1</sup>)];  $DNR_{0t}^{\pm}$ : dissolved nitrogen concentration of rural wastewater during period  $t$  (t/m<sup>3</sup>);  $\widetilde{ANL}_t^{\pm}$ : maximum allowable nitrogen loss from rural life section in period  $t$  (t);  $PCR_{it}^{\pm}$ : phosphorus concentration of raw wastewater from chemical plant  $i$  in period  $t$  (kg/m<sup>3</sup>);  $\eta_{TP,it}^{\pm}$ : phosphorus treatment efficiency in chemical plant  $i$  in period  $t$  (%);  $ASC_{it}^{\pm}$ : amount of slag discharged by chemical plant  $i$  in period  $t$  (kg/t);  $SLR_{it}^{\pm}$ : slag loss rate due to rain wash in chemical plant  $i$  during period  $t$  (%);  $PSC_{it}^{\pm}$ : phosphorus content in slag generated by chemical plant  $i$  in period  $t$  (%);  $\widetilde{APC}_{it}^{\pm}$ : allowable phosphorus discharge for chemical plant  $i$  in period  $t$  (kg/day);  $PS_{jk}^{\pm}$ : phosphorus content of soil in agricultural zone  $j$  planted with crop  $k$  (%);  $SL_{jkt}^{\pm}$ : average soil loss from agricultural zone  $j$  planted with crop  $k$  in period  $t$  (t/ha);  $RF_{jkt}^{\pm}$ : runoff from agricultural zone  $j$  with crop  $k$  in period  $t$  (mm);  $DP_{jkt}^{\pm}$ : dissolved phosphorus concentration in the runoff from agricultural zone  $j$  planted with crop  $k$  in period  $t$  (mg/L);  $MPL_{jt}^{\pm}$ : maximum allowable phosphorus loss in agricultural zone  $j$  during period  $t$  (t/ha);  $DPR_t^{\pm}$ : dissolved phosphorus concentration of rural wastewater during period  $t$  (t/m<sup>3</sup>);  $\widetilde{APL}_t^{\pm}$ : maximum allowable phosphorus loss from rural life during period  $t$  (t);  $PCM_{st}^{\pm}$ : phosphorus concentration of municipal wastewater at town  $s$  in period  $t$  (kg/m<sup>3</sup>);  $\eta_{TP,st}^{\pm}$ : phosphorus treatment efficiency of WTP at town  $s$  in period  $t$  (%);  $\widetilde{APW}_{st}^{\pm}$ : allowable phosphorus discharge for WTP at town  $s$  in period  $t$  (kg/day);  $WPM_{pt}^{\pm}$ : wastewater generation from phosphorus mining company  $p$  in period  $t$  (m<sup>3</sup>/t);  $MWC_{pt}^{\pm}$ : phosphorus concentration of wastewater from mining company  $p$  in period  $t$  (kg/m<sup>3</sup>);  $\theta_{pt}^{\pm}$ : phosphorus treatment efficiency in mining company  $p$

TABLE 2: Crop yields and net benefits.

	Agricultural zone			
	AZ1	AZ2	AZ3	AZ4
Yields (t/ha)				
Citrus	[10.3, 12.6]	[9.8, 11.9]	[8.4, 10.2]	[9.2, 11.2]
Tea	[0.1, 0.2]	[0.1, 0.2]	[0.3, 0.6]	[0.2, 0.4]
Wheat	[1.4, 2.1]	[1.3, 1.7]	[1.2, 2.5]	[2.3, 3.1]
Potato	[2.4, 3.2]	[2.0, 2.8]	[1.9, 2.8]	[2.8, 3.8]
Rapeseed	[1.6, 1.7]	[1.3, 1.5]	[1.3, 1.7]	[1.7, 1.8]
Alpine rice	[6.9, 9.6]	[6.7, 7.9]	[4.4, 6.6]	[5.7, 7.0]
Second rice	[7.4, 10.2]	[7.3, 8.5]	[4.7, 7.0]	[6.2, 7.4]
Maize	[2.9, 3.9]	[2.7, 2.9]	[2.5, 2.6]	[4.0, 4.7]
Vegetable	[21.6, 24.0]	[10.4, 13.4]	[21.8, 24.2]	[26.2, 29.1]
Net benefits (RMB¥/t)				
Citrus	[1082, 1350]	[1010, 1260]	[1126, 1405]	[1203, 1502]
Tea	[18000, 18900]	[19125, 20081]	[20170, 21178]	[22500, 23625]
Wheat	[1031, 1242]	[972, 1169]	[945, 1134]	[1010, 1218]
Potato	[915, 1001]	[827, 897]	[893, 969]	[846, 917]
Rapeseed	[2435, 2934]	[2191, 2640]	[2305, 2778]	[2490, 3000]
Alpine rice	[1105, 1214]	[1047, 1153]	[1084, 1178]	[1149, 1265]
Second rice	[1159, 1274]	[1098, 1209]	[1137, 1236]	[1205, 1327]
Maize	[1295, 1451]	[1267, 1422]	[1230, 1378]	[1308, 1467]
Vegetable	[2360, 2691]	[1613, 1865]	[1927, 2197]	[1845, 1950]

(%);  $ASM_{pt}^{\pm}$ : amount of slag discharged by mining company  $p$  during period  $t$  (kg/t);  $PCS_{pt}^{\pm}$ : phosphorus content in generated slag (%);  $SLW_{pt}^{\pm}$ : slag loss rate due to rain wash (%);  $APM_{pt}^{\pm}$ : allowable phosphorus discharge for mining company  $p$  during period  $t$  (kg/day);  $MSL_{jt}^{\pm}$ : maximum allowable soil loss agricultural zone  $j$  in period  $t$  (t/ha);  $NVF_t^{\pm}$ : nitrogen volatilization/denitrification rate of fertilizer in period  $t$  (%);  $NVM_t^{\pm}$ : nitrogen volatilization/denitrification rate of manure in period  $t$  (%);  $\varepsilon_{NF}^{\pm}$ : nitrogen content of fertilizer (%);  $\varepsilon_{PF}^{\pm}$ : phosphorus content of fertilizer (%);  $\varepsilon_{NM}^{\pm}$ : nitrogen content of manure (%);  $\varepsilon_{PM}^{\pm}$ : phosphorus content of manure (%);  $NR_{jkt}^{\pm}$ : nitrogen requirement of agricultural zone  $j$  with crop  $k$  during period  $t$  (t/ha);  $PR_{jkt}^{\pm}$ : phosphorus requirement of crop  $k$  in agricultural zone  $j$  during period  $t$  (t/ha);  $NEC_k^{\pm}$ : net energy content of crop  $k$  (Mcal/t);  $ERL_r^{\pm}$ : net energy requirement of livestock  $r$  (Mcal/unit);  $ERH_t^{\pm}$ : net energy requirement of human beings (Mcal/unit);  $DPC_k^{\pm}$ : digestible protein content of crop  $k$  (%);  $DRL_r^{\pm}$ : digestible protein requirement of livestock  $r$  (t/unit);  $DRH_t^{\pm}$ : digestible protein requirement of human beings (t/unit);  $MCY_{jkt}^{\pm}$ : minimum crop production requirement for crop  $k$  in period  $t$  (t);  $TPC_{st}^{\pm}$ : capacity of wastewater treatment capacity (WTPs) ( $m^3$ /day);  $TPD_{it}^{\pm}$ : capacity of wastewater treatment capacity (chemical plants) ( $m^3$ /day).

Table 1 provides the net benefits of chemical plant productions, phosphorus mining company, and municipal water supply. According to the crops' growth periods, dry season crops include wheat, potato, rapeseed and alpine rice; second rice, maize and vegetable are identified as main crops during

the wet season; citrus and tea grow over the entire year. Table 2 shows the net benefits of each crop in every AZ and yields of each crop. To guarantee the stream water quality, wastewater treatment measures have to be adopted at each point source. Based on the local environmental regulations, a safe level of water quality must be guaranteed to protect aquatic life and maintain aerobic condition in the stream system [2]. Thus, the BOD and TP loading amount would be controlled strictly. However, the imprecision of the allowable BOD and TP discharge could introduce uncertainties in the water quality management. For modeling purpose, the vagueness of the allowable BOD and TP loading amount are encoded by triangular fuzzy membership functions. Figure 1 presents the fuzzy set with triangular membership function. The minimum, maximum, and most likely values ( $\underline{b}$ ,  $b$ , and  $\bar{b}$ ) that define these fuzzy sets are estimated according to previous research regarding water quality monitoring and environmental capacities, as tabulated in Table 3. Moreover, by setting acceptable interval credibility levels, the constraints can be at least basically satisfied and at best practically satisfied. Lower-bound of the interval numbers would be no less than 0.5, and upper-bound of the interval numbers would be no more than 1 [16]. Lower-bound of credibility level represents a situation when the decision makers are optimistic about this study area, which may imply a higher risk of violating the river's self-purification capacity. Conversely, upper-bound of credibility level corresponds to a situation when the decision makers prefer a conservative policy that could guarantee that the river's self-purification capacity be satisfied.

TABLE 3: Allowable BOD and TP discharges.

	$\underline{b}$		$b$		$\bar{b}$	
	$t = 1$	$t = 2$	$t = 1$	$t = 2$	$t = 1$	$t = 2$
Allowable BOD loading discharge from chemical plant (kg/day)						
GF	0.76	0.78	0.82	0.85	0.88	0.92
BSH	437.2	442.97	444.265	448.605	451.33	454.24
PYK	7.25	7.83	7.53	7.89	7.81	7.95
LCP	95.43	97.23	97.82	102.83	100.21	108.43
XJLY	48.34	49.43	49.635	50.645	50.93	51.86
Allowable BOD loading discharge from WTP (kg/day)						
Gufu	145	143	150	148	155	153
Nanyang	7	6	10	9	13	12
Gaoyang	38	36	40	38	42	40
Xiakou	28	30	30	32	32	34
Allowable TP loading discharge from chemical plant (kg/day)						
GF	1.18	1.29	1.31	1.43	1.44	1.57
BSH	393.73	485.94	419.14	514.27	444.55	542.59
PYK	80.23	99.57	84.87	105.75	89.51	111.92
LCP	385.59	470.16	416.21	497.96	446.83	525.76
XJLY	259.81	330.52	276.46	355.02	293.1	379.52
Allowable TP loading discharge from WTP (kg/day)						
Gufu	13.00	13.50	15.22	15.68	17.43	17.85
Nanyang	0.36	0.42	0.55	0.6	0.74	0.78
Gaoyang	1.82	1.88	2.03	2.27	2.23	2.65
Xiakou	2.05	2.34	2.25	2.49	2.45	2.64
Allowable TP loading discharge from phosphorus mining company (kg/day)						
XL	157.70	143.31	175.60	192.45	193.49	241.59
XH	89.40	104.19	99.51	120.53	109.62	136.87
XC	108.20	110.74	120.48	138.25	132.75	165.76
GP	146.20	140.03	162.78	181.99	179.36	223.95
JJW	89.80	104.49	99.97	121.01	110.13	137.52
SJS	86.60	102.19	96.41	117.40	106.21	132.61
Allowable TP and TN loading discharge from rural life (kg/day)						
TP	21.5	20.5	24.45	24.4	27.4	28.3
TN	102.1	106.0	107.5	107.0	112.8	118.0

### 4. Result Analysis

Table 4 shows the solutions for industrial production and water supply during the two periods. The results show that significant variations in industrial production and water supply exist among different chemical plants, phosphorus mining companies, and towns. For chemical plants, the production scale of BSH (i.e., [536.23, 652.37] t/d (tonne/day) during period 1 and [530.78, 629.19] t/d during period 2) would be larger than the other chemical plants (especially

TABLE 4: Solutions for industrial productions and water supplies.

Main point sources	Period	
	$t = 1$	$t = 2$
Chemical plant (t/day)		
GF	[25.64, 27.41]	[21.13, 27.02]
BSH	[536.23, 652.37]	[530.78, 629.19]
PYK	[81.71, 102.09]	[75.98, 80.92]
LCP	[379.24, 403.72]	[357.33, 453.48]
XJLY	[280.87, 313.47]	[320.42, 337.81]
Phosphorus mining company (t/day)		
XL	[824.78, 1261.00]	[701.05, 1044.89]
XH	[326.00, 420.00]	[350.48, 400.00]
XC	[286.87, 400.00]	[260.38, 393.68]
GP	[534.99, 778.00]	[659.80, 778.00]
JJW	[425.99, 547.00]	[412.57, 547.00]
SJS	[510.53, 685.00]	[602.43, 685.00]
Water supply (m <sup>3</sup> /day)		
Gufu	[11723.79, 14859.14]	[12264.89, 21739.14]
Nanyang	[762.29, 987.64]	[859.73, 1109.84]
Gaoyang	[2783.46, 3225.87]	[2962.32, 3226.25]
Xiakou	[1656.71, 2083.18]	[1592.84, 2156.09]

GF) because of its higher allowable BOD and TP discharges and net benefits. For water supply, more water would be delivered to Gufu (i.e., [11723.79, 14859.14] m<sup>3</sup>/day in period 1 and [12264.89, 21739.14] m<sup>3</sup>/day in period 2) than those to the other towns due to its greater water demand, higher allowable BOD discharge, and higher economic return. For phosphorus mining company, the production scale of XL (i.e., [824.78, 1261.00] t/d in period 1 and [701.05, 1044.89] t/d in period 2) would be larger than the other chemical plants because of its higher allowable TP discharge and net benefit.

The results for total crop areas and manure/fertilizer applications are listed in Table 5. The areas of citrus and tea would maintain the low levels over the planning horizon. This may be attributed to their pollutant losses as well as their low net energy and digestible protein contents (supplied for livestock). In period 1, wheat, potato, rapeseed, and alpine rice should be cultivated. The potato area (i.e., [1459.8, 1620.3] ha) would account for the largest one of the entire croplands. In period 2, wheat, potato, rapeseed, and alpine rice would be harvested and second rice, maize, and vegetable would be sown. The vegetable area (i.e., [1745.2, 1915.6] ha) would be the largest one among all croplands. The results indicate that the high levels of area planted with potato and vegetable are associated with their high crop yields, good market price, and low pollutant losses. In terms of manure and fertilizer application, their quantities would vary with crop areas. The results indicate that manure would be the main nitrogen and phosphorus source which satisfy the requirements of most crops due to its availability and low price to collect. Solutions demonstrate that domestic fowl husbandry would reach the highest level

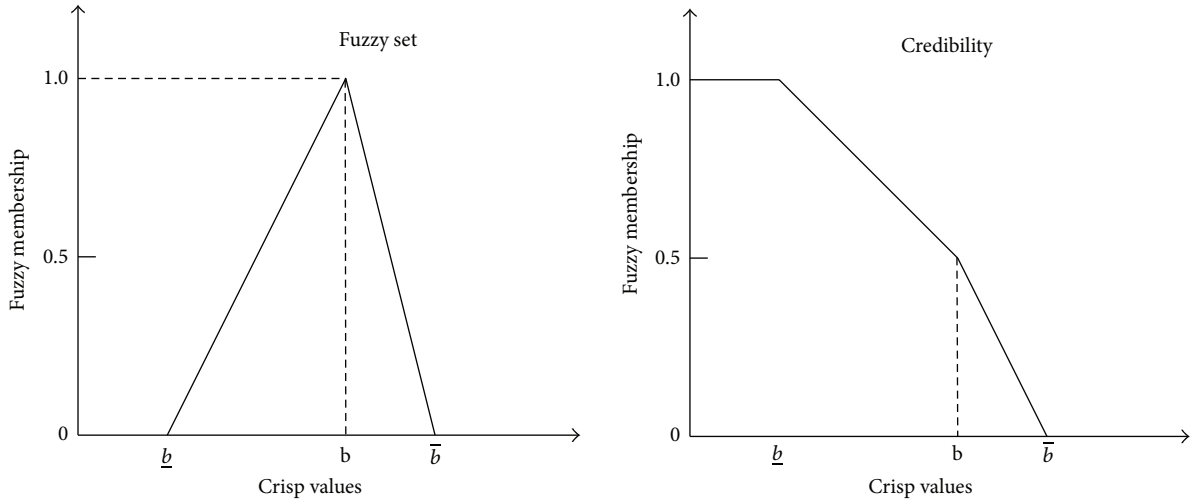


FIGURE 1: Fuzzy set and credibility.

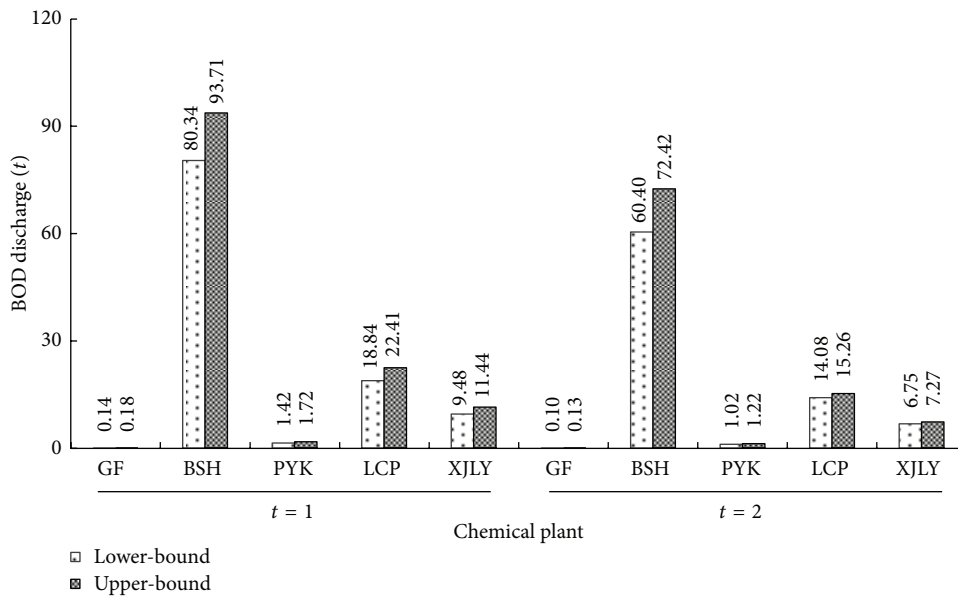


FIGURE 2: BOD discharges from chemical plants. Note: the five chemical plants are abbreviated as their initials in this figure. GF: Gufu,  $i = 1$ ; BSH: Baishahe,  $i = 2$ ; PYK: Pingyikou,  $i = 3$ ; LCP: Liucaopo,  $i = 4$ ; XJLY: Xiangjinlianying,  $i = 5$ .

(i.e.,  $[34.80, 132.56] \times 10^3$  unit) among all live stocks because it possesses more advantageous conditions than the other live stocks (i.e., higher allowable discharge, higher revenue parameter, and lower manure generation rate).

Figures 2 and 3 present the amounts of BOD discharges from chemical plants and WTPs, respectively. The amount of BOD discharge is associated with a number of factors (e.g., production scale, wastewater generation rate, and wastewater treatment facility). The BOD discharge from BSH would be more than those from the other chemical plants, which would be  $[80.34, 93.71]$  t (i.e., tonne) in period 1 and  $[60.40, 72.42]$  t in period 2. The BOD discharge from GF would be the lowest among all chemical plants, with  $[0.14, 0.18]$  t in period 1 and  $[0.10, 0.13]$  t in period 2. Among all WTPs, Gufu wastewater

treatment plant would discharge the highest BOD level, with  $[17.62, 28.69]$  t in period 1 and  $[26.72, 36.72]$  t in period 2; the BOD discharged from Nanyang WTP would be the lowest (i.e.  $[3.99, 4.39]$  t in period 1 and  $[5.01, 7.55]$  t in period 2).

Figure 4 shows TP discharges from point sources (i.e., chemical plants, WTPs, and phosphorus mining companies) and nonpoint sources (i.e., crop farming and agricultural life). In Figure 4, symbol “CP” denotes chemical plant; symbol “PMC” denotes phosphorus mining company; symbol “CF” denotes crop farming; symbol “AL” means agricultural life. For point sources, the chemical plants would be the major contributor to water pollution. The phosphorus pollutants can be discharged from wastewater and solid wastes (i.e., chemical wastes, slags, and tailings). The amount of TP

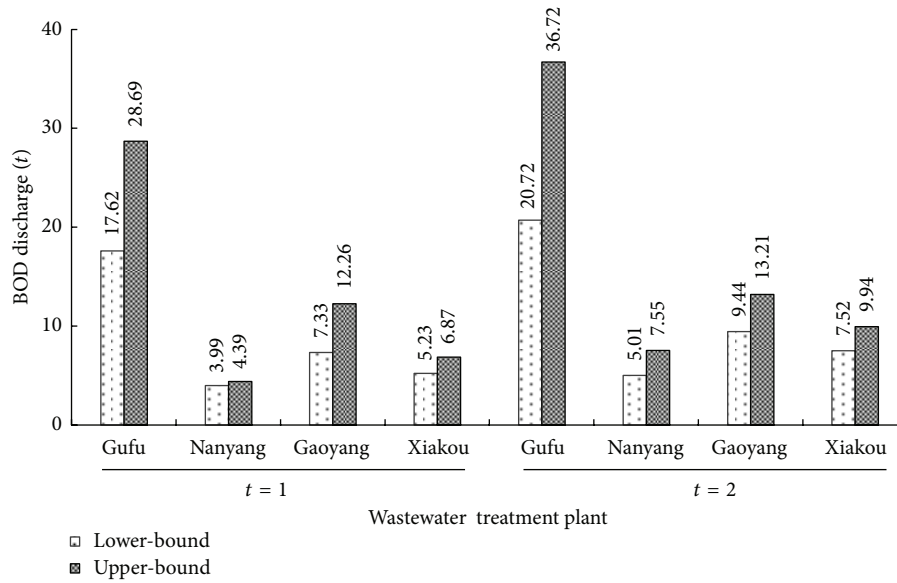


FIGURE 3: BOD discharges from WTPs.

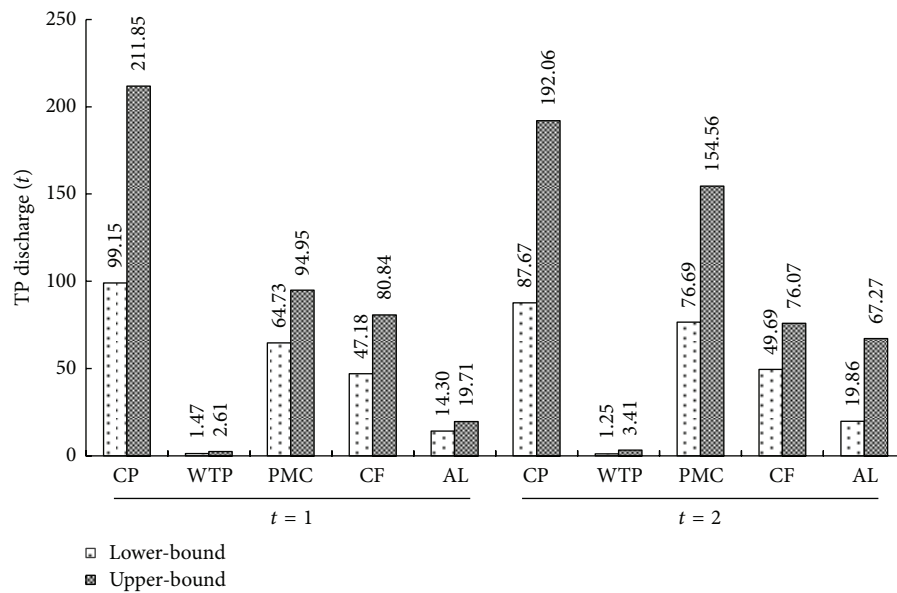


FIGURE 4: Solutions of TP discharge. Note: CP: chemical plant; WTP: wastewater treatment plant; PMC: phosphorus mining company; CF: crop farming; AL: agricultural life.

discharge from chemical plant would be [99.15, 211.85] t in period 1 and [87.67, 192.06] t in period 2. Since the wastewater should be sluiced strictly according to the integrated discharge standards, the amount of TP discharge from WTPs would stay at a low level. Most of the TP would be from phosphorus-containing wastes (i.e., discharged directly and washed by rainfall). For nonpoint sources, the phosphorus pollutants from crop farming which can be generated through runoff and soil erosion (the latter would be a larger proportion) would be more than that from agricultural life. The amount of TP discharge from crop farming would be

[47.18, 80.84] t in period 1 and [76.69, 154.56] t in period 2. This is associated with its high soil loss rate, low runoff, and low phosphorus concentration in the study area. Generally, TP discharge derives mainly from point sources, particularly from chemical plants. The results also indicate that the nitrogen pollutants would be generated by nonpoint sources (i.e., mainly from crop farming). TN discharge from citrus and tea can be neglected (i.e., nearly equal to zero). Figure 5 shows TN discharges from the other cropping areas. TN discharges from wheat and potato would be higher than those from rapeseed and alpine rice in period 1; TN discharges from

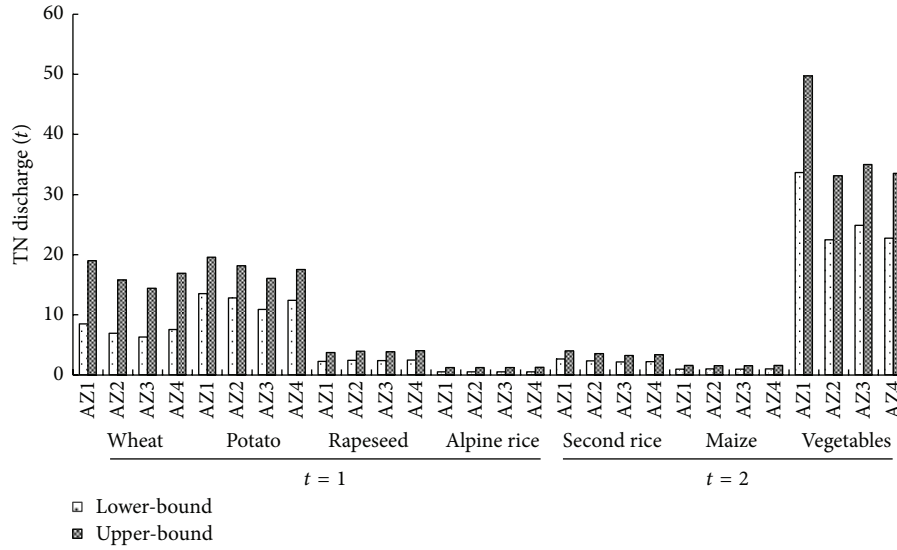


FIGURE 5: TN discharges from agriculture activities.

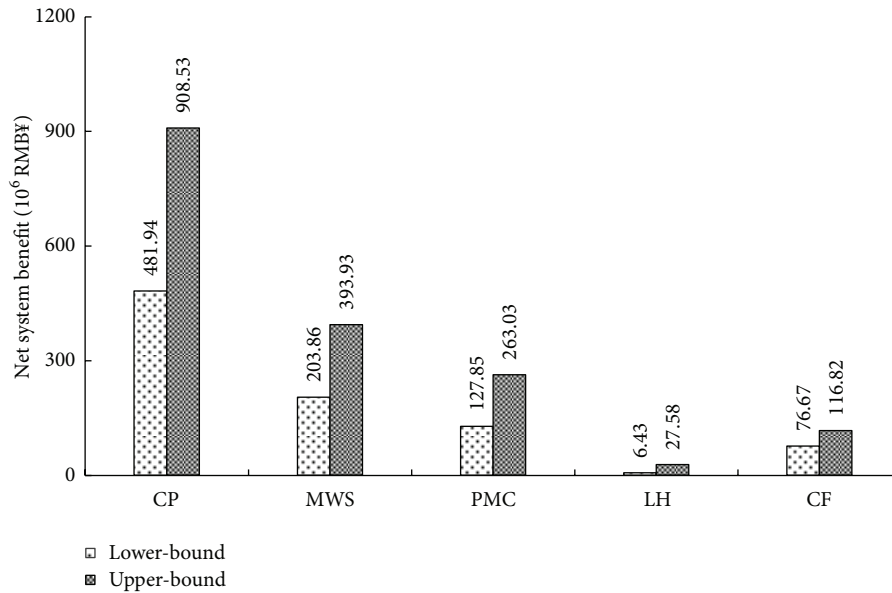


FIGURE 6: Net benefits from industrial and agricultural activities. Note: CP: chemical plant; MWS: municipal water supply; PMC: phosphorus mining company; CF: crop farming; LH: livestock husbandry.

vegetable would be higher than those from maize and second rice in period 2. This difference may be attributed to their planting areas, soil losses, runoff, and nitrogen concentration.

Net system benefit can be obtained from different industrial and agricultural activities, as shown in Figure 6. Chemical plants would be the major economic incoming source in the study area and could generate the highest revenue (RMB¥ [484.94, 906.53] × 10<sup>6</sup>). Municipal water supply and phosphorus mining company would also make certain contribution to the economic development; their net benefits would be RMB¥ [203.86, 393.93] × 10<sup>6</sup> and RMB¥ [127.85, 263.03] × 10<sup>6</sup>, respectively. Livestock husbandry would bring the lowest benefit. Such an industry-oriented pattern may be related

to the abundant mineral resources (particularly phosphorus ore) which can generate high economic return. Agricultural activities would make less contribution to the local economic development due to its topography which is not suitable for cultivation in large parts.

### 5. Conclusions

In this study, an interval fuzzy credibility-constrained programming (IFCP) has been advanced for water quality management under uncertainty. This method integrates interval-parameter programming (IPP) and fuzzy credibility-constrained programming (FCP) techniques within a general

TABLE 5: Solutions for agricultural production.

Crops and live stocks	Growth period	
Crop area (ha)		
Citrus	Whole year	[35.7, 72.8]
Tea	Whole year	[40.8, 53.4]
Wheat	Dry season	[1112.6, 1894.2]
Potato	Dry season	[1459.8, 1620.3]
Rapeseed	Dry season	[296.5, 369.4]
Alpine rice	Dry season	[206.5, 393.2]
Second rice	Wet season	[351.2, 387.4]
Maize	Wet season	[83.4, 97.8]
Vegetable	Wet season	[1745.2, 1915.6]
Manure application (10 <sup>3</sup> t)		
Citrus	Whole year	[10.4, 19.3]
Tea	Whole year	[8.2, 11.7]
Wheat	Dry season	[2.9, 7.8]
Potato	Dry season	[0.7, 2.8]
Rapeseed	Dry season	[4.1, 4.7]
Alpine rice	Dry season	[5.8, 6.3]
Second rice	Wet season	[5.2, 5.7]
Maize	Wet season	[0.8, 1.1]
Vegetable	Wet season	[1.2, 1.4]
Fertilizer application (t)		
Citrus	Whole year	[0.7, 1.0]
Tea	Whole year	[804.3, 893.6]
Wheat	Dry season	[824.4, 917.3]
Potato	Dry season	[1023.4, 1454.2]
Rapeseed	Dry season	[2.4, 3.6]
Alpine rice	Dry season	[39.6, 60.5]
Second rice	Wet season	[292.7, 316.3]
Maize	Wet season	[0.2, 0.3]
Vegetable	Wet season	[1520.4, 1632.1]
Size of livestock husbandry (10 <sup>3</sup> unit)		
Pig	Whole year	[0.121, 35.462]
Ox	Whole year	[0.688, 0.813]
Sheep	Whole year	[21.430, 34.478]
Domestic fowl	Whole year	[34.800, 132.561]

optimization framework. Generally, the IFCP model has advantages in (1) handling uncertainties presented in terms of interval values and possibility distributions in the model, and (2) providing bases for determining optimal water quality management plans with desired compromises between economic benefits and environmental capacity-violation risks.

The developed model has been applied to a real-world case of planning water quality management in the Xiangxi River of the Three Gorges Reservoir Region. The objective is to maximize the net system benefit subject to the environmental requirements under uncertainty over the planning

horizon. Pollutant discharges generated by various point and nonpoint sources were considered simultaneously. Interval solutions for production activities (i.e., industrial, municipal, and agricultural) and pollutant discharges (i.e., BOD, TP, and TN) under interval credibility levels have been generated by solving two deterministic submodels. The detailed results of related production scales and pollutant discharges can help identify desired water quality management schemes for developing the local economy in a sustainable manner. Some useful suggestions for the local economy development in a sustainable manner could be summarized: (i) advancing wastewater treatment technologies (e.g., tertiary treatment and depth processing technologies) to further improve pollutant removal efficiency; (ii) controlling the generation of phosphorus-containing wastes (from chemical plants and phosphorus mining companies) strictly in the production process and taking effective treatments and disposal measures to reach the goal of achieving TP abatement; (iii) taking control practices on soil erosion for reducing the transport of nitrogen and phosphorus pollutants to the river.

Although reasonable solutions and desired management policies have been obtained through the IFCP management model, there are still some extensive research works to be done. For example, the proposed IFCP method can deal with uncertainties expressed as fuzzy sets and interval numbers; however, the main limitations of the IFCP method remain in its difficulties in tackling uncertainties expressed as probabilistic distributions (stochastic uncertainties). Under such a circumstance, stochastic mathematical programming method is a suitable option to be introduced into the proposed IFCP method. Moreover, decision support regarding pollution management could be further provided by incorporating certain water quality simulation models into IFCP framework, which can effectively reflect dynamic interactions between pollutant loading and water quality.

## Acknowledgments

This research was supported by the Natural Sciences Foundation of China (Grant nos. 51379075, 51225904, and 51109077), the 111 Project (B14008), and the Program for Innovative Research Team in University (IRT1127). The authors are grateful to the editors and the anonymous reviewers for their insightful comments and suggestions.

## References

- [1] P. Du, Y. P. Li, and G. H. Huang, "Inexact chance-constrained waste-load allocation model for water quality management of Xiangxihe River," *Journal of Environmental Engineering*, vol. 139, pp. 1178–1197, 2013.
- [2] Y. P. Li and G. H. Huang, "Two-stage planning for sustainable water-quality management under uncertainty," *Journal of Environmental Management*, vol. 90, no. 8, pp. 2402–2413, 2009.
- [3] Y. P. Li, W. Li, and G. H. Huang, "Two-stage inexact-probabilistic programming model for water quality management," *Environmental Engineering Science*, vol. 29, no. 7, pp. 713–725, 2012.

- [4] Y. P. Li and G. H. Huang, "Fuzzy-stochastic-based violation analysis method for planning water resources management systems with uncertain information," *Information Sciences*, vol. 179, no. 24, pp. 4261–4276, 2009.
- [5] X. S. Qin, G. H. Huang, G. M. Zeng, A. Chakma, and Y. F. Huang, "An interval-parameter fuzzy nonlinear optimization model for stream water quality management under uncertainty," *European Journal of Operational Research*, vol. 180, no. 3, pp. 1331–1357, 2007.
- [6] B. Julien, "Water quality management with imprecise information," *European Journal of Operational Research*, vol. 76, no. 1, pp. 15–27, 1994.
- [7] C.-S. Lee and C.-G. Wen, "Fuzzy goal programming approach for water quality management in a river basin," *Fuzzy Sets and Systems*, vol. 89, no. 2, pp. 181–192, 1997.
- [8] P. P. Mujumdar and K. Sasikumar, "A fuzzy risk approach for seasonal water quality management of a river system," *Water Resources Research*, vol. 38, no. 1, pp. 51–59, 2002.
- [9] H.-W. Chen and N.-B. Chang, "Decision support for allocation of watershed pollution load using grey fuzzy multiobjective programming," *Journal of the American Water Resources Association*, vol. 42, no. 3, pp. 725–745, 2006.
- [10] S. Karmakar and P. P. Mujumdar, "Grey fuzzy optimization model for water quality management of a river system," *Advances in Water Resources*, vol. 29, no. 7, pp. 1088–1105, 2006.
- [11] Y. P. Li, G. H. Huang, S. L. Nie, and D. W. Mo, "Interval-parameter robust quadratic programming for water quality management under uncertainty," *Engineering Optimization*, vol. 40, no. 7, pp. 613–635, 2008.
- [12] X. H. Nie, G. H. Huang, D. Wang, and H. L. Li, "Robust optimisation for inexact water quality management under uncertainty," *Civil Engineering and Environmental Systems*, vol. 25, no. 2, pp. 167–184, 2008.
- [13] S. Maeda, T. Kawachi, K. Unami, J. Takeuchi, T. Izumi, and S. Chono, "Fuzzy optimization model for integrated management of total nitrogen loads from distributed point and nonpoint sources in watershed," *Paddy and Water Environment*, vol. 7, no. 3, pp. 163–175, 2009.
- [14] T. Y. Xu and X. S. Qin, "Solving water quality management problem through combined genetic algorithm and fuzzy simulation," *Journal of Environmental Informatics*, vol. 22, no. 1, pp. 39–48, 2013.
- [15] M. Liu, G. X. Nie, M. Hu, R. F. Liao, and Y. S. Shen, "An interval-parameter fuzzy robust nonlinear programming model for water quality management," *Journal of Water Resource and Protection*, vol. 5, pp. 12–16, 2013.
- [16] Y. M. Zhang and G. H. Huang, "Optimal water resource planning under fixed budget by interval-parameter credibility constrained programming," *Engineering Optimization*, vol. 43, no. 8, pp. 879–889, 2011.
- [17] M. S. Pishvaei, S. A. Torabi, and J. Razmi, "Credibility-based fuzzy mathematical programming model for green logistics design under uncertainty," *Computers and Industrial Engineering*, vol. 62, no. 2, pp. 624–632, 2012.
- [18] Y. P. Li, G. H. Huang, and S. L. Nie, "Optimization of regional economic and environmental systems under fuzzy and random uncertainties," *Journal of Environmental Management*, vol. 92, no. 8, pp. 2010–2020, 2011.
- [19] R. Brouwer and C. De Blois, "Integrated modelling of risk and uncertainty underlying the cost and effectiveness of water quality measures," *Environmental Modelling and Software*, vol. 23, no. 7, pp. 922–937, 2008.
- [20] Y. R. Fan and G. H. Huang, "A robust two-step method for solving interval linear programming problems within an environmental management context," *Journal of Environmental Informatics*, vol. 19, no. 1, pp. 1–9, 2012.
- [21] Y. Xu, G. H. Huang, and T. Y. Xu, "Inexact management modeling for urban water supply systems," *Journal of Environmental Informatics*, vol. 20, no. 1, pp. 34–43, 2012.
- [22] Y. Chen, S. Y. Cheng, L. Liu et al., "Assessing the effects of land use changes on non-point source pollution reduction for the Three Gorges Watershed using the SWAT model," *Journal of Environmental Informatics*, vol. 22, no. 1, pp. 13–26, 2013.
- [23] L. He, G. Q. Wang, and C. Zhang, "Application of loosely coupled watershed model and channel model in Yellow River, China," *Journal of Environmental Informatics*, vol. 19, no. 1, pp. 30–37, 2012.
- [24] Y. P. Li and G. H. Huang, "A recourse-based nonlinear programming model for stream water quality management," *Stochastic Environmental Research and Risk Assessment*, vol. 26, no. 2, pp. 207–223, 2012.
- [25] L. Ye, Q.-H. Cai, R.-Q. Liu, and M. Cao, "The influence of topography and land use on water quality of Xiangxi River in three Gorges Reservoir region," *Environmental Geology*, vol. 58, no. 5, pp. 937–942, 2009.
- [26] F. A. Deviney Jr., D. E. Brown, and K. C. Rice, "Evaluation of bayesian estimation of a hidden continuous-time markov chain model with application to threshold violation in water-quality indicators," *Journal of Environmental Informatics*, vol. 19, no. 2, pp. 70–78, 2012.

## Research Article

# Testing a Conceptual Lumped Model in Karst Area, Southwest China

Peng Shi,<sup>1,2</sup> Mi Zhou,<sup>2</sup> Simin Qu,<sup>2</sup> Xi Chen,<sup>1,2</sup> Xueyuan Qiao,<sup>2</sup>  
Zhicai Zhang,<sup>2</sup> and Xinxin Ma<sup>2</sup>

<sup>1</sup> State Key Laboratory of Hydrology-Water Resources and Hydraulic Engineering, Hohai University, Nanjing 210098, China

<sup>2</sup> College of Water Resources and Hydrology, Hohai University, Nanjing 210098, China

Correspondence should be addressed to Peng Shi; [ship@hhu.edu.cn](mailto:ship@hhu.edu.cn)

Received 21 September 2013; Revised 10 November 2013; Accepted 19 November 2013

Academic Editor: Y. P. Li

Copyright © 2013 Peng Shi et al. This is an open access article distributed under the Creative Commons Attribution License, which permits unrestricted use, distribution, and reproduction in any medium, provided the original work is properly cited.

Karst aquifers are known for their heterogeneous physical properties and irregular complex flow patterns which make it a challenge to describe the hydrological behavior and to quantitatively define the distribution of river flow components using hydrologic models. In this paper, a conceptual lumped hydrologic model, Xin'anjiang model (XAJ), was applied in Sancha River, which is a karst basin in southwest China, for the simulation of streamflow. The performance of XAJ model was evaluated based on the model's ability to reproduce the streamflow and baseflow. Percentage of bias (PBIAS), Nash-Sutcliffe efficiency (NSE), coefficient of determination ( $R^2$ ), and standard deviation (RSR) were calculated between the simulated and measured flow for both calibration and validation period. The low PBIAS and RSR (2.7% and 0.367 for calibration period, 1.3% and 0.376 for validation period) and the high NSE and  $R^2$  (0.866 and 0.866 for calibration period, 0.858 and 0.860 for validation period) indicate that the model structure and parameters are of reasonable validity. Furthermore, streamflow was separated to baseflow and surface flow using the "baseflow programme" and the calculated results indicate that the model could also reproduce the response of baseflow in such karst system.

## 1. Introduction

Karst terrain accounts for about 15% of the world's land and is home for around 1 billion people [1]. Water from Karst terrain supports upwards of 25% of the current world population [2]. Guizhou Province has one of the largest, continuous karst areas in the world. About 73% of Guizhou is karst, and 17.42% of the karst landforms are developed on continuously pure limestone [3, 4]. The importance of karst aquifers as a water resource has grown, as the population in this region continues to expand causing an increasing demand of water. However, Karst rocky desertification is a serious problem in this region, especially in limestone areas [5, 6]. It is a process featured by the degradation of karst areas originally covered by soil and vegetation into rocky landscapes or lithological deserts with little soil or vegetation covering. As a result, modeling the response of karst aquifers and water storage in such systems becomes an important challenge and is an important step to estimate the sustainable yield of karst aquifers as well as to evaluate future climatic

or anthropogenic impacts on the sustainability of groundwater resources in these systems. However, Karst aquifers are known for their heterogeneous physical properties and irregular complex flow patterns which make it a challenge to describe the hydrological behavior and to quantitatively define the distribution of river flow components using hydrologic models [7]. For reliable simulations, the used models require an adequate representation of hydrological systems, which is particularly true in karst regions. Both distributed and lumped hydrological models were used to simulate the hydrological processes in karst systems [8, 9]. Distributed models provide spatially distributed information about groundwater heads and flow, including karst processes in different degrees of complexity [10]. However, the application of distributed models is hampered by the complexity and heterogeneity of karst systems and the lack or limitation of detailed and quantifiable information about the physical parameters (soil, vegetation, fractures, conduits, and swallow holes). On the other hand, lumped models are based on a set of mathematical equations that represent the transfer from

input [11–15]. This has resulted in the use of lumped models in karst hydrology.

In karst hydrology, two main types of lumped models are generally used to simulate the rainfall-discharge relationship:

- (1) empirical models (also called “black box” models) that represent a completely unknown system, neither on the structure of the aquifer, nor on hydrodynamics parameters. This type of model aims to characterize the overall relationship between rainfall and discharge. Most of these models have been already applied to numerous karst systems [16–22];
- (2) reservoir models that are developed with simple discharge equation between linked reservoirs. The use of reservoir models is a simple and classical way which is being explored with software packages such as GARDENIA [23] or VENSIM, which has been used in surface hydrology for some years [24] and presently is being tested on karst aquifers.

From a physical point of view, the hydrologic functioning of a karst system is driven by the typical hydrodynamic behavior of each compartment that can be classified according to three distinct zones: epikarst, infiltration zone, and saturated/phreatic zone [25]. However, the abovementioned “black box” models and reservoir-based models poorly rely on the physical properties of functioning of karst systems. Thus, Xin’anjiang conceptual lumped models (LPM) were developed, not only for reproducing the dynamics of the catchment but also for understanding the relations between karst system and its geological and human environment for managing the resource.

Conceptual lumped models (LPM) are based on the conceptualization of the karst aquifer as a whole; that is, dependent variables are not a function of spatial position, and physical relationships are not considered explicitly but are represented in general terms through the conceptualization of the aquifer. Due to their simplicity, LPMs are particularly useful for the interpretation of data when it is neither possible nor justified to use distributed parameter models [26]. Albeit based on a simplified physical interpretation of the processes which transform inputs into outputs, Xin’anjiang conceptual lumped models are sufficient to help define the nature and behavior of the karst contribution to river flows and the impact of future change on karst water resources.

The Xin’anjiang model was developed on the basis of the analysis of data from the Xin’anjiang Reservoir located in the Zhejiang, China. It has been applied extensively in most humid regions in the south and east of China with warm climate and little snow for runoff simulation and water resources planning. It has been improved incrementally since it was proposed in 1973 [27–30]. The advantages of the Xin’anjiang model in this study are that it is based on a simplified physical interpretation of the processes which transform inputs into outputs, while all the model parameters have clear physical meanings. High accuracy alone is insufficient for our purposes. By the application of this model, the relations between parameter values and natural conditions will be found and it is valuable for extending and developing the model to meet with more miscellaneous surface conditions.

Based on the extensive field research, the hydrological features of karst catchments in southwest China can be described as below [31]. (1) Abundant precipitation serves as a principal source for soil water replenishment. Soil in karst regions, characterized by a strong permeability and coarse vegetation covering, usually has a depth of 20–50 cm. Thus we hold the opinion that runoff from karst catchments in southwest China occurred as stored-full runoff process. (2) Generally, two processes, quick flow and slow flow, are apparent and control the characteristics of a karst flow hydrograph [17, 32]. (3) The open conduit provides low resistance pathways for the subsurface flow, which often has more in common with surface water than with groundwater [33]. (4) The relationship between karst groundwater storage and discharge in southwest China can be regarded as linear system [34, 35]. These hydrological features satisfy some assumptions of Xin’anjiang model. Thus, we hold the opinion that the conceptual lumped Xin’anjiang model can be applied for predicting the flood processes in such area.

In this paper, the main features of flood and the applicability of Xin’anjiang model to such karst area in Southwest China are thoroughly analyzed through a successful case study and the possibility and difficulty to apply Xin’anjiang model in Karst area are pointed out. The main points explored in this paper are

- (1) testing the application of Xin’anjiang model in Sancha River Valley,
- (2) using precipitation, evapotranspiration and discharge data to calibrate model parameters,
- (3) analyzing the hydrological behavior in karst area Southwest China.

## 2. Methods and Materials

**2.1. Study Area.** Guizhou Province in Southwest China is located in the east side of the Yunnan-Guizhou Plateau and covers about 17,600 km<sup>2</sup>. This region is dominated by subtropical wet monsoon climate. The mean annual temperature is 20°C. The highest average monthly temperature is in July, and the lowest is in January. Annual precipitation is 1140 mm, with a distinct summer wet season and a winter dry season. Average monthly humidity ranges from 74% to 78%.

The Sancha River Valley (Figure 1), located in the northwest part of Guizhou Province, is a tributary of the Wujiang River with an area of 7264 km<sup>2</sup> and an elevation of 200–2010 m above sea level. The studied area has a subtropical monsoonal climate with an annual precipitation of 1000 mm. Rainfall mainly occurs between May and October. The temperature of this area ranges from –1°C to 28°C, with an annual average of 14°C. Sancha River is a typical mountain river of 325.6 km long. In Sancha River Valley, karst is well developed and the topography is marked by numerous abrupt ridges, fissures, channels, sink-holes, swallow-holes, and caverns. The dominant lithology in this catchment is the pure and thick limestone of the Guanling Formation of the Middle Triassic. The limestone has a less than 10° dip angle. Soil, commonly 20–50 cm in thickness, occurs on most slopes. The soil

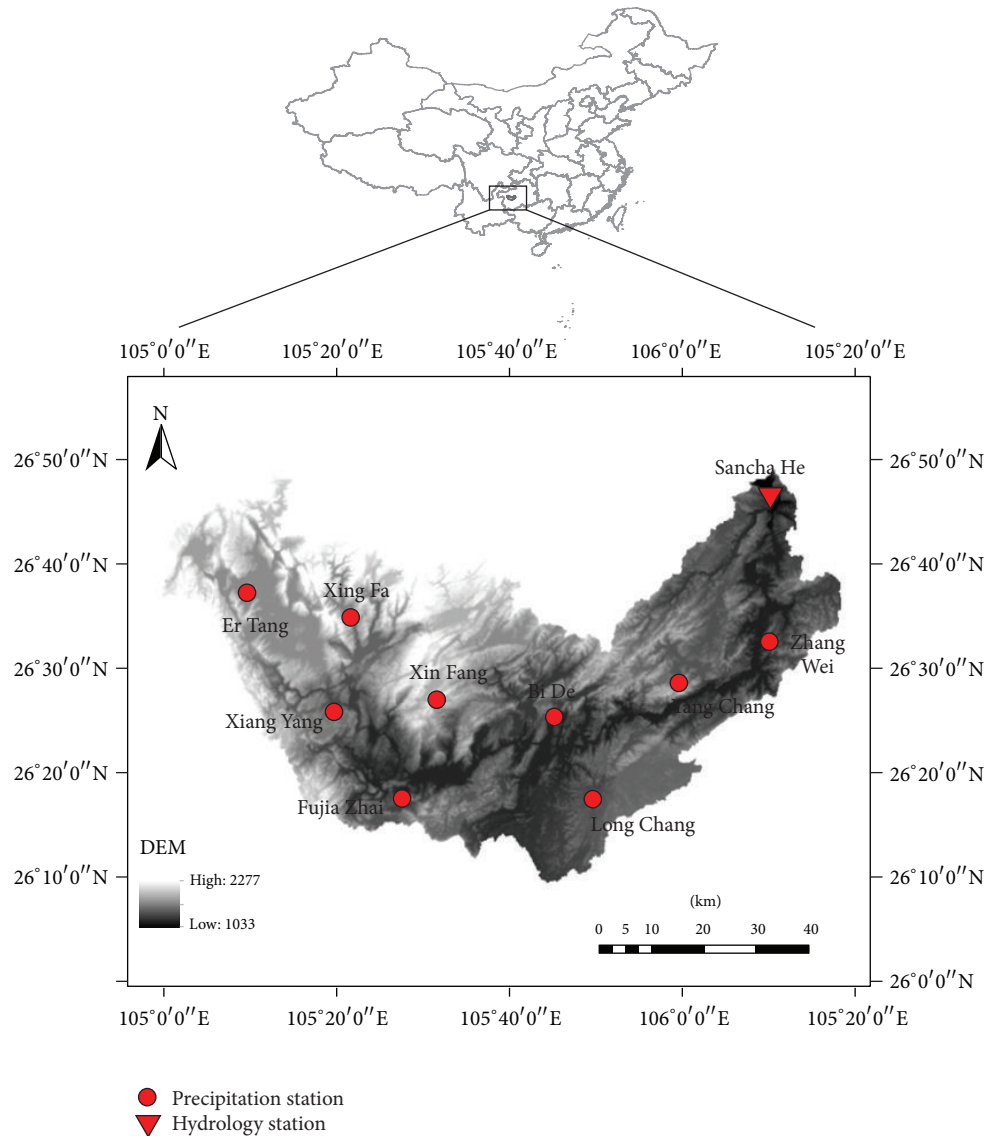


FIGURE 1: Location of Sancha River Valley.

has a clay content of 24–32.5% and a density of  $1.13 \text{ g/cm}^3$ . The organic matter content of the soil is 69.8–136.6 g/kg. The vegetation in the catchment is mainly broad-leaved deciduous shrubs and evergreens. The agriculture fields and pastureland are mainly located from mountain slope side to bottom. Crops commonly grown are corn, soybeans, and rape oil seed.

**2.2. Description of Xin'anjiang (XAJ) Model.** Xin'anjiang (XAJ) model is a conceptual hydrologic model developed by Zhao et al. [36] based on extensive observed data from the Xin'anjiang reservoir watershed. The XAJ model has been widely used in China for flood forecasting, hydrologic station network design, and water availability estimation [37]. XAJ has been used in all major river basins in China, including the Yellow River, Yangtze River, Huaihe River, and so forth.

According to the model structure, runoff was separated only into two components using the concept of a final,

constant, infiltration rate. However, in 1980, the model was modified to represent the three components of surface runoff, subsurface flow, and groundwater flow. The karst water is also composed by surface runoff, rapid and slow ground flow [38, 39]. The main feature of Xin'anjiang model is the concept of runoff formation on the depletion of storage, which means that runoff is not produced until the soil moisture content of the aeration zone reaches the field capacity, and thereafter runoff equals the rainfall excess without further loss. XAJ uses the runoff formation at natural storage mechanism to calculate runoff, making it valid only in humid and semihumid regions. The runoff-producing area is critical for calculating runoff. Runoff distribution is usually nonuniform across a region because the soil moisture deficit is heterogeneous. In order to accommodate the nonuniformity of the soil moisture deficit or the tension water capacity distribution, XAJ model adopted the storage capacity curve [36] to calculate total runoff. Shi et al. [40] proposed a method for calculating the

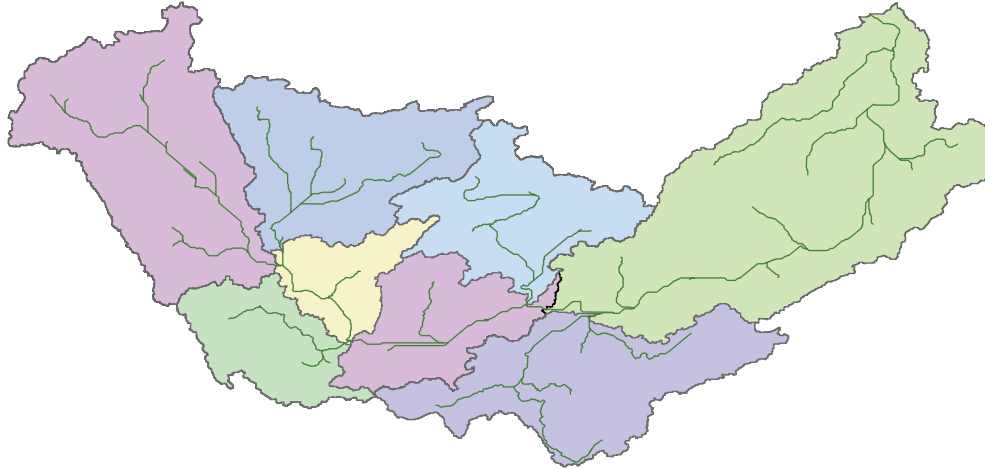


FIGURE 2: Subdivision of the study area.

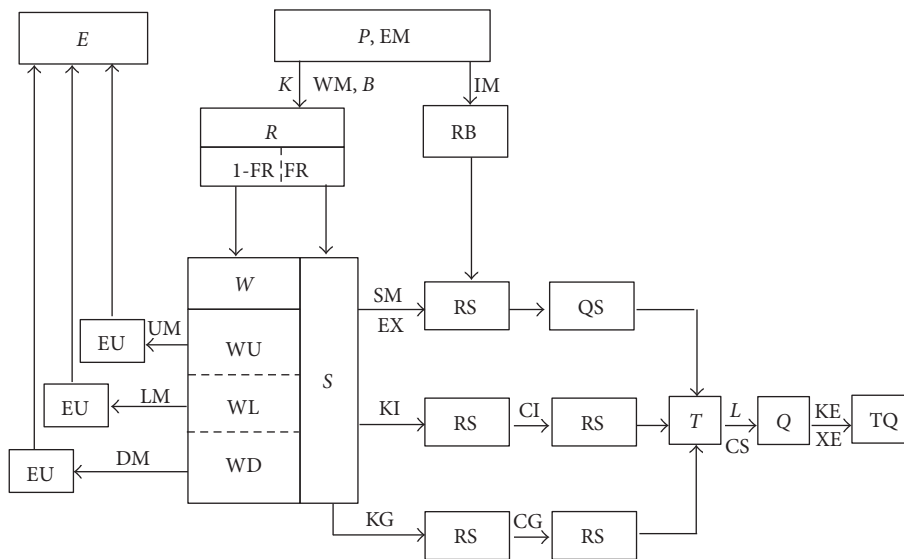


FIGURE 3: Flowchart for the Xin'anjiang model (adapted from Zhao, [37]).

water capacity from a topographic index. After calculating the total runoff, three components including surface runoff  $Q_{surf}$ , groundwater contribution  $Q_{gw}$ , and contribution to lateral flow  $Q_{lat}$  are separated [37]. By applying the Muskingum method to successive subreaches [41], flood routing from subbasin outlets to the total basin outlet is achieved.

XAJ divides a watershed into a set of subbasins (Figure 2) to capture the spatial variability of precipitation and the underlying surface. Instead of further delineating each sub-basin into HRUs, XAJ uses the subbasin as the basic operation unit. XAJ requires precipitation and measured pan evaporation inputs. Outflow simulation from each sub-basin consists of four major parts: (1) the evapotranspiration which generates the deficit of the soil storage divided into upper, lower, and deep layers; (2) the runoff production which produces the runoff according to the rainfall and soil storage deficit; (3) the runoff separation which divides the total runoff into three components, surface runoff, subsurface runoff and

groundwater, (4) the flow routing which transfers the local runoff to the outlet of each sub-basin forming the outflow of the sub-basin.

The flow chart of model calculation in each sub-basin is shown in Figure 3. All symbols inside the blocks are variables including inputs, outputs, state variables, and internal variables, while those outside the blocks are parameters. The inputs of the model are rainfall,  $P$ , and measured pan evaporation,  $EM$ . The outputs are the outlet discharge,  $Q$ , and the actual evapotranspiration,  $E$ . The function, methods, and corresponding parameters in every part (layer) are shown in Table 1.  $K$  is the ratio of potential evapotranspiration to pan evaporation if pan evaporation measurements are used as references.  $WM$  and  $B$  are two parameters describing the tension water distribution.  $WM$ , the areal mean tension water capacity, is the sum of  $UM$  in the upper layer,  $LM$  in the lower layer, and  $DM$  in the deeper layer.  $B$  is the exponent of the tension water capacity distribution curve.  $IM$  is the

TABLE 1: Function, methods, and parameters in Xin'anjiang model.

Layer	1st	2nd	3rd	4th	
Function	Evapotranspiration	Runoff generation	Water source separation	Overland flow	River network flow
Methods	Three-layer evaporation pattern	Runoff yield at natural storage	Free water storage reservoir model	Linear reservoir	Muskingum method
Parameters	KC, WUM, WLM, and C	WM, B	SM, EX, KI, and KG	CS, CI, CG	KE, XE

factor of impervious area. SM and EX are similar to WM and B, while they describe the free water capacity distribution. The areal mean of the free water capacity of the surface soil layer, SM, represents the maximum possible deficit of free water storage. Surface runoff is sensitive to the value of this parameter. EX is the exponent of the free water capacity curve. KG and KI are the outflow coefficients of the free water storage to groundwater and interflow. The sum of them determines the drainage rate from free water storage and their ratio determines the proportion going to interflow and groundwater flow, respectively. The daily recession constant of groundwater storage, CG, can be easily determined by the recession curve during the dry season. CS, the recession constant in the "lag and route" method for routing through the channel system within each sub-basin, is purely empirical. KE and XE are parameters of the Muskingum method which can be initially determined by hydraulic formulas. The more about physical meaning and value range of each parameter and the calculation are described in detail by [37].

The efficiency of the Xin'anjiang model has been established by long use in China, and use of the model has also spread to other fields of application such as water resources estimation, design flood and field drainage, water project programming, hydrological station planning, water quality accounting, and so forth. However the uncertainty problem in hydrological model is inevitable, which covers three aspects of data, model structure and parameters. Firstly, during the modeling of hydrological processes the chief question is data problem, as well as the main reason of the uncertain problems. Making the fullest use of existing information, and introducing new data, especially combining remote sensing data with different scales of hydrological simulation, will significantly lower the uncertainty problem in Xin'anjiang model. Secondly, enhance the fundamental research of hydrologic cycle. Based on the generalization and simplification of complex hydrology processes, the hydrological model should be improved continually during practical applications in order to promote the development of hydrological science. Thirdly, parameter is one of the key roles in analyzing model uncertainty problem. Usually, there is certain arbitrariness on parameters optimization based on traditional methods, and the results of parameters optimization in model are not the global optimal value which lack adequate stability [42]. The generalized likelihood uncertainty estimation (GLUE) methodology is an effective approach to study uncertainty of parameters. In the largest study of this kind, various computational approaches were investigated to analyze the impact of uncertainty on

predictions of streamflow. SHU [43] employ GLUE to examine the uncertainty in Xin'anjiang model. The propagation of precipitation uncertainty through the Xin'anjiang model and the effect on the discharge simulation were analyzed quantitatively based on the fuzzy membership grade theory and the Monte Carlo method [44]. These studies are favorable for understanding Xin'anjiang model so as to provide valuable scientific information for future uncertainties research in hydrological modeling.

**2.3. Data.** The rainfall data used in this study are the daily rainfall data from ten permanent rain gauges of the Sancha River Valley in Guizhou and they were employed: Ertang, Xingfa, Xiangyang, Xinfang, Fujiazhai, Bide, Longchang, Yangchang, Zhangwei, and Sanchahe, with equal weighing coefficients of 0.1. There is one evaporation station (Bide) in the middle part of the catchment and a discharge station (Sanchahe) in the outlet of the catchment. All stations in the catchment have nearly complete records for water years 1991 to 2012, providing a unique dataset to apply the model for discharge simulation. The data were split into two independent subsets for model calibration and validation, respectively. The data from 1991 to 2005 were used for parameter calibration, and residual seven years (2006 to 2012) were used for model validation.

**2.4. Model Calibration and Validation.** Daily runoff data from January 1, 1991 to December 31, 2005 were used for calibration, and the remaining data from January 1, 2006 to December 31, 2012 were used to validate model performance.

In this study, we followed Santhi et al. [45] and Moriasi et al. [46] by using the following statistical evaluation tools: percent bias (PBIAS), coefficient of determination ( $R^2$ ), Nash-Sutcliffe efficiency (NSE), and standard deviation (RSR). PBIAS is calculated as

$$PBIAS = \left( \frac{\sum_{t=1}^T (Q_{s,t} - Q_{m,t})}{\sum_{t=1}^T Q_{m,t}} \right) \times 100, \quad (1)$$

where  $Q_{s,t}$  is the model simulated value at time unit  $t$ ,  $Q_{m,t}$  is the observed data value at time unit  $t$ , and  $t = 1, 2, \dots, T$ . PBIAS measures the average tendency of the simulated data to be larger or smaller than their observed counterparts. PBIAS values with small magnitude are preferred. Positive values indicate model overestimation bias, while negative values indicate underestimation [47].

TABLE 2: Parameters for Xin'anjiang model after calibration.

Parameter	$K$	WM (mm)	WUM (mm)	WLM (mm)	$B$	$C$	SM (mm)	EX
Value	0.62	120.0	20.0	70.0	0.3	0.15	10	1.5
Parameter	KI	KG	CS	CI	CG	KE	XE	
Value	0.3	0.4	0.55	0.875	0.98	1.0	0.46	

The formula for calculating coefficient  $R^2$  is

$$R^2 = \left\{ \frac{\sum_{t=1}^T (Q_{m,t} - \bar{Q}_m)(Q_{s,t} - \bar{Q}_s)}{\left[ \sum_{t=1}^T (Q_{m,t} - \bar{Q}_m)^2 \right]^{0.5} \left[ \sum_{t=1}^T (Q_{s,t} - \bar{Q}_s)^2 \right]^{0.5}} \right\}^2, \quad (2)$$

where  $\bar{Q}_m$  is mean observed data value for the entire evaluation time period and  $\bar{Q}_s$  is the mean simulated data value for the entire evaluation time period. The other symbols have the same meaning defined above.  $R^2$  is equal to the square of Pearson's product moment correlation coefficient [48]. It represents the proportion of total variance in the observed data that can be explained by the model.  $R^2$  ranges between 0.0 and 1.0. Higher values mean better performance.

NSE is calculated as

$$\text{NSE} = 1.0 - \frac{\sum_{t=1}^T (Q_{m,t} - Q_{s,t})^2}{\sum_{t=1}^T (Q_{m,t} - \bar{Q}_m)^2}. \quad (3)$$

NSE indicates how well the plot of observed values versus simulated values fits the 1:1 line and ranges from  $-\infty$  to 1 [49]. Larger NSE values are equivalent with better model performance.

The standard deviation (RSR) is calculated as:

$$\text{RSR} = \frac{\text{RMSE}}{\text{STDEV}_{\text{obs}}} = \frac{\sqrt{\sum_{t=1}^T (Q_{m,t} - Q_{s,t})^2}}{\sqrt{\sum_{t=1}^T (Q_{m,t} - \bar{Q}_m)^2}}. \quad (4)$$

2.5. *Calibration Phase.* The calibration process is as follows.

- (1) Model parameters are assumed firstly using reasonable initial values according to their physical meaning and value range described in detail by Zhao [37].  $K$ ,  $UM$ ,  $LM$ , and  $C$  are evapotranspiration parameters.  $WM$ ,  $B$ , and  $IM$  are runoff production parameters.  $SM$ ,  $EX$ ,  $KG$ , and  $KI$  are parameters of runoff separation.  $CG$ ,  $CI$ ,  $CS$ , and  $L$  are runoff concentration parameters. The output is more sensitive to  $K$ ,  $SM$ ,  $KG$ ,  $KI$ ,  $CG$ ,  $CS$ , and  $L$ .  $K$ , as an empirical coefficient transferring the pan evaporation to potential evapotranspiration, and is calibrated alone firstly. Pan evaporation in Bide evaporation station is used as reference in this study area.  $C$  depends on the proportion of the basin area covered, and it can be adjusted after calibration of  $K$ . Parameters  $UM$  and  $LM$  are determined by experience.  $WM$  is the areal mean tension water capacity having components  $UM$ ,  $LM$ ,

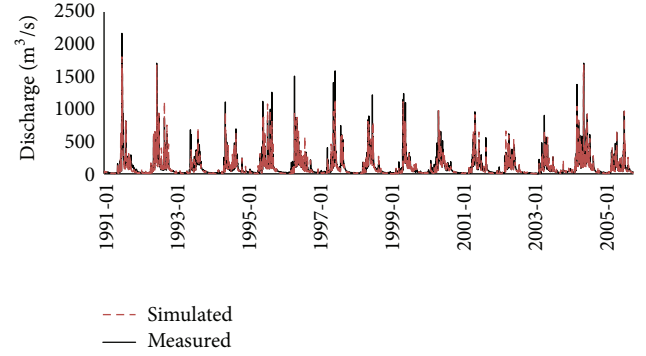


FIGURE 4: XAJ model simulation phase (1991 to 2005).

TABLE 3: The daily simulation results of the calibration and validation process.

	NSE	PBIAS	$R^2$	RSR
Calibration	0.866	2.7	0.866	0.367
Validation	0.858	1.3	0.860	0.376

and  $DM$ , and the value is provided large enough to ensure that the computed areal mean soil moisture content  $W$  does not become negative.  $SM$  is the areal mean of the free water capacity of the surface soil layer. It may be approximately 10 mm or less for thin soils, increasing to 50 mm or more for thick surface soils. The best choice for the value of  $EX$  is between 1 and 1.5 and a fixed value (0.7 or 0.8) is taken for the sum of  $KG$  and  $KI$ .

- (2) Next, by comparing the simulated and observed hydrographs, a manual calibration is applied to refine model parameters by a trial-and-error method because the number of parameters is limited and the range is relatively short. Table 2 shows the set of model parameters obtained from the calibration phase (years from 1991 to 2005) for the Xin'anjiang model. The hydrograph obtained using the model for this period is compared to the measured hydrograph in Figure 4.

The daily simulation results of the calibration process are reported in Table 3. From the table, it can be seen that the percent bias (PBIAS), coefficient of determination ( $R^2$ ), Nash-Sutcliffe efficiency (NSE), and standard deviation (RSR) for the calibration are 2.7, 0.866, 0.866, and 0.367. These results show that the calibrated parameters are realistic and reasonable.

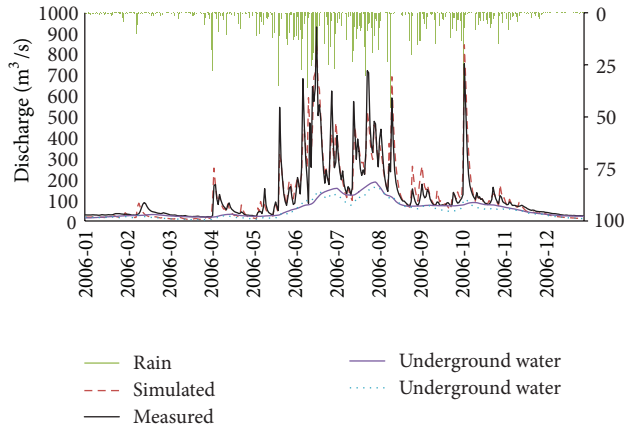


FIGURE 5: XAJ model validation phase (2006). Measured and simulated discharge, the groundwater runoff separated from the hydrograph and calculated by Xin'anjiang model, and catchment average rainfall time series.

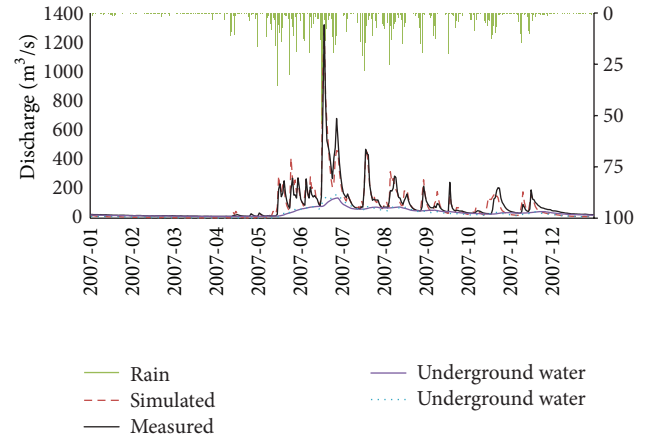


FIGURE 6: XAJ model validation phase (2007). Measured and simulated discharge, the groundwater runoff separated from the hydrograph and calculated by Xin'anjiang model, and catchment average rainfall time series.

2.6. *Validation Phase.* The hydrograph obtained using the model for the period 2006–2012 is compared to the measured hydrograph in Figures 5–11. The daily calculation results of the validation process are shown in Table 3. From the table, it can be seen that the percent bias (PBIAS), coefficient of determination ( $R^2$ ), Nash-Sutcliffe efficiency (NSE), and standard deviation (RSR) for the validation are 1.3, 0.860, 0.858, and 0.376. According to Moriasi et al. [46], the model performance is “very good.”

### 2.7. Model Response Analysis

- (1) Figures 5–11 present the observed and simulated total runoff and the groundwater runoff separated from the hydrograph and calculated by the model for study area. Both the calibration and validation graphs show very good similarity between observed and simulated total runoff. The goodness of fit of these graphs is measured by four statistical tests NSE, PBIAS,  $R^2$ , and RSR, which were described in Table 3. The results of these tests are given in Table 3 which indicate that the model is able to present reasonably well the runoff generated by rainfall events in study area. The groundwater runoff calculated by Xin'anjiang model also can be seen to reproduce the groundwater runoff separated from the hydrograph.
- (2) Results of simulations show that good agreement in aspect of both timing and flow quantity exists between the calculated and observed maximum flood peak. For instance, maximum flood peaks occurred in June 2006 (Figure 5), June 2007 (Figure 6), June 2008 (Figure 7), July 2009 (Figure 8), June 2010 (Figure 9), June 2011 (Figure 10), and June 2012 (Figure 11).
- (3) Hydrographs show the rapid confluence and precipitous fluctuation of flooding process following the intensive rainfall events when soil moisture content approach saturation. The response of runoff to rainfall

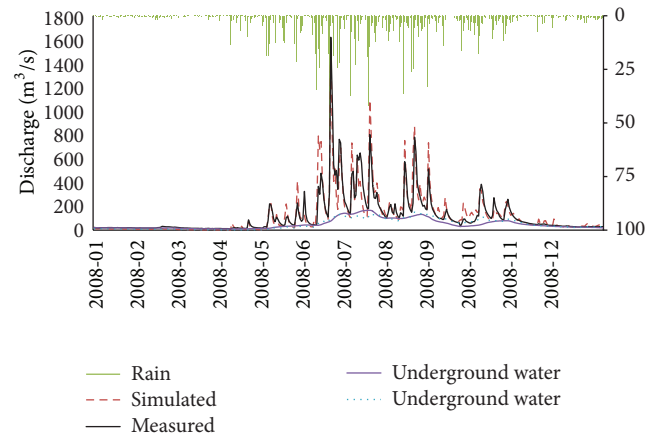


FIGURE 7: XAJ model validation phase (2008). Measured and simulated discharge, the groundwater runoff separated from the hydrograph and calculated by Xin'anjiang model, and catchment average rainfall time series.

implies a high sensitivity of runoff to the variation in rainfall quantity. They also show clearly the relatively steady groundwater runoff.

- (4) However, further limitations in the rainfall-runoff relationship exist. A single precipitation time series cannot fully describe the dynamic of the runoff in karst area. It could be seen that after long dry periods, rainfall events that occurred could not generate any discharge peak and all the rainfall formed the groundwater runoff; for instance, the rainfall events occurred in January 2010 (Figure 11), while moderate rainfall events could generate strong flow peaks after a long wet period. A closer inspection of the response of karst catchments to rainfall events indicates that the vadose zone needs to reach a minimum volume for the possibility of the fast transfer to the outlet. On the contrary, when water content is high enough, it

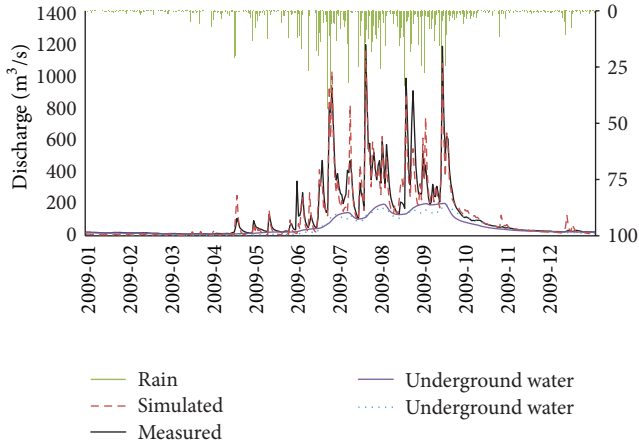


FIGURE 8: XAJ model validation phase (2009). Measured and simulated discharge, the groundwater runoff separated from the hydrograph and calculated by Xin'anjiang model, and catchment average rainfall time series.

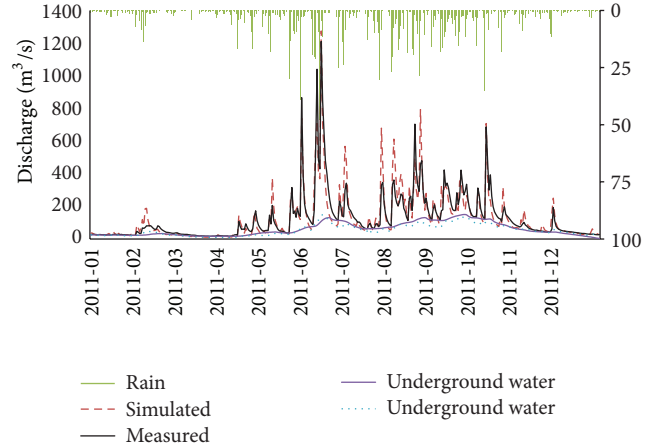


FIGURE 10: XAJ model validation phase (2011). Measured and simulated discharge, the groundwater runoff separated from the hydrograph and calculated by Xin'anjiang model, and catchment average rainfall time series.

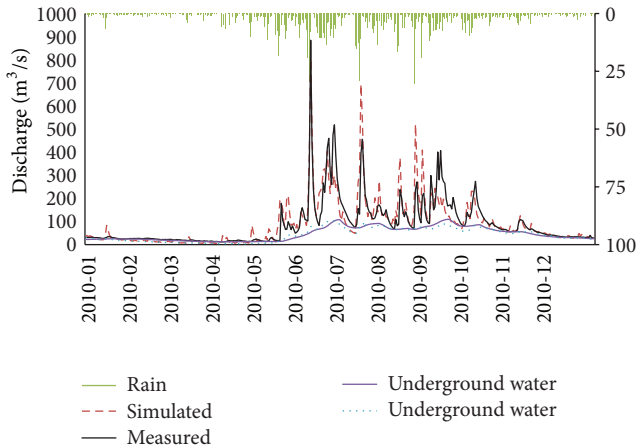


FIGURE 9: XAJ model validation phase (2010). Measured and simulated discharge, the groundwater runoff separated from the hydrograph and calculated by Xin'anjiang model, and catchment average rainfall time series.

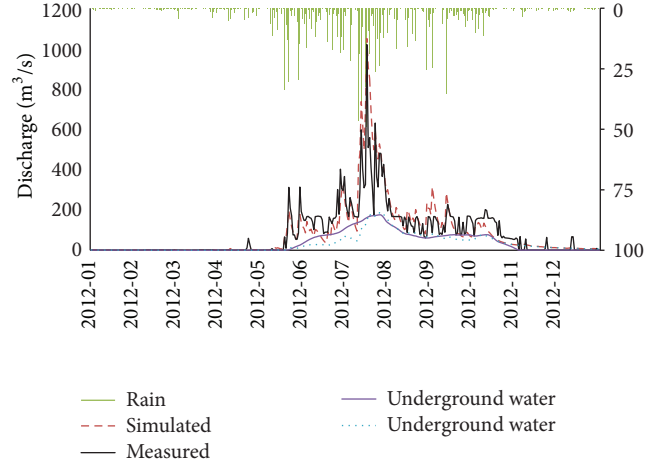


FIGURE 11: XAJ model validation phase (2012). Measured and simulated discharge, the groundwater runoff separated from the hydrograph and calculated by Xin'anjiang model, and catchment average rainfall time series.

activates the rapid transfer through the dissolution-widened fractures towards the main outlet of the karst system. However, water does not flow necessarily towards one single outlet in karst hydrology. During high water periods, many temporary outlets may also discharge from the karst system [50]. This may generate a large increase in the flood peak discharge of the river, compared to the discharge attributed only to surface runoff processes [51–53].

- (5) As mentioned above, the discharge peaks following a mild rainfall event in September 2010 (Figure 11) were overrated. The reason is that the runoff is strongly dependent on the initial state of karst system. As a result rainfall events occurring after long, dry periods and sparse, mild events are not able to generate any discharge peak or just generate small peak.

- (6) In low flow season, the baseflow could be reproduced accurately by the Xin'jiang model.

### 3. Conclusion

Xin'anjiang model has been applied for modeling hydrological response of Sancha River Valley (where a typical karst area). The applicability of Xin'anjiang model in this area depends on the quality of data and the accuracy of the results obtained by this model. The obtained values of the model precision show that the results from Xin'anjiang model can be considered as a reliable estimation of the flow process in Sancha River Valley.

Hydrograph of karst basins has a feature of steep up-down limbs. Precipitation after a preceding drought that endures a long time generally produces quite small discharge. However,

the peak flow, usually with a relatively high discharge rate, is observed shortly after the rainfall event, due to the fact that the system was already near-saturated before the rainwater drained into the main stream channel directly and quickly. Suitable parameters reflecting the hydrological and geomorphic condition are obtained by analyzing the hydrographic areas karst landform characteristics and karst features of flood in study area, and the simulation results indicate that Xin'anjiang model is reasonable and feasible to describe the hydrologic processes in this region.

The mode of recharge and transfer through the vadose zone (soil, epikarst, and infiltration zone) is a key variable in the development of a rainfall-discharge model. Structure of Xin'anjiang model is generally based on a production function and a transfer function and has the advantages of keeping in memory the previous water storage in each aquifer and simulating the main steps of the aquifer functioning and all the model parameters have clear physical meanings for finding relations between parameter values and natural conditions. That is the reason why Xin'anjiang models were developed and used for simulating karst aquifer functioning. However, small-flow peaks following long, dry periods are still hard to be exactly simulated because of the sophisticated flow regimes of karst groundwater systems originated from the complexity of karst aquifers. Moreover, the application of the model for hydrological prediction in regions outside our study area requires more calibration data, and the uncertainty problem in hydrological model is inevitable. Nowadays, there are a variety of hydrological models described in the literature. However, all surface hydrological models, in general, reach their limit of applicability in complex hydrological environments. The choice of a suitable model depends on the availability of data and the goals that are to be achieved.

## Acknowledgments

The first author thanks the following financial support: the National Natural Science Foundation of China (nos. 41001011/51190091/41101018/41371048/40930635); the Special Fund of State Key Laboratory of China (2009586412); the Ph.D. Programs Foundation of Ministry of Education, China (20090094120008); the Fundamental Research Funds for the Central Universities; and the Ground Project Granted by the Ministry of Education of China (20064). The paper was edited by Dr. Peng Jiang. Thanks are due to the editor and the anonymous reviewer for their constructive comments on the earlier paper that led to a great improvement of the paper.

## References

- [1] D. Yuan and G. Chai, *The Science of Karst Environment*, Chongqing Press, Chongqing, China, 1988.
- [2] D. Ford and P. Williams, *Karst Geomorphology and Hydrology*, Unwin Hyman, London, UK, 1989.
- [3] R. Li, S. Wang, D. Zhou et al., "The correlation between rock desertification and lithology in karst area of Guizhou," *Acta Geographica Sinica*, vol. 58, no. 2, pp. 314–320, 2003 (Chinese).
- [4] Y. B. Li, S. J. Wang, and Z. F. Wei, "The spatial distribution of soil loss tolerance in carbonate area in Guizhou province," *Earth and Environment*, vol. 34, pp. 36–40, 2006 (Chinese).
- [5] D. Yuan, "Rock desertification in the subtropical karst of south China," *Zeitschrift für Geomorphologie*, vol. 108, pp. 81–90, 1997.
- [6] S. J. Wang, Q. M. Liu, and D. F. Zhang, "Karst rocky desertification in southwestern China: geomorphology, landuse, impact and rehabilitation," *Land Degradation and Development*, vol. 15, no. 2, pp. 115–121, 2004.
- [7] M. Bakalowicz, "Karst groundwater: a challenge for new resources," *Hydrogeology Journal*, vol. 13, no. 1, pp. 148–160, 2005.
- [8] A. J. Jakeman and G. M. Hornberger, "How much complexity is warranted in a rainfall-runoff model?" *Water Resources Research*, vol. 29, no. 8, pp. 2637–2649, 1993.
- [9] M. Sauter, A. Kovács, T. Geyer, and G. Teutsch, "Modellierung der hydraulik von karstgrundwasserleitern—eine übersicht," *Grundwasser*, vol. 11, no. 3, pp. 143–156, 2006.
- [10] N. Goldscheider and D. Drew, "Hydrogeologists," in *Methods in Karst Hydrogeology*, IAH—International Contributions to Hydrogeology, Taylor and Francis Group, London, UK, 1st edition, 2007.
- [11] C. Butscher and P. Huggenberger, "Intrinsic vulnerability assessment in karst areas: a numerical modeling approach," *Water Resource Research*, vol. 44, no. 3, 2008.
- [12] P. Fleury, V. Plagnes, and M. Bakalowicz, "Modelling of the functioning of karst aquifers with a reservoir model: application to fontaine de vaucluse (South of France)," *Journal of Hydrology*, vol. 345, no. 1-2, pp. 38–49, 2007.
- [13] A. Hartmann, M. Kralik, F. Humer, J. Lange, and M. Weiler, "Identification of a karst system's intrinsic hydrodynamic parameters: upscaling from single springs to the whole aquifer," *Environmental Earth Sciences*, vol. 65, no. 8, pp. 2377–2389, 2012.
- [14] P. Shi, M. Wu, X. Chen, Z. C. Zhang, and S. M. Qu, "A conceptual distribution hydrologic model for karst area in Southwest China," *Tropical Geography*, vol. 33, no. 5, pp. 570–574, 581, 2013 (Chinese).
- [15] S. Tritz, V. Guinot, and H. Jourde, "Modelling the behaviour of a karst system catchment using non-linear hysteretic conceptual model," *Journal of Hydrology*, vol. 397, no. 3-4, pp. 250–262, 2011.
- [16] V. Denić-Jukić and D. Jukić, "Composite transfer functions for karst aquifers," *Journal of Hydrology*, vol. 274, no. 1-4, pp. 80–94, 2003.
- [17] D. Labat, R. Ababou, and A. Mangin, "Rainfall-runoff relations for karstic springs. Part I: convolution and spectral analyses," *Journal of Hydrology*, vol. 238, no. 3-4, pp. 123–148, 2000.
- [18] D. Labat, R. Ababou, and A. Mangin, "Rainfall-runoff relations for karstic springs. Part II: continuous wavelet and discrete orthogonal multiresolution analyses," *Journal of Hydrology*, vol. 238, no. 3-4, pp. 149–178, 2000.
- [19] D. Labat, A. Mangin, and R. Ababou, "Rainfall-runoff relations for karstic springs: multifractal analyses," *Journal of Hydrology*, vol. 256, no. 3-4, pp. 176–195, 2002.
- [20] M. Larocque, A. Mangin, M. Razack, and O. Banton, "Contribution of correlation and spectral analyses to the regional study of a large karst aquifer (Charente, France)," *Journal of Hydrology*, vol. 205, no. 3-4, pp. 217–231, 1998.
- [21] D. Jukić and V. Denić-Jukić, "Nonlinear kernel functions for karst aquifers," *Journal of Hydrology*, vol. 328, no. 1-2, pp. 360–374, 2006.
- [22] A. Rimmer and Y. Salingar, "Modelling precipitation-streamflow processes in karst basin: the case of the Jordan River sources, Israel," *Journal of Hydrology*, vol. 331, no. 3-4, pp. 524–542, 2006.

- [23] D. Thiery, "Forecast of changes in piezometric levels by a lumped hydrological model," *Journal of Hydrology*, vol. 97, no. 1-2, pp. 129-148, 1988.
- [24] A. Hreiche, D. Mezher, C. Bocquillon, A. Dezetter, E. Servat, and W. Najem, "Parallel processing for a better understanding of equifinality in hydrological models," in *Proceedings of the Integrated Assessment and Decision Support (IEMSS '02)*, vol. 1, Lugano, Switzerland, June 2002.
- [25] A. Mangin, *Contribution à l'étude hydrodynamique des aquifères karstique [Ph.D. thesis]*, University of Dijon, France, 1975.
- [26] P. Maloszewski and A. Zuber, "Manual on lumped-parameter models used for the interpretation of environmental tracer data in groundwaters," in *Use of Isotopes for Analyses of Flow and Transport Dynamics in Groundwater Systems*, Y. Yurtsever, Ed., pp. 1-50, Vienna, Austria, 2002.
- [27] Z. J. Li, X. G. Kong, and C. W. Zhang, "Improving Xin'anjiang model," *Hydrology in China*, no. 4, pp. 19-23, 1998 (Chinese).
- [28] Z. J. Li, K. Zhang, and C. Yao, "Comparison of distributed geological models based on GIS technology and DEM," *Journal of Hydraulic Engineering*, vol. 37, no. 8, pp. 1022-1028, 2006 (Chinese).
- [29] Z. J. Li, C. Yao, and Z. H. Wang, "Development and application of grid-based Xin'anjiang model," *Journal of Hohai University*, vol. 35, no. 2, pp. 131-134, 2007 (Chinese).
- [30] L. L. Wang, Z. J. Li, and H. J. Bao, "Application of hydrological models based on DEM in the Yihe basin," *Journal of Hydraulic Engineering*, no. 10, pp. 417-422, 2007 (Chinese).
- [31] Zhang Jianyun and Zhuang Yiling, "Study and application of hydrological model for karst catchments," *Journal of Hohai University*, vol. 16, no. 3, 1988.
- [32] V. Denić-Jukić and D. Jukić, "Composite transfer functions for karst aquifers," *Journal of Hydrology*, vol. 274, no. 1-4, pp. 80-94, 2003.
- [33] Y. Lizheng, "Distribution of subterranean rivers in South China," *Carsologica Sinica*, vol. 4, no. 1, pp. 92-100, 1985 (Chinese).
- [34] S. J. Dreiss, "Linear kernels for karst aquifers," *Water Resources Research*, vol. 18, no. 4, pp. 865-876, 1982.
- [35] D. M. Ristic, "Water regime of flooded poljes," *Karst Hydrology and Water Resources*, vol. 1, pp. 301-318, 1976.
- [36] R. J. Zhao, Y. L. Zhuang, L. R. Fang, X. R. Liu, and Q. S. Zhang, "The Xinanjiang model," in *Hydrological Forecasting*, IAHS Publication no. 129, pp. 351-356, IAHS, Wallingford, UK, 1980.
- [37] R. J. Zhao, "The Xinanjiang model applied in China," *Journal of Hydrology*, vol. 135, no. 1-4, pp. 371-381, 1992.
- [38] Y. Q. Huang and J. C. Weixin, "Discussion of rapid flow and retarded flow in karst water system," *Carsologica Sinica*, vol. 5, no. 4, 1986.
- [39] K. Torbarov, "Estimation of permeability and effective porosity in karst on the basis of recession curver analysis," in *Karst Hydrology and Water Resources*, WRP, 1976.
- [40] P. Shi, X. F. Rui, S. M. Qu, and X. Chen, "Calculating storage capacity with topographic index," *Advances in Water Science*, vol. 19, no. 2, pp. 264-267, 2008.
- [41] R. J. Zaho, "A non-linear system model for basin concentration," *Journal of Hydrology*, vol. 142, no. 1-4, pp. 477-482, 1993.
- [42] J. F. Chen, W. C. Zhang, and B. Wu, "Multi-objective calibration with predictive uncertainty analysis for conceptual hydrological model," *Bulletin of Soil and Water Conservation*, vol. 28, no. 3, pp. 107-112, 2008 (Chinese).
- [43] C. Shu, S. X. Liu, X. J. Mo, Z. M. Liang, and D. Dai, "Uncertainty analysis of Xinanjiang model parameter," *Geographical Research*, vol. 27, no. 2, pp. 343-352, 2008.
- [44] W. Liu, L. L. Ren, X. U. Jing, and X. F. Liu, "Propagation of precipitation uncertainty through the Xinanjiang model," *Water Resources Protection*, vol. 25, no. 6, 2009.
- [45] C. Santhi, J. G. Arnold, J. R. Williams, W. A. Dugas, R. Srinivasan, and L. M. Hauck, "Validation of the SWAT model on a large river basin with point and nonpoint sources," *Journal of the American Water Resources Association*, vol. 37, no. 5, pp. 1169-1188, 2001.
- [46] D. N. Moriasi, J. G. Arnold, M. W. Van Liew, R. L. Bingner, R. D. Harmel, and T. L. Veith, "Model evaluation guidelines for systematic quantification of accuracy in watershed simulations," *Transactions of the American Society of Agricultural and Biological Engineers*, vol. 50, no. 3, pp. 885-900, 2007.
- [47] H. V. Gupta, S. Sorooshian, and P. O. Yapo, "Status of automatic calibration for hydrologic models: comparison with multilevel expert calibration," *Journal of Hydrologic Engineering*, vol. 4, no. 2, pp. 135-143, 1999.
- [48] D. R. Legates and G. J. McCabe Jr., "Evaluating the use of "goodness-of-fit" measures in hydrologic and hydroclimatic model validation," *Water Resources Research*, vol. 35, no. 1, pp. 233-241, 1999.
- [49] J. E. Nash and J. V. Sutcliffe, "River flow forecasting through conceptual models part I—a discussion of principles," *Journal of Hydrology*, vol. 10, no. 3, pp. 282-290, 1970.
- [50] D. Jukić and V. Denić-Jukić, "Groundwater balance estimation in karst by using a conceptual rainfall-runoff model," *Journal of Hydrology*, vol. 373, no. 3-4, pp. 302-315, 2009.
- [51] H. Jourde, A. Roesch, V. Guinot, and V. Bailly-Comte, "Dynamics and contribution of karst groundwater to surface flow during Mediterranean flood," *Environmental Geology*, vol. 51, no. 5, pp. 725-730, 2007.
- [52] V. Bailly-Comte, H. Jourde, A. Roesch, and S. Pistre, "Mediterranean flash flood transfer through karstic area," *Environmental Geology*, vol. 54, no. 3, pp. 605-614, 2008.
- [53] V. Bailly-Comte, H. Jourde, and S. Pistre, "Conceptualization and classification of groundwater-surface water hydrodynamic interactions in karst watersheds: case of the karst watershed of the Coulazou River (Southern France)," *Journal of Hydrology*, vol. 376, no. 3-4, pp. 456-462, 2009.

## Research Article

# Detecting Runoff Variation of the Mainstream in Weihe River

**Qiang Huang and Jingjing Fan**

*Xi'an University of Technology, Xi'an 710048, China*

Correspondence should be addressed to Qiang Huang; [wresh@mail.xaut.edu.cn](mailto:wresh@mail.xaut.edu.cn)

Received 23 August 2013; Accepted 16 October 2013

Academic Editor: G. H. Huang

Copyright © 2013 Q. Huang and J. Fan. This is an open access article distributed under the Creative Commons Attribution License, which permits unrestricted use, distribution, and reproduction in any medium, provided the original work is properly cited.

The runoff change in Weihe River is significantly decreasing with the climate change and the huge increasing of human activities. The analysis of the variation changes of runoff would provide scientific understanding of Weihe River basin and similar basins. Mann-Kendall method is used to detect the variation changes of annual and seasonal runoff of 1919–2011 at the outlet station, that is, Huaxian station, in the mainstream of Weihe River. The results show that the runoff variation point is 1990, and there were significant changes in trends and periodicals, corroborated by wavelet variance analysis, Kendall's rank tests, and trends persistence test, in annual, seasonal, and monthly runoff at the variation point of 1990. Attribution analysis indicates that the primary drivers of the shift in runoff variation were human activities rather than climate change, as water consumption (particularly groundwater consumption) increased sharply in the 1990s.

## 1. Introduction

In recent decades, there are significantly changes in climate, such as temperature, precipitation, and hydrology as runoff, flood and drought. Runoff volumes in a catchment are influenced by numerous factors, like climatic variables (particularly precipitation), human activities, subsurface drainage patterns, and various other geographical and hydrological variables [1–3]. With the changing of the factors, runoff changes significantly. Many aspects of the Earth's climate system have changed abruptly and further variations are predicted [4, 5]. Runoff in catchments of various regions is changing [6]. Notably, the runoff is declining in catchments of the Haihe River [7], Yellow River [8], Liaohe River, and Yangtze River [9].

The sequential Mann-Kendall test is a statistical test that has been used (e.g., [1, 7]) in detecting variation changes in runoff volumes and many other variables. This test, initially developed by Mann [10] and modified by Kendall [11], is straightforward, robust, and can handle both missing values and values below detection limits [12–14]. It is recommended as a standard method for detecting variation changes in serially independent hydrological data [15, 16]. Using the Mann-Kendall method, Yang and Tian [7] found that variations in runoff in the Haihe River basin occurred in the period

of 1978–1985. Zhang et al. [17] found that the sediment and runoff in Yangtze River basin have a significant change in 1980s.

In this paper, the variation in Weihe River is analyzed using the sequential Mann-Kendall test method. It examines both seasonal and annual trends, using data obtained from the Huaxian hydrological station. A variation at around 1990 is then corroborated by wavelet variance analysis, which is used to detect changes in runoff periodicity [18–22], Kendall's rank test (a nonparametric method for detecting or testing trends), and rescaled range analysis (a nonlinear technique for evaluating the persistence of apparent trends), which are widely used in hydrology (e.g., [23–28]). Finally, we explore the probable causes of the shift in runoff by the analysis of attribution [29], focusing on the factors that contribute to reductions in precipitation and increases in human water consumption in the Weihe River catchment.

## 2. Methodology

The sequential Mann-Kendall test [10, 30] is used to detect variation changes in runoff (annual, seasonal, and monthly) from 1919 to 2011 at the Huaxian hydrological station. In this test, the null hypothesis is that a series of observations of a variable  $\tau_i$  (where  $i = 1, \dots, n$ ) are independent and

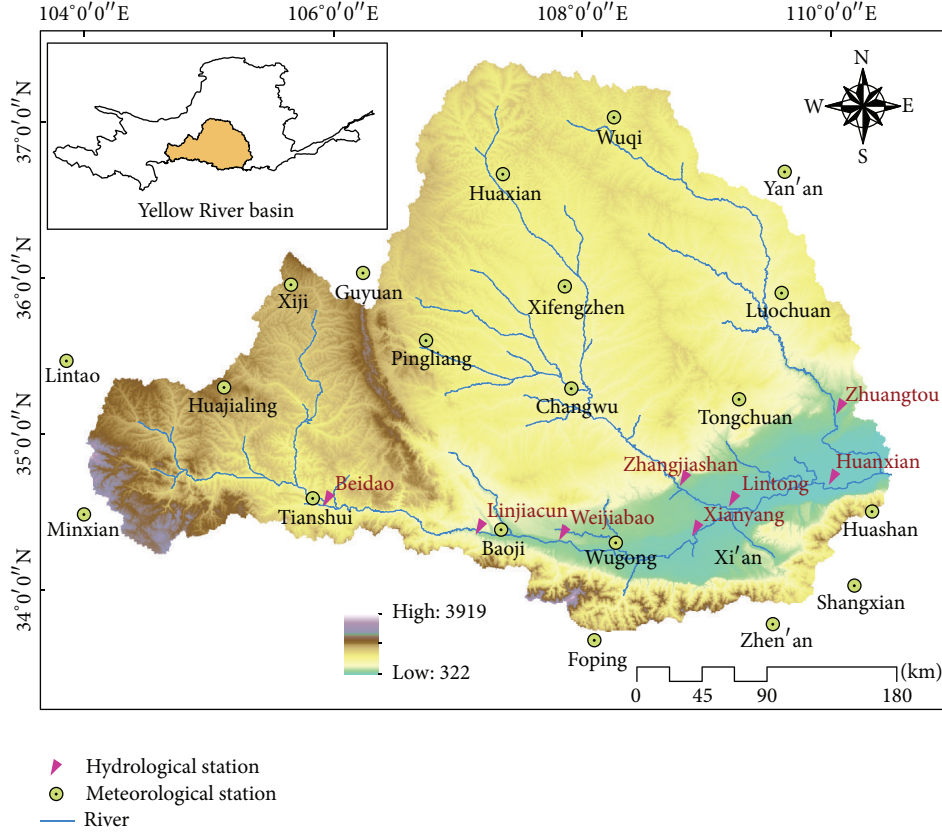


FIGURE 1: Map of the River Wei Basin.

identically distributed. The alternative hypothesis is that there is a monotonic trend in  $\tau_i$ . The Mann-Kendall test statistic,  $D_\tau$ , is calculated here using the following model:

$$D_\tau = \sum_{i=1}^{\tau} R_i \quad (\tau = 2, 3, \dots, i), \quad (1)$$

where

$$R_i = \begin{cases} +1, & x_i > x_j \\ 0, & x_i \leq x_j \end{cases} \quad (j = 1, 2, \dots, i) \quad (2)$$

$R_i$  is normally distributed with a mean and variance given by (3) and (4), respectively:

$$E(D_\tau) = \frac{\tau(\tau-1)}{4}, \quad (3)$$

$$V(D_\tau) = \frac{\tau(\tau-1)(2\tau+5)}{72}. \quad (4)$$

Sequential values of a statistic,  $UF_\tau$  (for which  $UF_1 = 0$ ), are now calculated from

$$UF_\tau = \frac{|D_\tau - E(D_\tau)|}{\sqrt{V(D_\tau)}}. \quad (5)$$

The data series is then reversed, and values corresponding to  $UF_\tau$  ( $UB_\tau = -UF_\tau$ ;  $\tau = n, n-1, \dots, 1$  and  $UB_1 = 0$ ) are calculated.

If the two sequences are accepted at a defined probability level,  $\alpha$ , then  $|UF_\tau| < UF_{1-\alpha/2}$ , where  $UF_{1-\alpha/2}$  is the critical value of a standard normal distribution for a probability exceeding  $\alpha/2$ .

A positive  $UF_\tau$  or  $UB_\tau$  value indicates an upward trend, and negative values indicate a downward trend in variable  $\tau$  with time. Further, if  $UF_\tau$  or  $UB_\tau > UF_{1-\alpha/2}$  there is a significant upward trend, while  $UF_\tau$  or  $UB_\tau < UF_{1-\alpha/2}$  indicates a significant downward trend.

In this study,  $\alpha$  is set at  $P < 0.05$ . The sequential Mann-Kendall test enables detection of the approximate time of changes in trends from intersections of the forward and backward curves of the test statistic. If the intersection point is significant at  $\alpha = 0.05$ , then the critical point of change is at that point [31]. Hence, the Mann-Kendall test provides an efficient method for pinpointing the starting times of trends [7].

### 3. Study Area and Data

**3.1. Study Area.** The Weihe River rises in the Niaoshu hill, in Gansu province, and flows into the Yellow River in Shaanxi province. Its catchment covers 132 million  $\text{km}^2$  ( $107^\circ 39' - 108^\circ 37' \text{ E}$  to  $33^\circ 42' - 34^\circ 14' \text{ N}$ ; Figure 1), and the mean annual streamflow amounted to 7.53 billion  $\text{m}^3$  (equivalent to an annual runoff depth of 572 mm/year) from 1951 to 2011. Huaxian station ( $34^\circ 35' \text{ E}$ ,  $109^\circ 42' \text{ N}$ ) is an important hydrological

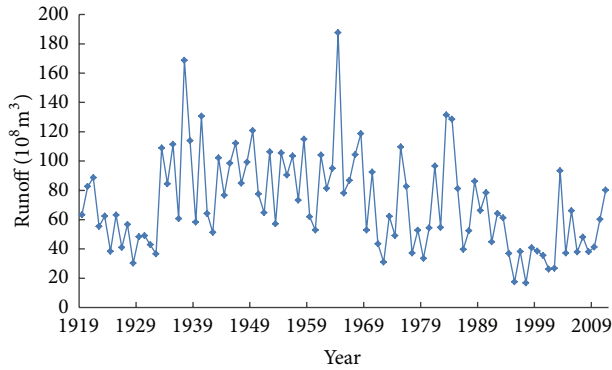


FIGURE 2: Annual runoff volumes in the Weihe River at the Huaxian hydrological station from 1919 to 2011.

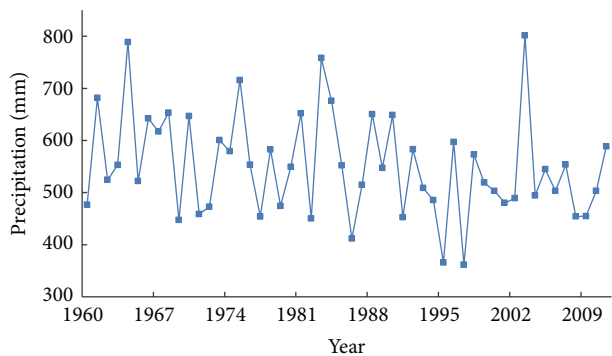


FIGURE 3: Estimated annual precipitation in the Weihe River basin from 1956 to 2011.

station, which monitors the flow from 105.3 million  $\text{km}^2$  of the catchment, that is, 81% of the total Weihe River basin area. It was established in 1919 and is the closest station to the confluence with the Yellow River. Mean annual streamflow is approximately 7.14 billion  $\text{m}^3$  from 1951 to 2011, and mean annual precipitation is 512 mm. However, the streamflow is distinctly seasonal and substantially higher in the period from July to October than in the following period from November to June of the next year.

**3.2. Data.** Monthly mainstream runoff data collected at Huaxian hydrological station from January 1919 to December 2011 (Figure 2) were obtained from the records. Monthly precipitation data from January 1956 to December 2011, collected from 18 monitoring stations in the Weihe River basin, were obtained from the Chinese meteorological data sharing system. Locations of the Huaxian hydrological station and rain gauging stations are shown in Figure 1 and Table 1. The annual areal precipitation of Weihe River basin (Figure 3) was calculated from the area-weighted monthly precipitation data collected at the 18 rain gauging stations.

## 4. Results and Discussion

**4.1. Annual Runoff Test.** The sequential Mann-Kendall test is used to diagnose the variations in annual, seasonal, and

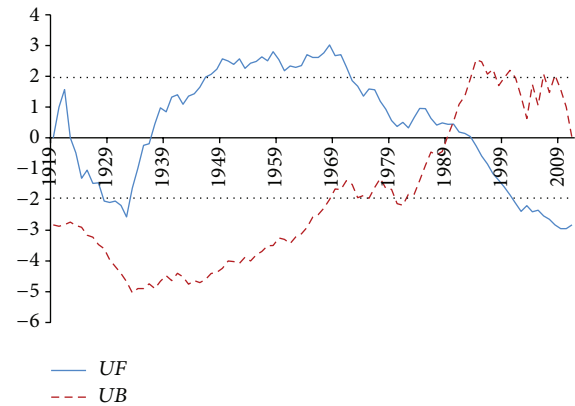


FIGURE 4: Mann-Kendall test statistics ( $UF$  and  $UB$  values) calculated from annual runoff data at the Huaxian station.

monthly runoff data obtained from the Huaxian station for the sequence from 1919 to 2011. Values of  $UF$  and  $UB$  sequence calculated from the annual runoff data show that runoff in the Weihe River basin significantly declined during the study period. The point of intersection of the  $UF$  and  $UB$  curves indicates that the variation of annual runoff began in 1990 (Figure 4), that of spring runoff (1 March–31 May) began in 1999, that of summer runoff (1 June–31 August) began in 1990, that of autumn runoff (1 September–31 November) began in 1989, that of winter runoff (1 December–28 January) began in 1977, that of wet season runoff (1 July–31 October) began in 1990, and that of dry season runoff (without wet season in a year) began in 1991 (Figure 5). Figures 4 and 5 show that annual runoff trend is similar to autumn wet and dry season. So, according to the results, 1990 is chosen as variation of the whole catchment. The result is similar to that of the previous study in the same area. Bai and Zhang [32] found that there are variation points in 1990s by using the rank sum test.

### 4.2. Basic Law Changes at Variation Point

**4.2.1. Mean Changes.** Aiming to verify the variation changes, mean change is an important factor. As the sequential Mann-Kendall test results show, 1990 is the year of the variation beginning time, so 1990 is chosen as a demarcation point. The sequence was divided into two parts, one is the former (1919–1989) and another is the latter (1990–2011). The identified time of the variation in the annual runoff is verified by a marked difference in mean values in the periods before and after it, which amounted to 8.74 billion  $\text{m}^3$  before 1990 and 4.67 billion  $\text{m}^3$  from 1990 to 2011, a decrease of 41%.

In order to analyze the seasonal variation changes in runoff in more detail, the time series can be divided into five periods: 1919–1969 (selected as a baseline), 1970–1979, 1980–1989, 1990–1999, and 2000–2011. Runoff values for each month during each of the periods are shown in Table 2. The data clearly show that the flow declined relative to the baseline period in all subsequent periods, particularly in 1990–1999 and 2000–2011, when the runoff volumes were lower than 50% compared to the baseline volumes in seven months.

TABLE 1: Locations of the 18 rain gauging stations that provided the precipitation data examined in this study.

Station no.	Station name	Province	Latitude (N)	Longitude (E)	Elevation (m)
52986	Lintao	Gansu	35/21	103/51	1893.8
52996	Huajialing	Gansu	35/23	105/00	2450.6
53817	Guyuan	Ningxia	36/00	106/16	1753.0
53821	Huanxian	Gansu	36/35	107/18	1255.6
53903	Xiji	Ningxia	35/58	105/43	1916.5
53915	Pingliang	Gansu	35/33	106/40	1346.6
53923	Xifengzhen	Gansu	35/44	107/38	1421.0
53929	Changwu	Shaanxi	35/12	107/48	1206.5
53947	Tongchuan	Shaanxi	35/05	109/04	978.9
56093	Minxian	Gansu	34/26	104/01	2315.0
57006	Tianshui	Gansu	34/35	105/45	1141.7
57016	Baoji	Shaanxi	34/21	107/08	612.4
57034	Wugong	Shaanxi	34/15	108/13	447.8
57036	Xi'an	Shaanxi	34/18	108/56	397.5
57046	Huashan	Shaanxi	34/29	110/05	2064.9
57134	Foping	Shaanxi	33/31	107/59	827.2
57144	Zhen'an	Shaanxi	33/26	109/09	693.7
57143	Shangzhou	Shaanxi	33/52	109/58	742.2

TABLE 2: Monthly runoff volumes during the five subperiods ( $10^8 \text{ m}^3$ ) and changes relative to baseline (1919–1969) values.

Year	1919–1969				1970–1979			1980–1989			1990–1999			2000–2011		
	Mean	Mean	Mean change	Percent change	Mean	Mean change	Percent change	Mean	Mean change	Percent change	Mean/ $10^8 \text{ m}^3/\text{s}$	Mean change	Percent change			
January	2.36	1.21	-1.16	-48.9%	1.52	-0.85	-35.8%	1.06	-1.30	-55.1%	<b>1.54</b>	-0.82	-34.8%			
February	2.37	1.39	-0.97	-41.1%	1.61	-0.76	-32.0%	1.18	-1.19	-50.2%	<b>1.37</b>	-1.00	-42.3%			
March	3.28	1.78	-1.50	-45.8%	2.04	-1.23	-37.6%	2.07	-1.21	-36.9%	<b>1.50</b>	-1.77	-54.1%			
April	4.53	3.17	-1.36	-29.9%	3.62	-0.91	-20.1%	3.32	-1.21	-26.8%	<b>1.79</b>	-2.74	-60.6%			
May	5.66	5.26	-0.40	-7.0%	5.86	0.20	3.6%	4.12	-1.54	-27.1%	<b>2.39</b>	-3.26	-57.7%			
June	5.09	2.38	-2.71	-53.2%	6.25	1.16	22.9%	4.05	-1.04	-20.4%	<b>2.33</b>	-2.76	-54.2%			
July	12.17	7.21	-4.95	-40.7%	11.58	-0.58	-4.8%	7.57	-4.59	-37.7%	<b>4.11</b>	-8.06	-66.3%			
August	13.74	7.37	-6.37	-46.3%	13.11	-0.63	-4.6%	6.64	-7.09	-51.6%	<b>7.10</b>	-6.63	-48.3%			
September	14.15	12.73	-1.42	-10.0%	15.89	1.73	12.3%	5.36	-8.79	-62.1%	<b>10.58</b>	-3.57	-25.3%			
October	10.73	10.65	-0.08	-0.7%	10.67	-0.06	-0.6%	4.63	-6.11	-56.9%	<b>10.17</b>	-0.57	-5.3%			
November	5.62	4.69	-0.93	-16.6%	5.14	-0.48	-8.5%	2.77	-2.85	-50.6%	<b>4.12</b>	-1.50	-26.6%			
December	3.10	1.63	-1.47	-47.5%	1.87	-1.23	-39.6%	1.01	-2.09	-67.3%	<b>2.23</b>	-0.87	-28.0%			

The most pronounced decline was during July in the most recent period (2000–2011), when the mean runoff volume was just 0.411 billion  $\text{m}^3$ , compared to the baseline volume of 1.217 billion  $\text{m}^3$ , a drop of 66.3%. In the second period (1970–1979), there is only one percent volumes above 50%, and 6 are before 40%, the high percent shows that it has an obviously change in the period. The main reason for the significant decline of runoff volumes is that there is a huge numbers of human activities happened in the periods. These findings confirm that the runoff variation changed substantially in the 1990s.

**4.2.2. Periodicity Changes.** Wavelet variance analysis is one of several methods based on wavelet functions that have been

developed and applied to detect changes in the periodicity of cycles of the data collected from hydrological system [18–22]. Application of this method, using equations presented by, clearly show that there were substantial reductions in annual runoff, the periodicity of two sequences. One is before variation point (1919–1989), and the other is after (1919–2011). Figure 6 shows that the before sequence has 18 and 37 years period and the after sequence has 7, 17, and 45 years. Because of the dramatically change after variation, the total has a short period. These results further corroborate the variation in runoff trends detected at around 1990.

**4.2.3. Trends and Persistence Changes.** As mentioned in the introduction, Kendall's rank test is a nonparametric method

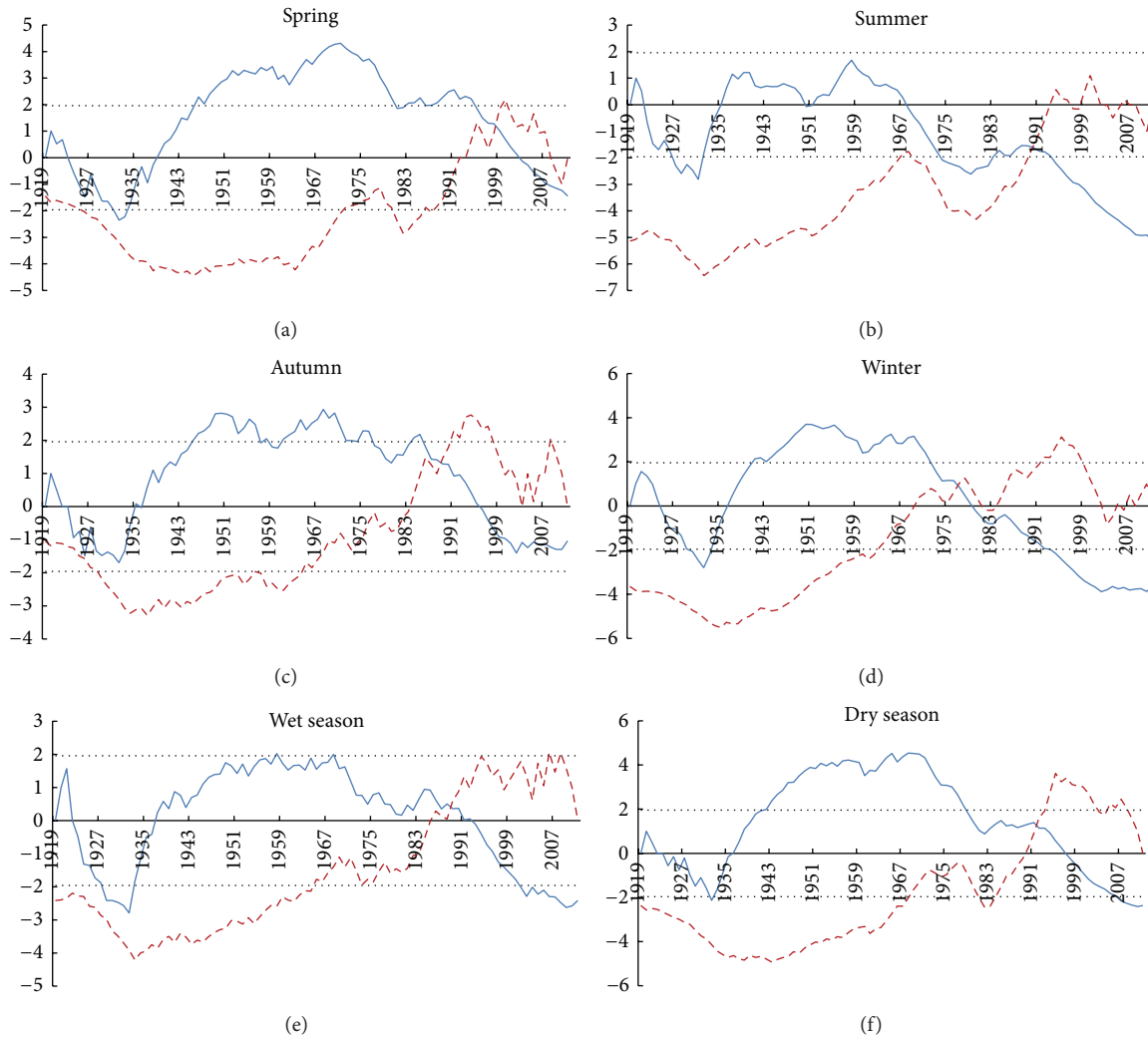


FIGURE 5: Mann-Kendall test statistics ( $UF$  and  $UB$  values) calculated from seasonal runoff data at the Huaxian station.

for detecting or testing trends, and rescaled range analysis is a nonlinear technique for evaluating the persistence of apparent trends, both of which are widely used in hydrology (e.g., [23–28]). Application of Kendall’s rank test to explore further the trend changes clearly shows that there was a highly significant ( $P < 0.001$ ) decline in runoff during the entire study period from 1919 to 2011, although there was a slight (nonsignificant) increase in the years before 1989 (Table 3). Furthermore, Hurst values [23], obtained from rescaled range analysis ( $R/S$ ), for the former series 1919–1989, have a slight (nonsignificant) increase, and positive persistence. Because of the dramatical change after the variation, the total trend is decline, but after the variation is increase. They all have positive persistence, but the total one is smaller.

**4.2.4. Hydrological Parameters Changes.** Key parameters for assessing changes in river runoff are the coefficient of variation ( $C_v$ ) and skewness ( $C_s$ ). Changes in these hydrological parameters during the study period are shown in Table 4. The data show that  $C_v$  slightly increased from 0.405 to 0.456

TABLE 3: Results of runoff trend and persistence tests of 1919–1989 and 1990–2011 (throughout the study period).

	1919–1989	1919–2011
Trends	0.442 Insignificantly upward	-2.828 Significantly downward
Persistence	0.978 Positive	0.762 Positive

TABLE 4: Coefficients of variation ( $C_v$ ) and skewness ( $C_s$ ) of annual runoff volumes of 1919–1989, 1919–2011 (the whole study period).

	1919–1989	1919–2011
$C_v$	0.405	0.456
$C_s$	0.802	0.841

between 1919–1989 and 1919–2011, while  $C_s$  significantly fell from 0.802 to 0.841, further corroborating the significant variation change that occurred around 1990.

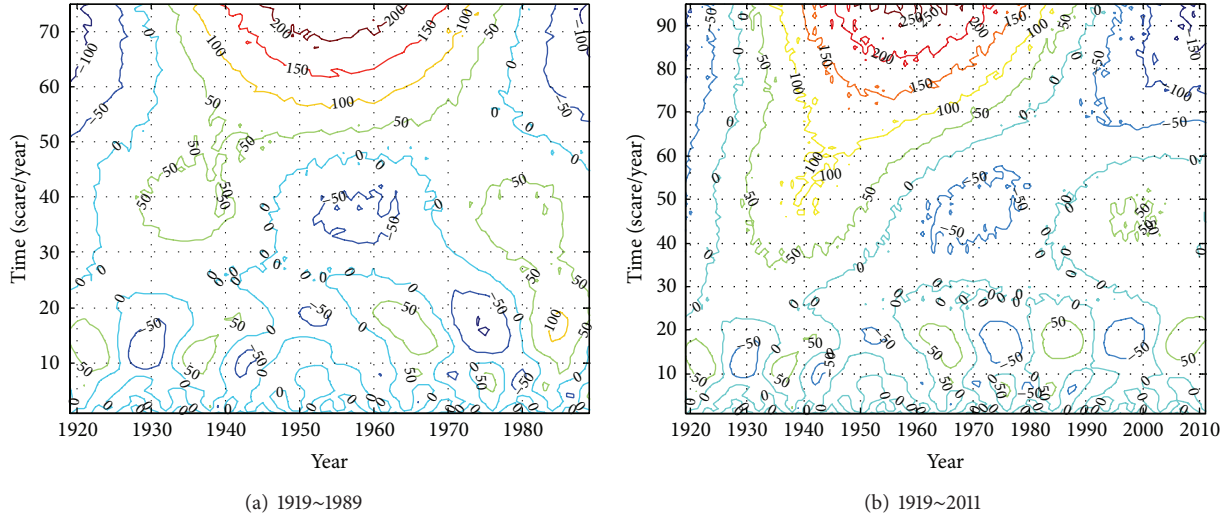


FIGURE 6: Results of the wavelet variance analysis for runoff periodicity in 1919–1989 and 1919–2011.

TABLE 5: Changes in mean precipitation (mm) and runoff ( $10^8 \text{ m}^3$ ) in the five periods from 1956 to 2011.

Period	Mean precipitation	Mean change	Percent change	Mean runoff / ( $10^8 \text{ m}^3/\text{s}$ )	Mean change	Percent change	Specific value / $10^8 \text{ m}^3$	Rate changes
1956–1969	594.48			93.95				
1970–1979	553.8	-40.67	-6.80%	59.41	-40.67	-43.30%	6.33	
1980–1989	576.09	-18.39	-3.10%	79.15	-14.8	-15.80%	5.09	0.19
1990–1999	509.46	-85.02	-14.30%	43.73	-50.22	-53.50%	3.74	0.41
2000–2011	530.83	-63.65	-10.70%	49.23	-44.72	-47.60%	4.45	0.3

TABLE 6: Changes in mean precipitation (mm) and runoff ( $10^8 \text{ m}^3$ ) from 1956–1989 to 1990–2011.

Period	Mean precipitation	Mean change	Percent change	Mean runoff	Specific value / $10^8 \text{ m}^3$	Rate of migration
1956–1989	506.02			69.04		
1990–2011	521.11	15.10	3.0%	46.73	-22.31	-32.3%

4.3. Attribution Analysis. In recent years, there are a lot of studies focusing on the driving factors in hydrological research [33–36]. Climate change and human activities are considered as the main factors driving runoff decline in most of river basins [6, 7]. In order to evaluate the contribution of these drivers to the changes in runoff in the Weihe River during the study period, the time series is divided into five periods 1956–1969 (baseline), 1970–1979, 1980–1989, 1990–1999, and 2000–2011.

(1) Contributions of Precipitation. Climate change has an important impact on runoff change [37, 38]. To assess the contribution of precipitation to the shift in runoff trends, changes of precipitation from baseline (1956–1969) values during subsequent periods are compared to changes of runoff (Table 5). There was a marked decline in both runoff at the Huaxian station and precipitation in the Weihe River basin. However, the relationships differ that precipitation was 6.80%, 3.10%, 14.30%, and 10.70% lower in the following

periods, while the falls in runoff were 43.30%, 15.80%, 53.50%, and 47.60%, respectively.

The precipitation and runoff values for the periods before and after the identified variation of 1990 are presented in Table 6. Precipitation in the catchment at the Huaxian station slightly increased, by 3.0%, in the latter period, but runoff volumes fell by 32.3%, confirming the substantial divergence between changes in precipitation and runoff before and after 1990.

(2) Human Water Consumption. Human water consumption in the Weihe River basin significantly increased in the 1990s, especially industrial and domestic water consumption, with rapid increases in groundwater consumption [39]. Total annual consumption increased by 56% from 2.793 billion  $\text{m}^3$  (2,383 million  $\text{m}^3$  of surface water and 410 million  $\text{m}^3$  of groundwater) before 1990s to 4.263 billion  $\text{m}^3$  (2.05 billion  $\text{m}^3$  of surface water and 2.213 billion  $\text{m}^3$  of groundwater) after 1990s. The increase in water consumption, mainly due

to a massive rise in exploitation of groundwater, closely correlates with the decrease in runoff carried by the Weihe River (Table 6). Soil and water conservation have an obviously increased, the mean annual runoff have an significantly increased, which is from 116 million  $m^3$  (before 10 1990s) upto 300 million  $m^3$  (after 1990s). The results clearly indicate that the decline in runoff in the Weihe River basin has been largely driven by human activities rather than climate change, as Yang and Tian [7] found in the Haihe River catchment.

## 5. Conclusion

The results obtained by applying the sequential Mann-Kendall test to a long series of runoff data (1919–2011) collected at the Huaxian station in the Weihe River in the Loess Plateau show that variations occurred in annual, seasonal, and monthly runoff volumes around 1990. This finding is strongly corroborated by the results of wavelet variance analysis, Kendall's rank tests, trend persistence tests, and shifts in skewness coefficients. Attribution analysis indicates that the primary drivers of the shift in runoff volumes were human activities rather than climate change, because water consumption increased sharply in the 1990s but not precipitation.

## Acknowledgments

This work was financially supported by the Natural Science Foundation of China (nos. 51190093, 51179148, 51179149), National Key Basic Research 973 of China (no. 2012CB417003), Governmental Public Industry Research Special Funds for Projects (no. 201101043), and Program for New Century Excellent Talents in University. Constructive comments from reviewers are gratefully acknowledged.

## References

- [1] S. Kumar, V. Merwade, J. Kam, and K. Thurner, "Streamflow trends in Indiana: effects of long term persistence, precipitation and subsurface drains," *Journal of Hydrology*, vol. 374, no. 1-2, pp. 171–183, 2009.
- [2] X. Wang, "Editorial: environmental informatics for environmental planning and management," *Journal of Environmental Informatics*, vol. 9, no. 1, pp. 1–3, 2007.
- [3] B. Chen, "Climate change and pesticide loss in watershed systems: a simulation modeling study," *Journal of Environmental Informatics*, vol. 10, no. 2, pp. 55–67, 2007.
- [4] X. S. Qin, G. H. Huang, A. Chakma, X. H. Nie, and Q. G. Lin, "A MCDM-based expert system for climate-change impact assessment and adaptation planning—a case study for the Georgia Basin, Canada," *Expert Systems with Applications*, vol. 34, no. 3, pp. 2164–2179, 2008.
- [5] B. Luo, I. Maqsood, Y. Y. Yin et al., "Adaption to climate change through water trading under uncertainty—an inexact two-stage nonlinear programming approach," *Journal of Environmental Informatics*, vol. 2, no. 2, pp. 58–68, 2003.
- [6] C. J. Vörösmarty, P. Green, J. Salisbury, and R. B. Lammers, "Global water resources: vulnerability from climate change and population growth," *Science*, vol. 289, no. 5477, pp. 284–288, 2000.
- [7] Y. Yang and F. Tian, "Abrupt change of runoff and its major driving factors in Haihe River Catchment, China," *Journal of Hydrology*, vol. 374, no. 3-4, pp. 373–383, 2009.
- [8] G. Fu, S. Chen, C. Liu, and D. Shepard, "Hydro-climatic trends of the yellow river basin for the last 50 years," *Climatic Change*, vol. 65, no. 1-2, pp. 149–178, 2004.
- [9] Z. Chen, J. Li, H. Shen, and W. Zhanghua, "Yangtze River of China: historical analysis of discharge variability and sediment flux," *Geomorphology*, vol. 41, no. 2, pp. 77–91, 2001.
- [10] H. B. Mann, "Nonparametric tests against trend," *Econometrica*, vol. 13, no. 3, pp. 245–259, 1945.
- [11] M. G. Kendall, *Rank Correlation Methods* Griffin, London, 1975.
- [12] Q. Zhang, C.-Y. Xu, Z. Zhang, Y. D. Chen, C.-L. Liu, and H. Lin, "Spatial and temporal variability of precipitation maxima during 1960–2005 in the Yangtze River basin and possible association with large-scale circulation," *Journal of Hydrology*, vol. 353, no. 3-4, pp. 215–227, 2008.
- [13] M. Sulkava, S. Luyssaert, P. Rautio, I. A. Janssens, and J. Hollmén, "Modeling the effects of varying data quality on trend detection in environmental monitoring," *Ecological Informatics*, vol. 2, no. 2, pp. 167–176, 2007.
- [14] J. Fan, Q. Huang, J. Chang et al., "Detecting abrupt change of streamflow at lintong station of wei river," *Mathematical Problems in Engineering*, vol. 2013, Article ID 976591, 9 pages, 2013.
- [15] W. Fengying, *Modern Technology of Statistics, Diagnosis and Forecast For Climate*, Meteorological Press, Beijing, China, 2007, Chinese.
- [16] K. H. Hamed and A. Ramachandra Rao, "A modified Mann-Kendall trend test for autocorrelated data," *Journal of Hydrology*, vol. 204, no. 1–4, pp. 182–196, 1998.
- [17] Q. Zhang, C. Xu, S. Becker et al., "Sediment and runoff changes in the Yangtze River basin during past 50 years," *Journal of Hydrology*, vol. 331, no. 3, pp. 511–523, 2006.
- [18] A. W. Galli, G. T. Heydt, and P. F. Ribeiro, "Exploring the power of wavelet analysis," *IEEE Computer Applications in Power*, vol. 9, no. 4, pp. 37–41, 1996.
- [19] S. Santoso, E. J. Powers, W. M. Grady, and P. Hofmann, "Power quality assessment via wavelet transform analysis," *IEEE Transactions on Power Delivery*, vol. 11, no. 2, pp. 924–930, 1996.
- [20] P. Pillaya Bhattacharjee, "Application of wavelets to model short-term power system disturbances," *IEEE Transactions on Power Systems*, vol. 11, no. 4, pp. 2031–2037, 1996.
- [21] W. A. Wilkinson and M. D. Cox, "Discrete wavelet analysis of power system transients," *IEEE Transactions on Power Systems*, vol. 11, no. 4, pp. 2038–2044, 1996.
- [22] P. F. Ribeiro, "Wavelet transform: an advanced tool for analyzing non-stationary harmonic distortions in power systems," in *Proceedings IEEE International Conference on Harmonics in Power Systems (ICHPS '94)*, 1994.
- [23] R. M. Hirsch, J. R. Slack, and R. A. Smith, "Techniques of trend analysis for monthly water quality data," *Water Resources Research*, vol. 18, no. 1, pp. 107–121, 1982.
- [24] R. M. Hirsch and J. R. Slack, "A nonparametric trend test for seasonal data with serial dependence," *Water Resources Research*, vol. 20, no. 6, pp. 727–732, 1984.
- [25] R. M. Hirsch, R. B. Alexander, and R. A. Smith, "Selection of methods for the detection and estimation of trends in water quality," *Water Resources Research*, vol. 27, no. 5, pp. 803–813, 1991.

- [26] D. P. Lettenmaier, "Detection of trends in water quality data from records with dependent observations," *Water Resources Research*, vol. 12, no. 5, pp. 1037–1046, 1976.
- [27] D. P. Lettenmaier, E. R. Hooper, C. Wagoner, and K. B. Faris, "Trends in stream quality in the continental United States, 1978–1987," *Water Resources Research*, vol. 27, no. 3, pp. 327–339, 1991.
- [28] J. Armengol, S. Sabater, A. Vidal et al., "Using the rescaled range analysis for the study of hydrological records: the river Ter as an example," *Oecologia Aquatica*, vol. 10, no. 10, pp. 21–34, 2012.
- [29] P. A. Stott, N. P. Gillett, G. C. Hegerl et al., "Detection and attribution of climate change: a regional perspective," *Wiley Interdisciplinary Reviews: Climate Change*, vol. 1, no. 2, pp. 192–211, 2010.
- [30] R. Sneyers, *Sur L'analyse Statistique Des Series D'observations*, Tech. Note, Geneva, Switzerland, 1975.
- [31] F.-W. Gerstengarbe and P. C. Werner, "Estimation of the beginning and end of recurrent events within a climate regime," *Climate Research*, vol. 11, no. 2, pp. 97–107, 1999.
- [32] C. Bai and S. Zhang, "Detection of the variation points of Weihe River watershed runoff process based on rank sum," *Journal of Northwest A&F University*, vol. 37, no. 10, pp. 215–220, 2009.
- [33] N. W. Arnell, "Climate change and global water resources," *Global Environmental Change*, vol. 9, pp. S31–S49, 1999.
- [34] D. Labat, Y. Godd ris, J. L. Probst, and J. L. Guyot, "Evidence for global runoff increase related to climate warming," *Advances in Water Resources*, vol. 27, no. 6, pp. 631–642, 2004.
- [35] C. d. Fraiture, "Integrated water and food analysis at the global and basin level. An application of WATERSIM," *Water Resources Management*, vol. 21, no. 1, pp. 185–198, 2007.
- [36] M. I. Hejazi and G. E. Moglen, "Regression-based approach to low prediction in the Maryland Piedmont region under joint climate and land use change," *Hydrological Processes*, vol. 21, no. 14, pp. 1793–1801, 2007.
- [37] V. K. Arora, "The use of the aridity index to assess climate change effect on annual runoff," *Journal of Hydrology*, vol. 265, no. 1–4, pp. 164–177, 2002.
- [38] C. M. Liu and J. Xia, *Global Water System Project*, 2004.
- [39] X. L. Su, S. Z. Kang, X. M. Wei et al., "Impact of climate change and human activity on the runoff of Wei River basin to the Yellow River," *Journal of Northwest A & F University*, vol. 2, p. 32, 2007.

## Research Article

# Uncertainty Analysis of Multiple Hydrologic Models Using the Bayesian Model Averaging Method

Leihua Dong,<sup>1,2</sup> Lihua Xiong,<sup>1</sup> and Kun-xia Yu<sup>1</sup>

<sup>1</sup> State Key Laboratory of Water Resources and Hydropower Engineering Science, Wuhan University, Wuhan 430072, China

<sup>2</sup> National Research Center for Sustainable Hydropower Development, China Institute of Water Resources and Hydropower Research, Beijing 100038, China

Correspondence should be addressed to Lihua Xiong; [xionglh@whu.edu.cn](mailto:xionglh@whu.edu.cn)

Received 30 August 2013; Accepted 6 November 2013

Academic Editor: Y. P. Li

Copyright © 2013 Leihua Dong et al. This is an open access article distributed under the Creative Commons Attribution License, which permits unrestricted use, distribution, and reproduction in any medium, provided the original work is properly cited.

Since Bayesian Model Averaging (BMA) method can combine the forecasts of different models together to generate a new one which is expected to be better than any individual model's forecast, it has been widely used in hydrology for ensemble hydrologic prediction. Previous studies of the BMA mostly focused on the comparison of the BMA mean prediction with each individual model's prediction. As BMA has the ability to provide a statistical distribution of the quantity to be forecasted, the research focus in this study is shifted onto the comparison of the prediction uncertainty interval generated by BMA with that of each individual model under two different BMA combination schemes. In the first BMA scheme, three models under the same Nash-Sutcliffe efficiency objective function are, respectively, calibrated, thus providing three-member predictions ensemble for the BMA combination. In the second BMA scheme, all three models are, respectively, calibrated under three different objective functions other than Nash-Sutcliffe efficiency to obtain nine-member predictions ensemble. Finally, the model efficiency and the uncertainty intervals of each individual model and two BMA combination schemes are assessed and compared.

## 1. Introduction

To date, various hydrological models have been put forward and widely used in flood forecasting, planning, and water resources management [1, 2]. Since different models have strengths in capturing different aspects of the real world processes, combining the results from diverse models by weighting procedures can present a better performance than any individual model [3–5]. The early model combination researches in hydrologic forecasting employed such tools as neural network [6] and fuzzy system [7]. Recently, Bayesian Model Averaging (BMA), a method for averaging over different competing models, has been introduced to ensemble hydrologic predictions.

Bayesian Model Averaging came to prominence in statistics in the mid-1990s, and Madigan and Raftery [8] were the first to propose this method for combining predictions. Subsequently, Raftery [9] and Draper [10] gave more detailed discussion about BMA. It has been applied in diverse fields

such as economics [11], biology [12], ecology [13], public health [14], toxicology [15], meteorology [16], and management science [17]. In many case studies, BMA produces accurate and reliable predictions and was shown to be a better scheme than other model-combining methods [18–20]. In recent years, hydrologists have also applied BMA to hydrologic modeling, such as groundwater [21] and rainfall-runoff modeling [22–24].

A prediction from a single model has been recognized to be associated with a certain degree of uncertainty, and so is the prediction from combining a number of different single models. Thus, uncertainty analysis is an indispensable element for any hydrologic modeling study. The uncertainty usually arises from errors during the calibration of parameters, the design of model structure, and measurements of input and output data [25, 26]. To account for these uncertainties, many uncertainty analysis techniques have been developed and applied to diverse catchments, such as Generalized Likelihood Uncertainty Estimation (GLUE),

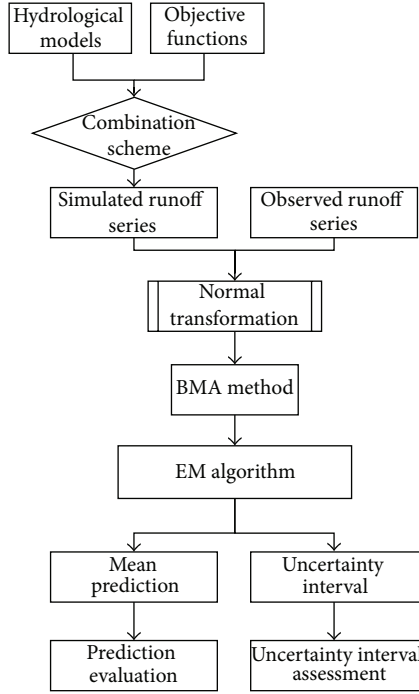


FIGURE 1: Flowchart of using BMA scheme for hydrological ensemble prediction as well as for prediction uncertainty analysis.

Parameter Solution (ParaSol), and Bayesian inference based on Markov chain Monte Carlo (MCMC) [27, 28]. Each of those techniques has its own advantage in uncertainty analysis. In the uncertainty analysis of BMA scheme, the composition of Monte Carlo method [29] is used to generate BMA probabilistic ensemble predictions, and then the 90% uncertainty intervals can be derived within the range of the 5% and 95% quantiles.

Previous studies of BMA in hydrology mostly focused on the comparison of the BMA mean prediction with each individual model's prediction, to prove the better performance of the prediction after weighted averaging. As BMA also has the ability to provide a statistical distribution of the quantity to be forecasted, the research focus in this study is shifted onto the comparison of the prediction uncertainty interval generated by the BMA with that of each individual model, in order to see if BMA can also improve the prediction reliability. The technical route of the research in this paper is described in Figure 1. Another purpose of this paper is that by calibrating different hydrological models under different objective functions, each of which has distinctive advantages in better modeling certain flow ranges, we can construct different sets of ensemble members for combination in order to fully explore the superiority of BMA. Therefore, two kinds of BMA combination schemes are designed, analyzed, and compared. In the first BMA scheme, we calibrate each of the three models under the same Nash-Sutcliffe efficiency objective function, thus providing three-member predictions ensemble for the BMA combination. In the second BMA scheme, three different objective functions other than

Nash-Sutcliffe efficiency are adopted, each of which is supposed to have some advantage of better simulating a certain range of flows (low flow, medium flow, and high flow). All three models are, respectively, calibrated for each of three objective functions to obtain the optimized parameter sets.

## 2. Methods

**2.1. Bayesian Model Averaging.** Bayesian Model Averaging (BMA) is a statistical technique designed to infer a prediction by weighted averaging over many different competing models. This method is not only a scheme for model combination but also a coherent approach for accounting for between-model and within-model uncertainty [22]. Below is a brief description of the basic ideas of this method.

Let us consider a quantity  $Q$  to be predicted on the basis of input data  $D = [X, Y]$  ( $X$  denotes the input forcing data, and  $Y$  stands for the observational flow data).  $f = [f_1, f_2, \dots, f_K]$  is the ensemble of the  $K$ -member predictions. The probabilistic prediction of BMA is given by

$$p(Q | D) = \sum_{k=1}^K p(f_k | D) \cdot p_k(Q | f_k, D). \quad (1)$$

The terms in (1) are explained as follows.  $p(f_k | D)$  is the posterior probability of the prediction  $f_k$  given the input data  $D$  and reflects how well model  $f_k$  fits  $Y$ . Actually  $p(f_k | D)$  is just the BMA weight  $w_k$ , and better performing predictions receive higher weights than the worse performing ones; all weights are positive and should add up to 1.  $p_k(Q | f_k, D)$  is the conditional probability density function (PDF) of the predictand  $Q$  conditional on  $f_k$  and  $D$ . For computation convenience,  $p_k(Q | f_k, D)$  is always assumed to be a normal PDF and is represented as  $g(Q | f_k, \sigma_k^2) \sim N(f_k, \sigma_k^2)$ , where  $\sigma_k^2$  is the variance associated with model prediction  $f_k$  and observations  $Y$ . In order to make this assumption valid, some techniques such as Box-Cox transformation are needed to make the data approximately normally distributed and to narrow the data range.

The BMA mean prediction is a weighted average of the individual model's predictions, with their posterior probabilities being the weights. In the case that the observations and individual model predictions are all normally distributed, the BMA mean prediction can be expressed as

$$E[Q | D] = \sum_{k=1}^K p(f_k | D) \cdot E[g(Q | f_k, \sigma_k^2)] = \sum_{k=1}^K w_k f_k. \quad (2)$$

**2.2. EM Algorithm for BMA Parameter Estimation.** To estimate BMA weight  $w_k$  and model prediction variance  $\sigma_k^2$ , the Expectation-Maximization (EM) algorithm, which has proved to be an efficient technique for BMA calculation based on the assumption that  $K$ -member predictions are normally distributed, is described in this section [23].

Firstly, if we denote the set of BMA parameters to be estimated by  $\theta = \{w_k, \sigma_k^2, k = 1, 2, \dots, K\}$ , the log form of likelihood function can be represented as

$$l(\theta) = \log(p(Q | D)) = \log\left(\sum_{k=1}^K w_k \cdot g(Q | f_k, \sigma_k^2)\right). \quad (3)$$

It is difficult to maximize the function (3) by analytical method. The EM algorithm is a method for finding the maximum likelihood by alternating between two steps, the expectation step and maximization step. The two steps are iterated to convergence when there is no significant change between two consecutive iterative log-likelihood estimations. In EM algorithm, a latent variable (unobserved quantity)  $z_k^t$  is used as an assistant for estimating BMA weight  $w_k$ . The procedure of EM algorithm for BMA scheme is described as follows.

- (1) *Initialization.* Set Iter = 0.  
Initialize

$$w_k^{(0)} = \frac{1}{K}, \quad (4)$$

$$\sigma_k^{2(0)} = \frac{\sum_{k=1}^K \sum_{t=1}^T (Y^t - f_k^t)^2}{K \cdot T},$$

where Iter is the number of iteration and  $T$  is the number of data in the calibration period.  $Y^t$  and  $f_k^t$  are denoted as the observation and the corresponding prediction by the  $k$ th model for the time  $t$ .

- (2) *Calculate the Initial Likelihood:*

$$l(\theta)^{(0)} = \sum_{t=1}^T \log\left(\sum_{k=1}^K (w_k^{(0)} \cdot g(Q | f_k^t, \sigma_k^{2(0)}))\right). \quad (5)$$

- (3) *Compute the Latent Variable.* Set Iter = Iter + 1, then calculate

$$z_k^{t(\text{Iter})} = \frac{g(Q | f_k^t, \sigma_k^{2(\text{Iter}-1)})}{\sum_{k=1}^K g(Q | f_k^t, \sigma_k^{2(\text{Iter}-1)})}. \quad (6)$$

- (4) *Update the Weight:*

$$w_k^{(\text{Iter})} = \frac{1}{T} \left( \sum_{t=1}^T z_k^{t(\text{Iter})} \right). \quad (7)$$

- (5) *Update the Variance:*

$$\sigma_k^{2(\text{Iter})} = \frac{\sum_{t=1}^T z_k^{t(\text{Iter})} \cdot (Y^t - f_k^t)^2}{\sum_{t=1}^T z_k^{t(\text{Iter})}}. \quad (8)$$

- (6) *Update the Likelihood:*

$$l(\theta)^{(\text{Iter})} = \sum_{t=1}^T \log\left(\sum_{k=1}^K (w_k^{(\text{Iter})} \cdot g(Q | f_k^t, \sigma_k^{2(\text{Iter})}))\right). \quad (9)$$

- (7) *Check for Convergence.* If  $l(\theta)^{(\text{Iter})} - l(\theta)^{(\text{Iter}-1)}$  is less than a prespecified tolerance level, stop the whole estimation procedure; else go back to Step (3).

*2.3. Estimation of Prediction Uncertainty Interval.* After BMA weight  $w_k$  and prediction variance  $\sigma_k^2$  being estimated, we use the composition of Monte Carlo method to generate BMA probabilistic predictions for any time  $t$  [29]. The procedures are described as follows.

- (1) Generate an integer value of  $k$  from  $[1, 2, \dots, K]$  with probability  $[w_1, w_2, \dots, w_K]$ . A specific procedure is described as follows.
  - (1a) Set the cumulative weight  $w'_0 = 0$  and compute  $w'_k = w'_{k-1} + w_k$  for  $k = 1, 2, \dots, K$ .
  - (1b) Generate a random number  $u$  between 0 and 1.
  - (1c) If  $w'_{k-1} \leq u < w'_k$ , it indicates that we choose the  $k$ th member of the ensemble predictions.
- (2) Generate a value of  $Q_t$  from the PDF of  $g(Q_t | f_k^t, \sigma_k^2)$ . Here,  $g(Q_t | f_k^t, \sigma_k^2)$  represents the normal distribution with mean  $f_k^t$  and variance  $\sigma_k^2$ .
- (3) Repeat the above steps (1) and (2) for  $M$  times.  $M$  is the probabilistic ensemble size. In this paper, we set  $M = 100$ .

After generating the BMA probabilistic ensemble predictions, sort them in the ascending order. Then the 90% uncertainty intervals can be derived within the range of the 5% and 95% quantiles.

For each individual model in the BMA scheme, the prediction uncertainty interval can also be constructed, with the Monte Carlo sampling method still being used to approximate the assumed PDF of  $g(Q_t | f_k^t, \sigma_k^2)$ .

### 3. Materials

*3.1. Study Area and Data.* The study area is Mumahe catchment, a branch of Han River. It is located in Shanxi Province of China and the total area is 1224 km<sup>2</sup>. The basin has a subtropical climate, and the area is humid with fairly high precipitation. The mean annual rainfall for the period of 1980–1987 is 1070 mm, and the mean annual runoff is 687 mm, or roughly 64% of the annual rainfall. The hydrological data include daily runoff, rainfall, and evaporation. There are 2992 data points in total, and 1825 (the period of 1980.1.1–1985.12.31) of them are used for calibration, while the rest 1167 data points (the period of 1986.1.1–1987.12.31) are used for validation.

*3.2. Hydrological Models and Optimization Algorithm.* In this study, three conceptual hydrological models are employed for testing the capability of BMA: the Xinanjiang Rainfall-Runoff Model (XAJ), the Soil Moisture Accounting and Routing Model (SMAR), and SIMHYD Rainfall-Runoff Model.

Xinanjiang Rainfall-Runoff Model was developed in 1970s. It is a conceptual hydrologic model, which has been widely used in humid and semihumid regions of China. And all the 15 parameters of this model have strong physical meanings. SMAR model is a lumped conceptual model with soil moisture as a central theme. The model consists of two

components in sequence: a water balance component with 5 water balance parameters and a routing component with 4 routing parameters. SIMHYD model is a daily conceptual model that estimates daily stream flow from daily rainfall and areal potential evapotranspiration data and it contains 7 parameters [30]. For calibrating these hydrological models, Shuffled Complex Evolution (SCE-UA) method is employed here for parameter optimization [31].

**3.3. Objective Functions.** The selection of objective function (OF) is of great importance since it will have great influence on the values of calibrated parameters and thus on simulation results of the rainfall-runoff model. Different objective functions can be adopted for different kinds of practical issues. For example, the objective function of squared model errors of squared transformed flow can be applied in high flow studies, and the objective function of squared model errors of logarithmic transformed flow can be applied in low flow studies [32]. In this study, four objective functions have been used for the parameter calibration.

(1) *OF1: The Nash-Sutcliffe Coefficient of Efficiency ( $R^2$ ):*

$$R^2 = 1.0 - \frac{\sum_{t=1}^T (Q_{\text{obs}}^t - Q_{\text{sim}}^t)^2}{\sum_{t=1}^T (Q_{\text{obs}}^t - \bar{Q}_{\text{obs}})^2}, \quad (10)$$

where  $Q_{\text{obs}}^t$  and  $Q_{\text{sim}}^t$  are observed and simulated data at time  $t$  and  $\bar{Q}_{\text{obs}}$  is the average of observed data in the calibration period.

(2) *OF2: Mean Squared Error of Squared Transformed (MSEST):*

$$\text{MSEST} = \frac{\sum_{t=1}^T (Q_{\text{obs}}^t{}^2 - Q_{\text{sim}}^t{}^2)^2}{T}. \quad (11)$$

Transforming the observed data in squared form puts great emphasis on fitting peak values.

(3) *OF3: Mean Squared Error of Squared Root Transformed (MSESRT):*

$$\text{MSESRT} = \frac{\sum_{t=1}^T (\sqrt{Q_{\text{obs}}^t} - \sqrt{Q_{\text{sim}}^t})^2}{T}. \quad (12)$$

MSESRT can be employed in the medium flow simulation.

(4) *OF4: Mean Squared Error of Logarithmic Transformed (MSELT):*

$$\text{MSELT} = \frac{\sum_{t=1}^T (\ln Q_{\text{obs}}^t - \ln Q_{\text{sim}}^t)^2}{T}. \quad (13)$$

This transformation helps model parameterization to better fit the low flow values.

**3.4. Construction of BMA(3) and BMA(9) Schemes.** When the prediction data are highly non-Gaussian, we should firstly transform the data to be normally distributed by Box-Cox transformation before using EM algorithm. OF1 is the most widely used objective function for parameter optimization

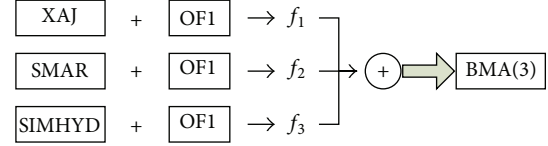


FIGURE 2: Diagram of BMA(3) combination scheme.

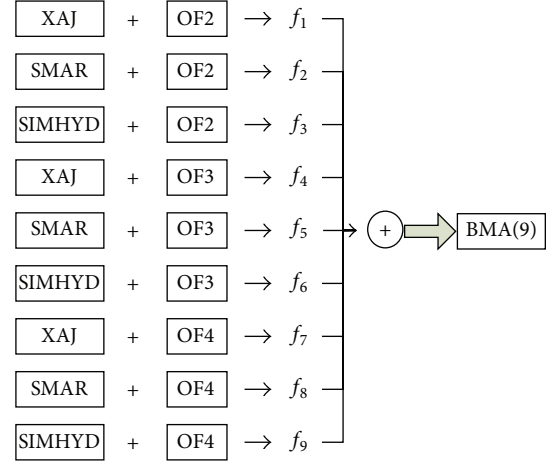


FIGURE 3: Diagram of BMA(9) combination scheme.

and is used in calibrating each of three hydrological models mentioned above to generate three different predictions. We combine these three different predictions by BMA to construct a three-member predictions ensemble; thus, we denote the first BMA scheme as BMA(3). Figure 2 shows the procedure of BMA(3) combination scheme. The other three objective functions, that is, OF2, OF3, and OF4 are, respectively, fit for high, medium, and low flow simulation. All three hydrological models are, respectively, calibrated for each of these three objective functions to obtain the optimized parameter sets. As the same model with different parameter sets will give rise to different outcomes, nine different predictions are generated. We can use BMA method to combine these nine different predictions to construct a nine-member predictions ensemble, which is just the second BMA scheme denoted as BMA(9). The procedure of BMA(9) combination scheme is described in Figure 3.

Let  $E$  denote the uncertainty of the forecast, and it can be written as  $E = [E_h, E_m, E_l]$ , including three components, that is, the high flow simulation uncertainty  $E_h$ , the medium flow simulation uncertainty  $E_m$ , and the low flow simulation uncertainty  $E_l$ . In BMA(9), the forecasts which are generated under OF2 have relatively small  $E_h$ , so they can get higher weights than other forecasts in high flow simulation. Similarly, the forecasts generated under OF3 have relatively high weights in medium flow simulation, while the ones generated under OF4 have higher weights than others in low flow simulation. By averaging the forecasts from a set of different combinations of hydrological model and objective function, the advantage of BMA(9) is its ability to reduce the simulation

errors by giving weights to each of the nine-member forecasts according to their performance in different flow ranges.

**3.5. Performance Criteria for Evaluating the Mean Prediction.** There are three indices for evaluating the mean prediction.

(1) *The Nash-Sutcliffe Coefficient of Efficiency ( $R^2$ )*. The definition of  $R^2$  has expressed in (10).  $R^2$  is not only an objective function but also a widely used performance criterion. It ranges from minus infinity to 1.0, with higher values indicating better agreement. It is difficult to evaluate the performance of the model with  $R^2$  in all flow ranges, since the value of  $R^2$  is always negative in the medium flow range.

(2) *Daily Root Mean Square Error (DRMS)*:

$$DRMS = \sqrt{\frac{\sum_{t=1}^T (Q_{obs}^t - Q_{sim}^t)^2}{T}}, \quad (14)$$

where  $Q_{obs}^t$  and  $Q_{sim}^t$  are observed and simulated data at time  $t$ .  $DRMS$  is sensitive to the differences between the observations and simulations. The lower the  $DRMS$  value is, the better the prediction performance is.

(3) *Relative Error of Total Runoff (RE)*:

$$RE = 1.0 - \frac{\sum_{t=1}^T Q_{sim}^t}{\sum_{t=1}^T Q_{obs}^t}. \quad (15)$$

It reflects the performance in the simulation of the total runoff amount. Lower values of  $RE$  indicate better agreement of total surface runoff.

**3.6. Performance Criteria for Assessing the Prediction Uncertainty Interval.** Xiong et al. [33] have presented a set of indices for assessing the prediction uncertainty intervals generated by the uncertainty analysis methods. Three main indices are selected here to assess the prediction uncertainty intervals produced by BMA schemes as well as from each individual hydrological model.

(1) *Containing Ratio (CR)*. The containing ratio is used for assessing the goodness of the uncertainty interval. It is defined as the percentage of observed data points that are covered in the prediction bounds.

(2) *Average Band-Width (B)*. Consider

$$B = \frac{1}{T} \sum_{t=1}^T (q_u^t - q_l^t), \quad (16)$$

where  $q_u^t$  and  $q_l^t$  are denoted as upper and lower prediction bounds at time  $t$ . The average band-width  $B$  is also an index for measuring the performance of estimated uncertainty interval.

(3) *Average Deviation Amplitude (D)*. The average deviation amplitude  $D$  is an index to quantify the average deflection of

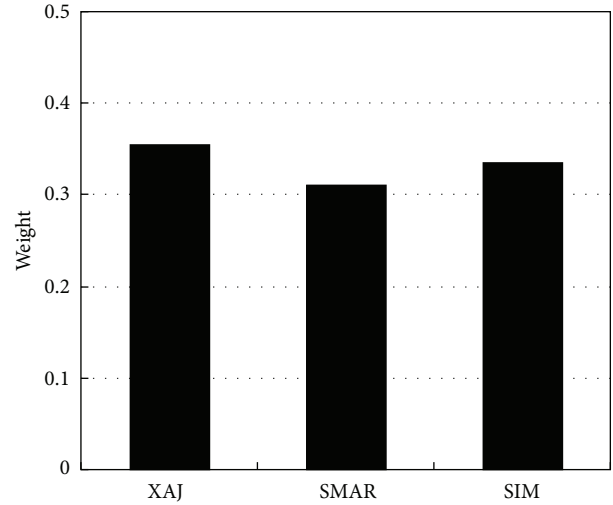


FIGURE 4: Histogram of weights of individual model predictions in BMA(3) scheme.

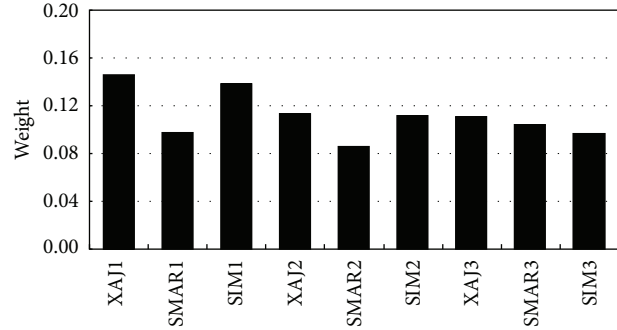


FIGURE 5: Histogram of weights of the individual model predictions in BMA(9) scheme.

the curve of the middle points of the prediction bounds from the observed streamflow hydrograph. It is defined as

$$D = \frac{1}{T} \sum_{t=1}^T \left| \frac{1}{2} (q_u^t + q_l^t) - Q_{obs}^t \right|, \quad (17)$$

where  $Q_{obs}^t$  is the observed discharge at time  $t$ .

## 4. Results and Discussion

The weights of individual models in BMA(3) scheme are displayed in Figure 4, while the weights in BMA(9) are showed in Figure 5. Moreover, in order to compare the performance of two BMA schemes in different flow ranges, according to the characteristics of the streamflow values of Mumahu catchment, data are broken into three flow ranges: high flow (top 10%), medium flow (middle 50%), and low flow (bottom 40%).

**4.1. BMA(3) Results.** We check the mean prediction of BMA(3) using three criteria illustrated in Section 4.1. Results of BMA(3) and its 3 individual models in the mean prediction

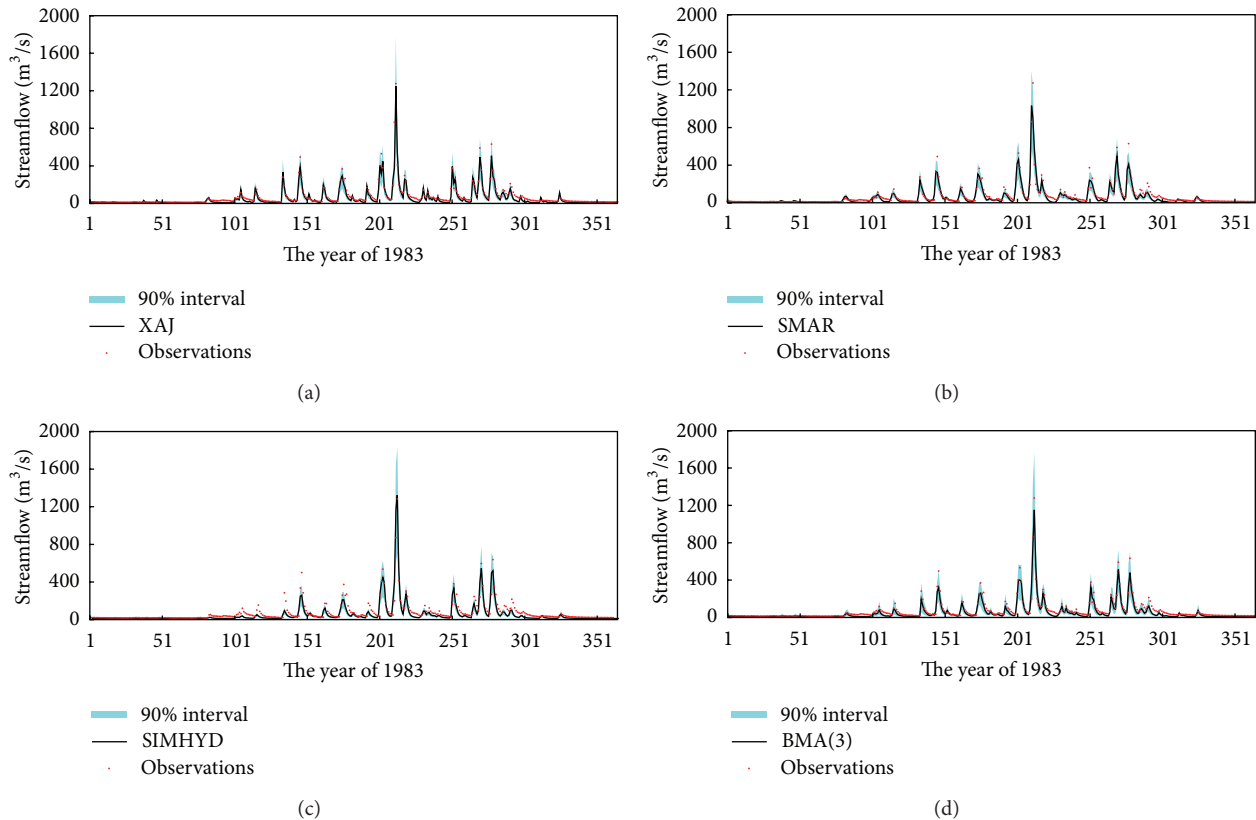


FIGURE 6: The mean prediction and 90% uncertainty interval of both BMA(3) and 3 individual models for the Mumaha catchment in 1983 during the calibration period.

for the whole flow series are presented in Table 1. In terms of  $R^2$ , the mean prediction of BMA(3) can achieve 90.68% in calibration period and 86.98% in validation period, which is better than its best individual model prediction (XAJ). However, in terms of RE, the mean prediction of BMA(3) performs much worse than its best individual model prediction.

Three indices illustrated in Section 4.2 are used for assessing the prediction uncertainty intervals of both BMA(3) and its three individual models. The results for the whole flow series are also showed in Table 1. It is clear that BMA(3) uncertainty interval has the largest values of CR and  $B$ , and almost the smallest  $D$ , in both calibration and validation periods. In other words, BMA(3) uncertainty interval has better properties than any individual model's uncertainty interval in terms of CR and  $D$ , but worse in terms of  $B$ . Then we compare the differences between BMA(3) and its individual model in uncertainty interval by the graph. Figure 6 displays the mean prediction and 90% uncertainty interval of both BMA(3) and its 3 individual models for Mumaha catchment in the year of 1983 during the calibration period. The observations of 1983 are shown as dots, and the BMA(3) mean prediction and its individual models' predictions are represented by solid curve. As the statistical results showed in Table 1, the uncertainty intervals of the individual models have low containing ratio and large deviation amplitude. But the uncertainty interval of BMA(3) is much broader than that of any of its individuals. It can be found from Figure 7 that the results of validation

period are similar to that of the calibration period. In general, the uncertainty interval of BMA(3) has better performance than its individual models for the whole flow series.

**4.2. BMA(9) Results.** Table 2 lists the results of BMA(9) and its 9 individual models in the mean prediction for the whole flow series. And from it we can easily find that in calibration period, the mean prediction of BMA(9) performs better than its best individual prediction according to the value of  $R^2$  and DRMS, though the mean prediction of BMA(9) does not have any advantage in comparison to its individual model predictions in terms of RE.

The results of the uncertainty intervals of BMA(9) and its 9 individual models are also listed in Table 2. The containing ratio of BMA(9) uncertainty interval reaches 91.11% in calibration period and 90.23% in validation period, which are much higher than those of the uncertainty intervals of any individual model. The average deviation amplitude of the BMA(9) uncertainty interval is smaller than that of the uncertainty intervals of most of its nine individual models. From Figures 8 and 9, the similar conclusion can be concluded both in calibration and validation periods.

**4.3. Comparison of BMA(3) and BMA(9).** The results of both BMA(3) and BMA(9) in terms of the mean prediction and 90% uncertainty interval for the whole flow series are listed

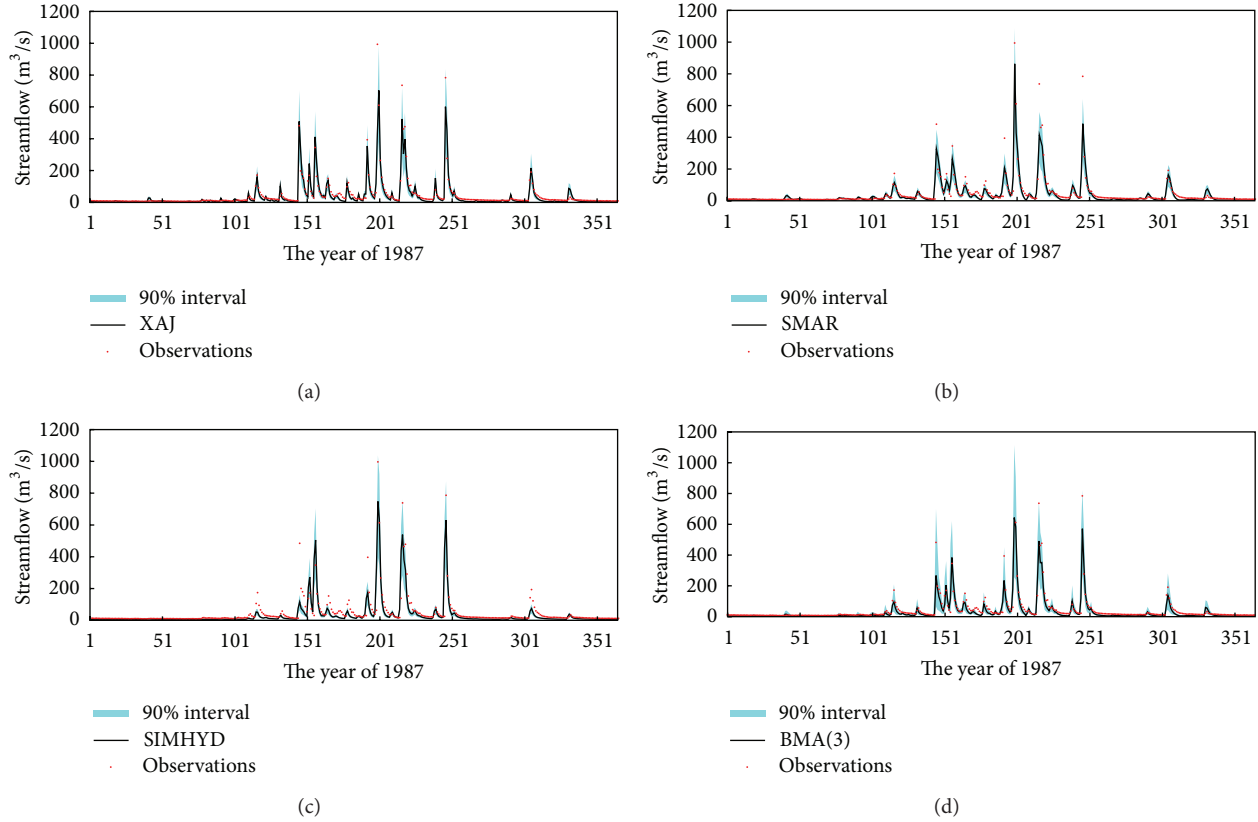


FIGURE 7: The mean prediction and 90% confidence interval of both BMA(3) and 3 individual models for the Mumaha catchment in 1987 during the validation period.

TABLE 1: Results of BMA(3) and its 3 individual models in the mean prediction as well as 90% uncertainty interval for the whole flow series.

Models	$R^2$ (%)	Mean prediction		90% uncertainty interval		
		DRMS	RE (%)	CR (%)	$B$ ( $m^3/s$ )	$D$ ( $m^3/s$ )
Calibration period:						
XAJ	88.69	30.77	21.04	24.83	31.41	16.69
SMAR	87.69	32.11	<b>16.21</b>	32.83	32.80	17.21
SIM	80.73	40.17	31.51	14.83	<b>27.38</b>	22.33
BMA(3)	<b>90.68</b>	<b>27.92</b>	27.87	<b>40.72</b>	43.76	<b>16.06</b>
Validation period:						
XAJ	85.77	29.22	17.79	24.28	24.66	14.09
SMAR	85.30	29.70	<b>14.19</b>	31.91	25.52	14.56
SIM	69.81	42.56	39.48	14.33	<b>18.40</b>	20.07
BMA(3)	<b>86.98</b>	<b>27.95</b>	30.72	<b>40.65</b>	36.71	14.13

Note: bolded values represent the best results.

in Table 3 for comparison. BMA(3) mean prediction has slightly better performance than BMA(9) mean prediction in terms of  $R^2$  and DRMS in both calibration and validation periods, while BMA(3) mean prediction is slightly worse than BMA(9) mean prediction in terms of RE. For the uncertainty intervals, some findings are listed as follows: (1) in terms of CR, BMA(9) uncertainty interval is much higher than BMA(3) uncertainty interval in both calibration and validation periods; (2) in terms of  $B$ , BMA(9) uncertainty

interval is obviously larger than BMA(3) uncertainty interval in both calibration and validation periods; (3) in terms of  $D$ , BMA(9) uncertainty interval performs slightly better than BMA(3) uncertainty interval in both calibration and validation periods.

Further, we compare the BMA(3) and BMA(9) mean predictions with respect to three flow ranges in Table 4. According to the values of three indices for mean prediction, BMA(3) mean prediction has better performance than BMA(9) mean

TABLE 2: Results of BMA(9) and its 9 individual models in the mean prediction and 90% uncertainty interval for the whole flow series.

Objective function	Models	Mean prediction			90% uncertainty interval		
		$R^2$ (%)	DRMS	RE (%)	CR (%)	$B$ (m <sup>3</sup> /s)	$D$ (m <sup>3</sup> /s)
Calibration period							
OF2 (MSEST)	XAJ	85.45	34.89	30.24	17.89	29.43	21.46
	SMAR	84.61	35.89	6.96	31.67	36.51	19.30
	SIM	80.73	40.17	31.51	15.39	<b>28.47</b>	22.67
OF3 (MSESRT)	XAJ	89.78	29.25	10.44	68.06	33.37	<b>11.75</b>
	SMAR	80.25	40.66	10.13	44.17	35.37	17.39
	SIM	72.42	48.05	<b>-5.82</b>	47.72	42.57	21.26
OF4 (MSELT)	XAJ	79.99	40.93	12.39	63.94	33.92	14.75
	SMAR	58.01	59.29	-9.22	42.28	43.45	28.32
	SIM	52.71	62.92	-41.07	38.89	55.51	26.93
BMA(9)		<b>90.49</b>	<b>28.22</b>	21.40	<b>91.11</b>	70.98	14.54
Validation period							
OF2 (MSEST)	XAJ	82.70	32.21	31.92	14.79	<b>21.56</b>	18.20
	SMAR	80.05	34.59	<b>0.66</b>	30.23	29.52	16.64
	SIM	69.81	42.56	39.48	20.84	24.43	22.32
OF3 (MSESRT)	XAJ	<b>88.52</b>	<b>26.25</b>	4.54	68.56	26.95	<b>9.62</b>
	SMAR	78.26	36.11	7.48	44.56	27.59	14.53
	SIM	71.09	41.64	8.98	53.86	27.69	16.47
OF4 (MSELT)	XAJ	77.25	36.94	8.74	63.07	26.68	11.85
	SMAR	43.43	58.25	-18.79	35.53	35.76	27.36
	SIM	72.27	40.79	-21.69	34.05	36.22	18.96
BMA(9)		84.54	30.46	25.42	<b>90.23</b>	55.91	13.20

Note: bolded values represent the best results.

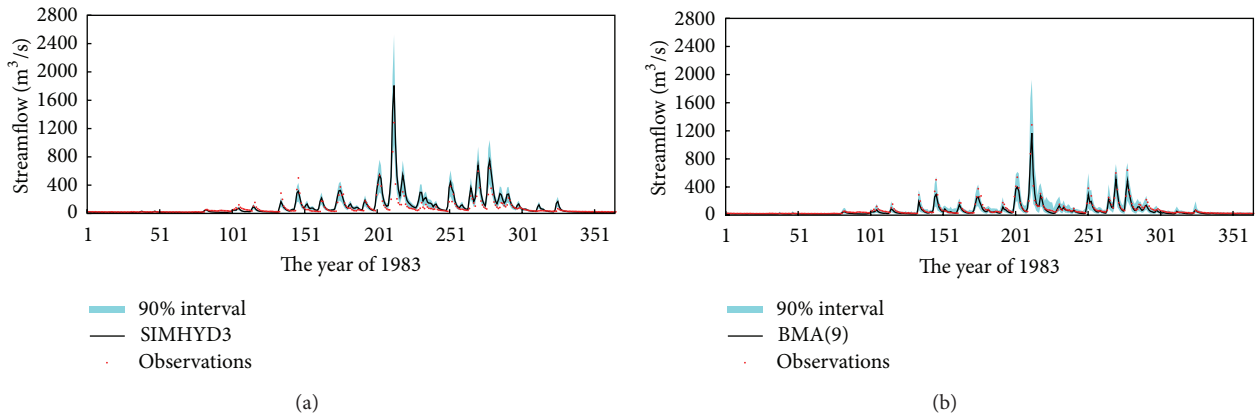


FIGURE 8: The mean prediction and 90% uncertainty interval of both BMA(9) and SIMHYD3 model (the SIMHYD with the objective function OF3) for the Mumahe catchment in 1983 during the calibration period.

prediction in high flow range, but has worse performance in medium and low flow ranges, during both calibration and validation periods. Then we compare the uncertainty intervals of BMA(3) and BMA(9) in three different flow ranges and have some findings as follows: (1) the CR value

of BMA(9) uncertainty interval has absolute predominance in comparison with that of BMA(3) uncertainty interval for each of three flow ranges in both calibration and validation periods; (2) the  $B$  value of BMA(9) uncertainty interval is larger than that of BMA(3) uncertainty interval for all three

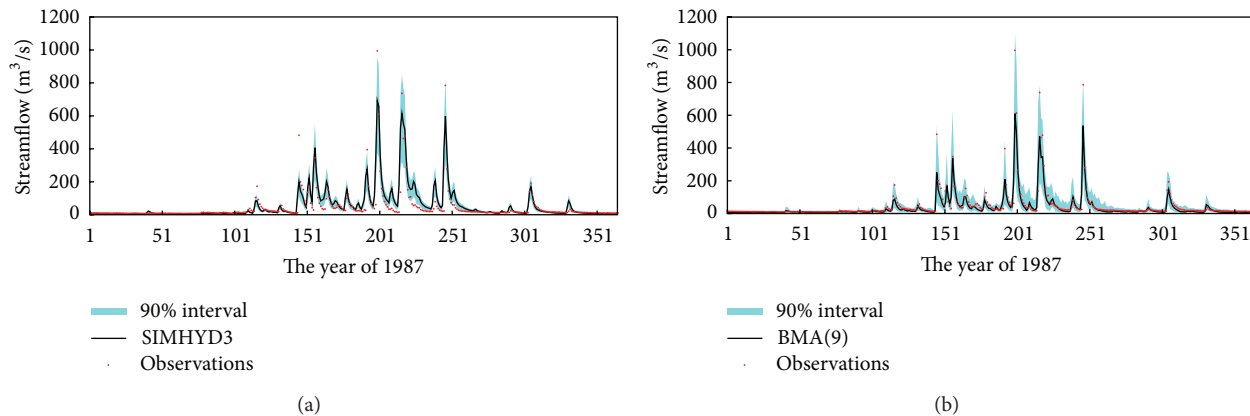


FIGURE 9: The mean prediction and 90% confidence interval of BMA(9) and SIMHYD3 model (the SIMHYD with the objective function OF3) for the Mumuhe catchment in 1987 during the validation period.

TABLE 3: The comparison of BMA(3) and BMA(9) in the mean prediction and 90% uncertainty interval for the whole flow series.

Indices	Calibration		Validation	
	BMA(3)	BMA(9)	BMA(3)	BMA(9)
Mean Prediction				
$R^2$ (%)	90.68	90.49	86.98	84.54
DRMS ( $m^3/s$ )	27.92	28.22	27.95	30.46
RE (%)	27.87	21.40	30.72	25.42
90% uncertainty interval				
CR (%)	40.72	91.11	40.65	90.23
$B$ ( $m^3/s$ )	43.76	70.98	36.71	55.91
$D$ ( $m^3/s$ )	16.06	14.54	14.13	13.20

TABLE 4: The comparison of BMA(3) and BMA(9) in the mean prediction and 90% uncertainty interval for three flow ranges.

Indices	High flow		Medium flow		Low flow	
	BMA(3)	BMA(9)	BMA(3)	BMA(9)	BMA(3)	BMA(9)
Calibration period						
Mean prediction						
$R^2$ (%)	93.01	91.74	32.28	52.76	95.83	96.39
DRMS ( $m^3/s$ )	78.15	84.90	23.24	19.41	7.81	7.27
RE (%)	15.48	17.44	35.66	21.51	69.29	46.73
90% uncertainty interval						
CR (%)	88.74	92.05	45.91	91.32	27.40	90.75
$B$ ( $m^3/s$ )	273.17	342.61	40.34	74.97	6.39	19.23
$D$ ( $m^3/s$ )	59.78	63.66	18.33	15.44	6.21	5.02
Validation period						
Mean prediction						
$R^2$ (%)	89.00	85.47	22.03	41.82	93.66	94.94
DRMS ( $m^3/s$ )	92.51	106.35	19.01	16.42	6.87	6.14
RE (%)	22.49	27.68	31.35	17.66	67.48	45.11
90% uncertainty interval						
CR (%)	85.33	88.00	46.76	90.81	28.60	90.02
$B$ ( $m^3/s$ )	252.88	282.17	34.97	61.22	7.19	18.45
$D$ ( $m^3/s$ )	65.67	66.12	14.90	14.03	5.99	4.82

flow ranges in both calibration and validation periods; (3) the  $D$  value of BMA(9) uncertainty interval is slightly larger than that of BMA(3) in high flow range but smaller in medium and low flow ranges in both calibration and validation periods.

## 5. Conclusions

In this paper, the Bayesian Model Averaging (BMA) method is employed to construct a three-member predictions ensemble, denoted by BMA(3), and a nine-member predictions ensemble, denoted by BMA(9), for ensemble prediction as well as for prediction uncertainty analysis. There are three kinds of comparisons made in terms of both mean prediction and prediction uncertainty interval in this study: BMA(3) with its three individual models, BMA(9) with its nine individual models, and BMA(3) with BMA(9). In particular, we break observational flows into three different ranges for detailed comparison and analysis. The performance of two BMA schemes can be summarized as follows.

- (1) In terms of mean predictions, BMA(3) performs generally better than any of its individual models. And BMA(9) mean prediction has generally higher accuracy than each of its individual model predictions. The comparison between BMA(3) and BMA(9) in mean predictions indicates that BMA(9) does not have any advantage compared to BMA(3) as far as the entire flow series is concerned. The performance of BMA(9) mean prediction is better than that of BMA(3) in both medium and low flow ranges, however, worse in the high flow range.
- (2) In terms of the containing ratio for assessing the uncertainty intervals, the BMA(3) has a larger CR value than any of its individual models. And the containing ratio of BMA(9) uncertainty interval is also markedly larger than that of all its individual models when the CR value is calculated for the whole flow series. When the CR value is compared for different flow ranges, BMA(9) uncertainty interval performs better than its individual models in high, medium, and low flow ranges. In comparison with BMA(3), BMA(9) uncertainty interval also has absolute predominance in terms of CR.
- (3) The average band-width  $B$  of BMA(3) uncertainty interval is larger than that of all its individuals. And the average band-width of BMA(9) uncertainty interval is even larger than that of BMA(3). It is found that, for uncertainty intervals, the increase of containing ratio is accompanied by the increase of band-width, which has already been pointed out by Xiong et al. [33].
- (4) The average deviation amplitude  $D$  of BMA(3) uncertainty interval is generally smaller than the best individual in the ensemble. In terms of  $D$ , BMA(9) uncertainty interval also has a better performance than the best individual among its nine-member ensemble, especially in high flow range. Moreover, in terms of  $D$ , BMA(9) uncertainty interval performs

better than BMA(3) uncertainty interval in medium and low flow ranges, but worse in the high flow range.

Based on this study, it is found that BMA is a particularly useful method for dealing with two issues. Firstly, when there are two or more competing models or methods available for the same problem, BMA can assess the relative performances of all models by assigning weights to each model or method and then produce more accurate mean prediction by weighted averaging of all predictions from those models or methods. Secondly, BMA can be used when there is uncertainty over control variables. The uncertainty intervals for both individual predictions and the BMA prediction can be derived when the distribution of the data is known or assumed.

Two issues from this study of BMA also need to be pointed out. The first is about the data transformation process. It is obvious that the daily flow data do not strictly obey the normal distribution even after the Box-Cox transformation. In fact, it is impossible to make every prediction from every model be normally distributed by using only a uniform transformation coefficient. Another problem is about the quality of the hydrological models chosen for combination. In this paper, the models employed here are all conceptual hydrological models. If better models are chosen as the ensemble members, then it is expected that the better results will come out of the BMA combination.

## Acknowledgments

This research is supported by the National Natural Science Foundation of China (Grant nos. 51190094, 51079098), which is greatly appreciated. The comments and suggestions from the editor and the reviewers are very helpful in the improvement of the paper and are greatly appreciated.

## References

- [1] WMO, "Intercomparison of conceptual models used in hydrological forecasting," Operational Hydrology Report 7, WMO, Geneva, Switzerland, 1975.
- [2] V. P. Singh, *Computer Models of Watershed Hydrology*, Water Resources Publications, 1995.
- [3] D. J. Reid, "Combing three estimates of gross domestic products," *Economica*, vol. 35, pp. 431–444, 1968.
- [4] J. M. Bates and C. W. J. Granger, "The combination of forecasts," *Operational Research Quarterly*, vol. 20, pp. 451–468, 1969.
- [5] J. P. Dickinson, "Some statistical results in the combination of forecasts," *Operational Research Quarterly*, vol. 24, no. 2, pp. 253–260, 1973.
- [6] A. Y. Shamseldin, K. M. O'Connor, and G. C. Liang, "Methods for combining the outputs of different rainfall-runoff models," *Journal of Hydrology*, vol. 197, no. 1–4, pp. 203–229, 1997.
- [7] L. Xiong, A. Y. Shamseldin, and K. M. O'Connor, "A non-linear combination of the forecasts of rainfall-runoff models by the first-order Takagi-Sugeno fuzzy system," *Journal of Hydrology*, vol. 245, no. 1–4, pp. 196–217, 2001.
- [8] D. Madigan and A. E. Raftery, "Model selection and accounting for model uncertainty in graphical models using Occam's

- window,” *Journal of the American Statistical Association*, vol. 89, pp. 1535–1546, 1994.
- [9] A. E. Raftery, “Bayesian model selection in social research,” *Sociological Methodology*, vol. 25, pp. 111–163, 1995.
- [10] D. Draper, “Assessment and propagation of model uncertainty,” *Journal of the Royal Statistical Society B*, vol. 57, no. 1, pp. 45–97, 1995.
- [11] C. Fernández, E. Ley, and M. Steel, “Benchmark priors for Bayesian model averaging,” *Journal of Econometrics*, vol. 100, no. 2, pp. 381–427, 2001.
- [12] K. Y. Yeung, R. E. Bumgarner, and A. E. Raftery, “Bayesian model averaging: development of an improved multi-class, gene selection and classification tool for microarray data,” *Bioinformatics*, vol. 21, no. 10, pp. 2394–2402, 2005.
- [13] B. A. Wintle, M. A. McCarthy, C. T. Volinsky, and R. P. Kavanagh, “The use of bayesian model averaging to better represent uncertainty in ecological models,” *Conservation Biology*, vol. 17, no. 12, pp. 1579–1590, 2003.
- [14] K. H. Morales, J. G. Ibrahim, C.-J. Chen, and L. M. Ryan, “Bayesian model averaging with applications to benchmark dose estimation for arsenic in drinking water,” *Journal of the American Statistical Association*, vol. 101, no. 473, pp. 9–17, 2006.
- [15] G. Koop and L. Tole, “Measuring the health effects of air pollution: to what extent can we really say that people are dying from bad air?” *Journal of Environmental Economics and Management*, vol. 47, no. 1, pp. 30–54, 2004.
- [16] A. E. Raftery, F. Balabdaoui, T. Gneiting, and M. Polakowski, “Using bayesian model averaging to calibrate forecast ensembles,” Technical Report 440, Department of Statistics, University of Washington, 2003.
- [17] V. Viallefont, A. E. Raftery, and S. Richardson, “Variable selection and Bayesian model averaging in case-control studies,” *Statistics in Medicine*, vol. 20, no. 21, pp. 3215–3230, 2001.
- [18] J. A. Hoeting, D. Madigan, A. E. Raftery, and C. T. Volinsky, “Bayesian model averaging: a tutorial,” *Statistical Science*, vol. 14, no. 4, pp. 382–417, 1999.
- [19] M. A. Clyde, “Bayesian model averaging and model search strategies,” in *Bayesian Statistics*, J. M. Bernardo, A. P. Dawid, J. O. Berger, and A. F. M. Smith, Eds., vol. 6, pp. 157–185, Oxford University Press, 1999.
- [20] A. E. Raftery and Y. Zheng, “Discussion: performance of bayesian model averaging,” *Journal of the American Statistical Association*, vol. 98, no. 464, pp. 931–938, 2003.
- [21] S. P. Neuman, “Maximum likelihood Bayesian averaging of uncertain model predictions,” *Stochastic Environmental Research and Risk Assessment*, vol. 17, no. 5, pp. 291–305, 2003.
- [22] N. K. Ajami, Q. Duan, and S. Sorooshian, “An integrated hydrologic Bayesian multimodel combination framework: confronting input, parameter, and model structural uncertainty in hydrologic prediction,” *Water Resources Research*, vol. 43, no. 1, Article ID W01403, 2007.
- [23] Q. Duan, N. K. Ajami, X. Gao, and S. Sorooshian, “Multi-model ensemble hydrologic prediction using Bayesian model averaging,” *Advances in Water Resources*, vol. 30, no. 5, pp. 1371–1386, 2007.
- [24] X. Zhang, R. Srinivasan, and D. Bosch, “Calibration and uncertainty analysis of the SWAT model using genetic algorithms and Bayesian model averaging,” *Journal of Hydrology*, vol. 374, no. 3–4, pp. 307–317, 2009.
- [25] K. Beven and A. Binley, “The future of distributed models: model calibration and uncertainty prediction,” *Hydrological Processes*, vol. 6, no. 3, pp. 279–298, 1992.
- [26] H. V. Gupta, K. J. Beven, and T. Wagener, “Calibration and uncertainty estimation,” in *Encyclopedia of Hydrological Sciences*, John Wiley and Sons, Chichester, UK, 2003.
- [27] L. Marshall, D. Nott, and A. Sharma, “A comparative study of Markov chain Monte Carlo methods for conceptual rainfall-runoff modeling,” *Water Resources Research*, vol. 40, no. 2, Article ID W02501, 2004.
- [28] J. A. Vrugt, H. V. Gupta, W. Bouten, and S. Sorooshian, “A Shuffled complex evolution metropolis algorithm for optimization and uncertainty assessment of hydrologic model parameters,” *Water Resources Research*, vol. 39, no. 8, 2003.
- [29] J. M. Hammersley and D. C. Handscomb, *Monte Carlo Methods*, Methuen, London, UK, 1975.
- [30] F. H. S. Chiew, M. C. Peel, and A. W. Western, “Application and testing of the simple rainfall runoff model SIMHYD,” in *Mathematical Models of Small Watershed Hydrology and Applications*, V. P. Singh and D. Frevert, Eds., pp. 335–366, Water Resources Publications, 2002.
- [31] Q. Duan, S. Sorooshian, and V. Gupta, “Effective and efficient global optimization for conceptual rainfall-runoff models,” *Water Resources Research*, vol. 28, no. 4, pp. 1015–1031, 1992.
- [32] L. Oudin, V. Andréassian, T. Mathevet, C. Perrin, and C. Michel, “Dynamic averaging of rainfall-runoff model simulations from complementary model parameterizations,” *Water Resources Research*, vol. 42, no. 7, Article ID W07410, 2006.
- [33] L. Xiong, M. Wan, X. Wei, and K. M. O’Connor, “Indices for assessing the prediction bounds of hydrological models and application by generalised likelihood uncertainty estimation,” *Hydrological Sciences Journal*, vol. 54, no. 5, pp. 852–871, 2009.